Journal of
Seismic Exploration

ISSN: 0963-0651



Processing four-dimensional vertical seismic profiling in the CO2CRC Otway Stage 4 Project

Volume 35 · Issue 3
June 2026

ACCSCIENCE PUBLISHING

State Key Laboratory for Fine Exploration and Intelligent Development of Coal Resources

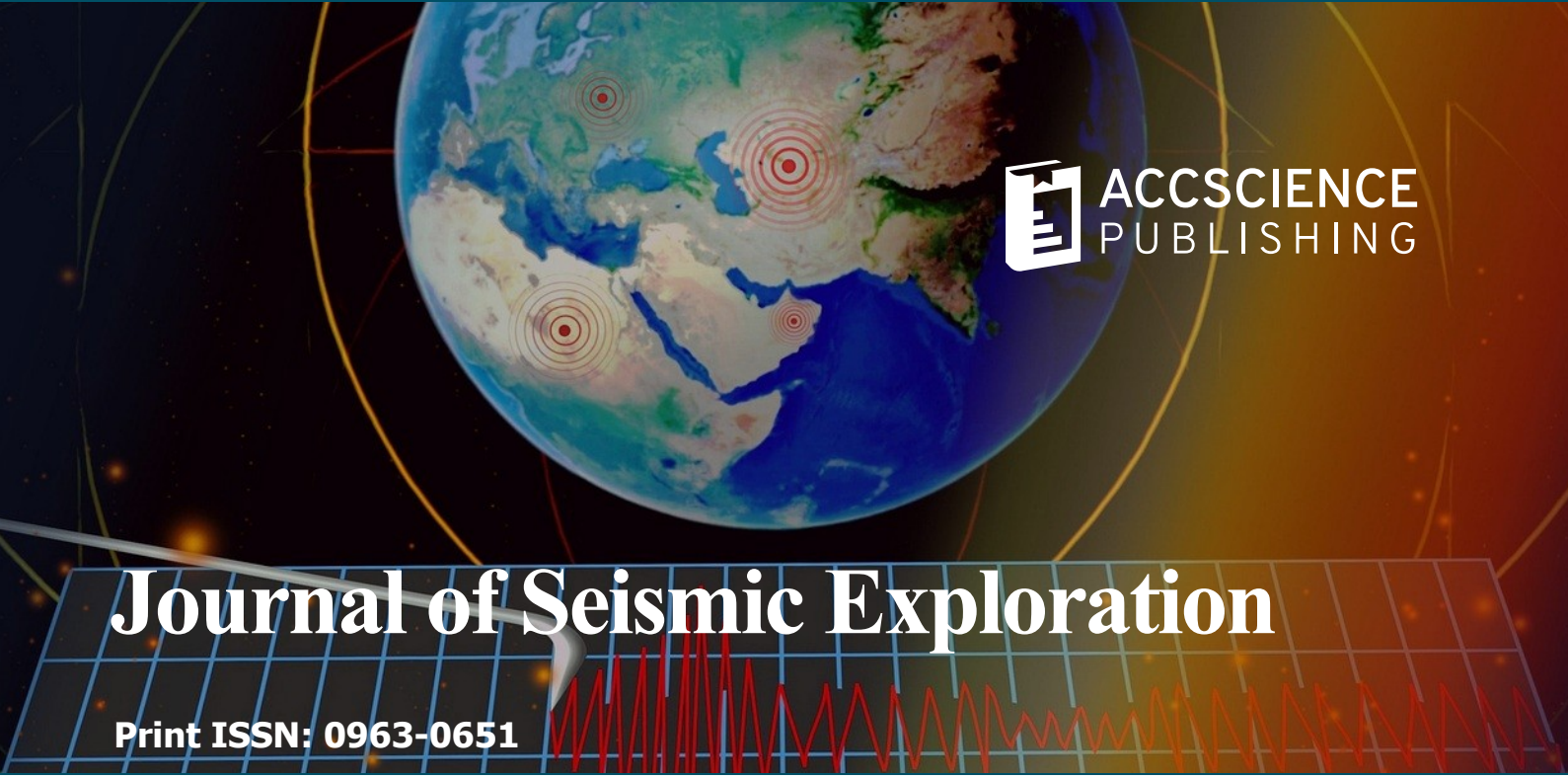

Journal of Seismic Exploration

Print ISSN: 0963-0651

The Journal of Seismic Exploration (JSE) aims to accelerate the development of smarter, more efficient, and more sustainable seismic solutions for energy, mineral, engineering, fluid, environmental, and planetary exploration.

The journal covers the full spectrum of seismic exploration, embracing both active- and passive-source methodologies across onshore, marine, borehole, and near-surface environments. Application domains include petroleum geology, reservoir characterization, unconventional resource assessment, geothermal exploration, coal and mineral prospecting, fluid investigations, engineering and environmental studies, as well as carbon storage monitoring and hazard assessment.

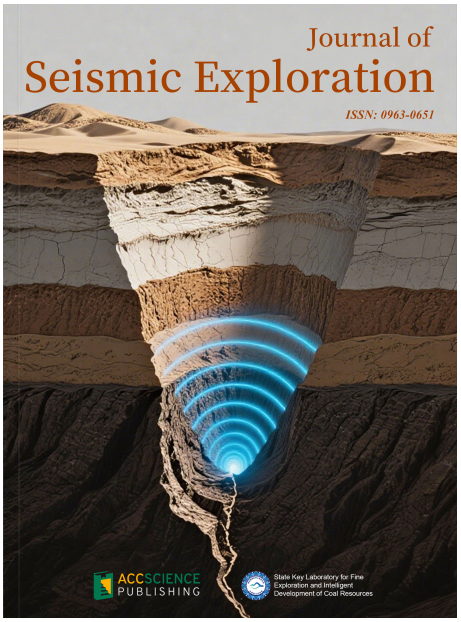

About the Publisher

AccScience Publishing is a publishing company based in Singapore. We publish a range of high-quality, open-access, peer-reviewed journals and books from a broad spectrum of disciplines.

Contact Us

Managing Editor
jse.office@accscience.sg

AccScience Publishing
2 Venture Drive, #07-06 Vision Exchange, Singapore 608526

Volume 35 • Issue 3 • 2026
ISSN 0963-0651 (print)

Journal of Seismic Exploration

Editors-in-Chief

Suping Peng
State Key Laboratory for Fine Exploration and Intelligent Development of Coal Resources

Arthur B. Weglein
University of Houston

ACCSCIENCE PUBLISHING

Access Science Without Barriers

Full issue copyright © 2026 AccScience Publishing
All rights reserved. Without permission in writing from the publisher, this full issue publication in its entirety may not be reproduced or transmitted for commercial purposes in any form or by any means, electronic or mechanical, including photocopying, recording, or any information storage and retrieval system. Permissions may be sought from jse.office@accscience.sg

Article copyright © Respective Author(s)
See articles for copyright year. All articles in this full issue publication are open-access. There are no restrictions in the distribution and reproduction of individual articles, provided the original work is properly cited. However, permission to reuse copyrighted materials of an article for commercial purposes is applicable if the article is licensed under Creative Commons Attribution-NonCommercial License. Check the specific license before reusing.

JOURNAL OF SEISMIC EXPLORATION

ISSN: 0963-0651 (print)

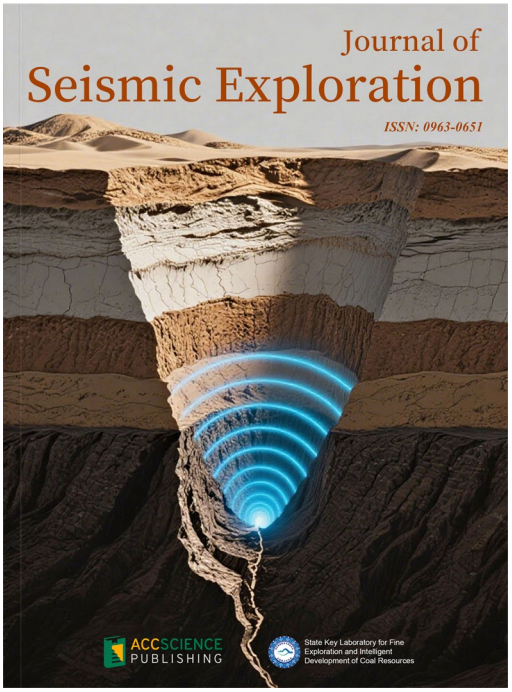

Editorial and Production Credits

Publisher: AccScience Publishing
Managing Editor: Gary Liu
Production Editor: Lim Mingyuan
Article Layout and Typeset: AccScience Publishing

For all advertising queries, contact jse.office@accscience.sg

Supplementary file

Supplementary files of articles can be obtained at https://accscience.com/journal/JSE/35/3.

Disclaimer

AccScience Publishing is not liable to the statements, perspectives, and opinions contained in the publications. The appearance of advertisements in the journal shall not be construed as a warranty, endorsement, or approval of the products or services advertised and/or the safety thereof. AccScience Publishing disclaims responsibility for any injury to persons or property resulting from any ideas or products referred to in the publications or advertisements. AccScience Publishing remains neutral with regard to jurisdictional claims in published maps and institutional affiliations.

Journal of Seismic Exploration

Editorial Board

Editors-in-Chief

Suping Peng
Arthur B. Weglein

Executive Editor-in-Chief

Jing Ba

Editorial Board Members

Mauricio Sacchi
Ilya Tsvankin
Li-Yun Fu
Boris Gurevich
José M. Carcione
Haijiang Zhang
Jun Matsushima
Fabio Trippetta
Qizhen Du
Lasse Amundsen
Jingyi Chen
Yangkang Chen
Lin Chen
Vladimir Cheverda
Eduardo Filpo
Doug Foster
Bill N. Goodway
Songfeng Guo
Zhiqi Guo
Cory Hoelting
Morten Jakobsen
Gilles Lambaré
Evgeny Landa
Jing Li
Huailiang Li
Chih-Ping Lin
José Eduardo M. Lira
Yang Liu
Jianwei Ma
George McMechan
Mark A. Meier
Roman Pevzner
Flavio Poletto
J. Germán Rubino
Mrinal K. Sen
Serge A. Shapiro
Changsoo Shin
Juan I. Soto
Paul L. Stoffa
Walter Söllner
Dinghui Yang
Umberta Tinivella
Peter Traynin
Arie Verdel
Dirk Jacob Eric Verschuur
Xiujuan Wang
Yibo Wang
Jincai Zhang
Lele Zhang
Gulan Zhang
Wei Zhang
Huai Zhang
Fons ten Kroode

Early Career Editorial Board

Cong Luo
Xintong Dong
Fei Gong
Qiang Guo
Guangtan Huang
Zhongxiao Li
Xingye Liu
Shaoyong Liu
Xinpeng Pan
Yingming Qu
Xiaokai Wang
Haibo Wu
Pan Zhang
Sheng Zhang
Jidong Yang
Peng Lin
Wei Chen
Yong Hu
Yaju Hao
Jiachun You

ACCSCIENCE PUBLISHING

June 2026 | Volume 35 | Issue 3 |

Journal of Seismic Exploration

https://accscience.com/journal/JSE

CONTENTS

REVIEW

1 **Wave-equation migration: Advances, artificial intelligence enhancement, comparisons, and outlook**
Yanlong Zhu, Anyu Li

ARTICLES

19 **DB-MS-CAN: A robust deep learning framework for microseismic velocity inversion via Dual-Branch Attention and Multi-Scale Feature Aggregation**
Aoyu Feng, Binxin Hu, Feng Zhu, Yang Gao, Feifei Jiang, Danya Ma, Rong Liu

40 **Thin-layer weak signal enhancement based on cyclic spectrum enhancement technology**
Hua Zhang, Yu Song, Wei Chen

57 **Geophysical prediction and evaluation of lacustrine shale oil and gas: Applications in the Fuxing area**
Kai Xu, Guangzhi Zhang, Yong Chen, Zhentao Sun, Wei Xie, Xinpeng Pan, Yu Zhong, Xiaohui Yang, Ling Su

73 **A Seislet U-Net for seismic data reconstruction**
Haixia Hu, Yankun Zhang, Youhua Wei, Xiaodong Luo, Yuefei Zhu, Yannan Wang

91 **Joint inversion of ambient noise and gravity to investigate crustal structure and dynamic processes in the southern Sichuan Basin**
Li Zhang, Guiju Wu, Rugang Xu, Yufei Xi, Jiapei Wang, Fan Wang

111 **Thin-bed reservoir characterisation using high-resolution ocean-bottom-node seismic data, seismic waveform indication inversion, and a Gaussian mixture model: A case study from the Guantao Formation, Bohai Bay Basin, China**
Yanjia Wu, Zhiwen Dong, Yiyao Zhang, Zekun Li, Shihao Liu, Xiaoxiao Shi, Hongke Zhou, Qunhu Wu, Shina Yu, Ahmed Bakry, Qamar Yasin

129 **Research on microseismic data noise suppression method based on adaptive spectral segmentation**
Mingyang Chang, Wenwu Zhou, Xiankai Wang, Huairui Su, Ziyi Na, Fuwu Ma, Yang Li

152 **Properties of fluids under multiphysical coupling and frequency-dependent rock physics modeling**
Lujia Ma, Guangtan Huang, Zhennan Yu, Haiyu Li, Mingliao Wu

172 **Three-dimensional high-order total variation regularized acoustic impedance inversion for thin coal seam thickness prediction in the Yushe East Area, China**
Yinping Dong, Youyi Shen, Zhongbin Tian, Wei Wei, Xiaodong Yang, Yaju Hao, Peng Zhang

187 **Coupled acoustic-elastic finite element modeling of underwater sound propagation**
Youngjae Shin, Won-Ki Kim, Eunpyo Lim, Youngseok Lee, Jaehwan Oh, Dawoon Lee, Ho Seuk Bae

209 **Fault prediction method for coalfields based on an SVD–ResCBAM–U-Net framework**
Guangui Zou, Jingwen Xue, Zeming Wang, Xiaopeng Jin, Chengyang Han

225 **Influence of filling characteristics on rock physical properties of deep carbonate reservoirs based on digital rock modeling**
Siqi Ji, Wei Cheng, Hui Shen, Wei-Hua Liu, Dechao Han

243 **An integrated approach of wavefield reconstruction and jointly constrained velocity modeling for seismic imaging in the complex foothill belt**
Lan-hua Wang, Wei-wei Duan, Hai-feng Wang, Xiao-nan Wang

225 **Processing four-dimensional vertical seismic profiling in the CO2CRC Otway Stage 4 Project**
Alina Almukhametova, Konstantin Tertyshnikov, Nikita Beloborodov, Olivia Collet, Boris Gurevich, Roman Isaenkov, Mustafa Al Marzooq, Pavel Shashkin, Mikhail Vorobev, Roman Pevzner

270 **Multi-constraint two-step intelligent prestack seismic inversion and its application: A case study in the Junggar Basin, Northwest China**
Hongyan Qi, Zhenlin Wang, Wei Li, Tingming Tang, Juqin Yao, Gang Chen, Qingyong Luo

286 **Full-wavefield modeling using a decoupled viscoacoustic wave equation with vector-reflectivity**
Fei Li, Zilong Ye, Jintao Liu, Jianping Huang, Mengmeng Wu, Mei Li, Yanjiao Dong

304 **Hierarchical division encoder–decoder network for distributed acoustic sensing-vertical seismic profile noise suppression**
Li Han, Dongyan Wang, Hang Yu

321 **CT-UNet: Curvelet transform-based component-wise deep learning framework for seismic trace interpolation**
Jiyun Yu, Young Kim, Daeung Yoon

346 **Deep learning for three-dimensional seismic fault prediction using convolutional neural networks**
Yasir Bashir, Dilek Yüksel, Begüm Akin, Derin Gezer, Muhsan Ehsan, Muhammad Khan, Syed Haroon Ali

ACCSCIENCE PUBLISHING

Journal of Seismic Exploration

REVIEW ARTICLE

Wave-equation migration: Advances, artificial intelligence enhancement, comparisons, and outlook

Yanlong Zhu[1,2,3,4] and Anyu Li[5]*

[1]Key Laboratory of Mineral Exploration (Gansu province), Lanzhou, Gansu, China

[2]Gold Mine Resource Exploration and Utilization Technology Innovation Center of Gansu Province, Lanzhou, Gansu, China

[3]The Third Institute of Geology and Minerals Exploration, Gansu Provincial Bureau of Geology and Minerals Exploration and Development, Lanzhou, Gansu, China

[4]Department of Geophysics, School of Geophysics and Information Technology, China University of Geosciences (Beijing), Beijing, China

[5]Department of Geophysics, School of Petroleum and Natural Gas Engineering, Chongqing University of Science and Technology, Chongqing, China

Abstract

Wave-equation–based seismic migration is a core technology for high-resolution subsurface imaging in applications such as hydrocarbon exploration and geothermal resource assessment. It provides a more complete physical description of seismic wave propagation than ray-based migration methods, and is therefore essential for imaging complex geological structures characterized by strong velocity contrasts and steeply dipping reflectors. This paper presents a systematic review and comparative analysis of wave-equation prestack depth-migration methods, including reference-velocity–based one-way wave-equation depth migration (OWDM), accurate-velocity–based OWDM, reverse-time migration, and full-wave-equation depth migration. The theoretical foundations, wavefield extrapolation characteristics, imaging mechanisms, and numerical implementations of these methods are examined within a unified framework. Particular emphasis is placed on clarifying the intrinsic limitations of one-way wave-equation migration in handling turning waves and large propagation angles, and on contrasting the strengths and weaknesses of time-domain versus depth-domain full-wave-equation migration. Based on representative numerical experiments and field data examples, the imaging performance, computational efficiency, and practical applicability of the four migration schemes are comprehensively compared. In addition, recent advances in artificial intelligence-assisted seismic imaging are reviewed, focusing on wavefield propagator design and migration artifact suppression. This review provides practical guidance for selecting appropriate migration strategies in complex geological settings and offers insights into future developments of wave-equation–based seismic imaging.

Keywords: Wave-equation migration; Seismic imaging; Research progress; Imaging comparison

***Corresponding author:**
Anyu Li
(li_anyu@cqust.edu.cn)

Citation: Zhu Y, Li A. Wave-equation migration: Advances, artificial intelligence enhancement, comparisons, and outlook. *J Seismic Explor*. 2026;35(3):025010137. doi: 10.36922/JSE025010137

Received: December 29, 2025

Revised: March 11, 2026

Accepted: March 12, 2026

Published online: May 8, 2026

Copyright: © 2026 Author(s). This is an Open-Access article distributed under the terms of the Creative Commons Attribution License, permitting distribution, and reproduction in any medium, provided the original work is properly cited.

Publisher's Note: AccScience Publishing remains neutral with regard to jurisdictional claims in published maps and institutional affiliations.

1. Introduction

Seismic imaging technology is of great significance in promoting oil and gas exploration and development, geothermal resource assessment, carbon dioxide sequestration monitoring, and related fields. As energy resources are extensively exploited, exploration has become increasingly challenging. The search for mid-to-deep reservoirs, ultra-shallow formations, buried hills, lithologic traps, and complex structural or fractured reservoirs has emerged as a key research focus, posing new challenges for exploration seismology—particularly in seismic-wave migration imaging. Advancements in high-resolution seismic imaging techniques are critical for improving the exploration of both conventional and unconventional hydrocarbon resources. Beyond hydrocarbon exploration, high-resolution seismic imaging is also critical for emerging energy technologies, such as carbon capture and storage (CCS) and geothermal energy development. Accurate migration methods are essential for monitoring fluid movement in CCS reservoirs and characterizing fracture networks in geothermal systems, highlighting the broader societal relevance of advancing wave-equation–based techniques.

Since its inception in the 1960s, seismic imaging has evolved significantly, progressing from early manual and human–computer migration methods to digital wave-equation–based techniques enabled by advances in scientific computing.[1] Early migration approaches were rooted in Huygens' principle, which treats every point on a wavefront as a secondary source. The exploding reflector model (ERM), which assumes simultaneous explosions of all points at the subsurface, laid the foundation for modern imaging.[2] Subsequent developments introduced frequency–wavenumber one-way wave migration derived from ERM and other wave-equation formulations.

One-way wave migration can be regarded as a practical implementation of ERM under the paraxial assumption. Integral migration methods based on ray-tracing theory also contributed to the theoretical foundation of modern imaging.[3] In addition to seismic reflection imaging, the diffraction imaging theory provides a special solution for small-scale structure.[4] These early techniques laid the groundwork for rapid advances in migration, with progress closely tied to improvements in computational hardware. Enhanced computing power has facilitated a transition from post-stack to prestack migration, from time migration to depth migration (which better accounts for velocity variations), from 2D to 3D migration, from ray-based algorithms to wave-equation migration employing exact solutions, from one-way wave migration to full-wave-equation migration, and, more recently, from traditional methods to artificial intelligence (AI)-assisted migration imaging.

This review systematically analyzes the evolution of one-way and full-wave-equation migration methods, focusing on comparisons of wavefield propagation and imaging performance among the current mainstream wave-equation–based migration methods. Specifically, it highlights advancements in wave-equation migration and their constraint, with discussions of their prospects for seismic exploration.

2. Research progress on wave-equation–based migration

Limited to a 2D case in this review, the acoustic constant-density second-order wave equation is given as:

$$\frac{\partial^2 u}{\partial x^2}+\frac{\partial^2 u}{\partial z^2}=\frac{1}{v^2}\frac{\partial^2 u}{\partial t^2} \tag{1}$$

where u is the pressure wavefield, v denotes the medium velocity, x and z are spatial coordinates, and t is time.

The full wave equation can be formulated in either the time or frequency domain as:

$$\frac{\partial^2 u}{\partial t^2}-Qu=0 \tag{2}$$

$$\frac{\partial^2 \tilde{u}}{\partial z^2}+H\tilde{u}=0 \tag{3}$$

where $\tilde{u}=\mathrm{FFT}\left[u\right]$ denotes the frequency-domain wavefield, $Q=v^2\left(\frac{\partial^2}{\partial x^2}+\frac{\partial^2}{\partial z^2}\right)$, and $H=\frac{\omega^2}{v^2}+\frac{\partial^2}{\partial x^2}$, where ω is frequency.

The wave-equation prestack depth migration can be categorized into one-way wave-equation migration and full-wave-equation migration based on the propagation characteristics of the wavefields.

2.1. Advances in one-way wave-equation depth migration

Over the past few decades, one-way wave-equation depth migration (OWDM) has played a crucial role in seismic imaging. From the perspective of wave-equation solutions, conventional seismic acquisition records only the wavefield

at the surface, providing a single boundary condition. To facilitate the solution process, the acoustic wave equation is decomposed into two independent one-way wave equations: the downgoing and upgoing wave equations.

Assuming a homogeneous medium, the one-way wave equation can be derived from the full second-order wave equation as:

$$\frac{\partial \tilde{u}}{\partial z} = \pm \mathrm{i} k_z \tilde{u} \tag{4}$$

where $k_z = \sqrt{\frac{\omega^2}{v^2} - k_x^2}$ is the square-root operator, also called the vertical wavenumber, at the core of depth-domain extrapolation.

Then, the adjacent-layer iteration equation can be written as:

$$\tilde{u}\left(z + \Delta z\right) = e^{\pm i k_z \Delta z} \tilde{u}\left(z\right) \tag{5}$$

where Δz is the depth-step length.

The fundamental strategy of OWDM involves extrapolating the source wavefield using the downgoing wave equation and backpropagating the receiver wavefield using the upgoing wave equation. These wavefields are then propagated downward in depth, and imaging is performed using an imaging condition. Since the one-way wave equations are derived from the full wave equation, OWDM retains its capability to handle complex media.

2.1.1. Reference-velocity–based one-way wave migration

The earliest OWDM method employs the Fourier transform to convert the original wave equation from the time–space domain to the frequency–wavenumber domain. It utilizes only the upgoing wave equation to compute the propagation operator and recursively extrapolate the wavefield for imaging. OWDM methods are computationally efficient and stable, making them suitable for large-scale imaging. As a classical migration scheme, the phase-shift (PS) method[5] assumes that velocity varies only in the depth direction. Therefore, this method is effective only when the velocity is uniform or varies strictly in the vertical direction, and it performs poorly in media with lateral velocity variations. Around the same period, frequency-domain finite-difference (FD) techniques were introduced into seismic migration imaging.[6] However, these methods suffered from severe limitations in imaging at large angles.

To address this limitation, OWDM algorithms have undergone extensive optimization, particularly in approximating the vertical wavenumber to better accommodate laterally varying velocity media. The PS plus interpolation method[7] and the split-step Fourier (SSF) migration algorithm[8] were subsequently developed. The SSF method introduces a time-shift correction term in the frequency–space domain to mitigate phase distortions caused by lateral velocity variations. Further refinements to the SSF algorithm partially improved phase accuracy, yet its fundamental limitation in imaging complex inhomogeneous media remains unresolved.[9]

Due to limited compensation for low-order perturbations, these algorithms only provide accurate imaging positions when lateral velocity variations are weak. By incorporating a quadratic correction term into the SSF method, the Fourier finite-difference (FFD) migration algorithm was proposed.[10] This approach significantly improved imaging for large-angle wave propagation and enhanced imaging accuracy in laterally varying velocity media. Based on the FFD method, researchers attempted to improve imaging precision in complex media by introducing more accurate polynomial coefficients derived from global optimization strategies, leading to the development of optimized FFD migration techniques.[11-13] Similar to the FFD approach, the generalized screen propagator (GSP) extends the phase-screen operator based on scattering theory.[14] GSP decomposes velocity perturbations into a background velocity field and an in-layer perturbation term. Various hybrid migration methods based on GSP operators have been developed to improve propagation angles, amplitude preservation, stability, adaptability, and amplitude compensation.[15-17]

Both the FFD and GSP methods employ higher-order corrections to address lateral velocity variations and operate in dual domains based on the SSF algorithm. However, their implementations differ: FFD expands the operator using a second-order Taylor series around the reference velocity, followed by continued fraction expansion and FD corrections in both the frequency and spatial domains. In contrast, GSP transforms the square-root operator from the reference velocity field to the correct velocity field and then applies a Taylor expansion to separate spatial and wavenumber variables, enabling alternating corrections in the frequency–space and frequency–wavenumber domains, as expressed as:

$$\begin{cases} k_z^{SSF} = \dfrac{\omega}{v(x,z)} - \dfrac{\omega}{v_r} + \sqrt{\dfrac{\omega^2}{v_r^2} - k_x^2} \\ k_z^{FFD} = k_z^{SSF} + \dfrac{\dfrac{v(x,z)-v_r}{\omega}\dfrac{\partial^2}{\partial x^2}}{a + b\dfrac{v^2(x,z)}{\omega^2}\dfrac{\partial^2}{\partial x^2}} \\ k_z^{GSP} = k_z^{SSF} + \omega\sum_{j=1}^{n} a_j \left(\dfrac{\omega}{v^2(x,z)} - \dfrac{\omega}{v_r^{\,2}}\right)^j \\ \qquad \times\left[\left(\dfrac{\omega}{\sqrt{\dfrac{\omega^2}{v_r^2} - k_x^2}}\right)^{2j-1} - v_r^{\,2j-1}\right] \end{cases} \tag{6}$$

where v_r is the reference velocity, which is often used as the mean velocity in the SSF and FFD method, and the minimum velocity in the GSP method.

Since OWDM methods separate the full acoustic wave equation into up- and downgoing components, imaging amplitude in one-way wave operators is typically achieved by introducing compensation factors or auxiliary functions in the equations. These methods have made progress in improving large-angle imaging and amplitude preservation.

2.1.2. Accurate-velocity–based one-way wave migration

Directly discretizing the lateral velocity and calculating the accurate value of the square-root operator at each discrete point are necessary to solve the wave equation in laterally varying velocity media. The idea of using accurate horizontal velocities to calculate one-way propagators with the generalized phase-shift (GPS) operator[18] was proposed to overcome the limitations of the traditional OWDM methods, which rely on reference-velocity approximations. Another way to solve the accurate one-way wave propagator is with an eigen decomposition (ED) of the Helmholtz operator,[19] enabling OWDM to image strongly laterally varying media. Specifically, in terms of matrix transformation theory, the self-adjoint matrix $H = k_z^2$ can be decomposed into a multiplication of eigenvalues and eigenvectors, so that:

$$H = VMV^T \tag{7}$$

where the superscripted T represents the matrix transpose and matrices and denote the eigenvalues and eigenvectors of , respectively.

$$H = \begin{bmatrix} \dfrac{\omega^2}{v^2(x_1)} & 0 & \cdots & 0 \\ 0 & \dfrac{\omega^2}{v^2(x_2)} & \cdots & 0 \\ \vdots & \vdots & \ddots & \vdots \\ 0 & 0 & \cdots & \dfrac{\omega^2}{v^2(x_n)} \end{bmatrix} + \begin{bmatrix} \dfrac{-2}{(\Delta x)^2} & \dfrac{1}{(\Delta x)^2} & 0 & 0 \\ \dfrac{1}{(\Delta x)^2} & \dfrac{-2}{(\Delta x)^2} & \ddots & 0 \\ 0 & \ddots & \ddots & \dfrac{1}{(\Delta x)^2} \\ 0 & 0 & \dfrac{1}{(\Delta x)^2} & \dfrac{-2}{(\Delta x)^2} \end{bmatrix} \tag{8}$$

Furthermore, the eigenvalues and eigenvectors of the sub-functions can be expressed as:

$$k_z = \sqrt{H} = V\sqrt{M}V^T \tag{9}$$

Following the above two solutions, improvements were made for an accurate one-way migration method. The migration/inversion methods driven by one-way wave operators for imaging multiples are constructed with a closed-loop least-squares framework. The GPS operator is fast and, therefore, frequently used in reflection waveform imaging and inversion.[20] The accurate one-way wave-migration operator can be enhanced by adding amplitude-correction terms to optimize true-amplitude calculation performance, with precise discrete velocities to compute the square root of the Helmholtz operator. By using a best-fit matrix decomposition operator based on the infinity norm, high-precision imaging was achieved with low-order expansions.[21] Also, with a Jacobi–Anger expansion to approximate the one-way operator[22] or using the Padé to approximate the propagator calculated in the pseudo-wavenumber domain via the Helmholtz operator,[23] the imaging results were more accurate than those using the Taylor series.

The generalized one-way wave PS operators were used to drive surface and internal multiple reflections and to estimate reflectivity, thereby proposing the full-wavefield migration (FWM) framework.[24] Subsequently, FWM was improved by combining surface multiples and internal multiples to image a 3D salt dome model.[25] The accurate one-way wave operator can also be integrated into the FWM framework,[26] thereby improving the accuracy of reflectivity estimation.

The comparison of propagating-phase accuracy is shown in Figure 1, which demonstrates that the ED operator fits the slowness in very strongly laterally varying media better than the GPS operator, owing to its avoidance of accuracy leakage from the Fourier transform, though both calculate full lateral velocity grids.

2.2. Progress on full-wave-equation migration

In homogeneous media, the phase and amplitude information calculated by the one-way wave migration is consistent with that of the full-wave-equation migration. For heterogeneous media, although the accurate-velocity–based one-way wave migration can achieve an imaging range of 90 degrees, it is essentially an approximation of the full wave equation and thus cannot fully support calculations for arbitrary propagation angles or achieve amplitude fidelity owing to a loss of traveling wavefield. Simplified propagation assumptions can lead to loss of resolution and inaccurate imaging in complex media.[27] In contrast, full-wave-equation migration, based on solving the complete wave equation, can handle turning waves and arbitrary angles. Therefore, since their introduction, full-wave-equation migration algorithms have gained widespread attention.

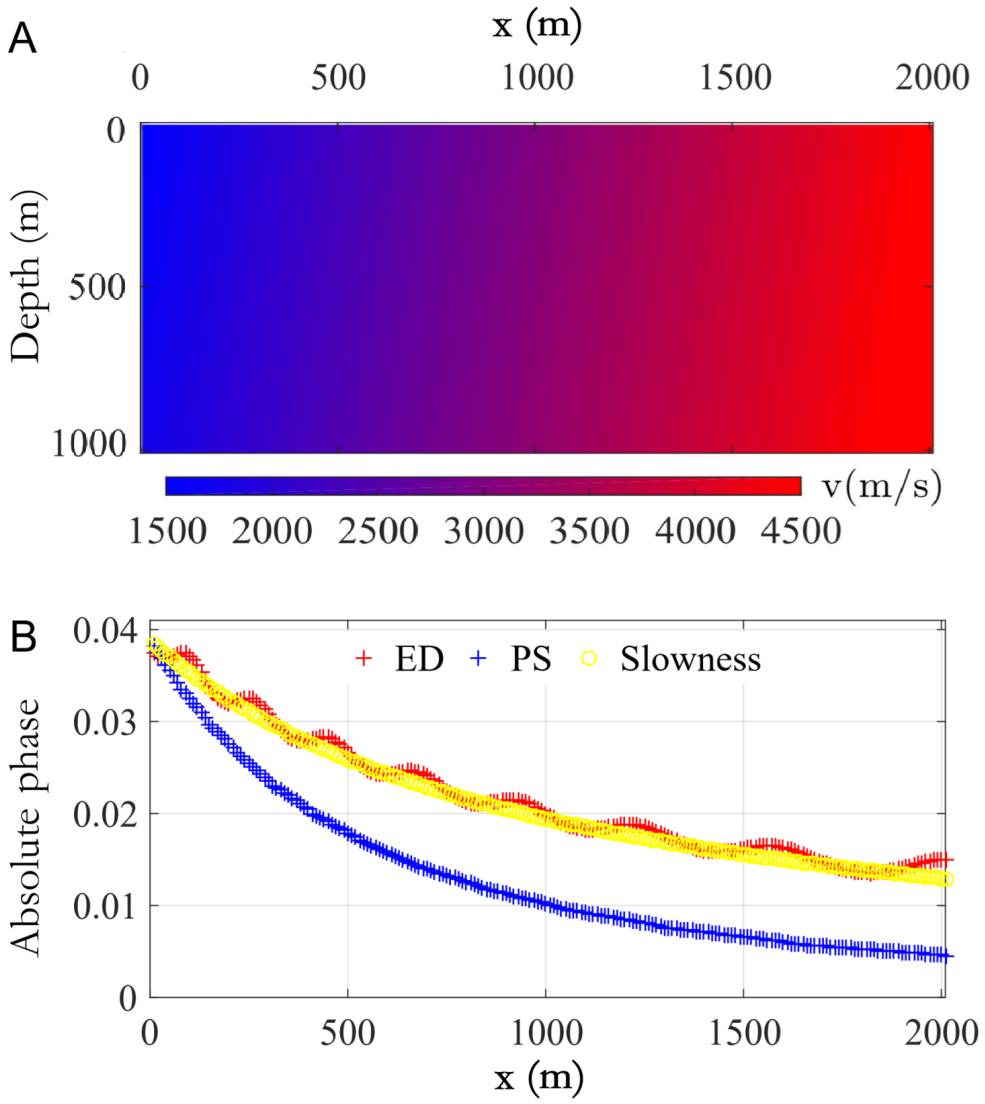

Figure 1. A comparison of propagating phase in inhomogeneous medium. (A) The inhomogeneous medium with strong lateral velocity gradients. (B) Comparison of the phase imaging accuracy between eigen decomposition (ED) and generalized phase-shift (GPS) operators. Reprinted with permission from Li *et al.*[26] Copyright © 2024 IEEE.

The wave equation is a function of time and space. To perform wave propagation, the wavefield is generally reconstructed in the time and space domains. With a space-independent and time-independent rewriting, by defining $U=\begin{bmatrix} u \\ u_t \end{bmatrix}$ and $\tilde{U}=\begin{bmatrix} \tilde{u} \\ \tilde{u}_z \end{bmatrix}$, the propagating wavefield can be further expressed regarding the full wave equation as:

$$\frac{\partial U}{\partial t}=\begin{bmatrix} 0 & 1 \\ Q & 0 \end{bmatrix}U \tag{10}$$

$$\frac{\partial \tilde{U}}{\partial z}=\begin{bmatrix} 0 & 1 \\ -H & 0 \end{bmatrix}\tilde{U} \tag{11}$$

Furthermore, the recursive equation can be formulated as:

$$\begin{cases} U\left(t+\Delta t\right)=\mathrm{e}^{\begin{bmatrix} 0 & 1 \\ Q & 0 \end{bmatrix}\Delta t}U\left(t\right) & \text{RTM} \\ \tilde{U}\left(z+\Delta z\right)=\mathrm{e}^{\begin{bmatrix} 0 & 1 \\ -H & 0 \end{bmatrix}\Delta z}\tilde{U}\left(z\right) & \text{FWDM} \end{cases} \tag{12}$$

where Δt is the time step.

According to execution principles, mainstream full-wave-equation migration is divided into reverse-time migration (RTM)[28,29] and full-wave-equation depth migration (FWDM),[30] based on **Equation 12**. Furthermore, wave-equation migration strategies can be further classified into one-step and two-step approaches based on how the wavefield is processed. One-step migration involves the concurrent extrapolation and imaging of the wavefield. In contrast, two-step strategies involve an initial wavefield decomposition—separating the recorded data into up- and downgoing components—followed by independent imaging. These two-step methods are particularly effective for improving numerical stability and preserving diffraction energy, thereby enhancing the resolution of small-scale geological features, such as faults and fractures, within wave-equation migration workflows.[31]

2.2.1. Progress on reverse-time migration

As a representative full-wave-equation migration method, RTM utilizes the FD technique to solve the wave equation by forward propagating the source wavefield and backward propagating the receiver wavefield. Theoretically, RTM offers superior accuracy in imaging complex structures because it is based on the two-way wave equation and does not rely on dip-angle limitations inherent in other migration methods. Research on RTM has primarily focused on three key areas: improving imaging accuracy, preserving amplitude, and improving computational efficiency.

Mainly caused by imaging upgoing and downgoing wavefields at large angles, and by a part of the interactions between forward–forward and backward–backward wavefields, strong low-frequency noise is introduced into RTM imaging results, severely degrading imaging accuracy and quality. Thus, prestack RTM filtering techniques were developed to suppress these noises.[32,33] Since RTM solves the full acoustic wave equation, it inherently possesses an amplitude-preserving imaging potential. True-amplitude recovery methods primarily account for spherical spreading and subsurface absorption effects. In high-frequency approximations, the angle-domain Hessian matrix was used as a weighting function for correction during wave propagation, or amplitude-compensated imaging conditions were applied to improve imaging amplitude.[34,35]

However, RTM requires storing either the forward-propagated or backward-propagated wavefield during computation, leading to huge memory consumption and low computational efficiency, which limits its industrial applications. Two primary strategies have been proposed to address this challenge: algorithmic optimization to reduce computational complexity and wavefield storage requirements, such as checkpointing, partial snapshot storage, and graphic processing unit acceleration, to enhance efficiency.[36-39]

Least-squares RTM (LS-RTM) reformulates imaging as a least-squares inversion, addressing issues such as migration artifacts, amplitude imbalances, and noise contamination caused by acquisition geometry and wave-propagation effects.[40-44] By accounting for the anisotropies of wave propagation, the method has also been extended to tilted transverse isotropic and vertical transverse isotropic media.[45-47] LS-RTM, when implemented with wavefield extrapolation in the time domain, can map primary and surface-related multiple reflections into the imaging results, showing significant progress in multiple-wave imaging.[48-51] With rapid development in recent decades, RTM has made significant progress and is widely used in the geophysical industry. However, it still suffers from high storage and computational costs, sensitivity to velocity model errors and data quality, and internal multiple cross-talk.

2.2.2. Progress on full-wave-equation depth migration

Depth migration propagates the wavefield along the depth axis. The FWDM was pioneered by solving the full acoustic

wave equation using the classical Runge–Kutta method, with a maximum-velocity truncation filter to suppress evanescent waves during wavefield extrapolation.[31] Building upon this framework, subsequent research has further advanced full-wave-equation–based algorithms.

Recent advancements in FWDM have revolutionized imaging capabilities through systematic improvements for the evanescent-wave filtering techniques, significantly enhancing energy preservation for steeply dipping geological structures.[52,53] Critical progress stems from three interconnected developments: the integration of physical boundary conditions to refine imaging fidelity, the inclusion of a wavefield separation strategy that enables precise depth-domain modeling of wavefield reception,[54-58] and the strategic expansion of FWDM frameworks through anisotropic media adaptations.[59] These synergistic innovations collectively broaden the operational scope of depth-migration algorithms while simultaneously elevating computational efficiency and imaging precision through the diversification of propagation-operator formulations to address complex wavefield dynamics.

3. Comparisons of the wave-equation migration method

The differences in wavefield propagation between RTM and FWDM are illustrated in Figure 2, which indicates reflected waves propagate from the reflection interface to the surface on the time profile in RTM; in contrast, in FWDM, they are mapped at the mirror position of the reflection interface (the bottom of the model), which is caused by a folding effect due to the incomplete propagating wavefield in the time domain.

In seismic imaging, the four wave-equation–based migration schemes—reference-velocity–based OWDM, accurate-velocity–based OWDM, RTM, and FWDM—differ significantly in imaging quality, computational efficiency, and geological applicability. RTM computes the wavefield in the time domain, while OWDM and FWDM are calculated in the frequency domain. RTM and FWDM both use the full wave equation; theoretically, they have similar imaging capabilities. Figure 3 shows a variable background velocity model. Figure 4 compares the impulse responses of RTM, reference-velocity–based OWDM, accurate-velocity–based OWDM, and FWDM. Using the FD-based RTM forward-modeling impulse response as the reference standard, the wavefront positions of the standard response pulse are outlined in white dashed lines in this figure. The comparison reveals that the phase information obtained by the accurate-velocity–based OWDM and FWDM methods aligns well with the RTM response curve; the reference-velocity–based OWDM method significantly deviates beyond about 75°, as indicated by the black arrow.

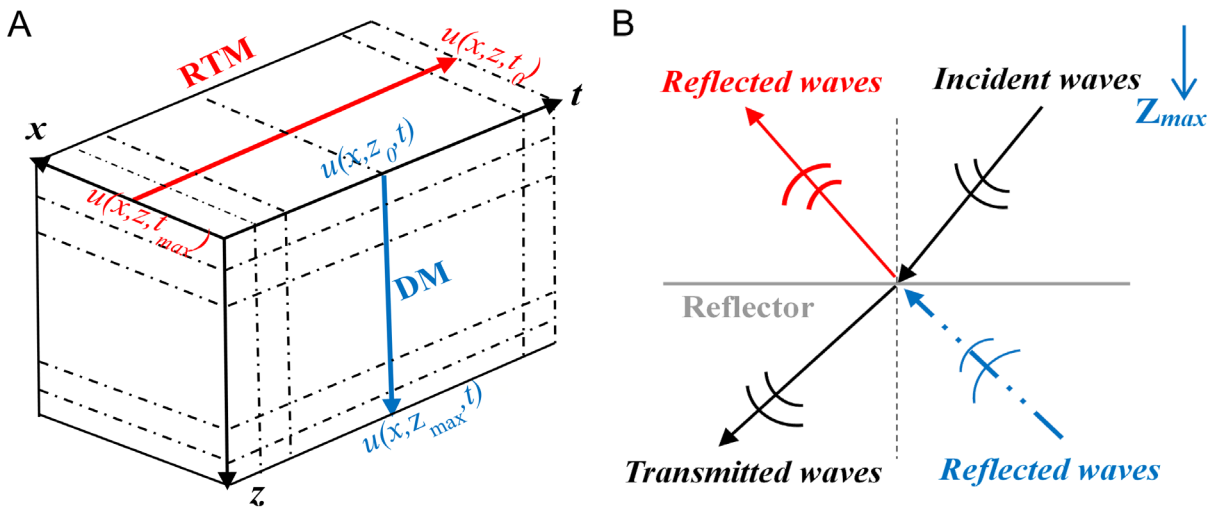

Figure 2. Comparison of wavefield extrapolation in reverse-time migration (RTM) and full-wave-equation depth migration (FWDM). (A) The difference in data extrapolation methods between RTM and depth migration (DM). (B) The difference in wave propagation between RTM and FWDM at the reflection interface: Reflected waves in RTM propagate from the reflection interface to the surface on the time profile, whereas in FWDM, they are mapped at the mirror position of the reflection interface, caused by the folding effect. Reprinted with permission from Li *et al.*[58] Copyright © 2024 Society of Exploration Geophysicists.

Figure 5 shows numerical results demonstrating that the reference-velocity–based OWDM method struggles to accurately image subsurface structures beneath the salt dome. This difficulty arises from phase errors induced by strong lateral velocity variations and steeply dipping reflectors with large scattering angles. Additionally, reference-velocity–based OWDM uses the minimum velocity as the reference velocity rather than the accurate lateral velocity, which tends to produce imaging artifacts due to phase errors (Figure 5B). The high-velocity salt body further complicates RTM, where internal multiples generate false reflectors below the salt. A comparison of the migrated sections in Figure 5C and 5D shows that the FWDM delivers a clearer and more coherent structural image with reduced noise compared to conventional RTM. However, the reflector polarity in the FWDM result is not fully consistent, because the bottom and top of the salt should be opposite. A slight phase difference between the two results stems from differences in their numerical implementations. The polarity discrepancy typically originates from the evanescent-wave filtering techniques or the specific PSs used to stabilize the Helmholtz operator in heterogeneous media. Furthermore, the folding effect at reflection interfaces, caused by the periodicity of the frequency domain and incomplete time-domain wavefield reconstruction, can lead to mirror-image artifacts that interfere with the primary reflector's phase.

This methodology capitalizes on turning wave energy to resolve vertical structural geometries, with quantitative validations presented in Figure 6. These comparisons substantiate that OWDM has the inherent constraint of imaging vertical structure, even when using accurate velocity. However, full-wave-equation migration schemes (RTM and FWDM) can image vertical formations—a capability fundamentally rooted in their rigorous incorporation of the full wave equation and propagating wavefield.

Figure 7 displays the Marmousi velocity model, while Figure 8 presents the imaging results obtained from four distinct wave-equation migration methodologies. The conventional OWDM method, employing the mean velocity in each lateral grid as the reference velocity, demonstrated limited efficacy in resolving dipping structures. The accurate-velocity–based OWDM, FWDM, and RTM approaches yielded comparable imaging accuracy. Notably, FWDM exhibited extended lateral imaging coverage in deeper model sections (below 2.5 km), as indicated by the red rectangles. A comparative analysis revealed RTM's superior performance in shallow structural imaging (0–1,000 m depth), contrasting with FWDM's enhanced imaging fidelity in deeper geological formations. This discrepancy stems from fundamental differences in wavefield extrapolation: RTM implementation delivers superior resolution in shallow layers through comprehensive wavefield reconstruction, whereas the FWDM preserves intricate structural features in deeper strata through rigorous acoustic wavefield modeling.

The comparative analysis of land seismic data imaging in Figure 9 compared the performances of the four migration

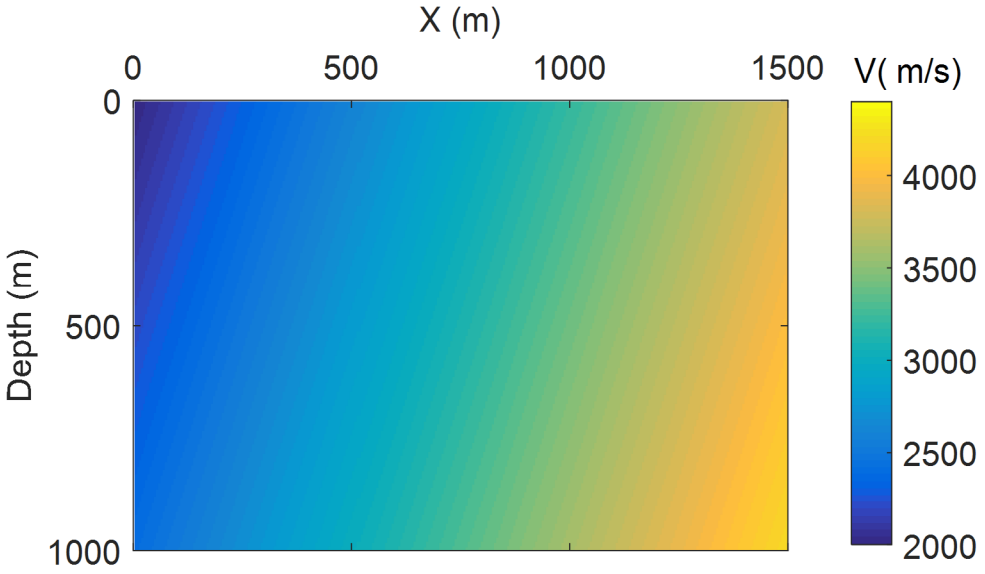

Figure 3. Background velocity model. Reprinted from Li and Liu.[21]

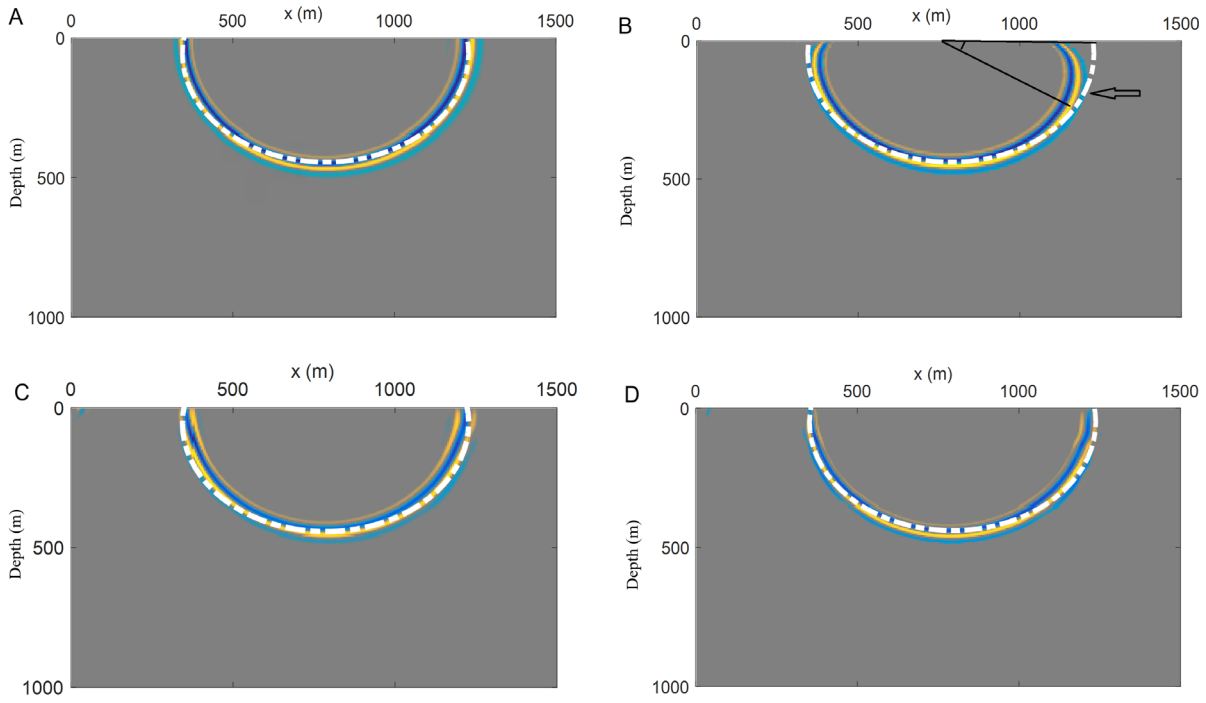

Figure 4. The impulse responses in media with lateral and vertical variations of velocity. (A) the finite-difference method. (B) Reference-velocity–based one-way wave-equation depth migration (OWDM). (C) Accurate-velocity–based OWDM. (D) Full-wave-equation depth migration. Reprinted from Li and Liu.[21]

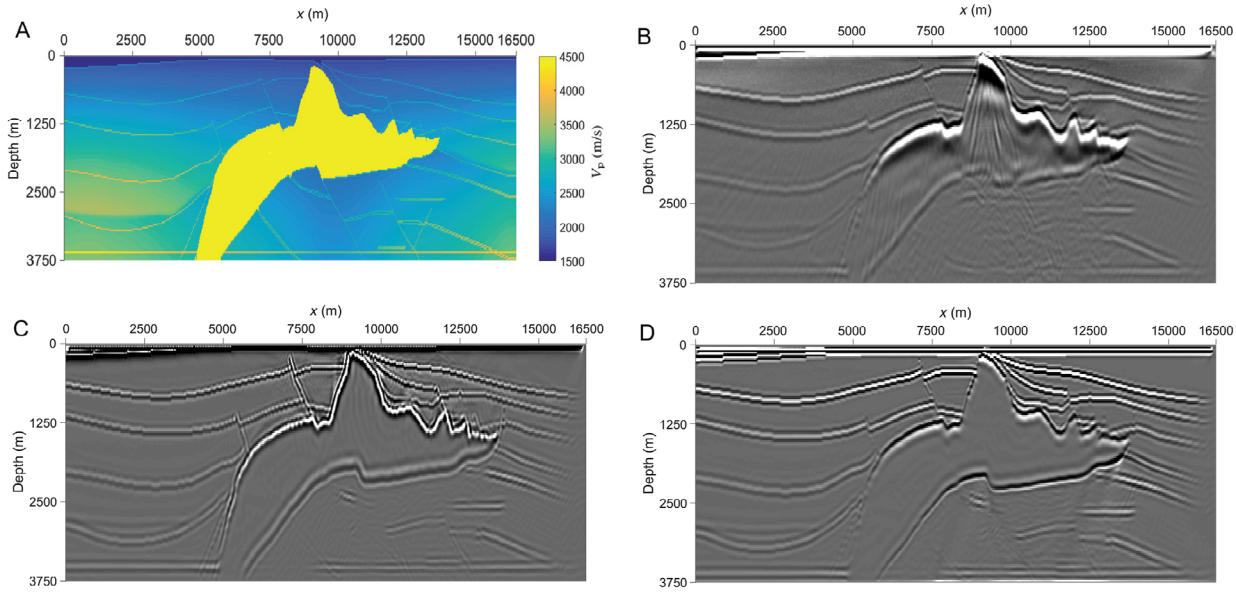

Figure 5. Velocity model and imaging results. (A) Velocity model. (B) Reference-velocity–based one-way wave-equation depth migration. (C) Reverse-time migration. (D) Full-wave-equation depth migration. Reprinted with permission from You and Cao.[55] Copyright © 2020 Society of Exploration Geophysicists.

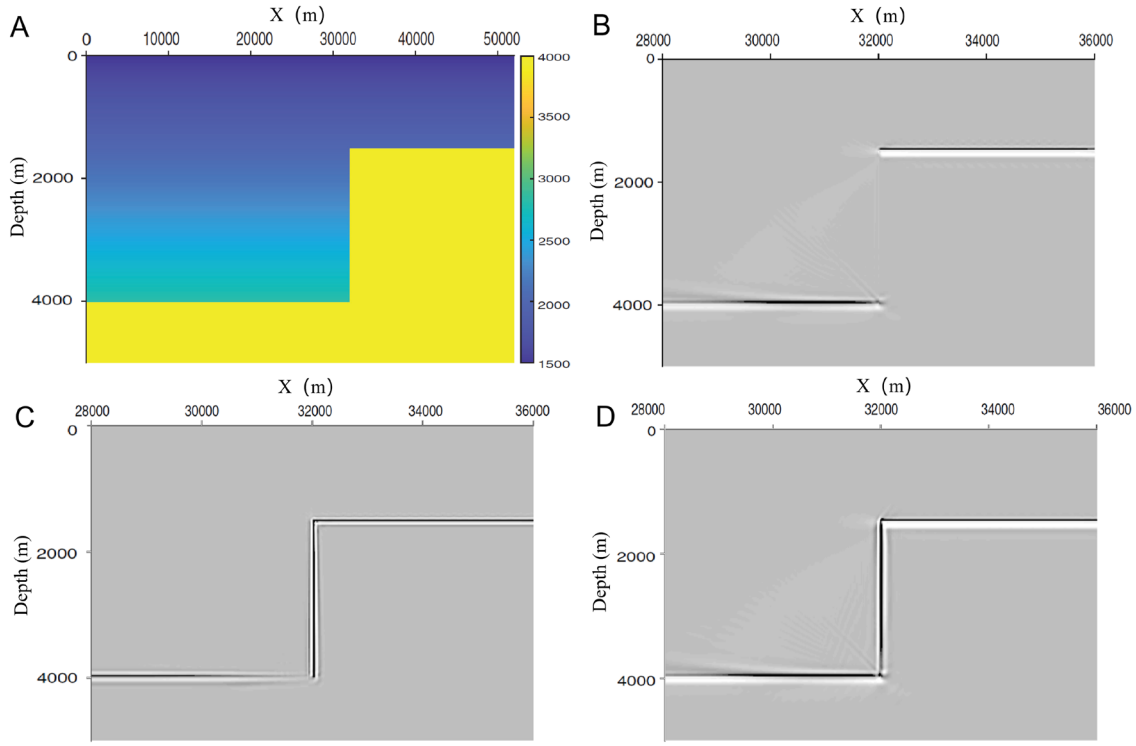

Figure 6. Comparison of depth-domain full-wavefield extrapolation based on wavefield separation imaging with one-way wavefield extrapolation and reverse-time migration (RTM). (A) Vertical velocity model. (B) One-way wave-equation depth migration. (C) Conventional RTM. (D) Full-wave-equation depth migration. Reprinted with permission from You *et al.*[57] Copyright © 2022 Society of Exploration Geophysicists.

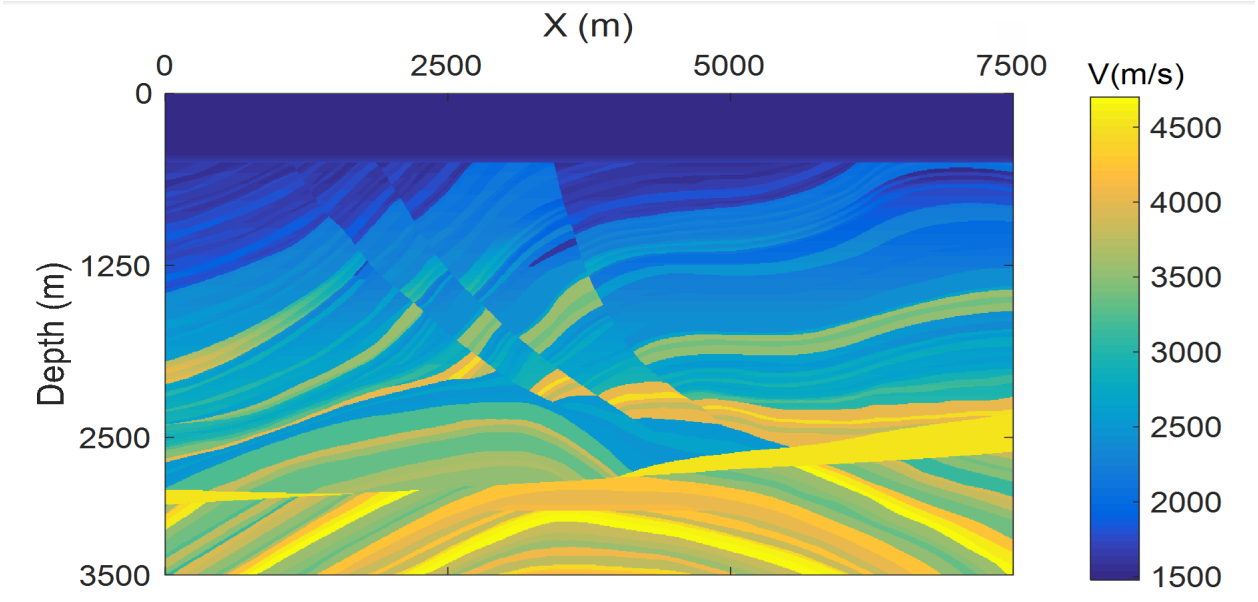

Figure 7. The Marmousi velocity model

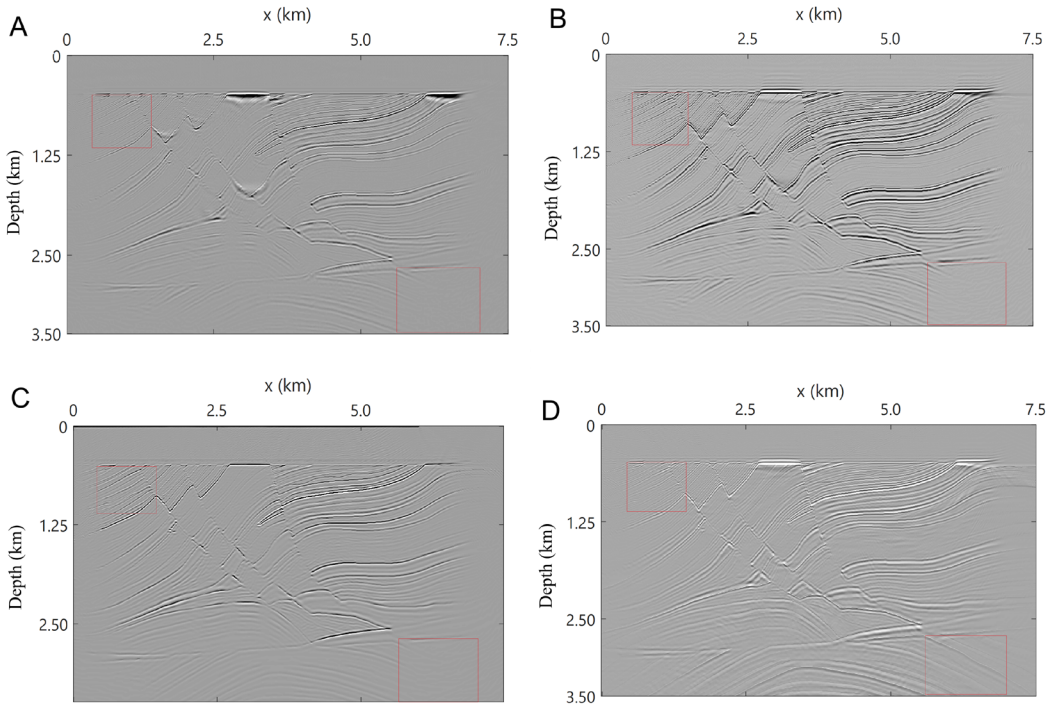

Figure 8. Migrated results. (A) Reference-velocity–based one-way wave-equation depth migration (OWDM). (B) Accurate-velocity–based OWDM. (C) Conventional reverse-time migration. (D) Full-wave-equation depth migration.

methods. The accurate-velocity–based OWDM method produced a clearer image than the reference-velocity–based OWDM technique. This enhancement is particularly evident in improving the phase continuity of seismic events and in delineating subtle stratigraphic features, as exemplified by micro-curved structural elements. The FWDM approach demonstrated superior geophysical fidelity, with more stable kinematic positioning, enhanced structural coherence, and higher-resolution imaging of complex geological interfaces. Although FWDM and RTM preserved two-way going-wave information and accounted for multi-directional wavefield propagation, the conventional RTM produced a slightly different profile, especially in deep layers, which may be due to sensitivity to an inaccurate migration velocity model and to noise in real data. This technological advancement primarily originates from extrapolating wavefield in depth direction, and it mitigates kinematic artifacts prevalent in conventional migration outputs.

A detailed feature comparison of these wave-equation migration algorithms is presented in Table 1. As exploration targets increasingly focus on deeper and more complex geological formations, selecting an optimal migration method has become critically important. Therefore, this table systematically evaluates the three types of schemes through comprehensive numerical examples, analyzing their imaging performance and practical suitability across diverse geological scenarios. The comparative results provide valuable guidance for field applications. Note that artifacts generated by FWDM are mostly at the bottom of the model due to the frequency-domain formulation and depth-marching strategy (only downward extension). While in RTM, the wavefield is propagated in the time domain, covering the entire propagation space, which mostly causes artifacts at the top of the model due to backscatter. Thus, the artifacts appear slightly less pronounced in FWDM than in RTM for the unfiltered migration profile. Furthermore, in terms of memory usage, while RTM can be formulated in the frequency domain, it is commonly implemented in the time domain in practice, whereas FWDM is naturally formulated in the frequency domain.

4. Progress on an artificial intelligence-assisted wave-equation migration

The integration of AI and deep learning extracts medium anisotropy parameters, velocity distributions, and attenuation characteristics from seismic data. It enhances velocity modeling accuracy, enables automatic noise identification/suppression, and reduces dependence on

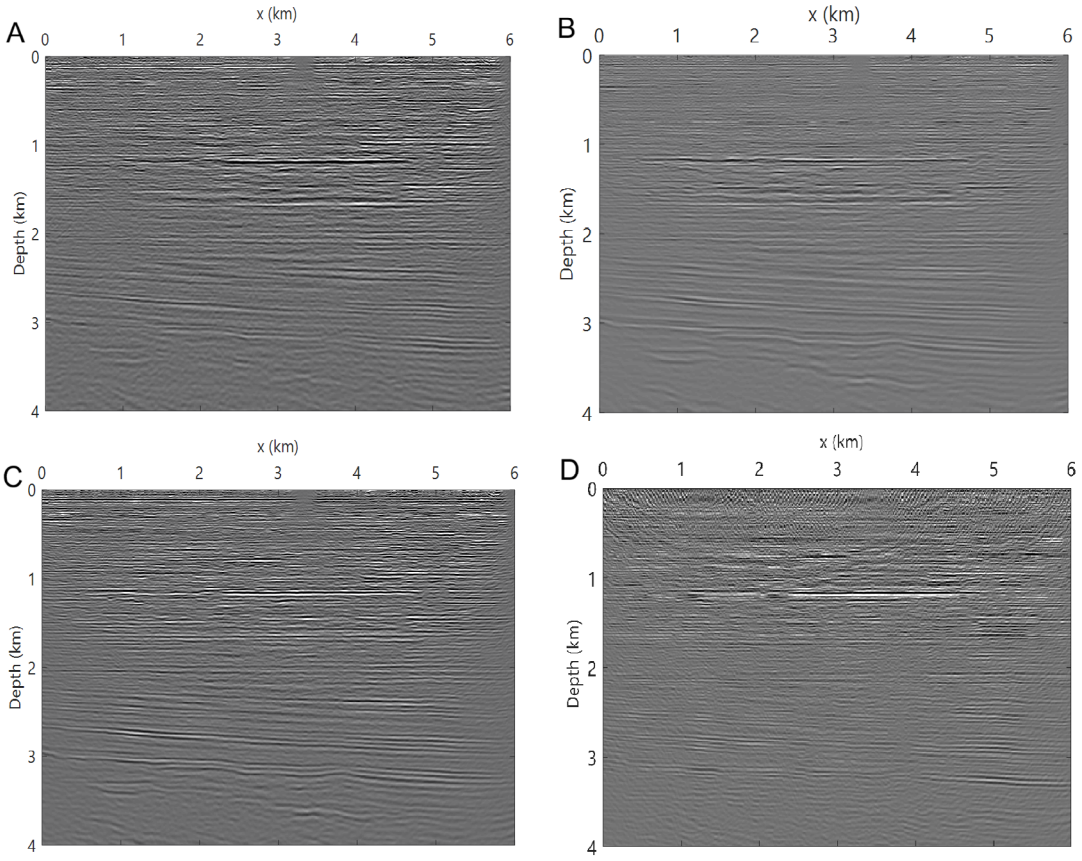

Figure 9. Migrated results from (A) reference-velocity–based one-way wave-equation depth migration (OWDM), (B) accurate-velocity–based OWDM, (C) full-wave-equation depth migration, and (D) conventional reverse-time migration.

Table 1. Comparisons of wave-equation–based migration schemes

Feature	OWDM	RTM	FWDM
Wavefield propagation	Solves the one-way wave equation in depth dimension	Solves the full wave equation in the time dimension	Solves the full wave equation in depth dimension
Dip handling	Limited to <90° dips (cannot handle turning waves)	Handles all dips (0–180°)	Handles all dips (0–180°)
Computational time cost	Low (efficient for large datasets, especially reference-velocity–based OWDM)	High (comparable to small-grid finite-difference schemes)	High (calculates Helmholtz operator and removes evanescent wave)
Memory usage	Minimal (2 × Nx × Nf)	High (2 × Nx × Nz × Nt)	Moderate (4 × Nx × Nf)
Artifacts	Low	High (same-directional wave)	High (same-directional wave)
Algorithm flexibility	Diverse operators (e.g., GSP, FFD, GPS, ED)	Typical finite difference-based	Diverse operators (Runge–Kutta, Padé approximation, deformed one-way wave operators, etc.)
Typical use case	Initial velocity model	Subsalt imaging	Complex structures with steep dips

Abbreviations: ED: Eigen decomposition; FFD: Fourier finite-difference; FWDM: Full-wave-equation depth migration; GPS: Generalized phase-shift; GSP: Generalized screen propagator; OWDM: One-way wave-equation depth migration; RTM: Reverse-time migration.

raw data quality. By developing neural network models trained on field and synthetic datasets, AI approaches effectively correct for the amplitude distortions and multipath effects inherent in conventional migration imaging. These technological breakthroughs can not only improve the precision and efficiency of migration imaging but also pioneer novel approaches for complex geological conditions, driving geophysical imaging toward intelligent development.[60-62]

4.1. Wavefield propagator design

Wavefield propagator design is a fundamental component of wave-equation–based high-resolution migration and modeling, as it directly governs the accuracy, stability, and computational efficiency of seismic imaging, emphasizing the importance of accurately describing wave-propagation physics for resolving complex subsurface structures.[63] These foundations underpin modern wave-equation migration methods and motivate ongoing developments in both numerical algorithms and data-driven approaches.

Recent advances in AI have enabled the development of surrogate modeling approaches that approximate wavefield propagation without traditional numerical integration. Neural operators, such as the Fourier neural operator (FNO), physics-informed neural networks (PINNs), physically constrained neural networks, and the Helmholtz neural operator, have shown strong potential in learning the mapping from model parameters to wavefields by training on high-fidelity numerical simulations and wavefield decomposition.[64-67] Use of PINNs enables grid-free, mesh-independent prediction of wavefield solutions, significantly reducing computational costs in large-scale or multi-shot imaging scenarios. Parallelized FNO variants and U-shaped neural operators could provide orders-of-magnitude acceleration while preserving wavefield accuracy in complex media. These models can generalize across varying velocity models and acquisition settings, providing efficient and scalable alternatives to conventional FD solvers.

In addition to pure surrogate modeling, hybrid strategies have been explored, in which AI models support conventional solvers by providing local error estimation, adaptive mesh refinement, or surrogate-based solution of Green's functions, or learning low-rank structure to approximate operator mappings.[68-70] These approaches not only enhance computational efficiency but also improve solver stability and resolution adaptivity in challenging geological settings. Furthermore, the integration of learned propagators into end-to-end differentiable modeling workflows allows for direct backpropagation through the wavefield modeling process, facilitating real-time seismic inversion and data assimilation. Such frameworks enable the computation of gradients concerning model parameters using automatic differentiation, thereby accelerating least-squares migration, full-waveform inversion, and tomographic updates.[71-74] Collectively, these AI-driven innovations represent a transformative direction for wave-equation–based imaging, blending physical principles with data-driven learning to achieve fast, flexible, and scalable seismic modeling.

4.2. Noise and artifact suppression

Noise and artifact suppression is a critical component of wave-equation–based migration, as these methods are inherently sensitive to both data quality and numerical implementation. Artifacts may originate from multiple sources, including limited acquisition aperture, inaccurate or poorly constrained velocity models, imperfect boundary conditions, and limitations in wavefield reconstruction or imaging conditions. The full-wave-equation migration method, in particular, is prone to generating low-frequency noise and spurious reflectors due to the cross-correlation of same-direction propagated wavefields under conditions of insufficient illumination or acquisition redundancy.

Deep learning has emerged as a transformative tool for noise and artifact suppression in seismic imaging. Supervised models, such as denoising autoencoders, support vector machines, convolutional residual networks, and generative adversarial networks (GANs), have been developed to attenuate artifacts—including backscattering, migration smiles, and acquisition footprints—without requiring explicit modeling of the underlying noise mechanisms.[75-77] These models can be applied either in the data domain, as a preprocessing step to enhance raw seismic traces before migration, or in the image domain, to refine migrated outputs by suppressing spatially incoherent or geologically implausible features.

Trained on curated synthetic or real datasets, AI-based denoisers learn to differentiate between primary reflections and multiples, enabling selective preservation of data features while reducing noise.[78-80] Some frameworks incorporate attention mechanisms to focus the network on geologically relevant areas and suppress irrelevant features, while others employ uncertainty-aware models to quantify confidence in the imaging output and highlight regions where noise may dominate.[81] Additionally, AI-enhanced imaging conditions—such as learned cross-correlation functions, adaptive stacking weights, and dynamic similarity metrics—can be integrated directly into the migration workflow to improve real-time artifact suppression during wave-equation–based migration.[82,83] Machine learning-based postprocessing techniques have

also shown promise in improving structural continuity and interpretability, particularly in challenging geological settings.[84] However, these approaches must be applied judiciously to avoid over-smoothing or introducing bias, especially in exploration contexts with high geological uncertainty.

Overall, a combination of improved physical imaging conditions, inversion-based regularization, and AI-driven filtering is redefining artifact-suppression strategies in wave-equation–based migration. The synergy between physics-based modeling and data-driven learning offers a path toward more accurate, efficient, and interpretable seismic imaging, while continuing challenges in generalization, training data quality, and physical interpretability remain active areas of research.

5. Discussion

Current wave-equation imaging techniques enable wavefield iteration driven by OWDM or RTM through least-squares iteration; however, one-way wave operators exhibit notable imaging-angle limitations, and LS-RTM still faces constraints from massive storage and computational demands due to time-domain wavefield backpropagation. Future improvements to least-squares–based migration could focus on computational efficiency. Considering the accuracy of wave-equation migration propagators, developing least-squares FWDM may hold significant promise for advancing reflectivity estimation accuracy through the closed-loop FWM framework for a multi-dimensional, large-scale database.

Multi-wave and multi-component seismic exploration technology acquires conventional P-wave data and captures converted PP and PS waves, substantially enriching wavefield information diversity. Compared to traditional P-wave exploration, converted waves demonstrate enhanced resolution for shallow, fine-scale structures, effectively improving imaging precision for specific geological features. Current research on FWDM remains predominantly focused on acoustic wave applications, while elastic wave and multi-wave/multi-component FWDM imaging technologies remain underdeveloped, offering substantial research value and developmental potential. A combination of separation and imaging diffractions can enhance the resolution of faults and discontinuities, particularly in complex velocity models.

Wave-equation migration with AI assistants has made great progress in enhancing imaging quality, computational efficiency, and parameter optimization, greatly advancing the practicality and intelligence of the wave-equation–based migration method. However, most AI models heavily rely on the quality and representativeness of training data; insufficient or geographically mismatched data can lead to poor generalization and reduced imaging accuracy. Moreover, almost all existing AI approaches operate as "black-box" models, lacking physical interpretability, thereby hindering their integration with traditional geophysical theories and reducing their reliability in complex subsurface scenarios. Additionally, handling high-dimensional, nonlinear input–output relationships demands substantial computational resources, making training and deployment costly. Finally, current AI methods still struggle with challenges such as anisotropy, multiphase wavefields, and multiscale geological features, underscoring the need to further develop AI architectures that integrate with physical constraints to better meet the demands of real-world seismic exploration.

Synergistically integrated with emerging innovations and multi-source information fusion strategies, wave-equation migration will play an increasingly vital role in imaging complex geological structures and hydrocarbon exploration. This technological convergence enhances characterization capabilities for intricate subsurface targets while providing sustained developmental momentum and directional guidance for seismic imaging innovation.

6. Conclusion

Wave-equation prestack migration is a core technique in seismic imaging for resolving complex geological structures and supporting reservoir prediction. This paper systematically reviewed and compared four representative wave-equation–based migration methods: reference-velocity–based OWDM, accurate-velocity–based OWDM, RTM, and FWDM, focusing on their theoretical characteristics and imaging performance.

The OWDM methods are computationally efficient and stable, making them suitable for large-scale imaging applications. However, their reliance on approximate wavefield propagation limits their ability to image dipping structures and complex wave phenomena in heterogeneous media. Accurate-velocity–based OWDM formulations improve phase accuracy and extend the imaging range by incorporating detailed velocity information, thereby enhancing the applicability of one-way wave migration.

Full-wave-equation methods provide a more complete physical description of seismic wave propagation. RTM and FWDM effectively image steep dips and complex structures by preserving two-way wavefield interactions. Comparative results indicate that RTM generally performs well in shallow regions, whereas FWDM offers improved stability and structural continuity in deeper or more complex settings. The integration of AI into wave-equation migration workflows has enhanced wavefield propagation

and noise suppression in the migration process.

Overall, this review clarifies the strengths and limitations of current wave-equation–based migration approaches through numerical examples and provides a practical reference for method selection in seismic imaging applications.

Acknowledgments

None.

Funding

This work was financially supported by the Natural Science Foundation of Chongqing (Grant No. CSTB2025NSCQ-GPX0927), the National Major Science and Technology Project for Deep Earth Exploration and Mineral Resources Exploration (Grant No. 2025ZD1009600), the Open Research Fund of Gansu Key Laboratory of Mineral Resources Exploration (Grant No. 202505), the Science and Technology Support Project for the New Round of Strategic Action for Prospecting Breakthrough (Grant No. ZKKJ202410), and the Research Foundation of Chongqing University of Science and Technology (Grant No. ckrc20241203).

Conflict of interest

The authors declare they have no competing interests.

Author contributions

Conceptualization: Yanlong Zhu, Anyu Li
Writing–original draft: Yanlong Zhu
Writing–review & editing: Anyu Li

Availability of data

Not applicable.

References

1. Bednar JB. A Brief History of Seismic Migration. *Geophysics*. 2005;70(3):3MJ-20MJ.

   doi: 10.1190/1.1926579

2. Claerbout JF. *Imaging the Earth's Interior*. Cambridge, MA, USA: Blackwell Scientific Publications; 1985.

3. Gray SH, Etgen J, Dellinger J, Whitmore D. Seismic migration problems and solutions. *Geophysics*. 2001;66(5):1622-1640.

   doi: 10.1190/1.1487107

4. Fomel S, Landa E, Taner MT. Poststack velocity analysis by separation and imaging of seismic diffractions. *Geophysics*. 2007;72(6):U89-U94.

   doi: 10.1190/1.2781533

5. Gazdag J. Wave equation migration with the phase-shift method. *Geophysics*. 1978;43(7):1342-1351.

   doi: 10.1190/1.1440899

6. Lee MW, Suh SY. Optimization of one-way wave equations. *Geophysics*. 1985;50(10):1634-1637.

   doi: 10.1190/1.1441853

7. Gazdag J, Sguazzero P. Migration of seismic data by phase shift plus interpolation. *Geophysics*. 1984;49(2):124-131.

   doi: 10.1190/1.1441643

8. Stoffa PL, Fokkema JT, de Luna Freire RM, Kessinger WP. Split-step Fourier migration. *Geophysics*. 1990;55(4):410-421.

   doi: 10.1190/1.1442850

9. Zhang L, James WRG, Michael HSF. Split-step complex Padé-Fourier depth migration. *Geophys J Int*. 2007;171(3):1308-1313.

   doi: 10.1111/j.1365-246X.2007.03610.x

10. Ristow D, Rühl T. Fourier finite-difference migration. *Geophysics*. 1994;59(12):1882-1893.

    doi: 10.1190/1.1443575

11. Biondi B. Stable-wide-angle Fourier finite-difference downward extrapolation of 3D wavefields. *Geophysics*. 2002;67(3):872-882.

    doi: 10.1190/1.1484530

12. Salcedo M, Novais A, Schleicher J, Costa JC. Optimization of the parameters in complex Padé FFD migration. *Geophysics*. 2017;82(3):S259-S269.

    doi: 10.1190/geo2016-0324.1

13. Huang J, Hu T, Wang S. Fourier finite-difference migration of internal multiples. *Chin J Geophys*. 2022;65(11):4394-4403. [In Chinese].

    doi: 10.6038/cjg2022P0790

14. Wu R. Wide-angle elastic wave one-way propagation in heterogeneous media and an elastic wave complex-screen method. *J Geophys Res Solid Earth*. 1994;99(B1):751-766.

    doi: 10.1029/93JB02518

15. Zhang Y, Zhang G, Bleistein N. True amplitude wave equation migration arising from true amplitude one-way wave equations. *Inverse Probl*. 2003;19(5):1113-1138.

    doi: 10.1088/0266-5611/19/5/307

16. Amazonas D, Aleixo R, Melo G, Schleicher J, Novais A, Costa JC. Including lateral velocity variations into true-amplitude common-shot wave-equation migration. *Geophysics*. 2010;75(5):S175-S186.

    doi: 10.1190/1.3481469

17. Zhu H, Wang D, Hu B, Zhang W, Chen Y. Sparsity-promoting wide-angle least-squares one-way migration. *Acta Geophys*.

2024;72(5):3091-3108.

doi: 10.1007/s11600-023-01215-0

18. Kosloff D, Kessler D. Accurate depth migration by a generalized phase-shift method. *Geophysics*. 1987;52(8):1074-1084.

doi: 10.1190/1.1442373

19. Grimbergen JLT, Dessing FJ, Wapenaar K. Modal expansion of one-way operators in laterally varying media. *Geophysics*. 1998;63(3):995-1005.

doi: 10.1190/1.1444410

20. Sun Y, Kim YS, Qu S, Verschuur E. Joint migration inversion: Features and challenges. *J Geophys Eng*. 2020;17(3):525-538.

doi: 10.1093/jge/gxaa012

21. Li A, Liu X. An optimised one-way wave migration method for complex media with arbitrarily varying velocity based on eigen-decomposition. *J Geophys Eng*. 2021;18(5):776-787.

doi: 10.1093/jge/gxab051

22. Revelo DE, Pestana RC. One-way wave-equation migration based on Jacobi-Anger expansion in arbitrarily lateral varying media. *IEEE Trans Geosci Remote Sens*. 2025;63:4501610.

doi: 10.1109/TGRS.2025.3533469

23. Li A. Efficient one-way wave-equation depth migration using fast Fourier Transform and complex Padé approximation via Helmholtz operator. *IEEE Trans Geosci Remote Sens*. 2026;64:5901211.

doi: 10.1109/TGRS.2026.3651624

24. Berkhout AJ. Review paper: An outlook on the future of seismic imaging, Part II: Full-wavefield migration. *Geophys Prospect*. 2014;62(5):931-949.

doi: 10.1111/1365-2478.12154

25. Davydenko M, Verschuur DJ. Full-wavefield migration: Using surface and internal multiples in imaging. *Geophys Prospect*. 2017;65(1):7-21.

doi: 10.1111/1365-2478.12360

26. Li A, Verschuur DJ, Liu X, Abolhassani S. An accurate propagator for heterogeneous media in full wavefield migration. *IEEE Trans Geosci Remote Sens*. 2024;62:4506210.

doi: 10.1109/TGRS.2024.3397887

27. Bashir Y, Babasafari AA, Alashloo SM, Muztaza NM, Ali SH, Imran QS. Seismic wave propagation characteristics using conventional and advance modelling algorithm for d-data imaging. *J Seism Explor*. 2021;30(1):21-44.

28. Whitmore ND. Iterative depth migration by backward time propagation. In: *SEG Technical Program Expanded Abstracts 1983*. 53rd SEG Annual International Meeting; 1983; Las Vegas, NV. Society of Exploration Geophysicists; 1983:382-385.

doi: 10.1190/1.1893867

29. Baysal E, Kosloff DD, Sherwood JWC. Reverse time migration. *Geophysics*. 1983;48(11):1514-1524.

doi: 10.1190/1.1441434

30. Kosloff DD, Baysal E. Migration with the full acoustic equation. *Geophysics*. 1983;48(6):677-687.

doi: 10.1190/1.1441498

31. Bashir Y, Waheed U, Ali SH, Karaman A, İmren C. Enhanced wave modeling & optimal plane-wave destruction (OPWD) method for diffraction separation and imaging. *Comput Geosci*. 2024;187:105576.

doi: 10.1016/j.cageo.2024.105576

32. Zhang L, Slob E, van der Neut J, Wapenaar K. Artifact-free reverse time migration. *Geophysics*. 2018;83(5):A65-A68.

doi: 10.1190/geo2017-0795.1

33. Xu Q, Wang Y. Seismic reverse time migration based on biaxial wavefield decomposition. *Geophysics*. 2024;89(1):S61-S70.

doi: 10.1190/geo2022-0698.1

34. Nguyen BD, McMechan GA. Excitation amplitude imaging condition for prestack reverse-time migration. *Geophysics*. 2013;78(1):S37-S46.

doi: 10.1190/geo2012-0079.1

35. Wang J, Li Q, Qiao B, Qi J. Reverse time migration using excitation amplitude imaging condition based on accurate first-arrival traveltimes calculation. *IEEE Trans Geosci Remote Sens*. 2025;63:5903111.

doi: 10.1109/TGRS.2025.3527144

36. Symes WW. Reverse time migration with optimal checkpointing. *Geophysics*. 2007;72(5):SM213-SM221.

doi: 10.1190/1.2742686

37. Sun W, Fu L. Two effective approaches to reduce data storage in reverse time migration. *Comput Geosci*. 2013;56:69-75.

doi: 10.1016/j.cageo.2013.03.013

38. Yang P, Brossier R, Métivier L, Virieux J. Wavefield reconstruction in attenuating media: A checkpointing-assisted reverse-forward simulation method. *Geophysics*. 2016;81(6):R349-R362.

doi: 10.1190/geo2016-0082.1

39. Cai W, Zhu P, Li Z. Simulation and reconstruction for 3D elastic wave using multi-GPU and CUDA-aware MPI. *Comput Geosci*. 2024;190:105616.

doi: 10.1016/j.cageo.2024.105616

40. Dai W, Schuster G. Plane-wave least-squares reverse-time migration. *Geophysics*. 2013;78(4):S165-S177.

doi: 10.1190/geo2012-0377.1

41. Yao G, Jakubowicz H. Least-squares reverse-time migration in a matrix-based formulation. *Geophys Prospect*. 2016;64(3):611-621.

doi: 10.1111/1365-2478.12305

42. Vamaraju J, Tuvi R, Zhao ZY, Sen MK. Optimal minibatch shot selection for target-oriented least-squares reverse time migration. *Geophysics*. 2022;87(4):A55-A60.

doi: 10.1190/geo2021-0579.1

43. Wang M, He B. Elastic least-squares reverse time migration based on integration of the Hessian. *IEEE Trans Geosci Remote Sens*. 2025;63:5912711.

doi: 10.1109/TGRS.2025.3563393

44. Li C, Huang J, Li Z, Wang R. Plane-wave least-squares reverse time migration with a preconditioned stochastic conjugate gradient method. *Geophysics*. 2018;83(1):S33-S46.

doi: 10.1190/geo2017-0339.1

45. Mu X, Huang J, Yang J, Guo X, Guo Y. Least-squares reverse time migration in TTI media using a pure qP-wave equation. *Geophysics*. 2020;85(4):S199-S216.

doi: 10.1190/geo2019-0320.1

46. Qiao Z, Chen T, Sun C. Anisotropic attenuation compensated reverse time migration of pure qP-wave in transversely isotropic attenuating media. *Surv Geophys*. 2022;43(5):1435-1467.

doi: 10.1007/s10712-022-09717-0

47. Huang J, Mu X, Yang J, Su L. Least-squares reverse time migration in viscoacoustic tilted transversely isotropic media. *Geophysics*. 2025;90(3):S69-S88.

doi: 10.1190/geo2023-0422.1

48. Zhang D, Schuster GT. Least-squares reverse time migration of multiples. *Geophysics*. 2013;79(1):S11-S21.

doi: 10.1190/geo2013-0156.1

49. Lu S, Liu F, Chemingui N, Valenciano A, Long A. Least-squares full-wavefield migration. *Leading Edge*. 2018;37(1):46-51.

doi: 10.1190/tle37010046.1

50. Liu Y, Zhang Y, Zheng Y. Reverse time migration of phase-encoded all-order multiples. *Geophysics*. 2022;87(2):S45-S52.

doi: 10.1190/geo2021-0004.1

51. Wu H, Lu S, Dong X, Deng X, Gao R. Least-squares full-wavefield reverse time migration using a modeling engine with vector reflectivity. *IEEE Trans Geosci Remote Sens*. 2023;61:5901112.

doi: 10.1109/TGRS.2023.3234902

52. Sandberg K, Beylkin G. Full-wave-equation depth extrapolation for migration. *Geophysics*. 2009;74(6):WCA121-WCA128.

doi: 10.1190/1.3202535

53. Wu B, Wu R, Gao J. Preliminary investigation of wavefield depth extrapolation by two-way wave equations. *Int J Geophys*. 2012;2012:968090.

doi: 10.1155/2012/968090

54. Pan J. A new upward and downward wavefield continuation for two-way wave equation migration. In: *SEG Technical Program Expanded Abstracts 2015*. 85th SEG Annual International Meeting; October 18-23, 2015; New Orleans, LA. Society of Exploration Geophysicists; 2015:4180-4184.

doi: 10.1190/segam2015-5829692.1

55. You J, Cao J. Full-wave-equation depth extrapolation for migration using matrix multiplication. *Geophysics*. 2020;85(6):S395-S403.

doi: 10.1190/geo2019-0323.1

56. Li A, Liu X, Zhao Q, You J, Zhu X. Hybrid boundary full-wave-equation depth migration based on dual-sensor acquisition system and its application. *J Appl Geophys*. 2022;203:104679.

doi: 10.1016/j.jappgeo.2022.104679

57. You J, Pan N, Liu W, Cao J. Efficient wavefield separation by reformulation of two-way wave-equation depth-extrapolation scheme. *Geophysics*. 2022;87(4):S209-S222.

doi: 10.1190/geo2021-0629.1

58. Li A, Zhu X, Liu T, Liao J, Liu X, You J. One-step sparse-matrix method for full wave equation depth migration. *Geophysics*. 2024;89(6):S405-S413.

doi: 10.1190/geo2023-0372.1

59. Li A, Li C, Lai F, Liao J, Liu T. An acoustic wave-equation depth migration method using generalized two-way phase shift operator for anisotropic media. *IEEE Geosci Remote Sens Lett*. 2025;22:7504505.

doi: 10.1109/LGRS.2025.3549919

60. Mousavi SM, Beroza GC. Deep-learning seismology. *Science*. 2022;377(6607):eabm4470.

doi: 10.1126/science.abm4470

61. Khosro Anjom F, Vaccarino F, Socco LV. Machine learning for seismic exploration: Where are we and how far are we from the holy grail? *Geophysics*. 2024;89(1):WA157-WA178.

doi: 10.1190/geo2023-0129.1

62. Sheng H, Wu X, Si X, Li J, Zhang S, Duan X. Seismic foundation model: A next-generation deep-learning model in geophysics. *Geophysics*. 2025;90(2):IM59-IM79.

doi: 10.1190/geo2024-0262.1

63. Bashir Y, Alashloo SYM, Ghosh DP. Chapter 3 - Seismic wave modeling and high-resolution imaging. In: Bashir Y,

ed. *Seismic Imaging Methods and Applications for Oil and Gas Exploration*. Elsevier; 2022:57-132.

64. Fu LY, Tang C, Wei W, Du Q. Data-driven double-focusing resolution analyses for seismic imaging. *Geophysics*. 2024;89(4):S311-S324.

doi: 10.1190/geo2023-0064.1

65. Vantassel JP, Bhochhibhoya S. Toward more-robust, AI-enabled subsurface seismic imaging for geotechnical applications. *Comput Geotech*. 2025;187:107443.

doi: 10.1016/j.compgeo.2025.107443

66. Song C, Wang Y. Simulating seismic multifrequency wavefields with the Fourier feature physics-informed neural network. *Geophys J Int*. 2023;232(3):1503-1514.

doi: 10.1093/gji/ggac399

67. Sun J, Zhao Z, Ma J, Yang J. Elastic wavefield decomposition using the physical-constrained neural network and its application on reverse-time migration. *IEEE Trans Geosci Remote Sens*. 2025;63:4505811.

doi: 10.1109/TGRS.2025.3571593

68. Yu Y, Li Y, Wu X, Jia X. Enhancing one-way wave equation-based migration with deep learning. *Geophysics*. 2023;88(1):WA105-WA114.

doi: 10.1190/geo2022-0159.1

69. Li F, Gao J, Sun W, *et al*. LSTM Network Assisted Construction of the Angle-Dependent Point Spread Function and Its Applications in Seismic Imaging. *IEEE Trans Geosci Remote Sens*. 2025;63:5906822.

doi: 10.1109/TGRS.2025.3535529

70. Zou C, Azizzadenesheli K, Ross ZE, Clayton RW. Deep neural Helmholtz operators for 3-D elastic wave propagation and inversion. *Geophys J Int*. 2024;239(3):1469-1484.

doi: 10.1093/gji/ggae342

71. Liu Z, Chen Y, Schuster G. Deep convolutional neural network and sparse least-squares migration. *Geophysics*. 2020;85(4):WA241-WA253.

doi: 10.1190/geo2019-0412.1

72. Torres K, Sacchi M. Least-squares reverse-time migration via deep-learning updated operators. *Geophysics*. 2022;87(6):S315-S333.

doi: 10.1190/geo2021-0491.1

73. Wu B, Hu H, Zhou HW. Convolutional neural network-assisted least-squares migration. *Surv Geophys*. 2023;44(4):1107-1124.

doi: 10.1007/s10712-023-09777-w

74. Mu X, Saad OM, Alkhalifah T. SiameseLSRTM: Enhancing least-squares reverse time migration with a Siamese network. *arXiv*. Preprint posted online May 13, 2025. Last accessed April 3, 2026.

doi: 10.48550/arXiv.2505.08305

75. Chen Y, Huang Y, Huang L. Suppressing migration image artifacts using a support vector machine method. *Geophysics*. 2020;85(5):S255-S268.

doi: 10.1190/geo2019-0157.1

76. Yoo J, Zwartjes P. Attenuation of seismic migration smile artifacts with deep learning. *Artif Intell Geosci*. 2022;3:123-131.

77. Yang L, Fomel S, Wang S, Chen X, Chen Y. Deep learning with soft attention mechanism for small-scale ground roll attenuation. *Geophysics*. 2024;89(1):WA179-WA193.

doi: 10.1190/geo2023-0150.1

78. Wang K, Hu T, Zhao B, Wang S. Surface-related multiple attenuation based on a self-supervised deep neural network with local wavefield characteristics. *Geophysics*. 2023;88(5):V387-V402.

doi: 10.1190/geo2022-0599.1

79. Liu X, Hu T, Wang S. Physics-informed self-supervised learning with phase resemblance constraint for internal multiple attenuation. *IEEE Trans Geosci Remote Sens*. 2024;62:5928113.

doi: 10.1109/TGRS.2024.3462440

80. Fernandez MR, Ettrich N, Delescluse M, Rabaute A, Keuper J. Towards deep learning for seismic demultiple. *Geophys Prospect*. 2025;73(4):1185-1203.

doi: 10.1111/1365-2478.13672

81. Lin L, Zhong Z, Li C, *et al*. Machine learning for subsurface geological feature identification from seismic data: Methods, datasets, challenges, and opportunities. *Earth Sci Rev*. 2024;257:104887.

doi: 10.1016/j.earscirev.2024.104887

82. Zhang W, Gao J, Cheng Y, Li Z, Jiang X, Zhu J. Deep-learning for accelerating least-squares reverse-time migration. *J Appl Geophys*. 2022;200:104645.

doi: 10.1016/j.jappgeo.2022.104645

83. Wu B, Yao G, Ma X, Chen H, Wu D, Cao J. Least-squares reverse time migration of simultaneous sources with deep-learning-based denoising. *Geophysics*. 2024;89(3):S289-S299.

doi: 10.1190/geo2023-0320.1

84. Zhao T, Di H, Abubakar A. Evaluating machine learning-predicted subsurface properties via seismic data reconstruction. *Geophysics*. 2024;89(6):R509-R519.

doi: 10.1190/geo2023-0124.1

ACCSCIENCE PUBLISHING

Journal of Seismic Exploration

ARTICLE

DB-MS-CAN: A robust deep learning framework for microseismic velocity inversion via Dual-Branch Attention and Multi-Scale Feature Aggregation

Aoyu Feng[1], Binxin Hu[2]*, Feng Zhu[1]*, Yang Gao[3], Feifei Jiang[3], Danya Ma[4], and Rong Liu[2]

[1]Shandong Key Laboratory of Optoelectronic Sensing Technologies / National-Local Joint Engineering Laboratory for Energy and Environment Fiber Smart Sensing Technologies, Laser Institute, Qilu University of Technology (Shandong Academy of Sciences), Jinan, Shandong, China

[2]Qilu Institute of Technology, Jinan, Shandong, China

[3]Institute of Rock and Soil Mechanics, Chinese Academy of Sciences, Wuhan, Hubei, China

[4]Jinan Institute of Semiconductor Devices, Jinan, Shandong, China

Abstract

Accurate real-time assessment of underground stress fields is critical for mine safety, yet conventional inversion methods struggle to balance precision with computational efficiency. To address these challenges, we propose the Dual-Branch Multi-Scale Convolutional Attention Network (DB-MS-CAN), which employs a decoupling-and-aggregation strategy. The framework integrates a Dual-Branch Fusion Module (BFM) to isolate sparse transient signals from persistent mining noise and a Multi-Scale Dense Feature Aggregation (MDFA) module to reconstruct complex geological structures across varying spatial scales. To ensure rigorous validation, the model was evaluated on both geologically constrained real-world datasets and an independent synthetic benchmark governed by wave propagation physics. Results demonstrate that DB-MS-CAN achieves a structural similarity index (SSIM) of 0.925 and an root mean square error (RMSE) reduction of approximately 40% compared to traditional ray-based tomography. The proposed model achieved significant performance improvements compared to advanced baselines, including CNN-LSTM and Vision Transformers. Notably, the model maintains high fidelity (correlation coefficient > 0.90) under extreme 0 dB SNR conditions and achieves an inference speed of ~7 seconds per event on a single GPU, outperforming iterative solvers by orders of magnitude. This framework provides a robust and efficient solution for dynamic hazard early warning in deep mining environments.

Keywords: Microseismic inversion; Deep learning; Dual-Branch Attention; Multi-Scale Feature Aggregation

***Corresponding authors:**
Binxin Hu (bxhu@qlu.edu.cn);
Feng Zhu (feng.zhu@sdlaser.cn)

Citation: Feng A, Hu B, Zhu F, *et al*. DB-MS-CAN: A robust deep learning framework for microseismic velocity inversion via Dual-Branch Attention and Multi-Scale Feature Aggregation. *J Seismic Explor*. 2026;35(3):025480121. doi: 10.36922/JSE025480121

Received: November 26, 2025

Revised: February 15, 2026

Accepted: March 9, 2026

Published online: May 6, 2026

Copyright: © 2026 Author(s). This is an Open-Access article distributed under the terms of the Creative Commons Attribution License, permitting distribution, and reproduction in any medium, provided the original work is properly cited.

Publisher's Note: AccScience Publishing remains neutral with regard to jurisdictional claims in published maps and institutional affiliations.

1. Introduction

As coal mining operations extend into deeper strata, dynamic disasters such as rockbursts have become increasingly frequent, posing severe threats to production

safety.[1] High stress concentration within coal-rock masses is the primary driver of such disasters; therefore, real-time and high-precision assessment of the subsurface stress state is critical for production safety.[2] Microseismic velocity inversion, which reconstructs the subsurface velocity field distribution, serves as a critical technique for safety assurance by intuitively reflecting stress concentration areas.[3] However, the complex geological environment of deep mines, coupled with strong background noise and the stringent requirement for real-time warning, imposes significant challenges on existing inversion methods.[4]

Traditional physics-driven methods, such as full waveform inversion FWI and computerized tomography (CT), struggle to balance accuracy with efficiency. Although FWI theoretically achieves high precision, its non-convex objective function leads to a heavy reliance on the initial model, and its iterative computation is too costly for real-time monitoring.[5-8] Conversely, while CT offers high efficiency, its reliance on ray theory often results in blurred boundaries and low resolution in complex heterogeneous structures.[9-11] Therefore, there is an urgent need for a data-driven approach that can deliver high-resolution imaging without the computational burden of iterative physics solvers.[12]

In recent years, deep learning (DL) has shown promise in geological inversion by learning non-linear mappings from data.[13,14] However, directly applying generic computer vision architectures, such as U-Net or Convolutional Neural Networks (CNNs), to microseismic velocity inversion is challenging because these techniques overlook the unique physical characteristics of microseismic data.[15-17] Unlike natural images with persistent objects, effective microseismic signals, such as P/S wave onsets, are sparse and transient, occupying only a fraction of the time series.[18,19] Generic convolutional operations treat all time steps equally, often obscuring critical spikes in continuous background noise, leading to feature dilution and noise overfitting.[20]

Furthermore, subsurface media exhibit extreme multi-scale heterogeneity, ranging from meter-scale micro-fractures to kilometer-scale fault zones.[21] Standard encoders with fixed receptive fields either fail to capture minor anomalies, resulting in underfitting, or blur large geological boundaries, leading to over-smoothing.[22]

Existing deep learning solvers usually handle spatiotemporal features ambiguously. Strictly spatial models, such as the standard U-Net, inherently struggle to capture the sequential dependencies in microseismic waveforms, resulting in temporal feature loss. While standard recurrent models, such as the Long Short-Term Memory (LSTM), can capture temporal dependencies, they incur high computational costs and do not explicitly address the extreme spatial-scale differences inherent in subsurface structures.

Moreover, emerging advanced paradigms also face specific limitations in microseismic velocity inversion. While Physics-Informed Neural Networks (PINNs) enforce consistency, they often suffer from over-smoothing and boundary blurring due to soft regularization constraints, which attenuates the peak velocity values of stress concentration zones. Conversely, Vision Transformer-based models, despite their superior global context modeling, inherently introduce blocky artifacts and jagged edges owing to their patch-based processing mechanisms, thereby compromising the pixel-level fidelity required for precise hazard detection.

To address these challenges, this study presents the Dual-Branch Multi-Scale Convolutional Attention Network (DB-MS-CAN). Built upon a "Decoupling-and-Aggregation" principle, the framework establishes a unified mapping mechanism to resolve the inherent conflict between transient signal extraction and multi-scale structural reconstruction. Recognizing that mining environments require resolving sharp velocity gradients, we employ a U-Net-based CNN architecture; its local receptive fields and skip connections are inherently superior for preserving high-frequency spatial information and recovering velocity extremums compared to global optimization or patch-based methods. Specifically, the architecture integrates two core components: the Dual-Branch Fusion Module (BFM), which decouples high-frequency transients from background noise, and the Multi-Scale Dense Feature Aggregation (MDFA) module, designed to capture geological heterogeneities across varying spatial scales. To ensure industrial relevance, the model was validated against geologically constrained offline tomography derived from borehole logging and active surveys. Experimental results demonstrate that DB-MS-CAN achieves a structural similarity index (SSIM) of 0.925, significantly outperforming baseline models and proving its efficacy for high-precision monitoring in complex coal mine settings.

2. Methods

2.1. Overall model architecture

As illustrated in Figure 1, the framework integrates two specialized components into a U-Net-like backbone.[23-25] The overall data flow within the network advances through a progressive processing cascade, comprising three distinct integration phases:

The network extracts hierarchical features via successive convolutions.[26-28] Unlike standard architectures, we embed the MDFA module directly into the deep encoding layers. By applying parallel dilated convolutions, MDFA encodes spatially enriched features that represent multi-scale structural information before significant downsampling occurs.

The data flow then converges at the network bottleneck, where the global context is compressed. At this critical junction, the BFM module is embedded to process the latent features. Through a dual-branch attention mechanism, BFM filters features along the temporal dimension, ensuring that only significant transient phases are preserved while background noise is suppressed.

Finally, the decoder reconstructs the velocity field via progressive upsampling.[29] The reconstruction process synergistically leverages the multi-scale spatial representations encoded by MDFA and the noise-suppressed temporal features refined by BFM, effectively mitigating the trade-off between structural continuity and boundary sharpness.

2.2. Multi-Scale Dense Feature Aggregation (MDFA)

To explicitly resolve the multi-scale heterogeneity of subsurface structures,[30] the MDFA module (Figure 2) employs parallel dilated convolutions with varying dilation rates as a scale-adaptive feature extractor.

We implemented the MDFA module using multi-scale dilated convolution and a spatial recalibration mechanism.

Multi-Scale Dilated Convolution: Distinct from generic multi-scale modules, we designed the dilation rates (d) to correspond to specific geological targets.[31] The small dilation branch with $d = 6$ is designed to capture high-frequency scattering effects induced by local micro-fractures and small voids. Conversely, the large dilation branches with $d = 12$ and 18 expand the receptive field to model macroscopic waveform variations caused by large-scale faults and lithological boundaries.

Mathematically, let the input feature tensor be $X \in \mathbb{R}^{C_{in} \times H \times W}$. The output Y_i of the i-th dilated convolutional branch is defined as:

$$\boldsymbol{Y}_i = \mathrm{ReLU}\left(\boldsymbol{W}_i \circledast_{d_i} \boldsymbol{X} + \boldsymbol{b}_i\right), i \in \{1,2,3\} \quad (1)$$

where $\circledast_{d_i}$ denotes the 2D dilated convolution operation with a dilation rate of d_i; W_i and b_i are the learnable weight matrix and bias vector for the i-th branch; $\mathrm{ReLU}(\cdot)$ is the Rectified Linear Unit activation function.

By aggregating these multi-branch features, the MDFA module effectively constructs a feature pyramid to ensure that the inverted velocity model preserves both the sharpness of micro-anomalies and the continuity of macro-structures.

Feature Fusion and Spatial Recalibration: The final high-accuracy velocity model is a synthesized representation of all these multi-scale features. However, simple

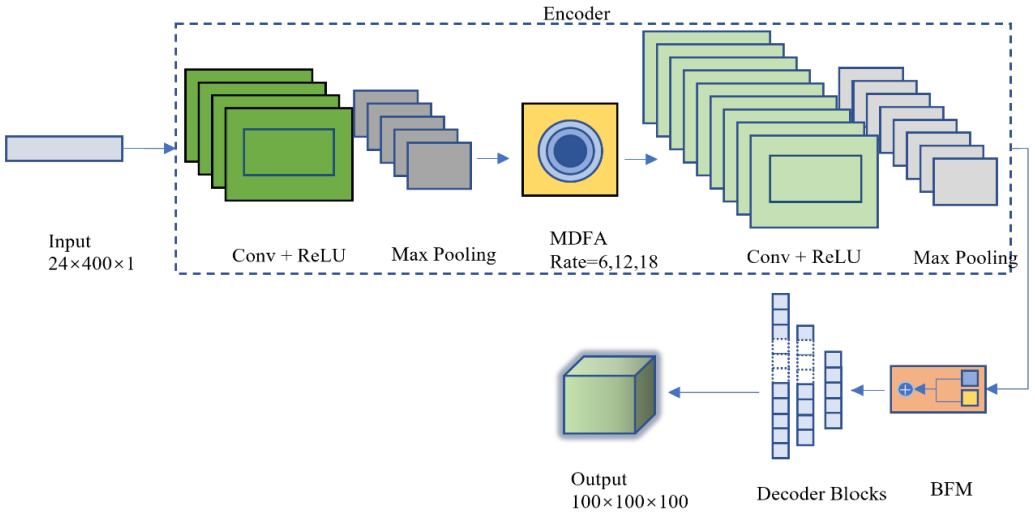

Figure 1. The overall network architecture
Abbreviations: BFM: Dual-Branch Fusion Module; MDFA: Multi-Scale Dense Feature Aggregation; ReLU: Rectified Linear Unit.

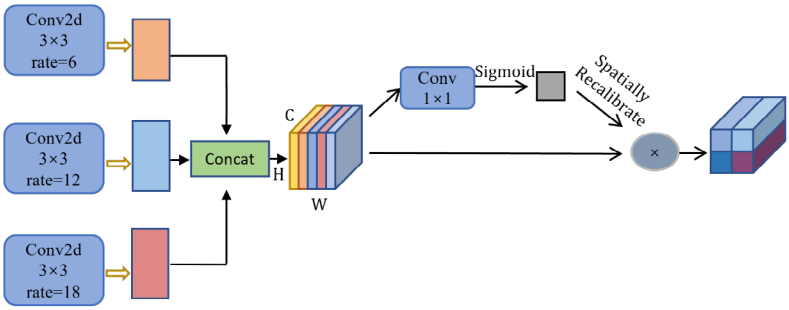

Figure 2. Multi-Scale Dense Feature Aggregation (MDFA) structure diagram

feature concatenation often struggles with semantic inconsistencies among features extracted at different scales. To ensure the coherent integration of information from micro-anomalies to macroscopic structures, we introduced a Spatial Recalibration Mechanism into our proposed MDFA module. This mechanism adaptively learns spatial attention weights to screen and strengthen the spatial locations most critical for the velocity inversion task.

First, the multi-scale features from all branches are concatenated along the channel dimension to obtain the aggregated feature U:

$$U = \mathrm{Concat}\left(Y_1, Y_2, Y_3\right) \in \mathbb{R}^{3C_{out} \times H \times W} \tag{2}$$

where Y_1, Y_2, and Y_3 correspond to the feature maps extracted by the branches with dilation rates $d = 6, 12$, and 18, respectively. C_{out} denotes the number of output channels for each individual branch (set to 64 in our experiments), and H and W represent the spatial height and width of the feature maps, which remain consistent due to padding operations.

Subsequently, a 1×1 convolutional layer is applied to the aggregated feature U to perform dimensionality reduction and cross-channel interaction, followed by a Sigmoid function to generate the spatial attention map A:

$$A = \sigma\left(W_{cal} \circledast_1 U + b_{cal}\right) \in \mathbb{R}^{1 \times H \times W} \tag{3}$$

where W_{cal} and b_{cal} denote the learnable weight matrix and bias vector of the spatial calibration convolution, respectively. The symbol $\circledast_1$ represents the 1×1 convolution operation, and $\sigma(\cdot)$ denotes the Sigmoid activation function used to normalize the attention weights to the range $(0,1)$.

Finally, the output Y_{out}—the spatially recalibrated feature—is obtained by applying the attention map to the aggregated feature via element-wise multiplication (Hadamard product):

$$Y_{out} = A \odot U \tag{4}$$

where $\odot$ is the Hadamard product.

This mechanism ensures that the model dynamically adjusts its focus based on the complexity of the geological structure. It produces a high-precision velocity model that retains local fracture details while accurately representing overall structural trends.

Figure 3 shows the intermediate feature maps from the encoder's bottleneck layer, illustrating how our proposed MDFA module addresses spatial-scale conflicts for a typical microseismic event. The red dashed lines are the ground truth reference for the velocity anomaly boundary. As observed in Figure 3A, the branch driven by small dilation rates (d = 6) prioritizes high-frequency scattering information. The resulting map exhibits rich textural details indicative of micro-fracture zones but suffers from a diffuse spatial distribution. In contrast, the large dilation branch (d = 18), shown in Figure 3C, captures the low-frequency envelope of the geological body, demonstrating strong morphological consistency with the ground-truth boundary. However, the internal activation intensity remains relatively subdued. Ultimately, the final spatially recalibrated output (Figure 3D) effectively synthesizes these complementary features. It retains the sharp, coherent structural boundaries derived from the macro-branch while simultaneously preserving the high-intensity internal details from the micro-branch. This visual evidence confirms that MDFA successfully mitigates the trade-off between boundary precision and internal detail resolution.

2.3. Dual-Branch Fusion Module (BFM)

The Dual-Branch Fusion Module (BFM), illustrated in Figure 4, employs a dual-path architecture. It is designed to mitigate the blurring of sparse high-frequency transients by decoupling the input into two streams and fusing them via a channel-spatial attention mechanism.[32,33]

Dual-Branch Structure: The local branch functions as a transient feature extractor. To adaptively capture waveform spikes with varying pulse widths, we employed a multi-kernel structure consisting of parallel 3 × 3, 5 × 5, and 7 × 7 convolutions to adaptively emphasize instantaneous P/S onsets. Mathematically, given the input feature X, the local feature map Y_{local} is defined as:

$$Y_{local} = \mathrm{ReLU}\left(\sum_{k\in\{3,5,7\}} W_{k\times k} \circledast X + b_{k\times k}\right) \tag{5}$$

where $W_{k\times k}$ and $b_{k\times k}$ denote the learnable weights and biases of the convolutional kernels with sizes $3\times3, 5\times5, 7\times7$, respectively; and $\circledast$ denotes the convolution operation; and $\mathrm{ReLU}(\cdot)$ is the activation function.

We created a Global Branch to serve as a context encoder, using Global Average Pooling (GAP) to model signal decay and background noise trends.[34] This technique provides the necessary context to distinguish real events from coherent noise.[35,36] The global feature vector V_{global} is computed as:

$$V_{global} = W_{1\times1} \circledast \left(\mathrm{GAP}\left(X\right)\right) + b_{1\times1} \tag{6}$$

where $\mathrm{GAP}(\cdot)$ denotes the Global Average Pooling operation, and $W_{1\times1}$ and $b_{1\times1}$ are the 1×1 Convolutional kernel weights and bias, respectively. Finally, the global feature is upsampled back to the dimension of Y_{local} to form the global feature map Y_{global}.

Channel-Spatial Attention Mechanism and Feature Fusion: Following the feature extraction, the dual (streams are integrated via element-wise summation ($F = Y_{local} \oplus Y_{global}$) and refined through an attention mechanism specifically tailored for multi-channel microseismic data. The Channel Attention mechanism serves as a sensor weighting filter. The mechanism autonomously learns to prioritize channels with coherent signal patterns. This is formulated as:

$$M_c\left(F\right) = \sigma\left(\mathrm{FC}\left(\mathrm{GAP}\left(F\right)\right) + \mathrm{FC}\left(\mathrm{GMP}\left(F\right)\right)\right) \tag{7}$$

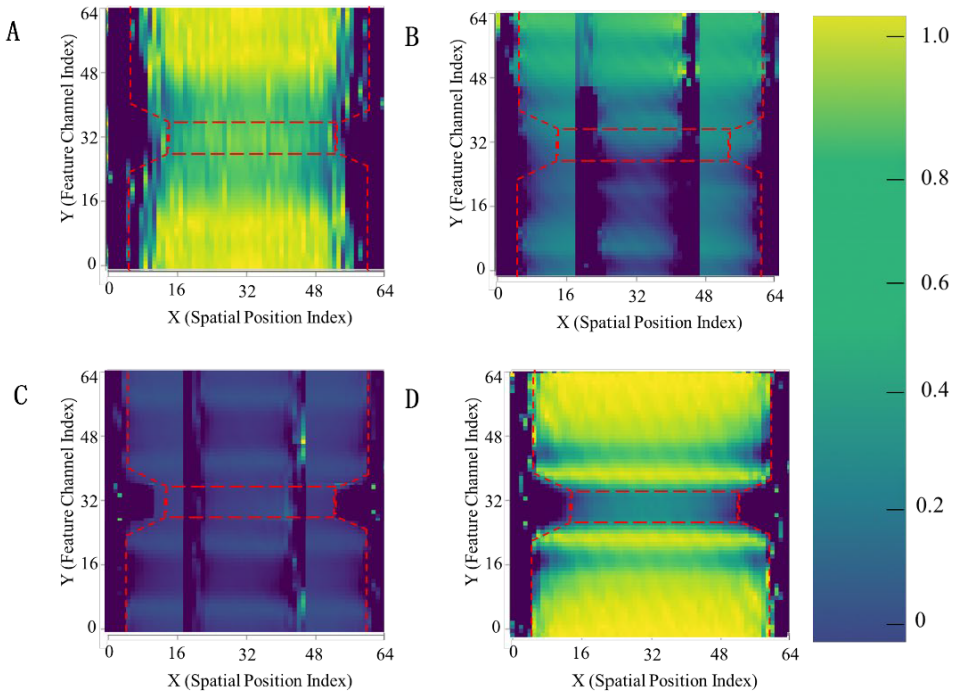

Figure 3. Visualization of intermediate feature maps from Multi-Scale Dense Feature Aggregation (MDFA) branches. The color scale indicates normalized activation intensity (0.0–1.0). The X and Y axes represent spatial position indices (64 × 64). Red dashed lines denote the reference boundary of the velocity anomaly. (A)–(C) Feature maps corresponding to dilation rates d = 6,12, and 18, respectively. (D) The final spatially recalibrated feature map after fusing (A), (B), and (C).

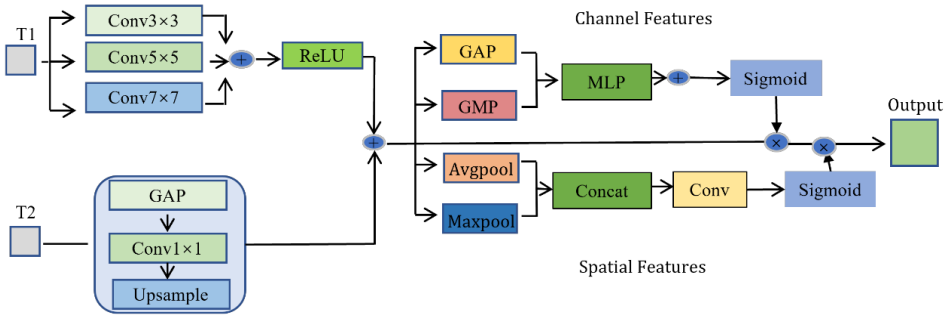

Figure 4. Branch Fusion Module (BFM) structure diagram
Abbreviations: GAP: Global Average Pooling; GMP: Global Max Pooling; MLP: Multilayer Perceptron; ReLU: Rectified Linear Unit.

where $GAP(\cdot)$ and $GMP(\cdot)$ denote the Global Average Pooling and Global Max Pooling operations, respectively. FC denotes the shared Fully Connected layers applied to the feature vectors, and σ denotes the Sigmoid activation function.

At the same time, the Spatial Attention mechanism provides temporal focus by highlighting critical arrival windows, reducing pre-event noise and coda waves. Its calculation is defined as:

$$M_s(F) = \sigma\left(W_{1\times1} \circledast \left[\text{AvgPool}(F); \text{MaxPool}(F)\right]\right) \tag{8}$$

where $AvgPool(\cdot)$ and $MaxPool(\cdot)$ represent average-pooling and max-pooling operations along the channel axis. The symbol $[;]$ denotes the concatenation operation. $W_{1\times1}$ represents the learnable weights of the 1×1 convolution (denoted as $\circledast$) used to compress the channel information into a single spatial map.

The final output Y_{fused} is obtained by modulating the fused features via element-wise multiplication, ensuring the network prioritizes significant spatiotemporal regions:

$$Y_{fused} = \left(M_c(F) \odot F\right) \odot M_s(F) \tag{9}$$

where $\odot$ denotes the Hadamard product (element-wise multiplication).

Figure 5 visualizes the intermediate activations of the BFM module to verify its decoupling capability. As shown in Figure 5A, the local branch exhibits a sharp activation peak at $t = 1.8s$ (normalized intensity approaching 0.95) effectively isolating the high-frequency P/S wave onsets from the background; whereas the global branch (Figure 5B) suppresses these transient pulses to retain the wavefield background trend. Regarding channel reliability, Figure 5C demonstrates distinct selectivity: the network assigns dominant weights to sensors with strong coherence (*e.g.*, Channel 7 = 0.78 and Channel 3 = 0.70), while heavily suppressing the noise-dominated Channel 2 (weight = 0.13). This significant quantitative disparity (> 6-fold difference) confirms that the mechanism has implicitly learned to prioritize high-quality signals through optimization. Finally, the spatial attention mask in Figure 5D reaches its maximum intensity (> 0.9) precisely at the 1.8 s window, aligning accurately with the signal arrival time, verifying that the model autonomously achieves temporal focusing without explicit physical programming.

3. Results

3.1. Data acquisition and preprocessing

The model proposed in this study was trained and validated using real-world microseismic monitoring data collected from an operating mine. The data acquisition zone is located near the deep mining face of a large-scale coal mine in Shanxi Province. Within this region, a high-density microseismic monitoring network comprising 24 triaxial geophones was deployed to capture microseismic events and subsurface velocity variations with high precision. The detailed sensor layout is illustrated in Figure 6.

3.1.1. Construction of the ground truth velocity field

To ensure the physical fidelity of the training labels, the velocity models used as ground truth, denoted as V_{gt}, were constructed through a geologically constrained offline inversion workflow, integrating *in situ* exploration data. This distinguishes them from the unconstrained real-time CT results used for baseline comparison.

The label generation process involves three key stages:

(i) Reference Model Construction: We utilized detailed geological logging data and exploration reports to build an initial velocity model. Precise travel-time pickings of P-wave and S-wave arrivals from a substantial historical dataset (exceeding 1,200 events)

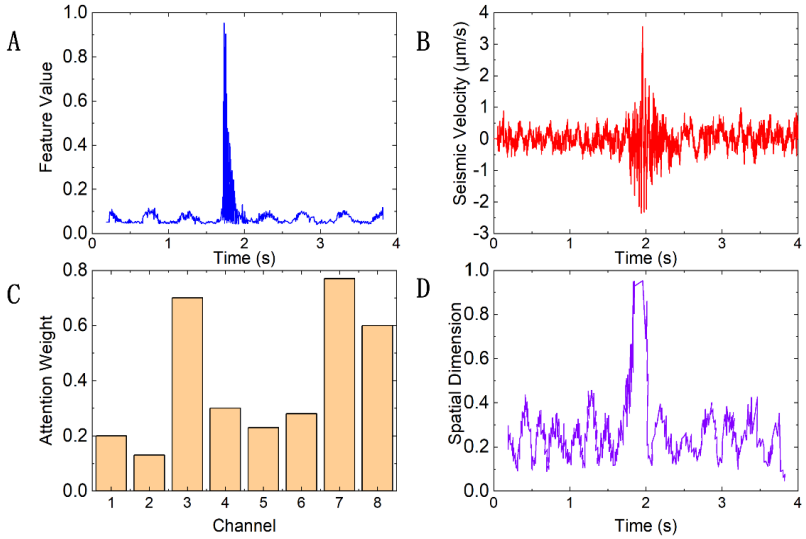

Figure 5. Visualization of intermediate variables within the Branch Fusion Module (BFM) module. (A) Local branch output captures high-frequency transient features, specifically responding to the sharp P/S wave onsets. (B) Global branch output represents the low-frequency background trends and global wavefield context. (C) Channel attention weights indicates the learned reliability of each sensor channel (treating sensors as feature channels). (D) Spatial attention weights defines the attention mask along the feature map's spatial dimension (which corresponds to the temporal axis in microseismic waveforms).

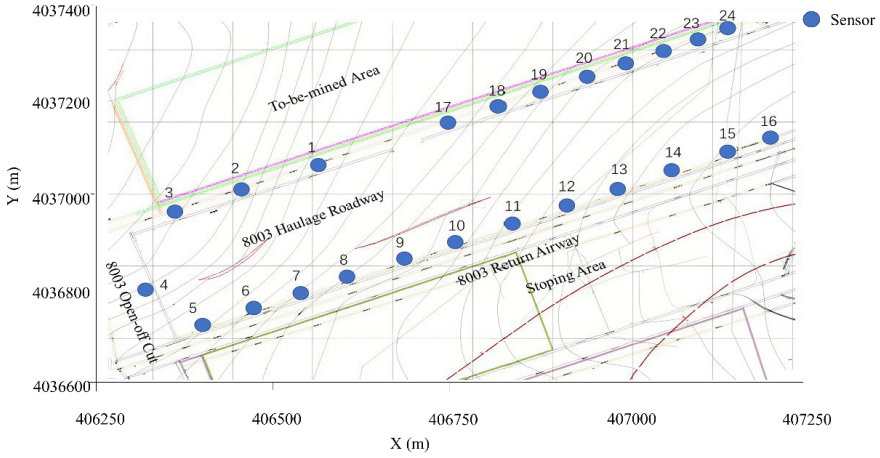

Figure 6. Sensor distribution diagram

were employed as constraints.[37]

(ii) Constrained Offline Tomography: Based on the reference model, we executed a Geologically Constrained offline inversion utilizing the Simultaneous Iterative Reconstruction Technique (SIRT). To ensure the high fidelity of the ground truth (V_{gt}), the input travel-time data underwent rigorous manual inspection by experienced geophysicists, achieving a picking precision of approximately 10 ms, followed by 30 iterations of recursive refinement to minimize the RMS error.

(iii) Grid Discretization: The final inverted velocity field was discretized into a 100×100×100 three-dimensional grid with a uniform spatial resolution of 10m×10m×10m. The resulting velocity values range between 3500 m/s and 5500 m/s.

The physically constrained tomographic result (V_{gt}) integrates actual geological measurements with large-scale microseismic data,[38] providing a high-quality target for the

deep learning model.

3.1.2. Data input and standardization

The model input consists of multi-channel waveforms recorded by 24 sensors for each microseismic event. All waveforms were uniformly truncated to 400 time sampling points, with a sampling rate of 2 kHz. The input tensor dimension is therefore $X \in \mathbb{R}^{24\times400\times1}$.

The dataset comprises 1,600 microseismic events. To ensure a rigorous evaluation and prevent data leakage, this dataset is strictly temporally mutually exclusive from the historical dataset (exceeding 1,200 events) used for ground truth construction. We partitioned the data into a training set (1,120 events), a validation set (240 events), and a testing set (240 events).

To eliminate dimensional differences among sensor channels, we standardized the input waveforms using the Z-score transformation. This standardization transformed the data to have a zero mean and unit standard deviation before passing it to the model for training. The output velocity model labels were also Min-Max normalized within a range of [0,1].

To comprehensively evaluate the proposed model's performance, a statistical analysis of the dataset's characteristics was conducted. The training, validation, and testing sets maintained consistent distributions across key attributes, including event magnitude, average signal-to-noise ratio (SNR), and spatial coverage, as detailed in Table 1. This process ensured fairness and the model's generalization assessment. Furthermore, the high-dimensional input tensor provides a rich feature space, offering sufficient information density for the network to extract robust physical representations.

3.2. Model training strategy and configuration

The proposed DB-MS-CAN was implemented using the PyTorch framework on a workstation equipped with an Intel Core i9-14900HX CPU and an NVIDIA GeForce RTX 4060 GPU. The training process utilized the Adam optimizer[39] with an initial learning rate of 1×10^{-4}, dynamically modulated by a Cosine Annealing schedule. We configured a batch size of 16 with a maximum duration of 500 epochs, employing an Early Stopping mechanism (patience = 20) based on validation loss to mitigate overfitting. The mean squared error (MSE) served as the objective function to minimize voxel-wise discrepancies between the predicted velocity field $\hat{V}$ and the ground truth V_{gt}. Regarding model complexity, the network comprises approximately 31.2 million trainable parameters. Notably, the proposed core innovations are designed to be extremely lightweight: the MDFA and BFM modules contain only 35,712 and 170,596 parameters, respectively. Together, they constitute less than 1% of the total model size while contributing to significant performance gains. The training phase required approximately 1.5 minutes per epoch, resulting in a total computation time of roughly 12 hours.

Figure 7 illustrates the training and validation loss curves of the DB-MS-CAN model, which show distinct trends reflecting the model's learning dynamics. As observed, the training loss exhibits a rapid descent within the first 50 epochs, indicating that the gradient descent algorithm effectively optimized the network weights. The validation loss closely follows the training loss trend without diverging, stabilizing at approximately 0.05 after 150 epochs. The minimal gap between the training and validation curves confirms that the Early Stopping mechanism (patience = 20) and Dropout layers successfully prevented overfitting. The smooth convergence behavior in the later stages demonstrates the stability of the proposed DB-MS-CAN architecture under the Adam optimizer.

3.3. Experimental results and analysis

3.3.1. Comparison with advanced deep learning models

Table 1. Microseismic dataset partition and feature statistics for the deep learning model

Dataset	Number of events	Magnitude range (ML)	Average SNR (dB)	Spatial distribution area
Training set	1120	[−1.5, 2.0]	15.2	Covers the entire working face
Validation set	240	[−1.3, 1.8]	14.8	Covers the entire working face
Test set	240	[−1.6, 1.9]	15.1	Covers the entire working face

To validate the effectiveness and superiority of the proposed DB-MS-CAN model, the U-Net, Attention U-Net,CNN,[40,41] Attention CNN,[42] CNN-LSTM,[43] and DB-MS-CAN architectures were trained and evaluated separately on the same dataset. The quantitative performance comparison is summarized in Table 2. All metrics in this and subsequent tables are reported as mean ± standard deviation, calculated across the 240 independent events in the test set. The visual comparison is presented in Figure 8.

Figure 8 visually compares the velocity inversion performance across different models, spanning from background low-velocity zones (~3500–4000 m/s) to high-velocity stress concentration areas (4800–5500 m/s). Visual inspection reveals clear limitations in the baseline architectures. The CNN and U-Net models (Figure 8A and 8C) suffer from significant over-smoothing, characterized by blurred boundaries in the left low-velocity anomaly and an inability to resolve fine textures in the bottom-right zone. They also tend to spatially exaggerate the central high-velocity core (> 5200 m/s), leading to an overestimated stress concentration area. These visual deficiencies align with their stagnant performance metrics, with root mean square error (RMSE) values persisting at 2.63–2.65 %. While adding spatial attention mechanisms (Figure 8Band 8D) yields slight morphological improvements in transitional layers, these models fail to correct global velocity deviations. Similarly, although the CNN-LSTM model (Figure 8E) improves structural continuity, it introduces local distortions by excessively enlarging the upper high-velocity region.

In contrast, the proposed DB-MS-CAN (Figure 8F) delivers an inversion result most consistent with the geological ground truth. It precisely reconstructs the low-velocity core (3600–3800 m/s) and resolves complex velocity gradients, effectively correcting the spatial artifacts observed in the baselines. This visual superiority is supported by rigorous statistical evidence. The model achieves a state-of-the-art SSIM of 0.925 ± 0.008 and reduces the RMSE to 2.17 ± 0.11 %. A paired *t*-test against the best-performing baseline (CNN-LSTM) yielded a *p*-value < 0.001, confirming that this performance gain is statistically significant rather than a result of random chance. Moreover, our method exhibits the lowest standard deviation among all models (*e.g.*, compared to CNN's ± 0.021), indicating that the architecture effectively mitigates stochastic instability and ensures consistent inversion results across diverse geological conditions.

3.3.2. Module ablation experiment

To further assess the specific contributions of the BFM and MDFA modules to the overall model performance, a module ablation study was designed in this research. Four distinct model variants were constructed for comparative analysis:

(i) Baseline Model (U-Net): Employs only the traditional U-Net structure, without incorporating any additional mechanisms.
(ii) BFM-Only (U-Net + BFM): Introduces the BFM solely at the bottleneck layer.
(iii) MDFA-Only (U-Net + MDFA): Integrates the

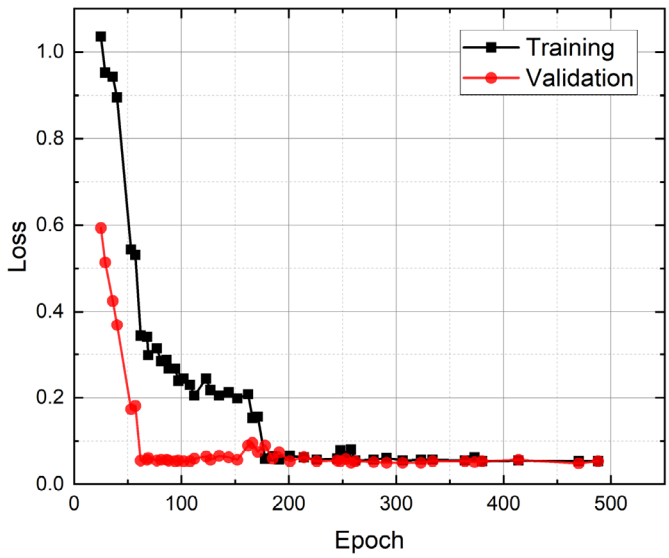

Figure 7. Training loss and validation loss

Table 2. Comparison of inversion results between DB-MS-CAN and existing deep learning models

Model	SSIM (mean ± SD)	RMSE (%) (mean ± SD)	R (mean ± SD)
CNN	0.715 ± 0.021	2.65 ± 0.28	0.940 ± 0.015
U-Net	0.735 ± 0.019	2.63 ± 0.25	0.939 ± 0.013
Attention CNN	0.785 ± 0.016	2.57 ± 0.19	0.945 ± 0.010
CNN-LSTM	0.865 ± 0.012	2.43 ± 0.15	0.954 ± 0.007
Attention U-Net	0.795 ± 0.014	2.59 ± 0.17	0.941 ± 0.009
DB-MS-CAN	0.925 ± 0.008	2.17 ± 0.11	0.968 ± 0.004

Abbreviations: CNN: Convolutional Neural Network; DB-MS-CAN: Dual-Branch Multi-Scale Convolutional Attention Network; LSTM: Long Short-Term Memory; RMSE: Root mean square error; SSIM: Structural similarity index.

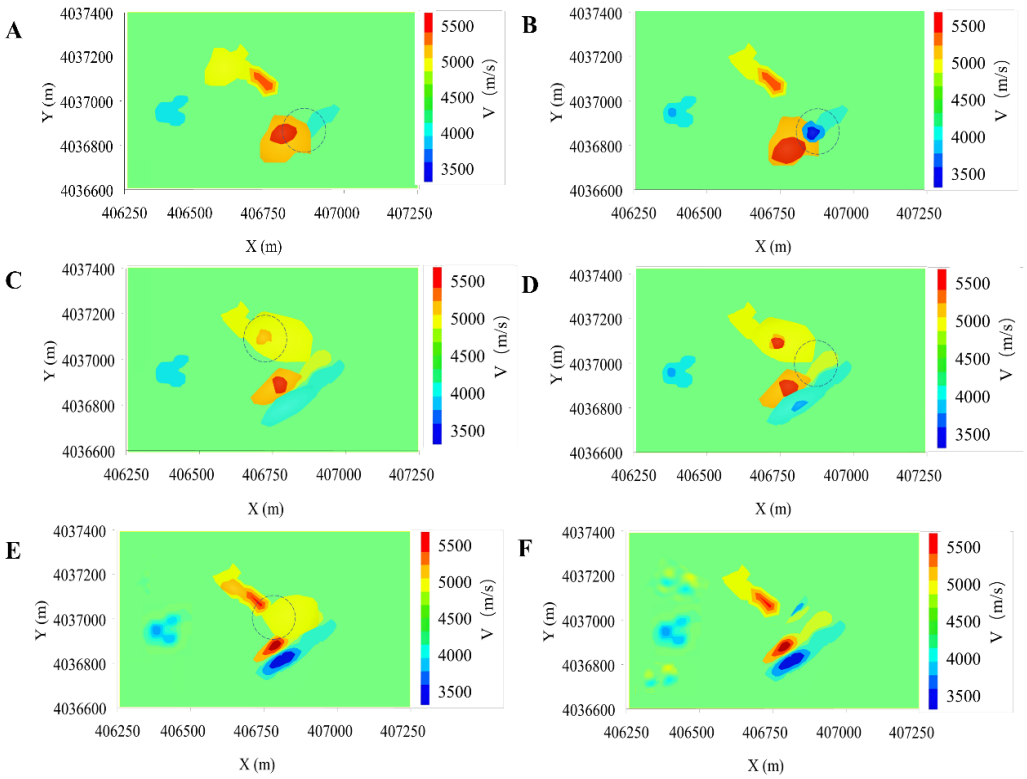

Figure 8. Visual comparison of microseismic velocity inversion results generated by various deep learning models. (A) U-Net; (B) Attention U-Net; (C) CNN; (D) Attention CNN; (E) CNN-LSTM; (F) DB-MS-CAN. The dashed-line circles point out the failure of baseline models to accurately reconstruct the local velocity anomalies, which are well preserved in (F).
Abbreviations: CNN: Convolutional Neural Network; DB-MS-CAN: Dual-Branch Multi-Scale Convolutional Attention Network; LSTM: Long Short-Term Memory.

MDFA mechanism solely within the intermediate layers of the encoder.

(iv) DB-MS-CAN: Represents the final, comprehensive network architecture proposed in this paper.

Figure 9 visualizes the ablation study results against this benchmark. The baseline U-Net (Figure 9A) exhibits characteristic over-smoothing, failing to resolve the high-velocity core or define the low-velocity zone (< 4000 m/s). This structural deficiency is reflected in the poorest performance metrics: an SSIM of 0.733 ± 0.019 and an RMSE of 2.65 ± 0.26 %.

Integrating specific modules yields distinct improvements. The MDFA module (Figure 9C) enhances macroscopic spatial continuity, evolving the patchy low-velocity structure into a coherent geological body. This improves the SSIM to 0.812 ± 0.015; however, the model struggles to recover peak high-velocity intensities, limiting RMSE reduction to 2.54 ± 0.18 %. In contrast, the U-Net-BFM variant (Figure 9B) excels at sharpening local boundaries and filtering noise. It successfully recovers the high-velocity core (> 5000 m/s), reducing the RMSE to 2.48 ± 0.14 %, though the background strata morphology remains discontinuous.

The proposed DB-MS-CAN (Figure 9D) integrates these complementary advantages, retaining MDFA-derived stratification and BFM-captured high-intensity cores. This completeness translates to state-of-the-art performance, achieving a peak SSIM of 0.925 ± 0.008 and a minimum RMSE of 2.17 ± 0.10 %.

Table 3 reveals a progressive reduction in metric variance as modules are integrated (SSIM standard deviation decreases from ± 0.019 to ± 0.008). This trend confirms that introducing domain knowledge—multi-scale constraints and transient signal decoupling—acts as a strong regularization factor. By constraining the solution space to geologically plausible manifolds, the full model significantly enhances inversion stability and reproducibility.

As additional modules are integrated, the overall running time of the model increases, as illustrated in Figure 10. However, this computational cost is acceptable considering the significant performance improvements.

3.3.3. Comparative verification with known ground truth

To mitigate field label uncertainty and evaluate the theoretical limits of DB-MS-CAN, we developed a synthetic benchmark following the microseismic perturbation framework. Unlike simplified layered models, our benchmark employs a physically-constrained stochastic strategy to embed high-contrast polygonal anomalies (V > 5200 m/s) and low-velocity voids (V < 3800 m/s). To bridge the 'simulation-to-reality' gap, high-order finite-difference modeling was employed, with site-specific industrial noise superimposed to ensure model robustness under complex field SNR conditions.

Utilizing this benchmark, we compare our method against two advanced baselines: PINN[44] (physics-driven) and a Vision Transformer-based network[45] (data-driven). To ensure a fair comparison, all baseline models were implemented using standard training protocols widely adopted in recent literature and were trained to convergence under identical hardware environments.

Figure 11A presents the ground truth velocity model, constructed based on rock mechanics principles to simulate a heterogeneous mining environment. Featuring a high-velocity stress concentration zone (> 5000 m/s) and a low-velocity void (< 3800 m/s), the significant contrast

Table 3. Ablation study results of components in the DB-MS-CAN model

Model	SSIM (mean ± SD)	RMSE (%) (mean ± SD)	R (mean ± SD)
U-Net	0.733 ± 0.019	2.65 ± 0.26	0.940 ± 0.014
U-Net-MDFA	0.812 ± 0.015	2.54 ± 0.18	0.947 ± 0.009
U-Net-BFM	0.855 ± 0.011	2.48 ± 0.14	0.951 ± 0.007
DB-MS-CAN	0.925 ± 0.008	2.17 ± 0.10	0.968 ± 0.004

Abbreviations: BFM: Dual-Branch Fusion Module; DB-MS-CAN: Dual-Branch Multi-Scale Convolutional Attention Network; MDFA: Multi-Scale Dense Feature Aggregation; RMSE: Root mean square error; SSIM: Structural similarity index.

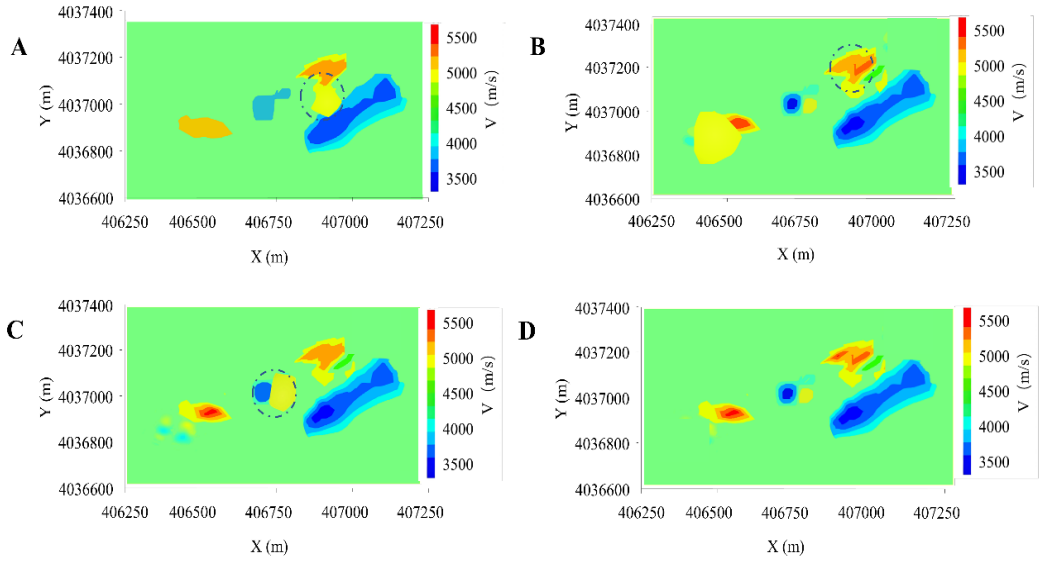

Figure 9. Velocity inversion images of (A) U-Net, (B) U-Net-BFM, (C) U-Net-MDFA, and (D) DB-MS-CAN. The dashed-line circles in (A) through (C) point out the reconstruction defects of the baseline and ablated models compared to the proposed architecture.
Abbreviations: BFM: Dual-Branch Fusion Module; DB-MS-CAN: Dual-Branch Multi-Scale Convolutional Attention Network; MDFA: Multi-Scale Dense Feature Aggregation.

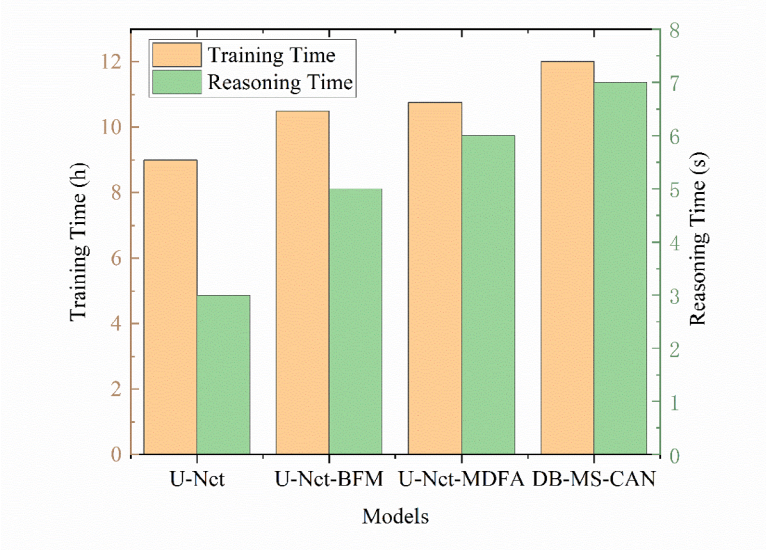

Figure 10. Training time and inference time
Abbreviations: BFM: Dual-Branch Fusion Module; DB-MS-CAN: Dual-Branch Multi-Scale Convolutional Attention Network; MDFA: Multi-Scale Dense Feature Aggregation.

(> 1200 m/s) serves as a precise benchmark for evaluating boundary delineation capabilities.

Against this benchmark, the PINN method (Figure 11B) successfully identifies the relative positions of the low-velocity void (blue region) and the high-velocity stress zone, demonstrating that physical constraints effectively guide the model toward a geologically plausible solution. However, visual inspection reveals significant over-smoothing, characterized by blurred high-stress zone boundaries and a failure to recover peak intensities. This amplitude attenuation, induced by soft physical regularization, results in suboptimal quantitative metrics: an SSIM of 0.875 ± 0.024 and an RMSE of 2.90 ± 0.32%. The notably large standard deviation (± 0.32) suggests

that convergence remains highly sensitive to initial weight distributions and the balancing of loss terms.

Similarly, the Vision Transformer-based network (Figure 11C) exhibits exceptional global context modeling capabilities. Benefiting from its self-attention mechanism, it achieves accurate macro-scale positioning of anomalies, which is reflected in a high Pearson correlation coefficient (R = 0.952). Nevertheless, the result is compromised by visible blocky artifacts and jagged discontinuities along anomaly boundaries, a consequence of its patch-based processing mechanism. This local fragmentation limits pixel-level fidelity, yielding an RMSE of 2.87 ± 0.25%, which offers no significant improvement over the PINN baseline.

In contrast, the proposed DB-MS-CAN (Figure 11D) delivers superior reconstruction performance. It is worth noting that its reconstruction of the homogeneous background is slightly less smooth than that of the PINN, with minor textural fluctuations observable. This is a characteristic behavior of CNN-based architectures inferring from local receptive fields rather than global governing equations. However, this minor background noise does not affect the identification of the high-stress anomaly, which is the primary objective of safety monitoring. Crucially, the model effectively eliminates baseline artifacts, precisely recovering sharp geometric boundaries and physical extremum values (> 5200 m/s). This fidelity translates into state-of-the-art metrics: a peak SSIM of 0.918 ± 0.009 and a minimum RMSE of 1.96 ± 0.12%. The significantly lower variance (±0.009) demonstrates the architecture's exceptional robustness in resolving complex geological heterogeneities.

3.4. Field validation

3.4.1. Comparison with traditional methods

To comprehensively evaluate the performance of the proposed method, this section compares the DB-MS-CAN model with two representative traditional velocity inversion techniques: passive seismic tomography (CT) and FWI. For a rigorous comparison, strictly identical test data from the mining area described in Section 3.1 were used for all inversion tasks. The implementation details and configuration strategies for the traditional methods are as follows:

(i) Passive CT: Implemented using the fast sweeping method (FSM) for forward modeling and the Least Squares with QR-factorization (LSQR) algorithm for inversion, with a grid resolution of 10 × 10 m.

(ii) FWI configuration: We employed a time-domain acoustic FWI with a multi-scale inversion strategy to effectively mitigate cycle-skipping. Specifically, a smoothed one-dimensional velocity model derived from pilot surveys was utilized as the initial model. The inversion process was executed sequentially across three frequency bands: 0–30 Hz, 0–60 Hz, and 0–120 Hz. We adopted the L-BFGS optimizer (memory depth of 10) with strict stopping criteria, terminating iterations when the relative change in the objective function fell below 1×10^{-4} or reached a maximum of 50 iterations per band. Finally, the inversion grid was refined to a resolution of 5 × 5 m to align with the output of the deep learning model.

Traditional methods relied on a workstation with an Intel Xeon Gold 6248R CPU (standard for parallelized iterative solvers), while the DB-MS-CAN inference was conducted on a single NVIDIA RTX 4060 GPU.

The quantitative performance comparison is summarized in Table 5 and Figure 12, while a comparison of the running time is provided in Figure 13.

Constrained by ray-theory approximations, the CT inversion (Figure 12A) exhibits severe spectral leakage and over-smoothing. It fails to resolve fine-grained geological textures or recover velocity extrema, missing both the deep

Table 4. Quantitative performance comparison of different inversion methods on the synthetic benchmark

Method	SSIM (mean ± SD)	RMSE (%) (mean ± SD)	R (Pearson) (mean ± SD)
PINN	0.875 ± 0.024	2.90 ± 0.32	0.924 ± 0.018
Transformer	0.885 ± 0.018	2.87 ± 0.25	0.952 ± 0.012
DB-MS-CAN	0.918 ± 0.009	1.96 ± 0.12	0.976 ± 0.005

Abbreviations: DB-MS-CAN: Dual-Branch Multi-Scale Convolutional Attention Network; PINN: Physics-Informed Neural Network; RMSE: Root mean square error; SSIM: Structural similarity index.

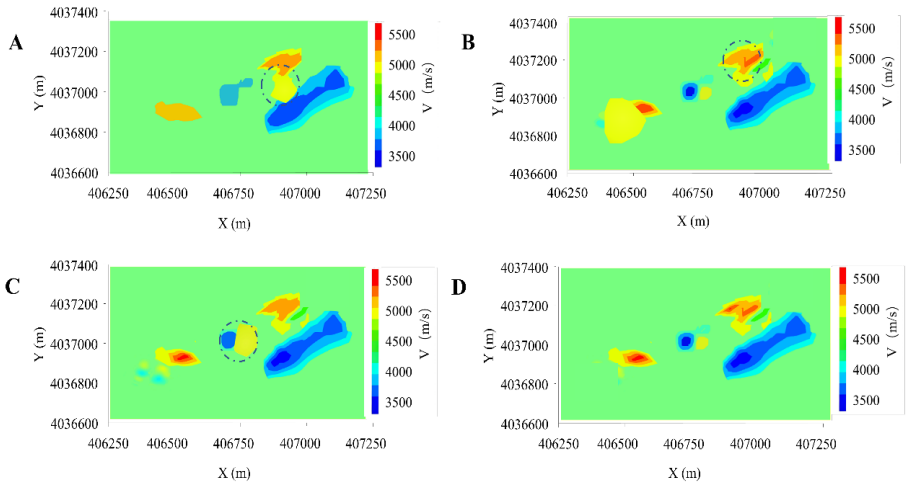

Figure 11. Comparison of velocity inversion results on the synthetic benchmark: (A) Ground truth model; (B) PINN; (C) Vision Transformer; (D) DB-MS-CAN. The dashed-line circles point out the key high-velocity and low-velocity anomalies, serving as a visual reference to compare the exact structures in (A) with the inaccurately reconstructed regions in (B) and (C).
Abbreviations: DB-MS-CAN: Dual-Branch Multi-Scale Convolutional Attention Network; PINN: Physics-Informed Neural Network.

blue intervals (< 3600 m/s) and deep red stress zones (> 5200 m/s). This limitation yields the poorest quantitative performance, characterized by an RMSE of 3.65 ± 0.52% and an SSIM of 0.720 ± 0.045. The notably large standard deviation (±0.52) highlights the inherent instability of ray-based tomography, which remains highly sensitive to ray coverage density and initial model selection.

The FWI result (Figure 12B) demonstrates marginal visual improvement by incorporating waveform information, reducing the RMSE to 2.87 ± 0.38%. However, structural definition remains indistinct, and boundary integrity is compromised by non-physical artifacts arising from cycle-skipping. The suboptimal SSIM (0.815 ± 0.032) and substantial metric variance indicate that optimization-based methods struggle to converge consistently under complex non-linear conditions, often trapping in local minima.

In contrast, the proposed DB-MS-CAN (Figure 12C) delivers the most geologically consistent reconstruction. It precisely delineates complex stratification within low-velocity zones and recovers the full dynamic range of the velocity field. This fidelity translates into state-of-the-art metrics: a peak SSIM of 0.925 ± 0.008 and a minimum RMSE of 2.17 ± 0.11% (a ~40% error reduction compared to CT). The minimal variance significantly outperforms traditional methods (CT's ± 0.52 and FWI's ± 0.38), demonstrating superior reproducibility for safety-critical monitoring. Additionally, the inference time of ~7 seconds achieves near-real-time performance, providing an optimal balance between accuracy and efficiency.

3.4.2. Robustness and noise tolerance experiment

The test dataset utilized in this study is derived from raw *in situ* microseismic monitoring. Consequently, the input waveforms inherently contain complex, real-world mining interference, including mechanical vibrations, electrical hum, and background blasting noise (as visualized in Figure 14). The model's high performance on this test set implicitly validates its robustness against realistic non-Gaussian noise.

To rigorously evaluate the model's theoretical stability limits under strictly controlled SNR conditions, we introduced Gaussian white noise as an additional stress test variable. We constructed a stress-test dataset by superimposing Gaussian white noise onto the test waveforms at SNRs of 10 dB, 5dB, and 0 dB. The performance degradation of the three methods is quantified in Figure 15.

To rigorously evaluate the theoretical stability limits under strictly controlled SNR conditions, we introduced Gaussian white noise as an additional stress test variable. We constructed a stress-test dataset by superimposing noise onto the test waveforms at varying levels: Noise-free, 10 dB, 5 dB, and 0 dB. The quantitative performance degradation of the three methods is illustrated in Figure 15.

As the noise level increases (*i.e.*, SNR decreases), a general decline in performance is observed across all inversion methods. However, the proposed DB-MS-CAN demonstrates exceptional robustness compared to

Table 5. Performance comparison of DB-MS-CAN with conventional inversion methods

Method	SSIM (mean ± SD)	RMSE (%) (mean ± SD)	R (mean ± SD)
CT wave velocity	0.720 ± 0.045	3.65 ± 0.52	0.85 ± 0.035
FWI	0.815 ± 0.032	2.87 ± 0.38	0.931 ± 0.022
DB-MS-CAN	0.925 ± 0.008	2.17 ± 0.11	0.968 ± 0.004

Abbreviations: CT: Computed tomography; DB-MS-CAN: Dual-Branch Multi-Scale Convolutional Attention Network; FWI: Full waveform inversion; RMSE: Root mean square error; SSIM: Structural similarity index.

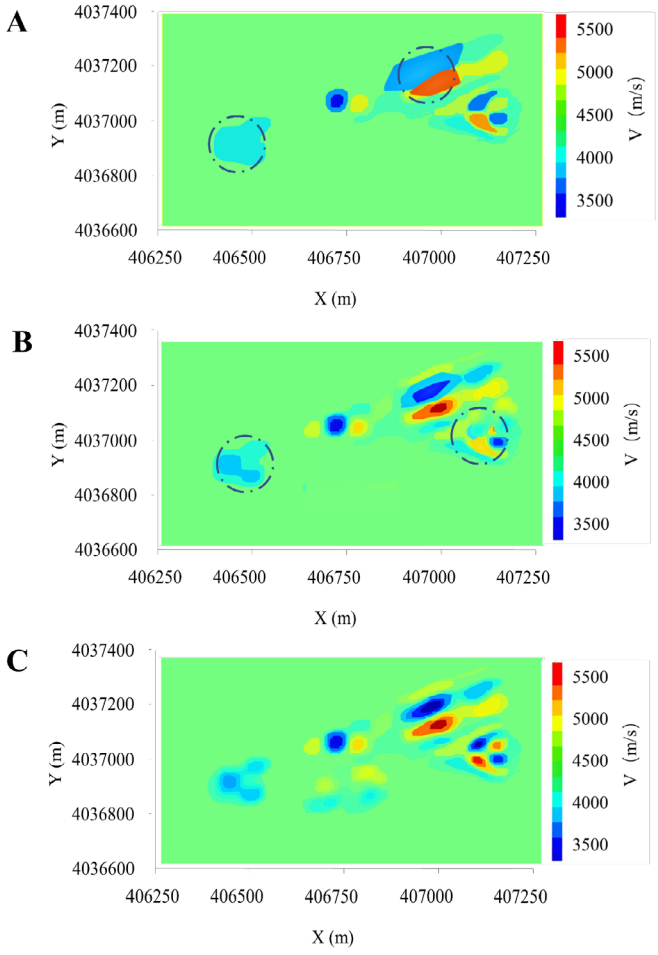

Figure 12. Visual comparison of velocity inversion results between traditional methods and the proposed DB-MS-CAN model. (A) CT velocity inversion image. (B) FWI inversion image. (C) DB-MS-CAN. The dashed-line circles point out local inversion inaccuracies and structural distortions in the traditional methods, which are effectively overcame by the DB-MS-CAN model in (C).
Abbreviations: CT: Computed tomography; DB-MS-CAN: Dual-Branch Multi-Scale Convolutional Attention Network; FWI: Full waveform inversion.

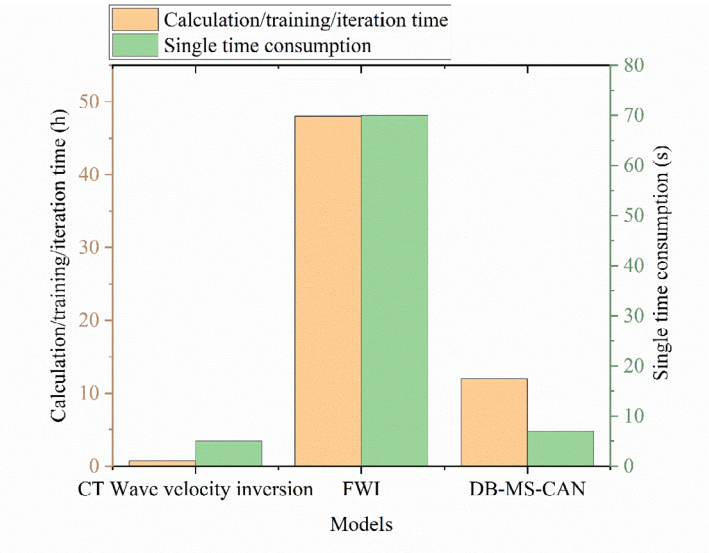

Figure 13. Running time of the three methods
Abbreviations: CT: Computed tomography; DB-MS-CAN: Dual-Branch Multi-Scale Convolutional Attention Network; FWI: Full waveform inversion.

traditional approaches.

First, regarding structural fidelity (Figure 15A), the SSIM of the traditional CT method (black line) drops precipitously from ~0.79 to ~0.63 as noise intensifies to 0 dB, indicating severe structural distortion. In contrast, DB-MS-CAN (blue line) maintains a high SSIM (> 0.92) even under the harshest 0 dB conditions, significantly outperforming FWI and CT. This suggests that the multi-scale aggregation mechanism effectively preserves geological structural details despite heavy interference.

Second, in terms of numerical accuracy (Figure 15B), the RMSE of the CT method exhibits a sharp linear increase, exceeding 5.4% at 0 dB. Conversely, DB-MS-CAN maintains the lowest error rate, with the RMSE rising only marginally to ~2.6%. The gentle slope of the blue curve confirms the model's stability in minimizing velocity deviations.

Finally, the correlation coefficient (R value) in Figure 15 further validates the model's reliability. While the R value for CT and FWI falls to approximately 0.70 and 0.85 respectively at 0 dB, DB-MS-CAN sustains a correlation above 0.92. This superior performance is attributed to the BFM, which adaptively assigns low attention weights to noise-dominated time steps, effectively "locking on" to effective signal phases and filtering out random interference.

4. Discussion

The primary bottleneck in microseismic monitoring for mine safety has consistently been the trade-off between inversion accuracy and computational efficiency. Traditional methods represent two extremes: travel-time tomography (CT) is fast but lacks detail, while FWI is precise but computationally intensive. The DB-MS-CAN model proposed in this study effectively bridges this gap. While there are formal differences in comparing an offline-trained deep learning model with online iteratively optimized traditional methods, this comparison possesses substantial fairness and significant industrial value within the specific context of dynamic mine safety monitoring. Traditional methods, particularly FWI, treat each microseismic event as an independent problem and must solve the wave equation from scratch. While this strategy is reasonable in exploration seismology, it appears redundant in real-time early warning scenarios. By shifting the heavy computational burden to the offline training phase, DB-MS-CAN achieves an online inference speed of approximately 7 seconds per event. This near-real-time processing capability allows the stress field to be updated dynamically at a speed synchronous with event occurrence, enabling engineers to promptly identify hazardous precursors such as high-stress concentration zones. Furthermore, both CT and FWI used for comparison in this paper employ industry-leading optimization algorithms to ensure performance, which further highlights the generational efficiency advantage of the proposed model.

Moreover, compared with current state-of-the-art models, the model in this paper maintains an advantage. Ablation experiments confirm the strengths and roles of each module within the model: the MDFA module focuses on the spatial continuity of low-frequency geological structures, while the BFM module focuses on the transient scattering of high-frequency P/S waves.

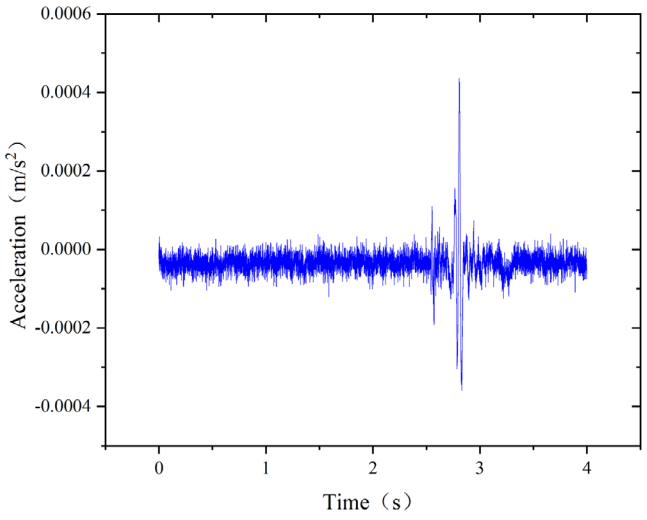

Figure 14. Raw microseismic signals featuring complex real-world noise

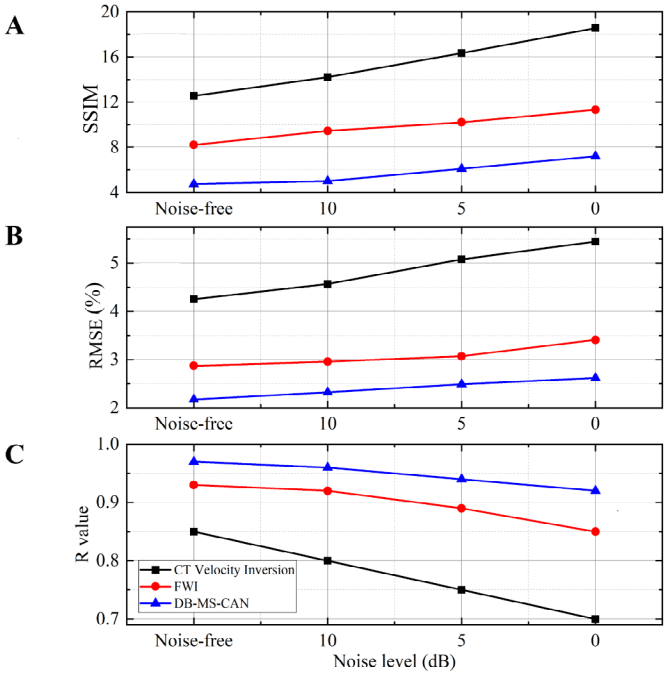

Figure 15. Evaluation metrics of the three methods after adding noise
Abbreviations: CT: Computed tomography; DB-MS-CAN: Dual-Branch Multi-Scale Convolutional Attention Network; FWI: Full waveform inversion; RMSE: Root mean square error; SSIM: Structural similarity index.

Although this study has achieved encouraging results in specific mining areas, to meet rigorous scientific standards, we must frankly discuss the limitations of the current method: synthetic vs. field data. Laboratory synthetic data are simpler than field data and struggle to restore the complex geological structures of mining environments. This paper adopts a strategy of synthesizing ground truth based on the actual physical environment of the mining area to ensure that the validation of the model under complex working conditions has practical significance. Additionally, to ensure data accuracy, our field labels are not purely data-driven results but are

subjected to strict geological constraints from currently publicly available borehole logging and active source detection, followed by manual screening by experienced experts. This minimizes the non-uniqueness errors inherent in offline CT itself. Nonetheless, we acknowledge that systematic errors in offline inversion may still set an upper bound on model accuracy, potentially introducing risks of bias transfer and circular validation. To verify the reliability of the proposed model, we introduced a synthetic benchmark dataset generated via physical equation forward modeling. In this experiment, the ground truth is absolutely precise and independent of any inversion algorithm. The performance of DB-MS-CAN over PINN and Transformer on synthetic data proves that the network has indeed learned spatiotemporal patterns consistent with wavefield propagation physics, rather than merely fitting specific artifacts of offline tomography. In comparative experiments, we found that PINN possesses a natural physical advantage in background smoothness, while Transformer excels in global macro-positioning. Future work will explore unsupervised learning or reference the advantages of PINN and Transformer by using wave equation residuals directly as a loss function to fundamentally escape dependence on labeled data.

Current validation is based on data from a single mine. While the dataset provides comprehensive spatial coverage, its "universal applicability" should currently be limited to engineering environments with similar geological backgrounds. The main challenge facing cross-mine application is domain drift. The different dilation rate features captured by MDFA correspond respectively to fractures and structures of different scales in the geological body. This "scale-independent" feature extraction capability gives it potential structural robustness when processing heterogeneities of different scales across mines. Future work for this model will focus on physics-driven transfer learning, utilizing the architecture's ability to capture physical laws to achieve small-sample fine-tuning for new scenarios.

The current model assumes a relatively fixed sensor layout. However, in actual mining, rock movement may lead to sensor displacement or failure, thereby causing changes in input tensor patterns. It is crucial to highlight that the Channel Attention mechanism within the BFM module provides an inherent degree of topological robustness against sensor malfunctions. As demonstrated in our quantitative analysis (Figure 5C), the proposed mechanism autonomously learns to evaluate sensor reliability. For noise-dominated or faulty channels, such as Channel 2, the network assigns a significantly suppressed weight (0.13), effectively filtering out misleading data. Conversely, the model prioritizes high-fidelity signals by assigning dominant weights to coherent channels like Channel 7 (0.78). This adaptive weighting capability ensures that the inversion process remains stable even under partial sensor failure, significantly enhancing the practical utility of DB-MS-CAN for continuous safety-critical monitoring in harsh industrial settings.

5. Conclusion

This study proposes the DB-MS-CAN deep learning framework to address the difficulty of balancing inversion accuracy and computational efficiency in microseismic passive tomography. By integrating multi-scale feature aggregation and a dual-branch attention mechanism, this method demonstrates potential superior to traditional methods in the studied mining environment. The core findings and contributions of this research are summarized as follows: The proposed framework, through an offline learning strategy, reduces the inference time for a single event to approximately 7 seconds while maintaining structural fidelity (SSIM 0.925) comparable to high-precision physical inversion, providing a feasible technical path for real-time dynamic disaster warning. The temporal decoupling mechanism of the BFM module endows the model with stability in strong noise environments. Even under stress tests with a 0 dB signal-to-noise ratio, the model maintains a high correlation coefficient, indicating its ability to adapt to complex industrial site noise environments. Compared to general computer vision models, the network architecture integrating the MDFA and BFM modules shows significant advantages in resolving micro-scale fractures and macro-scale fault zones.

Acknowledgments

None.

Funding

This work was supported by the Open Fund of State Key Laboratory of Geomechanics and Geotechnical Engineering (Grant No. SKLGGES-024034), the Key Research and Development Program of Jining City (Grant No. 2024AQGX009), and the Research Planning Project of Qilu Institute of Technology (Grant Nos. QIT24BZ002 and QIT25TP006).

Conflict of interest

The authors declare they have no competing interests.

Author contributions

Conceptualization: Aoyu Feng, Binxin Hu, Feng Zhu
Data curation: Aoyu Feng, Feifei Jiang
Formal analysis: Aoyu Feng, Danya Ma
Funding acquisition: Feng Zhu
Investigation: Aoyu Feng, Feifei Jiang
Methodology: Aoyu Feng, Binxin Hu, Yang Gao
Project administration: Binxin Hu
Resources: Yang Gao, Rong Liu
Software: Aoyu Feng
Supervision: Binxin Hu, Feng Zhu
Validation: Binxin Hu, Feng Zhu, Rong Liu
Visualization: Aoyu Feng, Danya Ma
Writing–original draft: Aoyu Feng
Writing–review & editing: Binxin Hu, Feng Zhu, Yang Gao

Availability of data

The authenticity of this study is grounded in a high-density microseismic dataset collected from an operational coal mine in Shanxi Province. As this is proprietary, sensitive monitoring data critical to mine safety and bound by non-disclosure agreements, the data cannot be shared publicly.

AI use statement

The authors affirm that AI tools were utilized solely for minor language refinement, grammar checking, and translation assistance during the preparation of this manuscript. All conceptualization, methodological design, experimental execution, result analysis, and interpretation were performed solely by the authors. The authors have reviewed and edited the content to ensure accuracy and original thought.

References

1. Feng F, Chen S, Zhao X, Li D, Wang X, Cui J. Effects of external dynamic disturbances and structural plane on rock fracturing around deep underground cavern. *Int J Coal Sci Technol*. 2022;9(1):15.

   doi: 10.1007/s40789-022-00487-z

2. Tang Z, Liu X, Xu Q, Li C, Qin P. Stability evaluation of deep-buried TBM construction tunnel based on microseismic monitoring technology. *Tunnelling and Underground Space Technology*. 2018;81:512-524.

   doi: 10.1016/j.tust.2018.08.02

3. Liu JP, Si YT, Wei DC, Shi HX, Wang R. Developments and prospects of microseismic monitoring technology in underground metal mines in China. *J Cent South Univ*. 2021;28(10):3074-3098.

   doi: 10.1007/s11771-021-4839-y

4. Dai R, Wang Y, Zhang D, Ji H. Automatic P-phase-onset-time-picking method of microseismic monitoring signal of underground mine based on noise reduction and multiple detection indexes. *Entropy*. 2023;25(10):1451.

   doi: 10.3390/e25101451

5. Aghamiry HS, Gholami A, Operto S, Malcolm A. ADMM-based full-waveform inversion for microseismic imaging. *Geophys J Int*. 2022;228(1):259-274.

   doi: 10.1093/gji/ggab332

6. Zhang B, Xia D, Tan J, *et al*. Acoustic wave equation full waveform inversion based on optimal transport and L2 norm hybrid weighting. *J Ocean Univ China*. Published online March 18, 2025.

   doi: 10.1007/s11802-026-6167-1

7. Zhang S, Li M, Cui G, Mao G. Jiyu xishu zhengzehua FWI he mOWL-QN de weidizhen zhenyuan weizhi yu zhenyuan zibo tongshi fanyan fangfa [A simultaneous inversion method for microseismic source location and source waveform based on sparse regularization FWI and mOWL-QN]. *Oil Geophysical Prospecting*. 2025;60(5):1146-1159. [In Chinese].

   doi: 10.13810/j.cnki.issn.1000-7210.20240309

8. Sun P, Zheng J, Zhao J, Yang Y, Wang Y. Fully automatic differentiation with coupling deep neural networks for full-waveform inversion. *J Seismic Explor*. 2025;34(6):16-28.

   doi: 10.36922/JSE025410085

9. Zhang J, Song G, Zhu F, Hu B, Zhang H. Elastic wave CT with multistage inversion process based on improved SIRT. *Phys Lett A*. 2024;522:129739.

   doi: 10.1016/j.physleta.2024.129739

10. Cai S. Zhu beidong shuangyuan weizhen CT fanyan suanfa yanjiu ji yingyong [Research and application of the active-passive dual-source microseismic CT inversion algorithm] [master's thesis]. Xuzhou, China: China University of Mining and Technology; 2024. [In Chinese].

    doi: 10.27623/d.cnki.gzkyu.2024.002106

11. Tian Z, Pei S, Yu Q. Inversion imaging research of cross hole seismic CT in complex Karst areas: Guiyang Metro Line 3 under construction presented as an example. *CT Theory and Applications*. 2024;33(5):561-567. [In Chinese].

    doi: 10.15953/j.ctta.2023.132

12. Yuan C, Zhang J. Vertical slowness-constrained joint anisotropic parameters and event-location inversion for downhole microseismic monitoring. *Remote Sensing*. 2025;17(3):529.

    doi: 10.3390/rs17030529

13. Olya BAM, Mohebian R, Moradzadeh A. A new approach for seismic inversion with GAN algorithm. *J Seismic Explor*.

2024;33(3):1-36.

14. Zhou Y, Han L, Zhang P, Zeng J, Shang X, Huang W. Microseismic data-direct velocity modeling method based on a modified attention U-Net architecture. *Applied Sciences*. 2023;13(20):11166.

    doi: 10.3390/app132011166

15. Li L, Zeng X, Pan X, Peng L, Tan Y, Liu J. Microseismic velocity inversion based on deep learning and data augmentation. *Applied Sciences*. 2024;14(5):2194.

    doi: 10.3390/app14052194

16. Chang A, Gross L, Hörning S. Full waveform inversion constrained to well log velocity data and seismic data using random mixing. *J Appl Geophys*. 2025;243:105968.

    doi: 10.1016/j.jappgeo.2025.105968

17. Gou R, Song D, He X, *et al*. Microseismic response characteristics and stress anomaly zoning in deep outburst-prone coal seams with multi-concealed structures: A case study. *J Appl Geophys*. 2025;242:105932.

    doi: 10.1016/j.jappgeo.2025.105932

18. Ma XP. Dadi dianci he yuanzhen zoushi shuju sanwei lianhe fanyan yanjiu [Research on three-dimensional joint inversion of magnetotelluric and teleseismic arrival time data] [PhD dissertation]. Changchun, China: Jilin University; 2025. [In Chinese].

    doi: 10.27162/d.cnki.gjlin.2025.000803

19. Wamriew D, Charara M, Pissarenko D. Joint event location and velocity model update in real-time for downhole microseismic monitoring: A deep learning approach. *Comput Geosci*. 2022;158:104965.

    doi: 10.1016/j.cageo.2021.104965

20. Cao D, Su Y, Cui R. Multi-parameter pre-stack seismic inversion based on deep learning with sparse reflection coefficient constraints. *J Pet Sci Eng*. 2022;209:109836.

    doi: 10.1016/j.petrol.2021.109836

21. Song C, Lu M, Li Y, *et al*. Spatial pattern learning: dip structure constraint multi-view convolutional neural network for pre-stacked seismic inversion. *IEEE Trans Geosci Remote Sens*. 2023;61:1-16.

    doi: 10.1109/TGRS.2023.3307897

22. Zou L, Jia J, Ye Y, Wu B. STA-Fault3D: a lightweight 3D seismic fault detection network based on spatial–temporal asymmetric convolution set. *Applied Sciences*. 2025;15(22):12153.

    doi: 10.3390/app152212153

23. Ou L, Huang L, Zhao Y, Wang Z, Shen H, Li X. Intelligent phase picking of microseismic signals based on ResUNet in underground engineering. *J Cent South Univ*. 2025;32(9):3314-3335. [In Chinese].

    doi: 10.1007/s11771-025-6077-1

24. Ma B, Han L, Liu W, Wu Z, Li C. A deep learning velocity modeling method based on a novel attention mechanism networks. *J Seismic Explor*. 2024;33(5):1-14.

25. Yang R. Convolutional neural network for image classification research - based on VGG16. In: *Proceedings of the 2024 International Conference on Image Processing, Computer Vision and Machine Learning (ICICML)*; November 22-24, 2024; Shenzhen, China. IEEE; 2024:213-217.

    doi: 10.1109/ICICML63543.2024.10958042

26. Li S, Xie B. Boosting UNet performance via VGG-based encoder for medical image segmentation. In: *Proceedings of the 2025 6th International Conference on Computer Engineering and Application (ICCEA)*. April 25-27, 2025; Hangzhou, China. IEEE; 2025:1964-1968.

    doi: 10.1109/ICCEA65460.2025.11102997

27. Tang W, Sun J, Wang S, Zhang Y. Review of AlexNet for Medical Image Classification. *EAI Endorsed Trans e-Learn*. 2023;9.

    doi: 10.4108/eetel.4389

28. Wei K, Liu H, Cao H, Chen M. Deep learning inversion research on frequency-domain borehole-to-surface electromagnetic method based on CNN-LSTM network. *Comput Tech Geophys Geochem Explor*. 2025. [In Chinese].

    doi: 10.12474/wthtjs.20250226-0001

29. Huang G, Liu Z, Van Der Maaten L, Weinberger KQ. Densely connected convolutional networks. In: *Proceedings of the 30th IEEE Conference on Computer Vision and Pattern Recognition (CVPR 2017)*. July 21-26, 2017; Honolulu, Hawaii, USA. IEEE; 2017:2261-2269.

    doi: 10.1109/CVPR.2017.243

30. Liu L, Song W, Zeng C, Yang X. Microseismic event detection and classification based on convolutional neural network. *J Appl Geophys*. 2021;192:104380.

    doi: 10.1016/j.jappgeo.2021.104380

31. Libby SA. Modelling faults as fracture swarms to introduce multi-scale heterogeneity. In: *Proceedings of the 58th U.S. Rock Mechanics/Geomechanics Symposium*. June 23-26, 2024; Golden, Colorado, USA. American Rock Mechanics Association; 2024.

    doi: 10.56952/ARMA-2024-0934

32. Chen F, Liang Z, Cao A. ConvLSTM for predicting short-term spatiotemporal distribution of seismic risk induced by large-scale coal mining. *Nat Resour Res*. 2023;32(3):1459-1479.

    doi: 10.1007/s11053-023-10193-5

33. Luo H, Xu X, Pan Y, Yu J, Zhang Y, Zhang L. The CGAS

deep learning algorithm for P-wave arrival time picking of mining microseismic events. *IEEE Access*. 2023;11:102961-102970.

doi: 10.1109/ACCESS.2023.3317084

34. He Z, Jia M, Wang L. UACNet: a universal automatic classification network for microseismic signals regardless of waveform size and sampling rate. *Eng Appl Artif Intell*. 2023;126:107088.

doi: 10.1016/j.engappai.2023.107088

35. Xu H, Li K, Shan P, *et al*. Automatic picking method for the first arrival time of microseismic signals based on fractal theory and feature fusion. *Fractal and Fractional*. 2025;9(11):679.

doi: 10.3390/fractalfract9110679

36. Yang Y, Wang H, Li Y, Birnie CE, Alkhalifah T. Automatic microseismic event location using deep neural networks in anisotropic media. In: *Proceedings of the 83rd EAGE Annual Conference & Exhibition*. June 6-9, 2022; Madrid, Spain. European Association of Geoscientists & Engineers; 2022:1-5.

doi: 10.3997/2214-4609.202210621

37. Aguiar AC, Myers SC. Microseismic event relocation based on PageRank linkage at the Newberry Volcano geothermal site. *Bull Seismol Soc Am*. 2018;108(6):3656-3667.

doi: 10.1785/0120180115

38. Antolik M, Ekstrom G, Dziewonski AM, Boschi L, Kustowski B, Pan J. Multi-resolution global models for teleseismic and regional event location. In: *Proceedings of the 23rd Seismic Research Review: Worldwide Monitoring of Nuclear Explosions*. October 2-5, 2001; Jackson Hole, Wyoming, USA. National Nuclear Security Administration; 2001:136-146.

39. Yang L. Theoretical analysis of Adam optimizer in the presence of gradient skewness. *Int J Appl Sci*. 2024;7(2):27-42.

doi: 10.30560/ijas.v7n2p27

40. Krizhevsky A, Sutskever I, Hinton GE. ImageNet classification with deep convolutional neural networks. *Commun ACM*. 2017;60(6):84-90.

doi: 10.1145/3065386

41. Bazulin M, Sabitov D, Charara M. Determination of the elastic parameters of a VTI medium from sonic logging data using deep learning. *Comput Geosci*. 2021;152:104759.

doi: 10.1016/j.cageo.2021.104759

42. Li W, Liu H, Wu T, Huo S. A high-resolution velocity inversion method based on attention convolutional neural network. *IEEE Trans Geosci Remote Sens*. 2023;61:1-14.

doi: 10.1109/TGRS.2023.3311788

43. Cao W, Guo XB, Tian F, *et al*. Seismic velocity inversion based on CNN-LSTM fusion deep neural network. *Appl Geophys*. 2021;18(4):499-514.

doi: 10.1007/s11770-021-0913-3

44. Sun QH, Zong ZY, Li X. Probabilistic seismic inversion based on physics-guided deep mixture density network. *Pet Sci*. 2024;21(3):1611-1631.

doi: 10.1016/j.petsci.2023.12.015

45. Lu J, Wu C, Huang J, Li G, Yuan S. Multi-receptive field distillation network for seismic velocity model building. *Eng Appl Artif Intell*. 2024;133:108547.

doi: 10.1016/j.engappai.2024.108547

ACCSCIENCE PUBLISHING

Journal of Seismic Exploration

ARTICLE

Thin-layer weak signal enhancement based on cyclic spectrum enhancement technology

Hua Zhang[1], Yu Song[1], and Wei Chen[2]*

[1]The National Key Laboratory of Uranium Resources Exploration-Mining and Nuclear Remote Sensing, East China University of Technology, Nanchang, Jiangxi, China

[2]Cooperative Innovation Center of Unconventional Oil and Gas, Yangtze University (Ministry of Education & Hubei Province), Wuhan, Hubei, China

Abstract

With the continuous growth of global energy demand, subtle reservoirs such as thin beds have become an important target for exploration and development. However, the identification accuracy of thin-layer seismic weak signals is limited by the physical resolution limit of traditional seismic exploration methods due to its small thickness, strong heterogeneity and significant interlayer interference effect. In order to solve the problem of weak signal recognition in thin layer, a method of weak signal recognition in thin layer based on cyclic spectrum enhancement technology is proposed in this paper, improving the sensitivity and accuracy of weak signal detection. The method preprocesses the original seismic data by Gauss filtering to suppress random noise while accurately preserving the main features of the signal, and then introduces even-order derivative operation, the high-frequency details of the weak signal in the thin layer are enhanced, and the reflection difference between the layers is highlighted. To mitigate the high-frequency artifacts inherently generated by high-order derivatives, a Butterworth low-pass filter is employed for directional spectral conditioning, facilitating the high-fidelity separation of the effective signal from noise. Finally, the optimal derivative order is dynamically determined through an adaptive termination criterion to prevent over-enhancement or under-enhancement. Numerical simulation and field seismic data test showed that the proposed method significantly improves the resolution of thin-layer horizons and enhances the detectability of subtle seismic signals.

Keywords: Differential operator; Thin layer; Weak signal; Forward simulation; Oil and gas exploration

***Corresponding author:**
Wei Chen
(chenwei2014@yangtzeu.edu.cn)

Citation: Zhang H, Song Y, Chen W. Thin-layer weak signal enhancement based on cyclic spectrum enhancement technology. *J Seismic Explor*. 2026;35(3):025010144. doi: 10.36922/JSE025010144

Received: December 31, 2025

Revised: February 17, 2026

Accepted: March 12, 2026

Published online: May 8, 2026

Copyright: © 2026 Author(s). This is an Open-Access article distributed under the terms of the Creative Commons Attribution License, permitting distribution, and reproduction in any medium, provided the original work is properly cited.

Publisher's Note: AccScience Publishing remains neutral with regard to jurisdictional claims in published maps and institutional affiliations.

1. Introduction

With the growth of global demand for oil and gas resources, the development of conventional oil and gas reservoirs is confronted with multiple challenges, making exploration of thin and unconventional reservoirs a research hotspot. Thin reservoirs have small thickness and strong heterogeneity, and the seismic response is mostly weak reflection or low signal-to-noise ratio (SNR), especially in complex geological areas such as Tarim basin. Research from recent years found that spectral inversion can invert λ/8 thin layer, diffraction wave separation imaging can distinguish fracture-cavity body

from matrix, and generalized S-transform can enhance time-frequency feature extraction, but the algorithm is time-consuming. In practical application, thin layer weak signal identification is the key to predict sweet spot distribution of unconventional oil and gas. Luo *et al.*[1] proposed a method based on improved empirical mode decomposition, using wavelet preprocessing to reduce noise, and combining segment control and superposition technology to improve decomposition accuracy. Paksima *et al.* used synchronous compression S-transform to identify thin gas reservoirs, improving the identification accuracy.[2-5] Wang *et al.*[6] proposed a multi-channel spectral fitting (MSF) method to improve seismic resolution. Although Shearlet transform can improve resolution and weak reflection energy, attention should be paid to noise amplification when dealing with low SNR data.

In terms of seismic frequency extension technology, complementary technical support for thin-layer identification has been provided by three-dimensional layered reflectivity inversion, frequency-domain thin-layer analysis, and frequency-enhanced imaging.[7] Deconvolution technology also has important applications in thin layer recognition. Chen *et al.*[8] improved the vertical resolution of logging curves via wavelet transforms to predict coal and rock textures. In terms of seismic noise suppression, Yang *et al.*[9] proposed an adaptive convolutional neural networks (CNN) for effective waveform reconstruction, while Song *et al.*[10] proposed a deep convolutional autoencoder denoising neural network to effectively attenuate random noise. Cheng *et al.*[11] proposed a broadband wavelet deconvolution method, and Meng *et al.*[12] proposed a deconvolution approach to preserve the SNR. Furthermore, Zhou *et al.*[13] introduced the support vector machine (SVM) method for fluid identification in thin reservoirs. Reflectivity inversion and sparse pulse deconvolution algorithms, such as those proposed by Chopra *et al.*[14] and Sui *et al.*,[15] have successfully bypassed traditional resolution limits. Recent advancements include frequency-dependent multi-scale networks,[16] high-resolution characterization for "ahead-of-the-bit" drilling scenarios,[17] and novel deep-learning-based inversion methods.[18] Ge *et al.*[19] demonstrated the effectiveness of modified reflectivity models for thin reservoir characterization. Additionally, Zhang *et al.*[20] used L1-norm sparse inversion to obtain reflection coefficients and performed clear imaging of thin interlayers. The rapid evolution of deep learning has revolutionized geophysical tasks.[21,22] For instance, Liu *et al.*[23] adopted the generative adversarial networks (GAN) network based on the deep residual channel attention mechanism to realize seismic profile reconstruction and random noise suppression. Ni *et al.*[24] used CNNs to establish mapping relationships for wavelet shaping deconvolution, verifying method reliability through thin-layer modeling. Finally, Manzoor *et al.*[25] inputted seismic data, 90° phase-shift data and discontinuity boundary attributes and used well high-frequency natural gamma as labels and multi-layer perceptron to predict cross-well gamma values to characterize thin reservoirs.

To enhance the recognition effect of thin layer weak signals, it is very important to increase the main frequency of the signal. Based on this understanding, this paper firstly studies the formation mechanism of thin layer weak signal through forward modeling. Especially, the influence of dominant frequency on signal strength is discussed. Then, the theory of cyclic spectrum enhancement technology is constructed, and the weak signal enhancement comparison analysis is carried out theoretically. Finally, the cyclic spectrum enhancement technology is applied to the actual data, and the actual processing effect is analyzed. In particular, it should be pointed out that thin layer weak signal identification belongs to the category of thin layer identification. Predecessors mainly identified the thickness and horizon of thin layers, usually focusing on thick thin layer signal identification. However, from the perspective of signal processing, this paper proposes a cyclic spectrum enhancement technology that can identify thin-layer extremely weak signals caused by interference effects.

2. Enhancement technique by cyclic spectrum

This paper intends to propose a weak signal enhancement method based on signal processing algorithms, especially one that can effectively enhance thin-layer weak signals. The main idea is to firstly use Gaussian filtering to initially smooth the noise, suppressing the noise while strengthening the low-frequency components of the signal. Then, the even-order derivatives of the original seismic trace are calculated to generate derivative seismic traces. Next, the even-order derivative seismic traces are superimposed onto the original seismic trace, and the smoothed seismic trace and the derivative seismic trace are subjected to cyclic superposition operations considering the adaptive loop termination condition. This process not only retains the low-frequency components but also enhances the high-frequency components, while increasing the energy of the main frequency band of the signal and broadening the frequency band width of the seismic signal. By using Butterworth low-pass filtering to handle the high-frequency interference generated by taking higher-order derivatives, the identification of thin-layer weak signals is ultimately achieved. The following sections introduce the theories including Gaussian smoothing, signal differentiation, and Butterworth low-pass filter. In

addition to giving a theoretical introduction, this paper provides an overview of practical problem to be solved, namely the enhancement of thin-layer weak signals.

2.1. Gaussian smoothing and signal derivation

Gaussian smoothing is a linear filtering method based on the Gaussian function. Its core principle is to use the weight distribution of the Gaussian function to perform weighted averaging on signals or images to achieve a smoothing effect, which is used for noise reduction, edge preservation, and multiscale analysis. Through weighted averaging, it can effectively suppress high-frequency noise and improve the quality of signals or images. Among them, the Gaussian function is the foundation of Gaussian smoothing, and its mathematical expression is as follows:

$$G(x) = \frac{1}{\sqrt{2\pi}\sigma} e^{-\frac{z^2}{2\sigma^2}} \quad (1)$$

where x is the offset from the center point; σ is the standard deviation, which controls the width of the Gaussian function. By adjusting σ, the degree of smoothing can be flexibly controlled. The larger is σ, the stronger the smoothing effect will be; $G(x)$ represents the weight at position x.

The purpose of differentiating seismic signals is to extract high-frequency components and detailed information by calculating the rate of change of seismic signals, which is particularly suitable for detecting thin-layer weak signals. Additionally, the differentiation operation can also enhance the reflection wave characteristics at thin-layer interfaces, highlighting the local abrupt change points of the top and bottom interface signals of thin layers, thereby improving the resolution of thin-layer weak signals. For a continuous signal $s(t)$, its n-th order derivative is defined as follows:

$$s^{(n)}(t) = \frac{d^n s(t)}{dt^n} \quad (2)$$

where n represents the order of the derivative.

Seismic differentiation enhances reflection characteristics at thin-layer interfaces by calculating signal change rates. Physically, lower-order derivatives identify structural abruptness, while higher-order derivatives refine thin-layer characterization by capturing signal curvature and local extrema. From a spectral perspective, differentiation acts as a high-pass filter. As shown in Figure 1, the amplitude spectra of the unit impulse response derivatives demonstrate that increasing the derivative order significantly boosts high-frequency energy while suppressing low-frequency components. This non-linear frequency enhancement mechanism broadens the bandwidth and improves vertical resolution without proportional amplification of ultra-high-frequency noise, thereby preserving the signal-to-noise ratio.

When selecting the order of derivative seismic traces, it is necessary to comprehensively consider the time shift, polarity and the balance between signal enhancement and noise suppression. From the perspective of derivative characteristics, odd-order derivation will introduce 90° phase shift, resulting in an asymmetric waveform relative to the original seismic trace. As demonstrated by the quantitative metrics in Table 1, the 1st -order derivative exhibits a phase shift of 90° and a significant zero-lag cross-correlation drop, leading to a noticeable peak time displacement. Such shifts can cause substantial positioning errors at thin-layer interfaces, making odd-order derivatives unsuitable for high-resolution thin-bed enhancement. In contrast, even-order derivatives possess zero-phase characteristics, maintaining waveform symmetry with the original trace, with only the polarity varying predictably with the order. For instance, the 2nd- and 6th-order derivatives have opposite polarities and require correction by a negative sign before superposition, whereas the 4th- and 8th-order derivatives share the same polarity.

The waveform comparison in Figure 2 and the quantitative indices in Table 1 reveal that, after polarity correction, even-order derivatives (such as 2nd and 4nd) maintain a phase shift of 0° and cross-correlation coefficients exceeding 0.95. While lower-order even derivatives are effective at preserving the overall signal trend, higher-order derivatives excel at extracting high-frequency details, albeit at the cost of amplified high-frequency noise. Therefore, this study integrates even-order derivatives with Gaussian smoothing to broaden the vertical resolution while effectively suppressing noise, thereby achieving precise characterization of thin-layer structures.

With the increase of derivative order, the ability of derivative operation to broaden the high frequency band is deteriorating; therefore, the order of cyclic superposition derivative seismic trace needs to be within a certain judgment criterion. Let S be the original seismic trace, S_n be its n-th derivative seismic trace, the dominant frequency of the n-th derivative seismic trace is denoted as D_n, and $S_n(f)$ is the spectrum of the n-th derivative seismic trace. The dominant frequency of S is as follows:

$$D_n = \frac{\int_0^\infty f S_n(f) df}{\int_0^\infty S_n(f) df} \quad (3)$$

where f in the above formula represents the frequency

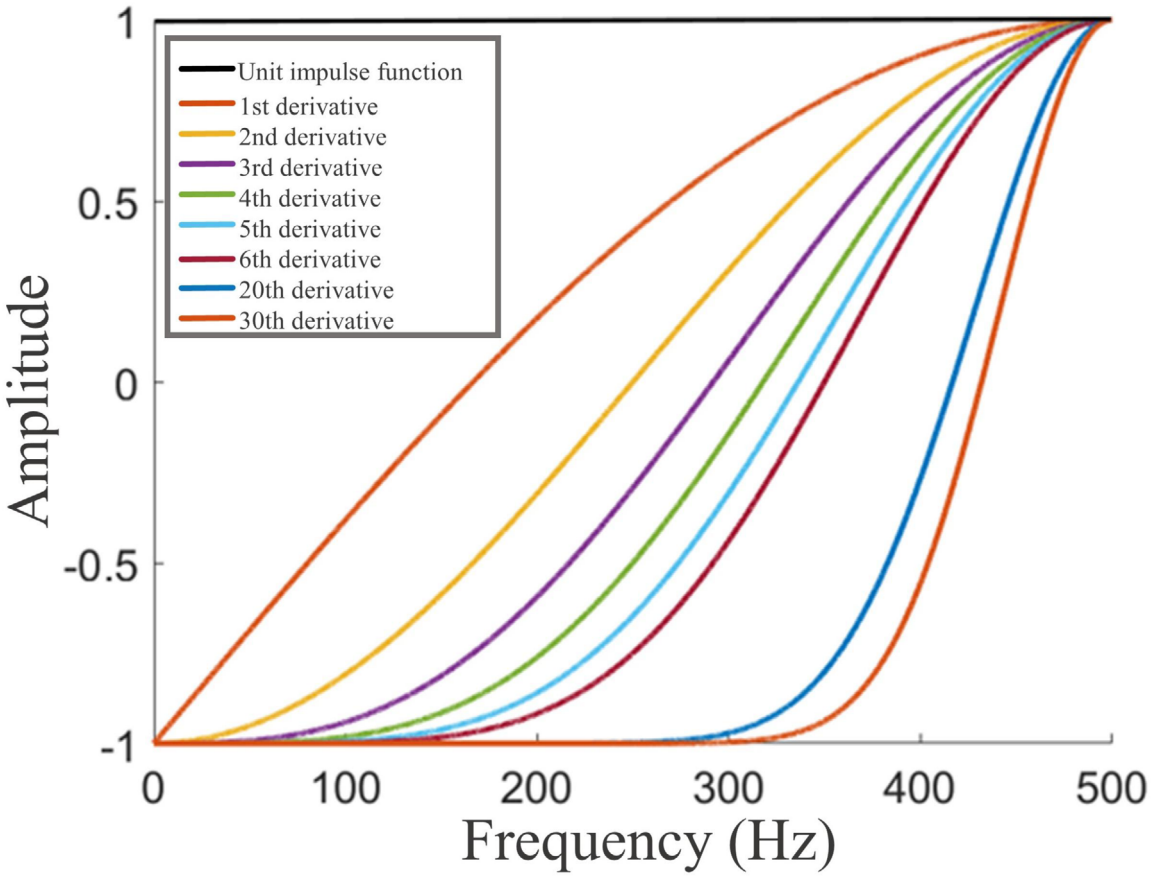

Figure 1. Unit impact function and amplitude spectrum of each derivative

Table 1. Quantitative evaluation of phase characteristics and fidelity of various derivative signals relative to the original signal

Order of derivative	Mean phase error	Correlation	Time shift (ms)
Original trace	0	1.000	0
1st derivative	90	0.052	Δt
2nd derivative	0	0.985	0
4th derivative	0	0.975	0
6th derivative	0	0.968	0

variable. Through many tests, this paper determines that the termination conditions of signal derivation are as follows:

$$\frac{D_{n+1}-D_n}{D_n-D_{n-1}} \le \varepsilon \quad (4)$$

The parameter ε in **Equation 4** acts as a critical threshold to balance resolution enhancement against high-frequency noise amplification. To clarify the physical significance and engineering criteria for selecting ε , we conducted a sensitivity analysis by testing values of 0.1, 0.2, 0.3, and 0.4. When ε = 0.1, the iterative process terminates prematurely, resulting in under-enhancement that fails to resolve λ/16 thin-layer reflections. Conversely, when ε =

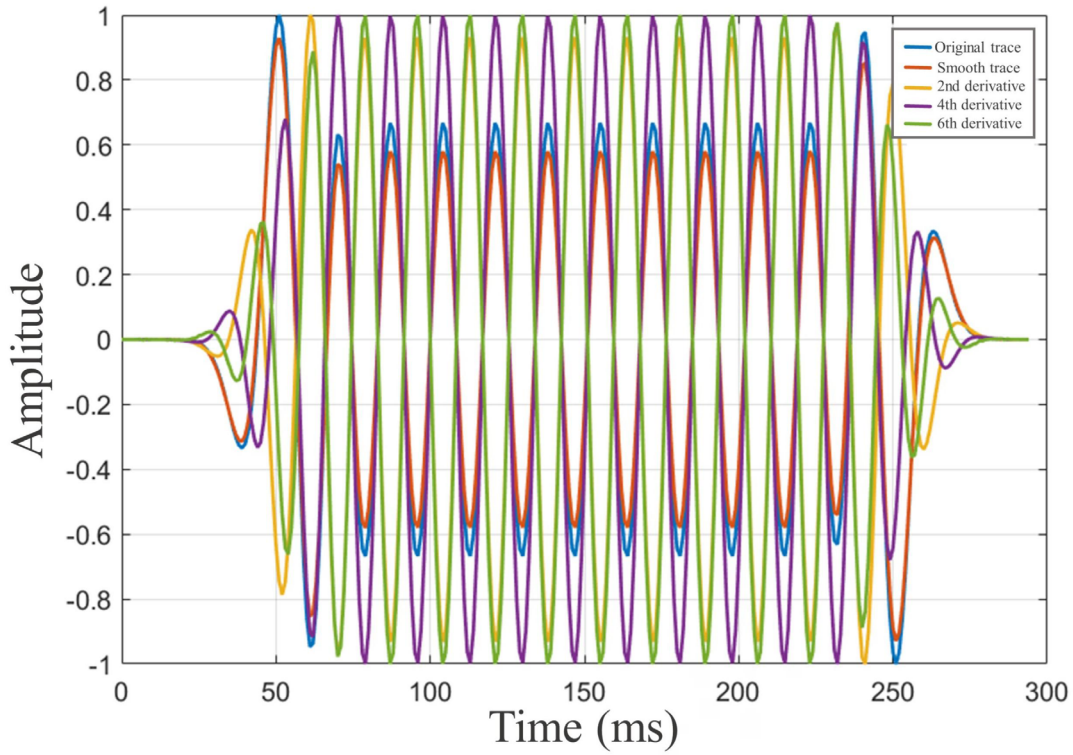

Figure 2. Original trace and derivative seismic trace of each order

0.4, excessive derivative orders lead to over-enhancement and the emergence of high-frequency artifacts. From an engineering perspective, the selection of ε is inversely related to the SNR of the raw data; lower-SNR records require a larger tolerance to ensure operator stability. Based on these comprehensive tests, this paper determines that the optimal range for the termination parameter ε is 0.2–0.3, which ensures maximum resolution improvement while strictly maintaining signal fidelity.

2.2. Cyclic spectrum enhancement technique

After high-order derivation operation, more high-frequency noise and numerical instability will be introduced. In this paper, Butterworth low-pass filter is selected to remove high-frequency noise interference. The characteristic of Butterworth low-pass filter is that the frequency response is flat in the passband, but the frequency value gradually decreases in the stopband. The mathematical formula of Butterworth low-pass filter is as follows:

$$H(s)=\frac{1}{\sqrt{1+\left(\frac{s}{\omega_c}\right)^{2n}}} \tag{5}$$

where $H(s)$ is the transfer function of the filter, ω_c is the cut-off frequency, and n is the order of the filter. In the process of designing Butterworth low-pass filters, the Butter function is used to determine the order and cut-off frequency of the filter to meet the predetermined performance indicators of the filter.

The SNR estimation of the low-pass filtered seismic traces is carried out to verify the accuracy of the derivative order selected in **Equation 4**. Generally speaking, the SNR of the filtered signal gradually decreases, because the higher the derivative order, the more serious the high-frequency interference will be, which will reduce the SNR of the filtered signal as a whole. After filtering the seismic trace, the SNR of the signal is in a constant stage, which indicates that further derivation and denoising can no longer improve the vertical resolution of the thin interlayer. At this time, the derivation order is the cyclic superposition termination order. The algorithm expression of the cyclic spectrum enhancement technology constructed in this paper is as follows:

$$S' = \mathrm{Butter}(\mathrm{Nor}(S)+\mathrm{Gao}(\mathrm{Nor}(S)) - \sum_{i=2}^{k=4m-2} R_k\left(\mathrm{Nor}(S^{(i)})\right) + \sum_{j=4}^{b=4n} R_b\left(\mathrm{Nor}(S^{(j)})\right) \tag{6}$$

where Nor means normalization of the signal, and normalization before and after processing can avoid incomplete display of the results due to the difference of data magnitude; Gao represents Gaussian smoothing, and $S^{(i)}$ represents the i-order derivative of the signal respectively; R represents the difference threshold of calculating the derivative seismic trace, and k is the order after the cycle termination condition is determined, which needs to be cyclically superimposed on the seismic trace by adding a negative sign; b is the order of the largest integer multiple of 4 derivative seismic trace under this condition. Let $k = 4m - 2$, $b = 4n$, find m and n and then cyclically superimpose them to the original seismic trace. Butter means Butterworth low-pass filtering of high-frequency noise, and S' is the processed normalized seismic trace.

The specific algorithm flowchart of the cyclic spectrum enhancement technology represented by **Equation 6** is shown in Figure 3.

3. Comparative analysis of different high frequency interference removal methods

To validate the low-frequency filtering performance of the Butterworth filter selected in **Equation 6,** this study compares the proposed approach against Complete Ensemble Empirical Mode Decomposition (CEEMD), a robust adaptive signal processing technique.[26] While both adaptive processing and traditional filtering are staples of digital signal processing, CEEMD provides a high-fidelity benchmark for denoising. Based on the cyclic superposition constraints in **Equation 4**, the Butterworth low-pass filter was configured to the 8th order to effectively eliminate high-frequency interference.

The denoising performance of CEEMD and the Butterworth low-pass filter was evaluated using single-channel seismic records with thin-layer thicknesses of λ/8 (Figure 4) and λ/16 (Figure 5). As illustrated, CEEMD results in significant amplitude attenuation in strong-signal regions and fails to effectively enhance weak reflections, particularly in the thinner λ/16 layer where residual noise and event dislocations are prominent (Figure 5a).

Conversely, the Butterworth filter, applied to high-order derivative traces, effectively suppresses high-frequency noise while preserving strong-signal amplitudes. It significantly improves the resolution of thin-layer horizons with 0.02 ms dislocation, as confirmed by the enlarged views. These comparisons demonstrate that for high-order derivative-induced noise, the Butterworth filter offers superior denoising stability and SNR over CEEMD.

Analysis indicates that derivative operations beyond the 8th order primarily amplify high-frequency noise rather than effective signals. While CEEMD-based denoising fails to enhance weak interlayer reflections and even attenuates strong-signal amplitudes, the proposed Butterworth filtering approach effectively suppresses derivative-induced noise while preserving strong signals and enhancing weak interlayer reflections.

Spectral analysis (Figure 6) confirms these advantages. For thin layers of λ/8 and λ/16, the cyclic spectrum enhancement significantly broadens the bandwidth and increases the dominant frequency. The rightward shift of low-frequency components and the boost in high-frequency content demonstrate the method's ability to improve resolution and restore subtle interlayer horizons. By expanding the high-frequency range while maintaining low-frequency integrity, the proposed technique effectively enhances seismic signal interpretability.

In order to demonstrate the effect of different signal processing methods on 2D seismic profiles, CEEMD and Butterworth low-pass filter are used to process 2D seismic records of 5 m (λ/8) thin layer weak signals, respectively. The processed seismic record is shown in Figure 7. It can be clearly seen that in the two-dimensional seismic record processed by Butterworth low-pass filter, the enhancement effect of thin layer weak signal area is more significant. This shows that using Butterworth low-pass filter can reduce the loss of thin layer weak signal to a greater extent, while retaining more high-frequency information.

Through the analysis of the processing effect of single-channel and two-dimensional seismic profiles above, it is proved that the noise suppression after weak signal enhancement by Butterworth low-pass filter is effective.

4. Numerical experiments

4.1. Single-channel seismic record

In order to verify the effect of cyclic spectrum enhancement technology on weak signal detection, single-channel seismic records with single layer thickness of 40 m and 5 m (λ/8) were simulated and enhanced. Figure 8 shows that the amplitude of the original seismic trace of 40 m is compensated to some extent after the cyclic spectrum is enhanced, and the degree of compensation for strong signals is low, indicating that this technology can enhance weak signals in thin layers without affecting the energy of strong signals in thick layers.

Figure 9 shows the waveforms of 5 m (λ/8) original seismic trace and cyclic spectrum enhancement trace. Based on the adaptive cycle stop criterion, even-order seismic guide traces are linearly superimposed to obtain enhanced tracks. The amplitude of the visible strong signal is basically consistent with that of the original track, while

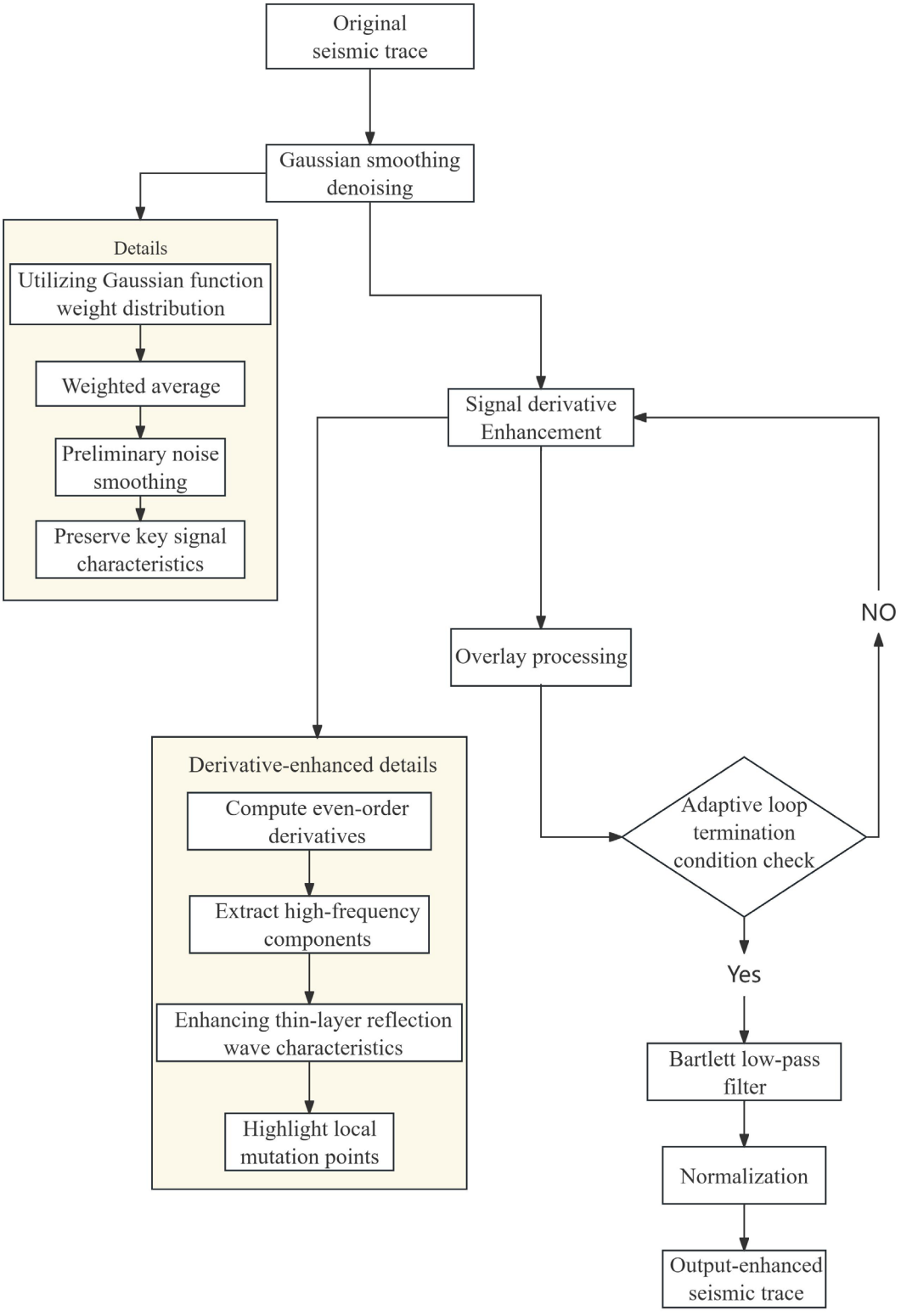

Figure 3. Flow chart of cyclic spectrum enhancement technology

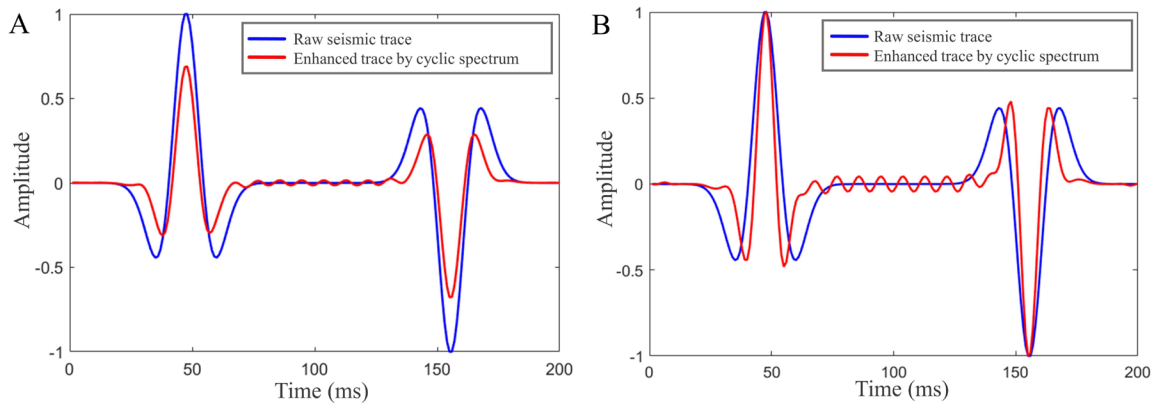

Figure 4. Comparison of waveforms processed by different denoising methods of λ/8 thin-layer. (A) Denoising results of Complete Ensemble Empirical Mode Decomposition (CEEMD) method; (B) Butterworth filter denoising results.

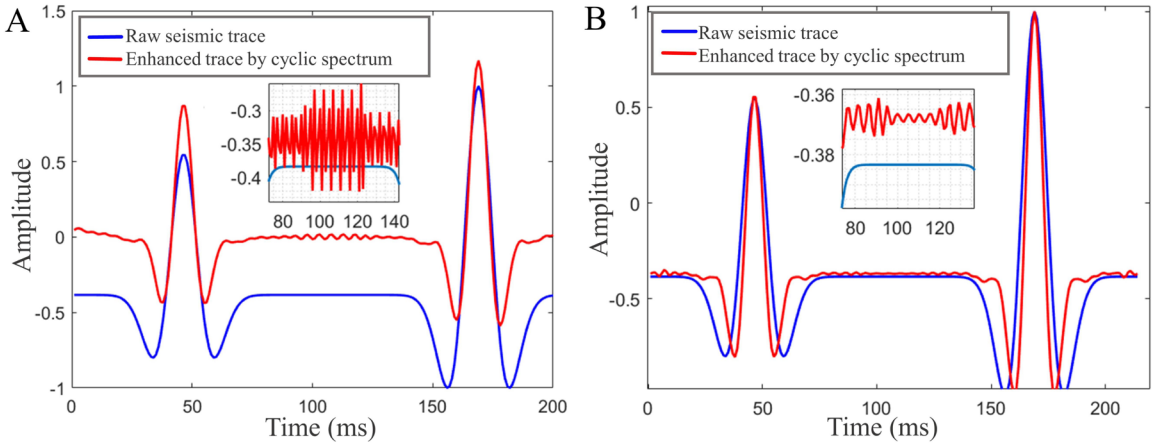

Figure 5. Comparison of waveforms processed by different denoising methods of λ/16 thin-layer. (A) Denoising results of Complete Ensemble Empirical Mode Decomposition (CEEMD) method; (B) Butterworth filter denoising results.

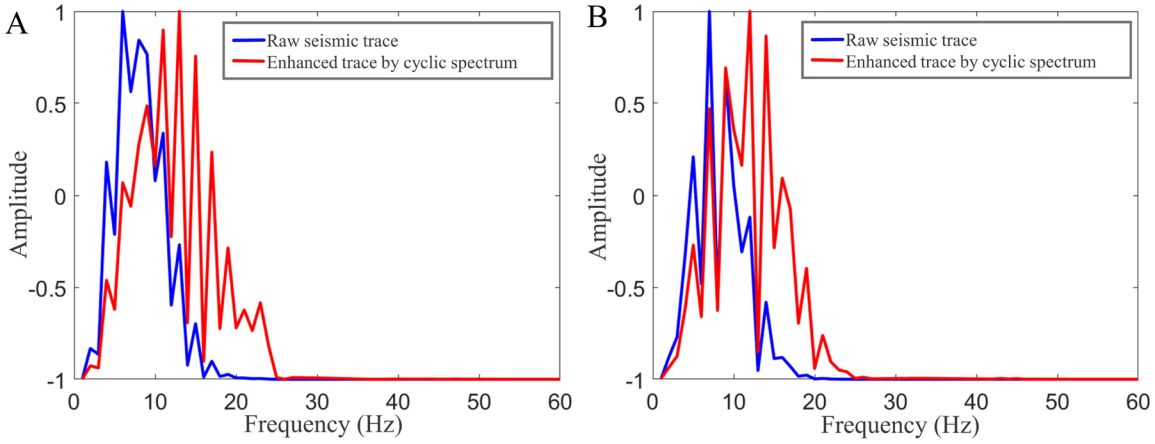

Figure 6. Comparison of amplitude spectra of two kinds of thin interlayer treatment. (a) λ/8; (b) λ/16.

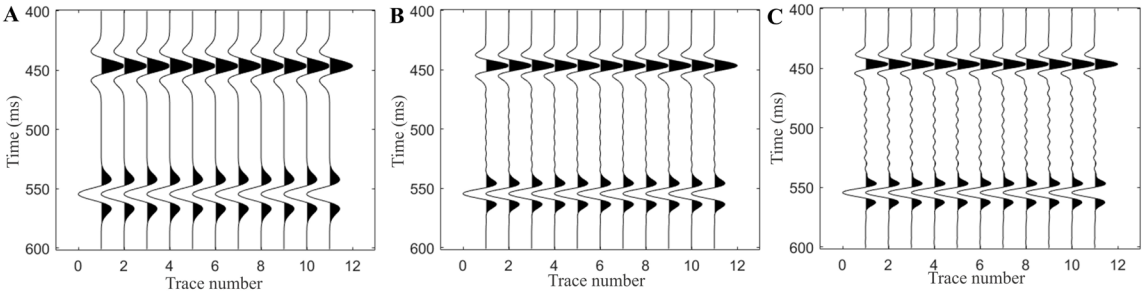

Figure 7. Comparison of seismic records processed by different denoising methods. (A) Raw seismic records; (B) CEEMD; (C) Butterworth filter.

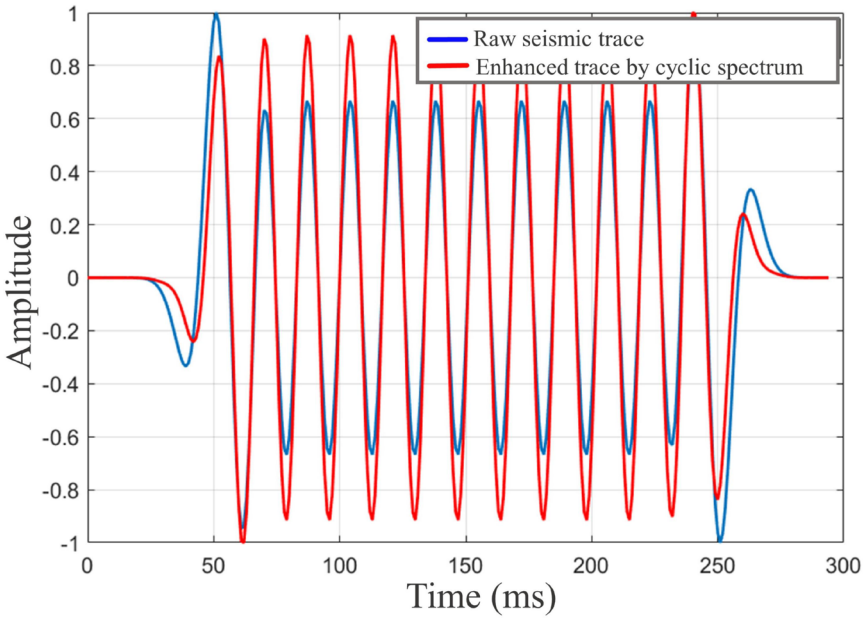

Figure 8. Thick layer numerical seismic traces and derivative seismic traces

the thin interlayer weak signal is enhanced from very weak to visible to the naked eye, which shows that this technology can enhance the thin interlayer weak signal and make it accurately recognized.

4.2. Two-dimensional seismic record

The two-dimensional thin interbedded seismic records of 40 m, 10 m and 5 m were subjected to cyclic spectrum enhancement, and the results are shown in Figure 10. It can be seen from the comparison chart before (Figure 10a) and after (Figure 10b) processing 40 m (1λ) record that the amplitude of strong reflection signal has not changed, indicating that this technology has no enhancement effect on thick layer strong seismic reflection signal. The amplitude of the 10 m (λ/4) original record (Figure 10c) increased after processing (Figure 10d), showing that the proposed method can enhance the moderate intensity signal. After 5 m (λ/8) original recording (Figure 10e) is processed (Figure 10f), the amplitude of the original weak signal near zero is significantly improved. To sum up, cyclic spectrum enhancement technology can compensate the amplitude of weak signals and extremely weak signals without losing strong signals, and the enhancement effect becomes more obvious as the thickness of the thin layer decreases.

5. Field data

Two-dimensional seismic data from an onshore exploration area in Jizhong, North China Plain, were used as the study dataset. The area lies within the tectonic transition zone of the western margin of Bohai Bay Basin, and has typical thin-layer geological characteristics of sandstone and mudstone. Numerous thin-layer structures are present, accompanied by pronounced weak-signal

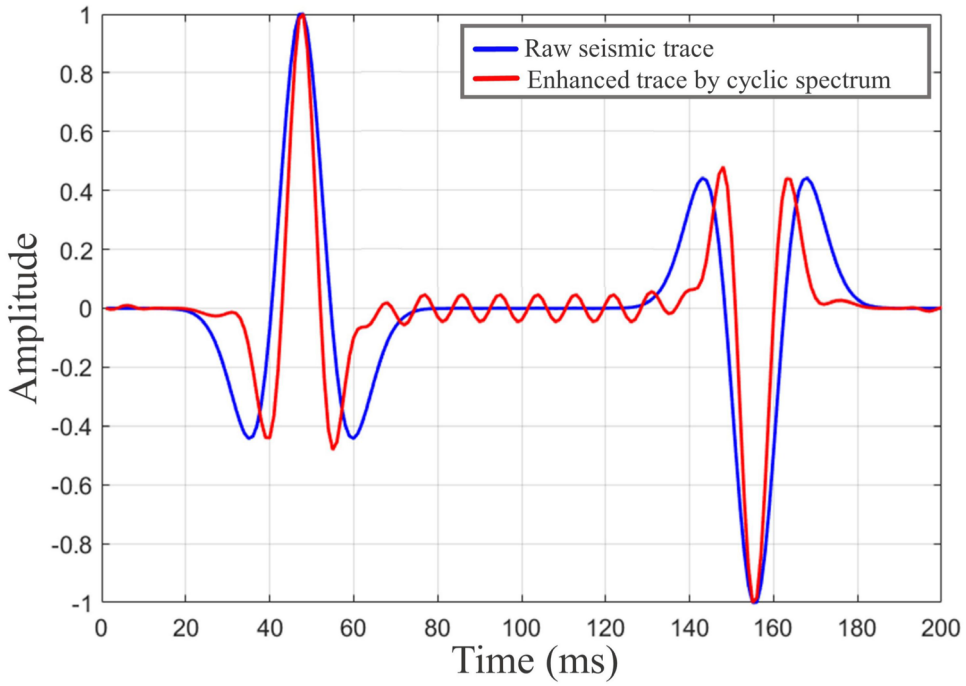

Figure 9. Thin layer numerical seismic traces and derivative seismic traces

characteristics, making this dataset particularly well suited for investigating identification of thin-layer weak signals. The length of each data in the experimental section is 3,000 sampling points, and the sampling rate is set to 1 ms, which contains 571 seismic data. In this paper, the classic thin-layer weak signal identification technology is compared experimentally through a predictive deconvolution method. Figure 11 shows the actual seismic record data. 1–100 thin-layer seismic records with actual data and a seismic record length of 2,000–2,200ms are selected for processing (as shown in the red box), and the amplitude spectrum, f-k spectrum and local similarity of the weak signal enhancement of the actual seismic data are analyzed.

Based on Figure 12a, the continuity of the in-phase axis of the seismic data before processing is poor, and there are many weak signals between layers. The results processed by the prediction deconvolution method are shown in the figure. The continuity of the in-phase axis of the processed seismic data is poor, and some strong signals are weakened, only part of the weak signals between layers are enhanced, and the extremely weak signals between layers have no enhancement effect. The seismic data processed by this method is shown in Figure 12c. The continuity of the in-phase axis at the arrow-indicated position is improved, and the weak signal between thin layers are markedly enhanced.

After the actual seismic data is processed by cyclic spectrum enhancement technology, the local similarity analysis is carried out on the two-dimensional seismic profile. The closer the color is to the yellow part on the color scale, the higher the similarity between the representative and the original data, and the closer the color scale is to the blue part on the lower color scale, the lower the similarity with the original data. The local similarity diagram of the actual seismic data processed by the predictive deconvolution method is shown in Figure 13a. Based on the diagram, it can be seen that the region with similarity coefficient close to zero appears in the strong reflection horizon (shown by the red arrow), indicating that the predictive deconvolution technology cannot guarantee the fidelity of the algorithm to the original data when processing strong signals. The local similarity diagram of this method is shown in Figure 13b, in which the weak signal enhancement region has good similarity with the original data.

The f-k spectrum of the original seismic data and the actual seismic data processed by different methods is shown in Figure 14. In the f–k spectrum, brighter colors indicate higher frequency values, greater energy concentration, and stronger effective signals. It can be seen from Figure 14b and 14c that the energy of the seismic data processed by the predictive deconvolution method and the method reported in this paper is concentrated, but the energy points in the f-k spectrum obtained by the

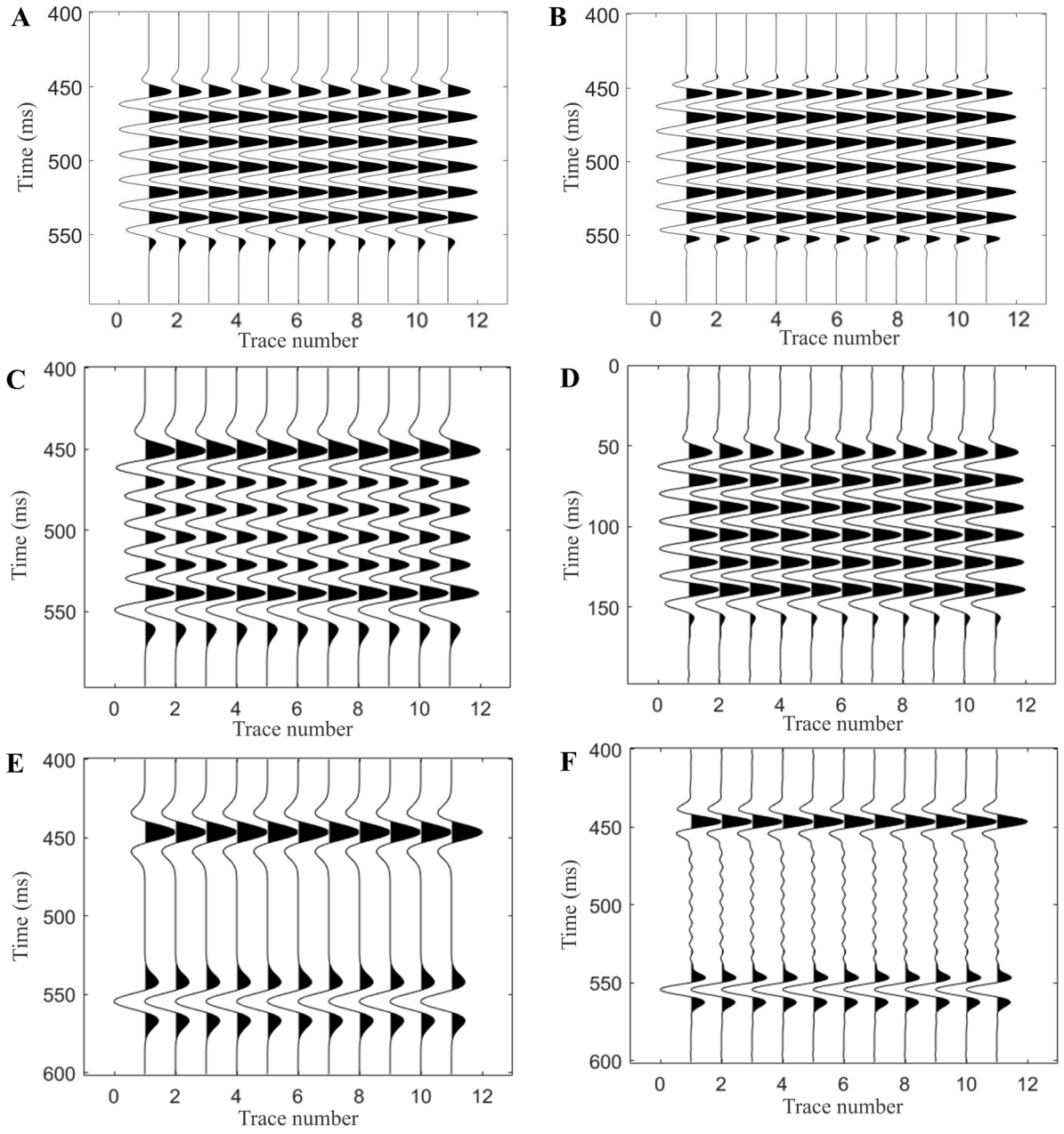

Figure 10. Comparison of effects before and after mutual recognition of different thicknesses. (A) 1λ original record; (B) post-process 1λ layers; (C) λ/4 original records; (D) post-process λ/4 layers; (E) λ/8 original records; (F) post-process λ/8 layers.

predictive deconvolution method are more scattered, and the randomly distributed energy points usually represent noise. The energy of f-k spectrum of this method is more concentrated, and the brightness of the effective signal is higher, indicating enhanced effective signal, but there are also scattered energy points that are unevenly distributed, suggesting the necessity of further algorithm optimization for removing high frequency interference.

Figure 15 shows the amplitude spectrum analysis of the two-dimensional seismic profiles before and after treatment. Compared with the predictive deconvolution method, the method in this paper has a better enhancement effect on weak signals, along with wider frequency band of the enhanced signal and better compensation effect in both low- and high-frequency directions, indicating that the method yields a better enhancement effect on weak

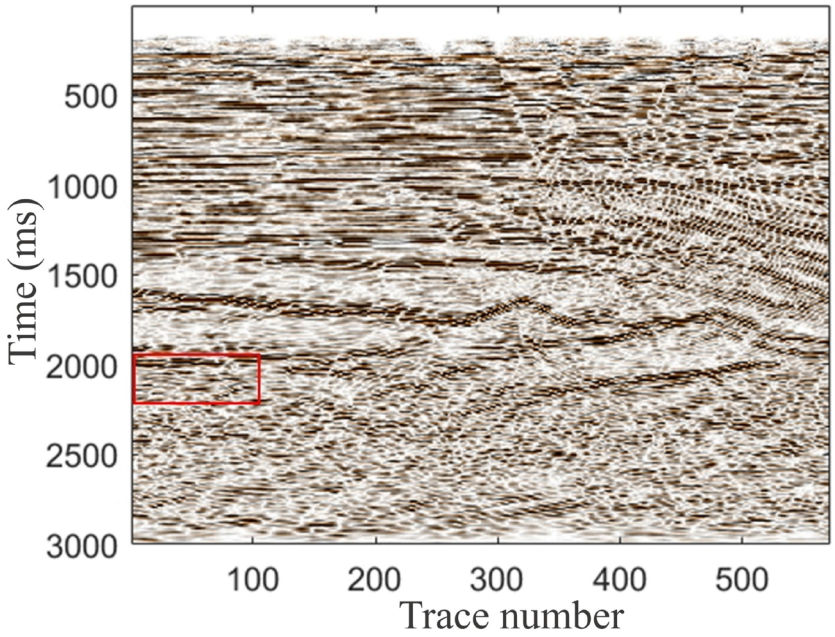

Figure 11. Sectional view of field data

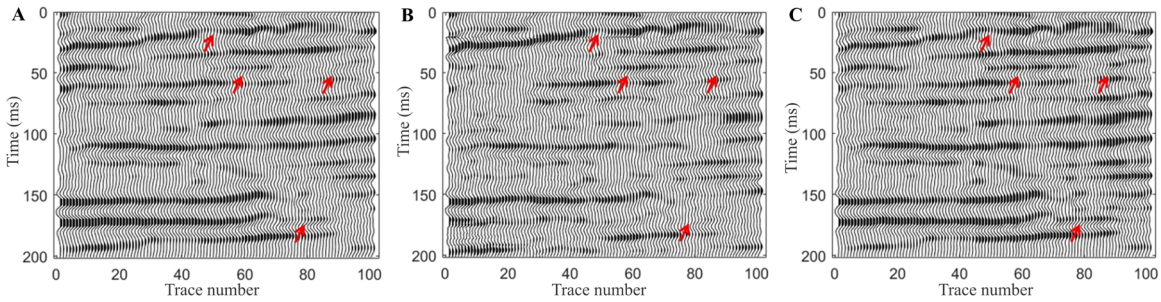

Figure 12. Different methods of processing cross-section enlargement effect. (A) Raw seismic data; (B) a predictive deconvolution method; (C) method reported in this paper.

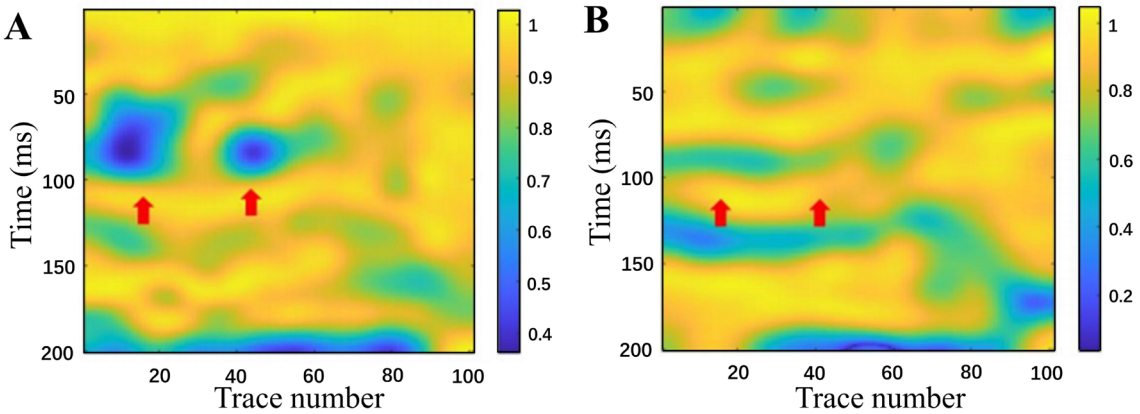

Figure 13. Local similarity diagram between data processed by different methods and original data. (A) A predictive deconvolution method; (B) method reported in this paper.

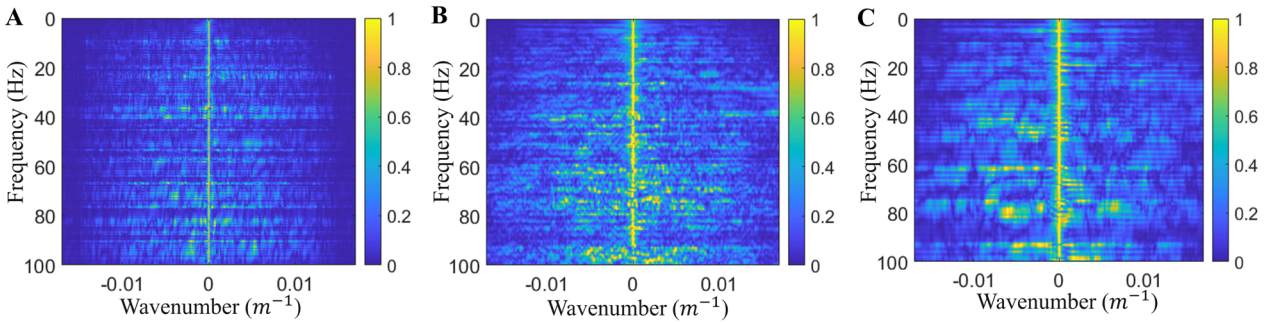

Figure 14. f-k spectra of different methods. (A) The original number of earthquakes; (B) predicting deconvolution; (C) Methods herein.

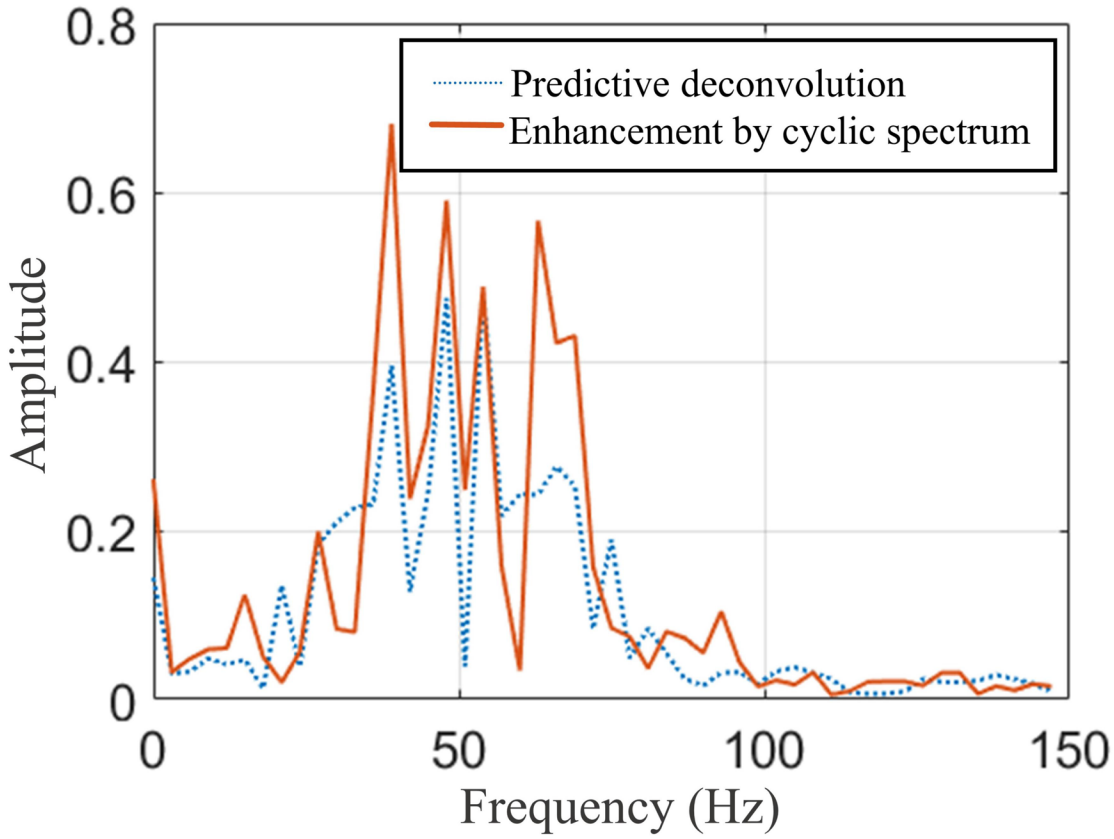

Figure 15. Post-processing profile amplitude spectra of predictive deconvolution and enhancement by cyclic spectrum

signals.

By applying the proposed method to the actual seismic data of Suning–Dawangzhuang area where thin layer development is extremely significant in Northern China, the accuracy of cyclic spectrum enhancement technology in thin layer recognition is verified by comparing the results before and after the processing of through-well seismic profiles. There are many layers of thin sandstone with a thickness of 3–5 m in this research area. Because of the delicate lithology of the thin sandstone layer, the wave impedance difference between the upper and lower strata is relatively small, and the interference between the thin sandstone layers makes its seismic reflection signal relatively weak. Figure 16a shows the original seismic profile, while Figure 16b presents the processed seismic profile. Some in-phase axes are added to the seismic profile

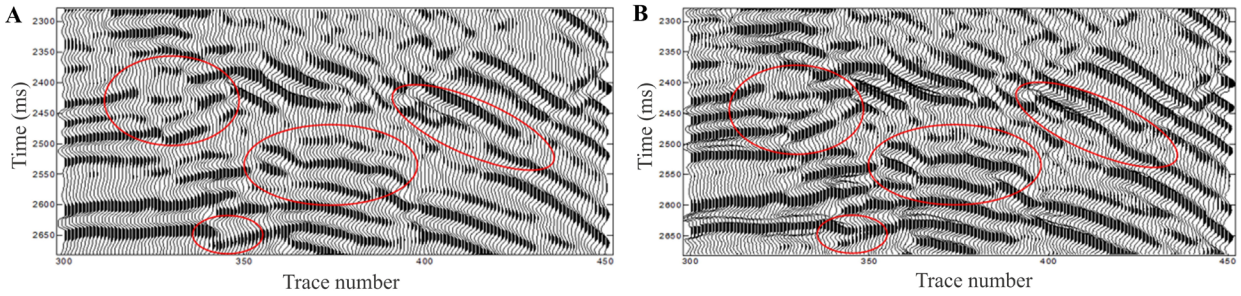

Figure 16. Comparison of seismic profiles before and after processing. (A) Original seismic data; (B) post-processing seismic profile.

processed by cyclic spectrum enhancement technology; the continuity of in-phase axes shows improvements, and the reflected signal becomes effectively enhanced.

Through the comparison of well-passing seismic profiles, the seismic reflection characteristics can be accurately matched with the actual drilling data (covering lithology, logging curves, oil and gas horizons). This process can not only effectively verify the reliability of seismic processing results, but also establish an accurate time-depth conversion relationship, thus verifying the accuracy of this method in structural interpretation and reservoir prediction. A comparison of the post-processing well-tie seismic profiles presented in Figure 17a and 17b revealed that the weak signals are significantly enhanced after the application of cyclic spectrum enhancement technology, along with substantial improvements in the continuity of the in-phase axis (as shown in the area marked by red circle) and enhanced clarity of the horizon information.

Figure 17 shows the macroscopic characteristics before and after well-tie profile processing, while Figure 18 (partial enlarged view of the red box area) reveals the significant advantages of this method in detail restoration. A comparison of results presented in Figure 18a and 18b indicated effective restoration of the amplitude characteristics of the reflected signal with weak energy and submerged in background noise in the original profile following processing using this method. Especially in the area marked by the red box in the figure, the original fuzzy weak reflection in-phase axis becomes clearer and sharper, and the background clutter is effectively suppressed. In the original section, some of the in-phase axes are intermittent and distorted, posing challenges in horizon tracking. After treatment, these breakpoints have been effectively bridged, the lateral continuity of the in-phase axis has been greatly improved, and the characteristics of the wave group become smoother and more natural, showing a good compliance with the stratigraphic deposition law. Integrated with the logging lithology column and curves shown in the center, the correspondence between the processed seismic waveform and the drilling layered interface is markedly improved. At the strong reflection horizon in the middle of Figure 18b, the enhanced wave group aligns closely with the key lithologic interface (yellow filling part) indicated by the logging data. This agreement confirms that this method enhances resolution while preserving the fidelity of the geological structure. This result strongly proves that the method utilized in this study can effectively mine the hidden information in seismic data, improve the resolution of the profile, and ensure high reliability of geological interpretation, which is of great value to address problems surrounding thin layer identification in complex structural areas.

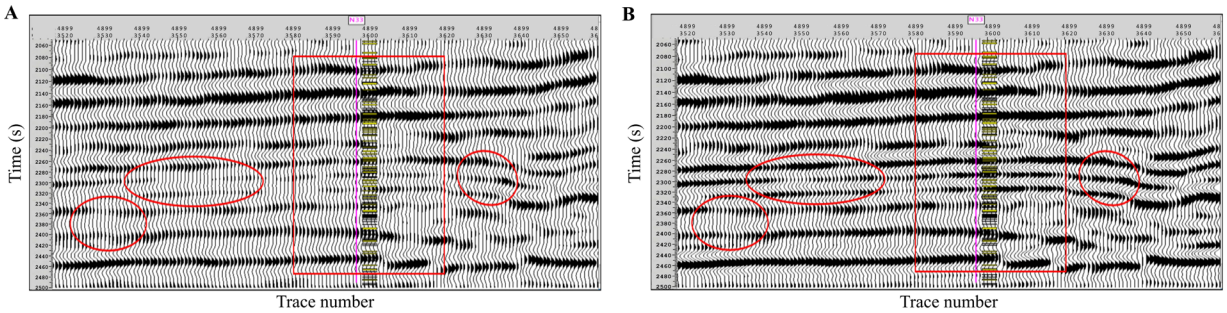

Figure 17. Comparison of seismic profiles before and after processing. (A) Original seismic data; (B) post-processing seismic profile.

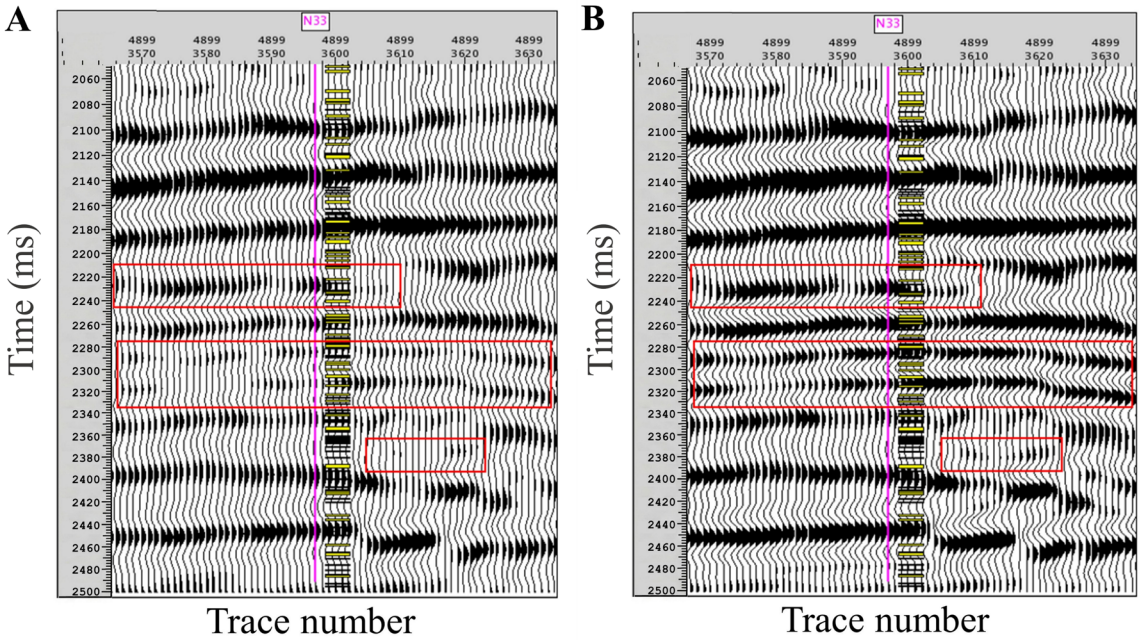

Figure 18. Enlarged comparison diagram of well-tie seismic profile. (A) Original seismic profile; (B) post-processing seismic profile.

6. Conclusion

In this paper, a cyclic spectrum enhancement technique is proposed to resolve weak reflections obscured by thin-layer interference. This methodology integrates Gaussian smoothing, derivative enhancement, and adaptive spectral conditioning to significantly improve the detectability of subtle seismic signals. Model tests and field data processing demonstrate that while the method maintains stability for thicker formations, it demonstrates exceptional performance in resolving weak signals at the tuning thickness (λ/4) and even extremely weak signals at λ/8, while maintaining high data fidelity and horizon consistency. However, the proposed technology struggles with several imitations in its application. For ultra-thin layers approaching the λ/32 limit, destructive interference becomes so pronounced that the effective signal spectrum is largely masked by the wavelet sidelobes, potentially leading to resolution instability or spurious events. Furthermore, beneath strong shielding layers (such as thick salt or basalt), severe energy attenuation and multiple-wave interference significantly reduce the SNR, thereby limiting the method's ability to recover weak deep-seated reflections. Future work will focus on integrating this technique with deep learning architectures to achieve adaptive parameter optimization and intelligent signal identification. By incorporating physics-informed neural networks, we aim to extend the method's applicability to ultra-deep, ultra-thin reservoirs and complex formations such as shale and tight gas, thereby facilitating high-precision sweet-spot prediction in challenging geological settings.

Acknowledgments

The authors would like to thank Dr. Yaming Yang (Yangtze University) for the excellent suggestions that greatly improved the original manuscript.

Funding

This work was supported in part by the Foundation National Key Laboratory of Uranium Resources Exploration-Mining and Nuclear Remote Sensing under Grant 2024QZ-TD-13, in part by the National Natural Science Foundation of China under Grant 42564006, and in part by the Natural Science Foundation of Jiangxi Province under Grant 20242BAB26051.

Conflict of interest

All authors declare no conflicts of interest.

Author contributions

Conceptualization: Hua Zhang
Formal analysis: Hua Zhang
Investigation: Hua Zhang
Methodology: Wei Chen
Writing–original draft: Hua Zhang
Writing–review & editing: Yu Song

Availability of data

Data are available from the corresponding author upon reasonable request.

References

1. Luo HM, Song WQ, Xing YR, Wang CJ, Mu X. Seismic weak signal enhancement processing method based on improved empirical mode decomposition. *Prog Geophys*. 2019;34(1):167-173.

   doi: 10.6038/pg2019BB0402

2. Gong D, Feng L, Xiao-Ting L, *et al*. The Application of S-transform Spectrum Decomposition Technique in Extraction of Weak Seismic Signals. *Chin J Geophys*. 2016;59(1):43-53.

   doi: 10.1002/cjg2.20212

3. Fan M, Wu S, Hu G, Qu J, Zhang J. A new method to enhance the characterisation of seismically thin beds based on the generalised S transform maximum modulus. *Explor Geophys*. 2018;49(4):559-571.

   doi: 10.1071/EG16123

4. Paksima S, Radad M, Roshandel Kahoo A, Soleimani Monfared MS. Identification of thin gas reservoir in reflection seismic data by synchrosqueezing S-transform in time-frequency representation. *Arab J Geosci*. 2023;16(6):376.

   doi: 10.1007/s12517-023-11464-4

5. Zhao Y, Cao H, Yang Z, Xu H, Nie R, Wang Z, *et al*. A seismic thin-layer detection factor calculated by integrated S transform with non-negative matrix factorization. *Geophys Prospect*. 2024;72(6):2274-2281.

   doi: 10.1111/1365-2478.13517

6. Wang SY, Chen H, Hu Y, Chen XP. Multichannel seismic resolution enhancement via spectral fitting for thin reservoir characterization. *Pet Sci*. 2025;22(7):2818-2827.

   doi: 10.1016/j.petsci.2025.04.008

7. Countiss ML. Frequency-enhanced imaging of stratigraphically complex, thin-bed reservoirs: A case study from South Marsh Island Block 128 Field. *Leading Edge*. 2002;21(9):826-836.

   doi: 10.1190/1.1508943

8. Chen S, Liu P, Tang D, Tao S, Zhang T. Identification of thin-layer coal texture using geophysical logging data: Investigation by Wavelet Transform and Linear Discrimination Analysis. *Int J Coal Geol*. 2021;239:103727.

   doi: 10.1016/j.coal.2021.103727

9. Yang L, Chen W, Wang H, Chen Y. Deep Learning Seismic Random Noise Attenuation via Improved Residual Convolutional Neural Network. *IEEE Trans Geosci Remote Sens*. 2021;59(9):7968-7981.

   doi: 10.1109/TGRS.2021.3053399

10. Song H, Gao Y, Chen W, Xue Y, Zhang H, Zhang X. Seismic random noise suppression using deep convolutional autoencoder neural network. *J Appl Geophys*. 2020;178:104071.

    doi: 10.1016/j.jappgeo.2020.104071

11. Cheng Z, Yuan Y, Liu S, Fan C, Li Z, Li Y. Application of wideband wavelet deconvolution for tight oil exploration. *Geophys Prospect Pet*. 2023;62(1):119-129.

    doi: 10.3969/j.issn.1000-1441.2023.01.010

12. Meng D, Wang D, Feng F, Huang F, Zhu H. Sparse deconvolution based on the Curvelet transform. *Acta Pet Sin*. 2013;34(1):107-114.

    doi: 10.7623/syxb201301012

13. Zhou X, Li Y, Song X, Jin L, Wang X. Thin Reservoir Identification Based on Logging Interpretation by Using the Support Vector Machine Method. *Energies*. 2023;16(4):1638.

    doi: 10.3390/en16041638

14. Chopra S, Castagna J, Portniaguine O. Thin-bed reflectivity inversion. In: *SEG Technical Program Expanded Abstracts 2006. 76th SEG Annual International Meeting; October 1-6, 2006; New Orleans, LA*. Society of Exploration Geophysicists; 2006:2057-2061.

    doi: 10.1190/1.2369941

15. Sui Y, Ma J. Blind sparse-spike deconvolution with thin layers and structure. *Geophysics*. 2020;85(6):V481-V496.

    doi: 10.1190/geo2019-0423.1

16. Xu Y, Yuan S, Zeng H, *et al*. Frequency-dependent multiscale network for seismic high-resolution processing. *Geophysics*. 2025;90(4):V297-V312.

    doi: 10.1190/geo2023-0682.1

17. Yuan S, Xu Y, Xie R, Chen S, Yuan J. Multi-scale intelligent fusion and dynamic validation for high-resolution seismic data processing in drilling. *Pet Explor Dev*. 2025;52(3):680-691.

    doi: 10.1016/S1876-3804(25)60596-9

18. Li M, Cao H, Yang Z, Yu Y, Ge Q, Yuan S. Intelligent prestack multitrace seismic inversion constrained by probabilistic geologic information. *Geophysics*. 2025;90(2):IM15-IM34.

    doi: 10.1190/geo2023-0638.1

19. Ge Q, Cao H, Yang Z, *et al*. High-resolution seismic impedance inversion integrating the closed-loop convolutional neural network and geostatistics: An application to the thin interbedded reservoir. *J Geophys Eng*. 2022;19(3):550-561.

    doi: 10.1093/jge/gxac035

20. Zhang R, Castagna J. Seismic sparse-layer reflectivity inversion using basis pursuit decomposition. *Geophysics*.

2011;76(6):R147-R158.

doi: 10.1190/geo2011-0103.1

21. Song H, Chen W. A method to predict reservoir parameters based on convolutional neural network-gated recurrent unit (CNN-GRU). *Pet Geol Recovery Effic*. 2019;26(5):73-78.

doi: 10.13673/j.cnki.cn37-1359/te.2019.05.009

22. Yang L, Chen W, Zha B. Prediction and application of reservoir porosity by convolutional neural network. *Prog Geophys*. 2019;34(4):1548-1555.

doi: 10.6038/pg2019CC0528

23. Liu J, Cao J, Zhao L, You J, Li H. Super-resolution reconstruction of seismic images based on deep residual channel attention mechanism. *IEEE Access*. 2024;12:149032-149044.

doi: 10.1109/ACCESS.2024.3477984

24. Ni W, Liu S, Wang L, Han B, Sheng S. Wavelet shaping deconvolution based on deep learning. *Oil Geophys Prospect*. 2023;58(6):1313-1321.

doi: 10.13810/j.cnki.issn.1000-7210.2023.06.002

25. Manzoor U, Ehsan M, Hussain M, Bashir Y. Improved reservoir characterization of thin beds by advanced deep learning approach. *Appl Comput Geosci*. 2024;23:100188.

doi: 10.1016/j.acags.2024.100188

26. Chen W, Zhang D, Chen Y. Random noise reduction using a hybrid method based on ensemble empirical mode decomposition. *J Seism Explor*. 2017;26(3):227-249.

ACCSCIENCE PUBLISHING

Journal of Seismic Exploration

ARTICLE

Geophysical prediction and evaluation of lacustrine shale oil and gas: Applications in the Fuxing area

Kai Xu[1,2]*, Guangzhi Zhang[1], Yong Chen[2], Zhentao Sun[2], Wei Xie[2], Xinpeng Pan[3], Yu Zhong[4], Xiaohui Yang[5], and Ling Su[2]

[1]Department of Geophysics, School of Geosciences, China University of Petroleum (East China), Qingdao, Shandong, China

[2]Department of Reservoir Geophysics, SINOPEC Geophysical Research Institute Co., Ltd., Nanjing, China

[3]Department of Geophysical Exploration, College of Geophysics, China University of Petroleum (Beijing), Beijing, China

[4]Department of Artificial Intelligence, School of Artificial Intelligence, Shiyan Key Laboratory of Electromagnetic Induction and Energy Saving Technology, Hubei Key Laboratory of Energy Storage and Power Battery, Hubei Key Laboratory of Automotive Power Train and Electronic Control, Hubei University of Automotive Technology, Shiyan, Hubei, China

[5]Department of Urban Underground Space, College of Civil Engineering, Xuzhou University of Technology, Xuzhou, Jiangsu, China

(This article belongs to the *Special Issue: Seismic Wave Propagation Theories and Reservoir Characterization Technologies for Complex Anisotropic Media*)

***Corresponding author:**
Kai Xu
(xukai.swty@sinopec.com)

Citation: Xu K, Zhang G, Chen Y, *et al*. Geophysical prediction and evaluation of lacustrine shale oil and gas: Applications in the Fuxing area. *J Seismic Explor*. 2026;35(3):026070030. doi: 10.36922/JSE026070030

Received: February 12, 2026

Revised: March 23, 2026

Accepted: March 23, 2026

Published online: May 11, 2026

Copyright: © 2026 Author(s). This is an Open-Access article distributed under the terms of the Creative Commons Attribution License, permitting distribution, and reproduction in any medium, provided the original work is properly cited.

Publisher's Note: AccScience Publishing remains neutral with regard to jurisdictional claims in published maps and institutional affiliations.

Abstract

The lacustrine shale reservoirs of Jurassic age in China's Sichuan Basin contain multiple hydrocarbon-bearing intervals and host substantial shale oil reserves, making them promising candidates as a significant replacement resource base for the region's petroleum production. However, the efficient exploration and development of lacustrine shale is confronted with two key geophysical challenges. Specifically, the first challenge involves identifying the location of the "sweet spot" with a primary emphasis on the engineering "sweet spot," characterized by critical parameters such as brittleness index and stress. The second challenge pertains to evaluating the effectiveness of hydraulic fracturing. To address these challenges, we first use engineering "sweet spot" seismic prediction technology to delineate the most favorable engineering zones, which subsequently guide well deployment and the design of horizontal well trajectories. We then use microseismic monitoring to assess the effects of hydraulic fracturing. Finally, we integrate these two technologies to form a complete geophysical workflow and conduct a comprehensive interpretation to understand the primary controlling factor. This integrated geophysical workflow effectively evaluated lacustrine shale reservoirs in the Sichuan Basin of China, providing robust recommendations for subsequent well placement, well trajectory design, and enhancing development efficiency in this complex geological setting. The analysis in this paper indicates that the brittleness index was the primary controlling factor in this geological setting, with higher values consistently corresponding to more microseismic events, and more extensive fracture networks.

Keywords: Lacustrine shale oil and gas; "Sweet spot" prediction; Brittleness; Differential horizontal stress ratio index; Microseismic monitoring; Comprehensive interpretation

1. Introduction

Recently, significant progress has been achieved in the exploration of marine shale gas within China's Sichuan Basin, leading to the successful commercial development of this resource.[1] In contrast, the Jurassic lacustrine shale oil and gas resources in the same region have not yet reached a comparable stage of development. Marine shale gas deposits are characterized by several distinct geological features that contribute to their commercial viability. These include extensive and stable lateral distributions, considerable burial depths, relatively substantial formation thicknesses, elevated concentrations of total organic carbon (TOC), and quartz content.[2] The geological characteristics of lacustrine shale formations, however, present a more complex scenario compared to their marine counterparts. Lacustrine shale typically exhibits shallower burial depths, thinner individual layers, intricate lithological associations with greater lithological variability, higher clay mineral content, more heterogeneous stress systems, more diverse fluid properties, and low permeability,[3] all of which contribute to the challenges in their exploration and development. Commercial lacustrine shale recovery necessitates extensive hydraulic fracturing treatments to establish adequate reservoir contact and conductivity pathways. Focusing on the complex geological characteristics of lacustrine shale, identifying the "sweet spot," assessing the effectiveness of hydraulic fracturing, and clarifying the factors that influence fracturing are key geophysical challenges.[4]

As one of the primary geophysical challenges in lacustrine shale studies, accurately identifying the double "sweet spot" is critical for guiding exploration and development efforts. This double "sweet spot" concept refers to formations that simultaneously satisfy the criteria of both geological and engineering "sweet spots." Specifically, the geological "sweet spot" is defined by high TOC content and optimal thermal maturity, whereas the engineering "sweet spot" is characterized by favorable friability and brittle mechanical properties.[5,6] In the subsequent analysis, particular attention will be devoted to the engineering "sweet spot" and its distinguishing characteristics within lacustrine shale systems.

The rock physics model is fundamental to the quantitative interpretation of engineering "sweet spots." Organic-rich lacustrine shale exhibits anisotropic characteristics, including both intrinsic anisotropy and fracture-induced anisotropy. Specifically, vertical transverse isotropy (VTI) arises from clay lamination, kerogen lamination, and horizontal fractures, while horizontal transverse isotropy (HTI) is induced by vertical fractures. Early theoretical foundations established that thin horizontal layering produces long-wave elastic anisotropy.[7] Subsequent developments introduced anisotropic effective medium models tailored to shale formations, incorporating the impacts of clay mineral orientation and microstructural anisotropy on elastic properties and anisotropic behaviour.[8,9] An orthorhombic medium model was later developed to characterize elastic wave propagation in vertically fractured geological formations, in which both VTI and HTI are considered.[10] The lacustrine shale exhibits pronounced orthorhombic anisotropy characteristics; therefore, the adoption of an orthorhombic rock physics model is essential for accurate characterization. More recent advances have integrated the effects of compaction, clay preferred orientation, and stress-dependent anisotropy into rock physics modeling frameworks.[11,12]

The key to predicting the engineering "sweet spot" of lacustrine shale lies in accurately estimating elastic and anisotropic parameters using an anisotropic rock physics model.[13] Traditional approaches estimate key parameters, such as brittleness and stress parameters, using elastic parameters derived from isotropic amplitude variation with offset inversion technology.[14-16] Building upon this foundation, subsequent advancements have integrated anisotropic medium theory with high-quality wide-azimuth seismic datasets to develop pre-stack amplitude variation with azimuth (AVAZ) inversion methodologies. These advanced techniques enable the three-dimensional (3D) spatial characterization of critical engineering "sweet spot" parameters.[17-19] When combined with geological knowledge and geomechanical principles, these prediction results provide valuable guidance for well placement optimization and horizontal well path planning in lacustrine shale formations.[20,21]

Focusing on the second critical geophysical challenge in lacustrine shale formations, evaluating hydraulic fracturing effectiveness and comprehending the influencing factors of fracturing play a vital role in achieving efficient development.[22-23] Microseismic monitoring offers opportunities to re-evaluate fractured

zones and gain insights into the progression of completion performance.[4,24] We utilize a practical and stable microseismic workflow that includes data acquisition, processing, and interpretation to accurately determine source locations and characterize the geometry of hydraulic fractures.[25-28] Leveraging real-time interpretation results from microseismic monitoring, we optimize horizontal well drilling designs and fracturing plans, and enhance production efficiency. Collectively, microseismic monitoring stands as a critical technique for the exploration and development of lacustrine shale reservoirs.

To address the requirements for high-quality exploration and development of lacustrine shale formations, we develop a comprehensive workflow by integrating engineering "sweet spot" seismic prediction techniques with microseismic monitoring technologies, thereby enabling detailed characterization of shale reservoirs both before and during hydraulic fracturing operations. This integrated workflow was validated in field applications at the Fuxing lacustrine shale formation in the Sichuan Basin, where it significantly improved well placement, trajectory planning, and fracturing design parameter optimization.

2. Methods

The geophysical workflow for lacustrine shale primarily comprises two key technologies. First, it incorporates "sweet spot" seismic prediction. It is widely recognized that key parameters defining "sweet spot" encompass TOC content, brittleness index, and stress state, among others. In this study, the engineering "sweet spot," encompassing both the brittleness index and the stress state, was the primary focus of analysis. We conducted quantitative seismic interpretation of the engineering "sweet spot" using pre-stack AVAZ inversion technology, thereby guiding well location deployment and horizontal well trajectory design. Second, the workflow involves microseismic monitoring, where we acquired, processed, and interpreted microseismic data to determine fracture geometry, enabling effective evaluation of hydraulic fracturing outcomes. Ultimately, we integrated "sweet spot" seismic prediction with microseismic monitoring to identify the primary controlling factor of hydraulic fracturing, thereby optimizing the fracturing plan in subsequent stimulation operations and improving the stimulated rock volume.

2.1. Rock physics modeling

The rock physics model establishes a quantitative correlation between reservoir properties and elastic parameters. The lacustrine shale has complex characteristics, including rapid facies transitions, heterogeneous lithological composition, high clay content, well-developed complex fractures, and the coexistence of oil and gas accumulations. To characterize the complex petrophysical properties of the lacustrine shale, we constructed an orthorhombic rock physics model, as illustrated in Figure 1, taking into account key influencing factors. The implementation process involved the following steps: first, we computed the equivalent modulus for each mineral in the matrix using the isotropic differential effective medium (DEM) model. Second, we computed the elastic matrix of the VTI background medium using the Backus average method.[7] Third, we added the horizontal fractures using the anisotropic DEM model.[8] Fourth, we added the vertical fractures into the model through the linear slip theory of Schoenberg.[10] Fifth, we computed the elastic modulus of pore fluid using the Voigt–Reuss weighted average. Sixth, we computed the orthorhombic elastic matrix of saturated rock matrix using the Brown–Korringa anisotropic fluid substitution formulation. Finally, an orthorhombic rock physics model specifically designed for lacustrine shale was established, enabling the computation of both elastic and anisotropic parameters for the study formation.

The orthorhombic rock physics model was successfully and effectively applied in the Fuxing area of Well-A. The input well logs included porosity, TOC, and mineralogical data (clay, quartz, and carbonate) (Figure 2). The predicted P- and S-wave velocities showed excellent agreement with the measured data, with an overall accuracy of 95%.

2.2. Stress prediction

Given the background of shale oil and gas exploration and development, the stress indicators included the magnitude and orientation of the differential horizontal stress ratio (DHSR), which serve as critical parameters for guiding well placement strategies and optimizing horizontal well trajectory design. The DHSR index is critical for hydraulic fracturing design because it controls fracture complexity and height growth. Low DHSR values indicate near-isotropic stress conditions favorable for complex fracture networks, while high values promote planar, bi-wing, and simple fracture networks.

In the present study, we analyzed stress magnitude and orientation predictions based on the pre-stack AVAZ inversion. The magnitude of the DHSR is defined as **Equation 1**:

$$\mathrm{DHSR} = \frac{\sigma_H - \sigma_h}{\sigma_H} \tag{1}$$

where σ_H is the maximum horizontal principal stress and σ_h is the minimum horizontal principal stress, respectively.

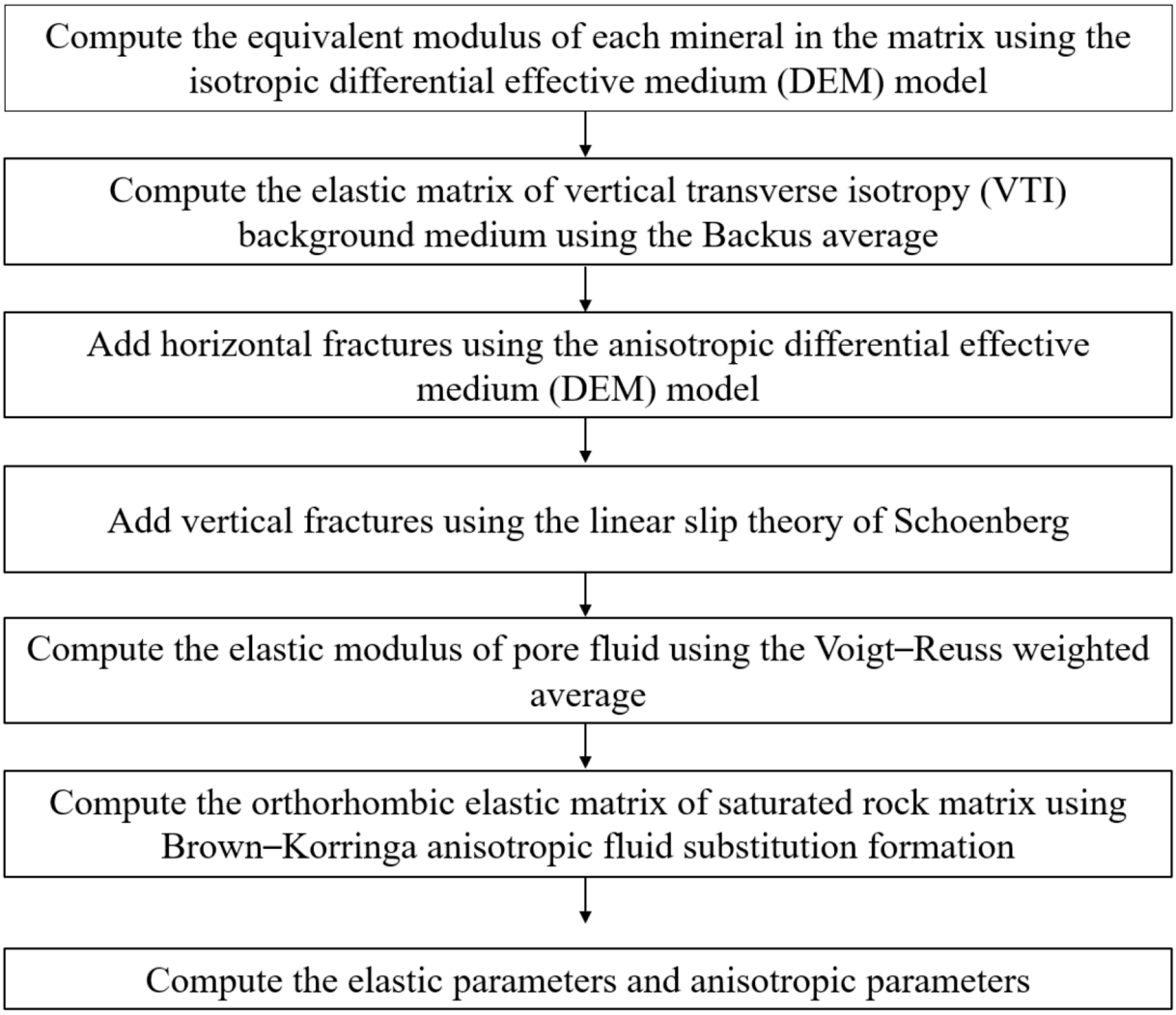

Figure 1. The lacustrine shale rock physics modeling workflow

Under the assumption of HTI anisotropy caused by vertically aligned fractures, DHSR can be related to seismic anisotropy parameters. To derive the DHSR formulation, we first adopted the HTI medium framework as proposed in previous studies,[29,30] which is specifically defined as **Equation 2**:

$$\mathrm{DHSR} = \frac{2I_S{}^2\Delta N}{I_P{}^2(1-\Delta N)+2I_S{}^2\Delta N} \tag{2}$$

where I_P represents P-wave impedance, I_S represents S-wave impedance, and ΔN denotes the normal weakness parameter characterizing fracture compliance.

Second, we derived the pre-stack AVAZ inversion formula by incorporating minor modifications to Shaw's equation,[31] and this modified formulation can be expressed as **Equation 3**:[32]

$$\begin{aligned} R_p(\theta,\varphi) = {} & sec^2\theta R_P - 8gsin^2\theta R_S - \\ & (gcos\varphi^2 sin^2\theta)(1-2g)\Delta N \\ & +(gcos^2\varphi sin^2\theta)\Delta T \end{aligned} \tag{3}$$

where θ denotes the incident angle, ϕ is the angle difference between the survey line's azimuth and the fracture orientation, g denotes the squared ratio of S-wave to P-wave velocity, R_{P} denotes P-wave impedance reflection coefficient, R_{S} denotes S-wave impedance reflection coefficient, ΔN is defined as the normal weakness

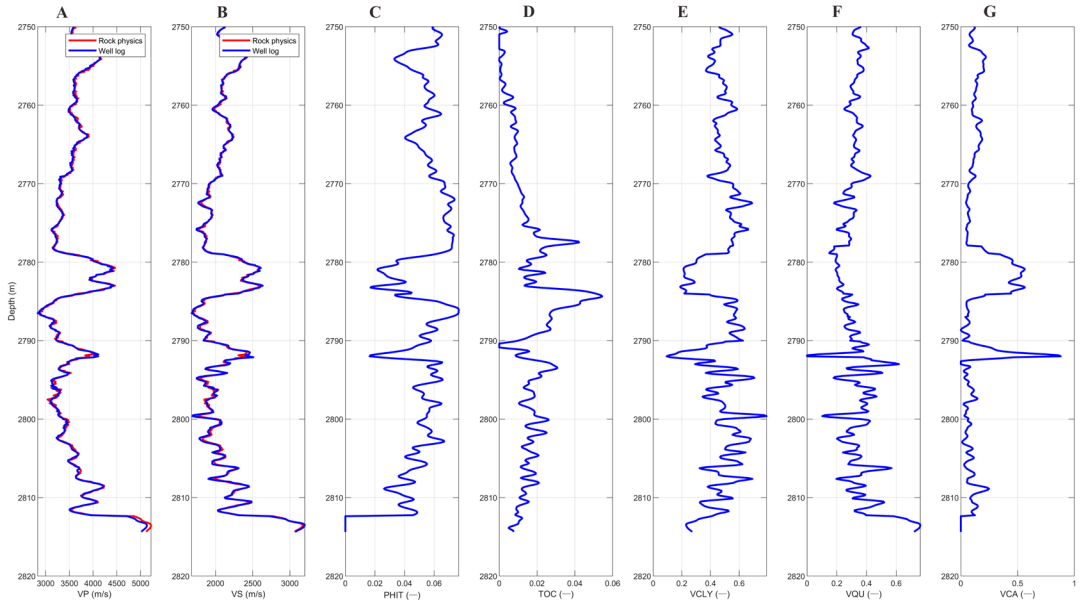

Figure 2. The orthorhombic rock physics modeling results of lacustrine shale. The well logs included (A) P-wave velocity, (B) S-wave velocity, (C) porosity, (D) total organic carbon (TOC), and mineralogical content of (E) clay, (F) quartz, and (G) carbonate. The blue curve indicates the measured well-log data, while the red curve indicates the rock physics-modeled results.

parameter of the fracture, and ΔT is defined as the tangential weakness parameter of the fracture.

According to convolution theory, seismic amplitude response can be represented as **Equation 4**:

$$d = G \cdot m \tag{4}$$

where d represents the observed data, G represents the forward operator, and m represents the model vector.

Assuming that seismic data background noise follows a Cauchy distribution, the correlation between real seismic data and reflection coefficients can be mathematically characterized through a likelihood function of a Cauchy distribution. By adding Cauchy constraints and model-constraint information, the stability and accuracy of the inversion are improved. The inversion estimation values can be obtained by solving the constructed inversion objective function. The specific form of the objective function is shown in **Equation 5**:

$$\begin{aligned} \min J(r') = {} & J_G(\underline{r}') + J_{Cauchy}(\underline{r}'_{Ip}) \\ & + J_p(\underline{r}'_{Ip}) + J_s(\underline{r}'_{Is}) \\ & + J_d(\underline{r}'_{\Delta N}) + J_d(\underline{r}'_{\Delta T}) \end{aligned} \tag{5}$$

where the first data misfit term describes the consistency between real seismic gathers and model-generated seismic gathers by the current model, ensuring consistency with measured data. The second term imposes a Cauchy sparsity constraint on the reflection coefficients, utilizing the heavy-tailed Cauchy distribution as a prior probability model, promoting sparse solutions in which significant reflectivity is concentrated at major geological boundaries. The remaining four terms are model-constraint terms that control the added low-frequency components, ensuring that the inversion results honor stratigraphic trends and petrophysical relationships. Taking the derivative of the objective function yields the final inversion equation shown as **Equation 6**:

$$\left(G^T G + \mu Q + P_3\right) \cdot m = \left(G^T d + Q_3\right) \tag{6}$$

where:

$$G = \begin{bmatrix} W \cdot a(\theta_1) & W \cdot b(\theta_1) & W \cdot c(\theta_1, \phi_1) & W \cdot d(\theta_1, \phi_1) \\ W \cdot a(\theta_2) & W \cdot b(\theta_2) & W \cdot c(\theta_2, \phi_2) & W \cdot d(\theta_1, \phi_1) \\ \vdots & & & \\ W \cdot a(\theta_l) & W \cdot b(\theta_l) & W \cdot c(\theta_l, \phi_n) & W \cdot d(\theta_l, \phi_n) \end{bmatrix} \tag{7}$$

$$P_3 = \alpha_{Ip} C^T C' + \alpha_{Is} C^T C + \alpha_{\Delta N} C^T C + \alpha_{\Delta T} C^T C \tag{8}$$

$$Q_3 = \alpha_{lp} C^T \underline{\xi}_{lp} + \alpha_{ls} C^T \underline{\xi}_{ls} + \alpha_{\Delta N} C^T \underline{\xi}_{\Delta N} + \alpha_{\Delta T} C^T \underline{\xi}_{\Delta T} \quad (9)$$

$$\mu = \frac{2\sigma_n^2}{\sigma_m^2} \quad (10)$$

W is wavelet matrix, $a(\theta_l)$, $b(\theta_l)$, $c(\theta_l, \phi_n)$, $d(\theta_l, \phi_n)$ are model parameter coefficients of AVAZ formula, $C = \begin{pmatrix} 1 & \cdots & 0 \\ \vdots & \ddots & \vdots \\ 1 & \cdots & 1 \end{pmatrix}$ is the lower triangular summation matrix, $\alpha_{IP,}\alpha_{IS,}\alpha_{\Delta N,}$ and $\alpha_{\Delta T}$ are the coefficient terms corresponding to the four parameters. Accounting for the thin-bed geological characteristic and well-logging responses of the lacustrine shale, we employ k-fold cross-validation to optimal μ and α parameters, thereby obtaining the stable, high-precision inversion results for elastic and anisotropic parameters. $\underline{\xi}_{lp}, \underline{\xi}_{ls}, \underline{\xi}_{\Delta N}$ and $\underline{\xi}_{\Delta T}$ are the reflection coefficients of the initial model. σ_n^2 is the noise variance, σ_m^2 is the model reflection coefficient variance. Q is the off-diagonal weighted matrix, and it is defined as follows:

$$Q_n = \begin{cases} \dfrac{1}{\left(\dfrac{r_n'^2}{2\sigma_1^2} + 1.0\right)^2}, n \le N \\ \dfrac{\sigma_1^2}{\sigma_2^2} \dfrac{1}{\left(\dfrac{r_n'^2}{2\sigma_2^2} + 1.0\right)^2}, N < n \le 2N \\ \dfrac{\sigma_1^2}{\sigma_3^2} \dfrac{1}{\left(\dfrac{r_n'^2}{2\sigma_3^2} + 1.0\right)^2}, 2N < n \le 3N \\ \dfrac{\sigma_1^2}{\sigma_4^2} \dfrac{1}{\left(\dfrac{r_n'^2}{2\sigma_4^2} + 1.0\right)^2}, 3N < n \le 4N \end{cases} \quad (11)$$

where σ_1, σ_2, σ_3, and σ_4 are the singular value decomposition components of the sparse covariance matrix of the inversion parameters, and r_n' is the initial model reflection coefficient.

By deriving and calculating using the aforementioned mathematical equation, the desired inversion parameters can be effectively retrieved. The input dataset for this inversion process primarily included the following essential components: well-logging curves characterizing formation properties; azimuth-dependent seismic wavelets capturing azimuthal variation characteristics; prior geological models incorporating key parameters such as P-wave and S-wave impedances; and azimuthally stacked seismic data volumes encompassing the study area. We had a brief discussion of uncertainty, which indicates that typical pre-stack gathers (signal-to-noise ratio ~ 3–5) can introduce ±5–8% relative uncertainty in final DHSR estimates and ±7–10% relative uncertainty in brittleness index estimates. Despite these uncertainties, the overall vertical and spatial trends remained geologically reasonable.

Finally, we used the elastic and anisotropic parameters obtained from the AVAZ inversion to compute DHSR. To address the problem of stress direction prediction, we used least-squares ellipse fitting to estimate orientation from wide-azimuth seismic datasets. By integrating these seismic-derived orientations with dipole acoustic logging measurements, we determined the minimum principal stress direction with enhanced reliability. Subsequently, we obtained the 3D spatial distribution of stress orientation and DHSR, thereby providing quantitative geomechanical constraints for optimal well placement and horizontal trajectory design.

2.3. Brittleness index prediction

The brittleness index is a critical parameter for identifying engineering "sweet spots," directly governing the feasibility and effectiveness of hydraulic fracturing operations. This study presents a methodology for predicting a brittleness index based on pre-stack seismic inversion. To differentiate brittle from ductile lithologies, we first established the brittleness index through rock physics analysis, defined as the ratio of Young's modulus to the Lamé constant. Higher values indicate increased brittleness in shale formations, whereas lower values signify greater ductility. The formulation is expressed as **Equation 12**:

$$Bi = E / \lambda \quad (12)$$

where B_i denotes brittleness index, and E and λ denote Young's modulus and the Lamé constant.

This mathematical formula, represented by P-wave impedance and S-wave impedance, can be formulated as **Equation 13**:

$$Bi = \frac{I_S^2\left(3I_P^2 - 4I_S^2\right)}{\left(I_P^2 - I_S^2\right)\left(I_P^2 - 2I_S^2\right)} \quad (13)$$

where I_P denotes P-wave and I_S denotes S-wave impedance.

The cross-plot of E/λ and E/σ (Figure 3) shows both of them have good correlation, and E/λ just need P-wave and S-wave impedance, which avoid density term, as we all known, the density inversion is difficult to obtain good

results.

Second, based on the elastic parameter inversion results from the AVAZ inversion analysis, we calculated the 3D brittleness index volume using both P-wave and S-wave impedance data. This approach enabled us to quantitatively characterize the brittleness properties of the target lacustrine shale formation using real data from the Sichuan Basin.

2.4. Microseismic monitoring

Microseismic monitoring is an effective tool for real-time characterization of hydraulic fracture propagation and for evaluating the effectiveness of hydraulic fracturing operations. We developed the technical workflow for surface microseismic fracturing monitoring, as illustrated in Figure 4. First, we developed a radially distributed ground-acquisition system specifically tailored for this work, enabling real-time detection of microseismic signals. It comprised 12 geophone arrays deployed in concentric rings centered on the treatment well pad, each array consisting of 24 vertical-component geophones. Second, we focused on enhancing microseismic weak signals through a systematic processing workflow that included time–frequency spectral decomposition, strong-noise attenuation, band-pass filtering, amplitude-energy gain, trace balancing, adaptive filtering, and higher-order moment filtering. When microseismic signals were automatically identified using the short-term average/long-term average (STA/LTA) algorithm, the Pwave arrival picking uncertainty ranged from 1–5 ms for high-quality data and from 5–20 ms for moderate-quality data. Third, we conducted microseismic source location and inversion analysis to determine the specific location and magnitude of each microseismic event. Finally, a comprehensive interpretation was performed to characterize the hydraulic fracture geometry and evaluate the effectiveness of hydraulic fracturing. The microseismic data processing workflow is shown in Figure 4.

By integrating "sweet spot" seismic prediction with microseismic monitoring data, this study first evaluates

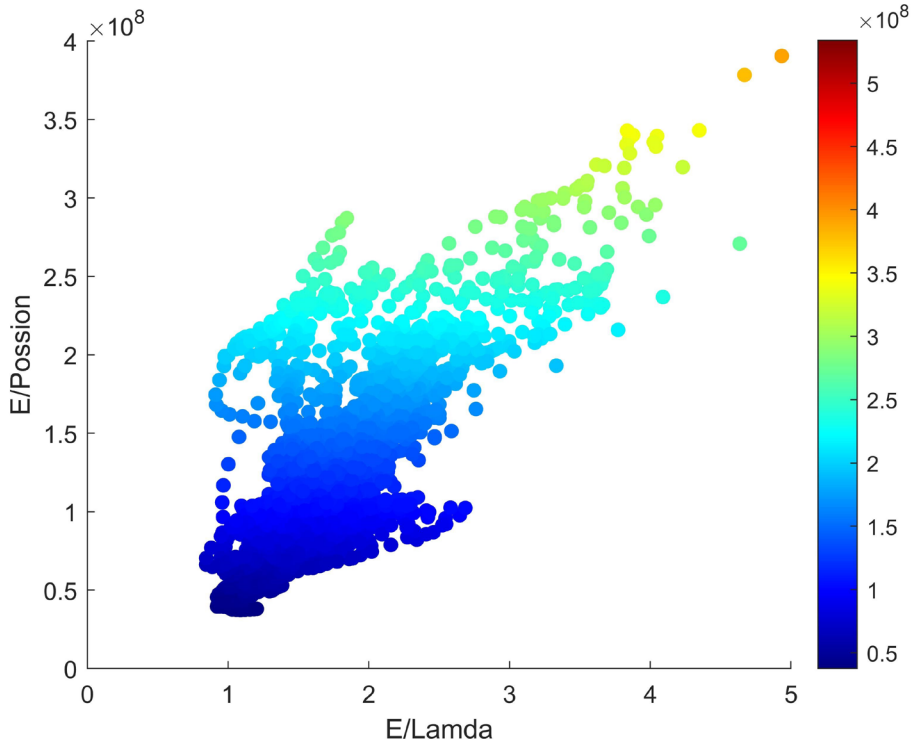

Figure 3. The Well-A cross plot of E/λ and E/σ; the color bar is E/σ

Note: E is the Young's modulus, which represents the ratio of normal stress to normal strain in uniaxial tension/compression, and measures material stiffness or resistance to axial deformation. λ is the Lamé-constant, which is related to volumetric deformation, and describes material response to hydrostatic pressure. σ is the Poisson's ratio, which is the ratio of transverse contraction strain to axial elongation strain under uniaxial stress, and describes lateral deformation behavior of materials.

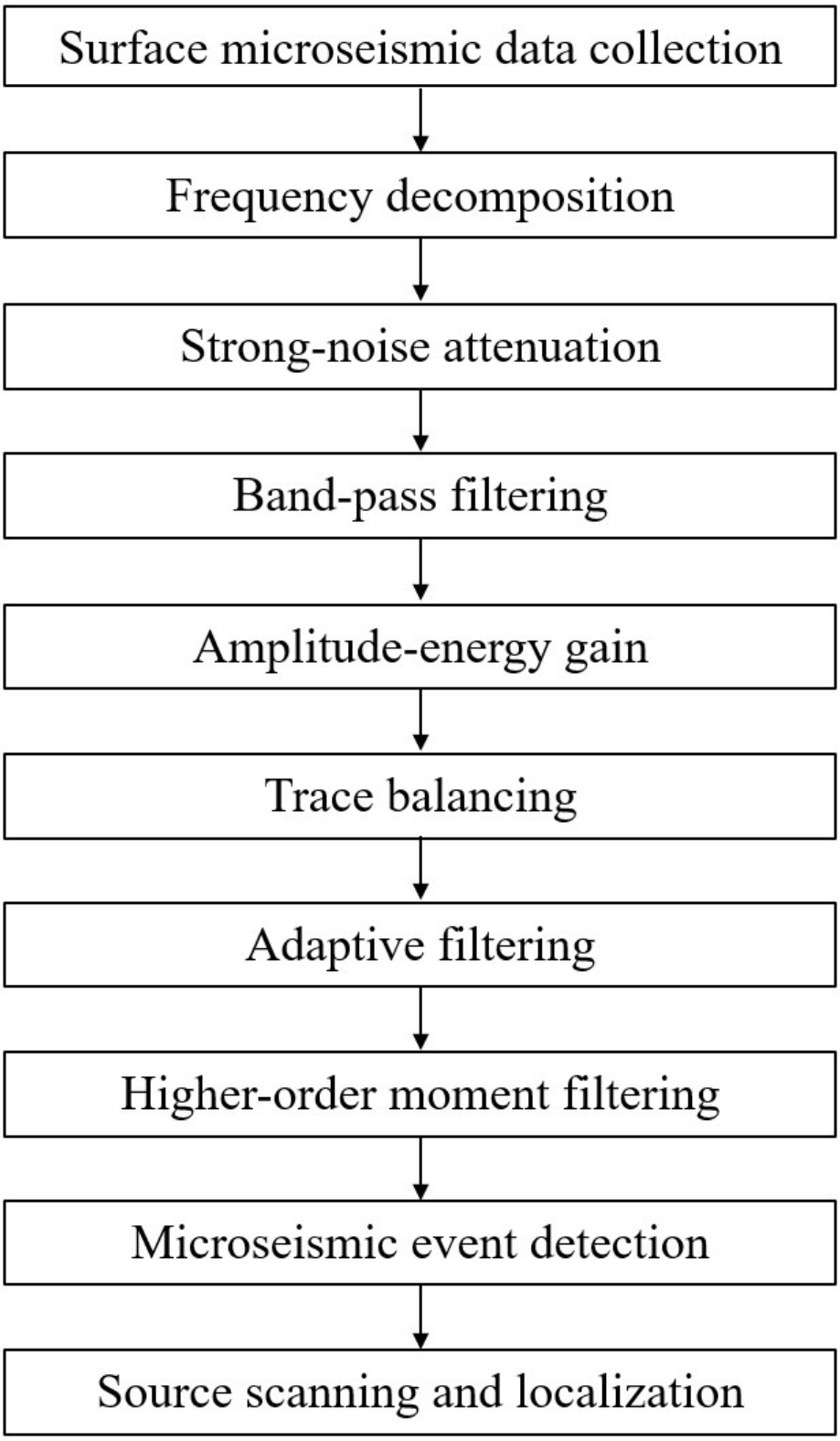

Figure 4. The microseismic data processing workflow

hydraulic fracturing performance and then analyzes the key controlling factors that govern its effects. This closed-loop workflow ensures continuous improvement in characterization accuracy and treatment effectiveness as more data are acquired throughout the oil and gas field exploration and development lifecycle. Building on the valuable insights and practical experiences from prior research and engineering practices, this study enables more precise well placement, optimized horizontal well trajectory design, and refined fracturing strategies tailored to the geological characteristics of the target formation. These comprehensive optimizations significantly enhance both production efficiency and economic viability of lacustrine shale oil and gas development in the Sichuan Basin.

3. Results

3.1. Work area overview

Southern China, particularly the Sichuan Basin, hosts substantial lacustrine shale reservoirs rich in organic matter. In contrast to North American shale systems, the Sichuan Basin's shale formations have undergone complex tectonic evolution involving multiple episodes of deformation, uplift, and erosion, resulting in intricate fracture networks and highly variable reservoir properties.[32] The study area encompasses approximately 2,500 km^2 in the Fuxing region of the Sichuan Basin, where geological structures exhibit diverse features, including both anticlinal and synclinal formations. Specifically, our investigation focuses on a synclinal structure within the high-steep fold belt of the eastern Sichuan Basin, targeting the Jurassic-aged Dongyuemiao Formation (Figure 5). This formation exhibits gentle dip angles and comprises lacustrine shale reservoirs ranging in thickness from 80 to 150 m, at depths of 2,500–3,500 m. Well-A was initially drilled at the syncline center, followed by the deployment of a horizontal well group, comprising Well-A1, Well-A2, and Well-A3, and was subsequently hydraulically fractured. Production data from these wells indicate favorable oil and gas productivity.

A wide-azimuth, long-offset 3D seismic survey was acquired, processed, and interpreted to characterize lacustrine shale reservoirs for exploration and development (Figure 6). The 3D seismic survey was a high-fold (120-fold) wide-azimuth survey with a bin size of 25 m × 25 m. The data were processed using an offset vector tile pre-stack time migration with anisotropic velocity analysis, preserving azimuthal information for AVAZ inversion, and yielded magnitudes of DHSR and a brittleness index from the elastic and anisotropic parameters.

High-quality data were obtained and interpreted, indicating that the study area lies between the yellow and pink lines, encompassing the main lacustrine shale body. This region contains extensive, laterally continuous shale reservoirs. The seismic data in this area had a high signal-to-noise (S/N) ratio. According to outcrops and logging data, the stable Lgs and J1dy formations were designated as potential reservoirs. The vertical logging data from Well-A, presented in Figure 2D, provide detailed insights into the basin's stratigraphic evolution. Within the target shale interval, TOC content ranged from 2% to 4% (Figure 2) and showed an overall increasing trend with depth. Furthermore, the target shale formation was characterized by well-developed roof and floor lithology that provide effective sealing conditions. These geological characteristics collectively indicate significant potential for lacustrine shale oil and gas exploration and development in this interval.

3.2. Comprehensive interpretation results

Following the offset vector tile pre-stack migration processing of the seismic data, wide-azimuth seismic gathers were generated. Pre-stack AVAZ inversion of these gathers yielded DHSR magnitudes and i*n situ* stress directions (Figure 7). DHSR values across the study area ranged from 0.08 to 0.18 (Figure 7). The range of DHSR reflects geological variability; lower magnitudes indicate higher potential for complex fracture network development during hydraulic fracturing, whereas higher values tend to produce simpler fracture geometries. In Figure 8, the minimum principal stress direction derived from seismic data is compared with the maximum principal stress direction obtained from dipole acoustic logging in Well-A. These orientations exhibited a nearly orthogonal relationship, consistent with the observation that microseismic event propagation is approximately perpendicular to the minimum principal stress direction. This multi-source consistency verifies the reliability of the stress field characterization methodology. Building upon these findings, three horizontal well trajectories were strategically designed parallel to the minimum principal stress direction. This placement strategy was expected to reduce mechanical resistance during hydraulic fracturing and enhance fracture propagation efficiency, ultimately improving estimated ultimate recovery.

Following well placement and horizontal well trajectory design, microseismic monitoring and integrated interpretation were initiated. Surface microseismic acquisition employed a 12-line array comprising 2,026 active channels, enabling real-time processing throughout hydraulic fracturing operations. A total of 2,640 microseismic events were identified across 88 fracturing stages, with magnitudes ranging from −1.98

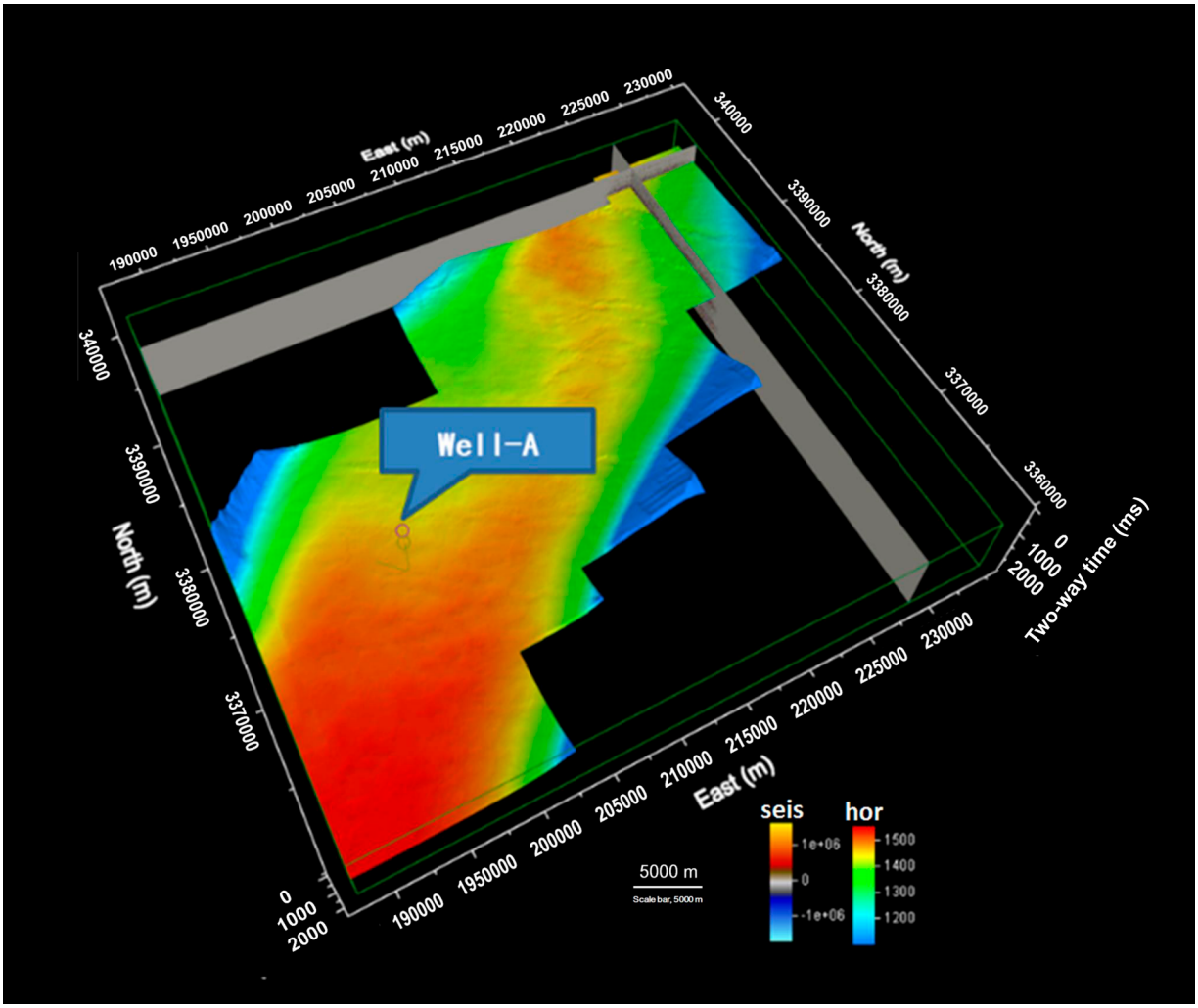

Figure 5. The three-dimensional structural map of the target shale interval. Well-A is positioned at the center. Scale bar: 5,000 m. Abbreviations: seis: Seismic; hor: Horizon.

to −1.08. Event locations were determined using a robust source-location algorithm. The spatial distribution of microseismic events is shown in Figure 9. Second, based on the observed fracture geometry, there are evident remaining spaces between adjacent wells in the current 300 m well-spacing configuration. Consequently, the fracture spacing in the hydraulic stimulation design for subsequent horizontal well pads in this region may be appropriately reduced to enhance the reservoir utilization rate and optimize development efficiency. Third, based on microseismic event locations, the statistical interpretations of fracture length, width, and height are presented in Table 1. The average fracture lengths were Well-A2 > Well-A1 > Well-A3, and the average fracture heights were Well-A1 > Well-A2 > Well-A3; the average widths of hydraulic fracture from different wells were broadly comparable.

We conducted an integrated interpretation by correlating the pre-stack inversion-derived brittleness index volume (Figure 10) with microseismic event distributions. Spatial variability analysis revealed moderate planar variations in brittleness across the study area, consistent with the regional geological framework. Microseismic monitoring data from the Well-A platform exhibited distinct clustering on both sides of the wellbore trajectories, with hydraulic fracture propagation orientations approximately orthogonal to the horizontal well paths, thereby supporting the validity of the well deployment design. Stratigraphic brittleness evaluation across the three horizontal wells indicated a descending trend: Well-A2 > Well-A1 > Well-A3. This brittleness gradient correlates positively with both the quantity and

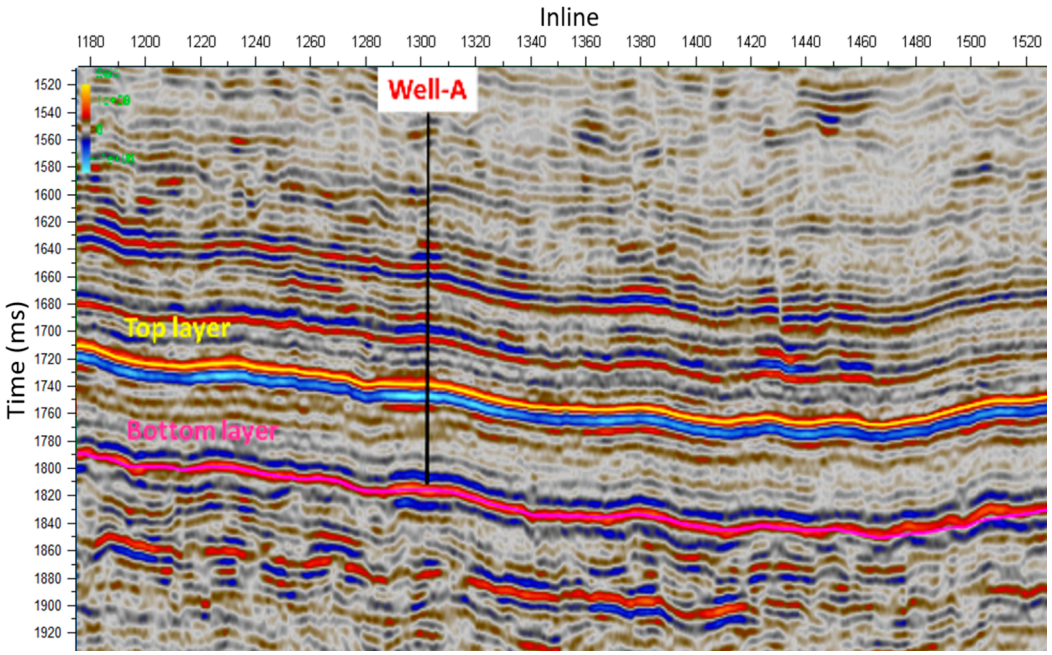

Figure 6. The seismic profile along the inline crossing of Well-A, with the target shale interval bounded by the yellow and pink lines

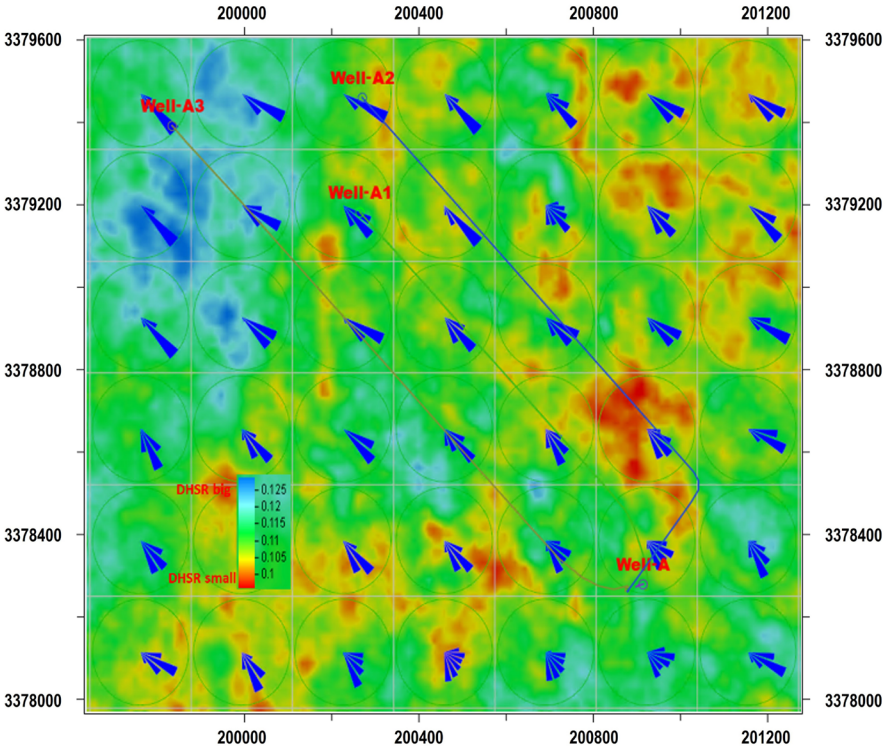

Figure 7. The Well-A platform map, constructed from differential horizontal stress ratio (DHSR) and orientation data, illustrates the minimum principal stress orientation within the target formation and the trajectories of three horizontal wells, with each trajectory distinguished by a distinct color. The warm colors on the map indicate lower DHSR values, and the cool colors indicate higher DHSR values.

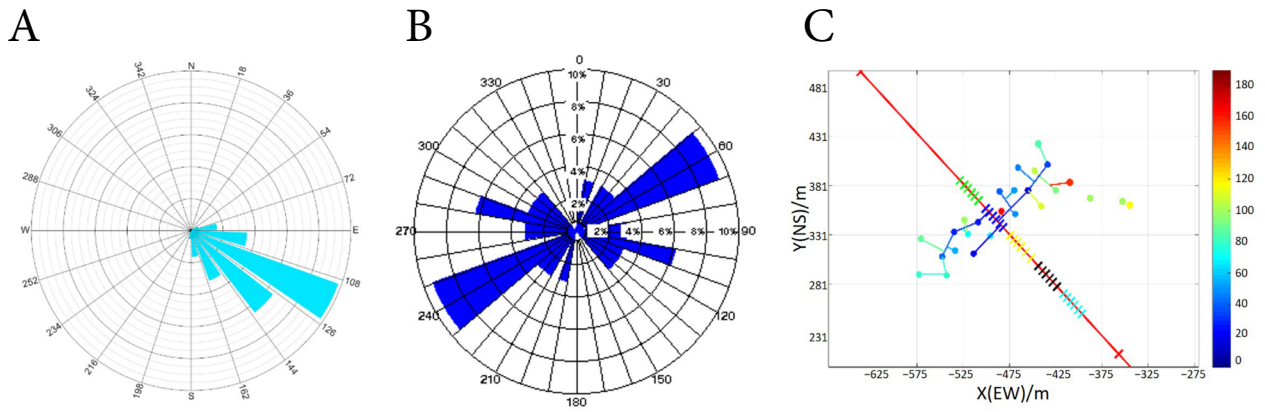

Figure 8. Rose diagrams of stress orientations and microseismic results at Well-A. (A) Minimum principal stress orientation from pre-stack AVAZ inversion. (B) Maximum principal stress orientation from dipole acoustic logging. (C) Microseismic interpretation of hydraulic fractures for the fracturing stage 29 of horizontal well-A3. The red line indicates the horizontal well trajectory, the colored dots indicate microseismic events, and the colored lines between microseismic events indicate the extension trajectories of hydraulic fractures; warm colors indicate higher fracture energy.

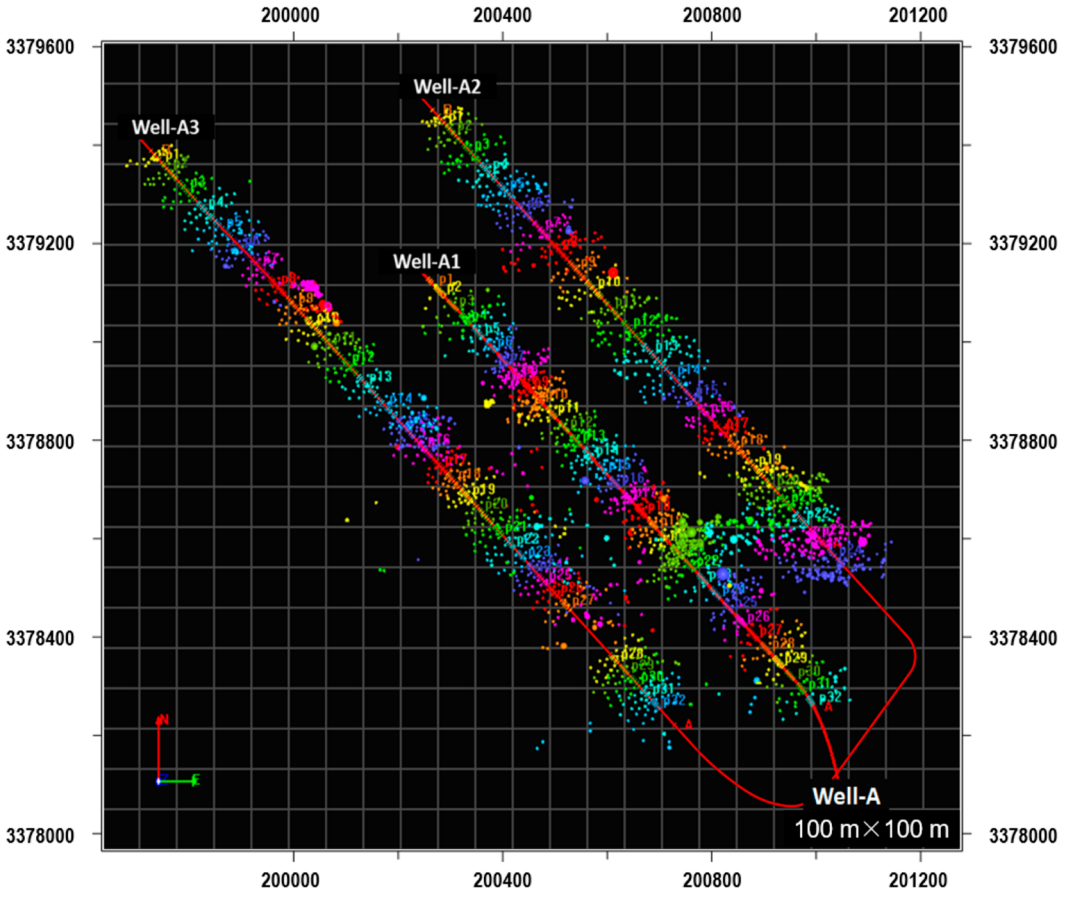

Figure 9. Plan view of microseismic event locations for the Well-A platform. The red lines indicate the horizontal well trajectory, the colored dots indicate the microseismic events at different stages, and the different sizes of dots indicate different fracture energies. The size of each grid square indicates the scale of 100 m × 100 m.

Table 1. The statistical geometry shape of hydraulic fracture based on microseismic monitoring

Geometry shape \ Well name	Well-A1	Well-A2	Well-A3
Average number of events per fracturing stage	31	38	23
Average length (m)	176	188	154
Average width (m)	61	62	64
Average height (m)	52.5	37	30

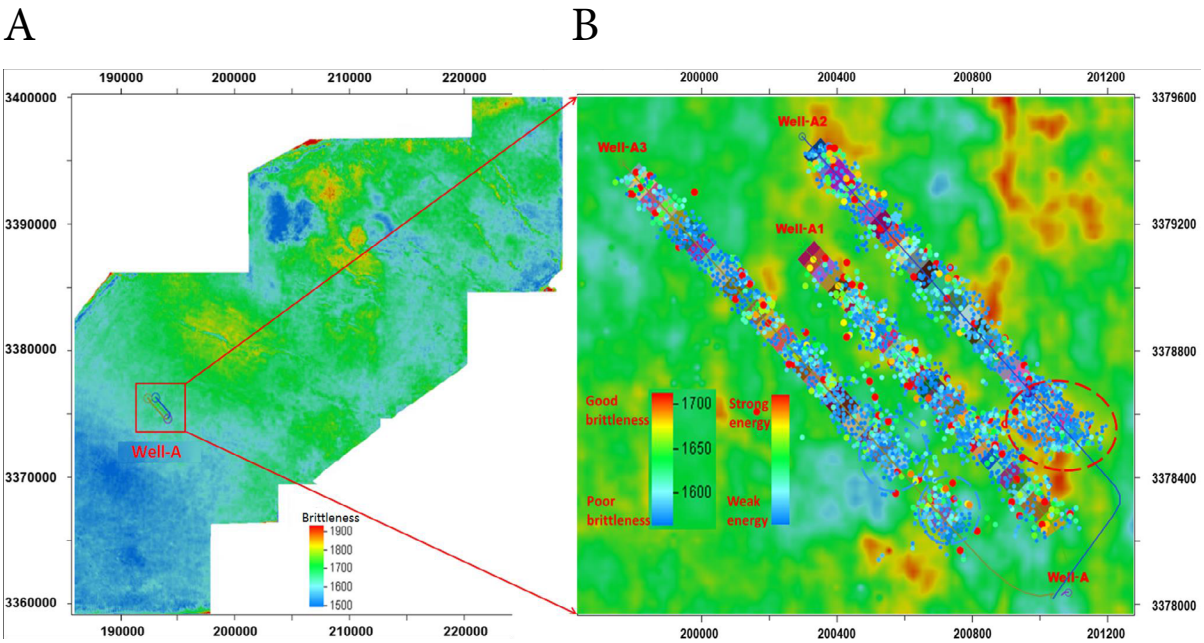

Figure 10. Brittleness index slices along the target horizon. (A) Full three-dimensional survey extent. (B) A detailed view of microseismic events and stage information for three horizontal wells. Colored dots denote microseismic events of varying magnitudes, overlain on the background brittleness index; colored rectangles indicate individual fracturing stages.

the magnitude of recorded microseismic events, suggesting a direct relationship between rock mechanical properties and the intensity of fracture development. Detailed examination of high-brittleness zones (red circles) revealed concentrated microseismic activity with morphologically similar distribution patterns, whereas low-brittleness regions (blue circles) exhibited significantly reduced event counts. These correlative analyses demonstrate strong consistency between brittleness index predictions and microseismic interpretations, confirming the reliability of the geomechanical characterization approach.

4. Discussion

In this study, the geophysical prediction and evaluation technologies for lacustrine shale oil and gas were successfully applied to real Fuxing data from the Sichuan Basin. First, engineering "sweet spot" prediction technologies based on a rock physics model characterized the compressibility of lacustrine shale in 3D space; the prediction results were in seismic scale, which are tens to

hundreds of meters. Second, the microseismic monitoring technology evaluated the hydraulic fracturing effect in real time; the acquisition method of surface microseismic monitoring technology has a longer propagation and stronger attenuation, whereas the acquisition method of downhole microseismic monitoring technology is close to the source. It exhibited detection thresholds of moment magnitude (Mw) from shear-wave source between −1.0 and −2.0 for surface configuration, whereas downhole configuration typically achieved lower thresholds of Mw −3.0 to −3.5. Consequently, the microseismic monitoring technology had detection limits of approximate magnitude, and potentially missed small-scale fracture events that contribute to permeability enhancement. This resultant sampling bias introduced systematic uncertainty into the interpretation of fracture network intensity and stimulated reservoir volume estimates; the limitation underscores the necessity of microseismic with complementary diagnostics (e.g., reservoir characterization, distributed acoustic sensing). Third, we performed a comprehensive interpretation that included static and dynamic data. The resulting analysis guided subsequent well placement and optimization of fracturing designs. Additionally, hydraulic fracturing operational parameters were significant factors influencing fracture geometry and production performance, highlighting the importance of this research.

5. Conclusion

This study presents an integrated application of "sweet spot" seismic prediction and microseismic monitoring for lacustrine shale formations in the Sichuan Basin. The research framework comprised three interconnected methodological components. First, engineering "sweet spot" seismic prediction was conducted using an orthorhombic anisotropic rock physics model, enabling 3D characterization of critical reservoir parameters, including brittleness index, DHSR, and *in situ* stress orientation, and guiding horizontal well trajectory optimization. Second, the high-precision microseismic monitoring was implemented to precisely locate hydraulic fracture initiation throughout the stimulation process. Third, comprehensive data interpretation facilitated quantitative evaluation of fracturing effectiveness and identification of the primary controlling factor. Analysis indicates that the brittleness index was the primary controlling factor in this geological setting, with higher values consistently corresponding to more extensive fracture networks. Field application of this integrated methodology in the Fuxing area of the Sichuan Basin yielded promising results, validating the proposed approach. These findings suggest significant potential for broader application in enhancing the efficiency of exploration and development in unconventional reservoirs.

Acknowledgments

We thank Sinopec for granting permission to publish this work, and gratefully acknowledge Sinopec Jianghan Oilfield and Sinopec Exploration Company for providing the data.

Funding

This work is supported by the Natural Science Foundation of China (Grant No. U23B6010) and the National Natural Science Foundation of China (Grant No. U24B6001).

Conflict of interest

Xinpeng Pan is an Editorial Board Member of this journal, but was not in any way involved in the editorial and peer-review process conducted for this paper, directly or indirectly. All the authors have no conflicts of interest.

Author contributions

Conceptualization: Kai Xu
Data curation: Kai Xu
Formal analysis: Kai Xu, Guangzhi Zhang, Wei Xie, Xinpeng Pan, Yu Zhong, Xiaohui Yang
Funding acquisition: Yong Chen, Zhentao Sun
Investigation: Kai Xu
Methodology: Kai Xu, Guangzhi Zhang, Wei Xie, Xinpeng Pan, Yu Zhong, Xiaohui Yang
Project administration: Kai Xu
Resources: Guangzhi Zhang, Yong Chen, Zhentao Sun
Software: Wei Xie, Xiaohui Yang
Supervision: Guangzhi Zhang
Validation: Xinpeng Pan, Yu Zhong
Writing-original draft: Kai Xu, Wei Xie, Ling Su
Writing-review & editing: Kai Xu

Availability of data

The data analyzed in the study can be requested via Sinopec and Sinopec Geophysical Research Institute (xukai.swty@sinopec.com).

References

1. Guo X, Li Y, Borjigen T, *et al*. Hydrocarbon generation and storage mechanisms of deep-water shelf shales of Ordovician Wufeng Formation–Silurian Longmaxi Formation in Sichuan Basin, China. *Pet Explor Dev*. 2020;47(1):204-213.

   doi: 10.1016/S1876-3804(20)60019-2

2. Hu DF, Wei ZH, Wei XF, Shi WB, Wang DJ, Liu XJ. Breakthrough in the exploration of continental shale oil/gas of Jurassic Lianggaoshan Formation in the Fuxing area of the Sichuan Basin and its inspiration. *Nat Gas Ind*. 2025;45(1):1-

13. [In Chinese].

doi: 10.3787/j.issn.1000-0976.2025.01.001

3. Yang Z, Zou CN, Wu ST, *et al*. Characteristics, Types, and Prospects of Geological Sweet Sections in Giant Continental Shale Oil Provinces in China. *J Earth Sci*. 2022;33(5):1260-1277.

doi: 10.1007/s12583-022-1735-9

4. Teng L, Yang XC, Lin ZL, Cheng JB. Combine prestack inversion and microseismic to understand hydraulic fracturing performance in gas shale of Sichuan Basin, China. In: *SEG Technical Program Expanded Abstracts 2016. 86th SEG International Exposition and Annual Meeting; October 16-21, 2016; Dallas, TX, USA*. Society of Exploration Geophysicists; 2016:5017-5021.

doi: 10.1190/segam2016-13530388.1

5. Tang JM, Xu TJ, Cheng BJ, Shen J, Yu Q. Sweet-spot prediction and aided design for drilling engineering: Application to deep shale gas reservoirs in the Sichuan Basin. *Geophys Prospect Pet*. 2021;60(3):479-487. [In Chinese].

doi: 10.3969/j.issn.1000-1441.2021.03.014

6. Chen C, Yin XY, Chen ZQ, Liu XJ. A seismic prediction strategy for engineering "sweet spots" in deep shale gas exploration: A case study in DS area. *Geophys Prospect Pet*. 2021;60(4):632-642. [In Chinese].

doi: 10.3969/j.issn.1000-1441.2021.04.012

7. Backus GE. Long-wave elastic anisotropy produced by horizontal layering. *J Geophys Res*. 1962;67(11):4427-4440.

doi: 10.1029/JZ067i011p04427

8. Hornby BE, Schwartz LM, Hudson JA. Anisotropic effective-medium modeling of the elastic properties of shales. *Geophysics*. 1994;59(10):1570-1583.

doi: 10.1190/1.1443546

9. Sayers CM. The elastic anisotropy of shales. *J Geophys Res*. 1994;99(B1):767-774.

doi: 10.1029/93JB02579

10. Schoenberg M, Helbig K. Orthorhombic media: modeling elastic wave behavior in a vertically fractured earth. *Geophysics*. 1997;62(6):1954-1974.

doi: 10.1190/1.1444297

11. Luo K, Zong ZY, Yin XY, Ji LX, Yang YM. Shale anisotropic rock-physics model incorporating the effect of compaction and nonplate mixtures on clay preferred orientation. *Geophysics*. 2024;89(6):MR309-MR323.

doi: 10.1190/geo2023-0591.1

12. Xu Y, Zhang F, Li XY. A stress-dependent anisotropic rock-physics model for shale with bedding-parallel cracks. *Geophysics*. 2025;90(6):M261-M270.

doi: 10.1190/geo2025-0037.1

13. Sarkar D, Bakulin A, Kranz RL. Anisotropic inversion of seismic data for stressed media: Theory and a physical modeling study on Berea sandstone. *Geophysics*. 2003;68(2):690-704.

doi: 10.1190/1.1567240

14. Buland A, Omre H. Bayesian linearized AVO inversion. *Geophysics*. 2003;68(1):185-198.

doi: 10.1190/1.1543206

15. Yin XY, Ma N, Ma ZQ, Zong ZY. Review of in-situ stress prediction technology. *Geophys Prospect Pet*. 2018;57(4):488-504. [In Chinese].

doi: 10.3969/j.issn.1000-1441.2018.04.001

16. Bi CC, Wang YC, Xie W, Sun W, Liu W. Prestack AVO inversion for brittleness index of shale based on BI_Zoeppritz equation and NSGA II. *Acta Geophys*. 2020;68(4):1067-1082.

doi: 10.1007/s11600-020-00461-w

17. Ma N, Yin XY, Sun CY, Zong ZY. Inversion for crustal stress based on azimuthal seismic data. *Chin J Geophys*. 2018;61(2):697-706. [In Chinese].

doi: 10.6038/cjg2018L0183

18. Sharifi J. Implications of static low-frequency model on seismic geomechanics inversion. *Geophysics*. 2023;88(1):R39-R48.

doi: 10.1190/geo2021-0797.1

19. Huang GT, Wei SY, Yang CH, Guo YT. The in situ stress prediction of a fractured shale reservoir based on amplitude variation with angle and azimuth inversion: A case study from Southwest China. *Geophysics*. 2024;89(5):B415-B430.

doi: 10.1190/geo2023-0393.1

20. Liu W, Zhang GL, Cao JX, Zhang JJ, Yu G. Combined petrophysics and 3D seismic attributes to predict shale reservoirs favourable areas. *J Geophys Eng*. 2019;16(5):974-991.

doi: 10.1093/jge/gxz060

21. Cheng LX, Gao HX, Li H. Quantitative characterization and optimization of fracability in continental shale reservoirs. *Sci Rep*. 2025;15(1):39271.

doi: 10.1038/s41598-025-23091-y

22. Li BQ, Einstein HH. Direct and Microseismic Observations of Hydraulic Fracturing in Barre Granite and Opalinus Clayshale. *J Geophys Res Solid Earth*. 2019;124(11):11900-11916.

doi: 10.1029/2019JB018376

23. Zhang BH, Tian XP, Ji BX, Zhao JZ, Zhu ZM, Yin SD. Study on microseismic mechanism of hydro-fracture propagation in shale. *J Pet Sci Eng*. 2019;178:711-722.

doi: 10.1016/j.petrol.2019.03.085

24. Chen XX, Meng XB, Chen HC, Chen XY, Li QY, Guo MY. Research on focal mechanism of microseismic events and the regional stress during hydraulic fracturing at a shale play site in southwest China. *Geophysics*. 2024;89(2):L21-L31.

doi: 10.1190/geo2023-0046.1

25. Grechka V, De La Pena A, Schisselé-Rebel E, Auger E, Roux PF. Relative location of microseismicity. *Geophysics*. 2015;80(6):WC1-WC9.

doi: 10.1190/geo2014-0617.1

26. Miao SY, Zhang HJ, Chen YK, *et al*. Surface microseismic monitoring of shale gas hydraulic fracturing based on microseismic location and tomography. *Geophys Prospect Pet*. 2019;58(2):262-271, 284. [In Chinese].

doi: 10.3969/j.issn.1000-1441.2019.02.012

27. Huang C, Zhu TY. Passive seismic imaging of subsurface natural fractures: application to Marcellus shale microseismic data. *Geophys J Int*. 2019;218(2):1087-1099.

doi: 10.1093/gji/ggz214

28. Liu QJ, Xue L, Sarout J, *et al*. Automatic history matching of multistage fractured shale gas reservoir constrained by microseismic data. *J Pet Sci Eng*. 2022;213:110357.

doi: 10.1016/j.petrol.2022.110357

29. Sayers CM. *Geophysics Under Stress: Geomechanical Applications of Seismic and Borehole Acoustic Waves*. Vol 13. Society of Exploration Geophysicists; 2010.

doi: 10.1190/1.9781560802129

30. Gray D, Anderson P, Logel J, Delbecq F, Schmidt D, Schmid R. Estimation of stress and geomechanical properties using 3D seismic data. *First Break*. 2012;30(3):59-68.

doi: 10.3997/1365-2397.2011042

31. Shaw RK, Sen MK. Born integral, stationary phase and linearized reflection coefficients in weak anisotropic media. *Geophys J Int*. 2004;158(1):225-238.

doi: 10.1111/j.1365-246X.2004.02283.x

32. Xu K, Li BH, Xiao PF, Lin ZL. Stress Prediction Technology Based on AVAZ Inversion and its Application in Sichuan Basin of China. In: *79th EAGE Conference and Exhibition 2017; June 12-15, 2017; Paris, France*. European Association of Geoscientists and Engineers; 2017:1-5.

doi: 10.3997/2214-4609.201700551

ACCSCIENCE PUBLISHING

Journal of Seismic Exploration

ARTICLE

A Seislet U-Net for seismic data reconstruction

Haixia Hu[1,2,3], Yankun Zhang[1,3]*, Youhua Wei[1,3], Xiaodong Luo[4], Yuefei Zhu[5], and Yannan Wang[1,3]

[1]Geomathematics Key Laboratory of Sichuan Province, Chengdu University of Technology, Chengdu, Sichuan, China

[2]College of Computer and Software, Chengdu Jincheng University, Chengdu, Sichuan, China

[3]School of Mathematical Sciences, Chengdu University of Technology, Chengdu, Sichuan, China

[4]School of Artificial Intelligence, Sichuan Tourism University, Chengdu, Sichuan, China

[5]College of Geoscience and Surveying Engineering, China University of Mining and Technology-Beijing, Beijing, China

(This article belongs to the *Special Issue: Advanced Artificial Intelligence Theories and Methods for Seismic Exploration*)

Abstract

Field seismic data often suffer from trace missing due to acquisition constraints. While deep learning has advanced reconstruction tasks, existing models often lack physical interpretability, risking geologically implausible results. To bridge this gap, we propose Seislet U-Net, which integrates forward and inverse Seislet transforms into a U-Net encoder-decoder. By leveraging local slope information to guide predictions along dominant seismic dips, this design enforces feature extraction and reconstruction in a physically consistent, sparse domain that aligns with seismic wavefront structures, thereby enhancing interpretability. Training uses a composite loss that balances sparsity, spatial smoothness, and structural fidelity. Experiments on synthetic and field datasets demonstrate that Seislet U-Net outperforms U-Net, denoising convolutional neural network, discrete wavelet transform U-Net, and AU-Net, achieving signal-to-noise ratio improvements of 1.47 dB and 4.49 dB, respectively, compared to U-Net. The framework integrates data-driven learning with domain-specific constraints, offering a reliable solution for seismic reconstruction.

Keywords: Seismic data reconstruction; Deep learning; U-Net; Seislet transforms

***Corresponding author:**
Yankun Zhang
(zhangyk@cdut.edu.cn)

Citation: Hu H, Zhang Y, Wei Y, Luo X, Zhu Y, Wang Y. A Seislet U-Net for seismic data reconstruction. *J Seismic Explor*. 2026;35(3):026040014. doi: 10.36922/JSE026040014

Received: January 23, 2026

Revised: March 20, 2026

Accepted: March 27, 2026

Published online: May 11, 2026

Copyright: © 2026 Author(s). This is an Open-Access article distributed under the terms of the Creative Commons Attribution License, permitting distribution, and reproduction in any medium, provided the original work is properly cited.

Publisher's Note: AccScience Publishing remains neutral with regard to jurisdictional claims in published maps and institutional affiliations.

1. Introduction

During seismic exploration, data integrity is often compromised by various factors. The complexity of geological structures may introduce uncertainty in seismic wave propagation paths, while geographical features, such as mountains, rivers, and prohibited mining areas, constrain the layout of seismic traces, resulting in data loss. In addition, equipment and transmission system failures, such as data collector transmission interruptions and artificial source excitation failures (such as a dumb source), might also lead to the loss of seismic channel data.[1-3]

Missing seismic exploration data results in incomplete underground physical

information, which can easily lead to problems such as spatial aliasing and weaken the integrity of the seismic wavefield. This can severely affect the quality of seismic data and, in turn, subsequent geological interpretation and resource assessment. Developing high-precision seismic data reconstruction methods is not only a technical means to improve the efficiency of oil and gas exploration and development, but also an urgent and important task in current seismic data processing. Therefore, effectively reconstructing seismic data has become a key issue in oil and gas exploration.

Traditional seismic data reconstruction methods are often limited by their reliance on prior information and are difficult to meet the needs of modern high-precision exploration. In recent years, deep learning has attracted much attention in seismic exploration for its ability to automatically extract features and process complex nonlinear relationships. Although scholars have applied deep learning to seismic data reconstruction, challenges remain, including limited physical interpretability. How to embed physical constraints, such as time-frequency analysis, into the deep learning framework and ensure the physical rationality of the results while maintaining the expressive capabilities of the model, remains a key issue.

In traditional seismic data processing, methods based on sparse transformations play an important role in reconstructing data with irregularly missing values. The basic idea is to find a mathematical transformation that makes the seismic signal express the sparsity, and then use this sparsity prior to constrain the solution to the inverse problem. Specifically, in the selected optimal sparse domain, the reflection signal of the real underground structure appears as a few large coefficients with highly concentrated energy, whereas the discontinuity caused by data gaps is dispersed into numerous small, weak coefficients. Based on this characteristic, the reconstruction process is transformed into a signal denoising and enhancement problem in the transform domain: retaining large coefficients and eliminating small ones through thresholding to filter out irregular components arising from missing values. Finally, by performing an inverse transformation on the purified coefficients, high-precision recovery of the missing position signal can be achieved. Commonly used sparse methods include the Fourier transform,[4] wavelet transform,[5] Radon transform,[6] Curvelet transform,[7] Seislet transform,[8] Shearlet transform,[9] and others. To optimize the solution, Projection Onto Convex Sets[10] gradually converges to the reconstruction that best fits the sparsity and the original observation data by alternately applying threshold filtering and enforcing data consistency constraints. The success of the traditional sparse transformation algorithm depends heavily on the selected sparse transformation. When the underground structure is complex (e.g., high- and steeply dipping faults, complex salt bodies) or the noise type does not match, the signal may not achieve optimal sparse representation on the preset basis, resulting in a sharp decline in reconstruction accuracy.

In recent years, deep learning technology has provided new approaches for efficiently solving the complex, nonlinear problem of seismic data reconstruction, especially the recovery of irregularly missing data, by virtue of its powerful ability to automatically learn multi-scale, abstract features from massive data. Therefore, it has received widespread attention and in-depth research from academia and industry. The following is a comprehensive analysis of the domestic and international research status and development trends related to this topic, focusing on the status of seismic exploration data reconstruction technology based on deep learning. Ronneberger *et al.*[11] proposed the U-Net, a symmetric encoder–decoder convolutional network with skip connections for precise biomedical image segmentation, particularly effective with limited training data. Wang *et al.*[1] proposed an attention-guided convolutional neural network for denoising that selectively suppresses various noise patterns while preserving seismic signals. The network is trained to transform ghost-contaminated seismic data into its clean version, operating without dependence on an explicit ghost model. Zhao *et al.*[2] presented a deep learning deghosting method that employs a convolutional neural network to suppress source-ghost reflections. Zhu *et al.*[3] developed a seismic data reconstruction method employing an attention U-N*et al*ongside transfer learning, where attention modules amplify relevant signal features and pre-trained knowledge improves performance in data-scarce scenarios.

For denoising multi-type noise in distributed acoustic sensing data, generative adversarial networks (GANs) have been adapted with novel architectures and loss functions to address complex reconstruction challenges. Dou *et al.*[12] introduced a multi-domain adaptation GAN, a framework utilizing adversarial learning to interpolate and reconstruct three-dimensional (3D) seismic data with intricate missing patterns. To enforce statistical fidelity, Liu *et al.*[13] designed a GAN constrained by a moment reconstruction error, thereby aligning the higher-order statistics of the generated data with those of the target distribution. Zhang *et al.*[14] presented an integrated GAN-based approach that concurrently performed seismic data reconstruction and denoising within a single adversarial network. Yu *et al.*[15] presented the masked autoencoder

GAN framework to address the combined task of super-resolution and denoising in post-stack seismic profiles. Dong *et al.*[16] developed a multitasked self-guided network for reconstruction, using cascaded self-attention modules to fuse multi-scale features to improve local and global consistency. Expanding on architectural advances, Dong *et al.*[17] proposed a transformer-based encoder to capture long-range dependencies across seismic sections, leveraging broader contextual information to recover missing data. Liu *et al.*[18] proposed a framework based on polarity-constrained dual-cycle GANs that incorporated physical constraints on waveform polarity during adversarial training. Wang *et al.*[19] addressed non-repeatable land time-lapse seismic data by combining interpolation with quality-control metrics to ensure reliable interpretation despite acquisition variations. Wu *et al.*[20] implemented conditional GANs with spectral reconstruction-based data augmentation, improving model generalization. Addressing the specific issue of consecutively missing traces, Yu and Wu[21] guided a deep learning model with a combination of attention mechanisms and a hybrid loss function to recover continuous gaps. Huang *et al.*[22] adopted a self-supervised learning strategy, enabling the reconstruction of consecutively missing traces without relying on fully labeled training datasets. However, these methods mostly follow a purely data-driven paradigm, and their core network architecture and optimization goals are not explicitly embedded in the inherent physical laws governing seismic data; as a result, their reconstructions lack physical consistency and interpretability.

Recent developments in seismic data processing demonstrate a clear trend towards integrating advanced signal-processing concepts with a flexible deep-learning framework. Liu *et al.*[23] proposed a wavelet-based residual deep learning model for reconstruction; this method decomposed seismic data using wavelet transforms and trained a network to predict the residual between incomplete and complete data within this multi-resolution domain, thereby refining recovery across different frequency bands. Similarly, Chen *et al.*[24] introduced a sparse reconstruction technique in the synchroextracting transform domain, which first obtained a high-concentration time-frequency representation before applying sparse inversion to recover missing traces, effectively preserving detailed time-frequency features. Saad *et al.*[25] developed a guided unsupervised deep network for distributed acoustic sensing data. This framework employed a custom loss function derived from the physical properties of seismic data to distinguish and attenuate noise without requiring clean training data. Extending the unsupervised paradigm to joint reconstruction and denoising, Li *et al.*[26] designed an off-the-grid unsupervised framework. This method simultaneously inferred missing seismic samples and unknown source locations by minimizing a physics-informed loss function, thereby effectively handling irregular acquisition patterns. Further innovation is seen in novel network architectures combined with flexible learning schemes. Cao *et al.*[27] presented a semi-supervised approach using a wavelet-informed Kolmogorov–Arnold Network (KAN) for reconstructing regular missing traces. The model leveraged the interpretable structure of KANs and was trained with a mix of labeled and unlabeled data, enhancing its ability to generalize from limited examples. These studies jointly promote the technological evolution from traditional sparse transformations based on fixed basis functions to highly adaptive, data-driven sparse representations enabled via deep learning.

Traditional methods effectively restore missing data by leveraging the sparsity prior of the signal in the preset transform domain, but their performance depends heavily on how well the transform basis matches the signal structure. When the underground structure is complex, the reconstruction effect will drop sharply. Purely data-driven deep learning models often lack physical constraints, leading to uncertainty about the fidelity and interpretability of their reconstruction results. Current cutting-edge research is focusing on integrating the advantages of both by embedding physical mechanisms, such as sparse constraints, into deep learning frameworks, moving from pure data-driven to a deeper integration of physical constraints and data-driven approaches.

We introduce a Seislet U-Net, a physically interpretable framework achieved through the dual embedding of the Seislet sparse transform (in the encoder) and its inverse (in the decoder). Unlike generic multi-scale transforms (e.g., Curvelet, Contourlet) designed for general image processing, the Seislet transform is specifically tailored to seismic data by incorporating local slope information to predict along dominant seismic dips. This unique feature enables it to represent seismic common-phase lines. This integration intrinsically confines both feature extraction and signal reconstruction within a physically consistent sparse domain. To guide this process, a multi-component loss function is introduced that explicitly optimizes reconstruction by jointly enforcing sparsity (via a sparsity [L_1] loss), spatial smoothness (via a total variation [TV] loss), and structural preservation (via a structural similarity [SSIM] loss).

2. Methods

2.1. Net structure

This study integrates the Seislet transform into the U-Net framework. The Seislet sparse transform was selected for its

unique ability to sparsely represent curved seismic events and its clear physical background. In the implementation, a differentiable forward Seislet transform layer was inserted between the double convolution and pooling layers of the U-Net encoder's down-sampling path, ensuring that the intermediate representations directly conformed to physical sparsity priors during feature extraction. Symmetrically, in the decoder, the inverse Seislet transform was inserted between the up-sampling operations (double convolution and transposed convolution), constraining the decoding process within a physically invertible transform domain. This design ensured the network's reconstruction results were physically rigorous. The proposed network architecture is illustrated in Figure 1.

Let y denote the fully sampled seismic data and y_{obs} the incompletely sampled data. The seismic data missing process can thus be represented as **Equation 1**:

$$y_{obs} = M \odot y \tag{1}$$

where M denotes a sampling matrix with entries of 0 or 1 (1 for retained traces and 0 for missing traces, corresponding to the sampling positions) and dimensions identical to those of y. The symbol $\odot$ denotes the Hadamard product. To reconstruct the full wavefield y based on the available (incomplete) data y_{obs}, the sampling matrix M is the central task of seismic data reconstruction.

Neural networks serve as universal approximators, capable of modeling complex, nonlinear mappings in high-dimensional spaces. A network was parameterized as $SU(x;\theta)$, where x denotes the input and θ encompasses all trainable weights and biases. Consequently, a neural network-based approach to seismic data reconstruction can be formulated as **Equation 2**:

$$SU(x;\theta) = \mathrm{y} \tag{2}$$

All reconstruction methods introduce errors; to enhance accuracy, the solution is refined to honor the originally observed data y_{obs}, yielding the final product y_{pre}. This process takes the form of **Equation 3**:

$$y_{pre} = (1-M) \odot SU(y_{obs};\theta) + y_{obs} \tag{3}$$

The signal-to-noise ratio (SNR) is adopted to measure the neural network's reconstruction quality. It is calculated as in **Equation 4**:

$$SNR = 10log_{10}\left(\frac{\sum_{i=1}^{n}\sum_{j=1}^{m}\left(X(i,j)-\bar{X}\right)^2}{\sum_{i=1}^{n}\sum_{j=1}^{m}\left(Y(i,j)-X(i,j)\right)^2}\right) \tag{4}$$

where $X(i,j)$ denotes the amplitude at a single point, while $\bar{X}$ represents the average (mean) of the entire data block. $Y(i,j)$ is defined as the reconstructed data point. Consequently, a higher SNR directly indicates improved

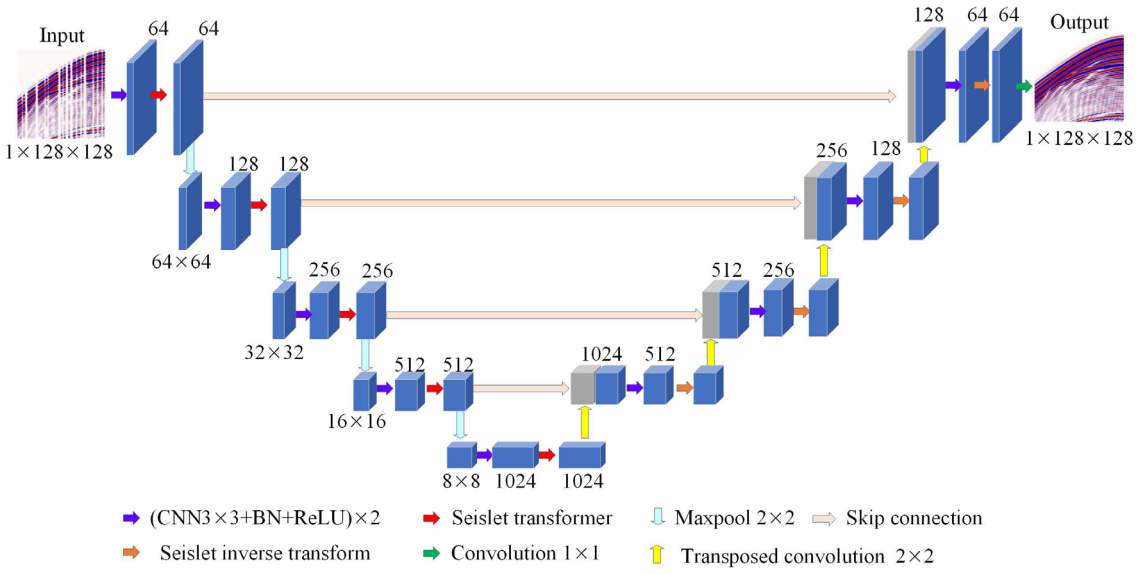

Figure 1. Structure of a Seislet U-Net neural network
Abbreviations: BN: Batch normalization; CNN: Convolutional neural network; ReLU: Rectified linear unit.

reconstruction fidelity.

2.2. Seislet transform

The Seislet transform is a sparse representation method that tailors the classical wavelet transform to the inherent patterns of seismic data.[8] It operates within a unified framework that integrates the intrinsic structure of seismic data and the discrete wavelet transform (DWT). Built on the lifting scheme of the second-generation wavelet transform, it incorporates specific modifications tailored to seismic signal characteristics, leading to significant advantages in compressing and representing seismic data.[8] This transform effectively exploits the spatial correlations between seismic traces. Through specifically designed prediction and update operators in its lifting algorithm, it progressively achieves efficient compression of the data sequence, ultimately producing a multi-resolution transform result.

According to the Seislet transform implementation principle, the core step is to compute the residual between the odd-trace sequence and the predicted even-trace sequence. Specifically, this step assumes that seismic events are predictable in the spatial domain. First, the preset prediction operator P is applied to the even-trace sequence e to generate a predicted version of the even-trace sequence. Then, the difference between the original odd-trace sequence o and this predicted value is calculated, yielding the residual trace (**Equation 5**).[28]

$$r = o - P(e) \tag{5}$$

In this process, the goal of the prediction operator P is to make the predicted even-trace sequences as close as possible to the original odd-trace sequences o in terms of both waveform and amplitude.

According to the standard definition of the two-dimensional (2D) Seislet transform, when the Haar wavelet basis is applied, its prediction operator P can be expressed mathematically as **Equation 6**:

$$P = (+k) \text{ or } P = (-k) \tag{6}$$

where P represents a linear prediction operator that estimates odd-trace sequences from even-trace sequences. The preceding positive (+) or negative (−) sign indicates whether the prediction is performed in the forward or backward direction along the seismic event. This direction is determined by the local dip attribute of the seismic event itself. The variable k denotes the grouping index of the data. During the actual iterative computation, the prediction process is executed sequentially in descending order of the grouping index k.

The Seislet inverse transform is a critical step for data reconstruction. Starting from the coarsest-scale low-frequency coefficients c and the sparse transform coefficients r obtained at each scale through multi-scale decomposition, it progressively recovers the even- and odd-trace sequences at each scale in a top-down, coarse-to-fine manner. The specific reconstruction procedure is as follows:[27]

First, the scaling coefficients c at the coarsest scale and the corresponding transform coefficients r are obtained from the decomposed data. Next, the update operator U is applied to the transform coefficients r at the current scale to compute an updated value. The scaling coefficients c are then subtracted from this updated value to reconstruct the even-trace sequence e at that scale (**Equation 7**):

$$e = c - U(r) \tag{7}$$

Next, the prediction operator P is applied to the recently restored even-trace sequence e to derive the predicted values. The predicted result is then added to the transform coefficients r of the current level, thereby reconstructing the corresponding odd-trace sequence o (**Equation 8**).

$$o = r + P(e) \tag{8}$$

Finally, the reconstructed odd-trace sequence o and even-trace sequence e at this scale are interleaved back into their original order, completing the data reconstruction. This merged result then serves as the input for the next finer scale. By recursively repeating the steps of coefficient extraction, even-trace reconstruction, odd-trace reconstruction, and sequence merging, the process proceeds iteratively from the coarsest to the finest scale, ultimately fully reconstructing the original seismic data.

2.3. Loss function

The core innovation of this work is the embedded Seislet U-Net, which incorporates the Seislet transform into the compression and decompression stages of the U-Net. This imposes a physics-based constraint across the network, ensuring an interpretable reconstruction process. Furthermore, training is guided by a combined loss function that strategically balances L_1,[29] TV,[30] spatial smoothing loss, and SSIM Loss,[29] thereby enforcing a geophysically optimal reconstruction (**Equation 9**).

$$L_{combined} = 0.7 * L_1 + 0.2 * L_{TV} + 0.1 * L_{SSIM} \tag{9}$$

For N samples with predictions $\hat{y}_i$ and ground truth values $\hat{y}_i$, the L_1 loss is defined as **Equation 10**:

$$L_1 = \frac{1}{N}\sum_{i=1}^{N}\left|y_i - \hat{y}_i\right| \tag{10}$$

For a reconstructed data matrix U of size $H \times W$ (the network's output), the discrete TV loss is typically computed as the sum of the absolute differences in both the horizontal and vertical directions between adjacent samples (traces or pixels) (**Equations 11–13**).

$$\begin{aligned} L_{tv} = &\sum_{i=1}^{H-1}\sum_{j=1}^{W}\left|U_{i+1,j} - U_{i,j}\right| \\ &+\sum_{i=1}^{H}\sum_{j=1}^{W-1}\left|U_{i,j+1} - U_{i,j}\right| \end{aligned} \tag{11}$$

$$L_{SSIM}\left(X,Y\right) = 1 - \frac{1}{M}\sum_{m=1}^{M} SSIM\left(x_m, y_m\right) \tag{12}$$

$$SSIM\left(x,y\right) = \left[l\left(x,y\right)\right]^{\alpha}\cdot\left[c\left(x,y\right)\right]^{\beta}\cdot\left[s\left(x,y\right)\right]^{\gamma} \tag{13}$$

in which, $l\left(x,y\right) = \frac{2\mu_x\mu_y + c_1}{\mu_x^2 + \mu_y^2 + c_1}$, $c\left(x,y\right) = \frac{2\sigma_{xy} + c_2}{\sigma_x^2 + \sigma_y^2 + c_2}$, and $s\left(x,y\right) = \frac{\sigma_{xy} + c_3}{\sigma_x\sigma_y + c_3}$, μ_x and μ_y are the average values of x and y, σ_x and σ_y are the standard deviations of x and y, σ_{xy} is the covariance of x and y, $l\left(x,y\right)$ is the comparison of brightness, $c\left(x,y\right)$ is the comparison of contrast, and $s\left(x,y\right)$ is the comparative structure.

3. Network training and synthetic experiment

The 3D seismic forward-modeling data used for network training were generated using the Society of Exploration Geophysicists-Computational Challenge 3 salt model.[31] This synthetic dataset was 45 shot records with 201 × 201 geophones arranged in a 20 m grid spacing horizontally and vertically, at a sampling rate of 8 ms (625 samples/trace). Each shot produced a 625 × 201 2D record. A subset of 1,809 records from shots 1–9 was used to train the network. To improve convergence, the input data was scaled to the range (−1, 1). This normalization step centered the data and reduced its variance, thereby accelerating and stabilizing the network training.

The dataset was constructed as follows: the 1,809 records were first randomized. For each record, 40%–60% of traces were randomly discarded to create incomplete data. This corpus was then segmented into 28,944 subsets of dimensions 128 × 128. These subsets were allocated for training (23,156), validation (2,894), and testing (2,894), maintaining an 8:1:1 split.

The denoising convolutional neural network (DnCNN),[32] U-Net,[11] DWT U-Net,[33] and AU-Net[3] models were benchmarked using identical datasets and hyperparameters. Training was conducted for 100 epochs with a batch size of 32, an initial learning rate of 0.001, a fixed step size of 5, and a decay coefficient of 0.8. Validation loss was monitored after each training epoch. Final model performance was evaluated by computing the average SNR on the reconstructed test set. All experiments were implemented in PyTorch and accelerated on an NVIDIA GeForce RTX 5090 D V2 graphics processing unit.

3.1. Seismic data reconstruction with different models

The loss curves for the five network architectures are presented in Figure 2, with an inset magnifying iteration of 50–100. A key observation is that incorporating the Seislet transform notably enhanced both convergence speed and final accuracy compared to the AU-Net, DWTU-Net, U-Net, and DnCNN baselines. To quantify this, reconstruction tests were conducted on the entire test set, with the resulting average SNR values serving as the performance metric. The superior performance of Seislet U-Net over AU-Net, DnCNN, DWT U-Net, and U-Net is demonstrated in Figure 3. This enhancement in seismic data reconstruction, which we attribute to its integrated Seislet transform, is visually evident from the comparative outputs.

For the complete data shown in Figure 4, 40%, 50%, and 60% random missing data were generated, with SNRs of 4.0438 dB, 2.9216 dB, and 2.2081 dB.

Figure 5 shows the reconstruction of 40% random missing data for the five methods. Seislet U-Net achieved the highest SNR, 25.5181 dB, followed by AU-Net (25.4102 dB), DnCNN (25.2920 dB), DWT U-Net (24.1147 dB), and U-Net (24.0446 dB). When the proportion of missing traces is limited, the reconstruction performance of U-Net is on par with other deep learning methods, as evidenced by the results in Figure 5B and 5F. Nevertheless, the reconstruction fails or produces severe artifacts when faced with consecutively missing channels. In Figure 6, Seislet U-Net and AU-Net had lower residual errors (Figure 6B–F). The Seislet transform sparsely represents seismic curved events along their dominant dips, ensuring that feature extraction and reconstruction are constrained within a physically consistent domain, and finally, outputs results with multi-scale resolution.

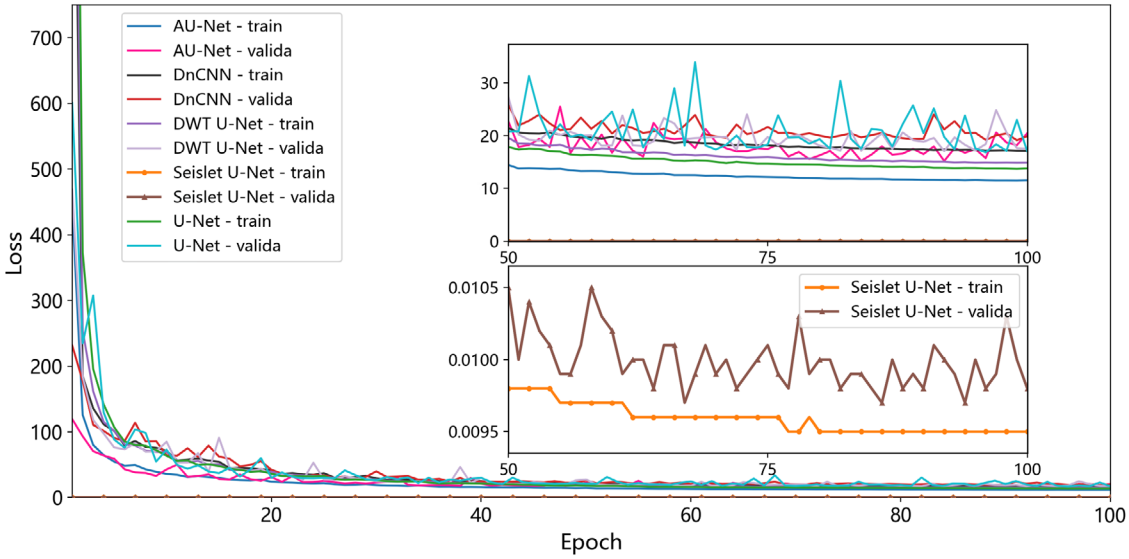

Figure 2. Training loss curve of the Seislet U-Net, DWT U-Net, AU-Net, U-Net, and DnCNN
Abbreviations: DnCNN: Denoising convolutional neural network; DWT: Discrete wavelet transform.

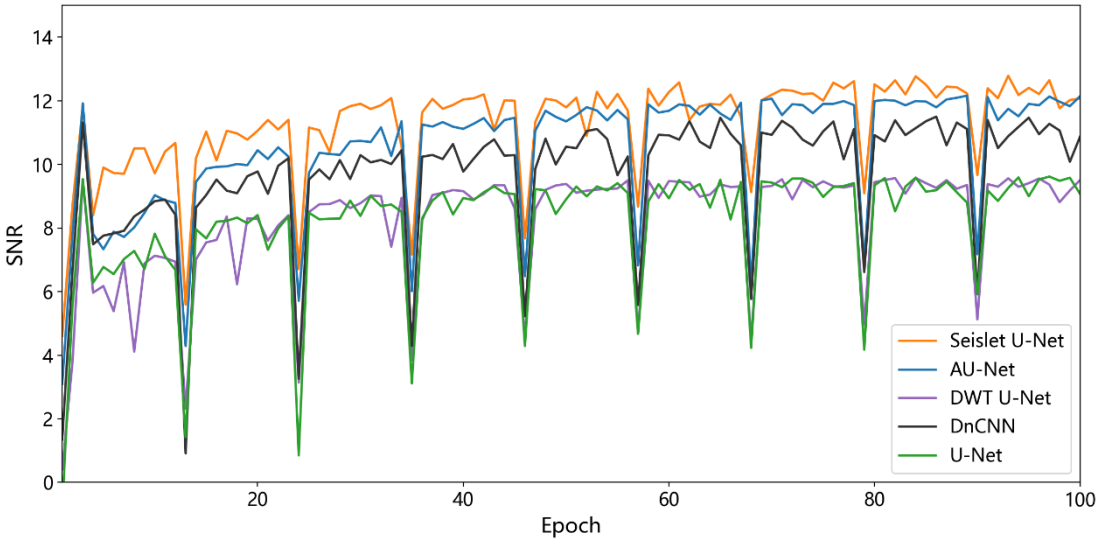

Figure 3. Signal-to-noise ratio (SNR) curve of Seislet U-Net, Discrete wavelet transform (DWT) U-Net, AU-Net, U-Net, and denoising convolutional neural network (DnCNN)

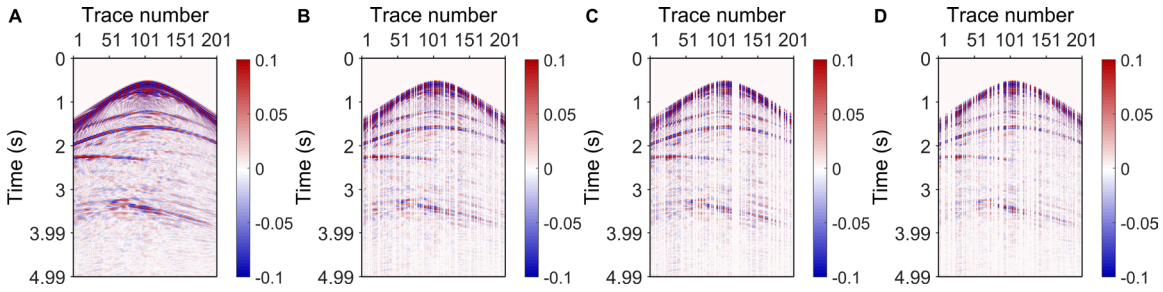

Figure 4. Complete and missing data. (A) Complete data. (B) Missing 40%. (C) Missing 50%. (D) Missing 60%.

With 50% random missing data (Figure 7), Seislet U-Net achieved the highest SNR, 22.8099 dB, followed by AU-Net (21.7144 dB), DnCNN (21.1228 dB), DWT U-Net (20.8605 dB), and U-Net (20.5555 dB). With 60% random missing data (Figure 8), Seislet U-Net achieved the highest SNR, 22.8260 dB, followed by AU-Net (22.2142 dB), U-Net (21.3801 dB), DWT U-Net (20.9596 dB), and DnCNN (20.6745 dB). The increasing proportion of missing data led to a progressive decline in the performance of DnCNN, exacerbated by consecutive data gaps. The superior performance of Seislet U-Net became more pronounced than that of U-Net and DnCNN. It achieved this by effectively balancing the precise reconstruction of high-energy regions with the careful recovery of low-energy regions. Seislet U-Net exhibited reduced reconstruction error and fewer artifacts (Figures 9 and 10), while also preserving seismic amplitudes more faithfully in areas of consecutive trace loss.

The frequency–wavenumber (F–K) spectra of the complete data, the data with 40% random-trace loss, and the corresponding reconstructions from all five methods are shown in Figure 11. While each method successfully mitigated the spatial aliasing artifacts present in the incomplete data (Figure 11A), subtle differences in reconstruction fidelity were discernible. Specifically, Seislet U-Net and AU-Net maintained higher accuracy in the low-frequency/wavenumber regions (Figure 11B and 11C), whereas U-Net and DnCNN exhibit slightly larger errors in these areas (Figure 11E and 11F).

A comparative analysis of the F–K error spectra for the five reconstruction methods is presented in Figure 12. The spectra reveal that U-Net and DnCNN exhibited pronounced reconstruction errors within the low-wavenumber domain. This limitation correlates with their reduced effectiveness in recovering the primary reflection events, as observable in Figure 12E and 12F. In contrast, Seislet U-Net demonstrated superior performance across all wavenumbers (Figure 12B). This capability is attributed to its mechanism for emphasizing differences in signal energy, yielding the lowest overall errors and making it the most suitable for practical seismic data applications.

The quantitative SNR results compiled in Table 1 reveal several findings. First, all methods showed reduced performance as the proportion of missing traces rose. Second, Seislet U-Net achieved the highest SNR at all missing data levels, confirming its advantage over the baseline U-Net. Third, DnCNN outperformed U-Net and DWT U-Net. Ultimately, Seislet U-Net was the most robust solution, delivering top-tier reconstruction accuracy regardless of the severity of data loss.

Table 1. Reconstructed SNR of synthetic data using different methods

Reconstruction methods	Seismic data missing 40% (dB)	Seismic data missing 50% (dB)	Seismic data missing 60% (dB)
Seislet U-Net	25.5181	22.8099	22.8260
AU-Net	25.4102	21.7144	22.2142
DnCNN	25.2920	21.1228	20.6745
DWT U-Net	24.1147	20.8605	20.9596
U-Net	24.0446	20.5555	21.3801
SNR of missing seismic data	4.0438	2.9216	2.2081

Abbreviations: DnCNN: Denoising convolutional neural network; DWT: Discrete wavelet transform; SNR: Signal-to-noise ratio.

3.2. Ablation experiment

3.2.1. Noise intensity levels

During training, noise levels of 0.1, 0.25, and 0.5 were added to each batch of data in each epoch. The ablation results in Tables 2–4 reveal several important insights. First, Seislet U-Net consistently outperformed all other methods across all combinations of missing trace ratio and noise level, as shown in Figure 13B, which presents reconstruction results for 40% missing traces and a noise level of 0.25. confirming the effectiveness of embedding physical constraints via the Seislet transform. Second, as noise intensity increased, Seislet U-Net exhibited the smallest SNR degradation among all models. For instance, at 40% missing traces, its SNR decreased by 6.09 dB from noise level 0.1 to 0.5, compared to 6.08–6.65 dB for other methods. This indicates that the physically aligned sparse representation helps the network distinguish signal from noise more effectively. Third, Seislet U-Net maintained its advantage, outperforming U-Net by 1.15 dB and achieving up to 2.42 dB higher SNR than DnCNN under 60% missing traces and noise level 0.1. These findings collectively demonstrate that integrating the Seislet transform not only improves reconstruction accuracy but also enhances

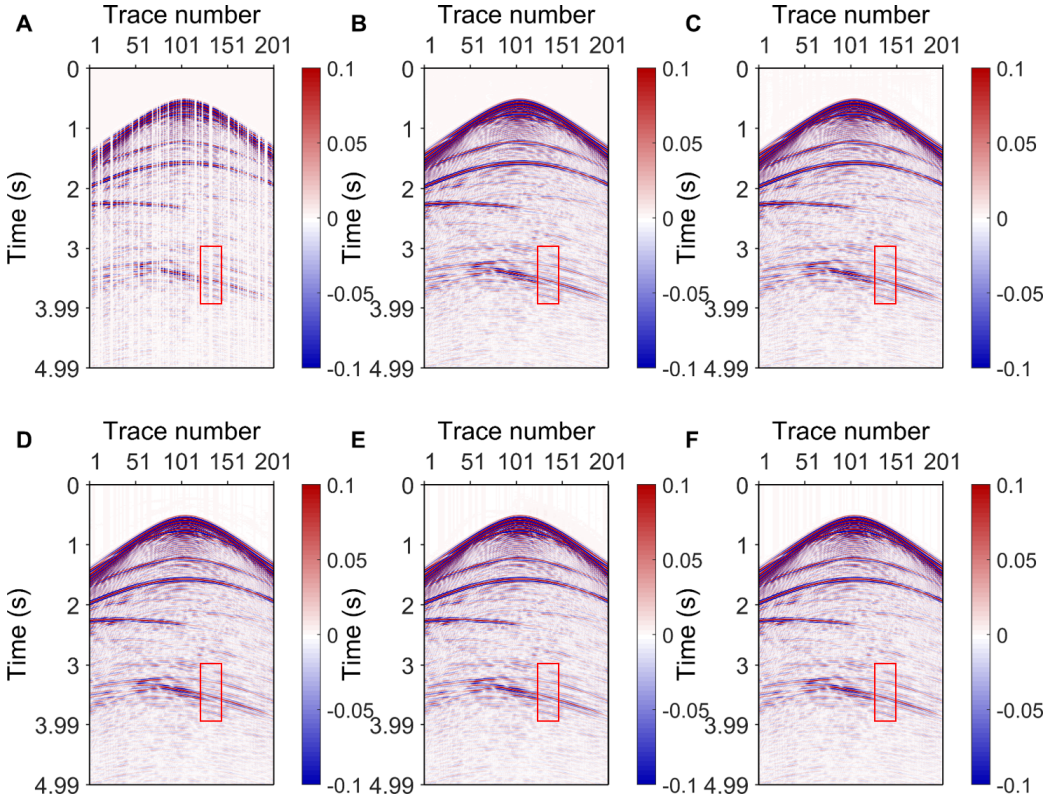

Figure 5. Reconstruction results with (A) 40% traces missing using (B) Seislet U-Net, (C) AU-Net, (D) discrete wavelet transform U-Net, (E) U-Net, and (F) denoising convolutional neural network

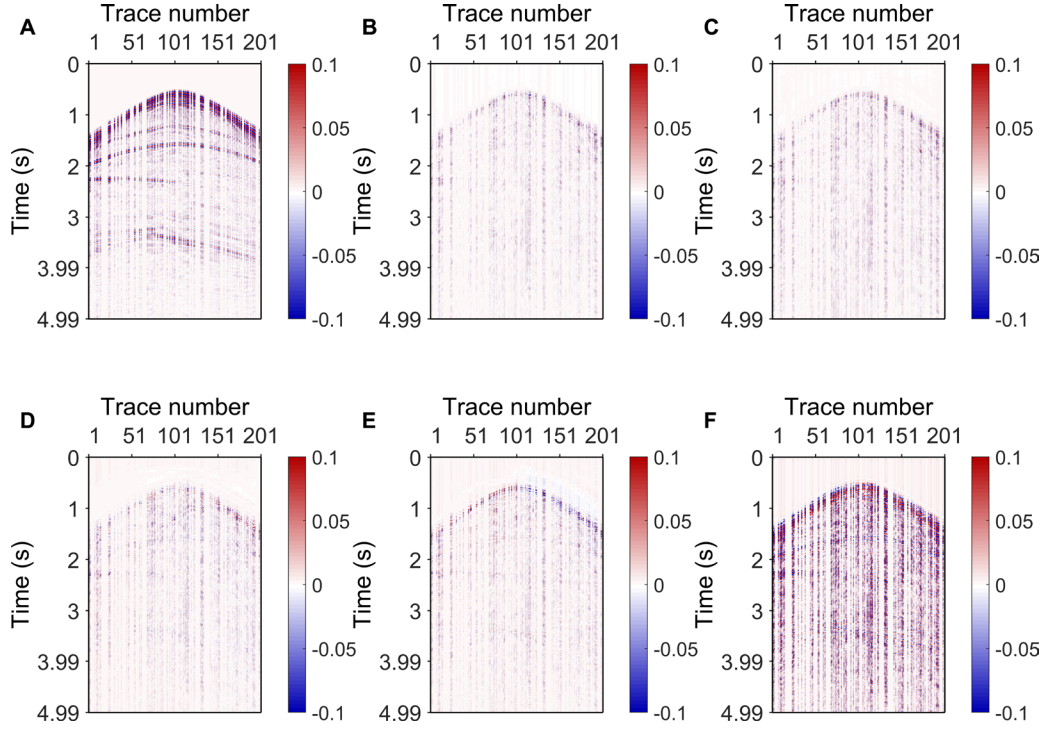

Figure 6. Reconstruction errors with (A) 40% traces missing of (B) Seislet U-Net, (C) AU-Net, (D) discrete wavelet transform U-Net, (E) U-Net, and (F) denoising convolutional neural network

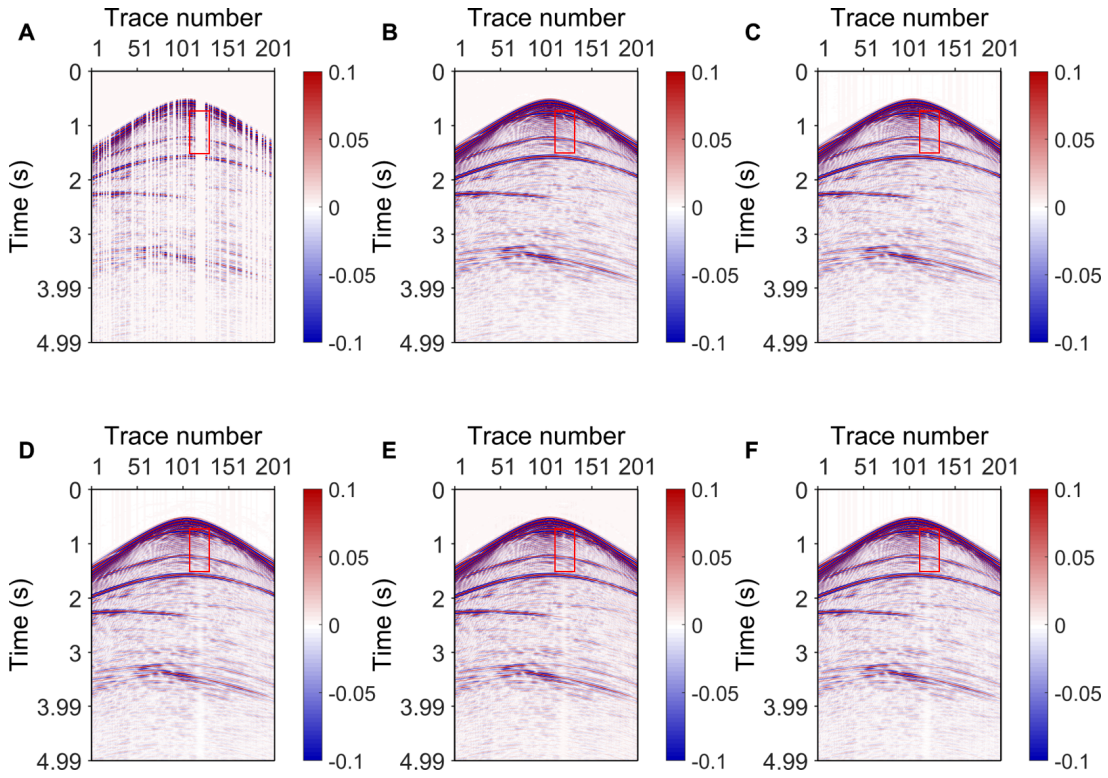

Figure 7. Reconstruction results with (A) 50% traces missing using (B) Seislet U-Net, (C) AU-Net, (D) discrete wavelet transform U-Net, (E) U-Net, and (F) denoising convolutional neural network

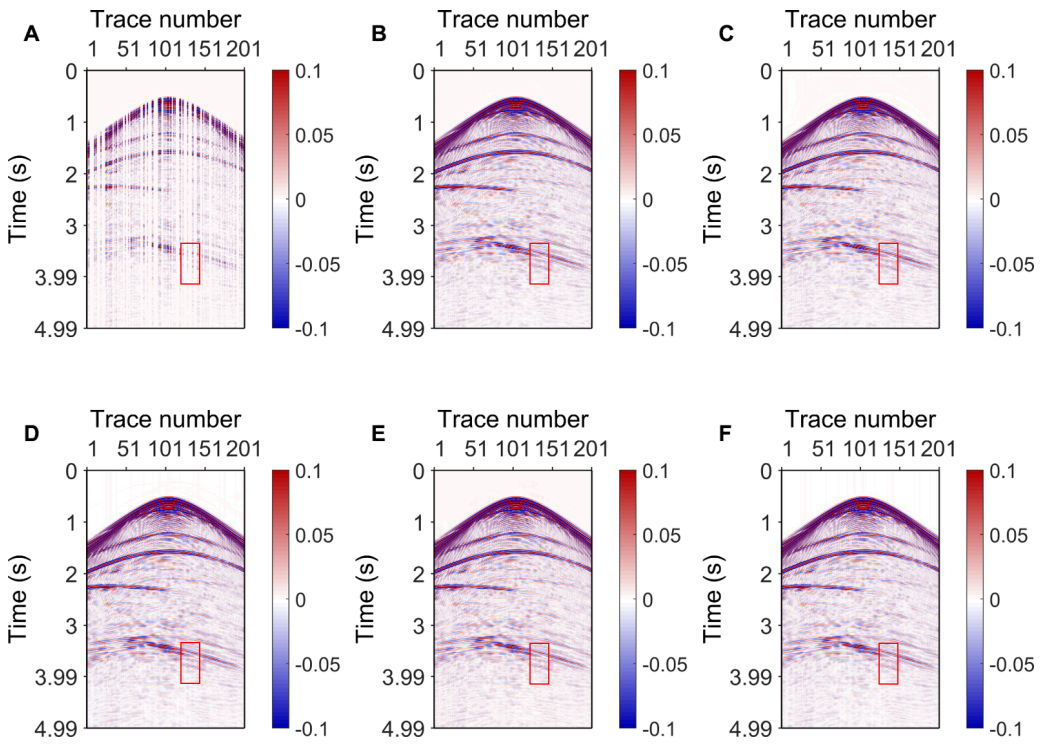

Figure 8. Reconstruction results with (A) 60% traces missing using (B) Seislet U-Net, (C) AU-Net, (D) discrete wavelet transform U-Net, (E) U-Net, and (F) denoising convolutional neural network

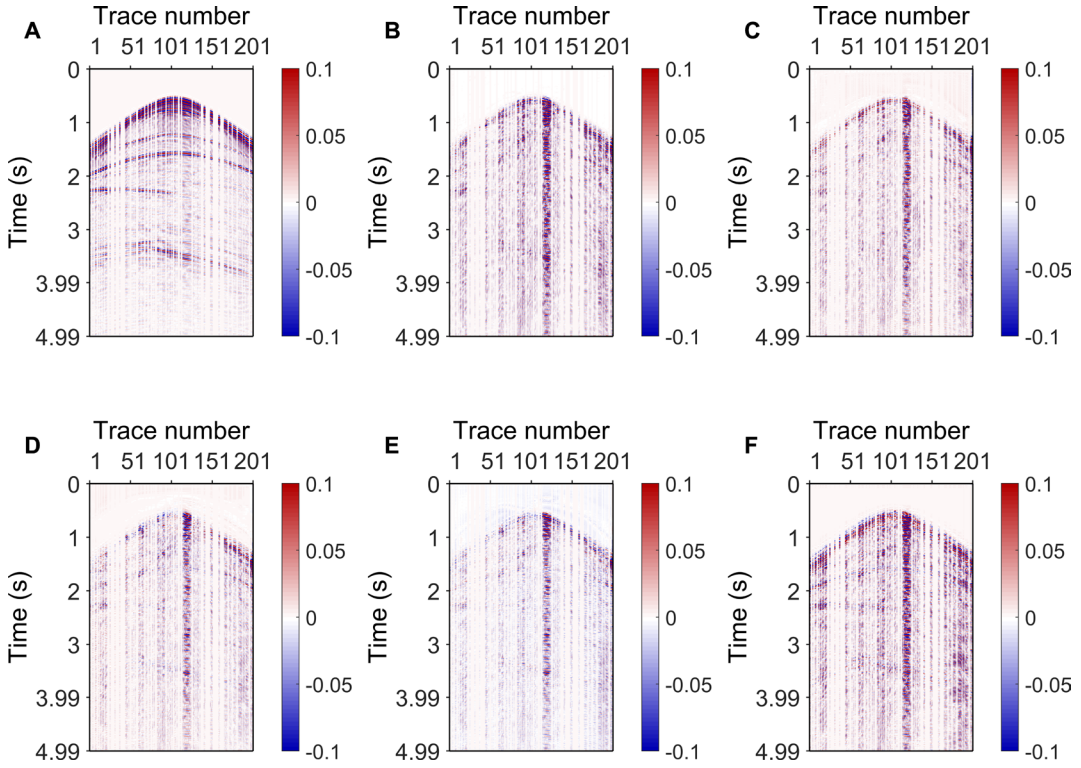

Figure 9. Reconstruction errors with (A) 50% traces missing of (B) Seislet U-Net, (C) AU-Net, (D) discrete wavelet transform U-Net, (E) U-Net, and (F) denoising convolutional neural network

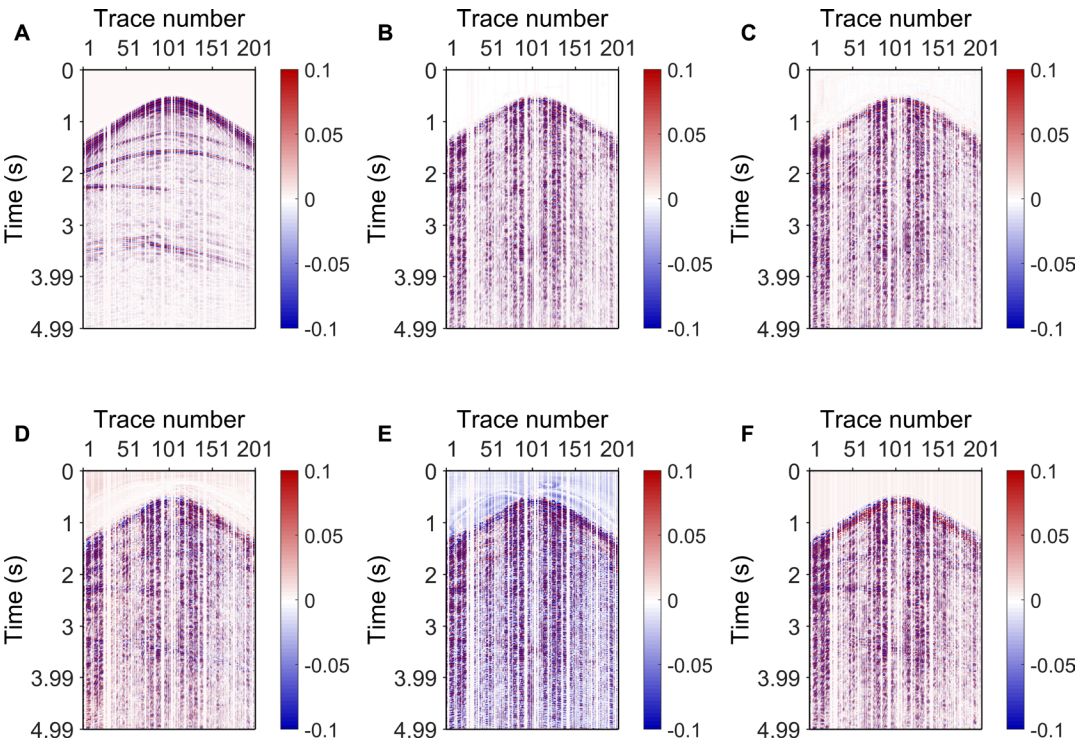

Figure 10. Reconstruction errors with (A) 60% traces missing of (B) Seislet U-Net, (C) AU-Net, (D) discrete wavelet transform U-Net, (E) U-Net, and (F) denoising convolutional neural network

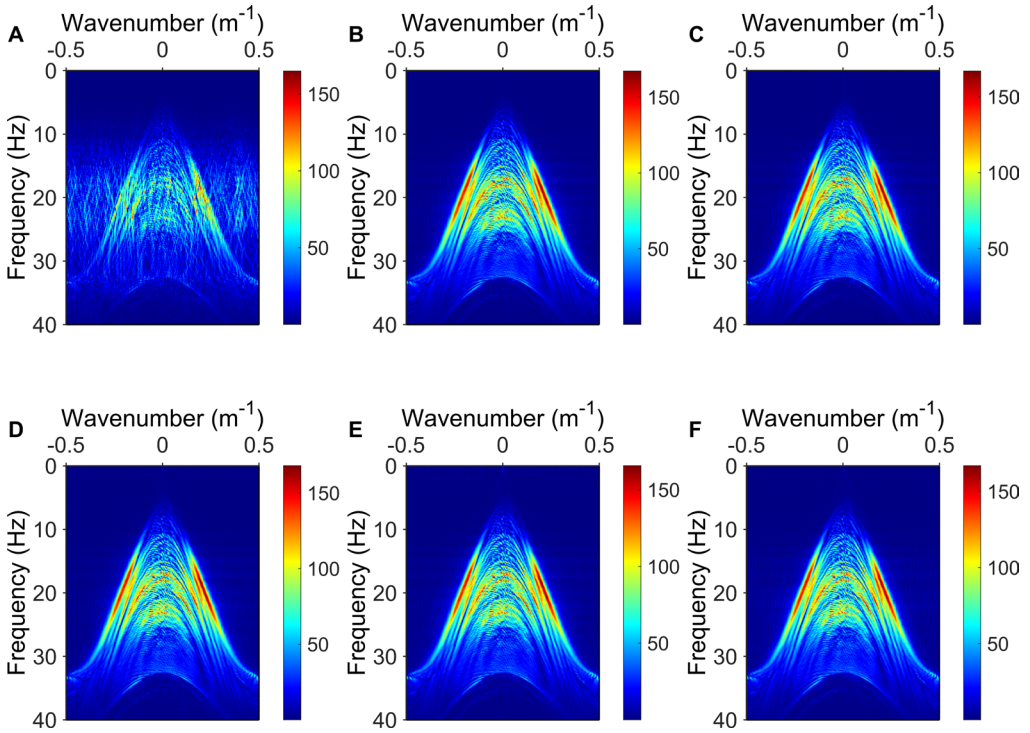

Figure 11. Frequency–wavenumber spectrum of raw and reconstructed data. (A) Data with 40% traces missing. (B) Seislet U-Net reconstruction results. (C) AU-Net reconstruction results. (D) Discrete wavelet transform U-Net reconstruction results. (E) U-Net reconstruction results. (F) Denoising convolutional neural network reconstruction results.

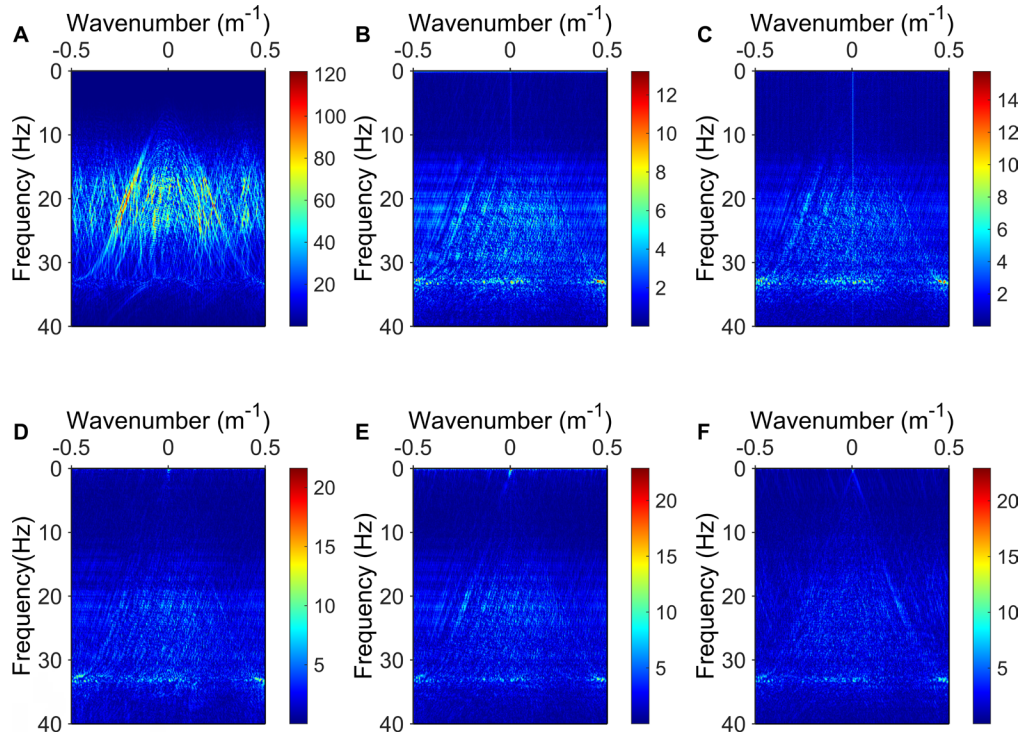

Figure 12. Frequency–wavenumber error spectrum of the reconstructed data. (A) 40% traces missing errors. (B) Seislet U-Net reconstruction errors. (C) AU-Net reconstruction errors. (D) Discrete wavelet transform U-Net reconstruction errors. (E) U-Net reconstruction errors. (F) Denoising convolutional neural network reconstruction errors.

model robustness to noise and missing data—a critical requirement for real-world seismic applications.

Table 2. Reconstructed SNR of different models in different noise intensity levels of 40% missing seismic data

Noise intensity level	0.10	0.25	0.50
Seislet U-Net	22.1732	19.4886	16.0818
AU-Net	18.3845	17.7059	15.3197
DWT U-Net	20.5782	18.5153	15.4185
U-Net	21.3966	18.3046	15.8810
DnCNN	21.2448	18.5814	15.4794
SNR of 40% missing seismic data	3.9761	3.6394	2.628

Abbreviations: DnCNN: Denoising convolutional neural network; DWT: Discrete wavelet transform; SNR: Signal-to-noise ratio.

Table 3. Reconstructed SNR of different models in different noise intensity levels of 50% missing seismic data

Noise intensity level	0.10	0.25	0.50
Seislet U-Net	20.434	18.3914	15.5307
AU-Net	18.9075	17.2694	15.0328
DWT U-Net	18.6609	17.0576	14.9401
U-Net	19.1627	17.3988	15.2021
DnCNN	18.769	17.1248	14.4938
SNR of 50% missing seismic data	2.87964	2.6635	1.9963

Abbreviations: DnCNN: Denoising convolutional neural network; DWT: Discrete wavelet transform; SNR: Signal-to-noise ratio.

Table 4. Reconstructed SNR of different models in different noise intensity levels of 60% missing seismic data

Noise intensity level	0.10	0.25	0.50
Seislet U-Net	20.6869	18.6653	15.7871
AU-Net	18.3845	17.1776	14.8468
DWT U-Net	19.1434	17.5488	14.9334
U-Net	19.5369	17.4993	15.2996
DnCNN	18.2676	17.0789	14.3972
SNR of 60% missing seismic data	2.1817	2.0359	1.5439

Abbreviations: DnCNN: Denoising convolutional neural network; DWT: Discrete wavelet transform; SNR: Signal-to-noise ratio.

3.2.2. Weight of loss function

The ablation results in Table 5 demonstrate that the proposed composite loss function with fixed weights of 70% L_1, 20% TV, and 10% SSIM achieved the highest reconstruction SNR across all missing trace ratios (25.52 dB at 40% missing data, 22.81 dB at 50% missing data, and 22.83 dB at 60% missing data), outperforming all other weighting configurations. Compared to using only L_1 loss or only SSIM loss, the composite loss improved SNR by 1.11–3.88 dB and 3.28–3.50 dB, respectively, indicating that no single loss function can simultaneously capture sparsity, spatial smoothness, and structural fidelity. The inclusion of both TV and SSIM was proven essential, as the full composite loss outperformed the 70% L_1 and 30% TV variant by up to 3.20 dB and the 70% L_1 and 30% SSIM variant by up to 2.32 dB. Notably, adaptive loss weighting performed substantially worse than the fixed 70/20/10 weighting, particularly at higher missing ratios (4.72 dB lower at 50% missing), suggesting that carefully tuned fixed weights provided more reliable guidance under severe data loss. The consistent ranking of the proposed configuration across all missing-ratio settings further confirmed that the synergistic combination of L_1 sparsity, TV smoothness,

Table 5. Reconstructed SNR of different weights of the loss function

Weight of the loss function	Seismic data missing 40% (dB)	Seismic data missing 50% (dB)	Seismic data missing 60% (dB)
70%L_1+20%TV+10%SSIM	25.5181	22.8099	22.826
Adaptive loss weighting	24.0201	18.0862	19.7523
70%L_1+30%TV	22.3154	20.1372	19.644
70%L_1+30%SSIM	23.2026	20.9447	20.5981
100%L_1	24.4033	18.9255	20.0406
100%SSIM	22.2343	19.3144	19.5053
SNR of missing and noisy seismic data	4.0438	2.9216	2.2081

Abbreviations: L_1: Sparsity; SNR: Signal-to-noise ratio; SSIM: Structural similarity; TV: Total variation.

and SSIM structural fidelity was robust to varying levels of data incompleteness and essential for achieving high-quality seismic data reconstruction.

4. Field data experiment

To assess the generalization capability of Seislet U-Net, marine seismic data from Petroleum Geosystems[34] were employed. The dataset comprises 256 shots, each with 256 traces at 25 m spacing; each trace contains 2,768 time samples at a 4 ms sampling rate, of which the first 1,344 samples were used. The 256 records were first normalized and then subjected to random trace deletion at 40%–60%. The processed data was divided into 15,360 patches of size 128 × 128, which were subsequently partitioned into 12,289 for training, 1,536 for validation, and 1,535 for testing.

The single-shot seismic record shown in Figure 14A, comprising 256 traces with 1,344 time samples each, was used for testing. After introducing 40% random missing traces, the input SNR was reduced to 5.9155 dB in Table 6. When benchmarked against the other four deep learning methods, the Seislet U-Net model (Figure 14B) achieved the best reconstruction performance, with a value of 20.4611 dB. Compared to AU-Net, it improved by 3.136 dB. Compared with the U-Net, it improved by 4.4932 dB in Table 6. In Figure 15, the Seislet U-Net model's error is relatively low (Figure 15B). This indicates that the Seislet U-Net model has certain generalization capabilities for seismic data reconstruction and denoising.

Table 6. SNR of reconstructed field data using different methods

Reconstruction methods	Seismic data missing 40% (dB)
Seislet U-Net	20.4611
AU-Net	17.3251
DWT U-Net	16.1146
U-Net	15.9679
DnCNN	13.2411
SNR of missing seismic data	5.9155

Abbreviations: DnCNN: Denoising convolutional neural network; DWT: Discrete wavelet transform; SNR: Signal-to-noise ratio.

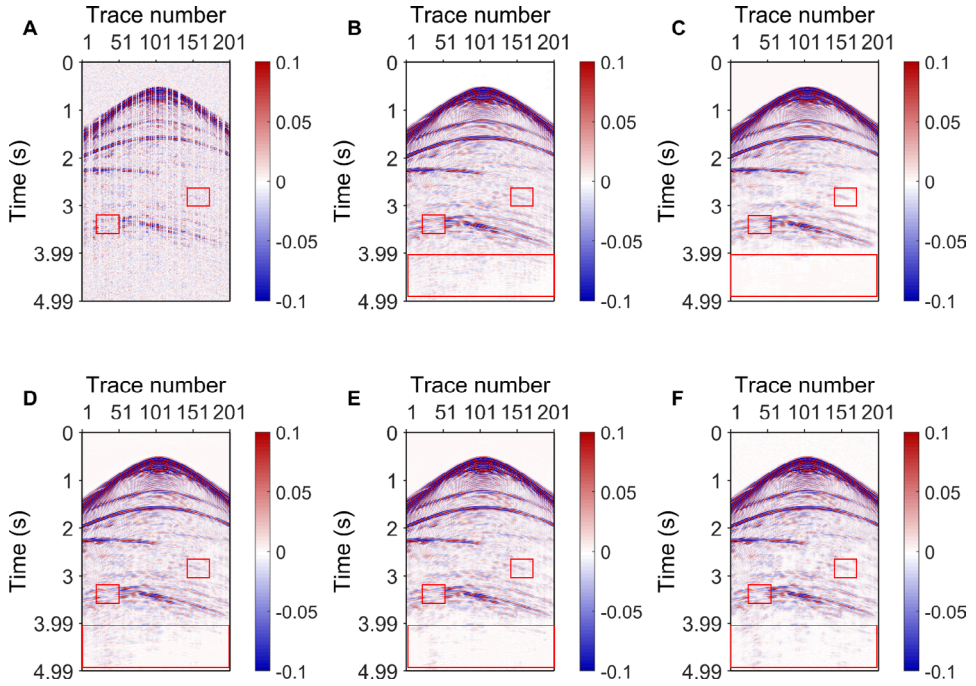

Figure 13. Reconstruction results under (A) 40% missing traces and noise level 0.25 of (B) Seislet U-Net, (C) AU-Net, (D) Discrete wavelet transform U-Net, (E) U-Net, (F) Denoising convolutional neural network

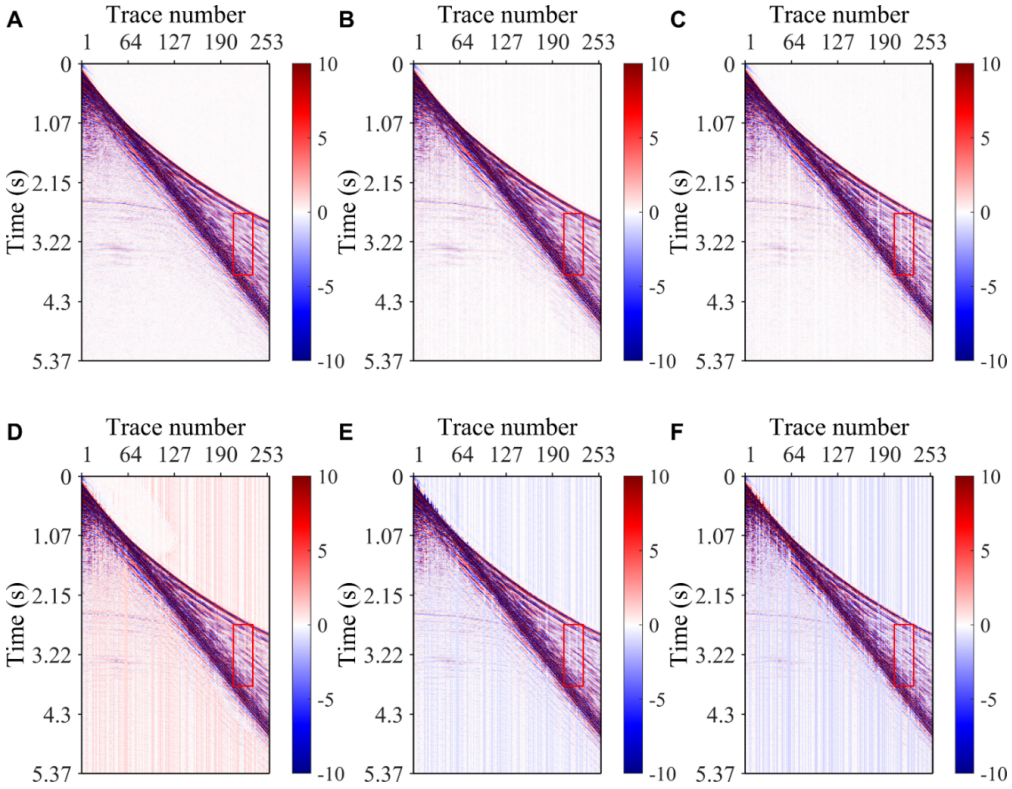

Figure 14. Reconstruction results with 40% traces missing. (A) Complete data. (B) Seislet U-Net reconstruction results. (C) AU-Net reconstruction results. (D) Discrete wavelet transform U-Net reconstruction results. (E) U-Net reconstruction results. (F) Denoising convolutional neural network reconstruction results.

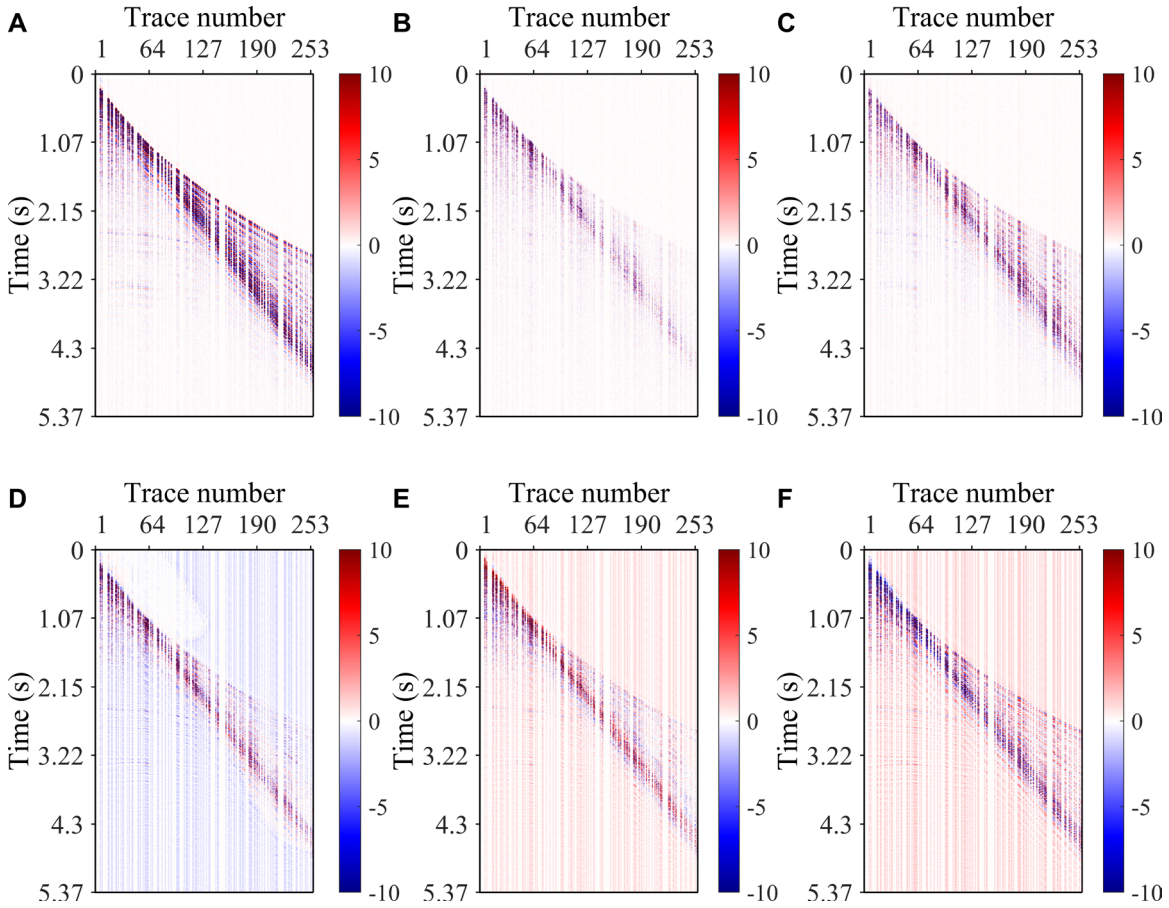

Figure 15. Reconstruction errors with 40% traces missing. (A) 40% traces missing errors. (B) Seislet U-Net reconstruction errors. (C) AU-Net reconstruction errors. (D) Discrete wavelet transform U-Net reconstruction errors. (E) U-Net reconstruction errors. (F) Denoising convolutional neural network reconstruction errors.

5. Conclusion

This study proposed Seislet UNet, a physically interpretable network that integrates the Seislet transform and its inverse into a UNet to reconstruct irregularly missing seismic data. By embedding sparse, physics-aware representations directly into the encoder–decoder flow, the model ensures reconstruction remains consistent with seismic-domain principles. A combined loss function that enforces L_1, spatial smoothness, and SSIM further guides the training. Evaluations on synthetic and field datasets demonstrated that Seislet UNet consistently outperformed UNet, DnCNN, DWT UNet, and AUNet in terms of SNR, artifact suppression, and fidelity across varying missingtrace ratios. The framework effectively integrates datadriven learning with geophysical constraints, offering a reliable, generalizable solution for seismic data recovery. Future improvements should focus on adaptive sparse-basis learning and extending the architecture to 3D reconstruction scenarios. The current method employs a fixed Seislet transform based on a pre-estimated dip field. Future work could explore learning the sparse representation basis endtoend within the network, allowing the model to adapt to complex geological structures (e.g., intersecting dips, faults) while maintaining physical interpretability. Key challenges in this direction include ensuring the learned basis remains invertible and geophysically meaningful, while balancing flexibility with computational efficiency. For 3D reconstruction, volumetric seismic data pose challenges, including increased memory requirements, higher dimensionality, and the need for accurate 3D dip estimation. Potential solutions include employing patchbased training strategies or designing hybrid 2D/3D networks to capture both inline and crossline correlations.

Acknowledgments

The authors gratefully acknowledge Sandia National Laboratories, USA, for providing the SEG-C3 dataset and

Petroleum Geosystems (PGS) for the Ocean Mixed Source Acquisition (OMSA) data.

Funding

This work was supported in part by the Natural Science Foundation of Sichuan (No.2026NSFSC0239), in part by the Sichuan Science and Technology Program (No.24ZYZYTS0010), and in part by the Opening Fund of Geomathematics Key Laboratory of Sichuan Province (No. scsxdz2026-14).

Conflict of interest

The authors declare no conflicts of interest.

Author contributions

Conceptualization: Haixia Hu, Yankun Zhang
Formal analysis: Haixia Hu
Investigation: Haixia Hu, Yankun Zhang, Yannan Wang
Methodology: Haixia Hu, Yankun Zhang, Youhua Wei
Software: Haixia Hu, Yuefei Zhu
Validation: Haixia Hu, Youhua Wei
Writing–original draft: Haixia Hu
Writing–review & editing: Yankun Zhang, Youhua Wei, Xiaodong Luo

Availability of data

All seismic datasets used in this study are sourced from the open-access resources released by the Society of Exploration Geophysicists (SEG; https://wiki.seg.org/wiki/SEG/EAGE_3D_modeling_Salt_Model_Phase-C_1996 and https://wiki.seg.org/wiki/PGS_Simultaneous_Source_Marine_Line).

References

1. Wang C, Huang X, Li Y, Jensen K. Removing multiple types of noise of distributed acoustic sensing seismic data using attention-guided denoising convolutional neural network. *Front Earth Sci*. 2022;10:986470.

   doi: 10.3389/feart.2022.986470

2. Zhao Y, Li Y, Jia X, Wu X. A deghosting method based on deep learning. In: *Journal of Physics: Conference Series*. 2023 Conference on Geophysics and Deep Learning; May 12-14, 2023; Beijing, China. IOP Publishing; 2023;2651(1):012126.

   doi: 10.1088/1742-6596/2651/1/012126

3. Zhu Y, Cao J, Yin H, Zhao J, Gao K. Seismic data reconstruction based on attention U-net and transfer learning. *J Appl Geophys*. 2023;219:105241.

   doi: 10.1016/j.jappgeo.2023.105241

4. Sacchi MD, Ulrych TJ, Walker CJ. Interpolation and extrapolation using a high-resolution discrete Fourier transform. *IEEE Trans Signal Process*. 1998;46(1):31-38.

   doi: 10.1109/78.651165

5. Cao S, Chen X. The second-generation wavelet transform and its application in denoising of seismic data. *Appl Geophys*. 2005;2(2):70-74.

   doi: 10.1007/s11770-005-0034-4

6. Thorson JR, Claerbout JF. Velocity-stack and slant-stack stochastic inversion. *Geophysics*. 1985;50(12):2727-2741.

   doi: 10.1190/1.1441893

7. Neelamani R, Baumstein AI, Gillard DG, Hadidi MT, Soroka WL. Coherent and random noise attenuation using the curvelet transform. *Lead Edge*. 2008;27(2):240-248.

   doi: 10.1190/1.2840373

8. Fomel S, Liu Y. Seislet transform and seislet frame. *Geophysics*. 2010;75(3):V25-V38.

   doi: 10.1190/1.3380591

9. Kong D, Peng Z. Seismic random noise attenuation using shearlet and total generalized variation. *J Geophys Eng*. 2015;12(6):1024-1035.

   doi: 10.1088/1742-2132/12/6/1024

10. Abma R, Kabir N. 3D interpolation of irregular data with a POCS algorithm. *Geophysics*. 2006;71(6):E91-E97.

    doi: 10.1190/1.2356088

11. Ronneberger O, Fischer P, Brox T. U-Net: convolutional networks for biomedical image segmentation. In: Navab N, Hornegger J, Wells WM, eds. **Medical Image Computing and Computer-Assisted Intervention – MICCAI 2015**. 18th International Conference; October 5-9, 2015; Munich, Germany. Springer; 2015:234-241.

    doi: 10.1007/978-3-319-24574-4_28

12. Dou Y, Li K, Duan H, Li T, Dong L, Huang Z. MDA GAN: Adversarial-learning-based 3-D seismic data interpolation and reconstruction for complex missing. *IEEE Trans Geosci Remote Sens*. 2023;61:5905014.

    doi: 10.1109/TGRS.2023.3249476

13. Liu B, Dong X, Xu L, Qin B. Seismic data reconstruction method using generative adversarial network based on moment reconstruction error constraint. *Sci Prog*. 2024;107(2).

    doi: 10.1177/00368504231208497

14. Zhang Y, Zhang Y, Dong H, Song L. An integrated method of seismic data reconstruction and denoising based on generative adversarial network. *Oil Geophys Prospect*. 2024;59(4):714-723. [In Chinese].

    doi: 10.13810/j.cnki.issn.1000-7210.2024.04.008

15. Yu W, Dong S, Lu S, Dong X. A novel strategy for simultaneous super-resolution reconstruction and denoising of post-stack

seismic profile. *Geophys Prospect*. 2025;73(1):96-112.

doi: 10.1111/1365-2478.13646

16. Dong X, Wei C, Zhong T, Cheng M, Dong S, Li F. Seismic data reconstruction based on a multicascade self-guided network. *Geophysics*. 2024;89(3):V179-V195.

doi: 10.1190/geo2022-0712.1

17. Dong X, Wei C, Lin J, Lu S, Cheng M, Zhang R. Deep-learning-based Global Feature Capture for Seismic Data Reconstruction. *Geophysics*. 2025;90(5):V499-V511.

doi: 10.1190/geo2024-0445.1

18. Liu N, Liu K, Wu L, Wu H, Zhang Y, Gao J. Polarity-constrained dual-cycle generative adversarial networks for irregularly sampled seismic data reconstruction. *IEEE Trans Geosci Remote Sens*. 2024;62:5918410.

doi: 10.1109/TGRS.2024.3411782

19. Wang Y, Xu X, Wang X. Reconstruction and quality control of non-repeatable land time-lapse seismic data. *J Seism Explor*. 2025;34(3):76-92.

doi: 10.36922/JSE025230010

20. Wu H, Feng J, Liu X, *et al*. Seismic Impedance Inversion Using Conditional Generative Adversarial Networks Assisted by Spectral Reconstruction-based Data Augmentation. *IEEE Trans Geosci Remote Sens*. 2025;63:5923712.

doi: 10.1109/TGRS.2025.3621119

21. Yu J, Wu B. Attention and hybrid loss guided deep learning for consecutively missing seismic data reconstruction. *IEEE Trans Geosci Remote Sens*. 2022;60:5902108.

doi: 10.1109/TGRS.2021.3068279

22. Huang H, Wang T, Cheng J, Xiong Y, Wang C, Geng J. Self-supervised deep learning to reconstruct seismic data with consecutively missing traces. *IEEE Trans Geosci Remote Sens*. 2022;60:5911514.

doi: 10.1109/TGRS.2022.3148994

23. Liu N, Wu L, Wang J, Wu H, Gao J, Wang D. Seismic data reconstruction via wavelet-based residual deep learning. *IEEE Trans Geosci Remote Sens*. 2022;60:4508213.

doi: 10.1109/TGRS.2022.3152984

24. Chen X, Chen H, Hu Y, Xie Y, Wang S. A sparse time-frequency reconstruction approach from the synchroextracting domain. *Signal Process*. 2024;222:109517.

doi: 10.1016/j.sigpro.2024.109517

25. Saad OM, Ravasi M, Alkhalifah T. Noise attenuation in distributed acoustic sensing data using a guided unsupervised deep learning network. *Geophysics*. 2024;89(6):V573-V587.

doi: 10.1190/geo2024-0109.1

26. Li C, Saad OM, Chen Y. Unsupervised deep learning for off-the-grid seismic reconstruction and denoising. *Geophysics*. 2025;90(3):V241-V254.

doi: 10.1190/geo2024-0189.1

27. Cao W, Lu W, Li Y. Semi-Supervised W-KAN for Regularly Missing Seismic Data Reconstruction. *IEEE Geosci Remote Sens Lett*. 2025;22:7507405.

doi: 10.1109/LGRS.2025.3583567

28. Peng T, Liu Y, Liu C, Chen C, Chen J. Seislet weighted stacking method with high resolution for low SNR seismic data. *Chin J Geophys*. 2025;68(3):1087-1101. [In Chinese].

doi: 10.6038/cjg2024R0866

29. Zhao H, Gallo O, Frosio I, Kautz J. Loss functions for image restoration with neural networks. *IEEE Trans Comput Imaging*. 2017;3(1):47-57.

doi: 10.1109/TCI.2016.2644865

30. Chen Y, Ma J, Fomel S. Double-sparsity dictionary for seismic noise attenuation. *Geophysics*. 2016;81(2):V103-V116.

doi: 10.1190/geo2014-0525.1

31. SEG Wiki. *SEG/EAGE 3D modeling Salt Model Phase-C 1996*. SEG Wiki. Updated May 2, 2016. Available from: https://wiki.seg.org/wiki/SEG/EAGE_3D_modeling_Salt_Model_Phase-C_1996 [Last accessed on October 5, 2023].

32. Zhang K, Zuo W, Chen Y, Meng D, Zhang L. Beyond a Gaussian denoiser: Residual learning of deep CNN for image denoising. *IEEE Trans Image Process*. 2017;26(7):3142-3155.

doi: 10.1109/TIP.2017.2662206

33. Lou Y, Wu L, Liu L, *et al*. Irregularly sampled seismic data interpolation via wavelet-based convolutional block attention deep learning. *Artif Intell Geosci*. 2022;3:192-202.

doi: 10.1016/j.aiig.2022.12.001

34. SEG Wiki. *PGS Simultaneous Source Marine Line*. SEG Wiki. Updated May 17, 2018. Available from: https://wiki.seg.org/wiki/PGS_Simultaneous_Source_Marine_Line [Last accessed on October 5, 2023].

ACCSCIENCE PUBLISHING

Journal of Seismic Exploration

ARTICLE

Joint inversion of ambient noise and gravity to investigate crustal structure and dynamic processes in the southern Sichuan Basin

Li Zhang[1], Guiju Wu[1]*, Rugang Xu[2], Yufei Xi[3], Jiapei Wang[1], and Fan Wang[1]

[1]Key Laboratory of Earthquake Geodesy, Institute of Seismology, China Earthquake Administration, Wuhan, Hubei, China

[2]Anhui Earthquake Agency, Hefei, Anhui, China

[3]Institute of Hydrogeology and Environmental Geology, Chinese Academy of Geological Sciences, Shijiazhuang, Hebei, China

Abstract

The southern Sichuan Basin, particularly the Changning area, is characterized by intense tectonic activity and frequent earthquakes. However, crustal structure models derived from different geophysical methods exhibit significant discrepancies, which impede an in-depth understanding of the tectonic evolution and earthquake genesis in this region. In this study, a joint inversion integrating surface-wave dispersion and Bouguer gravity anomaly data is adopted. By employing empirical velocity–density relations, the two datasets are coupled into a unified linearized least-squares inversion framework, in which local optimization is achieved through iterative solving. This approach is utilized to obtain the crustal density structure of the southern Sichuan Basin. The joint inversion results reveal an intracrustal low-density layer in the southern Sichuan Basin, inferred to originate from plastic deformation or partial melting of felsic components at relatively high temperatures. Driven by the topographic pressure gradient, this low-density layer undergoes ductile flow toward the Sichuan Basin. Obstructed by the rigid crust of the Sichuan Basin, the material migrates along both the eastern and western margins of the basin, with a broader eastward migration range. The leading edge of the low-density layer shows a distinct special correspondence with the seismic activity concentration zone in the Changning area, a stress concentration zone jointly shaped by deep material migration and tectonic blocking. This stress accumulation serves as the key controlling factor for the frequent earthquakes in the Changning area.

Keywords: Joint inversion; Seismic tomography; Crustal structure; Changning earthquakes

***Corresponding author:**
Guiju Wu
(wugjsky@126.com)

Citation: Zhang L, Wu G, Xu R, Xi Y, Wang J, Wang F. Joint inversion of ambient noise and gravity to investigate crustal structure and dynamic processes in the southern Sichuan Basin. *J Seismic Explor*. 2026;35(3):025010143. doi: 10.36922/JSE025010143

Received: December 31, 2025

Revised: March 23, 2026

Accepted: March 27, 2026

Published online: May 12, 2026

Copyright: © 2026 Author(s). This is an Open-Access article distributed under the terms of the Creative Commons Attribution License, permitting distribution, and reproduction in any medium, provided the original work is properly cited.

Publisher's Note: AccScience Publishing remains neutral with regard to jurisdictional claims in published maps and institutional affiliations.

1. Introduction

With significant improvements in seismic station coverage and the continuous accumulation and extensive application of geophysical exploration data, numerous studies on geophysical inversion have emerged, including magnetotelluric imaging, seismic body-wave tomography, surface-wave tomography, and receiver function

analysis.[1-5] However, constrained by the limited sensitivity of single geophysical data and insufficient sampling of observational data, a specific type of geophysical data usually imposes strong constraints only on physical parameters at certain subsurface locations or of specific scales.[6] In contrast, the joint inversion method can integrate multiple types of observational data, leverage their complementary advantages, and thus yield more reliable inversion results. The concept of joint inversion can be traced back to the work of Vozoff and Jupp,[7] who performed joint inversion of direct current and magnetotelluric data. Subsequently, the idea of joint inversion has been applied to various fields of geophysical inversion and diverse combinations of datasets. A pioneering work in joint inversion was conducted by Julià *et al.*,[8] who performed the joint inversion of receiver functions and surface-wave dispersion. They systematically accounted for differences in sensitivity and error characteristics across observational datasets, adjusted the constraining influence of each data type via weighting during inversion, and established a unified objective function framework for joint inversion, laying a key methodological foundation for subsequent joint inversion studies. At present, seismic surface-wave tomography and gravity inversion are the primary methods for obtaining crust-mantle shear-wave velocity and density structure, respectively. Although gravity data are highly sensitive to lateral density variations, their radial resolution is often limited. In contrast, seismic surface-wave data offer high radial resolution for shear-wave velocity but provide insufficient velocity constraints for short-distance observations. Therefore, joint inversion of surface-wave and gravity data can leverage the strengths of the two individual geophysical inversion methods, thereby improving the reliability of the inversion results.

The core of performing joint inversion across models with different physical parameters lies in establishing relationships among these physical models. Two common methods are currently used for this purpose: one is based on empirical or statistical relations between different physical properties, and the other is based on structural similarity between different physical property models, such as the cross-gradient method.[9] Numerous studies and applications of these two methods have been carried out in recent years. Maceira and Ammon[10] adopted the Nafe–Drake and Birch laws, optimized the velocity modeling process in complex basin areas by using piecewise velocity–density relations to adapt to lithological differences between shallow sedimentary layers and deep basements, and applied this method to Central Asian basins to obtain a three-dimensional (3D) shear-wave velocity model with richer shallow details and physical self-consistency. Chen *et al.*[11] derived a 3D shear-wave velocity model of the lithosphere in the Sichuan area via joint inversion of gravity and surface-wave data, using the empirical relations proposed by Maceira and Ammon,[10] and Brocher.[12] Wan *et al.*[13] inverted the density model of the lithosphere beneath the Qinghai–Xizang Plateau by jointly using gravity and surface-wave phase velocity data based on the Nafe–Drake curve and Brocher's empirical relations. Han[14] developed a joint inversion algorithm for various types of seismic and gravity data based on the cross-gradient structure and applied it to regional imaging studies in different regions.

The Yangtze Craton acts as a natural tectonic barrier, effectively impeding the eastward expansion of the Qinghai–Xizang Plateau. Situated between the eastern segment of the Qinghai–Xizang Plateau and the Yangtze Craton, the Eastern Tibetan Bounding Block is a seismically active zone. Over the past two decades, a series of strong earthquakes have occurred successively within this tectonic belt and its adjacent areas; typical examples include the 2008 Wenchuan M_S8.0 earthquake and the 2013 Lushan M_S7.0 earthquake. Most of these earthquakes exhibit a close genetic relationship with the Longmenshan Fault Zone, thereby providing critical observational evidence for deciphering the tectonic dynamic processes governing the eastern Qinghai–Xizang Plateau.[15] This study focuses on the southern Sichuan Basin (Figure 1B), a core transitional zone between the southeastern Qinghai–Xizang Plateau and the southwestern Sichuan Basin. Spanning the high-relief, steep terrain of the southeastern Qinghai–Xizang Plateau and the relatively low-lying, gentle landscape of the southwestern Sichuan Basin, this region exhibits remarkable topographic variation. As a critical zone for plate compression and block interaction, it is characterized by the development of multiple faults, including the Ebian Fault, Xihe–Meigu Fault, Mabian Fault, Guancun Fault, Wulianfeng Fault, Huayingshan Fault, and Zhaotong–Ludian Fault. Seismic activity in this region is frequent, and the processes of its earthquake preparation and occurrence are directly controlled by the properties of the crustal materials, fault characteristics, and deep tectonic stress states in the southern Sichuan Basin. Consequently, constructing a high-resolution 3D model of shear-wave velocity and density structure is a key foundation for analyzing the crust–mantle tectonic evolution and dynamic mechanisms. This model further provides essential support for investigating the correlation between the deep structure of the southern Sichuan Basin and the genesis of the Changning earthquake. In summary, there is an urgent need to develop a subsurface structure model of the southern Sichuan Basin through effective inversion methods, thereby providing key support for the genetic interpretation of seismic activity in the Changning area.

With significant improvement in the coverage density of seismic stations, research on the subsurface structure of the southern Sichuan Basin has advanced considerably. Li *et al.*[16] conducted a joint inversion of receiver functions and surface-wave dispersion data, and their results revealed that the regional crustal thickness increases from 30 km in southern Yunnan to 62 km in the southeastern margin of the Qinghai–Xizang Plateau, and there are two continuous low-velocity zones in the middle-lower crust serving as core channels for crustal flow, providing key seismological evidence for the study of the lateral extrusion mechanism of the Qinghai–Xizang Plateau. He *et al.*[17] systematically investigated the tectonic and geological background and mechanism of earthquakes in the Changning area by integrating multiple technical approaches, including seismic relocation, tectonic modeling, and evolutionary restoration analysis. Their findings indicated that earthquakes in the Changning area are associated with the southeastward advance of the southeastern Qinghai–Xizang Plateau, whereas moderate-to-large earthquakes in the southwestern Sichuan Basin are predominantly controlled by Cenozoic fault activity and subsurface structures. Long *et al.*[18] performed 3D velocity structure inversion and demonstrated that the velocity anomalies in the Changning–Gongxian area are highly consistent with known fault zones, and small earthquake swarms mainly occur in areas with high P-wave or S-wave velocity anomalies, which are closely related to the subsurface structure. Li *et al.*[19] employed double-difference seismic tomography to invert the 3D P-wave velocity structure of the upper crust in the earthquake area. Their study revealed the deep structural characteristics and seismogenic setting of the Changning M_S6.0 earthquake area, providing a detailed explanation of the tectonic background and genesis of seismic activity.

A comprehensive review of the literature indicates that numerous geophysical exploration projects have been conducted in the southern Sichuan Basin and its surrounding areas, yielding valuable insights into the subsurface structure and the depth of the Moho discontinuity in this region. However, significant debates persist regarding the fundamental causes of frequent earthquakes in the area and the corresponding seismogenic models. Therefore, this study aims to develop a subsurface structural model of the southern Sichuan Basin, identify intracrustal density anomalies and their spatial distribution, and elucidate the relationship between deep structural anomalies, tectonic stress accumulation, and frequent earthquakes in the Changning area. This study adopts a joint inversion method integrating surface-wave dispersion and Bouguer gravity anomaly data.[20] The empirical velocity–density relations are employed to couple the two datasets into a unified linearized least-squares inversion framework,[12] where local optimization is achieved through iterative solving to obtain the 3D crustal density structure model of the southern Sichuan Basin. This study not only provides a more reliable and accurate 3D structural model of the southern Sichuan Basin by integrating complementary constraints from multi-physical field data, but also discusses in detail the genesis of the intracrustal low-density layer in the southern Sichuan Basin by integrating previous geological and geophysical observation results. Furthermore, it innovatively analyzes the deep-dynamic processes of earthquake preparation in the Changning area from a macroscopic perspective of deep material flow and rigid block interaction, thereby offering a novel explanatory framework for the genesis of regional strong earthquakes.

2. Data and methods

2.1. Surface-wave dispersion data

Surface-wave dispersion data were extracted from ambient seismic noise data. The noise data consist of annual waveform records collected in 2016 from 87 stations deployed in the region by the China National Seismic Network.[24] The station locations are illustrated in Figure 1A. Ultimately, 3,127 fundamental-mode Rayleigh wave phase velocity dispersion curves and 2,167 fundamental-mode Rayleigh wave group velocity dispersion curves within the period range of 4–40 s were extracted from the ambient noise cross-correlation data.[25] This study utilized the data that underwent quality control of the extracted dispersion curves, as conducted by Du *et al.*[20] (Figure 2).

To ensure data reliability, the surface-wave ray-path coverage was evaluated. As presented in Figure 3, ray-path coverage maps are shown for periods of 8 s, 12 s, 16 s, 20 s, 24 s, 28 s, 32 s, and 36 s. It can be observed that most areas are covered by stations, with dense ray distribution, and the ray paths adequately cover the entire study area, indicating that this dataset can effectively resolve the crustal structure of the area.

2.2. Bouguer gravity anomaly data

The Bouguer gravity anomaly data are derived from the Earth Gravitational Model 2008 (EGM2008), with a grid spacing set to 3'×3'. The model's primary data sources include terrestrial gravity, satellite altimetry, and satellite gravity observations.[26] Figure 4 presents the distribution of the Bouguer gravity anomaly utilized in this study. To eliminate high-frequency disturbances caused by the dramatic topographic relief along the southeastern margin of the Qinghai–Xizang Plateau, this study processed EGM2008 gravity field data using a matched-filter method

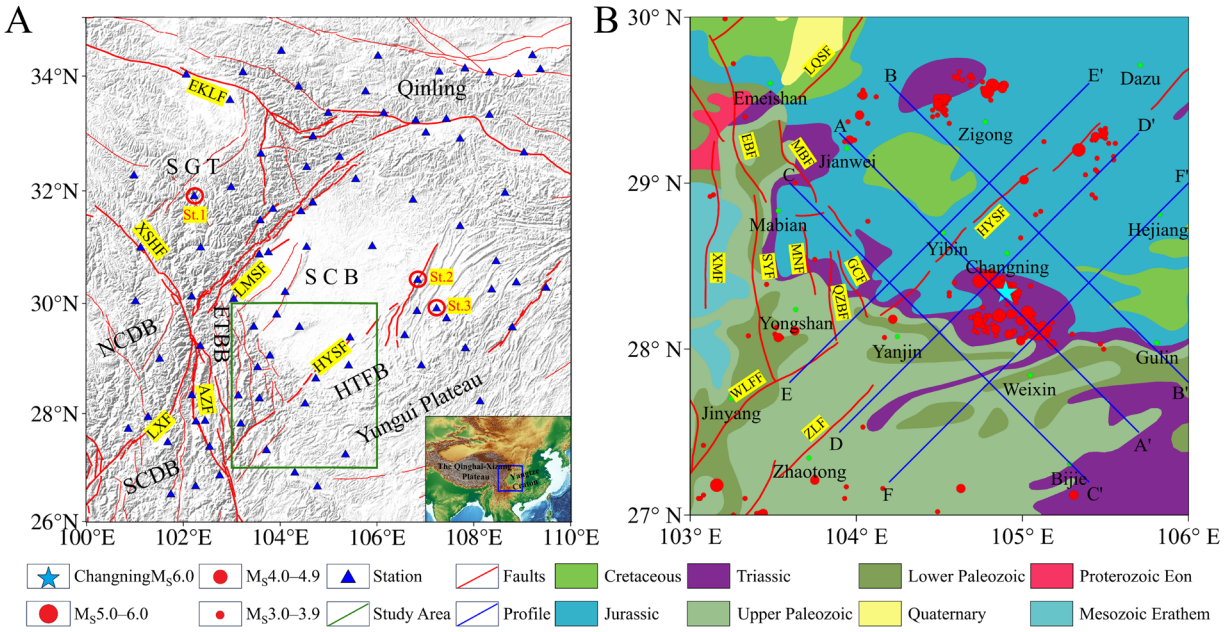

Figure 1. Distribution of tectonic blocks and major faults in the Sichuan Basin and surrounding areas. (A) Major active tectonic units in the southeastern Qinghai–Xizang Plateau and distribution of stations used in this study. The main tectonic blocks and faults are as follows:[21-23] AZF: Anninghe–Zemuhe Fault; EKLF: east Kunlun Fault; ETBB: Eastern Tibetan Bounding Block; HTFB: Huayingshan Thrust and Fold Belt; HYSF: Huayingshan Fault; LMSF: Longmenshan Fault; LXF: Lijiang–Xiaojinhe Fault; NCDB: North Chuan–Dian Block; SCB: Sichuan Basin; SCDB: South Chuan–Dian Block; SGT: Songpan–Ganzi Block; XSHF: Xianshuihe Fault. (B) Stratigraphic distribution and earthquake distribution (2019–2025) in the southern Sichuan Basin.[21-23] The main faults include: EBF: Ebian Fault; GCF: Guancun Fault; LQSF: Longquanshan Fault; MBF: Mabian Fault; MNF: Manao Fault; QZBF: Xieziba Fault; SYF: Sanhekou–Yanfeng Fault; WLFF: Wulianfeng Fault; XMF: Xihe–Meigu Fault; ZLF: Zhaotong–Ludian Fault.

based on logarithmic power spectrum analysis. By analyzing the slope of the logarithmic power spectrum, we selected 20 km as the cut-off wavelength for the matched filter. This procedure separated shallow and deep field sources, effectively suppressed high-frequency noise from the shallow crust, and obtained the Bouguer gravity anomalies caused by crustal materials at depths of approximately 5 km and greater in the study area. Meanwhile, since this study focused on regional tectonic features, relative gravity anomalies were adopted in the analysis. Therefore, mean removal was applied to the gravity data before inversion, which effectively eliminates the influence of the regional gravity background field associated with large-scale structures in the deep mantle.

2.3. Joint inversion method

2.3.1. The forward problem

According to the statistical theory of ambient noise,[27] cross-correlating long-time series of ambient noise signals can extract the Green's function, which is dominated by surface waves. Subject to the constraint of surface-wave dispersion effects, the computation of frequency-dependent travel time $t(\omega)$ should be viewed as a ray-tracing problem at each period on the Earth's free surface:

$$T(\omega) = \int_A^B \frac{dl}{c(\omega)} \tag{1}$$

where ω is the angular frequency, $c(\omega)$ is the dispersion map for every period, and the integral is computed along the ray-path connecting point A and B. As for the ray-path used to compute travel time, a more accurate approach to modeling the surface-wave travel time is to utilize a two-dimensional eikonal equation in spherical coordinates:

$$\frac{1}{R}\left(\frac{\partial T}{\partial \theta}\right)^2 + \frac{1}{R^2 \sin^2\theta}\left(\frac{\partial T}{\partial \phi}\right)^2 = \frac{1}{c^2(\omega)} \tag{2}$$

where $T = T(\theta, \phi, \theta_0, \phi_0)$ is the arrival time of the surface-wave propagating from spherical coordinates (θ_0, ϕ_0) to (θ, ϕ) at a given period, and R is the Earth's radius. This equation can be efficiently solved using the fast marching

method.[28,29] Given the enormous computational cost, a localization approach is adopted to calculate the dispersion map, in which the dispersion map at each point on the free surface is determined solely by the one-dimensional (1D) layered model beneath that point. Subsequently, the Thomson–Haskell algorithm[30,31] is utilized for forward computation. With this method, surface-wave travel times for each period can be directly calculated from a given 3D model.

The radial component of the gravity field produced by the density distribution of a spherical prism can be expressed as:[32]

$$g_r(r_o,\theta_0,\phi_0)=\int_{r_1,\theta_1,\phi_1}^{r_2,\theta_2,\phi_2}\frac{G\rho_S r_s^2\sin\theta_s(-r_o+r_s\cos\delta)}{R_{os}^3}dr_s d\theta_s d\phi_s \quad (3)$$

where G is the gravitational constant, g_r is the radial component of gravity at (r_o,θ_0,ϕ_0), R_{os} is the straight-line distance between source and receiver, and δ is the epicentre distance. For complex density distributions, the Gauss–Legendre numerical integration method can be used, such that the above integral can be expressed as:

$$g_r^n=\sum_{i=1}^{I}\sum_{j=1}^{J}\sum_{k=1}^{K}\omega_i\omega_j\omega_k g(r_i,\theta_j,\phi_k),n=1,2,..,N \quad (4)$$

where I,J,K denotes the order of Gauss–Legendre integration used in each direction, $\omega_{i,j,k}$ denotes the weight coefficient in each direction, and (r_i,θ_j,ϕ_k) denotes the position of the Gauss–Legendre integration node in each direction.

Since a longitude–latitude oriented grid is utilized to solve **Equation 2**, for computational convenience, this grid is required to coincide with that adopted in gravity forward modeling. Notably, different prisms contribute unequally to gravity observations owing to their sizes and distances from the observation point, making it extremely time-consuming to use an identical number of Gauss–Legendre points in each prism. To tackle this problem, the number of grid points and the order of the Gauss–Legendre polynomial for each prism can be adaptively determined based on the distance between a grid point and its adjacent points,[33] which significantly improves computational efficiency.

2.3.2. The inverse problem

To enable joint inversion, the surface-wave and gravity inversion equations need to be unified into a single system. Surface-wave dispersion data are mainly related to shear-wave velocity, and Bouguer gravity anomaly data, after conversion between velocity and density, are also related to shear-wave velocity. During the inversion process, surface-wave travel-time residuals and gravity residuals can be correlated with shear-wave velocity perturbations via sensitivity kernel matrices. Joint inversion can assemble the surface-wave travel-time and gravity data residuals into a sparse linear system in each iteration:

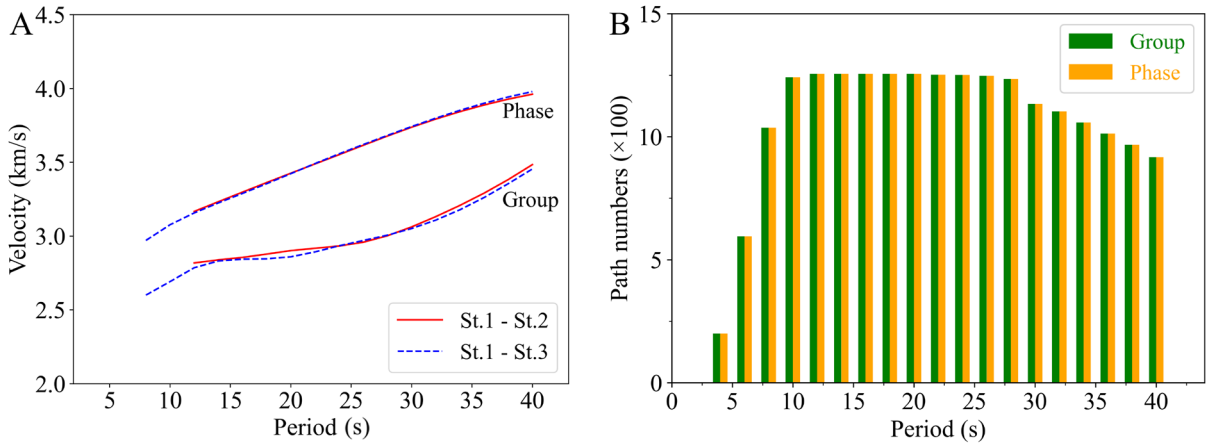

Figure 2. Surface-wave dispersion data for inversion. (A) Group velocity and phase velocity dispersion curves between station pairs St.1–St.2 and St.1–St.3 (Figure 1A); (B) number of group velocity and phase velocity paths used for each period in the inversion.

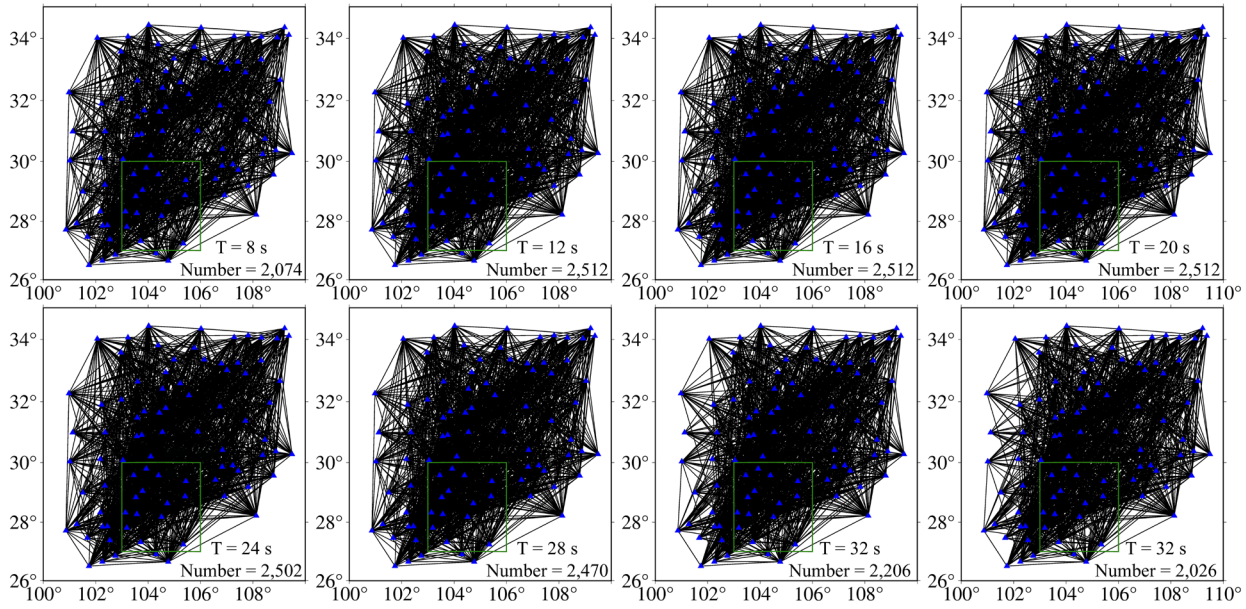

Figure 3. Ray-path coverage maps for different periods. The study area is the region enclosed by the green rectangle, and blue triangles represent stations used in this study.

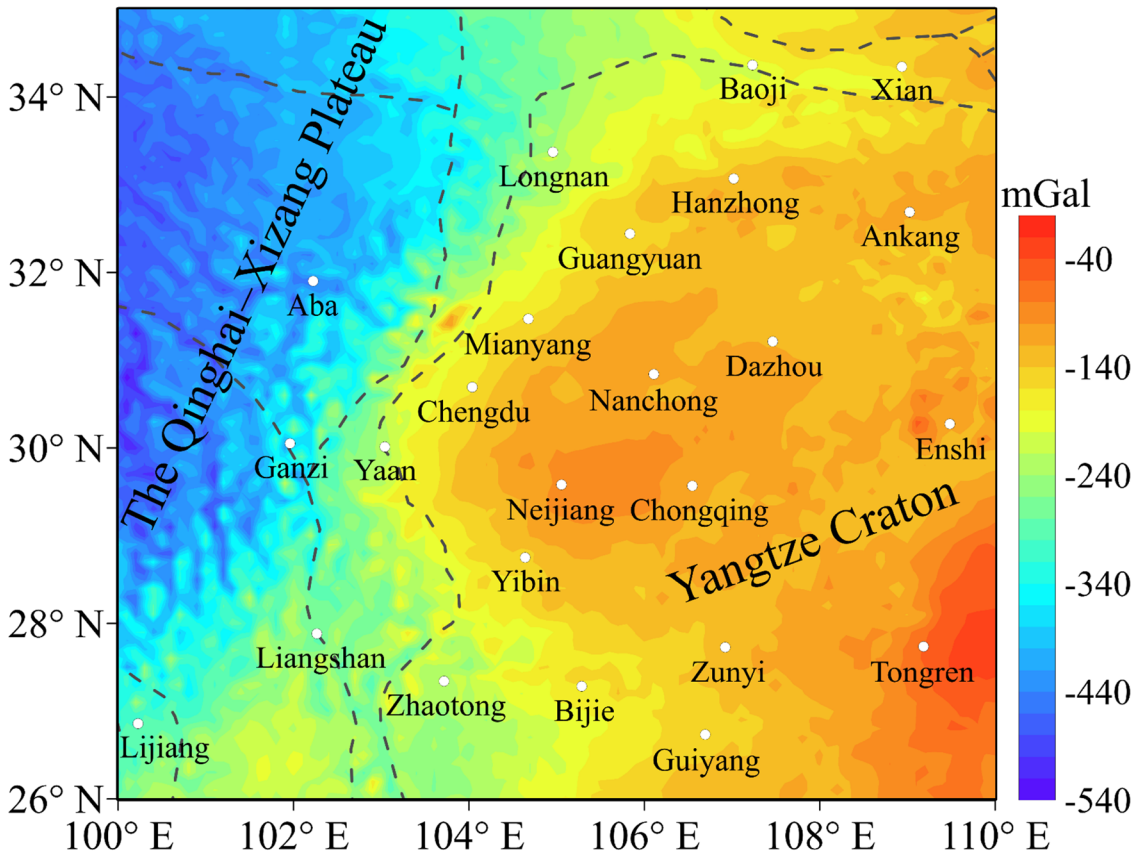

Figure 4. Distribution of Bouguer gravity anomaly data obtained from the Earth Gravitational Model 2008. Dashed lines represent the block boundaries in this region.[23]

$$\begin{bmatrix} G_s \\ G_g \end{bmatrix} \delta\beta_i = \begin{bmatrix} \delta t \\ \delta g_g \end{bmatrix} \tag{5}$$

The solution to **Equation 5** can be formulated as a weighted least-squares optimization problem with second-order Tikhonov regularization and damping:[10,34-36]

$$\delta\beta_i = \underset{m}{argmin} \left\| \begin{bmatrix} W_s G_s \\ W_g G_g \\ \sigma S \\ \gamma I \end{bmatrix} m - \begin{bmatrix} W_s \delta t \\ W_g \delta g \\ 0 \\ 0 \end{bmatrix} \right\|_L \tag{6}$$

where G_s and G_g are the sensitivity kernel matrix of surface-wave and gravity anomaly to shear-wave velocity, respectively; σ and S are the second-order Tikhonov regularization coefficient and matrix, respectively; γ is the damping factor; I is the identity matrix; W_S and W_g are diagonalized weight matrices for surface-wave and gravity data, respectively:[8]

$$W_s = diag\left\{ \sqrt{\frac{p}{N_s \left(\sigma_i^s\right)^2}}, i = 1, 2, ..N_s \right\} \tag{7}$$

$$W_g = diag\left\{ \sqrt{\frac{1-p}{N_g \left(\sigma_i^g\right)^2}}, i = 1, 2, ..N_g \right\} \tag{8}$$

where p is a parameter between 0 and 1. $N_{s,g}$ are the number of data for surface-wave and gravity data, respectively, and $\sigma_{s,g}$ are the standard variations of the two datasets.

This augmented linear system is efficiently solved under the L_2-norm using the least-squares minimum residual (LSMR) iterative method.[37] Based on the standard derivative property of the L_2-norm, the gradient of the objective function $J(m)$ with respect to the variable m can be explicitly expanded as:

$$\begin{aligned} \nabla J(m) = 2\Big[& G_s^T W_s^T W_s (G_s m - \delta t) \\ & + G_g^T W_g^T W_g (G_g m - \delta g) \Big] + 2\left[\sigma^2 S^T S + \gamma^2 I\right] m \end{aligned} \tag{9}$$

By progressively searching along these gradient directions toward the local minimum, LSMR identifies the optimal solution.

Subsequently, the model is updated using **Equation 10** until the residuals are in a reasonable range.

$$\beta_{i+1} = \beta_i + \delta\beta_i \tag{10}$$

3. Joint inversion of the southern Sichuan Basin

3.1. Model setup and parameter selection

Based on the ray-path distribution in the study area and extensive tests, the initial velocity model was configured to divide the study area into a latitude–longitude grid with a 0.3° horizontal interval. In the vertical direction, the shallow layer is the main seismogenic layer in the study area, encompassing key structures such as sedimentary layers and active faults, and thus requiring high-resolution characterization of structural heterogeneity. In contrast, the deep crustal structure is relatively homogeneous, with lateral inhomogeneity weakening with increasing depth, and thus, sparse layering can also reflect the overall trend. To balance resolution and computational efficiency, the model is divided into 21 layers with gradually increasing grid spacing with depth, spanning 0 km to 70 km, as detailed in Table 1. Since linearized methods rely on the initial model, the inversion results of Xia[25] for this region were adopted for the crust and upper mantle in this study. In this initial model, the shear-wave velocity from these inversion results increases with depth. The shallow layer at 0–6 km is controlled by the sedimentary layers of the Sichuan Basin, where basin velocities are significantly lower than those in the surrounding mountainous areas. In the 6–20 km depth range, the extent of low-velocity anomalies inside the basin shrinks gradually, and the lateral inhomogeneity of the medium weakens markedly. Starting from 20 km depth, a remarkable reversal occurs in the velocity structural pattern: the shear-wave velocity in the Sichuan Basin becomes progressively higher than that in the eastern margin of the Qinghai–Xizang Plateau, and a distinct and prominent velocity difference forms on both sides of the basin–mountain boundary. In terms of the Moho depth, the Moho discontinuity beneath the Sichuan Basin and its adjacent areas is generally at 40–60 km, and it deepens gradually from the basin westward to the southeastern margin of the Qinghai-Xizang Plateau. This model accurately delineates the velocity differences among the thick sedimentary layers, the rigid basin basement of the Sichuan Basin, and the surrounding orogenic belts, as well as the lateral variation law of the Moho discontinuity, and is highly consistent with the regional tectonic setting. Therefore, selecting this model can provide a rational and stable initial constraint for linearized inversion, effectively reduce the non-uniqueness of inversion solutions, and simultaneously enhance the inversion process's convergence efficiency and the credibility of the final results.

For the velocity–density empirical relationship, a general relationship proposed by Brocher was employed in this study:[12]

Table 1. Three-dimensional model settings of the study

Depth/km	Thickness/km	Number of layers
0–20	2	10
20–40	4	5
40–70	5	6

$$\rho = 1.6612\alpha - 0.4721\alpha^2 + 0.0671\alpha^3 - 0.0043\alpha^4 + 0.000106\alpha^5 \quad (11)$$

$$\alpha = 0.9409 + 2.0947\beta - 0.8206\beta^2 + 0.2683\beta^3 - 0.0251\beta^4 \quad (12)$$

where ρ denotes density, α denotes P-wave velocity, and β denotes S-wave velocity. This empirical relationship is established based on global datasets of crustal borehole logging, laboratory petrophysical measurements, and seismic tomography. It covers a variety of common crustal lithologies, including sedimentary rocks, granitic rocks, and metamorphic rocks, and is applicable to seismically active continental margins, which is highly consistent with the geological and tectonic setting of the study area. Furthermore, this empirical relationship is valid for the ranges of 1.5 km/s < V_p < 8.5 km/s and V_s < 4.5 km/s. Since this study focuses on the density structure of the crust and upper mantle, the empirical relationship is applicable over most depths in the research region.

To determine the weight matrices in **Equation 6**, it is necessary to estimate the measurement uncertainties of the two datasets. For the EGM2008 data, the uncertainty is typically 10.5 mGal.[38] For surface-wave dispersion data, the uncertainties were estimated as 1.4 s by Du *et al.*[20] using **Equation 13**.

$$\delta t = d\frac{\delta c}{c_o} \quad (13)$$

where δt is the surface-wave travel-time error, d is the average interstation distance, δc is the average error of the observed phase and group dispersion velocities, and c_o is the average dispersion velocity.

To accelerate convergence of the inversion, it is essential to ensure that low-frequency information in the model is recovered as much as possible in the initial iterations. Therefore, the method proposed by Roecker[39] was adopted. Only surface-wave travel-time data were fitted in the first 10 iterations, and gravity data were incorporated for joint inversion in subsequent iterations. In the final 10 iterations, different values of P were tested, and both datasets could be fitted with root-mean-square (RMS) residuals close to the noise level, with negligible differences. Therefore, the value of P was set to 0.5, indicating that the weights of the two datasets are determined solely by their statistical uncertainties, and no additional artificial weighting is applied to either dataset.

In the recursive solution of algebraic equations during each iteration, the damping and smoothing factors control the amplitude of velocity variation per iteration. In the numerical experiments, the effects of the damping factor are much smaller than those of the smoothing factor. Therefore, in this study, the damping factor is ultimately fixed to a very small value. To select an appropriate smoothing factor, the model regularization norm and data residual norm corresponding to different smoothing factors were calculated, and an L-curve was plotted for analysis (Figure 5). The parameter value was determined based on the L-curve.[40] In the L-curve, the optimal smoothing factor corresponding to the inflection point was selected as 30.

3.2. Checkerboard test

Based on the ray-path distribution in the study area and extensive tests, the size of the velocity anomaly body was finally set to 1.2°×1.2°, with a velocity perturbation of ±5%. In the vertical direction, intervals of 10 km were used for the 0–20 km depth range, and 20 km for the 20–70 km depth range. The forward method was applied to compute the synthetic surface-wave travel-time and Bouguer gravity anomaly data sets for this model. Then, random Gaussian noise was added to the synthetic observations, with a standard error of 1.4 s for the surface-wave travel-time data and 10.5 mGal for the gravity data. Finally, the same inversion strategy used for the real data was applied to recover the checkerboard model.

Figure 6 presents the inversion results of surface-wave-only inversion and joint inversion at four depths (6 km, 16 km, 32 km, 50 km). The surface-wave-only inversion generally recovered the velocity structure (Figure 6A–D). However, due to uneven ray distribution, the checkerboard pattern in edge regions with sparse coverage was not well recovered by surface-wave-only inversion, and the recovery performance of inversion deteriorated progressively with increasing depth. In contrast, the joint inversion results (Figure 6E–H) show improved recovery both outside

the ray-paths and across all depth ranges up to 60 km, outperforming the surface-wave-only inversion and closely reproducing the true model. This depth-dependent degradation is further confirmed by the extracted 1D velocity profile (Figure 7).

3.3. Results

3.3.1. Fitting analysis of surface-wave travel-time and gravity data

The residuals between theoretical travel times calculated from the initial model and observed travel times are distributed primarily within ±12 s, with an RMS of 4.71 s (Figure 8A). After surface-wave-only inversion, the distribution of travel-time residuals clearly converged toward the center, mostly within ±6 s, and the RMS reduced to 2.69 s (Figure 8B). The distribution of travel-time residuals after joint inversion was similar, also concentrated within ±6 s. However, the RMS is 2.73 s (Figure 8C), slightly higher than that of the surface-wave-only inversion.

The initial density model was derived by converting the initial velocity model using an empirical relationship. Forward modeling of gravity anomalies was then performed on this initial density model to obtain the residuals between theoretical and observed gravity anomalies (Figure 9A). The results show that the gravity anomaly residuals range from −300 to 200 mGal, with an RMS of 86.3 mGal. The spatial distribution of residuals shows a distinct pattern: high values at the eastern and western edges and low values in the center. The gravity anomaly residuals from the surface-wave-only inversion results are smaller than those from the initial model. Compared with the residuals from the forward modeling of the initial model, larger residuals are concentrated in the Sichuan Basin, with the RMS decreasing to 83.8 mGal (Figure 9B). The gravity anomaly residuals are mainly distributed between −220 and 260 mGal and do not fit the gravity anomaly data well. In contrast, the gravity anomaly residuals after joint inversion are significantly reduced. Regions with relatively large residuals are concentrated in the Songpan–Ganzi Block and Sichuan–Yunnan Block, and the residuals are mainly confined to a small range of approximately ± 20 mGal, with the RMS reduced to 14.7 mGal (Figure 9C). Therefore, the joint inversion results can effectively fit both surface-wave travel times and gravity data.

3.3.2. Comparison of results from different inversion methods

The results of surface-wave-only and joint inversions were converted using the velocity–density empirical relationship to obtain the density structure of the study area at different depths (Figure 10). The density structure obtained from surface-wave-only inversion and joint inversion is generally similar, but there are still some differences. At a depth of 6 km, the density difference between the two sides bounded roughly by the Wulianfeng Fault and Xieziba Fault is more pronounced in the joint inversion results, which is consistent with the findings of Xia *et al.*[25] At 12 km depth, the joint inversion results reveal a larger-scale high-density anomaly southwest of the epicenter of the Changning M_S6.0 earthquake, with obvious density differences from other directions, exhibiting distinct lateral inhomogeneous distribution.[18,19] At a depth of 32 km, the boundary between the Sichuan Basin and the adjacent orogen is more distinct in the tomographic results from the surface-wave-only inversion.

3.3.3. Results of joint inversion

In the horizontal direction, the density structure at different depths in the joint inversion results (Figure 11) exhibits significant lateral inhomogeneity. At a depth of 6 km (Figure 11A), the density structure is consistent with the surface geological structure, with a distinct boundary between mountainous areas and the basin.[20,25,41] A prominent low-density anomaly develops within the Sichuan Basin, further confirming the presence of a thick sedimentary layer.

At a depth of 12 km (Figure 11B), the low-density anomaly in the Sichuan Basin gradually concentrates toward the southwest margin, and the density in the central part of the basin is higher than that in the southwest part of the basin; low-density anomalies appear on the eastern side of the Xihe–Meigu Fault and the eastern side of the Zhaotong–Ludian Fault. Additionally, the Changning M_S6.0 earthquake and its surrounding area exhibit distinct lateral inhomogeneity in density structure.[18]

As depth increases to 20 km (Figure 11C), the density in the basin increases rapidly, and the low-density anomaly basically disappears. The Sichuan Basin exhibits a high-density anomaly, while its surrounding areas have relatively low density, in stark contrast to the density structure at 6 km depth. Within the Sichuan Basin, the density gradually exceeds that in the southeastern Qinghai–Xizang Plateau. This density reversal pattern is caused by the greater crustal thickness of the Qinghai–Xizang Plateau: at the same depth, the Qinghai–Xizang Plateau is still within the crust, whereas the Sichuan Basin has already entered the lower crust or even the crust–mantle transition zone.[20,42,43] Furthermore, the low-density anomaly on the eastern side of the Zhaotong–Ludian Fault at 12 km depth extends northward to the southern margin of the Sichuan Basin, and then spreads along both sides of the margin after reaching it, with a larger eastward extension.[43]

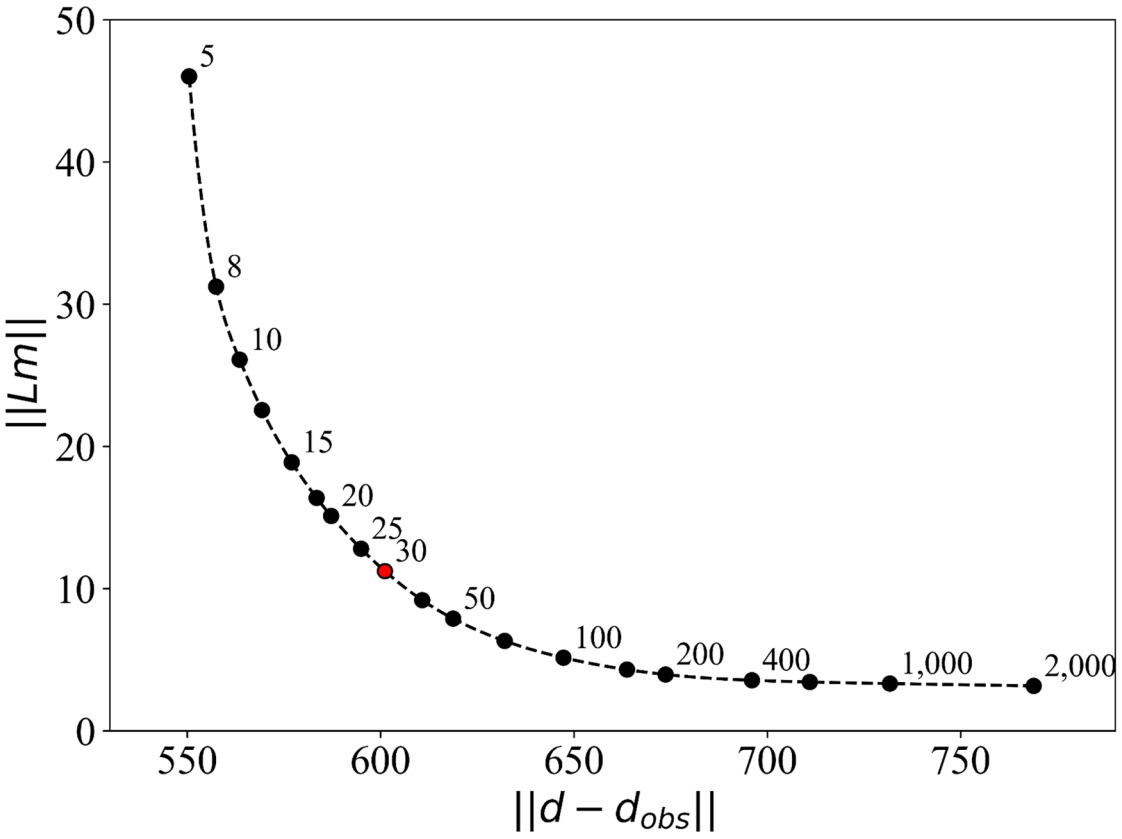

Figure 5. L-curve analysis in the joint inversion method. The red dot represents the optimal smoothing factor

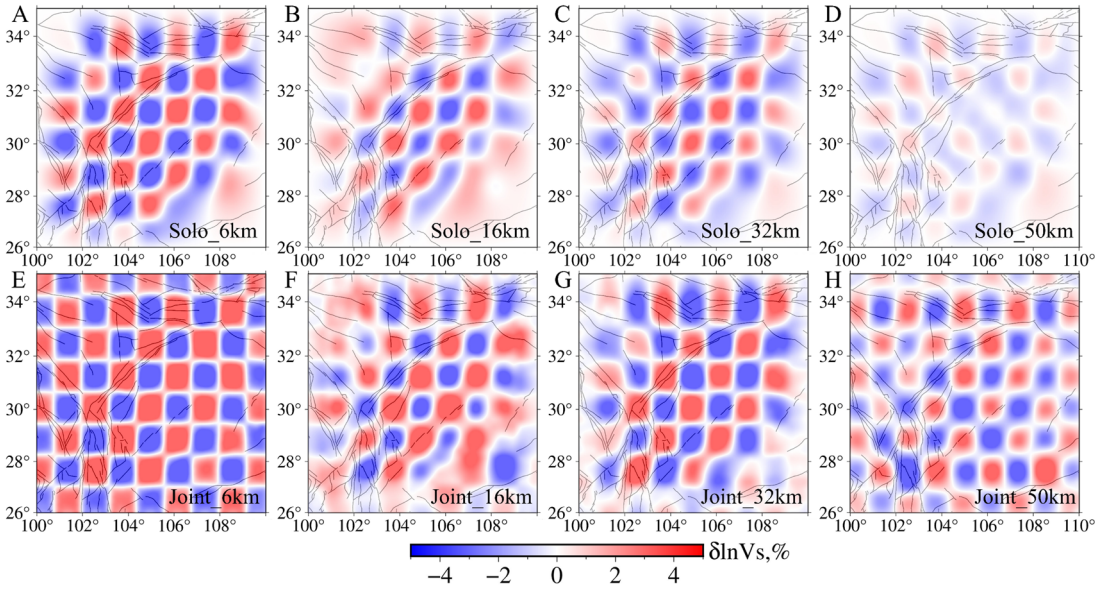

Figure 6. Horizontal slices of the inversion model at 6, 16, 32, and 50 km depth. (A–D): Results of surface-wave-only inversion; (E–H): Results of joint inversion.

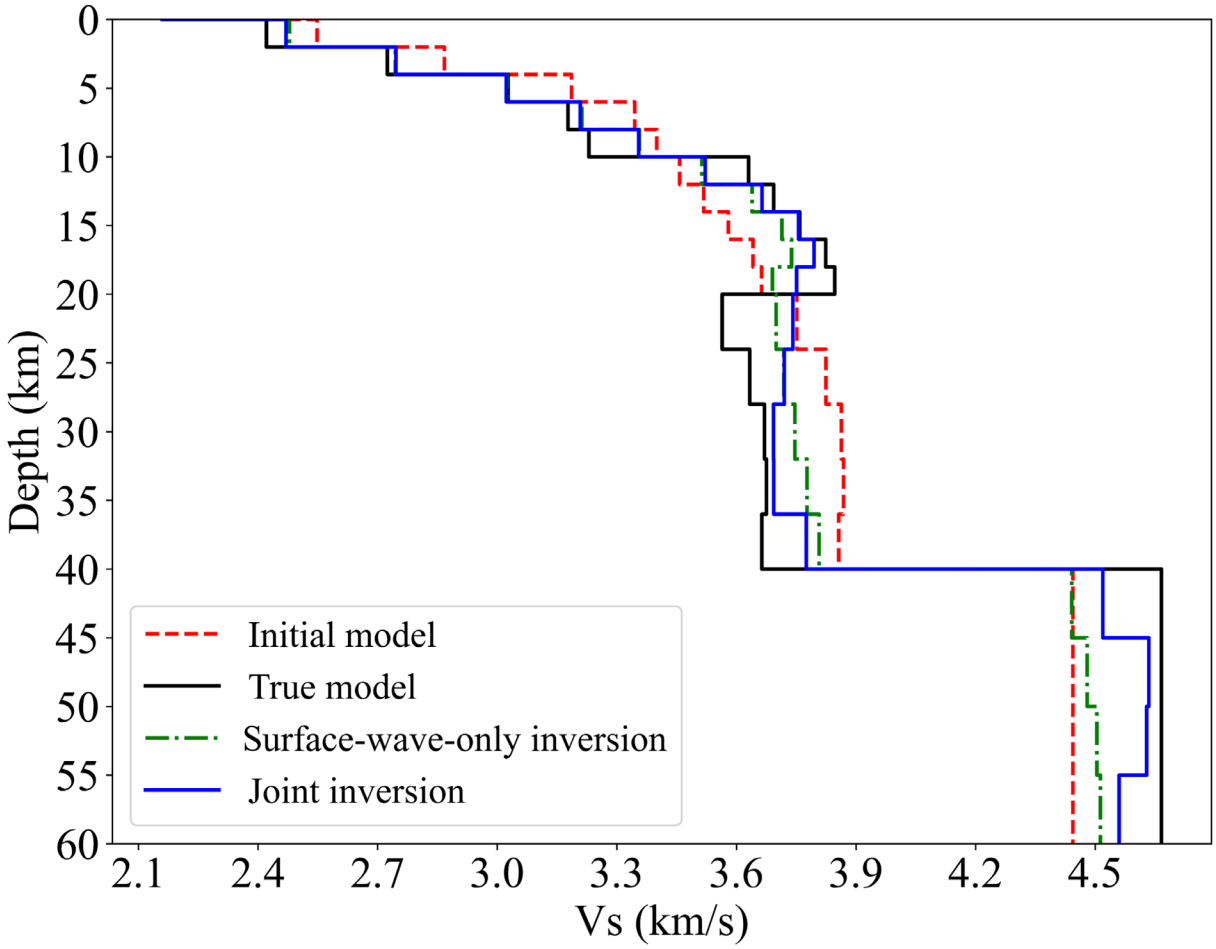

Figure 7. One-dimensional velocity profile comparison from the checkerboard test

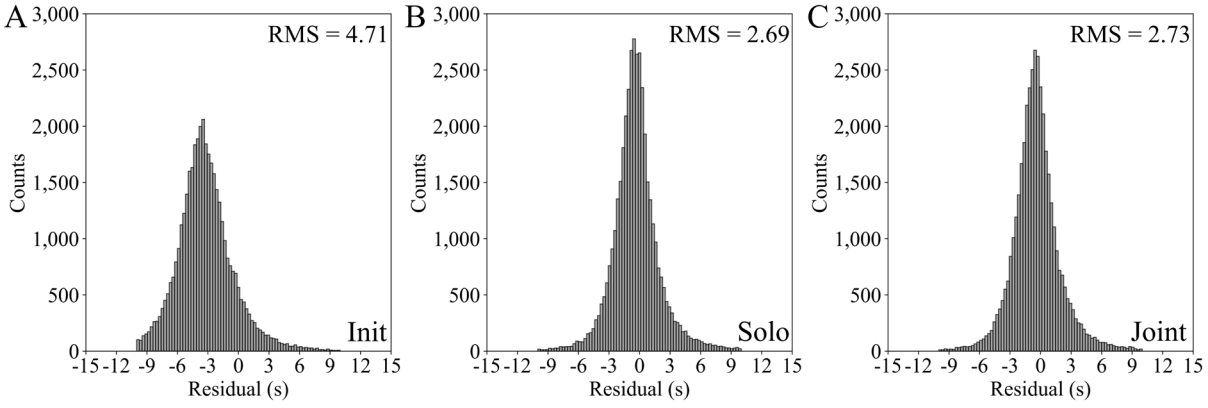

Figure 8. Histograms of travel-time residual distribution. (A) Travel-time residuals of the initial model; (B) travel-time residuals after surface-wave-only inversion; (C) travel-time residuals after joint inversion.
Abbreviation: RMS: Root mean square.

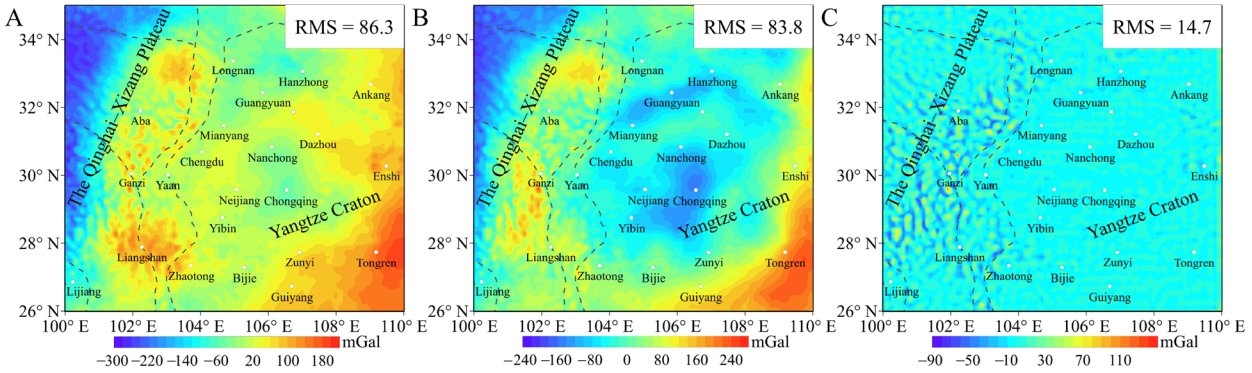

Figure 9. Residuals between observed and theoretical gravity anomalies for different models. (A) Gravity anomaly residuals of the initial model; (B) gravity anomaly residuals from surface-wave-only inversion; (C) gravity anomaly residuals from joint inversion.
Abbreviation: RMS: Root mean square.

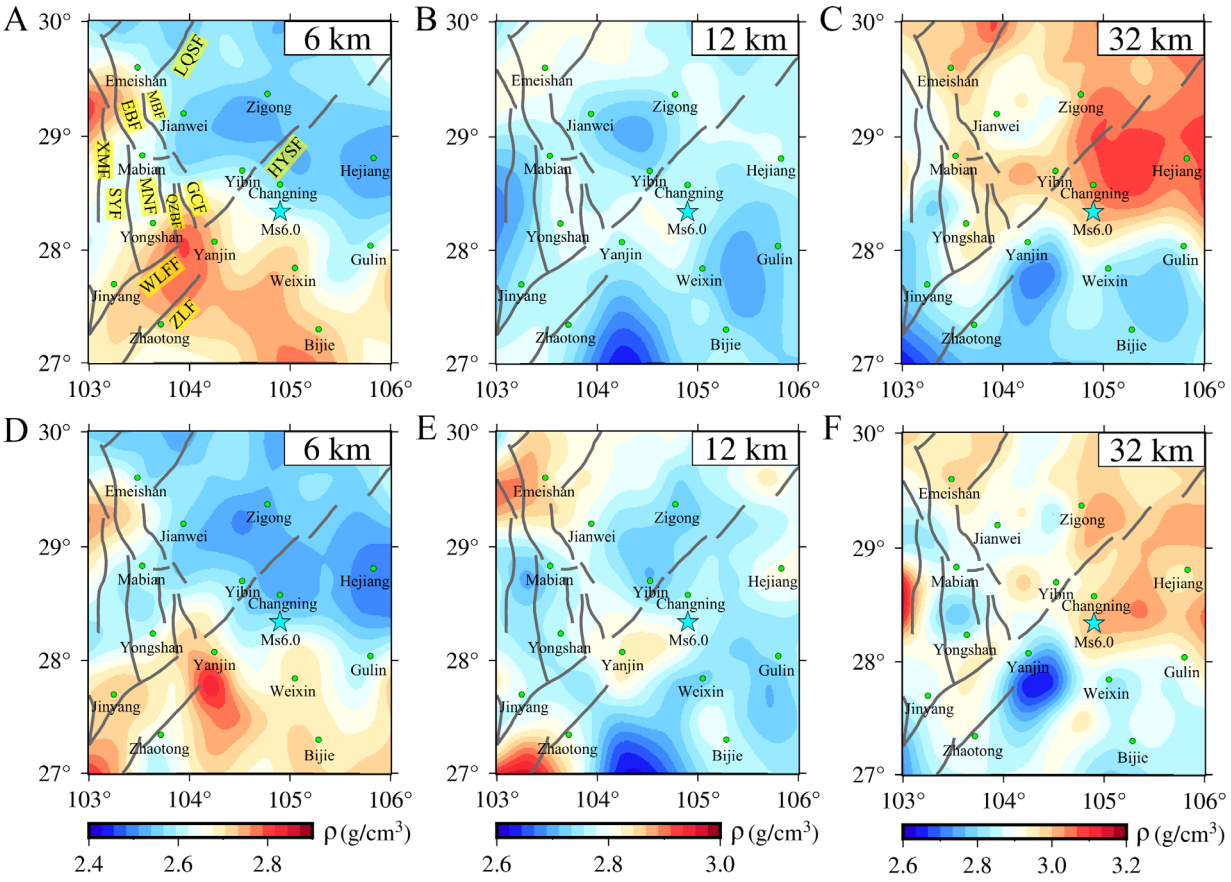

Figure 10. Comparison of tomography results from surface-wave-only inversion and joint inversion at depths of 6 km, 12 km, and 32 km. (A–C): Results of surface-wave-only inversion; (D–F): Results of joint inversion. Gray solid lines represent major active faults, and the cyan five-pointed star represents the 2019 Changning M_S6.0 earthquake.

At a depth of 28 km (Figure 11D), the low-density anomaly on the eastern side of the Zhaotong–Ludian Fault extends northward, with an area smaller than that at 20 km depth, and only extends on the eastern side of the southern Sichuan Basin. The epicenter of the Changning M_S6.0 earthquake is located in the gradient zone where the center of the low-density anomaly transitions into the high-density anomaly inside the basin; the low-density anomaly on the eastern side of the Xihe–Meigu Fault still persists.[20]

At a depth of 32 km (Figure 11E), the low-density anomaly on the eastern side of the Zhaotong–Ludian Fault continues to shrink, and its extension trend almost disappears; the range of the low-density anomaly on the eastern side of the Xihe–Meigu Fault shrinks, while the high-density anomaly on its western side gradually expands compared with that at 28 km.

At a depth of 36 km (Figure 11F), the low-density anomaly on the eastern side of the Zhaotong–Ludian Fault almost disappears, while the high-density anomaly on the western side of the Xihe–Meigu Fault continues to expand eastward. However, overall lateral inhomogeneity weakens with increasing depth.[18,42,43]

In the vertical direction, density tomography was performed along the six profiles shown in Figure 1B, producing the results displayed in Figure 12. The joint inversion results show that a prominent, continuous low-density anomaly develops in the middle-lower crust of the southern margin of the Sichuan Basin. Along the northwest–southeast direction, the low-density anomaly extends horizontally for approximately 220 km along profile CC′, occurring between approximately 30 km and 250 km along the profile. It has a vertical thickness of 10–30 km and forms a large-scale continuous low-density anomaly. Before reaching profile AA′, the anomaly expands both eastward and westward, with a markedly greater eastward extent. At profile BB′, only the eastward extension remains, whereas the westward extension is nearly absent.

From the southwest–northeast direction, the low-density anomaly develops in the tectonic transition zone between the high-topographic mountainous area in the southeastern Qinghai–Xizang Plateau and the low-topographic Sichuan Basin. Vertically, it gradually extends toward the Sichuan Basin from a depth of 15 km, thins toward the northeast, and eventually disappears at 35 km. The anomaly is most prominently developed on Profile DD'. On Profile EE', the low-density anomaly almost disappears, while on Profile FF', the anomaly still maintains a prominent low-density anomaly and extends continuously toward the southeast direction. Furthermore, the Wulianfeng Fault and Zhaotong–Ludian Fault develop on the left side of Profile DD', which is also adjacent to the eastern boundary of the Sichuan–Yunnan Block. In contrast, the regions on the right side of Profile DD' and where Profile FF' is located exhibit weak fault activity and limited ability to restrict the development of the anomaly, accounting for the significant differences in the degree of anomaly development across different directions.

4. Discussion and analysis

4.1. Intracrustal low-density layer in southern Sichuan Basin

A prominent, continuous intracrustal low-density layer occurs along the southern margin of the Sichuan Basin (Figure 12), exhibiting a zonal distribution mainly along the eastern side of the Zhaotong–Ludian Fault and along the southern margin of the Sichuan Basin. Its spatial location is consistent with previous studies' results.[20,25,44-46] However, due to the limitations of research scope and imaging resolution, the detailed distribution pattern of this low-density layer has not been specifically demonstrated. The findings from this study clearly show that the low-density layer is centered on Yanjin, with its western extent extending to the Xieziba Fault and Guancun Fault, and its eastern limit terminating at the study area (Figure 11C). This low-density layer is predominantly hosted within the Upper Paleozoic strata (Figure 1B). Notably, the southern Sichuan Basin lies within the active tectonic belt at the southeastern Qinghai–Xizang Plateau. The continuous convergence between the Indian Plate and the Eurasian Plate has not only induced intense deformation of the lithosphere in the Qinghai–Xizang Plateau but also driven substantial volumes of low-density crustal material to escape toward the plateau's southeastern margin.[47-49] Thus, the low-density layer identified in this study may be genetically linked to the crustal flow escaping southeastward from the Qinghai–Xizang Plateau. However, previous studies have shown that as the crustal material migrates southeastward, passes through the Lijiang–Xiaojinhe Fault zone, and enters the South Chuan–Dian Block, its movement is obstructed by the Emeishan Large Igneous Province. Instead of continuing southeastward, the crustal material turns to migrate southwestward.[48,50] Furthermore, this low-density layer is separated from the low-velocity layer of the Sichuan–Yunnan rhombic block by the high-velocity body adjacent to the Anninghe–Zemuhe Fault Zone.[46] Collectively, these lines of evidence indicate that the identified low-density layer is not the ductile material escaping from the Qinghai–Xizang Plateau toward its southeastern margin.

To further elucidate its material composition and formation mechanism, this study integrates multi-source observational data to conduct a comprehensive analysis.

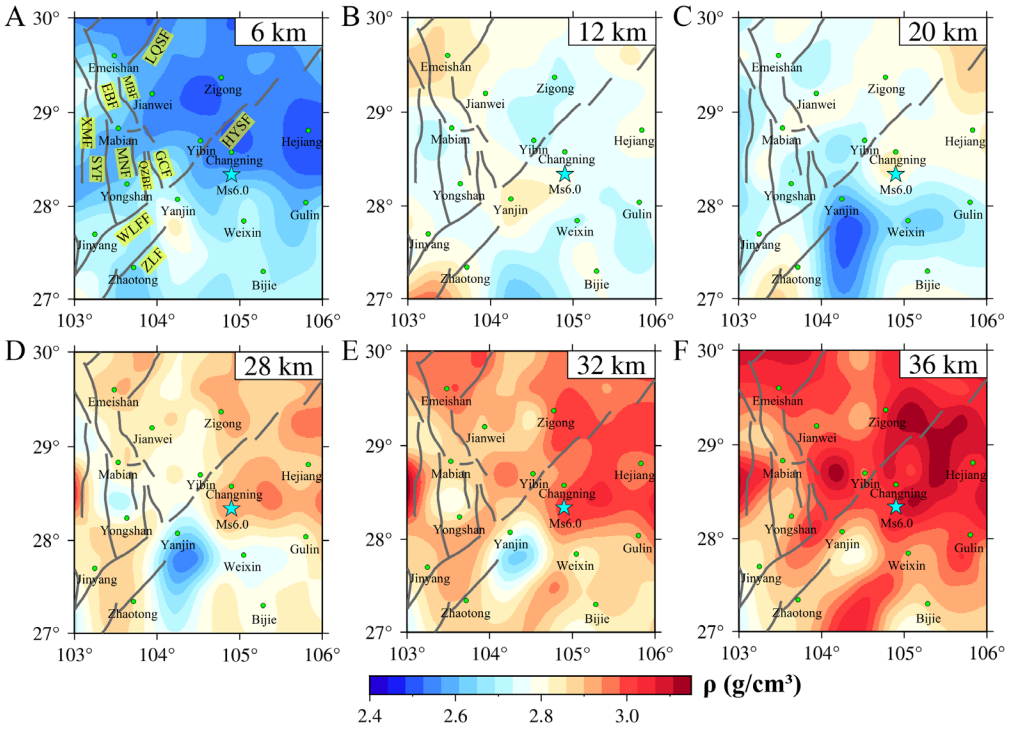

Figure 11. Density tomography results of the joint inversion at different depths. (A) 6 km; (B) 12 km; (C) 20 km; (D) 28 km; (E) 32 km; (F) 36 km.

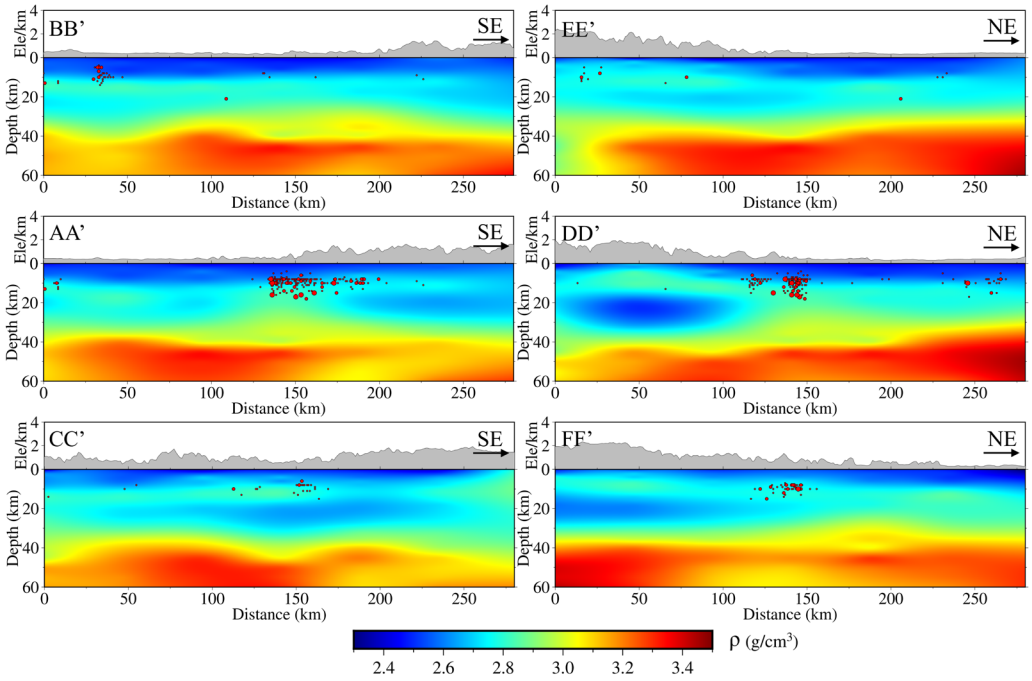

Figure 12. Density tomography results of the joint inversion along six profiles. Red dots represent $M_S \geq 3.0$ earthquakes recorded between 2019 and 2025 within 25 km of the profiles, with dot size indicating magnitude.
Abbreviations: NE: Northeast; SE: Southeast.

Poisson's ratio is quite sensitive to rock composition, and the low-density layer region exhibits a low Poisson's ratio.[51] Low Poisson's ratio corresponds to more felsic components, leading to the inference that the crustal components in this area are likely dominated by felsic materials.[51] Felsic materials, compared with mafic materials, have lower densities, as well as relatively lower solidus temperatures and rheological strengths, making them more susceptible to melting.[51-53] Additionally, the Moho discontinuity depth in this region indicates that the crustal thickness is moderately greater than the average continental crustal thickness. Thus, crustal thickening caused by plateau uplift may have elevated crustal temperature in this region.[51,54] Meanwhile, seismic attenuation is more sensitive to temperature and hydrothermal activity, and Lg waves undergo strong attenuation as they pass through this region.[48,50] Additionally, the terrestrial heat flow in this region is relatively high.[55] Magnetotelluric results also show that the crust east of the Zhaotong–Ludian Fault is characterized by low resistivity and high conductivity, suggesting the presence of fluids or partial melting.[56,57] Based on the comprehensive analysis above, it can be inferred that the low-density layer in this area is formed by plastic deformation or partial melting of felsic crustal components at relatively high temperatures.

The presence of partial melting not only significantly reduces viscosity but also greatly weakens the crustal strength in this region, providing a prerequisite for the lateral flow of this low-density layer.[52,53] This allows the low-density layer to undergo ductile flow driven by the topographically induced pressure gradient.[58] Located in the southern Sichuan Basin, this region forms a steep topographic transition zone with the Sichuan Basin's interior. Therefore, it can be inferred that the low-density material in the southern margin undergoes ductile flow toward the Sichuan Basin driven by the topographic pressure gradient.

4.2. Relationship between dynamic processes and seismic activity

As illustrated in Figure 1B, most seismic activity in the study area has been concentrated in the Changning area in recent years. To further analyze the relationship between seismic activity and density structure, seismic events within approximately 25 km on both sides of the profiles are projected onto the density structure, as shown in Figure 12. Profiles DD', EE', FF', and Figure 13 collectively demonstrate that seismic activity in the study area is concentrated mainly in the junction zone between the low-density layer and the edge of the Sichuan Basin, where Triassic strata dominate (Figure 1B). Meanwhile, existing studies suggest that if the weak, low-velocity zone material in the mid-lower crust is blocked by rigid high-velocity bodies, it will result in steep topographic changes on the surface; otherwise, relatively gentle topographic changes will occur.[47,59] The crust of the Sichuan Basin is cold, rigid, and thin, lacking developed low-velocity zones or Cenozoic magmatic activities. It has high strength and good stability, forming a rigid block that resists deformation.[60,61] Therefore, evidence from three aspects, including seismic distribution, surface topographic relief, and lateral flow of the low-density layer, directly or indirectly proves that this low-velocity layer is expanding toward the Sichuan Basin. Blocked by the strong crustal block of the Sichuan Basin, the crustal material cannot penetrate the strong crustal block and instead flows parallel to the edge or expands around both sides of the basin[58] (Figure 13). Furthermore, during the lateral expansion of the low-density layer, the western side is affected by active faults, such as the Huayingshan Fault and block compression constraints. The shear deformation of the fault zone absorbs part of the material's momentum during migration.[47] In contrast, the eastern side is not cut by large strike-slip faults, and the crustal medium is relatively homogeneous, allowing it to extend continuously eastward along the southern margin of the Sichuan Basin, forming a broader eastward extension range (Figure 11C).

Due to the obstruction, the leading edge of the low-density layer cannot expand, resulting in strain and stress accumulation in the leading edge region of the contact zone. When the accumulated stress exceeds the fracture threshold of the overlying brittle crust, energy is released in the form of earthquakes. The middle part of profile AA' in Figure 12 is the stress concentration zone formed by the low-density layer and the edge of the Sichuan Basin. The frequent seismic activity in this region is a direct manifestation of the high regional stress concentration caused by the blocked lateral expansion of the low-density material generated by melting toward the Sichuan Basin. Based on the comprehensive analysis above, the low-density layer and stress accumulation resulting from its interaction with the rigid Sichuan Basin are the key controlling factors for the frequent earthquakes in the Changning area.

5. Conclusion

This study utilizes surface-wave dispersion data and EGM2008 Bouguer gravity anomaly data, coupled with a joint tomographic inversion of ambient noise and gravity data to obtain the subsurface density structure of the southern Sichuan Basin, yielding the following key conclusions:

(i) The joint inversion significantly improves reliability and effectively compensates for the limitations of inversion with a single dataset. Compared with surface-

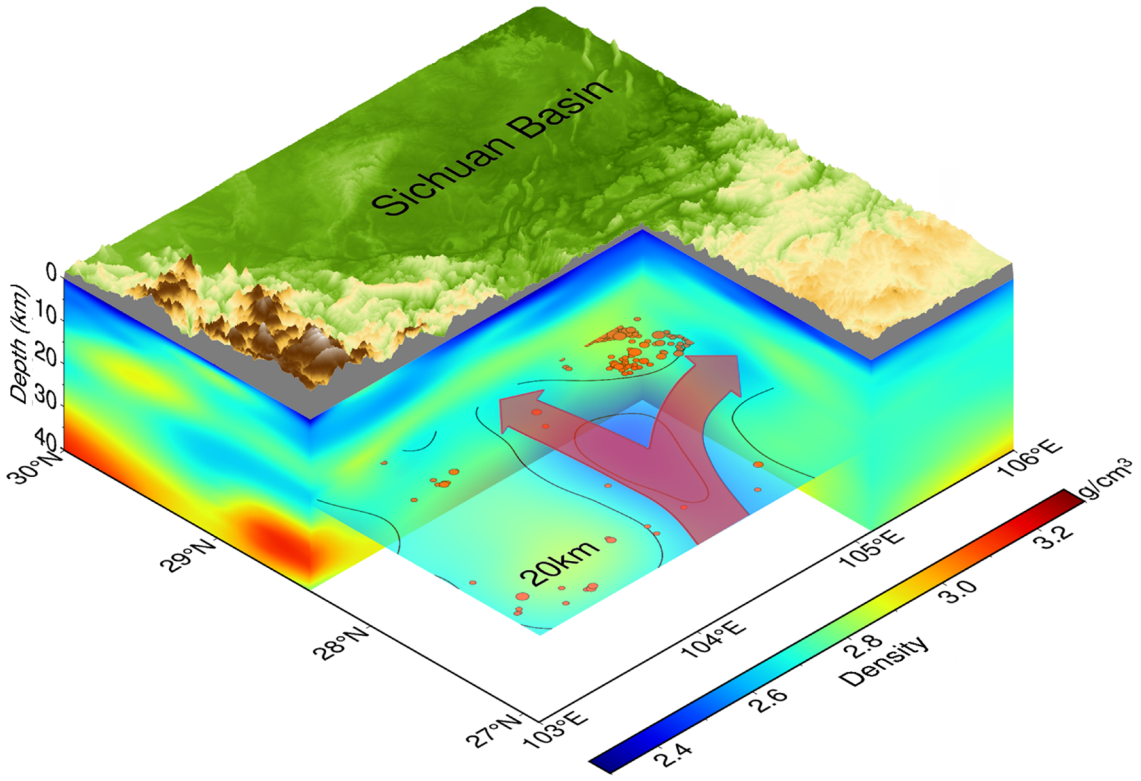

Figure 13. Three-dimensional density structure and the low-density layer in the southern Sichuan Basin. Red dots represent earthquakes. Red arrows denote the migration direction of low-density materials, which, after being obstructed by the rigid crust of the Sichuan Basin, migrate along both the eastern and western margins of the basin.

wave-only inversion, the combination of surface-wave dispersion data and Bouguer gravity anomaly data enables better recovery of the true subsurface model in edge regions with sparse ray coverage, and across all depth ranges within 60 km. Additionally, the RMS of surface-wave travel-time residuals from the initial model decreases from 4.71 s to 2.73 s, while the RMS of gravity anomaly residuals decreases from 86.3 mGal to 14.7 mGal. The results demonstrate good fitting performance with both surface-wave travel-time and Bouguer gravity anomaly observations, reducing the non-uniqueness of the inversion solutions and improving the reliability of the inverted model.

(ii) The joint inversion reveals that an intracrustal low-density layer exists in the southern Sichuan Basin. Comprehensive analysis, combined with other geophysical data, indicates that this low-density layer is not the ductile material escaping from the Qinghai–Xizang Plateau toward its southeastern margin, but rather a low-density layer formed by plastic deformation or partial melting of felsic components within the crust under relatively high-temperature conditions. Driven by the topographic pressure gradient, the low-density layer undergoes ductile flow toward the Sichuan Basin. Obstructed by the rigid crust of the Sichuan Basin, the material migrates along both the eastern and western margins of the basin, with a broader eastward migration range.

(iii) The stress accumulation induced by the interaction between the low-density layer and the rigid Sichuan Basin is the key controlling factor for frequent earthquakes in the Changning area. Seismic activity in the study area is predominantly concentrated in the junction zone between the low-density layer and the margin of the Sichuan Basin, with the leading edge of the low-density layer exhibiting a distinct spatial correspondence to the seismic activity concentration zone in the Changning area. This region is a stress-concentration zone jointly shaped by deep material migration and tectonic obstruction. Blocked by

the rigid basement of the Sichuan Basin, the lateral flow of low-density material is hindered, leading to continuous accumulation of regional stress, which acts as the key controlling factor responsible for the frequent earthquakes in the Changning area.

Acknowledgments

We sincerely acknowledge Nanqiao Du from the Institute of Geology and Geophysics, Chinese Academy of Sciences, for assistance and valuable suggestions provided during the experimental process.

Funding

This research was supported by the Deep Earth Probe and Mineral Resources Exploration-National Science and Technology Major Project (2025ZD1010201), the National Natural Science Foundation of China (42574074), the Hubei Provincial Natural Science Foundation of China (2025AFB854), and the Scientific Research Fund of the Institute of Seismology, China Earthquake Administration (IS202456377).

Conflict of interest

The authors declare that they have no competing interests.

Author contributions

Conceptualization: Li Zhang, Guiju Wu, Rugang Xu
Formal analysis: Guiju Wu, Rugang Xu, Yufei Xi
Investigation: Rugang Xu, Yufei Xi, Fan Wang, Li Zhang
Methodology: Guiju Wu, Li Zhang, Fan Wang
Writing–original draft: Li Zhang, Jiapei Wang, Rugang Xu
Writing–review & editing: Guiju Wu, Li Zhang, Yufei Xi

Availability of data

The surface-wave travel times at the different periods described in this study are available at https://github.com/nqdu/JDSurfG, and the EGM2008 data are available at http://earth-info.nga.mil/GandG/wgs84/gravitymod/egm2008/egm08_wgs84.html.

References

1. Yao H, van der Hilst RD, Montagner JP. Heterogeneity and anisotropy of the lithosphere of SE Tibet from surface wave array tomography. *J Geophys Res Solid Earth*. 2010;115(B12):B12307.

   doi: 10.1029/2009JB007142

2. Jiang F, Chen X, Unsworth MJ, *et al*. Mechanism for the uplift of Gongga Shan in the southeastern Tibetan Plateau constrained by 3D magnetotelluric data. *Geophys Res Lett*. 2022;49(9):e2021GL097394.

   doi: 10.1029/2021GL097394

3. Hu L, Zhang F, Li Y. Crustal Velocity Structure of the Sichuan–Yunnan Block Revealed by High-Quality Crustal Phase Travel Time. *Seismol Res Lett*. 2024;95(3):1913-1925.

   doi: 10.1785/0220230181

4. Berg EM, Lin F, Allam A, Schulte-Pelkum V, Ward KM, Shen W. Shear velocity model of Alaska via joint inversion of Rayleigh wave ellipticity, phase velocities, and receiver functions across the Alaska transportable Array. *J Geophys Res Solid Earth*. 2020;125(2):e2019JB018582.

   doi: 10.1029/2019jb018582

5. Liu L, Gao SS, Liu KH, *et al*. Mantle dynamics of the North China Craton: new insights from mantle transition zone imaging constrained by P-to-S receiver functions. *Geophys J Int*. 2022;231(1):629-637.

   doi: 10.1093/gji/ggac210

6. Tarantola A. Inversion of seismic reflection data in the acoustic approximation. *Geophysics*. 1984;49(8):1259-1266.

   doi: 10.1190/1.1441754

7. Vozoff K, Jupp DLB. Joint Inversion of Geophysical Data. *Geophys J Int*. 1975;42(3):977-991.

   doi: 10.1111/j.1365-246X.1975.tb06462.x

8. Julià J, Ammon CJ, Herrmann RB, Correig AM. Joint inversion of receiver function and surface wave dispersion observations. *Geophys J Int*. 2000;143(1):99-112.

   doi: 10.1046/j.1365-246x.2000.00217.x

9. Gallardo LA. Joint two-dimensional DC resistivity and seismic travel time inversion with cross-gradients constraints. *J Geophys Res Solid Earth*. 2004;109(B3):B03311.

   doi: 10.1029/2003jb002716

10. Maceira M, Ammon CJ. Joint inversion of surface wave velocity and gravity observations and its application to central Asian basins shear velocity structure. *J Geophys Res Solid Earth*. 2009;114(B2):B02314.

    doi: 10.1029/2007jb005157

11. Chen F, Yu HY, Gao LN. Three-dimensional lithospheric shear wave tomography beneath Sichuan region from joint inversion of gravity anomalies and surface-wave. *Comput Tech Geophys Geochem Explor*. 2018;40(3):277-289. [In Chinese].

    doi: 10.3969/j.issn.1001-1749.2018.03.01

12. Brocher TM. Empirical Relations between Elastic Wavespeeds and Density in the Earth's Crust. *Bull Seismol Soc Am*. 2005;95(6):2081-2092.

    doi: 10.1785/0120050077

13. Wan JK, Luo ZC, Wu YL. Lithospheric density structure beneath the Tibetan Plateau from the joint inversion of gravity and seismic data. *Chin J Geophys*. 2025;68(2):470-

482. [In Chinese].

doi: 10.6038/cjg2023R0073

14. Han SC. *Joint Inversion Algorithms of Multiple Types of Seismic Data and Gravity Data and Their Applications in the China Region*. Dissertation. University of Science and Technology of China; 2022.

doi: 10.27517/d.cnki.gzkju.2022.001743

15. Liang C, Liu Z, Hua Q, Wang L, Jiang N, Wu J. The 3D seismic azimuthal anisotropies and velocities in the eastern Tibetan Plateau extracted by an azimuth-dependent dispersion curve inversion method. *Tectonics*. 2020;39(4):e2019TC005747.

doi: 10.1029/2019tc005747

16. Li M, Zhang S, Wang F, Wu T, Qin W. Crustal and upper-mantle structure of the southeastern Tibetan Plateau from joint analysis of surface wave dispersion and receiver functions. *J Asian Earth Sci*. 2016;117:52-63.

doi: 10.1016/j.jseaes.2015.12.002

17. He D, Lu R, Huang H, Wang X, Jiang H, Zhang W. Tectonic and geological setting of the earthquake hazards in the Changning shale gas development zone, Sichuan Basin, SW China. *Pet Explor Dev*. 2019;46(5):1051-1064.

doi: 10.1016/S1876-3804(19)60262-4

18. Long F, Zhang Z, Qi Y, *et al*. Three dimensional velocity structure and accurate earthquake location in Changning-Gongxian area of southeast Sichuan. *Earth Planet Phys*. 2020;4(2):163-177.

doi: 10.26464/epp2020022

19. Li D, Zhan Y, Ding Z, *et al*. Upper crustal velocity and seismogenic environment of the Changning MS6.0 earthquake region in Sichuan, China. *Chin J Geophys*. 2021;64(1):18-35. [In Chinese].

doi: 10.6038/cjg2021O0241

20. Du N, Li Z, Hao T, Xia X, Shi Y, Xu Y. Joint tomographic inversion of crustal structure beneath the eastern Tibetan Plateau with ambient noise and gravity data. *Geophys J Int*. 2021;227(3):1961-1979.

doi: 10.1093/gji/ggab299

21. Deng Q, Zhang P, Ran Y, Yang X, Min W, Chu Q. Basic characteristics of active tectonics of China. *Sci China Ser D-Earth Sci*. 2003;46(4):356-372.

doi: 10.1360/03yd9032

22. Zhang P, Deng Q, Zhang G, *et al*. Active tectonic blocks and strong earthquakes in the continent of China. *Sci China Ser D-Earth Sci*. 2003;46(2):13-24.

doi: 10.1360/03dz0002

23. Wu X, Xu X, Yu G, *et al*. The China Active Faults Database (CAFD) and its web system. *Earth Syst Sci Data*. 2024;16(7):3391-3417.

doi: 10.5194/essd-16-3391-2024

24. Zheng X, Yao Z, Liang J, Zheng J. The Role Played and Opportunities Provided by IGP DMC of China National Seismic Network in Wenchuan Earthquake Disaster Relief and Researches. *Bull Seismol Soc Am*. 2010;100(5B):2866-2872.

doi: 10.1785/0120090257

25. Xia X, Li Z, Bao F, *et al*. Sedimentary structure of the Sichuan Basin derived from seismic ambient noise tomography. *Geophys J Int*. 2021;225(1):54-67.

doi: 10.1093/gji/ggaa578

26. Pavlis NK, Holmes SA, Kenyon SC, Factor JK. An Earth Gravitational Model to Degree 2160: EGM2008. In: *Proceedings of the European Geosciences Union General Assembly 2008*; April 13-18, 2008; Vienna, Austria. European Geosciences Union; 2008.

27. Wapenaar K. Retrieving the Elastodynamic Green's Function of an Arbitrary Inhomogeneous Medium by Cross Correlation. *Phys Rev Lett*. 2004;93(25):254301.

doi: 10.1103/physrevlett.93.254301

28. Rawlinson N, Sambridge M. Wave front evolution in strongly heterogeneous layered media using the fast marching method. *Geophys J Int*. 2004;156(3):631-647.

doi: 10.1111/j.1365-246x.2004.02153.x

29. Sethian JA. Advances in Fast Marching and Level Set Methods for Propagating Interfaces. In: Jeltsch R, Fey M, eds. *Hyperbolic Problems: Theory, Numerics, Applications*. Seventh International Conference on Hyperbolic Problems; February 1998; Zürich, Switzerland. Birkhäuser; 1999:855-864.

doi: 10.1007/978-3-0348-8724-3_36

30. Thomson WT. Transmission of elastic waves through a stratified solid Medium. *J Appl Phys*. 1950;21(2):89-93.

doi: 10.1063/1.1699629

31. Haskell NA. The dispersion of surface waves on multilayered media. *Bull Seismol Soc Am*. 1953;43(1):17-34.

doi: 10.1785/BSSA0430010017

32. Afnimar, Koketsu K, Nakagawa K. Joint inversion of refraction and gravity data for the three-dimensional topography of a sediment-basement interface. *Geophys J Int*. 2002;151(1):243-254.

doi: 10.1046/j.1365-246x.2002.01772.x

33. Li Z, Hao T, Xu Y, Xu Y. An efficient and adaptive approach for modeling gravity effects in spherical coordinates. *J Appl Geophys*. 2011;73(3):221-231.

doi: 10.1016/j.jappgeo.2011.01.004

34. Fang H, Yao H, Zhang H, Huang YC, van der Hilst RD. Direct inversion of surface wave dispersion for three-dimensional

shallow crustal structure based on ray tracing: methodology and application. *Geophys J Int*. 2015;201(3):1251-1263.

doi: 10.1093/gji/ggv080

35. Roecker S, Ebinger C, Tiberi C, *et al*. Subsurface images of the Eastern Rift, Africa, from the joint inversion of body waves, surface waves and gravity: investigating the role of fluids in early-stage continental rifting. *Geophys J Int*. 2017;210(2):931-950.

doi: 10.1093/gji/ggx220

36. Ahmed N, Weibull WW, Grana D. Constrained non-linear AVO inversion based on the adjoint-state optimization. *Comput Geosci*. 2022;168:105214.

doi: 10.1016/j.cageo.2022.105214

37. Fong DCL, Saunders M. LSMR: An Iterative Algorithm for Sparse Least-Squares Problems. *SIAM J Sci Comput*. 2011;33(5):2950-2971.

doi: 10.1137/10079687x

38. Zhang C, Guo C, Chen J, Zhang L, Wang B. EGM 2008 and Its Application Analysis in Chinese Mainland. *Acta Geod Cartogr Sin*. 2009;38(4):283-289. [In Chinese].

doi: 10.3321/j.issn:1001-1595.2009.04.001

39. Roecker S, Thurber C, McPhee D. Joint inversion of gravity and arrival time data from Parkfield: New constraints on structure and hypocenter locations near the SAFOD drill site. *Geophys Res Lett*. 2004;31(12):L12S04.

doi: 10.1029/2003gl019396

40. Hansen PC, O'Leary DP. The use of the L-curve in the regularization of discrete ill-posed problems. *SIAM J Sci Comput*. 1993;14(6):1487-1503.

doi: 10.1137/0914086

41. Liu Z, Liang C, Hua Q, *et al*. The seismic potential in the seismic gap between the Wenchuan and Lushan earthquakes revealed by the joint inversion of receiver functions and ambient noise data. *Tectonics*. 2018;37(11):4226-4238.

doi: 10.1029/2018TC005151

42. Wu Z, Zou K, Su J, Hua Y, Li P, Xu T. Crustal velocity structure beneath the eastern Tibetan Plateau derived from double-difference travel-time tomography. *Chin J Geophys*. 2024;67(3):871-888. [In Chinese].

doi: 10.6038/cjg2024R0746

43. Sun H, Wang X, Chang L. S-wave velocity and radial anisotropy structure in Southeastern Tibetan Plateau and the deep seismogenic environment of Luding MS6.8 earthquake and Lushan MS7.0 earthquake. *Chin J Geophys*. 2024;67(1):108-127. [In Chinese].

doi: 10.6038/cjg2023Q0810

44. Bao XW, Sun X, Xu M, *et al*. Two crustal low-velocity channels beneath SE Tibet revealed by joint inversion of Rayleigh wave dispersion and receiver functions. *Earth Planet Sci Lett*. 2015;415:16-24.

doi: 10.1016/j.epsl.2015.01.020

45. Fu YV, Jia R, Han F, Chen A. SH wave structure of the crust and upper mantle in southeastern margin of the Tibetan Plateau from teleseismic Love wave tomography. *Phys Earth Planet Inter*. 2018;279:15-20.

doi: 10.1016/j.pepi.2018.04.002

46. Zhang Z, Yao H, Yang Y. Shear wave velocity structure of the crust and upper mantle in Southeastern Tibet and its geodynamic implications. *Sci China Earth Sci*. 2020;63(9):1278-1293.

doi: 10.1007/s11430-020-9625-3

47. Clark MK, Royden LH. Topographic ooze: Building the eastern margin of Tibet by lower crustal flow. *Geology*. 2000;28(8):703-706.

doi: 10.1130/0091-7613(2000)28<703:Tobtem>2.0.Co;2

48. He X, Zhao LF, Xie XB, Tian X, Yao ZX. Weak crust in southeast Tibetan Plateau revealed by Lg-wave attenuation tomography: Implications for crustal material escape. *J Geophys Res Solid Earth*. 2021;126(3):e2020JB020748.

doi: 10.1029/2020JB020748

49. Royden LH, Burchfiel BC, King RW, *et al*. Surface deformation and lower crustal flow in eastern Tibet. *Science*. 1997;276(5313):788-790.

doi: 10.1126/science.276.5313.788

50. Liu H, Pei S, Liu W, *et al*. Crustal and upper mantle attenuation structure beneath the southeastern Tibetan Plateau and its implications on plateau outgrowth. *J Geophys Res Solid Earth*. 2004;129(2):e2023JB026977.

doi: 10.1029/2023jb026977

51. Wang W, Wu J, Fang L, Lai G, Cai Y. Crustal thickness and Poisson's ratio in southwest China based on data from dense seismic arrays. *J Geophys Res Solid Earth*. 2017;122(9):7219-7235.

doi: 10.1002/2017JB013978

52. Rosenberg CL, Handy MR. Experimental deformation of partially melted granite revisited: implications for the continental crust. *J Metamorph Geol*. 2005;23(1):19-28.

doi: 10.1111/j.1525-1314.2005.00555.x

53. Kohlstedt DL, Evans B, Mackwell SJ. Strength of the lithosphere: constraints imposed by laboratory experiments. *J Geophys Res Solid Earth*. 1995;100(B9):17587-17602.

doi: 10.1029/95jb01460

54. He R, Shang X, Yu C, Zhang H, Van der Hilst RD. A unified map of Moho depth and VP/VS ratio of continental China by receiver function analysis. *Geophys J Int*. 2014;199(3):1910-

1918.

doi: 10.1093/gji/ggu365

55. Shi Z, Wang G. Evaluation of the permeability properties of the Xiaojiang Fault Zone using hot springs and water wells. *Geophys J Int*. 2017;209(3):1526-1533.

doi: 10.1093/gji/ggx113

56. Cheng Y, Tang J, Chen X, Dong Z, Xiao Q, Wang L. Electrical structure and seismogenic environment along the border region of Yunnan, Sichuan and Guizhou in the south of the North-South seismic belt. *Chin J Geophys*. 2015;58(11):3965-3981. [In Chinese].

doi: 10.6038/cjg20151107

57. Cui T, Chen X. Magnetotelluric imaging and tectonic movement characteristics of the central Yunnan sub-block and its adjacent areas. *Sci China Earth Sci*. 2023;66(2):377-392.

doi: 10.1007/s11430-021-9997-y

58. Cook KL, Royden LH. The role of crustal strength variations in shaping orogenic plateaus, with application to Tibet. *J Geophys Res Solid Earth*. 2008;113(B8):B08407.

doi: 10.1029/2007JB005457

59. Royden LH, Burchfiel BC, van der Hilst RD. The geological evolution of the Tibetan Plateau. *Science*. 2008;321(5892):1054-1058.

doi: 10.1126/science.1155371

60. Burchfiel BC, Royden LH, Van der Hilst RD, *et al*. A geological and geophysical context for the Wenchuan earthquake of 12 May 2008, Sichuan, People's Republic of China. *GSA Today*. 2008;18(7):4-11.

doi: 10.1130/GSATG18A.1

61. Zhang P, Wen X, Xu X, *et al*. Tectonic model of the great Wenchuan earthquake of May 12, 2008, Sichuan, China. *Chin Sci Bull*. 2009;54(7):944-953. [In Chinese].

doi: 10.1360/csb2009-54-7-944

ACCSCIENCE PUBLISHING

Journal of Seismic Exploration

ARTICLE

Thin-bed reservoir characterisation using high-resolution ocean-bottom-node seismic data, seismic waveform indication inversion, and a Gaussian mixture model: A case study from the Guantao Formation, Bohai Bay Basin, China

Yanjia Wu[1], Zhiwen Dong[1], Yiyao Zhang[1], Zekun Li[1], Shihao Liu[1], Xiaoxiao Shi[1], Hongke Zhou[1], Qunhu Wu[1], Shina Yu[1], Ahmed Bakry[2], and Qamar Yasin[2]*

[1]Offshore Production Plant, Sinopec Shengli Oilfield Company, Dongying, Shandong, China

[2]National Key Laboratory of Continental Shale Oil, Northeast Petroleum University, Daqing, Heilongjiang, China

***Corresponding author:**
Qamar Yasin
(qyasin@nepu.edu.cn)

Citation: Wu Y, Dong Z, Zhang Y, *et al*. Thin-bed reservoir characterisation using high-resolution ocean-bottom-node seismic data, seismic waveform indication inversion, and a Gaussian mixture model: A case study from the Guantao Formation, Bohai Bay Basin, China. *J Seismic Explor*. 2026;35(3):026060026.
doi: 10.36922/JSE026060026

Received: February 6, 2026

Revised: March 25, 2026

Accepted: March 31, 2026

Published online: May 13, 2026

Copyright: © 2026 Author(s). This is an Open-Access article distributed under the terms of the Creative Commons Attribution License, permitting distribution, and reproduction in any medium, provided the original work is properly cited.

Publisher's Note: AccScience Publishing remains neutral with regard to jurisdictional claims in published maps and institutional affiliations.

Abstract

Targeting reservoirs that fall below seismic resolution remains a primary challenge in reservoir characterisation. High-resolution ocean-bottom-node seismic data are essential for imaging oil-bearing thin-sand facies, particularly in the Guantao Formation of the Bohai Bay Basin. The basin is rich in hydrocarbon resources but underexplored due to the difficulty of identifying thin-sand bodies. This study investigated thin beds below the tuning thickness to determine reservoir quality and oil–water distribution within this formation. By applying seismic waveform indication inversion (SWII) at the reservoir level, we generated a high-frequency and high-resolution facies model validated against existing geological data. Simultaneously, a Gaussian mixture model (GMM) was utilised to detect anomalies in well-log data (gamma ray, velocity ratio [Vp/Vs], and density), leveraging inter-variable relationships to enhance geological interpretability. Results demonstrated an excellent correlation between GMM anomalies and high-resolution seismic data, significantly improving prediction accuracy in complex structural regimes. SWII effectively identified thin sand-shale layers, reflecting various stacking patterns and the effects of porosity and oil-bearing properties on sand-body velocity. Forward modelling analysis revealed the seismic-resolvable thicknesses of sand bodies, the seismic response characteristics associated with various stacking patterns, and the influence of physical properties and oil-bearing characteristics on sand-body velocity, among other factors. This integrated approach effectively resolves thin-bed distributions and identifies potential hydrocarbon traps, providing a robust foundation for future multilayer system deployment in the Bohai Bay Basin.

Keywords: Anomaly detection; Gaussian mixture model; Thin-bed reservoir characterisation; Well-log analysis, Seismic data inversion

1. Introduction

Well-log acquisition serves as the cornerstone of subsurface geological characterisation, providing high-resolution, in situ measurements of formation physical properties. The integration of nuclear logs (gamma ray [GR], bulk density [DEN], and neutron porosity [CNL]), acoustic logs (downhole travel-time of P-wave [DTP] and downhole travel-time of S-wave [DTS]), and electrical logs (deep resistivity) enables precise lithological discrimination and the quantification of storage capacity.[1,2] For example, cross-validation of density and CNL is essential for fluid typing, while the DTP and DTS ratios are critical for delineating lithofacies classification. Consequently, the rigorous interpretation of these multi-physical datasets is a prerequisite for efficient reservoir management, serving as the basis for calculating reserves and optimising drilling trajectories.[3] Moreover, advanced anomaly detection in these datasets is essential for preserving data integrity. Automated outlier identification enables effective reservoir modelling and facilitates early detection of geomechanical risks, such as overpressure zones and borehole instability.[4-6]

Gaussian mixture models (GMMs) have emerged as powerful tools for anomaly detection due to their capacity to model complex, multi-modal data distributions.[7] As probabilistic models, GMMs assume data points are generated from a mixture of Gaussian distributions, allowing them to approximate any continuous probability density function with high precision, provided the components (means, covariances, and weights) are properly optimised.[8] Unlike deterministic clustering approaches, GMMs provide probability-based membership estimates, enabling quantification of uncertainty and identification of low-probability observations that may correspond to subtle lithological variations, such as thin-sand interbeds.

While well logs and core data provide vertical detail, seismic data inversion is pivotal for understanding the lateral distribution of anomaly zones and identifying hydrocarbon-bearing formations.[9-11] As global energy demand grows, advanced inversion techniques are increasingly necessary to optimise well placement and minimise environmental impact.[12-14] By providing detailed information on reservoir properties, such as reservoir facies distribution, porosity, permeability, and fluid saturation, seismic inversion significantly reduces uncertainties associated with oil and gas reservoir characterisation and management.[15]

However, traditional methods face significant challenges, e.g., P-wave impedance inversion using post-stack data often suffers from the "tuning effect," where the lack of direct correspondence between seismic signals and thin beds prevents effective lateral prediction.[16-18] While geostatistical inversion integrates diverse datasets to improve vertical resolution, its accuracy often falters in the high-frequency band, leading to inconsistencies with sedimentary models.[19-22] However, this method's prediction accuracy is reduced in the high-frequency band, and the lateral prediction accuracy of the inversion results is often inconsistent with the sedimentary model.[16,23,24]

To overcome these limitations, the seismic waveform indication inversion (SWII) method was developed. By utilising the lateral change information inherent in seismic waveforms, this method ensures reservoir predictions are less dependent on well distribution. This approach establishes an interpolation model aligned with geological and sedimentary characteristics, making it uniquely suited for high-precision predictions in areas characterised by fast lateral changes, strong heterogeneity, and thin interbeds.[23,25,26]

Recent literature supports the efficacy of such advanced inversion workflows, with studies demonstrating improved accuracy in complex lithological environments and tight sandstone reservoirs. Helgesen *et al.*[27] found that the sparse pulse inversion method provides more accurate and detailed reservoir property predictions in a complex reservoir than traditional inversion methods. Li *et al.*[28] showed that the SWII method can accurately predict the spatial distribution of reservoir properties in a tight sandstone gas reservoir with complex geological structures. SWII establishes a relationship between seismic waveforms and high-frequency well logs by dynamically clustering seismic waveforms. This process aims to enhance the vertical and horizontal resolution of the inversion results, providing a more detailed and accurate depiction of subsurface geological features. Nizarul *et al.*[29] introduced the short-time Fourier transform half cepstrum method for enhancing thin-bed identification in the Sarawak Basin, emphasising its significance for improved hydrocarbon exploration and seismic interpretation. Babasafari *et al.*[30] proposed an approach for petro-elastic modelling that significantly improves the accuracy of elastic property estimation by simplifying the modelling process and optimising parameters. This ultimately enhances predictions and supports seismic inversion in carbonate reservoirs in Central Luconia, offshore Sarawak, Malaysia. Fateh *et al.*[31] introduced an azimuthal deep resistivity technology and customised workflows for proactive geosteering in thin, heterogeneous carbonate reservoirs. Purnomo *et al.*[32] introduced an improvement to the elastic inversion technique that allows the extraction of petrophysical characteristics from low-amplitude seismic data. This enhancement was implemented to calculate petrophysical parameters in a gas field characterised by

thin sand-shale layers in the Sarawak Basin, Malaysia. The study also demonstrated that the SWII method can help identify potential bypassed pay zones and optimise well placement and completion design.

Despite these advances, previous studies typically treat seismic inversion, rock physics, and machine learning techniques as parallel workflows rather than as a unified probabilistic framework. In many cases, machine learning methods are applied for supervised facies classification without explicitly constraining seismic inversion. In contrast, inversion studies often rely on deterministic impedance thresholds without incorporating statistical anomaly structure derived from multi-parameter log space. Consequently, a clear probabilistic linkage between anomaly detection in well-log data and waveform-controlled seismic inversion remains insufficiently explored—particularly for ultra-thin interbeds below seismic tuning thickness.

This study introduces a probabilistically constrained thin-bed characterisation framework that integrates unsupervised GMM, rock physics validation, forward seismic modelling, and SWII into a unified interpretive workflow. Unlike conventional approaches that treat anomaly detection and inversion as independent tasks, the proposed methodology uses GMM to quantify anomaly likelihood in multi-dimensional log space (GR, velocity ratio [Vp/Vs], DEN), identifies statistically significant thin-bed signatures, and cross-validates these signatures using rock-physics relationships and forward modelling. The inversion results are then evaluated within this probabilistic and physically consistent framework, thereby reducing interpretational ambiguity and enhancing lateral prediction reliability.

The primary methodological contributions of this study are: (i) the integration of probability-based anomaly quantification with waveform-controlled inversion; (ii) the explicit coupling of statistical log-space anomalies with rock physics consistent seismic responses; and (iii) the demonstration of enhanced thin-bed detectability (<10 m) using high-frequency ocean-bottom-node (OBN) data within a structurally complex fluvial system.

Building upon this framework, we applied the integrated methodology to the Guantao Formation in the Bohai Bay Basin. By merging probabilistic anomaly detection with SWII, we generated high-frequency and high-resolution imaging of thin-sand reservoirs in a tectonically complex setting. This approach not only improves thin-bed discrimination below the tuning thickness but also establishes a statistically robust, physically grounded workflow for reservoir characterisation in heterogeneous fluvial systems. The findings expand understanding of the Guantao Formation and provide a transferable methodology for thin-bed exploration in similar geological environments worldwide.

2. Geological overview

The Guantao Formation is a Miocene-age stratigraphic unit that forms a foundational component of the Neogene succession within the Bohai Bay Basin (Figure 1A), one of China's most prolific hydrocarbon regions.[33] Its deposition occurred during the regional post-rift thermal subsidence phase that followed the intense Paleogene extensional rifting. This shift to a more stable tectonic regime led to widespread, blanket-like deposition of the Guantao Formation across the previously fractured basin architecture. It unconformably overlies the older Paleogene formations.

Lithologically, the Guantao Formation is characterised by coarse-grained, clastic sediments with a distinct vertical evolution. The lower section typically consists of thick, poorly sorted conglomerates and coarse sandstones deposited by high-energy braided river systems, which grade upward into finer-grained sandstones and interbedded mudstones deposited in meandering-river and flood-plain environments.[34] This fining-upward sequence reflects the gradual decrease in topographic relief and sediment supply as the basin continued to subside.

The primary significance of the Guantao Formation lies in its exceptional reservoir characteristics, making it a major exploration target for both conventional and heavy oil accumulations.[33] The coarse-grained, clean sandstones of the lower braided river channels exhibit high primary porosity and permeability, resulting in excellent reservoir quality (Figure 1B). These rocks play a crucial role in a highly effective petroleum system. The hydrocarbons generated from the underlying, organic-rich Palaeogene Shahejie Formation source rocks migrate vertically along faults and laterally along the regional unconformity at the base of the Guantao to charge these reservoirs. Trapping mechanisms are varied, including gentle anticlines and, most notably, stratigraphic and lithologic traps such as sand bodies pinching out against the basal unconformity or "buried hill" structures of the pre-Cenozoic basement. The widespread distribution and consistent reservoir properties of the Guantao Formation have therefore cemented its status as a key hydrocarbon-producing formation in the Bohai Bay Basin.

Figure 1 illustrates the regional geological framework and the location of the Bohai Bay Basin along China's eastern coast, within the broader North China Craton. The basin's proximity to the Yellow Sea and Bohai Sea provides the structural context for its evolution as a major

intracontinental rift system and hydrocarbon province. A regional summary structural map (Figure 1B) reveals the basin's characteristic graben-horst architecture developed during Cenozoic extension. The Guantao Formation (highlighted as dark brown in Figure 1A) unconformably overlies the fault-controlled Paleogene sequence, demonstrating the transition from syn-rift to post-rift sedimentation.

3. Methodology and data preparation

An extensive dataset of borehole well logs was compiled from six actively producing wells, accompanied by 3D OBN seismic data in the study area (Figure 1). The investigation encompassed a thorough analysis of key logging measurements, including calliper (CAL), GR, DTP, DTS, DEN, and CNL. This dataset comprises 10,000 measurements of GR (API), DEN (g/cm^3), and Vp/Vs over a depth range of 1,200 to 2,400 m (the upper and lower Guantao Formation). Two wells were specifically chosen for model training due to their high data quality and complete log coverage.

Before clustering and probabilistic modelling, several preprocessing steps were applied to ensure statistical consistency. Missing values were imputed using the mean. All variables were subsequently standardised using z-scores so that each feature contributed equally to the distance metrics and likelihood calculations. An initial unsupervised partitioning of the standardised dataset was then carried out using K-means clustering with 10 clusters (n_init = 10; random seed = 42). Only the two clusters that displayed a clear lithological separation between sand-prone and shale-prone responses were retained for subsequent anomaly detection and GMM analysis.

3.1. Unsupervised anomaly detection

To uncover geologically meaningful patterns, the data were clustered using the K-means algorithm following standardisation. These clusters align with known lithofacies (sand and mudstone) and present a petrophysically diverse yet interpretable subset for anomaly detection.

Following the initial clustering phase, the isolation forest (IF) algorithm was deployed to identify potential anomalies within the selected lithological clusters. Unlike distance-based or density-based methods, IF is an ensemble learning approach that isolates anomalies by recursively partitioning the feature space into random binary trees.[35] The fundamental idea is that anomalous observations, being rare and distinct, are more easily isolated and therefore exhibit shorter average path lengths, whereas normal samples require more partitions.

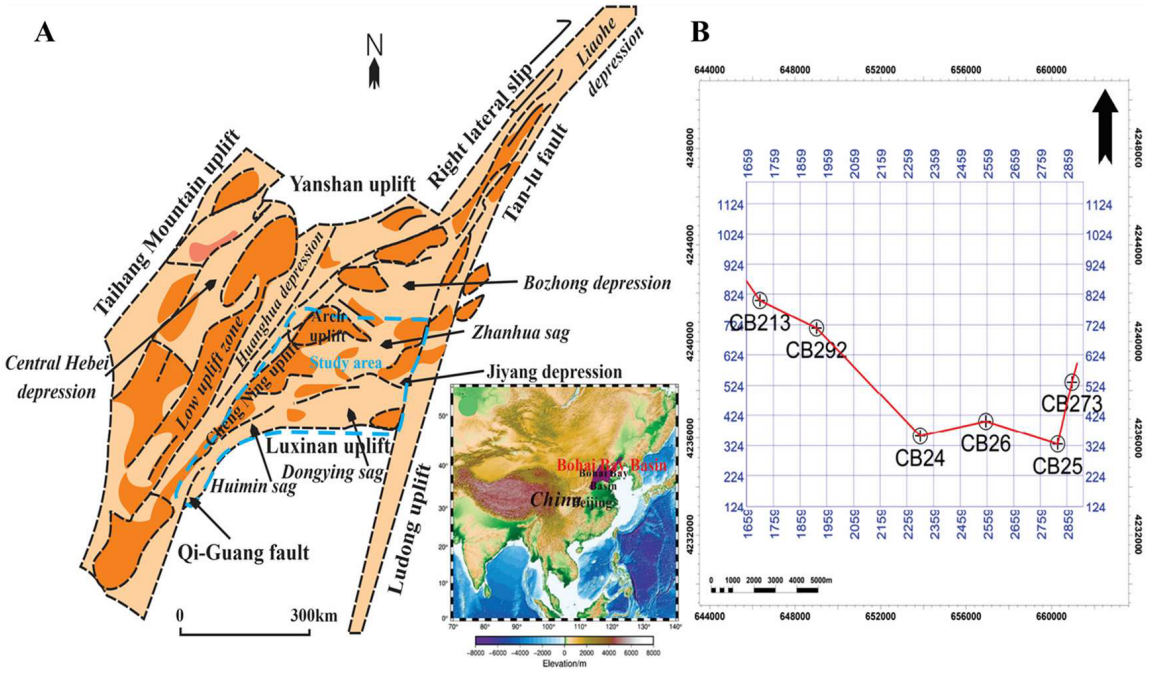

Figure 1. Regional geological framework of the study area. (A) Location of the Bohai Bay Basin. (B) Seismic and well location map displaying the spatial distribution of study wells across major structural elements.

In this study, the filtered dataset was divided into training (70%) and testing (30%) subsets using a fixed random seed (42) to ensure reproducibility. The IF model was built with 100 trees (the default in scikit-learn) and a contamination factor of 0.10, indicating that approximately 10% of the samples were expected to be anomalous. The algorithm outputs binary labels, where −1 indicates an anomaly and +1 denotes normal behaviour. It is important to stress that IF predictions were not treated as ground truth; rather, they provided an objective statistical reference for comparison with the probability-based anomalies derived from the GMM.

Figure 2 visualises the integration of clustering and anomaly detection across the GR, DEN, and Vp/Vs logs. The subplots contrast the measurements from both wells, delineating the distribution of training and testing samples. Notably, the visualisation highlights the distinct petrophysical separation between clusters 0 and 1, while revealing the stratigraphic and spatial distribution of the anomalies flagged by the algorithm.

3.2. Gaussian mixture model configuration

Data were collected from six wells that penetrated the Guantao Formation, which consists of mudstones and sandstones as the major lithologies, with minor conglomerates. Rigorous quality control procedures were implemented to minimise noise and bias, including outlier detection using both the three-sigma rule and interquartile range analysis, and verification of borehole conditions via CAL logs.

The GMM was configured with customised hyperparameters to optimise its performance. The GMM implementation followed the scikit-learn framework. A mixture of two Gaussian components was selected to represent the primary lithological populations in the feature space. Full covariance matrices were adopted to allow each component to capture anisotropic variance and inter-variable correlations. Parameter estimation was performed using the expectation–maximisation algorithm with 10 independent initialisations (n_init = 10), and the solution with the highest log-likelihood was retained. The convergence tolerance and maximum number of iterations were kept at the default values of 10^{-3} and 100, respectively. A fixed random seed was applied to ensure reproducibility of the optimisation. To maintain stable geological interpretation across runs, the resulting mixture components were sorted by the ascending mean of the first feature dimension. This ordering prevents label switching and enables consistent comparison among wells. To ensure comparability across wells and lithologies, all features were standardised using z-score normalisation (**Equation 1**).

$$X_{norm} = \frac{X - \mu}{\sigma} \tag{1}$$

where x denotes an individual data point, μ denotes the sample mean of the input dataset, and σ denotes the sample standard deviation.

After training, each observation was evaluated against the learned probability density function. Samples located within the high-density core of the distributions were classified as background lithology, whereas points falling in the low-probability tails were considered anomaly candidates. Operationally, this corresponds to observations lying outside the three-sigma confidence envelope of the Gaussian components.

3.3. Seismic waveform indication inversion framework

The SWII method is a geostatistics-based approach that combines well logging, geological, and seismic data to establish probability models for reservoir attributes.[23,27] Unlike conventional inversion, which relies on existing well configurations to initialise models, SWII focuses on lateral seismic waveform indicators derived from well data.

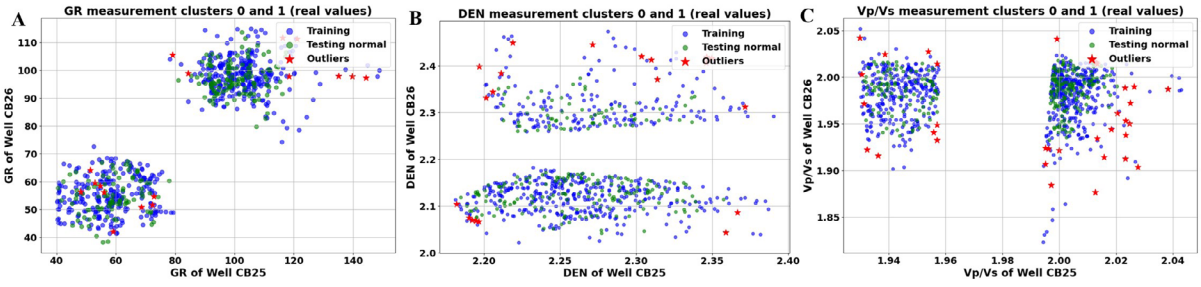

Figure 2. Clustering results and isolation forest anomaly detection for (A) gamma ray (GR), (B) density (DEN), and (C) velocity ratio (Vp/Vs) logs in wells CB25 and CB26. Red points indicate detected anomalies, highlighting their distribution relative to the main litho-fluid clusters.

It utilises a stochastic function model to obtain multiple high-resolution realisations aligned with both well and seismic data, inferring spatial distribution characteristics with high vertical resolution.

The objective function for waveform inversion is represented as (**Equation 2**):

$$E_{(m)} = min_m \left(d - F_m\right)_2^2 \quad (2)$$

where d represents the observed seismic data (waveforms), and F is the forward modelling operator that generates synthetic data from the model m, which is the vector of subsurface properties (e.g., velocity and DEN) we aimed to estimate. The objective of the E(m) function is to minimise the misfit between the observed and synthetic data, ultimately refining the model parameters m.

The SWII utilises a deterministic method to derive impedance volumes, followed by the Markov Chain Monte Carlo algorithm to generate interwell impedance. The resulting impedance is converted into reflection coefficients and convolved with wavelets to produce synthetic traces. By comparing these synthetic traces to the original seismic data, we identified sandstone and shale layers through impedance matches. This process integrates information across multiple scales to achieve accurate inversion results that align with the inherent phase-contrast capabilities of seismic data (Figure 3).

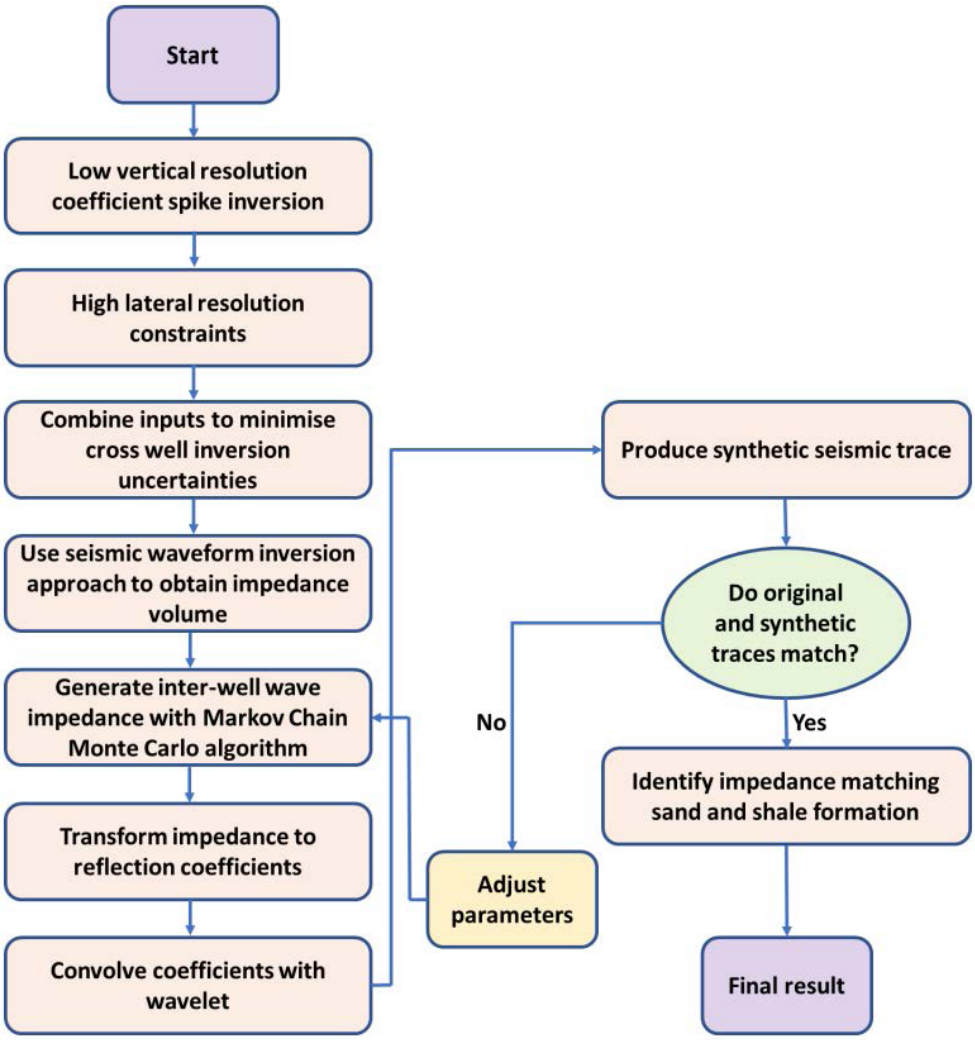

Figure 3. Simplified workflow illustrating the seismic inversion process used to construct a geological model containing thin interbeds

3.4. The challenges of seismic inversion in the Guantao Formation

After an extensive and detailed analysis of the reservoir's essential characteristics through the use of GMM, it became evident that applying the post-stack elastic parameter inversion technique to the Guantao Formation across the CB24, CB25, CB26, CB273, CB292, and CB213 wells facilitates an accurate distinction between sandstone and shale layers.

As illustrated in Figure 4, the Vp/Vs and Poisson's ratios derived from the sparse spike inversion method in the Guantao Formation revealed a consistent pattern. Notably, low Vp/Vs and low Poisson's ratios indicate the presence of sandstone beds. However, it is important to note the challenges presented by seismic data in effectively detecting all the thin interbedded sand layers. The variability in seismic waveforms, caused by the diverse configurations of these sand bodies, poses significant challenges to obtaining a clear and definitive identification in the Guantao Formation.

It is important to emphasise that over 80% of the individual sand layers within the Guantao Formation's targeted strata tend to be thin, with thicknesses measuring less than 10 m, as depicted in Figure 5. This illustration plays a crucial role in analysing the difficulties encountered when trying to differentiate these complex and interbedded sand layers within the formation. The challenge is intensified by the predominantly thin profile of these sand layers, combined with the distinctive characteristics of the seismic data.

In high-resolution OBN seismic data, sand bodies exceeding 20 m in thickness are particularly notable. They are distinguished by complex waveforms and strong amplitudes that unmistakably signal their presence. Conversely, sand bodies that measure between 10 and 15 m are characterised by more streamlined waveforms and lower amplitudes. Meanwhile, smaller sand bodies measuring 5 m or less are often undetected, becoming nearly invisible in seismic data.

Thoroughly exploring the complexity beneath the tuning thickness distribution is essential to utilise SWII. This sophisticated technique unveils the hidden layers of thin sand with remarkable accuracy and insight, allowing us to uncover the complexities of these subtle geological features.

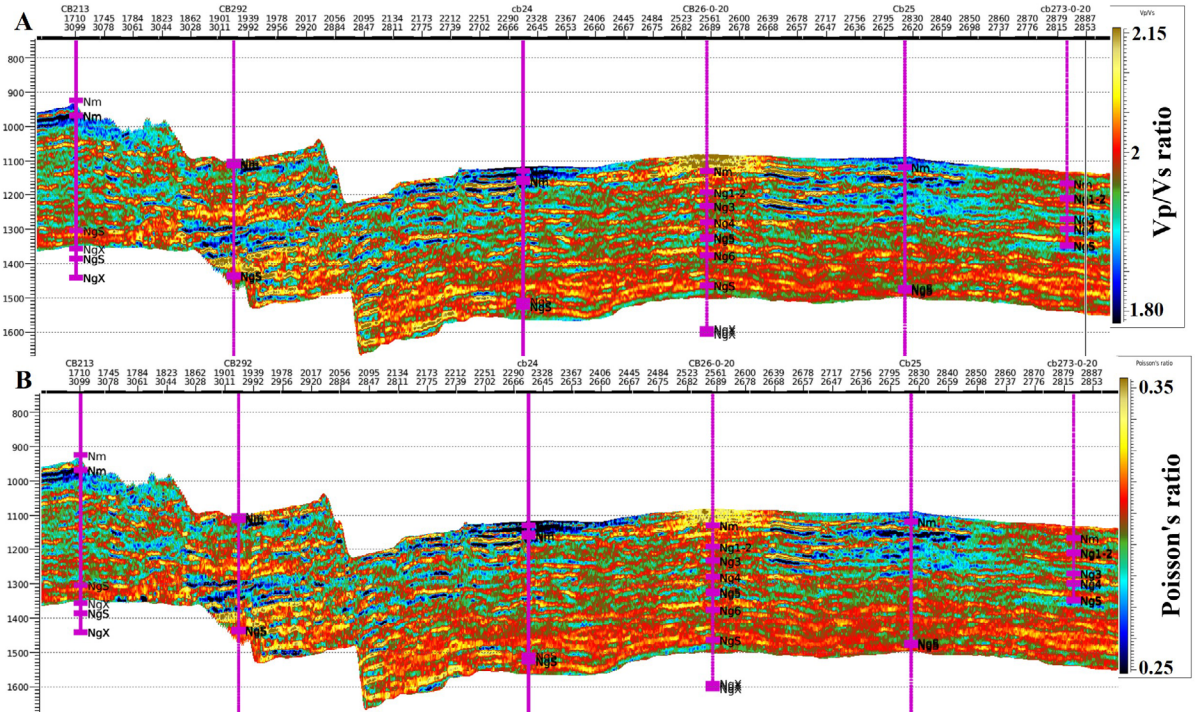

Figure 4. Seismic interpretation of the Guantao Formation. (A) Inverted velocity ratio (Vp/Vs) and (B) Poisson's ratio seismic sections of the Guantao Formation, showing consistent low-value anomalies associated with sandstone layers (for cross-section analysis, refer to Figure 1).

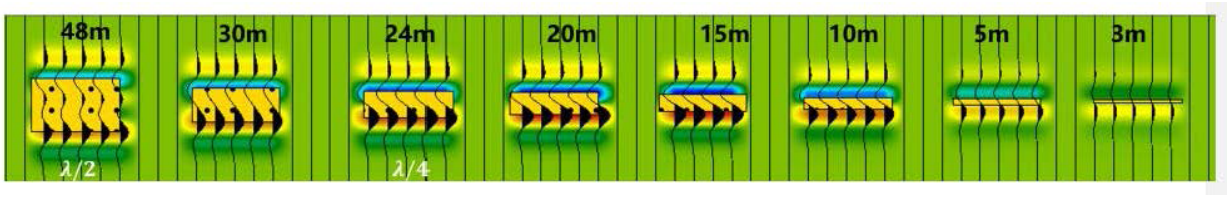

Figure 5. Thickness distribution of individual sand layers within the Guantao Formation

4. Results and discussion

4.1. Gaussian mixture model analysis of thin beds

Figure 6 illustrates the application of GMM to GR, Vp/Vs, and DEN logs. The first row shows the initial anomaly detection results from the IF algorithm. The IF method effectively delineated outliers (marked in red) from the nominal data clusters, revealing that anomalies are predominantly concentrated at the periphery of the data distribution. This step established a baseline for distinguishing between standard lithological responses and potential thin-bed occurrences.

The second row depicts the unsupervised training phase of the GMM. Because the dataset was unlabelled, the model approximated the underlying structure of the log data by fitting two distinct Gaussian components to the clusters. These components, visualised as ellipses, represented the high-probability regions of the dataset. By optimising parameters to fit these components, the GMM captured the intrinsic variance of the normal formation data, creating a probabilistic reference model against which deviations could be measured.

The third row presents the testing stage, visualising the model's predictions against the probability density functions of the learned distributions. Contour lines indicate the model's confidence levels; data points in high-density regions are classified as normal (blue), while those in lower-density regions that fall below a defined probability threshold are flagged as anomalies (red). Significantly, the concentration of anomalies within these low-probability tails correlated with the expected log responses of thin sand beds. This alignment confirms the GMM's efficacy in isolating subtle lithological features that deviate from the background trend.

To further clarify how the probabilistic structure governs the classification, the maximum-posterior cluster memberships were projected back into the original measurement space. The resulting Gaussian components formed compact, clearly separated populations, while their covariance matrices define ellipsoidal envelopes whose orientations reflect inter-variable dependence rather than isotropic spread. The majority of background samples fell within the one- to two-sigma regions, demonstrating that the mixture adequately represents the dominant lithofacies.

In contrast, predicted anomalies were preferentially located near the margins of the distributions or beyond the three-sigma confidence limits, where the probability density decreased sharply. This geometric relationship provides a transparent explanation for the link between statistical rarity and geological distinctiveness: intervals that are difficult to represent with the learned background model correspond to thin, heterogeneous, or fluid-affected sand bodies.

The stability of the separation observed in Figure 6 further indicates that a two-component mixture is sufficient for the investigated interval. Tests with additional components yielded only marginal improvements in probability while reducing geological interpretability and were therefore not adopted.

4.2. Rock physics analysis

4.2.1. Fluid discrimination

Accurate reservoir characterisation and thin-bed detection rely on the identification of distinct fluid- and lithology-dependent signatures within well-log data. The porosity–resistivity crossplot, commonly referred to as the Pickett plot, provides a fundamental diagnostic framework based on the Archie equation, which relates porosity to resistivity and fluid saturation. In this study, the clean water-saturated trend (the "clean sand line") established a baseline at a water saturation of 1, corresponding to fully saturated formations. Data points clustered along this line exhibited a predictable pattern: resistivity increased as porosity decreased, thereby calibrating the model to local reservoir conditions (Figure 7A).

Hydrocarbon-bearing zones deviated significantly from this water-saturated baseline due to the distinctively high resistivity of hydrocarbons relative to water.[36] On the Pickett plot, these zones appeared as clusters shifted toward higher resistivity values and lower water saturation (indicated by yellow points), representing the primary targets for completion and evaluation (Figure 7B). The analysis also delineated geologically complex formations, such as shaly sands and tight zones. Shaly sands, which

contain conductive clay minerals, can complicate fluid discrimination by occupying the region between the clean sand line and hydrocarbon clusters. Conversely, tight zones are characterised by low porosity and elevated resistivity; however, they are considered non-economic due to insufficient storage capacity and are typically bypassed during production planning.

4.2.2. Sensitivity analysis and crossplot validation

A comprehensive sensitivity analysis revealed the hierarchical importance of reservoir parameters in distinguishing sand from clay. The crossplot framework leveraged the differential sensitivity of elastic parameters to pore-fluid properties, utilising the relationship between DEN and Vp/Vs (Figure 8). Oil-saturated intervals (yellow clusters; DEN: 2,350–2,370 g/cm^3, Vp/Vs: 1.90–2.0) displayed intermediate properties, reflecting high-porosity (> 15%) sands. In contrast, water-saturated rocks (green clusters; DEN: 2,400–2,500 g/cm^3, Vp/Vs: 2.00–2.05) maintained high elastic parameter values, consistent with the behaviour of incompressible pore fluids. Colour-coding by oil saturation revealed additional control mechanisms: zones with higher oil saturation exhibited enhanced fluid sensitivity due to increased pore-volume fractions, whereas tight rocks showed reduced discrimination capability.

The consistent clustering patterns observed across wells CB25 and CB26 validate the predictions for pore-fluid type and lithology discrimination (Figure 8A and 8B). Zones where fluid types overlap corresponded to intervals with mixed saturation (oil and water). Furthermore, production data from these wells confirms the presence of the identified water- and/or oil-saturated reservoirs. This quantitative framework enables probabilistic fluid

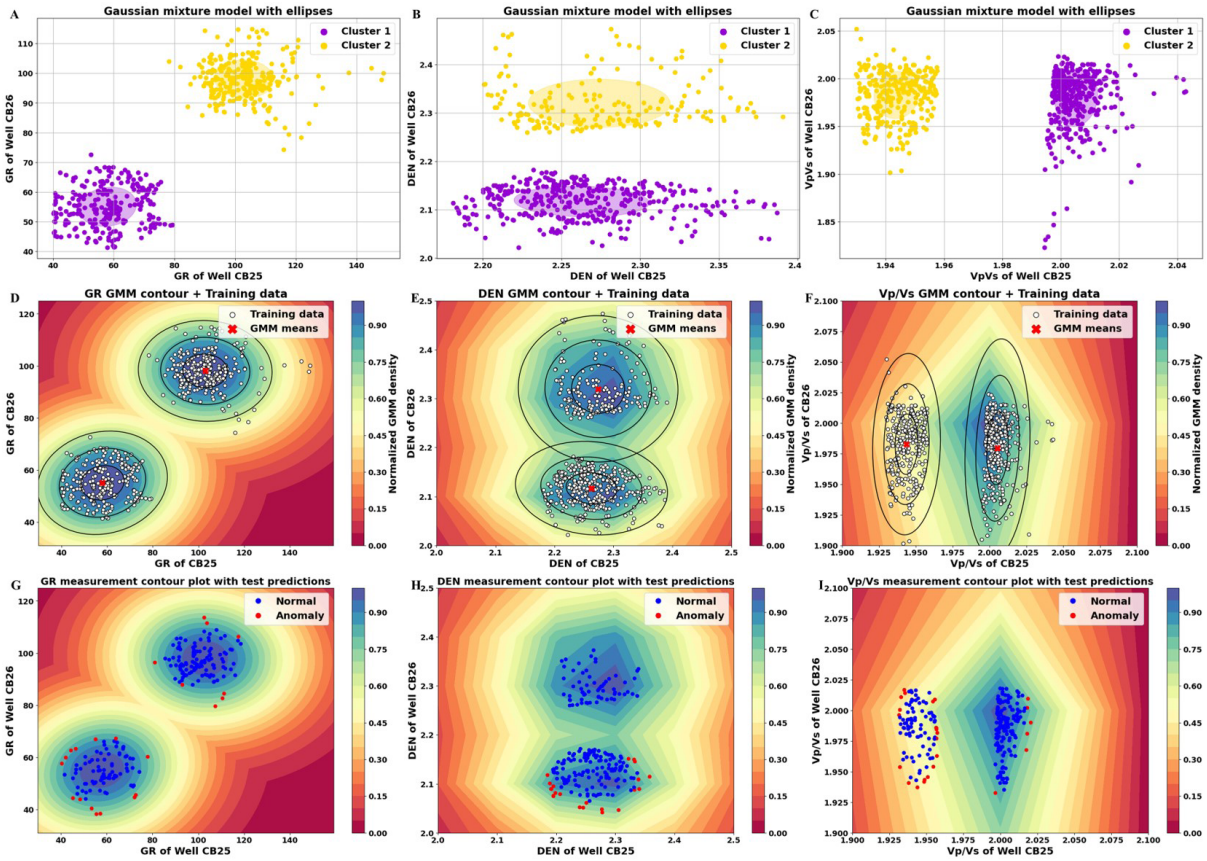

Figure 6. Unsupervised lithofacies clustering and anomaly detection using a Gaussian mixture model (GMM) applied to gamma ray (GR), velocity ratio (Vp/Vs), and density (DEN) logs. (A–C) Results of the isolation forest algorithm for (A) GR, (B) DEN, and (C) Vp/Vs, identifying initial statistical outliers (red) versus normal clusters. (D–F) GMM training phase showing the unsupervised fitting of Gaussian components (ellipses) to the data structure for (D) GR, (E) DEN, and (F) Vp/Vs. (G–I) Probability density function contours from the testing phase for (G) GR, (H) DEN, and (I) Vp/Vs. Points located in high-density regions are classified as normal background lithology (blue), while points falling below the probability threshold in low-density regions are flagged as anomalies (red), corresponding to thin sand beds.

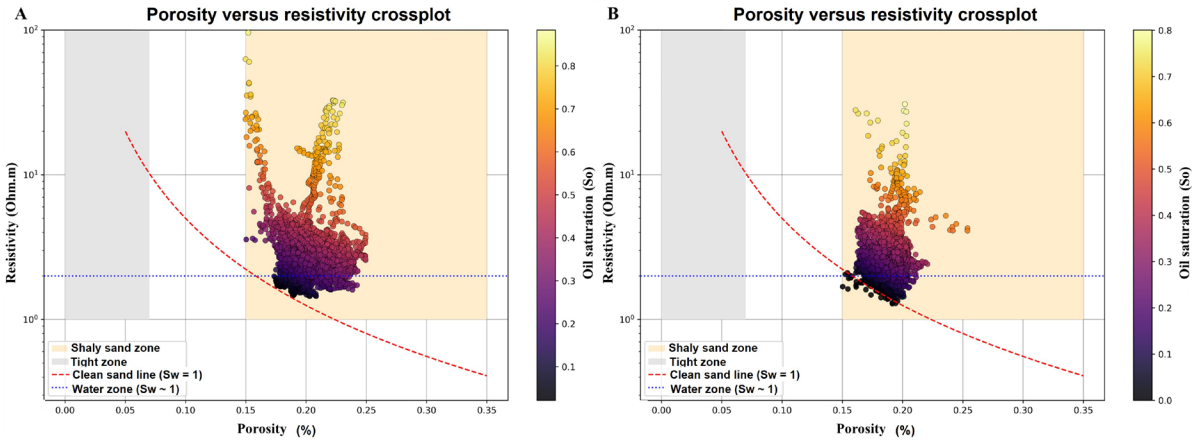

Figure 7. Porosity–resistivity (Pickett) crossplots used for fluid and lithology discrimination (CB25 and CB26; see Figure 1). (A) Establishment of the clean water-saturated baseline (water saturation [Sw] = 1), showing the inverse relationship between porosity and resistivity in water-bearing zones. (B) Identification of hydrocarbon potential. Hydrocarbon-bearing zones (yellow points) deviate significantly from the water line toward higher resistivities. The plot also distinguishes non-economic tight zones (low porosity and high resistivity) and shaly sands (intermediate resistivity) from the primary reservoir targets.

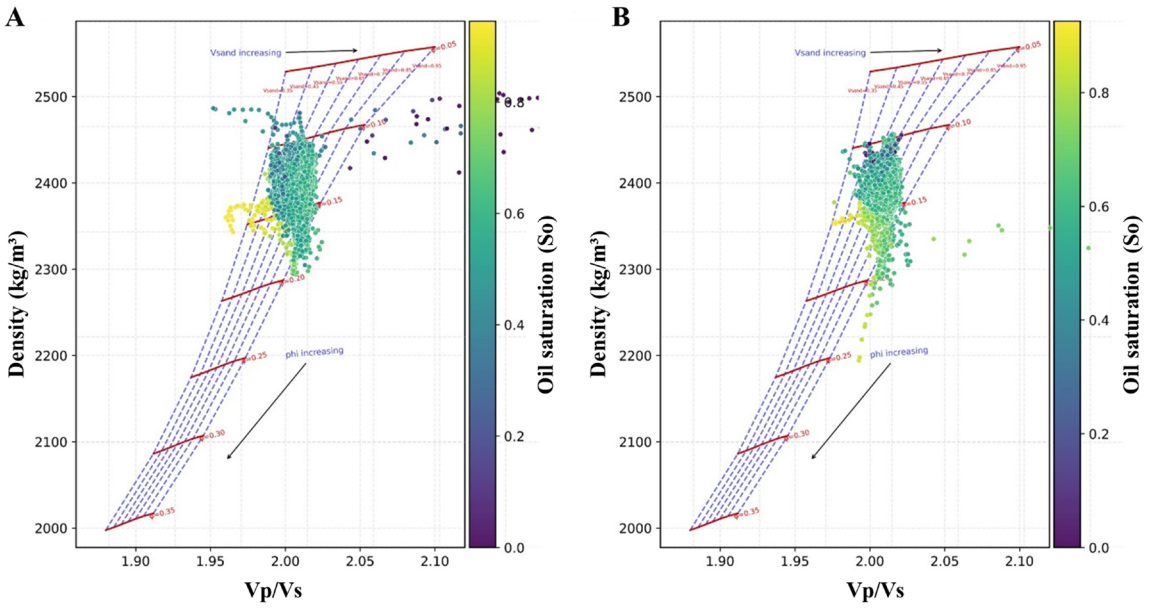

Figure 8. Crossplots of density versus velocity ratio (Vp/Vs) used for fluid and lithology discrimination in wells (A) CB25 and (B) CB26. The plots reveal distinct clustering based on pore fluid content. Oil-saturated sands (yellow clusters) are characterised by lower density and Vp/Vs values (1.90–2.0) compared to water-saturated zones (green clusters), which exhibit higher elastic parameters due to fluid incompressibility. Overlap regions between clusters indicate intervals of mixed fluid saturation.

prediction and supports the economic evaluation of potential well-completion intervals.

4.3. Forward seismic modelling

To evaluate the validity of the SWII approach and its effectiveness at identifying thin interbeds, we generated synthetic seismic sections for different geological reservoir scenarios. Based on well profile analysis and existing literature on stacking patterns in the Guantao Formation, sedimentary facies were classified into channel sands, mudstones, and point bar sands, with thicknesses ranging from 3 to 50 m. The background velocities were defined as

2,720 m/s for mudstone and 2.670 m/s for sandstone.

Figure 9 shows the geological interpretations of seismic responses derived from forward seismic modelling. The orange colour suggests a mixed lithology or perhaps a facies change, while the yellow represents "cleaner" sand. Forward modelling was performed for various sand-body superposition patterns. Channel sand bodies were characterised by large-scale and regular morphology, reflecting the migration and amalgamation of river channels. In contrast, point bar sand bodies were smaller, isolated lens-shaped features resulting from the lateral accretion and abandonment of meandering rivers. Both facies consist of sandstone interbedded with flood-plain or abandoned-channel mudstones. These distinct lithological contrasts provide the physical basis for generating seismic reflections.

Different stacking patterns altered the interference of seismic waves, causing observable changes in attributes such as waveform symmetry, amplitude, and frequency. These variations serve as diagnostic criteria for distinguishing sand body patterns. Forward modelling at a dominant frequency of 120 Hz proved effective for identifying thin interbedded sands, as significant waveform variations were observed across different combinations of channel and point-bar sands (Figure 9).

Subsequently, the forward seismic modelling was performed for porosity, oil saturation, and velocity. The study accounted for the influence of physical properties on seismic response by modelling varying porosity and saturation levels. The forward seismic modelling results at 120 Hz are presented in Figures 10 and 11.

We observed that as porosity increased, sandstone velocity decreased. While low-porosity sandstone might exhibit velocities higher than mudstone, high-porosity sandstone dropped below the mudstone velocity. This transition creates a distinctive velocity contrast that is visually resolvable in the amplitude response (Figure 10).

Conversely, sandstone velocity decreased monotonically with increasing oil saturation. This amplifies the velocity difference relative to the surrounding mudstone, resulting in increased seismic amplitude (Figure 11).

In the study area, the baseline velocity of sandstone was slightly lower than that of mudstone. High porosity (25–35%) further reduced formation velocity and DEN, thereby enhancing impedance contrast and amplitude response. Oil-bearing sandstone exacerbated this velocity reduction, creating a strong impedance contrast with the surrounding mudstone, often resulting in "bright spot" reflections, as shown in Figure 12. Additionally, the dominant frequency tended to shift downward due to velocity attenuation. Thus, the patterns derived from forward modelling are consistent with the well-log responses and rock physics analysis shown in Figure 8.

4.4. Seismic inversion and 3D visualisation

Previous studies have shown that SWII is highly effective for detecting thin interbedded sand layers. Specifically, the inverted acoustic impedance provides a robust tool for identifying oil-bearing sand layers within the target distribution. Figure 13 shows the results of waveform indication inversion of P-wave impedance. The lower P-impedance (pink and blue) revealed a remarkable capability to accurately identify thin sand layers in reservoirs to a depth of 3 m.

The SWII method offers notably superior vertical resolution, adapts well to lateral variations, and provides robust, precise prognostication.

P-impedance is an effective tool for identifying sand and shale and for locating the oil layer within a specific distribution range in the Guantao Formation. SWII was applied for lithofacies characterisation because the algorithm can better identify facies changes given the similarities and variations in these waveforms. Figure 14 visualises the spatial distribution and resource potential of these sand bodies. Overall, the results indicate significant potential for oil extraction in this area, suggesting that targeted exploration and drilling could yield promising results. These findings confirm that the inversion method is reliable for predicting the location and properties of subsurface formations.

The success of this approach lies in the methodology; waveform indication inversion is a phase-controlled method that does not rely on sparsity assumptions. It utilises waveform differences to constrain the inversion, facilitating the resolution of thinner layers. Because waveform disparity is a key parameter independent of seismic wavelet frequency, this method provides higher-resolution identification of thin beds within the seismic frequency band. Moreover, SWII uses a Markov Chain Monte Carlo approach to integrate well-log data with seismic texture, thereby resolving lithological units thinner than the tuning thickness (1/4 wavelength).

The analysis of lithofacies profiles across wells CB25, CB26, CB213, CB273, CB292, and CB24 revealed that sand and shale boundaries are clearly defined (Figure 15). These profiles confirm the extent of the sand bodies within the Guantao Formation oil layer.

The high concordance between the drilled well data and the inversion results further confirms the reliability of the inversion. The strong correlation between well points

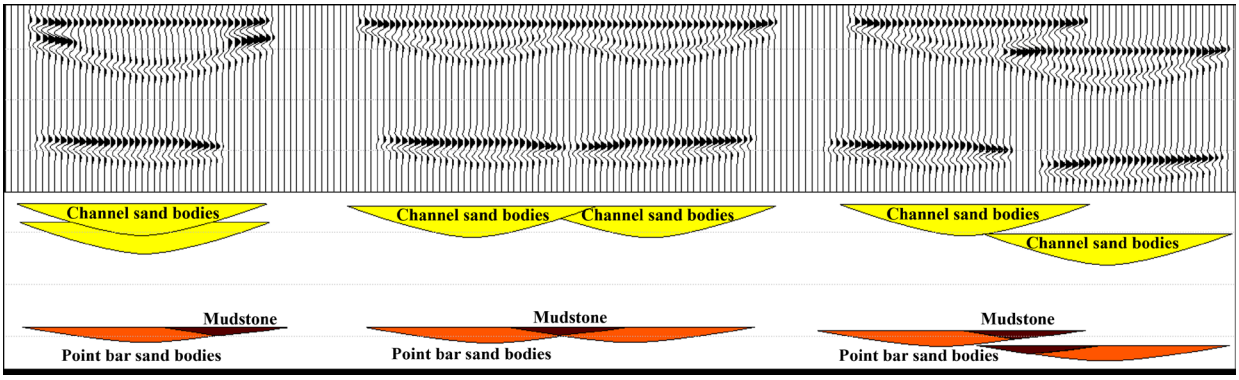

Figure 9. Forward geological model illustrating stacked channel and point-bar sand bodies within mudstone. Variations in sand-body geometry and thickness (3–50 m) generate distinct seismic waveform responses, providing a basis for evaluating the ability of waveform-indication inversion to resolve thin interbeds.

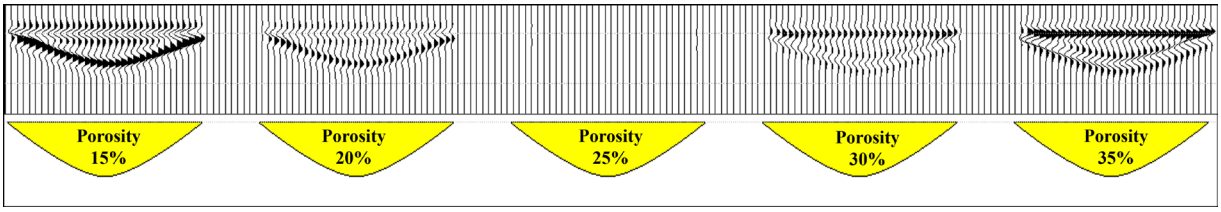

Figure 10. Focus on porosity sensitivity. Seismic amplitude response as a function of increasing porosity.

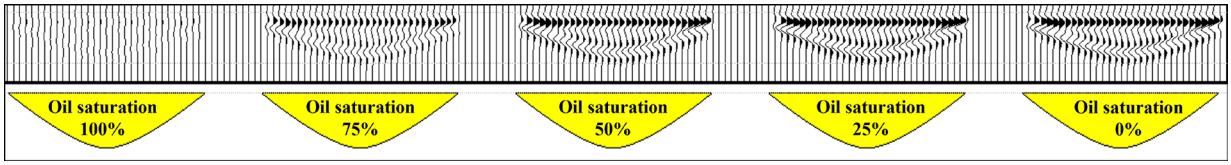

Figure 11. Focus on fluid sensitivity. Effect of oil saturation on sandstone velocity and seismic amplitude with different saturation levels.

and inverted parameters indicates that the model is both physically reasonable and highly predictive (Table 1).

Furthermore, 3D visualisation enables the identification of "sweet spots" and optimal drilling targets by illustrating the spatial continuity of reservoir properties. The lithofacies inversion elucidates structural and stratigraphic features, with colour-coded values highlighting lateral facies changes and depositional architecture (Figure 16A). The porosity distribution revealed variations in reservoir quality; prospective zones (porosity > 20% within sandstone lithofacies) are concentrated around the key wells CB24 and CB25, corresponding to channel sand systems (Figure 16B). In contrast, low-porosity zones (< 10%) associated with mixed sand–shale layers or mudstone lithofacies around wells CB273, CB26, CB213, and CB292 correspond to water-saturated or non-reservoir intervals.

This study demonstrates that integrating rock physics analysis with seismic inversion provides a robust, interpretable, and physically grounded framework for characterising thin-bed reservoirs. It enables the accurate estimation of reservoir characteristics, elastic parameters, and fluid discrimination across various lithologies. Consequently, this workflow has the potential to significantly improve exploration efficiency, optimise well-completion selection, and reduce uncertainties in subsurface modelling.

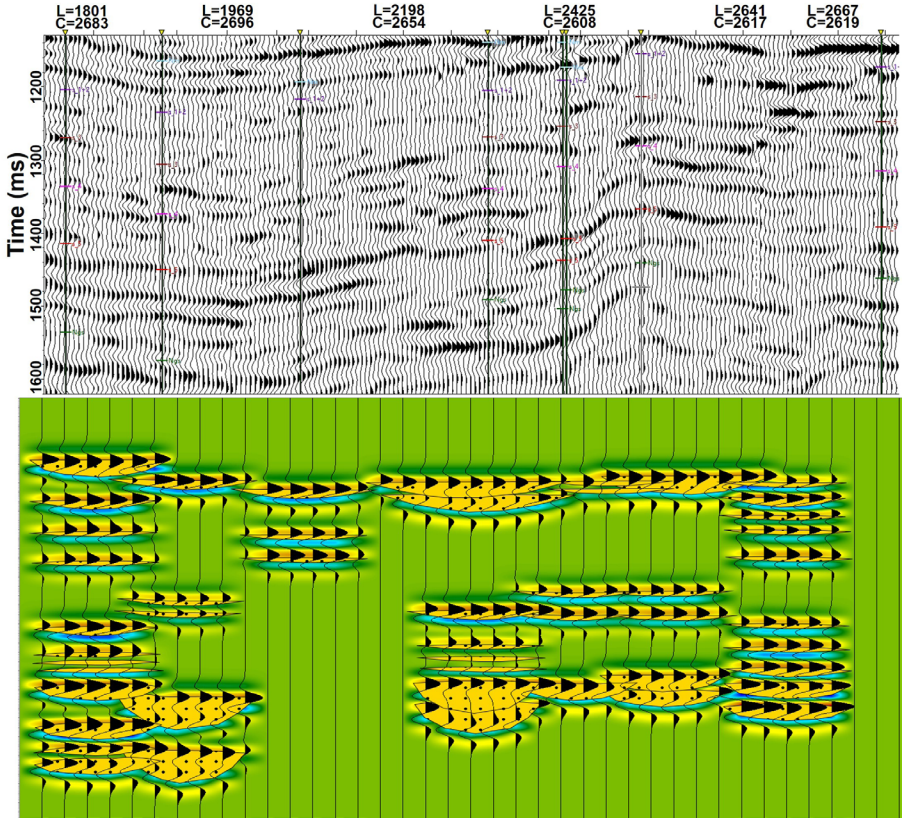

Figure 12. Comparison of forward-modelling results showing bright-spot characteristics in high-porosity, oil-bearing zones

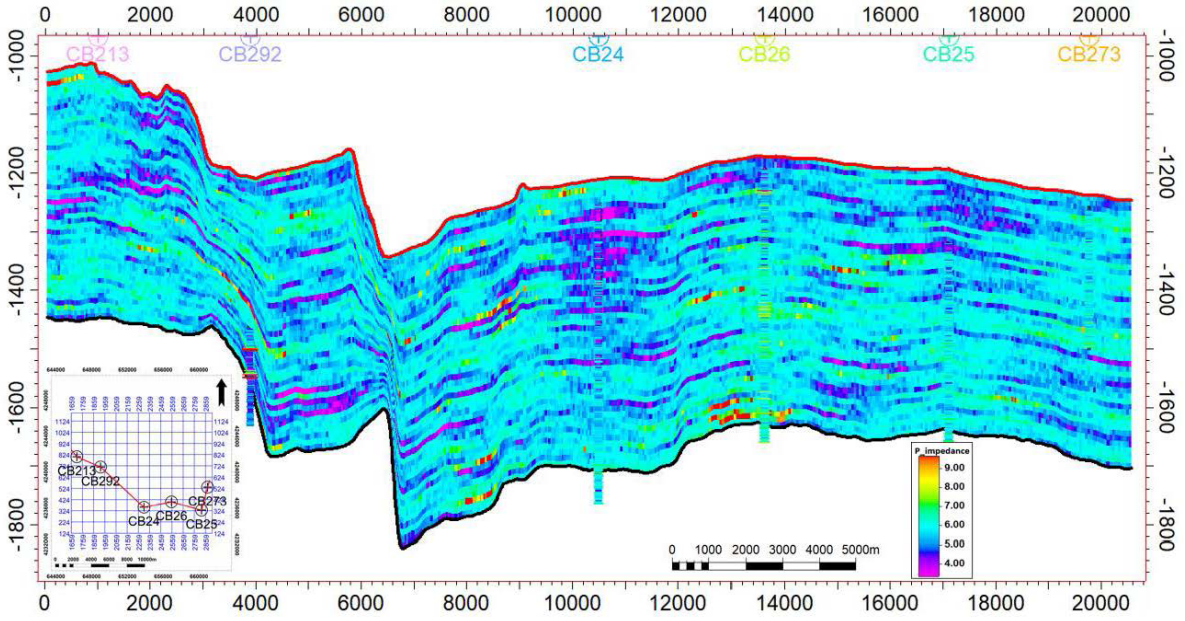

Figure 13. Cross-sectional view of P-impedance (g/cm^3 × km/s) inversion profile in Guantao Formation

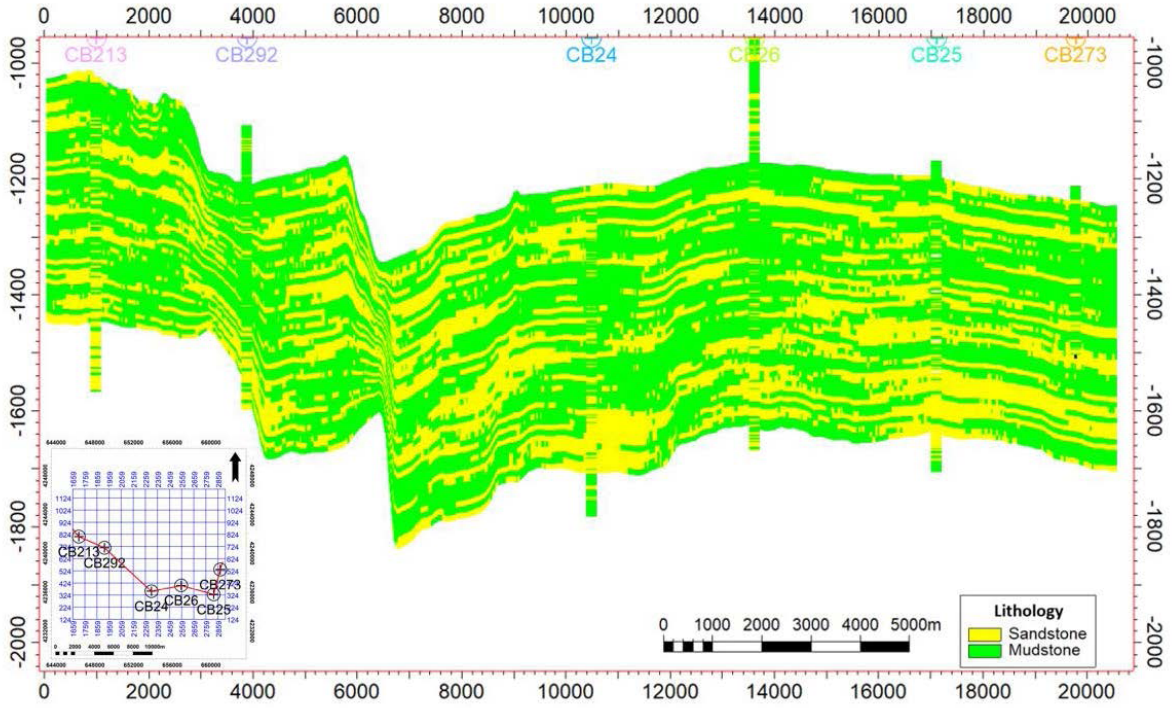

Figure 14. Visualisation of the spatial extent and hydrocarbon potential of the identified sand bodies. The distribution map highlights the favourable zones within the oil-bearing layers, suggesting significant extraction potential.

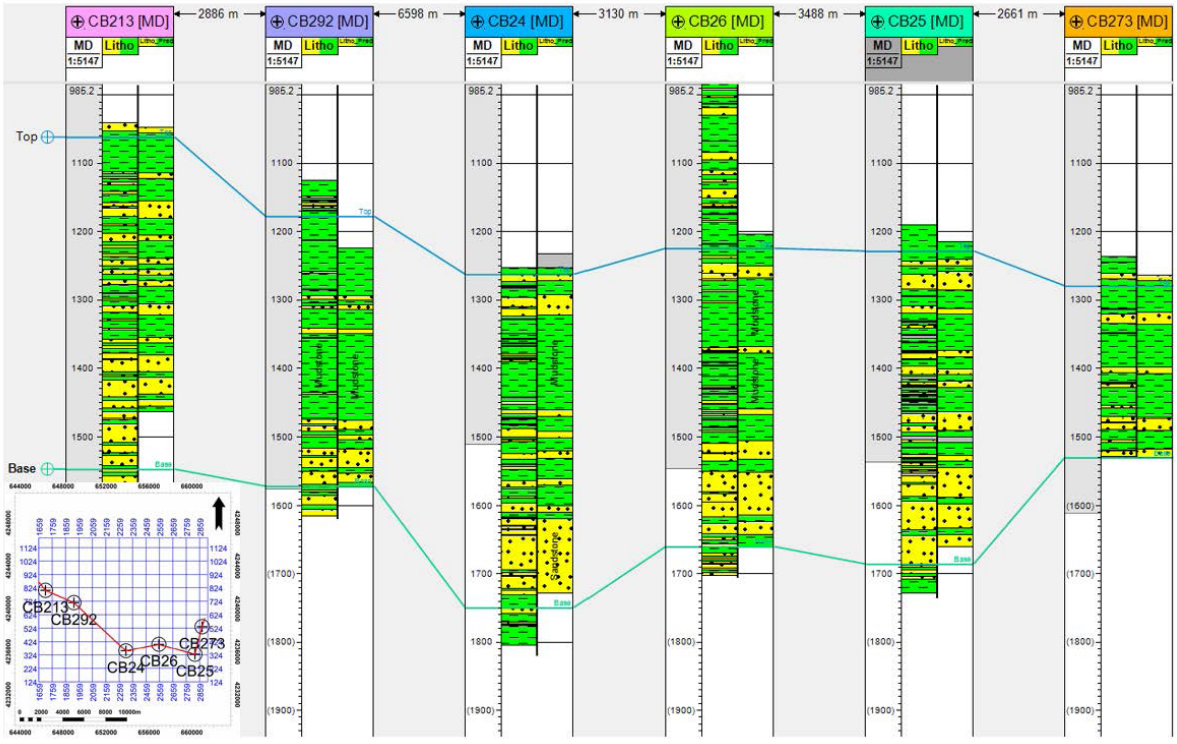

Figure 15. Seismically inverted lithofacies profiles across wells CB25, CB26, CB213, CB273, CB292, and CB24. The inversion results clearly delineate the boundaries between sand and shale, confirming the lateral extent and continuity of the sand bodies within the target Guantao Formation (for cross-section analysis, refer to Figure 1).

Table 1. Depth uncertainty through the studied wells

Well	Depth (Logs; m)	Depth (Seismic; m)	Difference (m)
CB213	−1,044.40	−1,043.90	−0.50
CB292	−1,160.40	−1,162.50	2.40
CB24	−1,241.50	−1,241.00	−0.50
CB26	−1,193.00	−1,192.90	−0.10
CB25	−1,208.00	−1,207.95	−0.05
CB273	−1,254.88	−1,254.18	−0.70
CB213	−1,529.40	−1,528.30	−1.10
CB292	−1,554.40	−1,554.40	0.00
CB24	−1,728.50	−1,728.50	0.00
CB26	−1,628.50	−1,628.50	0.00
CB25	−1,665.00	−1,664.80	−0.20
CB273	−1,504.88	−1,507.68	2.80

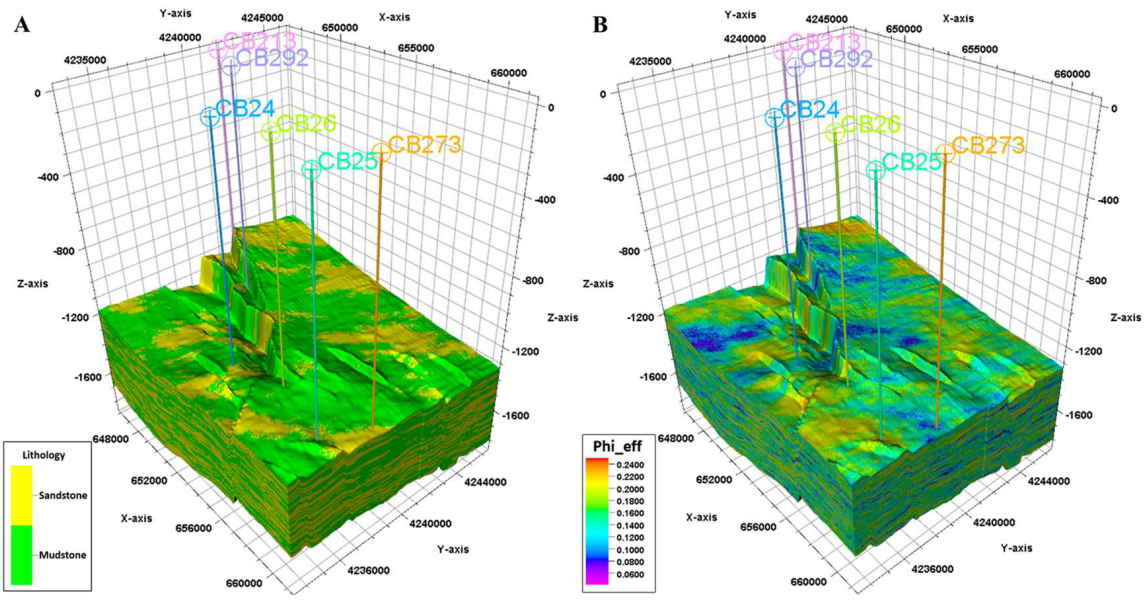

Figure 16. 3D visualisation of reservoir properties for "sweet spot" identification. (A) Lithofacies inversion volume illustrating the structural features, depositional architecture, and lateral facies changes. (B) 3D porosity distribution showing variations in reservoir quality. High-quality prospective zones (porosity > 20%) are concentrated in sandstone channels near wells CB24 and CB25, while low-porosity zones correspond to mudstone-rich intervals.

5. Conclusion

This study provides critical insights into the distribution of the Guantao Formation, emphasising the challenges of identifying thin sand layers less than 10 m thick. By employing SWII, we addressed the difficulty in distinguishing these layers, achieving high-precision reservoir prediction. The SWII effectively identifies thin sand-shale layers, reflecting various stacking patterns and the effects of porosity and oil saturation on sand-body velocity.

The integration of GMM provides a promising alternative for anomaly detection, leveraging inter-variable relationships (GR, Vp/Vs, and DEN) to improve geological interpretability and facies classification. The results demonstrate reliable effects and considerable predictive power, with inversion parameters coinciding closely with rock physics and GMM analysis. Consequently, this research establishes a robust foundation for future multilayer system deployment and efficient oil and gas exploration in the Bohai Bay Basin and similar geological settings.

Acknowledgments

None.

Funding

This research was financially supported by the offshore production plant, Sinopec Shengli Oilfield Company, Dongying, China (30200012-25-ZC0699-0008).

Conflict of interest

Yanjia Wu, Zhiwen Dong, Yiyao Zhang, Zekun Li, Shihao Liu, Xiaoxiao Shi, Hongke Zhou, Qunhu Wu, Shina Yu are employees of Sinopec Shengli Oilfield Company; however, they were not involved in any activities that could constitute a conflict of interest in relation to this study. The authors confirm that they have no conflicts of interest, financial or non-financial, associated with the material presented in this manuscript.

Author contributions

Conceptualization: Yanjia Wu, Qamar Yasin
Formal analysis: Zhiwen Dong, Hongke Zhou, Shina Yu
Investigation: Qunhu Wu, Shihao Liu, Xiaoxiao Shi
Methodology: Yanjia Wu, Qamar Yasin
Validation: Zekun Li, Ahmed Bakry, Qamar Yasin
Visualization: Yanjia Wu, Qamar Yasin, Ahmed Bakry
Writing–original draft: Yanjia Wu, Yiyao Zhang
Writing–review & editing: Shina Yu, Yiyao Zhang, Ahmed Bakry

Availability of data

All datasets, trained models, and analysis code will be made available upon publication through a code repository (https://github.com/qamarquaidian/Pore-Structure-Analysis).

References

1. Darling T. *Well Logging and Formation Evaluation*. Gulf Professional Publishing; 2005.

   doi: 10.1016/B978-0-7506-7883-4.X5000-1

2. Lai J, Su Y, Xiao L, *et al*. Application of geophysical well logs in solving geologic issues: Past, present and future prospect. *Geosci Front*. 2024;15(3):101779.

   doi: 10.1016/j.gsf.2024.101779

3. Zhu J, Qu Y, Duan W, Zhang Q, Yang C. Frequency Domain Acoustic Wave Full Waveform Inversion Based on Average-Derivative Optimization. *J Seism Explor*. 2024;33(5):21-38.

4. Pe'er U, Dy JG. Automated target detection for geophysical applications. *IEEE Trans Geosci Remote Sens*. 2016;55(3):1563-1572.

   doi: 10.1109/TGRS.2016.2627245

5. Struminskiy K, Klenitskiy A, Reshytko A, *et al*. Well log data standardization, imputation and anomaly detection using hidden Markov models. In: *Petroleum Geostatistics 2019*; September 2-6, 2019; Florence, Italy. European Association of Geoscientists & Engineers; 2019:1-5.

   doi: 10.3997/2214-4609.201902208

6. Al-Fakih A, Kaka SI, Koeshidayatullah AI. Reservoir property prediction in the North Sea using machine learning. *IEEE Access*. 2023;11:140148-140160.

   doi: 10.1109/ACCESS.2023.3336623

7. Liu J, Zhu H, Liu Y, Wu H, Lan Y, Zhang X. Anomaly detection for time series using temporal convolutional networks and Gaussian mixture model. In: *Journal of Physics: Conference Series*. 2018 International Symposium on Power Electronics and Control Engineering (ISPECE 2018); December 28-30, 2018; Xi'an, China. IOP Publishing; 2019;1187(4):042111.

   doi: 10.1088/1742-6596/1187/4/042111

8. Reynolds D. Gaussian mixture models. In: Li SZ, Jain AK, eds. *Encyclopedia of Biometrics*. Springer; 2015:827-832.

   doi: 10.1007/978-1-4899-7488-4_196

9. Jia J, Zheng X, Wang Y, *et al*. The effect of artificial intelligence evolving on hyperspectral imagery with different signal-to-noise ratio, spectral and spatial resolutions. *Remote Sens Environ*. 2024;311:114291.

   doi: 10.1016/j.rse.2024.114291

10. Sun M, Yasin Q, Daniel E, *et al*. Swin-UNETR: A transformer-based model for 3D pore network segmentation

in low-permeability sedimentary rocks. *Int J Coal Geol*. 2026;315:104951.

doi: 10.1016/j.coal.2026.104951

11. Ashraf U, Zhang H, Anees A, *et al*. Controls on reservoir heterogeneity of a shallow-marine reservoir in Sawan Gas Field, SE Pakistan: Implications for reservoir quality prediction using acoustic impedance inversion. *Water*. 2020;12(11):2972.

doi: 10.3390/w12112972

12. Yasin Q, Ding Y, Baklouti S, Boateng CD, Du Q, Golsanami N. An integrated fracture parameter prediction and characterization method in deeply-buried carbonate reservoirs based on deep neural network. *J Pet Sci Eng*. 2022;208:109346.

doi: 10.1016/j.petrol.2021.109346

13. Jackson CA, Larsen E. Temporal constraints on basin inversion provided by 3D seismic and well data: a case study from the South Viking Graben, offshore Norway. *Basin Res*. 2008;20(3):397-417.

doi: 10.1111/j.1365-2117.2008.00359.x

14. Chetia B, Nagaraju J, Sharma SK, Kumar A. Reservoir characterization through seismic inversion: A case study. In: *SEG Technical Program Expanded Abstracts 2019*. 89th Society of Exploration Geophysicists International Exposition and Annual Meeting 2019; September 15-20, 2019; San Antonio, TX. SEG; 2019:3215-3219.

doi: 10.1190/segam2019-3216159.1

15. Ali M, Zhu P, Jiang R, *et al*. Data-driven lithofacies prediction in complex tight sandstone reservoirs: a supervised workflow integrating clustering and classification models. *Geomech Geophys Geo-Energy Geo-Resour*. 2024;10(1):70.

doi: 10.1007/s40948-024-00787-5

16. Zhang R, Sen MK, Phan S, Srinivasan S. Stochastic and deterministic seismic inversion methods for thin-bed resolution. *J Geophys Eng*. 2012;9(5):611-618.

doi: 10.1088/1742-2132/9/5/611

17. Ashraf U, Zhang H, Anees A, *et al*. Application of unconventional seismic attributes and unsupervised machine learning for the identification of fault and fracture network. *Appl Sci*. 2020;10(11):3864.

doi: 10.3390/app10113864

18. Yakovleva IP, Filippova KE, Kuznetsov VI, Keller TE. Comparison of deterministic and geostatistical inversion results-a case study for a gas-saturated reservoirs with coals. In: *Proceedings of the 78th EAGE Conference and Exhibition 2016*; May 30 - June 2, 2016; Online. European Association of Geoscientists & Engineers; 2016:1-5.

doi: 10.3997/2214-4609.201601337

19. Haas A, Dubrule O. Geostatistical inversion-a sequential method of stochastic reservoir modelling constrained by seismic data. *First Break*. 1994;12(11).

doi: 10.3997/1365-2397.1994034

20. Liu X, Li J, Chen X, *et al*. Stochastic inversion of facies and reservoir properties based on multi-point geostatistics. *J Geophys Eng*. 2018;15(6):2455-2468.

doi: 10.1088/1742-2140/aac694

21. Li X, Shen Y, Chen W, Feng S, Zhang Z, Hong H. Seismic response of ice-water-covered two-layer seabed under obliquely incident P/SV-wave considering imperfect interface condition. *Ocean Eng*. 2025;342:122872.

doi: 10.1016/j.oceaneng.2025.122872

22. Ullah J, Luo M, Ashraf U, *et al*. Evaluation of the geothermal parameters to decipher the thermal structure of the upper crust of the Longmenshan fault zone derived from borehole data. *Geothermics*. 2022;98:102268.

doi: 10.1016/j.geothermics.2021.102268

23. Gao J, Bi JJ, Zhao HS, Fu ZF. Seismic waveform inversion technology and application of thinner reservoir prediction. *Prog Geophys*. 2017;32(1):142-145. [In Chinese].

doi: 10.6038/pg20170119

24. Ashraf U, Zhang H, Thanh HV, *et al*. A robust strategy of geophysical logging for predicting payable lithofacies to forecast sweet spots using digital intelligence paradigms in a heterogeneous gas field. *Nat Resour Res*. 2024;33(4):1741-1762.

doi: 10.1007/s11053-024-10350-4

25. Cheng Z, Liang Z, Han J, *et al*. Application of pre-stack geostatistical inversion in prediction of thin high-quality conglomerate reservoir in Shawan Depression, Junggar Basin. *Front Earth Sci*. 2025;19(4):498-504.

doi: 10.1007/s11707-025-1159-9

26. Wang J, Li Z, Chen C, Meng C. Predicting gas content in coalbed methane reservoirs using seismic waveform indication inversion: a case study from the Upper Carboniferous Benxi Formation, eastern Ordos Basin, China. *Acta Geophys*. 2022;70(2):623-638.

doi: 10.1007/s11600-022-00745-3

27. Helgesen J, Magnus I, Prosser S, *et al*. Comparison of constrained sparse spike and stochastic inversion for porosity prediction at Kristin Field. *Leading Edge*. 2000;19(4):400-407.

doi: 10.1190/1.1438620

28. Li B, Bi J, Wei S, Liu M, Han S. Application of waveform inversion technique in prediction of beach bar sandstone reservoir. In: *Proceedings of the International Geophysical Conference*; April 17-20, 2017; Qingdao, China. Society of Exploration Geophysicists and Chinese Petroleum Society; 2017:686-689.

doi: 10.1190/IGC2017-174

29. Nizarul O, Hermana M, Bashir Y, Ghosh DP. Improving thin bed identification in Sarawak Basin field using short time Fourier transform half Cepstrum (STFTHC) method. In: *IOP Conference Series: Earth and Environmental Science*. 3rd International Conference on Geological, Geographical, Aerospace and Earth Science 2015 (AeroEarth 2015); September 26-27, 2015; Jakarta, Indonesia. IOP Publishing; 2016;30(1):012003.

doi: 10.1088/1755-1315/30/1/012003

30. Babasafari AA, Bashir Y, Ghosh DP, *et al*. A new approach to petroelastic modeling of carbonate rocks using an extended pore-space stiffness method, with application to a carbonate reservoir in Central Luconia, Sarawak, Malaysia. *Leading Edge*. 2020;39(8):592a1-592a10.

doi: 10.1190/tle39080592a1.1

31. Fateh A, Al-Haji A, Elmasry H, Bikchandaev E. Customized workflow for proactive geosteering in thin heterogeneous carbonate reservoirs utilizing deep resistivity inversion. In: *Proceedings of the SPWLA 64th Annual Logging Symposium*; June 10-14, 2023; Lake Conroe, TX. Society of Petrophysicists and Well Log Analysts; 2023:D041S008R003.

doi: 10.30632/SPWLA-2023-0046

32. Purnomo EW, Abdul Latiff AH, Elsaadany MA. Predicting reservoir petrophysical geobodies from seismic data using enhanced extended elastic impedance inversion. *Appl Sci*. 2023;13(8):4755.

doi: 10.3390/app13084755

33. Liu H, Lin C, Zhang X, Wang H, Fu X. Sedimentological characteristics and controlling factors on fluvial styles of the Guantao Formation, Kongdian Oilfield, China. *J Earth Syst Sci*. 2019;128(2):37.

doi: 10.1007/s12040-018-1058-5

34. Wang J, Li ZG. Lacustrine Facies Sedimentary Characteristics of Guantao Formation in Zhanhua Sag. *Appl Mech Mater*. 2014;522-524:1337-1340.

doi: 10.4028/www.scientific.net/AMM.522-524.1337

35. Liu FT, Ting KM, Zhou ZH. Isolation forest. In: Giannotti F, Gunopulos D, Turini F, Zaniolo C, Ramakrishnan N, Wu X, eds. *Proceedings of the 2008 Eighth IEEE International Conference on Data Mining*; December 15-19, 2008; Pisa, Italy. IEEE; 2008:413-422.

doi: 10.1109/ICDM.2008.17

36. Xue S, Li Z, Feng G, *et al*. Visualization characterization of void structure evolution in broken limestone and its influence on permeability. *Fuel*. 2026;405:136412.

doi: 10.1016/j.fuel.2025.136412

ACCSCIENCE PUBLISHING

Journal of Seismic Exploration

ARTICLE

Research on microseismic data noise suppression method based on adaptive spectral segmentation

Mingyang Chang[1], Wenwu Zhou[1], Xiankai Wang[1], Huairui Su[1]*, Ziyi Na[2], Fuwu Ma[1], and Yang Li[1]

[1]Department of Comprehensive Exploration Technology, Shandong Provincial Research Institute of Coal Geology Planning and Exploration, Jinan, Shandong, China

[2]Geological Exploration Center, Shandong Provincial Coalfield Geology Bureau, Jinan, Shandong, China

Abstract

Microseismic monitoring data are characterized by strong background noise and low signal-to-noise ratio (SNR), posing challenges for effective signal identification and real-time processing. Existing methods generally suffer from poor adaptability, low processing accuracy, and insufficient computational efficiency. To address these issues, this study proposes an adaptive spectral segmentation method for microseismic signal extraction. First, the Ramanujan subspace method is employed to suppress periodic noise and eliminate spectral peak interference. Subsequently, an adaptive band number determination criterion based on the sampling rate is established, and adaptive empirical Fourier decomposition is adopted to achieve optimized spectral segmentation. Finally, the Gini coefficient is introduced to establish an adaptive threshold screening mechanism for automatic reconstruction of effective signals. For real-time processing of multi-channel data, a unified filtering strategy based on statistical overlapping bands is proposed, enabling rapid processing of subsequent data using common bands. Experiments on synthetic and field data demonstrate that the proposed adaptive spectral segmentation method yields significant advantages: on synthetic data, SNR improvements of up to 4.65 dB over modal decomposition methods (e.g., empirical mode decomposition, ensemble empirical mode decomposition, and variational mode decomposition) and wavelet packet decomposition, along with a 72% reduction in multi-channel processing time using the unified filtering strategy. These results highlight its high adaptability and practicality for low-SNR microseismic signal processing.

Keywords: Adaptive spectral segmentation; Microseismic signal processing; Noise suppression; Microseismic monitoring

***Corresponding author:**
Huairui Su
(beyondwaterloo@163.com)

Citation: Chang M, Zhou W, Wang X, *et al*. Research on microseismic data noise suppression method based on adaptive spectral segmentation. *J Seismic Explor*. 2026;35(3):026050018.
doi: 10.36922/JSE026050018

Received: January 28, 2026

Revised: March 18, 2026

Accepted: March 23, 2026

Published online: May 15, 2026

Copyright: © 2026 Author(s). This is an Open-Access article distributed under the terms of the Creative Commons Attribution License, permitting distribution, and reproduction in any medium, provided the original work is properly cited.

Publisher's Note: AccScience Publishing remains neutral with regard to jurisdictional claims in published maps and institutional affiliations.

1. Introduction

Microseismic signals serve as critical information for revealing subsurface medium activities and are widely applied in geological exploration and engineering monitoring.[1,2] However, these signals typically exhibit weak energy and are severely contaminated by strong background noise, resulting in extremely low signal-to-noise ratios (SNRs) and

posing significant challenges for effective information extraction.[3] Therefore, the development of adaptive denoising techniques capable of adapting to complex noise environments has become an important research direction in this field.

Regarding microseismic noise suppression, existing methods have formed multiple technical routes. Traditional fixed-band filtering methods,[4,5] though simple to implement, often lead to effective signal loss or noise residual when facing scenarios where signal and noise bands are intertwined, due to their fixed cutoff frequencies. Adaptive filtering techniques (e.g., least mean squares algorithms and their variants,[6,7] Kalman filtering[8]) improve adaptability through dynamic parameter adjustment; however, their performance largely depends on accurate assumptions regarding noise statistical characteristics or system models.[9] Deep learning methods, such as convolutional neural networks (CNN) and recurrent neural networks (RNN),[10,11] demonstrate powerful performance when sufficient training data are available. However, their generalization capability is severely limited by the completeness of training sets; when geological conditions change or noise patterns are unknown, model transfer effects are often unsatisfactory. Additionally, they face inherent limitations, including high computational resource demands and weak process interpretability.

In contrast to the aforementioned methods, modal decomposition methods—including empirical mode decomposition (EMD),[12] its noise-assisted variants (e.g., ensemble EMD [EEMD]/complete EEMD)[13-15] designed to alleviate mode mixing, and variational mode decomposition (VMD)[16,17] grounded in a variational framework—share a common theoretical foundation: they decompose signals into basis functions or modes according to intrinsic time–frequency characteristics without prior model assumptions. However, these methods encounter a shared fundamental bottleneck: their decomposition processes are inherently susceptible to noise interference and lack effective component screening mechanisms. Specifically, the essence of modal decomposition lies in adaptively decomposing signals into intrinsic mode functions or sub-signals, with the decomposition logic relying on the signal's own time–frequency features. Yet under strong background noise, noise energy permeates multiple components, causing severe feature aliasing between noise-contaminated modes and signal-dominant modes across both frequency and time domains.

More critically, existing methods predominantly employ statistical criteria (e.g., correlation coefficient, kurtosis, sample entropy) for component selection; however, these criteria exhibit fundamental limitations. The correlation coefficient method requires clean signals as references, which are unavailable under low-SNR conditions. Kurtosis is sensitive to non-Gaussian noise and is prone to misclassifying impulsive noise as effective signals; sample entropy tends to identify highly random noise as "complex signals." These theoretical limitations of the screening mechanisms ultimately force effective signal reconstruction to rely on subjective manual judgment, severely restricting the degree of automation and engineering practicality of such methods.

The recently proposed empirical Fourier decomposition (EFD) method[18,19] provides novel insights for signal decomposition by performing band segmentation based on empirical features such as local maxima of the signal's Fourier spectrum. Compared with EMD-like methods, EFD is built upon the solid theoretical foundation of the Fourier transform, offering a more deterministic and interpretable decomposition process. In contrast to VMD, EFD adaptively partitions frequency band boundaries, circumventing the need to preset the number of modes and thus exhibiting greater flexibility for microseismic signals with unknown frequency bands. However, this segmentation strategy, which relies on fixed empirical rules, still has notable limitations. On one hand, the strong periodic noise commonly present in actual microseismic data (manifested as discrete spectral spikes) severely interferes with its empirical criteria, leading to inaccurate band segmentation. On the other hand, the EFD method itself only performs signal decomposition without incorporating mechanisms for noise identification and component screening, making it difficult to apply directly to microseismic data processing in strongly noisy environments.

To address these issues, this study proposes an adaptive spectral segmentation (ASS) method. Specifically, for microseismic monitoring data, the Ramanujan subspace method (RSM) is employed to extract and suppress periodic noise, eliminating interference from discrete spectral peaks in subsequent segmentation processes.[20,21] Based on microseismic signal spectral characteristics, an adaptive band number determination criterion is established, and an adaptive EFD (AEFD) is adopted to achieve optimized band segmentation. The Gini coefficient is introduced as a sparsity measure for components, and an adaptive threshold screening mechanism is established to automatically identify and reconstruct effective microseismic signals through superposition.

For processing multi-channel microseismic data, the overlapping band ranges from each channel are further statistically analyzed and used as the effective signal band for the entire fracturing monitoring segment. Based on this

unified band, rapid bandpass filtering can be implemented for subsequent microseismic data, significantly improving processing efficiency while also correcting single-channel data with poor reconstruction results, thereby ensuring the reliability and consistency of overall denoising effects. To validate the effectiveness of the ASS method, this study processes both synthetic and field data, conducting comparative analyses with traditional methods including EMD, EEMD, VMD, and wavelet packet decomposition (WPD). The results demonstrate that the ASS method exhibits excellent performance in improving SNR, maintaining signal waveform integrity, and adapting to complex noise environments, providing a highly adaptive and practical solution for microseismic monitoring data processing.

2. Methodology

The primary objective of this study is to suppress background noise in microseismic data to improve the SNR and enhance the identifiability of effective signals. To achieve this, we propose an ASS method. Its core idea is to automatically identify and reconstruct signal-dominated spectral components through a three-stage process: (i) periodic noise suppression using the RSM to eliminate discrete spectral interference; (ii) AEFD to partition the spectrum into meaningful bands based on the signal's sampling rate and spectral characteristics; and (iii) automatic component screening based on the Gini coefficient to select and reconstruct effective signals. The overall workflow of the ASS method is illustrated in Figure 1.

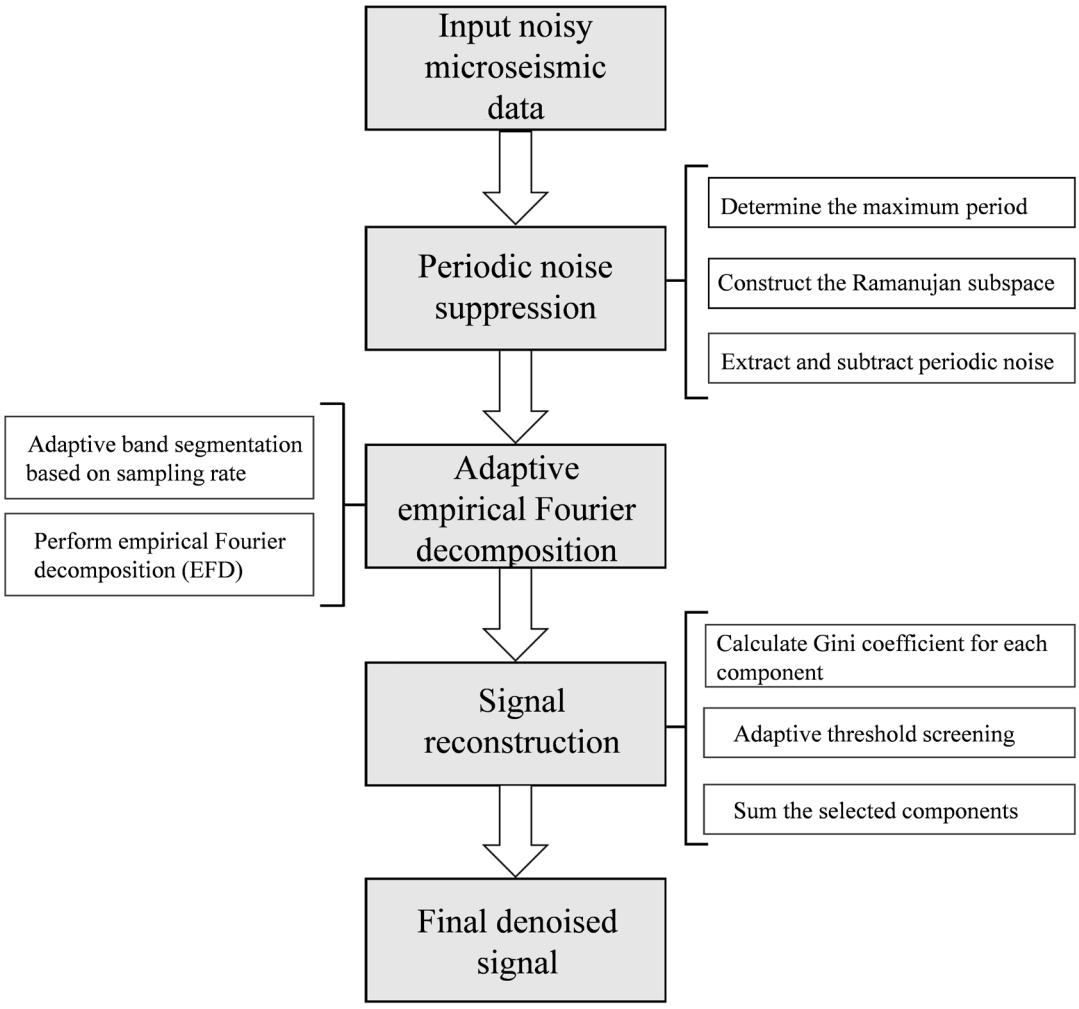

Figure 1. Flowchart of the proposed method

2.1. Periodic noise suppression

Periodic noise (e.g., power frequency interference and mechanical vibration) manifests as discrete spectral spikes in microseismic data, severely interfering with the accuracy of spectral segmentation. This study employs the RSM for periodic noise extraction and suppression.[22] First, potential periodic components are identified based on the signal autocorrelation function. Let the microseismic signal be denoted as $x(n), n = 0,1,\ldots,N-1$. Its autocorrelation function is defined as:

$$R_{xx}(\tau) = \frac{1}{N}\sum_{n=1}^{N-k} x(n)x(n+k) \tag{1}$$

where τ represents the time lag. The peaks of $R_{xx}(\tau)$ correspond to periodic components in the signal. The threshold is set to 70% of the maximum autocorrelation function value (determined through sensitivity analysis), and the maximum lag exceeding this threshold is recorded as the maximum period P_{max} of the periodic noise.

After determining the maximum period $R_{xx}(\tau)$, the Ramanujan subspace is constructed based on $R_{xx}(\tau)$. The Ramanujan subspace is composed of Ramanujan sums $C_T(n)$, defined as:

$$C_T(n) = \sum_{\substack{k=1 \\ \gcd(k,T)=1}}^{T} e^{j2\pi kn/T} \tag{2}$$

where n is the index, T is equal to $P_{\max}$, $\gcd(k,T)$ is the greatest common divisor of K and T, and $\gcd(k,T)=1$ indicates that K and T are coprime.

The orthogonal projection of the signal x onto the Ramanujan subspace can be represented as:

$$x_T = B_T x / T \tag{3}$$

where B_T is the Ramanujan subspace matrix.

The periodicity measure $P(x_T,T)$ is calculated to identify and extract periodic noise, where this measure is determined by selecting basis vectors with relatively high energy in x_T. The periodic noise $x_{periodic}$ is reconstructed and subtracted from the original signal to obtain the preprocessed signal:

$$\tilde{x} = x - x_{periodic} \tag{4}$$

2.2. Adaptive empirical Fourier decomposition

Conventional EFD methods typically employ a fixed band number for segmentation, making it difficult to adapt to variations in sampling rates and signal characteristics.[18,19] For microseismic monitoring data, this study proposes an adaptive band number determination method based on the signal sampling rate. The preprocessed signal $\tilde{x}(t)$ is subjected to Fourier transform to obtain its spectrum $\tilde{X}(f)$: $\tilde{X}(f) = \mathcal{F}[\tilde{x}(t)]$. Here, $\mathcal{F}$ denotes the Fourier transform operation. For microseismic data with sampling rate f_s, the Nyquist frequency is $f_N = f_s/2$, and the spectral analysis range is $[0, f_N]$.

According to the energy distribution characteristics of microseismic signals, the effective frequency band range of microseismic signals typically does not exceed 60 Hz. To ensure that band segmentation covers the full frequency domain while maintaining the integrity of signal characteristics within individual bands, this study establishes the following adaptive band number determination criterion:

$$K = \left\lfloor \frac{f_s/2}{60} \right\rfloor = \left\lfloor \frac{f_s}{120} \right\rfloor \tag{5}$$

where $\lfloor \cdot \rfloor$ denotes the floor operation, and K is the band number. The physical significance of this criterion is: using 60 Hz as the characteristic bandwidth unit, the Nyquist frequency range is divided into several continuous bands. This adaptive mechanism ensures that under different sampling rate conditions, band segmentation can match the spectral characteristics of microseismic signals, avoiding over-decomposition (for high sampling rates) or under-decomposition (for low sampling rates) problems caused by fixed band numbers. It should be noted that the 60 Hz characteristic bandwidth originates from the spectral properties of hydraulic fracturing microseismic signals—effective event energy typically concentrates below 100 Hz, with dominant frequency bands often below 60 Hz. This observation is consistent with numerous studies in this field.[22,23]

From a signal processing perspective, setting the characteristic bandwidth to 60 Hz ensures that the Nyquist frequency range ($f_s/2$) is divided into sufficiently fine bands to capture detailed spectral structures of effective signals, while avoiding excessive computational costs and spectral fragmentation from over-decomposition. The adaptive mechanism in **Equation 5** automatically adjusts the band number K according to the sampling rate, ensuring consistent physical interpretation of "one band per 60 Hz" across different acquisition systems.

It is important to emphasize that the 60-Hz value is not a fixed parameter, but a configurable prior that can be adapted to different applications. For example, natural

seismic signals with higher frequency content may require a larger unit, whereas mining-induced microseismicity with lower dominant frequencies may benefit from a smaller one. To validate this configurability and the appropriateness of the 60-Hz setting, we conducted a sensitivity analysis using bandwidths of 30 Hz, 80 Hz, and 120 Hz as the lower and upper limits. The results confirm that 60 Hz provides the optimal balance between resolution and robustness: 30 Hz leads to excessive spectral fragmentation (K = 8), while 80 Hz (K = 3) and 120 Hz (K = 2) suffer from insufficient resolution, causing signal-noise mixing. Therefore, 60 Hz was chosen as the default parameter used throughout the study.

The spectral maximum points $\{f_{peak}^{(m)}\}_{m=1}^{M}$ are selected and combined with initial uniform division boundaries $f_k^{(0)} = k \cdot f_s/(2K)$ uniform to optimize band boundaries:

$$f_k = \arg\min_{f_{peak}^{(m)}} \left| f_{peak}^{(m)} - f_k^{(0)} \right|, \quad \text{s.t.} \left| f_{peak}^{(m)} - f_k^{(0)} \right| < \frac{f_s}{4K} \quad (6)$$

A zero-phase filter bank $H_k(f)$ is constructed, and each band is filtered and inverse transformed to reconstruct time-domain components:

$$\hat{X}_k(f) = \hat{X}_{pre}(f) \cdot H_k(f), \quad x_k(t) = \mathcal{F}^{-1}[\hat{X}_k(f)] \quad (7)$$

yielding K band components $\{x_k(t)\}_{k=1}^{K}$.

2.3. Signal reconstruction and output

Automatically selecting effective microseismic signal components from the *K* components requires establishing a discrimination criterion. Microseismic signals exhibit significant sparsity (energy concentrated in a few sampling points), while noise energy is relatively uniformly distributed. The Gini coefficient can effectively measure this characteristic. The Gini coefficient is a statistical measure that quantifies the degree of inequality in a probability distribution. Its value ranges between 0 and 1, where a smaller value indicates a more uniform distribution, and a larger value indicates a more uneven distribution. In the fields of signal processing and machine learning, the Gini Coefficient is commonly used to assess the concentration of feature values.[24,25] The calculation steps for the Gini coefficient are as follows:

For a given signal $f_k^{(0)} = k \cdot f_s/(2K)$, the steps to calculate its Gini coefficient $G(x)$ are:

(i) Step 1: First, sort the absolute values of the signal in ascending order to obtain $x' = [x'_1, x'_2, \ldots, x'_n]$, $x'_i \le x'_{i+1}$.

(ii) Step 2: Compute the cumulative sum of the sorted signal: $S_i = \sum_{j=1}^{i} x'_j$.

(iii) Step 3: Compute the total sum of the absolute values of the signal: $S = \sum_{i=1}^{n} x_i$.

(iv) Step 4: The Gini coefficient $G(x)$ is given by the following formula:

$$G(x) = \frac{1}{n-1}\left(n + 2\sum_{i=1}^{n} \frac{i}{n}\frac{S_i}{S} - 2\right) \quad (8)$$

This study proposes an adaptive threshold based on statistical distribution:

$$G_{th} = \mu_G + \alpha \cdot \sigma_G \quad (9)$$

where $\mu_G = \frac{1}{K}\sum_{k=1}^{K} G$, $\sigma_G = \sqrt{\frac{1}{K}\sum_{k=1}^{K}(G_k - \mu_G)^2}$. σ is a tuning coefficient (typically ranging from 0.5 to 1.0, with a default value of 0.8). Lower σ increases threshold stringency, reducing false positives but risking signal loss; higher σ relaxes threshold, improving signal completeness but increasing noise retention. The default σ = 0.8 is validated through sensitivity analysis as providing optimal balance for typical microseismic SNR ranges. This threshold dynamically adjusts according to data characteristics, enhancing the algorithm's robustness. Components that satisfy condition $G_k > G_{th}$ are selected for superposition reconstruction:

$$x_{signal}(t) = \sum_{k \in \mathcal{K}_{valid}} x_k(t), \quad \mathcal{K}_{valid} = \{k | \ G_k > G_{th}\} \quad (10)$$

The reconstructed signal constitutes the final denoising result. To validate the effectiveness of the method proposed in this section, we designed a set of experiments, including microseismic signals, periodic noise, and random noise. Specifically, the periodic noise was composed of sinusoidal signals with an amplitude of 0.5 and frequencies of 30 Hz and 130 Hz; the random noise was Gaussian white noise, and the microseismic signals were based on real, clean microseismic data.

We calculated the Gini coefficient and sample entropy values for these signals and conducted a comparative analysis. Sample entropy is a common parameter for measuring the complexity of time series, which reflects signal complexity by estimating the probability of new pattern generation within the time series. A larger sample entropy value indicates a more chaotic waveform, higher frequency, and greater complexity of the signal; conversely, a smaller sample entropy value suggests a more regular pattern and lower complexity of the signal. Specific details are illustrated in Figure 2.

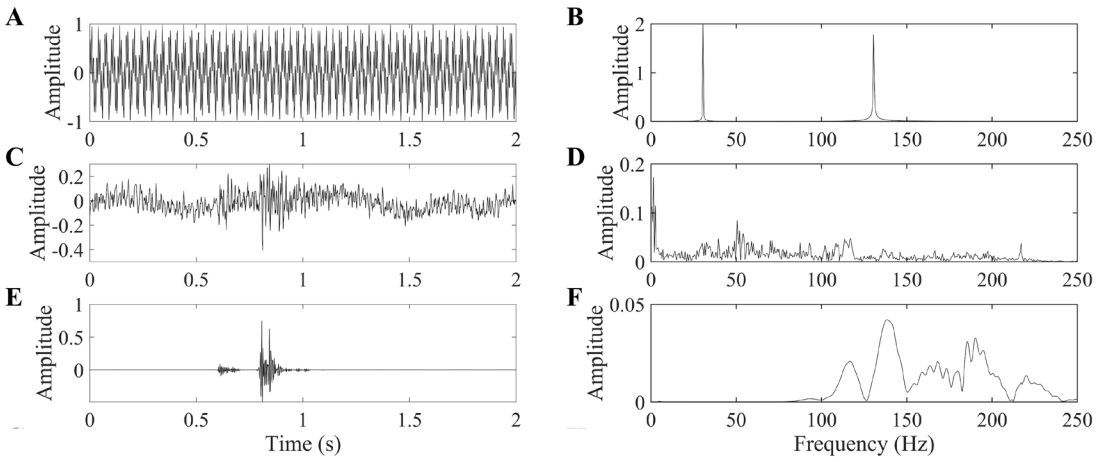

Figure 2. Composition of synthetic data. (A, C, E) The time-domain waveforms of (A) periodic noise, (C) random noise, and (E) the clean microseismic signal. (B, D, F) The corresponding frequency spectra of (B) periodic noise, (D) random noise, and (F) the clean microseismic signal.

We calculated the sample entropy and Gini coefficient for these three types of signals, and the results are shown in Figure 3. Sample entropy is a commonly used indicator for measuring the complexity of time series, reflecting the randomness and structural complexity of a signal by assessing the likelihood of new pattern generation within the sequence. A higher sample entropy value indicates a more irregular signal with more complex dynamic characteristics; conversely, it suggests that the signal pattern tends to be more regular.

The experimental results show that the Gini coefficient performs well in distinguishing the three types of signals: the maximum Gini coefficient appears in Group 3, corresponding to the real microseismic signal, while the Gini coefficients for periodic noise and random noise are relatively lower. In contrast, sample entropy failed to accurately identify the microseismic signal, with its maximum value appearing in Group 2 (random noise), indicating that sample entropy tends to misclassify highly random noise as "complex signals." This demonstrates that, in the task of microseismic signal identification, the Gini coefficient possesses higher discriminative accuracy and robustness.

3. Application

3.1. Processing of simulated data

The synthetically generated microseismic data were used to mimic actual monitoring environments, with a sampling frequency of 500 Hz. The noise composition was designed based on the dominant interference characteristics observed in hydraulic fracturing monitoring: (i) periodic noise from pumping equipment, power lines, and mechanical vibrations, which manifests as discrete spectral spikes; and (ii) random background noise from environmental sources and sensor electronics, which exhibits broadband Gaussian characteristics.

Based on field data analysis from the southwestern China monitoring site (Section 3.2), these two noise types collectively account for approximately 80–90% of the total noise energy in typical surface and near-surface microseismic arrays. Pulse noise (e.g., from electrical discharges, traffic, or drilling operations) and non-stationary harmonic interference, while present in some field conditions, represent secondary contamination sources whose suppression will be addressed in subsequent work.

Random noise was modeled as Gaussian white noise, and periodic noise was synthesized from sinusoidal signals with frequencies of 30 Hz and 130 Hz, respectively. The experiment sets the SNR to −19 dB. This value was selected to approximate the typical low-SNR conditions encountered in field microseismic monitoring, with the noise energy adjusted accordingly based on this SNR. The final synthesized simulated signal has a duration of 2 s. The structural composition of the simulated data and its spectral information are shown in Figure 4. The definitions of SNR and mean squared error (MSE) are as follows:

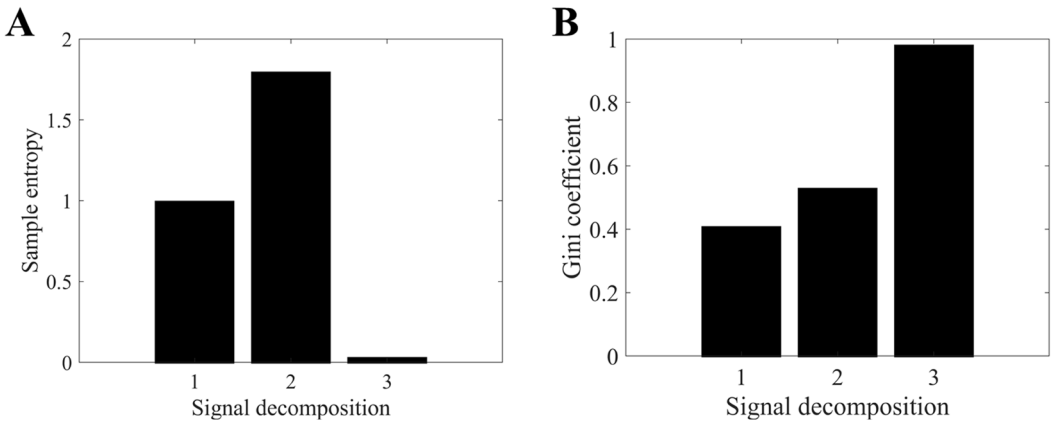

Figure 3. Comparison of (A) sample entropy and (B) Gini coefficient across the three types of signals

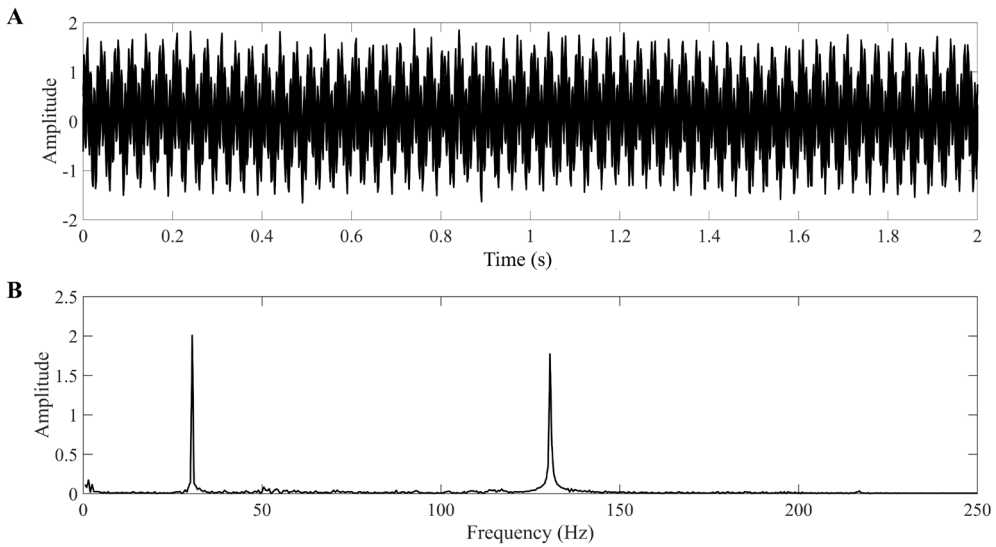

Figure 4. Synthetic simulated data showing the (A) time-domain waveform and (B) the frequency-domain spectrum.

$$SNR = 10\lg\left(\sum_{t=1}^{N}\frac{F(t)^2}{(\hat{F}(t)-F(t))^2}\right) \tag{11}$$

$$MSE = \frac{1}{N}\sum_{t=1}^{N}(F(t)-\hat{F}(t))^2 \tag{12}$$

where $F(t)$ is the clean signal, $\hat{F}(t)$ is the noisy data, and N is the length of the signal $F(t)$, that is, the number of sampling points.

Periodic noise components were clearly observed in the synthetic data, which were processed using the proposed Ramanujan subspace method. First, periodic components were identified through autocorrelation function analysis, with the threshold set to 70% of the maximum autocorrelation value, determining the maximum period as 50 sampling points (Figure 5). Based on this period, the Ramanujan subspace was constructed, and periodic noise components were extracted for spectral analysis. Results showed that the extracted noise spectrum was consistent with the preset 30 Hz and 130 Hz sinusoidal noise (Figure 6). After subtracting the extracted periodic noise from the original data, the denoised signal was obtained (Figure 7), demonstrating that periodic noise was effectively suppressed while the waveform and spectral structure of the effective signal remained intact.

To verify the rationality of the 70% threshold selection, processing effects under different thresholds (50%, 60%,

70%, 80%, and 90%) were tested. Results indicated that thresholds below 70% led to incomplete periodic noise removal, while thresholds above 70% increased the loss of effective signal; 70% was the optimal balance point (see Table 1). The 70% threshold used for periodic component detection in the autocorrelation function is determined based on sensitivity analysis of the synthetic data in this study. While this value proves effective for the hydraulic fracturing microseismic data, its optimal setting may vary across different application scenarios depending on the relative strength and characteristics of periodic noise.

In practice, this threshold can be adjusted according to two guiding principles: (i) if periodic noise components are exceptionally strong and well-separated from the signal in the frequency domain, a lower threshold (e.g., 60%) may suffice for reliable detection; (ii) if periodic noise is weak or spectrally overlapping with the signal, a higher threshold (e.g., 80%) is recommended to avoid false detection and signal distortion.

After completing periodic noise suppression, the AEFD method was applied to the processed data for frequency-domain segmentation. Based on the adaptive band-number determination criterion proposed in this study (**Equation 5**), the 0–250 Hz frequency range was partitioned into four bands. The segmentation results are shown in Figure 8. Zero-phase filters were constructed for each band, and the corresponding time-domain signals were reconstructed, yielding four time-domain signal components associated with distinct frequency bands, as shown in Figure 9.

To validate the appropriateness of the 60 Hz characteristic bandwidth, a sensitivity analysis was performed using bandwidth settings of 30 Hz, 80 Hz, and 120 Hz as the lower and upper limits. These settings resulted in band numbers of 8, 3, and 2, respectively, according to **Equation 5**. The corresponding spectral segmentation results are presented in Figure 10. A qualitative assessment of segmentation performance indicates that the 60–80 Hz range provides an appropriate balance between resolution and completeness. The 30 Hz setting leads to excessive fragmentation (K = 8), dispersing effective signal energy across multiple adjacent bands, whereas the 120 Hz setting results in insufficient resolution (K = 2), causing merging of signal and noise components. In contrast, both the 60 Hz (K = 4) and 80 Hz (K = 3) configurations preserve the effective signal within one or two contiguous bands, thereby confirming the adaptability and robustness of the proposed criterion.

To select effective signals from each component, the Gini coefficient of each component was calculated (Figure 11). According to the adaptive threshold determination method (**Equation 9**), for this dataset G_1 = 0.62, G_2 = 0.58, and a G_3 = 0.86, with α =0.8, the resulting threshold was G_{th} = 0.8. Components satisfying $G_k > G_{th}$, specifically the third component, were identified as effective signals and reconstructed. These were superimposed and reconstructed as the final denoising signal.

As shown in Figure 12, after processing, the signal SNR improved from −19 dB to 3.11 dB, and the MSE decreased to 0.0073. Compared with the original noisy signal, background noise was significantly suppressed, and the waveform characteristics of effective microseismic signals became clearly distinguishable.

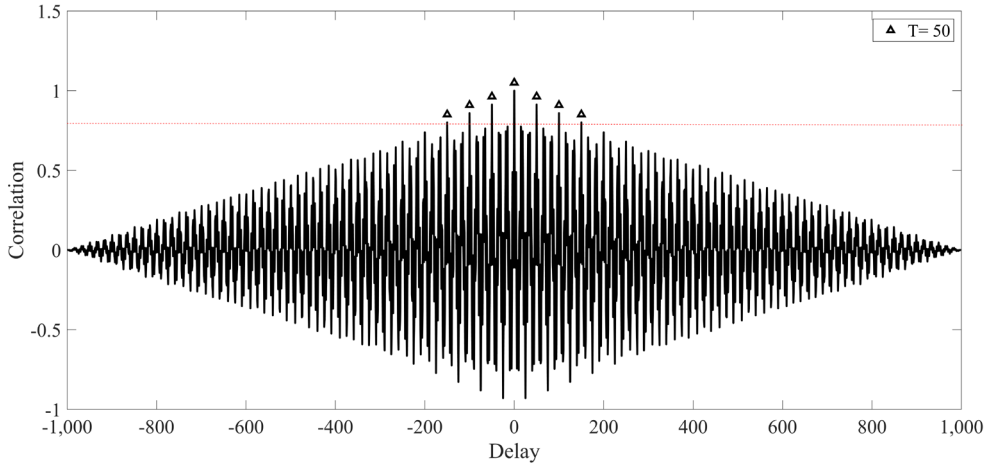

Figure 5. Autocorrelation function and period extraction results

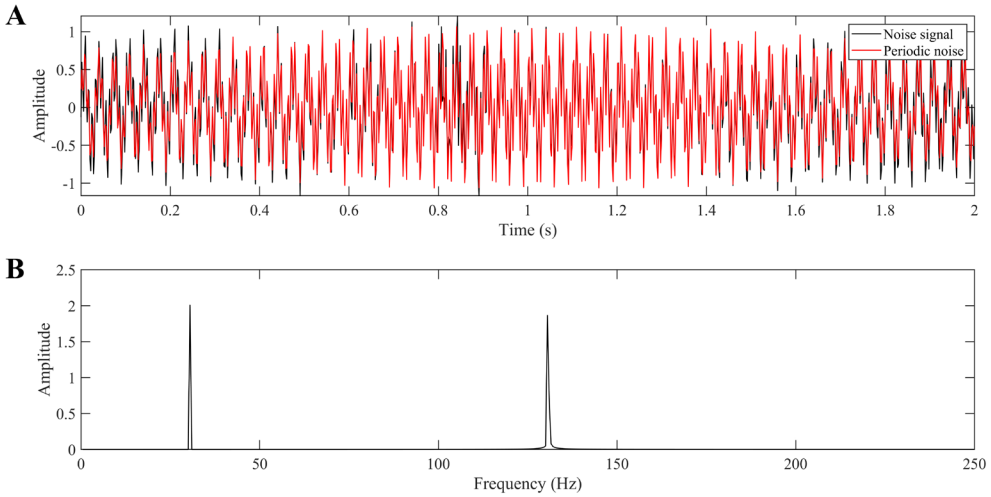

Figure 6. Extracted periodic noise and its spectrum. (A) The time-domain waveform. (B) The frequency-domain spectrum.

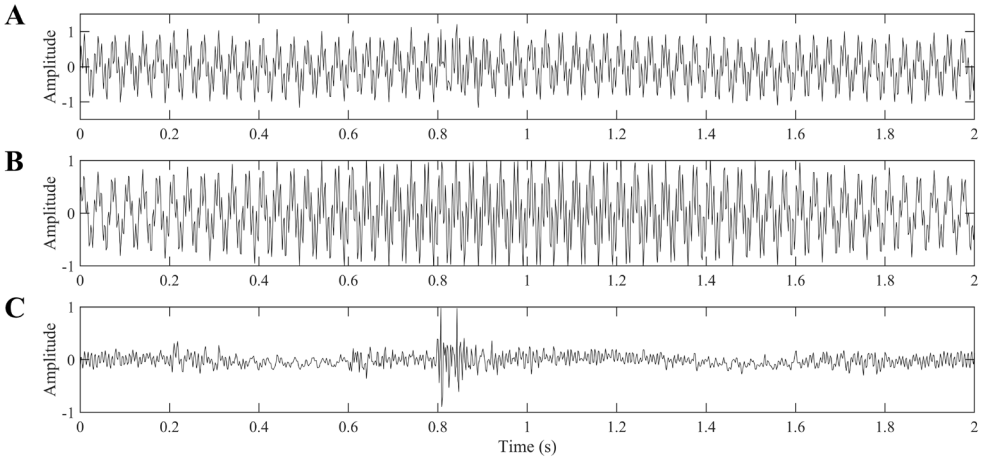

Figure 7. Periodic noise suppression of (A) simulated data, (B) the removed periodic noise, and (C) the denoised results.

Table 1. Sensitivity analysis of period detection threshold

Threshold coefficient	Periodic noise removal rate (%)	Effective signal fidelity (%)
0.5	62.3	98.7
0.6	78.5	97.2
0.7[a]	94.2[a]	95.8[a]
0.8	96.8	89.1
0.9	98.5	82.3

Note: [a] indicates the optimal parameter result.

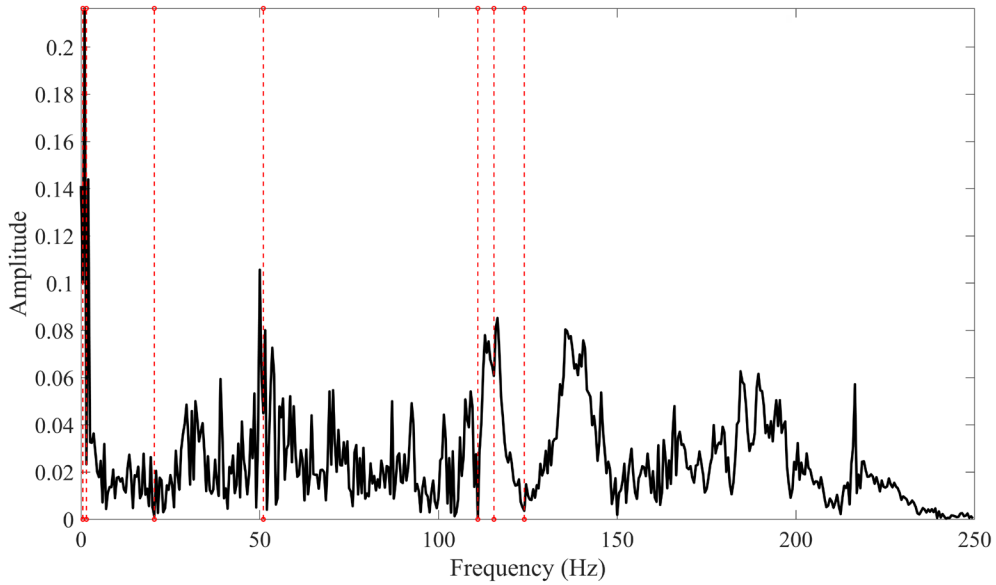

Figure 8. Frequency-domain segmentation

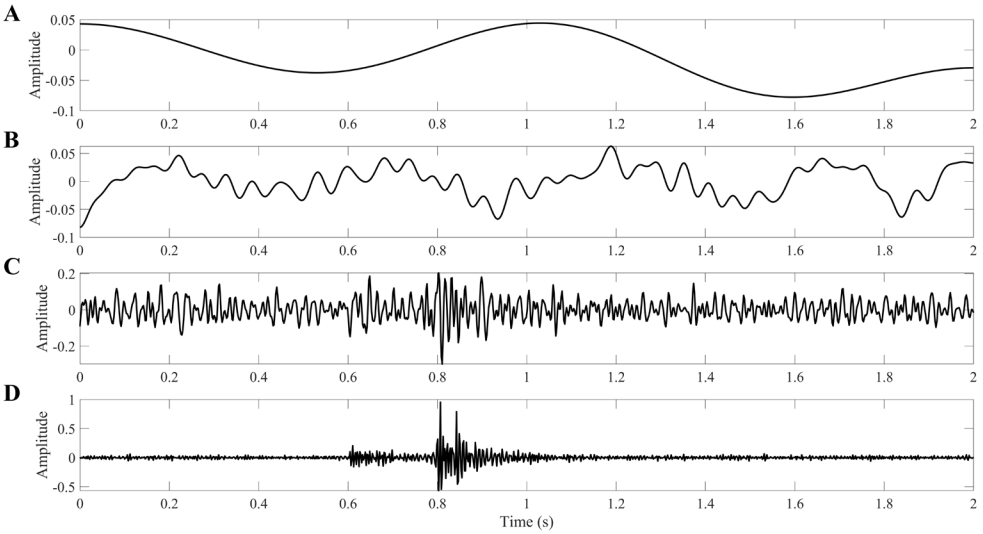

Figure 9. Waveforms corresponding to different segmented frequency bands. (A) 0–2 Hz, (B) 2–20 Hz, (C) 20–110 Hz, and (D) 110–250 Hz.

The adaptive threshold in **Equation 9** employs a tuning coefficient σ (default = 0.8) to balance signal preservation and noise rejection. To evaluate the stability of the algorithm with respect to this parameter, σ was systematically varied within the range [0.5, 1.0], and denoising performance was evaluated on the synthetic dataset. The results are presented in Table 2.

Based on Table 2, performance varies moderately with λ in the range [0.6, 1.0], with σ = 0.8 achieving the optimal balance, including the lowest MSE (0.0035), the highest signal preservation (95.6%), and an acceptable SNR (2.11 dB). While σ = 0.9 yields a slightly higher SNR (3.01 dB), it results in increased MSE and reduced signal retention, indicating over-thresholding and the rejection of valid components. Conversely, σ ≤ 0.7 leads to insufficient noise rejection. These results demonstrate that the algorithm maintains robust performance within σ ∈ [0.7, 0.9], with 0.8 selected as the default for the studied microseismic

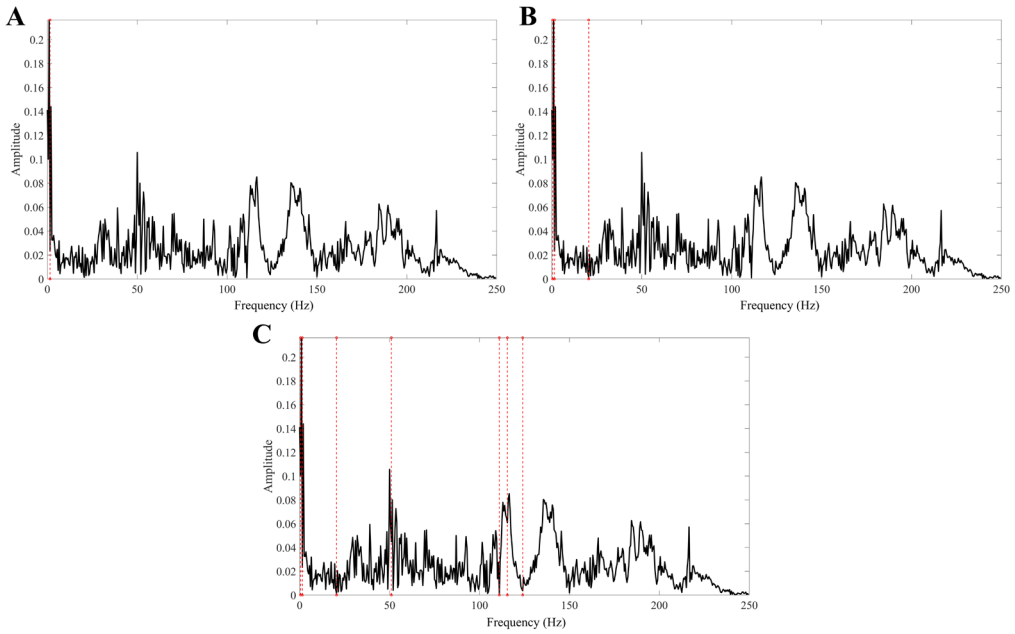

Figure 10. Results of spectral segmentation using different bandwidth units. (A) 120 Hz (K = 2), (B) 80 Hz (K = 3), and (C) 30 Hz (K = 8).

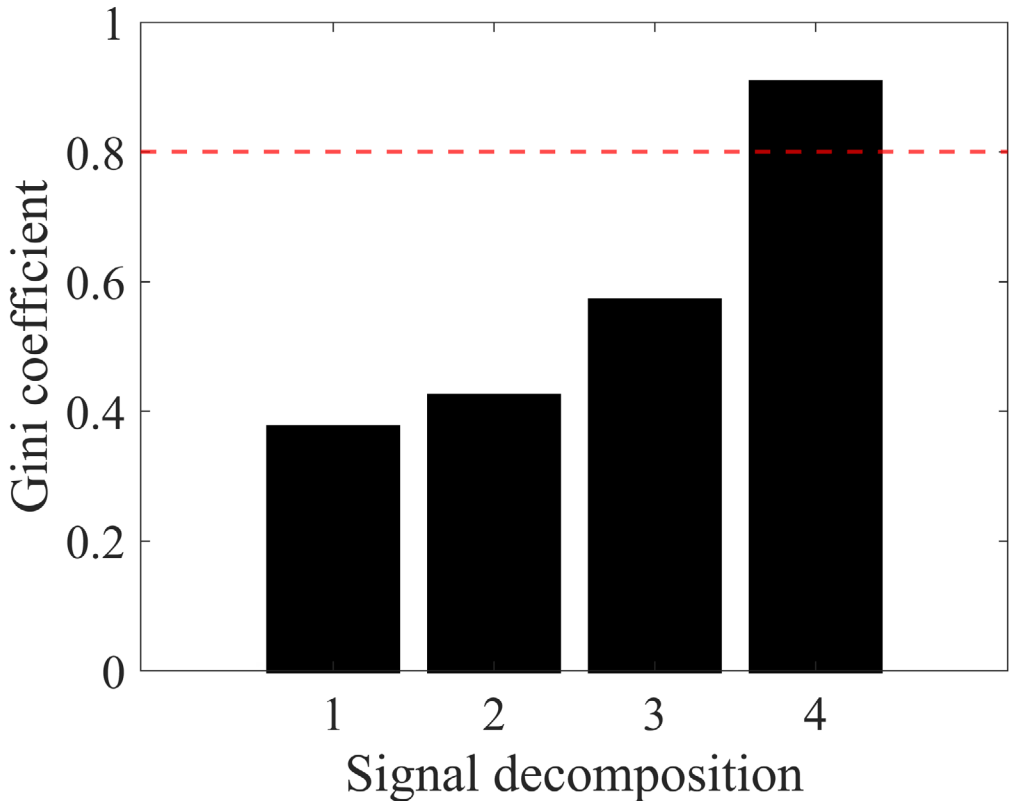

Figure 11. Gini coefficients calculated across different frequency ranges

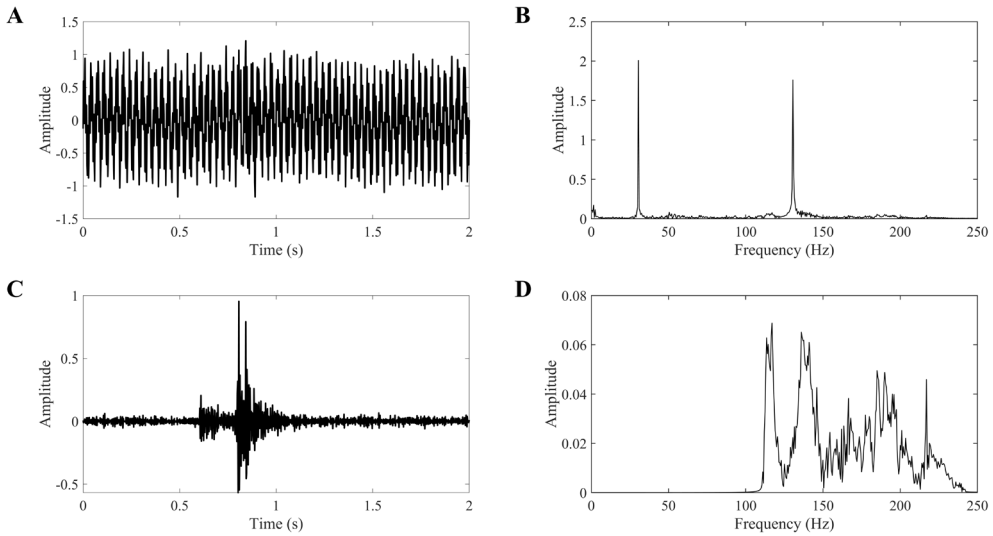

Figure 12. Results obtained using the adaptive spectral segmentation method. (A) original signal and (B) its frequency spectrum, and (C) denoised signal and (D) its frequency spectrum.

Table 2. Sensitivity analysis of Gini coefficient threshold parameter σ

Threshold	Output signal-to-noise ratio (dB)	Mean squared error	Signal preservation rate (%)
0.6	1.85	0.0081	77.1
0.7	2.16	0.0076	80
0.8[a]	2.11[a]	0.0035[a]	95.6[a]
0.9	3.01	0.0075	79.6
1.0	2.34	0.0097	75

Note: [a] indicates the optimal parameter result.

data.

To illustrate the necessity of periodic noise suppression, a comparison was conducted using only AEFD processing (without periodic noise suppression). As shown in Figures 13 and 14, interference from periodic spectral peaks degrades the frequency-domain segmentation performance of AEFD, resulting in residual noise in the reconstructed waveforms and reduced denoising effectiveness (SNR = −5.23 dB, MSE = 0.0415). This comparison demonstrates the importance of incorporating periodic noise preprocessing prior to AEFD.

Empirical mode decomposition, EEMD, and VMD were used as comparative methods to process the same simulated data. The parameters for each method were set as follows: EEMD noise standard deviation = 0.2, iteration count = 100; VMD bandwidth constraint = 2,000, noise tolerance = 0, mode number = 4, convergence tolerance = 1×10^{-7}. WPD was additionally employed, using the Daubechies 8 (db8) wavelet with decomposition level 4, soft thresholding with "sqtwolog" universal threshold, and Shannon entropy-based optimal basis selection. The decomposition results and reconstructed signals after Gini coefficient screening are shown in Figure 15. From the time-domain waveforms and frequency spectrum comparisons, while traditional methods partially suppress noise, they suffer from mode mixing, residual periodic noise, and wavelet-induced artifacts, leading to signal distortion.

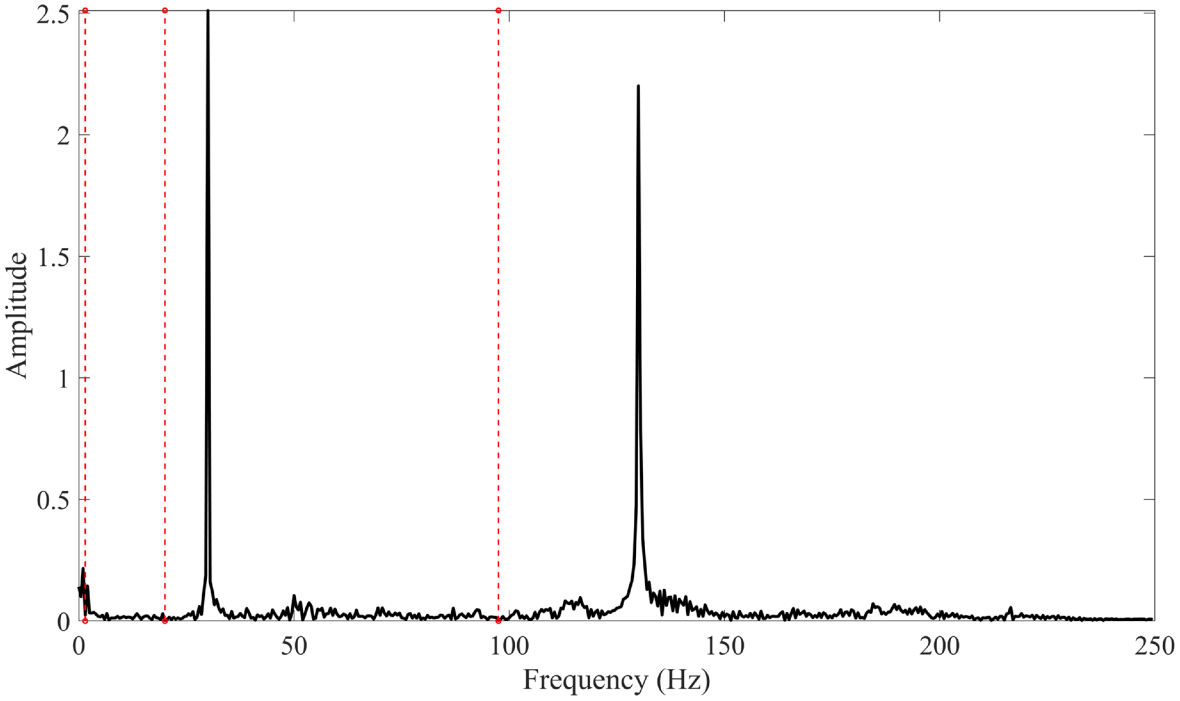

Figure 13. Frequency-domain segmentation results obtained by applying adaptive empirical Fourier decomposition directly to the original data without periodic noise suppression

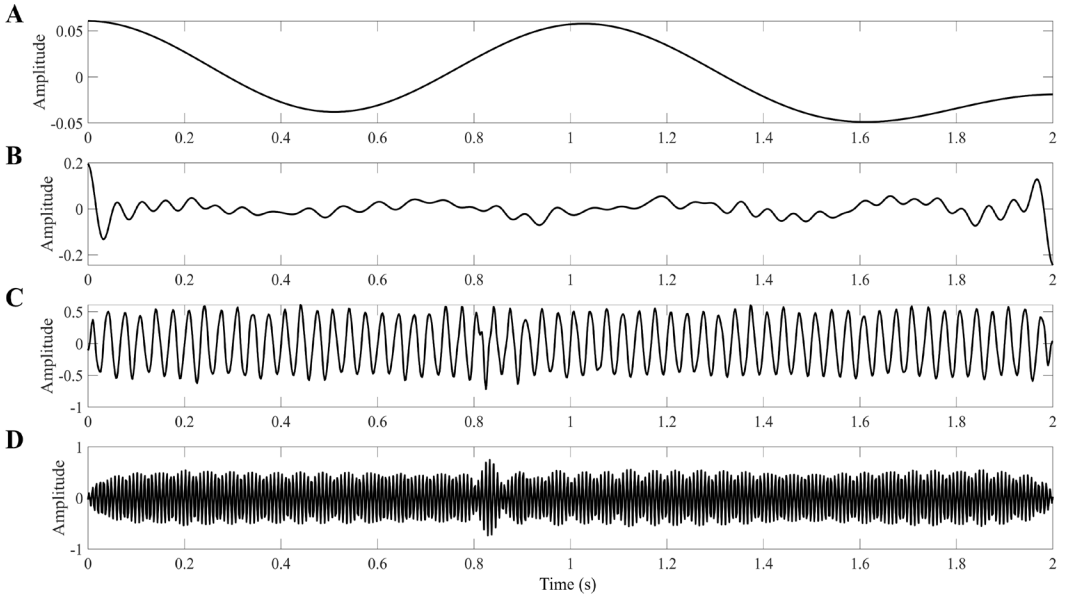

Figure 14. Waveform components obtained from frequency-domain segmentation without periodic noise suppression. (A) 0–2 Hz, (B) 2–20 Hz, (C) 20–96 Hz, and (D) 96–250 Hz.

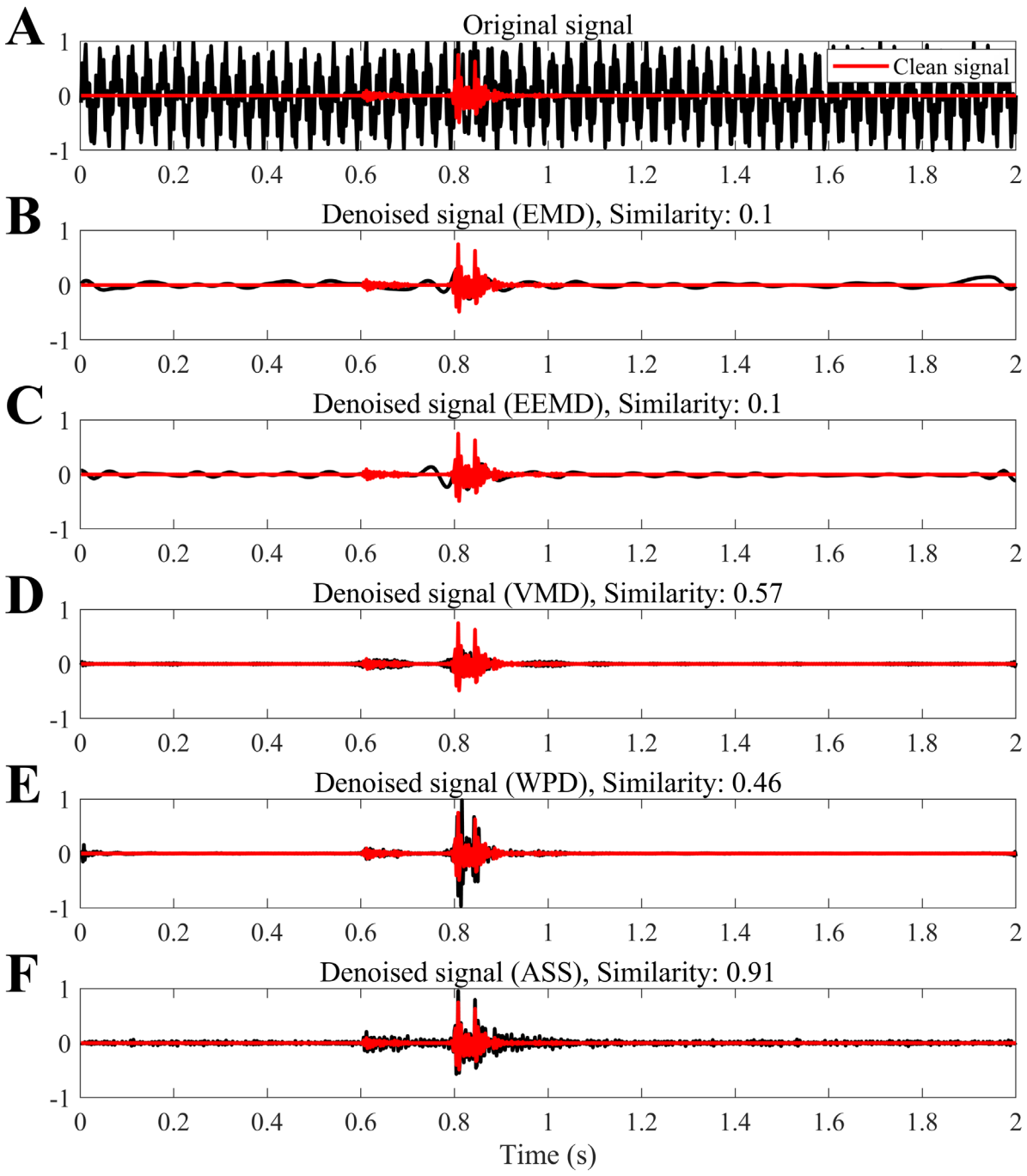

Figure 15. Comparison of denoising results obtained using different methods. Clean signal versus (A) original signal, (B) EMD results, (C) EEMD results, (D) VMD results, (E) WPD results, and (F) ASS results.
Abbreviations: ASS: Adaptive spectral segmentation; EEMD: Ensemble empirical mode decomposition; EMD: Empirical mode decomposition; VMD: Variational mode decomposition; WPD: Wavelet packet decomposition.

The quantitative results are shown in Table 3. The proposed ASS method significantly outperforms the three traditional methods in both SNR and MSE metrics, achieving the best denoising effect. Furthermore, the waveform correlation coefficient of the ASS method (0.91) is significantly higher than that of EMD (0.1), EEMD (0.1), WPD (0.46), and VMD (0.18), demonstrating its advantage in preserving signal waveform integrity.

Table 3. Comparison of signal-to-noise ratio and mean square error results of different denoising methods

Method	SNR (dB)	MSE
ASS	3.11[a]	0.0073[a]
EMD	−0.67	0.0258
EEMD	−0.39	0.0241
VMD	−1.14	0.0315
WPD	−1.46	0.0402

Note: [a] indicates the optimal parameter result.
Abbreviations: ASS: Adaptive spectral segmentation; EEMD: Ensemble empirical mode decomposition; EMD: Empirical mode decomposition; MSE: Mean squared error; SNR: Signal-to-noise ratio; VMD: Variational mode decomposition; WPD: Wavelet packet decomposition.

To validate the suppression performance against random noise (non-periodic noise), frequency components identified as invalid by AEFD decomposition (primarily high-frequency bands) were reconstructed as residual noise and compared with the original random noise added in the synthetic experiment.

Figure 16 illustrates the comparison between the removed random noise and the original random noise. Both waveform structures and spectral distributions exhibit high similarity in terms of frequency range and energy distribution, indicating effective identification and separation of random noise components. It should be noted that due to the band-segmentation characteristic of AEFD, a proportion of high-frequency effective signal energy may be filtered together with noise, resulting in slight energy deficiency in the low-frequency band of the removed noise spectrum compared to the original noise. Overall, the method demonstrates satisfactory performance in suppressing random noise.

To validate method performance across different sampling rates, synthetic microseismic data were generated using a three-layer velocity model (2,500, 3,000, and 3,200 m/s; thickness: 500, 700, and 600 m) with impulsive source excitation. Noise was added to achieve SNR = −19 dB. Two sampling rates were tested—250 Hz and 1,000 Hz—with results shown in Figure 17 (250 Hz) and Figure 18 (1,000 Hz). Table 4 presents quantitative comparisons.

Table 4. Comparison of signal-to-noise ratio and mean squared error results across different sampling rates

Signal type	250 Hz		1,000 Hz	
	SNR	MSE	SNR	MSE
Original signal	−19	0.2375	−19	0.9486
Periodic denoised	−1.2	0.0039	1.69	0.0081
Final denoised	13.9	0.0001	6.47	0.0026

Abbreviations: MSE: Mean squared error; SNR: Signal-to-noise ratio.

The results demonstrate that the ASS method maintains effective noise suppression across varying sampling rates. To systematically verify the robustness of the proposed method under varying noise conditions, six channels of synthetic microseismic data were constructed, as shown in Figure 19A. While the effective microseismic waveform remains identical across all channels, independent noise realizations with different energies were added to each channel, generating a sequence of synthetic records with progressively varying SNRs. Specifically, the SNRs for the six channels were set from −26 dB to −21 dB, with an increment of 1 dB per channel. This design aims to: (i) evaluate the method's sensitivity and robustness to different noise energy levels, and (ii) simulate the trace-to-trace SNR variations commonly encountered in field monitoring due to changes in noise sources or signal attenuation.

For this dataset, the proposed ASS algorithm, along with traditional EMD, EEMD, and VMD algorithms, were used for denoising. The processing flow and corresponding results of the ASS algorithm are shown in Figure 19. Firstly, periodic noise suppression was independently applied to each trace of data (Figure 19B), followed by AEFD for ASS and Gini coefficient screening (Figure 19C). After processing each trace independently, the effective signal frequency bands identified by the Gini coefficient in each trace were statistically analyzed. The analysis revealed that the effective signal spectra primarily overlapped in the

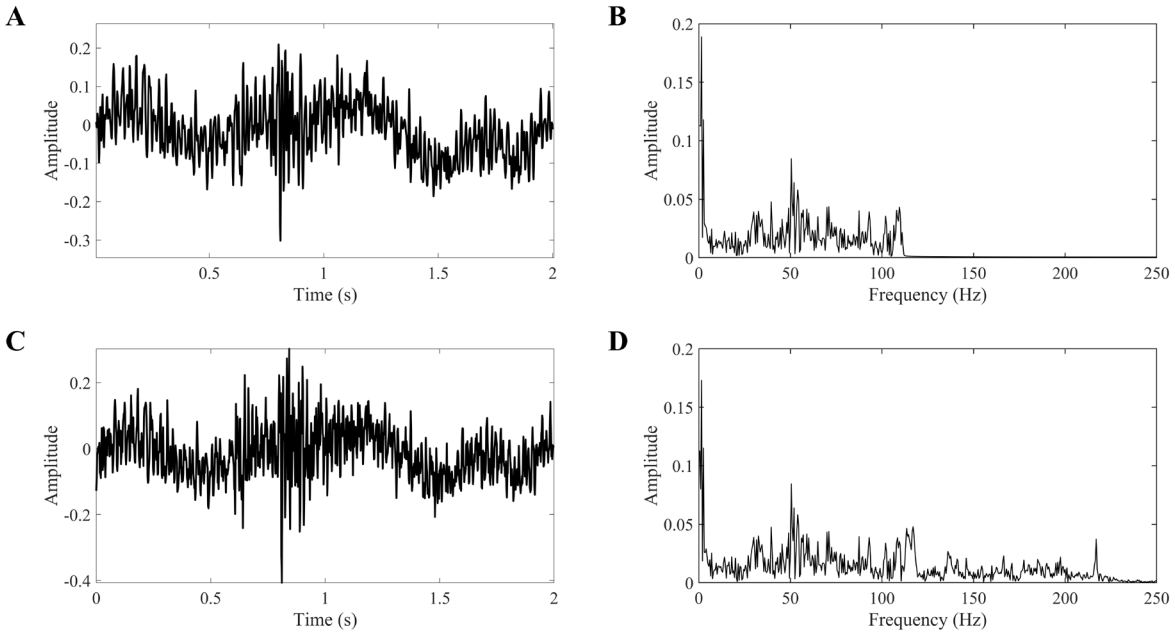

Figure 16. Random noise suppression results. (A) Random noise removed by the proposed method and (B) its corresponding amplitude spectrum, and (C) actual random noise added to the synthetic data and (D) its corresponding amplitude spectra.

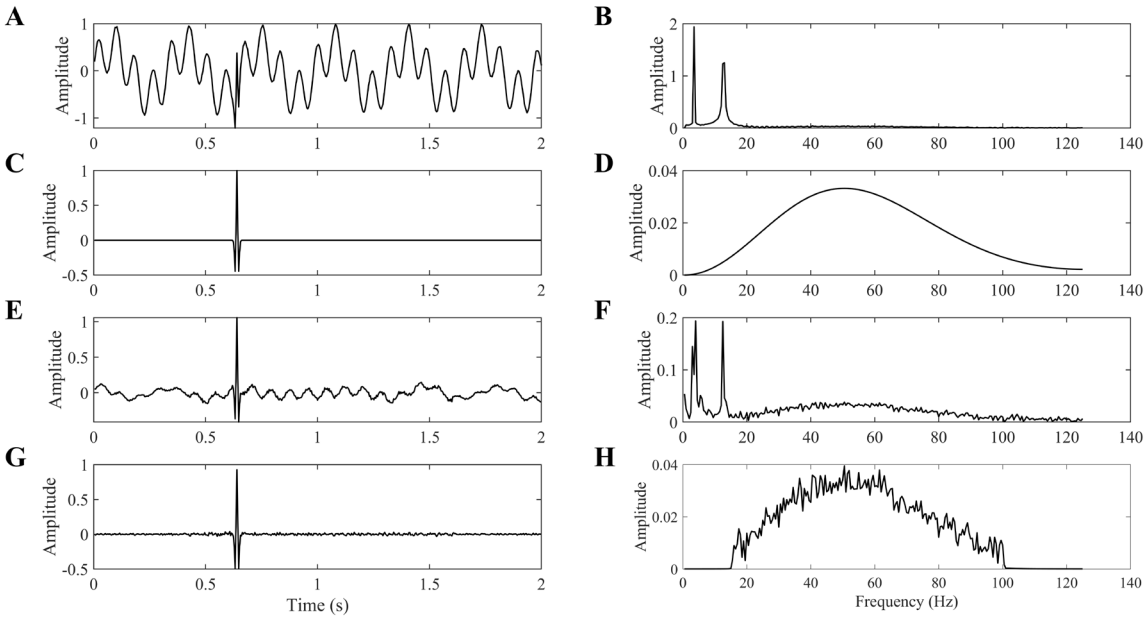

Figure 17. Denoising results for the 250 Hz sampling rate. (A) Noisy data and (B) its corresponding amplitude spectrum, (C) clean signal and (D) its corresponding amplitude spectrum, (E) periodic noise suppression result and (F) its corresponding amplitude spectrum, and (G) final denoised result and (H) its corresponding amplitude spectrum.

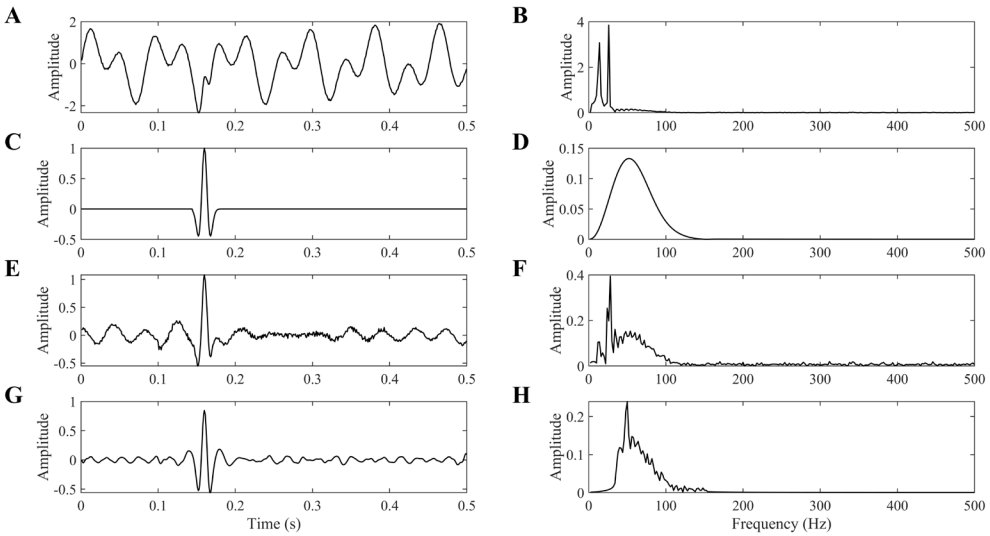

Figure 18. Denoising results for the 1,000 Hz sampling rate. (A) Noisy data and (B) its corresponding amplitude spectrum, (C) clean signal and (D) its corresponding amplitude spectrum, (E) periodic noise suppression result and (F) its corresponding amplitude spectrum, and (G) final denoised result and (H) its corresponding amplitude spectrum.

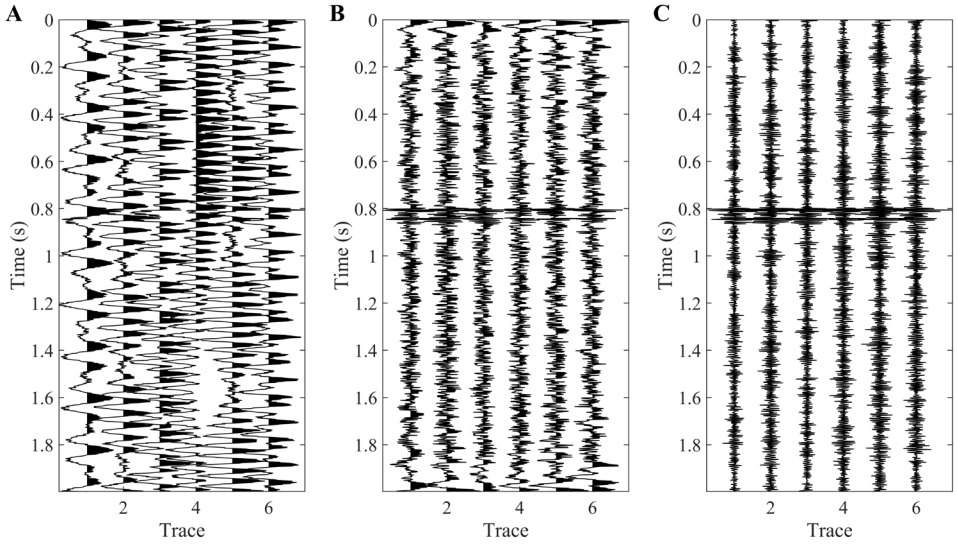

Figure 19. Processing of multi-channel simulated data using the adaptive spectral segmentation method. (A) Original microseismic data, (B) results after periodic noise suppression, and (C) denoising results obtained using the adaptive empirical Fourier decomposition method.

100–200 Hz range (occurrence frequency: 83%). Based on this statistical pattern, a uniform 100–200 Hz band-pass filter was applied to the preliminary ASS results of all traces, yielding the final multi-trace denoising result, as shown in Figure 19C.

The denoising results from different methods are compared in Figure 20. Although EMD, EEMD, VMD, and WPD methods can suppress background noise to some extent, their denoising results still retain significant periodic and random noise components, leading to insufficient clarity and continuity of the effective signals. The quantitative comparison results are shown in Figure 21. The ASS method maintains the highest output SNR and lowest MSE across all SNR levels, attributable to its adaptive signal decomposition, which more accurately distinguishes effective signal characteristics from noise.

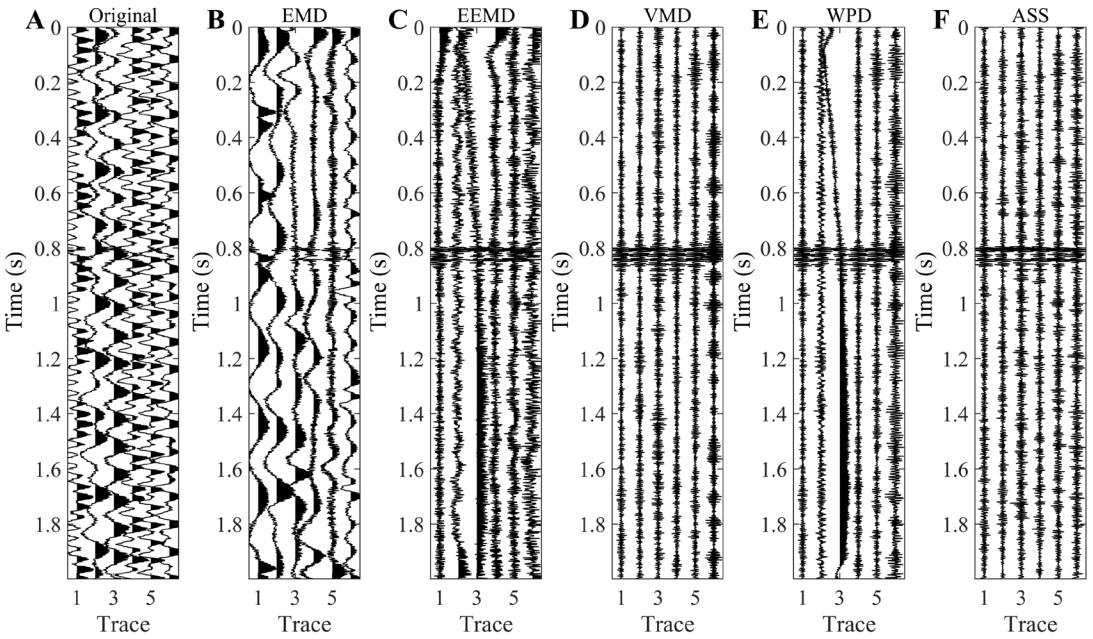

Figure 20. Comparison of denoising results obtained using different methods. (A) Original data, (B) EMD results, (C) EEMD results, (D) VMD results, (E) WPD results, and (F) ASS results.
Abbreviations: ASS: Adaptive spectral segmentation; EEMD: Ensemble empirical mode decomposition; EMD: Empirical mode decomposition; VMD: Variational mode decomposition; WPD: Wavelet packet decomposition.

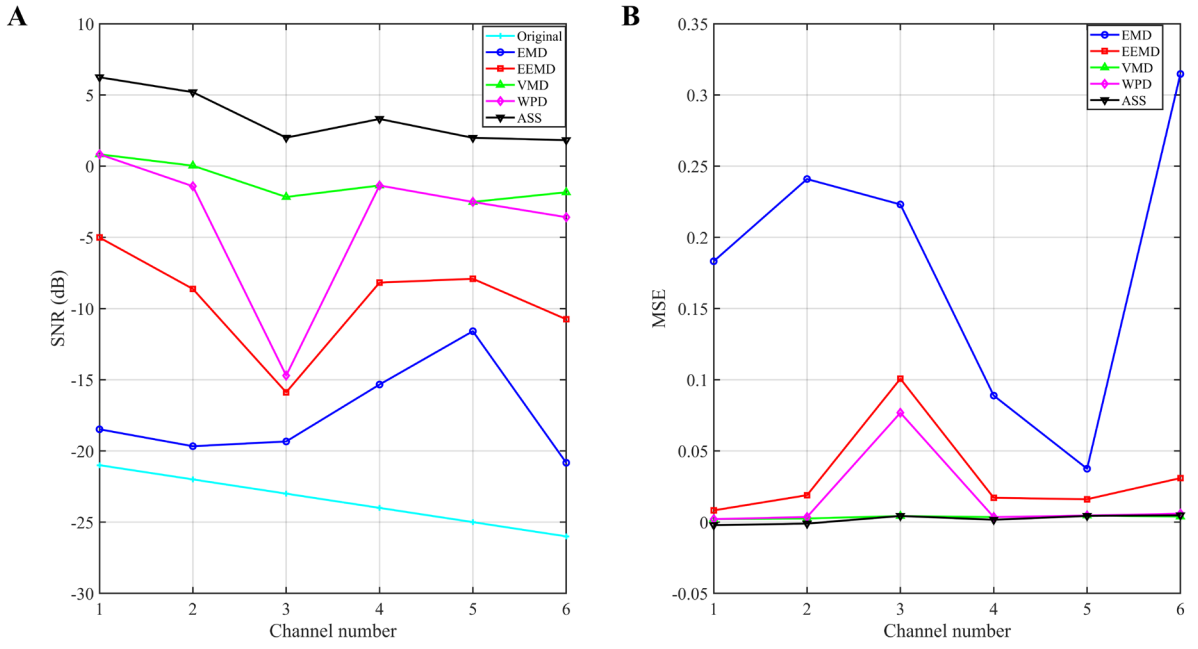

Figure 21. Comparison of (A) signal-to-noise ratio and (B) mean squared error results obtained using different denoising methods.
Abbreviations: ASS: Adaptive spectral segmentation; EEMD: Ensemble empirical mode decomposition; EMD: Empirical mode decomposition; VMD: Variational mode decomposition; WPD: Wavelet packet decomposition.

To comprehensively evaluate computational efficiency, we recorded the average processing time for single-trace data (2 s, 500 Hz sampling rate, 1,000 sampling points) across 100 independent runs. Although the ASS method requires slightly more single-trace processing time than VMD due to the RSM preprocessing step, it possesses a decisive efficiency advantage in multi-channel applications: when processing batches of microseismic data from the same region, representative effective signal frequency bands can be statistically derived from preliminary multi-trace analysis. This frequency range can then be applied for rapid band-pass filtering of subsequent data.

In this experiment, complete ASS processing for the first trace took 0.15 s, statistical analysis of the common frequency band took 0.05 s, and rapid filtering for each subsequent trace took 0.01 s, yielding a total time of 0.25 s for six traces. This represents a 72% reduction in total processing time compared to independent ASS processing (0.90 s), 67% versus EMD (0.76 s), 65% versus EEMD (0.72 s), 63% versus WPD (0.61 s), and 58% versus VMD (0.60 s). Furthermore, the common frequency band determined by majority rule enables identification and correction of abnormal traces, enhancing reliability in practical monitoring.

3.2. Processing of field data

The measured data used in this study were collected from a hydraulic fracturing unconventional oil and gas extraction area in southwestern China, with a sampling rate of 500 Hz. To conduct an in-depth analysis of microseismic signal characteristics, a segment of fracturing microseismic data from one well was selected. Multi-channel waveform data containing the effective fracturing signal period (mainly concentrated between 0.9–1.1 s) were extracted for analysis (Figure 22A). Affected by various interferences such as environmental noise, fracturing equipment vibration, and human activities, the data exhibit an extremely low SNR, with effective signals being strongly masked and accompanied by noticeable periodic noise. The estimated SNR of the field microseismic data used in this analysis ranges from approximately –15 dB to –5 dB.

The proposed ASS method was employed to process this adjacent multi-channel microseismic data. The specific steps include: (i) using the RSM to suppress periodic noise; (ii) applying AEFD to partition the signal in the frequency domain (with the adaptive determination of $K = 4$ based on the 500 Hz sampling rate); and (iii) screening effective components for reconstruction based on the adaptive Gini threshold.

During the processing of the nine adjacent channels, some channels—due to complex noise composition—resulted in suboptimal AEFD spectral partitioning, making it difficult to clearly identify the effective signal's phase axis (Figure 22C). To address this issue, by statistically analyzing the effective frequency bands determined by the Gini coefficient from each channel, it was found that the 1–35 Hz range was the most common overlapping band (seven times, 77.8%). Based on this statistical result, a uniform 1–35 Hz band-pass filter was applied to all channel data. The corrected results are shown in Figure 22D. This correction strategy effectively enhanced the overall noise suppression performance and waveform consistency.

To further validate the effectiveness of the ASS method, the processing results were compared with those from three traditional methods: EMD, EEMD, VMD, and WPD. The comparison results are shown in Figure 23. The comparative analysis based on Figure 23 indicates that the ASS method has a clear advantage in suppressing both periodic and random noise, enabling more distinct recovery of effective signals. In contrast, under the same conditions, the traditional methods still exhibit residual noise and poorer signal continuity. This demonstrates that while traditional methods possess some noise suppression capability, their adaptive decomposition ability is limited when dealing with low-SNR, complex noise backgrounds in real-world microseismic data, making it difficult to achieve reliable and effective signal extraction.

To quantitatively evaluate the denoising performance of different methods on the same field dataset, we conducted a comparative analysis using P-wave first arrival picking as an objective metric. The short-term average/long-term average algorithm[26] was applied to the denoised results from each method to automatically detect P-wave arrivals, with a short-term window length of 40 samples and a long-term window length of 80 samples. The picking errors were then calculated by comparing these automated picks with the manually picked reference arrivals, with the statistical results summarized in Table 5.

Table 5. Quantitative comparison of P-wave arrival picking errors for different denoising methods

Method	Mean absolute error (ms)
EMD	272
EEMD	80
VMD	190
WPD	247
ASS	15

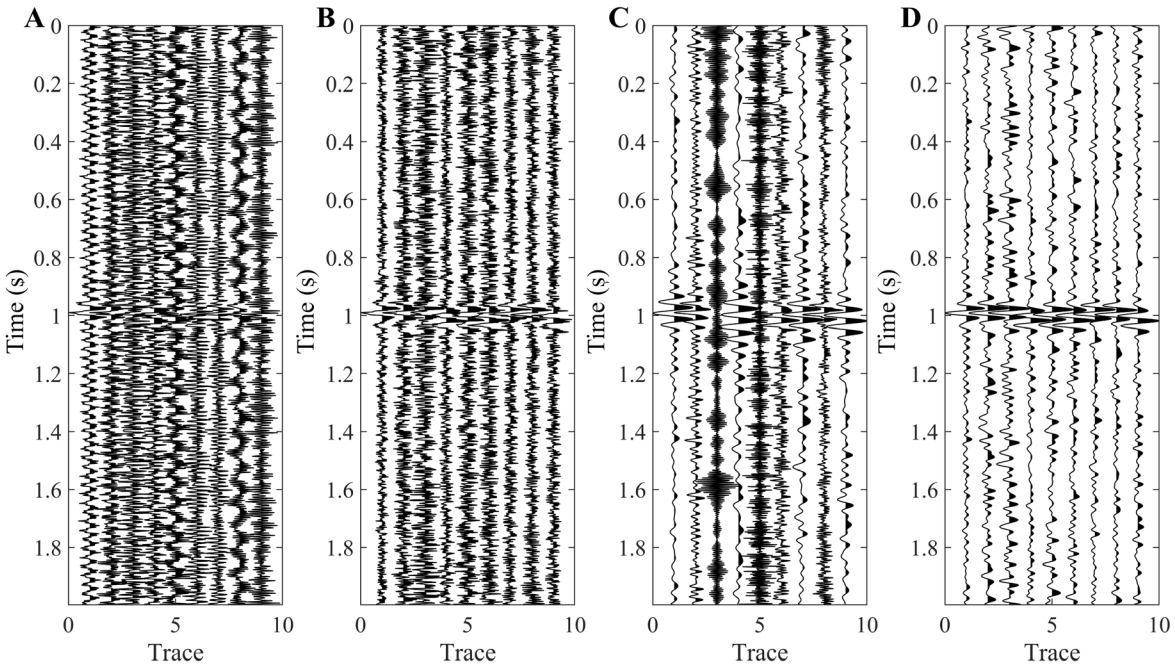

Figure 22. Processing of field data using the adaptive spectral segmentation method. (A) Original microseismic data, (B) results after periodic noise suppression, (C) denoising results obtained using the adaptive empirical Fourier decomposition method, and (D) results after applying appropriate filtering.

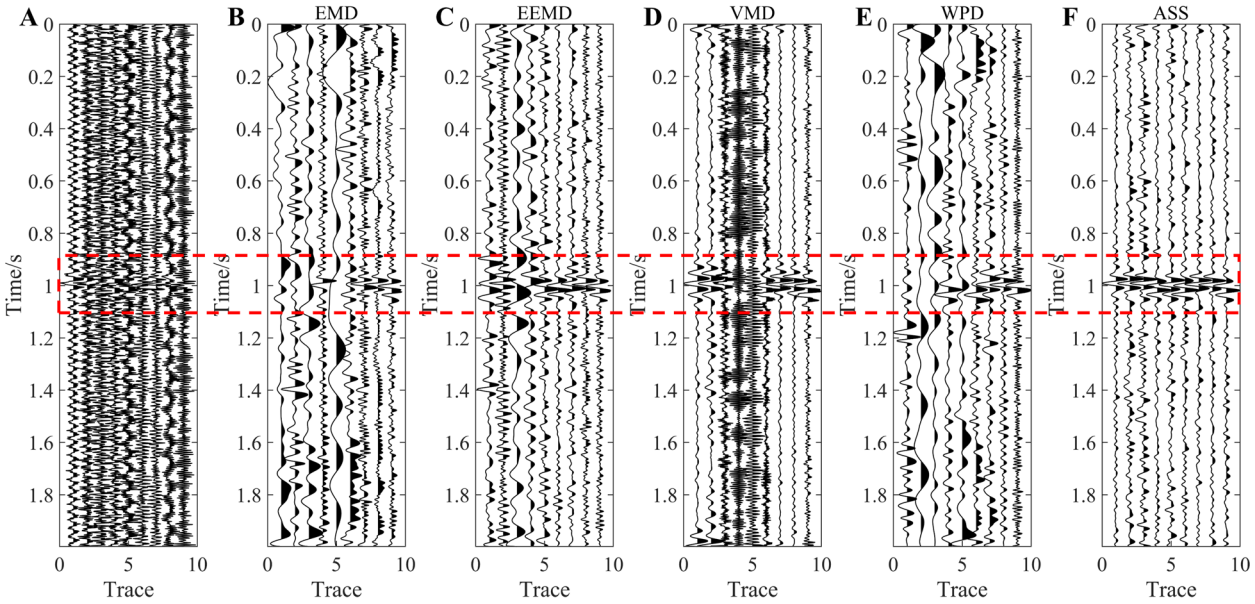

Figure 23. Comparison of denoising results for field data obtained using different methods. (A) Original microseismic data, (B) EMD results, (C) EEMD results, (D) VMD results, (E) WPD results, and (F) ASS results. The red dashed boxes indicate the main distribution regions of the effective signals. Abbreviations: ASS: Adaptive spectral segmentation; EEMD: Ensemble empirical mode decomposition; EMD: Empirical mode decomposition; VMD: Variational mode decomposition; WPD: Wavelet packet decomposition.

As shown in Table 5, the ASS method achieves the highest picking accuracy, with a mean absolute error of only 15 ms. In comparison, EMD, EEMD, VMD, and WPD all exhibit significantly larger deviations. These results indicate that traditional methods suffer from either incomplete suppression of in-band noise or excessive attenuation of signal components when processing complex field data. The quantitative evidence confirms that while conventional decomposition-based methods possess some noise suppression capability, their limited adaptive decomposition capacity makes it difficult to achieve reliable signal extraction when dealing with low-SNR microseismic data characterized by complex noise backgrounds. In contrast, the ASS method demonstrates superior performance in both noise reduction effectiveness and signal fidelity.

4. Discussion

4.1. Theoretical advances beyond empirical Fourier decomposition

The AEFD method builds directly upon the EFD framework by Zhou *et al.* [18], inheriting its core philosophy of ASS based on Fourier spectrum extrema. Both methods operate in the frequency domain and construct zero-phase filter banks without predefined basis functions. However, AEFD introduces two critical advances: (i) an adaptive band number criterion (**Equation 5**) that ensures consistent physical interpretability across varying sampling rates, preventing over- or under-segmentation; and (ii) the Gini coefficient-based adaptive threshold (**Equation 9**) that enables fully automated component screening, eliminating EFD's reliance on manual inspection.

4.2. Theoretical affinities with modal decomposition methods

Beyond its EFD lineage, AEFD shares fundamental behaviors with established methods. Both VMD and AEFD implement frequency-domain filtering, yielding comparable results for clean signals with well-separated spectral peaks. However, VMD's fixed bandwidth constraints may merge adjacent peaks under noisy conditions, whereas AEFD's adaptive boundaries preserve resolution. Similarly, EMD and AEFD both pursue data-driven decomposition without prior models—EMD through time-domain sifting, whereas AEFD through frequency-domain segmentation. Both face noise-induced feature confusion: EMD suffers mode mixing from spurious extrema; AEFD is affected by spectral distortion induced by periodic noise. The RSM preprocessing in ASS addresses this shared vulnerability through deterministic subspace projection, analogous to EEMD's stochastic ensemble averaging but with deterministic guarantees.

4.3. Limitations and future directions

The proposed method's primary boundary lies in ultra-low SNR conditions (below approximately −26 dB), where signal sparsity characteristics diminish and Gini coefficient discrimination becomes unreliable. Additionally, while validated against periodic and Gaussian noise, robustness against impulsive noise remains unverified due to its sparsity similarity to effective signals.

Future work should focus on: (i) integrating deep learning for enhanced ultra-low SNR detection; (ii) developing robust strategies for impulsive and non-stationary noise; and (iii) validating across diverse scenarios (e.g., natural seismicity, mining microseismicity) to establish the boundaries of generalization.

5. Conclusion

This study addresses the challenges of severe background noise interference, low SNR, and difficulties in real-time processing of microseismic monitoring data. An ASS-based method for microseismic signal extraction is proposed, with the following main achievements:

(i) RSM was employed to construct a periodic subspace projection, effectively identifying and removing periodic noise such as power frequency interference and mechanical vibrations from microseismic data. This avoids interference from discrete spectral peaks in subsequent frequency band segmentation, providing a clean spectral foundation for further processing.

(ii) An adaptive frequency band number determination criterion based on the sampling rate was established, using the characteristic frequency bandwidth unit of microseismic signals for spectral segmentation. This overcomes the limitation of fixed frequency band numbers in traditional EFD. By optimizing frequency band boundaries in conjunction with spectral maxima, the segmentation accuracy and adaptability to signals are improved.

(iii) The Gini coefficient was introduced as a measure of component sparsity, and an adaptive threshold screening criterion based on statistical distribution was established. This enables automatic discrimination and reconstruction of noise components and effective signal components, avoiding the subjectivity of manual judgment and enhancing the level of automation of the method.

(iv) For real-time application scenarios such as fracturing monitoring, a unified filtering method based on statistically overlapping frequency bands is proposed. By determining a common effective frequency band through preliminary multi-channel data analysis,

rapid band-pass filtering of subsequent data is achieved. This significantly improves computational efficiency while ensuring processing consistency, with a total processing efficiency improvement of up to 72%.

The method proposed in this study is primarily designed for microseismic monitoring data in hydraulic fracturing. Its applicability to different scenarios, such as natural earthquakes, mine microseismicity, and geothermal development, requires further validation with more measured data. Additionally, its effectiveness in suppressing non-periodic narrowband noise (e.g., environmental interference at specific frequencies) warrants further testing.

Acknowledgments

None.

Funding

This work was supported by the Natural Science Foundation of Shandong Province (Youth Project) (Grant No. ZR2023QD038): "Dynamic Response Characteristics of Surrounding Rock in Large-Height Fully-Mechanized Mining Roadways under Hard-Thick Strata and Mechanism of Pressure Relief by Deep-Hole Presplitting Blasting."

Conflict of interest

The authors have no conflicts to disclose.

Author contributions

Conceptualization: Mingyang Chang, Huairui Su
Formal analysis: Mingyang Chang, Xiankai Wang
Investigation: Wenwu Zhou, Ziyi Na
Methodology: Mingyang Chang, Fuwu Ma
Supervision: Huairui Su, Yang Li
Validation: Mingyang Chang
Visualization: Xiankai Wang, Ziyi Na
Writing–original draft: Mingyang Chang
Writing–review & editing: Wenwu Zhou, Huairui Su, Fuwu Ma

Availability of data

Data supporting the findings of this study are available from the corresponding author upon reasonable request.

References

1. Shu H, Dawod AY. Microseismic monitoring signal waveform recognition and classification: review of contemporary techniques. *Appl Sci*. 2023;13(23):12739.

doi: 10.3390/app132312739

2. Zeng Z, Zhang D, Han P, *et al*. A review of microseismic source location techniques in underground mining. *MetaResource*. 2025;2(3):157-181.

doi: 10.23919/METAR.2025.000011

3. Li J, Stankovic L, Pytharouli S, Stankovic V. Automated platform for microseismic signal analysis: denoising, detection, and classification in slope stability studies. *IEEE Trans Geosci Remote Sens*. 2020;59(9):7996-8006.

doi: 10.1109/TGRS.2020.3032664

4. Ma H, Qian Z, Li Y, Lin H, Shao D, Yang B. Noise reduction for desert seismic data using spectral kurtosis adaptive bandpass filter. *Acta Geophys*. 2019;67(2):123-131.

doi: 10.1007/s11600-018-0232-0

5. Feng Z. Robust ground roll noise suppression based on dictionary learning and bandpass filtering. *IEEE Geosci Remote Sens Lett*. 2021;19:1-5.

doi: 10.1109/LGRS.2021.3107722

6. Donatus IB, Theopilus A. Noise reduction and signal estimation for 5G antenna using least mean square (LMS) algorithm and Kalman filter. *Int J Latest Technol Eng Manag Appl Sci*. 2026;15(1):246-264.

doi: 10.51583/IJLTEMAS.2026.150100019

7. Lin J, Du Y, Qiu Y, Lin Z, Huang B, Tong B. Implementation of an LMS adaptive noise filter with automated parameter configuration. In: *Proceedings of the 2025 5th International Conference on Communication Technology and Information Technology (ICCTIT)*; December 26-28, 2025; Guangzhou, China. IEEE; 2025:207-212.

doi: 10.1109/ICCTIT68197.2025.11406624

8. Yang Y, Nagayama T, Xue K. Structure system estimation under seismic excitation with an adaptive extended Kalman filter. *J Sound Vib*. 2020;489:115690.

doi: 10.1016/j.jsv.2020.115690

9. Xu R, Feng B, Wang H, Wu C, Nie Z. Nonlinear seismic signal denoising using template matching with time difference detection method. *Remote Sens*. 2025;17(4):674.

doi: 10.3390/rs17040674

10. Fang W, Fu L, Li H. Unsupervised CNN based on self-similarity for seismic data denoising. *IEEE Geosci Remote Sens Lett*. 2021;19:1-5.

doi: 10.1109/LGRS.2021.3131046

11. Liu L, Song W, Zeng C, Yang X. Microseismic event detection and classification based on convolutional neural network. *J Appl Geophys*. 2021;192(6):104380.

doi: 10.1016/j.jappgeo.2021.104380

12. Long L, Wen X, Lin Y. Denoising of seismic signals based on empirical mode decomposition-wavelet thresholding. *J Vib Control*. 2021;27(3-4):311-322.

doi: 10.1177/1077546320926846

13. Peng K, Guo H, Shang X. EEMD and multiscale PCA-based signal denoising method and its application to seismic P-phase arrival picking. *Sensors*. 2021;21(16):5271.

doi: 10.3390/s21165271

14. Qiao Y, Li Q, Qian H, Song X. Seismic signal denoising method based on CEEMD and improved wavelet threshold. In: *IOP Conference Series: Earth and Environmental Science*. 2nd International Conference on Geology, Resources Exploration and Development; January 15-17, 2021; Zhuhai, China. IOP Publishing; 2021;671(1):012036.

doi: 10.1088/1755-1315/671/1/012036

15. Sun M, Li Z, Li Z, Li Q, Liu Y, Wang J. A noise attenuation method for weak seismic signals based on compressed sensing and CEEMD. *IEEE Access*. 2020;8:71951-71964.

doi: 10.1109/ACCESS.2020.2982908

16. Yao X, Zhou Q, Wang C, Hu J, Liu P. An adaptive seismic signal denoising method based on variational mode decomposition. *Measurement*. 2021;177(2):109277.

doi: 10.1016/j.measurement.2021.109277

17. Liu W, Liu Y, Li S, Chen Y. A review of variational mode decomposition in seismic data analysis. *Surv Geophys*. 2022;44(2):323-355.

doi: 10.1007/s10712-022-09742-z

18. Zhou W, Feng Z, Xu YF, Wang X, Lv H. Empirical Fourier decomposition: an accurate signal decomposition method for nonlinear and non-stationary time series analysis. *Mech Syst Signal Process*. 2022;163(9):108155.

doi: 10.1016/j.ymssp.2021.108155

19. Zhu D, Liu G, Wu X, Yin B. An enhanced empirical Fourier decomposition method for bearing fault diagnosis. *Struct Health Monit*. 2024;23(2):903-923.

doi: 10.1177/14759217231178653

20. Vaidyanathan PP. Ramanujan sums in the context of signal processing—Part I: fundamentals. *IEEE Trans Signal Process*. 2014;62(16):4145-4157.

doi: 10.1109/TSP.2014.2331617

21. Vaidyanathan PP. Ramanujan sums in the context of signal processing—Part II: FIR representations and applications. *IEEE Trans Signal Process*. 2014;62(16):4158-4172.

doi: 10.1109/TSP.2014.2331624

22. Wang X, Zhang J, Huang Z. A Ramanujan subspace and dynamic time warping and adaptive singular value decomposition combined denoising method for low signal-to-noise ratio surface microseismic monitoring data in hydraulic fracturing. *Geophys Prospect*. 2025;73(1):251-265.

doi: 10.1111/1365-2478.13634

23. Huang W, Wang R, Li H, Chen Y. Unveiling the signals from extremely noisy microseismic data for high-resolution hydraulic fracturing monitoring. *Sci Rep*. 2017;7(1):11996.

doi: 10.1038/s41598-017-09711-2

24. Chen C, Xu W, Dai J, Zhou Y, Zhang Y. Performance analysis of Gini correlator for detecting known signals in impulsive noise. *IEEE Access*. 2019;7:153300-153316.

doi: 10.1109/ACCESS.2019.2948403

25. Albezzawy MN, Nassef MG, Sawalhi N. Rolling element bearing fault identification using a novel three-step adaptive and automated filtration scheme based on Gini index. *ISA Trans*. 2020;101:453-460.

doi: 10.1016/j.isatra.2020.01.019

26. Stevenson PR. Microearthquakes at Flathead Lake, Montana: a study using automatic earthquake processing. *Bull Seismol Soc Am*. 1976;66(1):61-80.

doi: 10.1785/BSSA0660010061

ACCSCIENCE PUBLISHING

Journal of Seismic Exploration

ARTICLE

Properties of fluids under multiphysical coupling and frequency-dependent rock physics modeling

Lujia Ma[1], Guangtan Huang[2]*, Zhennan Yu[2], Haiyu Li[3], and Mingliao Wu[3]

[1]School of Earth Sciences and Engineering, Hohai University, Nanjing, Jiangsu, China

[2]The State Key Laboratory of Geomechanics and Geotechnical Engineering, Institute of Rock and Soil Mechanics, Chinese Academy of Sciences, Wuhan, Hubei, China

[3]The Key Laboratory of Exploration Technology for Oil and Gas Resources of Ministry of Education, College of Geophysics and Petroleum Resources, Yangtze University, Wuhan, Hubei, China

Abstract

In fluid underground storage and seismic monitoring, accurately characterizing the physical properties of fluid-bearing rocks under multiphysical coupling is crucial. However, in deep geological environments, fluids often exist in a supercritical state with highly nonlinear acoustic properties. Moreover, most existing models lack a unified framework for multiple gas types, often treating fluid properties as constants, which does not adequately reflect their actual state. This study proposes a method for constructing a frequency-dependent rock physics model for fluid-bearing rocks. Three equations of state were used to calculate the density, bulk modulus, and acoustic velocity of carbon dioxide, methane, and hydrogen, which were then compared with reference data from the National Institute of Standards and Technology. The properties of brine under varying temperature and pressure conditions were derived from the Batzle–Wang model, and the properties of mixed fluids were obtained using Wood's equation, before being integrated into a sandstone matrix. To account for inelastic behavior, the Johnson and White models were applied to analyze the effects of fluid distribution on compressional wave velocity and the attenuation factor under different conditions. The results show that the acoustic properties of fluids are significantly influenced by phase changes. This frequency-dependent rock physics model improves upon most conventional models that treat fluid properties as fixed constants, enabling more accurate calculation of acoustic properties in deep environments. It thus provides a theoretical basis for underground fluid storage and monitoring in practical applications.

Keywords: Multiphysical coupling; Supercritical fluids; Equations of state; Geological storage of carbon dioxide/methane/hydrogen; Johnson model; White model

***Corresponding author:**
Guangtan Huang
(gthuang@whrsm.ac.cn)

Citation: Ma L, Huang G, Yu Z, Li H, Wu M. Properties of fluids under multiphysical coupling and frequency-dependent rock physics modeling. *J Seismic Explor.* 2026;35(3):026070033. doi: 10.36922/JSE026070033

Received: February 13, 2026

Revised: March 26, 2026

Accepted: April 2, 2026

Published online: May 15, 2026

Copyright: © 2026 Author(s). This is an Open-Access article distributed under the terms of the Creative Commons Attribution License, permitting distribution, and reproduction in any medium, provided the original work is properly cited.

Publisher's Note: AccScience Publishing remains neutral with regard to jurisdictional claims in published maps and institutional affiliations.

1. Introduction

Energy security and the sustainable development of the ecological environment are global issues. Over the past 150 years, the increase in atmospheric carbon dioxide (CO_2) concentration has contributed to a global average temperature rise of 0.3–0.6

°C.[1] The construction of a new energy system urgently requires vigorous development of renewable energy and effective management of carbon emissions. In this context, utilizing underground geological formations for the large-scale sequestration and storage of CO_2, methane (CH_4), and hydrogen (H_2) has become a key technological pillar supporting the energy transition, ensuring energy security, and achieving deep decarbonization. Among these, CO_2 geological sequestration stands as one of the most feasible and scalable technological pathways for serving global carbon neutrality goals.[2] Underground CH_4 gas storage represents the most mature and largest-scale practice of underground energy storage today, directly contributing to energy security.[3] As a clean and renewable energy source, hydrogen plays a significant role in the global energy transition.[4] Underground H_2 storage is a strategic technology for the future hydrogen-based society, offering clean energy solutions in sectors such as transportation and power generation, and enabling large-scale reductions in greenhouse gas emissions.

However, the effective implementation of these underground energy storage technologies relies on accurate monitoring of the distribution and migration of the sequestered fluids. The key to achieving this monitoring lies in establishing robust rock physics models, which must fully consider the influence of the supercritical state on fluid properties and be capable of characterizing the differences in acoustic properties among the three gases. In early rock physics, research on the propagation of elastic waves in fluid-containing porous media was primarily based on the assumption of macroscopic homogeneity. Biot[5] first provided a theoretical framework for elastic wave propagation in fluid-saturated porous media, analyzing the acoustic characteristics of fluid-saturated porous permeable media. The work of Batzle and Wang[6] provided a reliable quantitative calculation method for the acoustic properties of hydrocarbon gases, crude oil, and brine. Murphy[7] verified that the Wood's[8] equation can be used to calculate the effective modulus of two-phase fluids. In the study of wave propagation in porous media, White[9] first introduced the concept of mesoscopic heterogeneity. Johnson[10] then provided a closed-form analytical expression to approximate frequency-dependent physical quantities in fluid-saturated porous media.

Regarding underground fluid modeling for storage, Picotti *et al.*[11] and Carcione *et al.*[12] calculated gas properties using equations of state (EoS) and analyzed changes in seismic response before and after CO_2 injection. The former described the seismic characteristics of reservoir rocks saturated with CO_2, CH_4, and brine, while the latter constructed an integrated model capable of predicting changes in seismic signals following CO_2 injection. In terms of field measurements and experimental studies, Wang *et al.*[13] and Oldenburg[14] noted that the phase changes of CO_2 and its injection can lead to significant changes in pore pressure and density. Xue *et al.*[15] found that injecting gaseous CO_2 into a reservoir significantly alters the seismic wave attributes of the reservoir. Daniele *et al.*[16] suggested that within rock–brine and hydrogen storage systems, the structural and trapping capacity of H_2 reservoirs is generally higher than that of CO_2 and CH_4 reservoirs. Carcione *et al.*[17] emphasized that obtaining accurate acoustic property data is crucial for implementing underground storage and monitoring. Depleted reservoirs and saline aquifers possess the potential for the required storage capacity. Meanwhile, Heinemann *et al.*[18] indicated that in studies on storing H_2 in such reservoirs, gas injection should be conducted under supercritical pressure to avoid the presence of a gaseous phase. Ali *et al.*[19] further highlighted that due to its thermodynamic properties, such as specific heat capacity and entropy, H_2 becomes a practical energy source in many industrial applications.

While previous research has achieved significant progress, applying rock physics models to the practical monitoring of multiple gas storage (e.g., CO_2, CH_4, and H_2) still faces several core challenges. Firstly, regarding the accurate calculation of complex fluid acoustic properties, when fluids are in deep geological environments, CO_2 and CH_4 tend to exist in a supercritical state, whereas H_2 generally does not. This leads to highly nonlinear acoustic behaviors, making it difficult to determine their precise property parameters.[20] Secondly, traditional EoS exhibit significant errors when calculating properties such as density and bulk modulus, which directly impact the reliability of input parameters for subsequent rock physics models and result in distorted seismic response predictions.[21] Furthermore, most existing rock physics models are developed for specific single gases, such as CO_2 storage or CH_4 exploration scenarios.[22] There is a lack of a unified modeling framework, and fluid parameters are often treated as constants within the models. This significantly reduces the models' adaptability to varying environmental conditions and prevents a systematic comparison and prediction of the differences in seismic responses among the three key gases—CO_2, CH_4, and H_2—under varying depths, temperature–pressure conditions, and different patch morphologies.

Based on the aforementioned background and challenges, this study aims to develop a systematic, accurate, and universally applicable frequency-dependent rock physics model. First, by comparing the van der Waals EoS, the Peng–Robinson EoS, and its modified form

(MPR EoS) for calculating the acoustic properties of CO_2, CH_4, and H_2—and validating them against the National Institute of Standards and Technology (NIST) database—the most accurate EoS is selected to simulate the P-wave velocity, density, and viscosity of gases under varying temperature and pressure conditions corresponding to depth. Subsequently, the Batzle–Wang model is employed to calculate the seismic P-wave velocity, density, and viscosity of brine. The three gases are then mixed with brine to simulate the actual fluid mixture in rock pores, and Wood's[8] equation is used to derive the equivalent P-wave velocity, density, and viscosity of the mixed fluid.

To capture the inelastic behavior of the rock, the Johnson model is introduced for analysis, with the seismic frequency set to 30 Hz. For comparison, the White model is also applied to systematically examine the suitability of both models in describing fluid states in deep geological environments and to provide practical criteria for selecting between them in real reservoir scenarios. This research not only offers a unified rock physics framework for modeling the underground storage of CO_2, CH_4, and H_2, but also provides theoretical references and practical recommendations for selecting seismic interpretation and monitoring models tailored to different reservoir conditions.

2. Gas acoustic properties

In the calculation of thermodynamic properties of gases, the primary factors are temperature and pressure. However, as these vary with formation depth, a constant geothermal gradient G may be adopted to quantitatively describe the changes in temperature and pressure with depth. The change in temperature can be expressed as:

$$T_c = \mathrm{T}_0 + \mathrm{G}\,z \tag{1}$$

where z represents formation depth, T_c denotes the temperature at depth, and T_0 denotes the surface temperature (at zero depth), with an average surface temperature of approximately 15 °C. Therefore, in this study, T_0 = 15 °C. Similarly, for the constant geothermal gradient G, its common value ranges between 20–30 °C/km. For computational convenience, G = 30 °C/km is adopted in this study.

Regarding pore pressure, it is primarily influenced by depth, lithology, fluid properties, and geological structure. For simplicity, we adopt the hydrostatic pressure assumption, expressed as:

$$P_c = \mathrm{P}_0 + \mathrm{P}_\mathrm{b}\mathrm{g}z \tag{2}$$

where P_c represents the pore pressure at depth z, P_0 is the standard atmospheric pressure, P_b is the average brine density from the surface to depth z, and g is the gravitational acceleration.

In this study, P_b = 1,030 kg/m^3 and g = 9.8 m/s^2. This approach allows for the determination of the values of temperature and pressure—the two factors exerting the most significant influence on thermodynamic properties—as they vary with depth.

Once temperature and pressure are determined, the thermodynamic parameters of supercritical-state fluids—such as those of CO_2, CH_4, and H_2—can generally be calculated using the van der Waals EoS.[23] Although experimental measurements can also be employed to obtain these thermodynamic parameters,[24] this study focuses on computational modeling approaches. The VDW equation is expressed as:

$$P_c = \frac{\mathrm{R}T_c}{V\text{-}\mathrm{b}} - \frac{\mathrm{a}}{V^2} \tag{3}$$

where P_c represents the gas pressure, V is the molar volume (in m^3/mol), R is the universal gas constant (taken here as R = 8.31 J/mol), and a and b are the attraction and repulsion parameters, respectively, which depend primarily on the specific compound.[25] The parameters a and b are further defined as follows:

$$\mathrm{a} = \frac{\mathrm{R}^2\mathrm{T}_{\mathrm{cr}}{}^2}{\mathrm{P}_{\mathrm{cr}}}\Omega_\mathrm{a} \tag{4}$$

$$\mathrm{b} = \frac{\mathrm{R}\mathrm{T}_{\mathrm{cr}}}{\mathrm{P}_{\mathrm{cr}}}\Omega_\mathrm{b} \tag{5}$$

where T_{cr} and P_{cr} represent the critical temperature and critical pressure of the gas, respectively, and $\Omega_\mathrm{a} = 0.4218$ and $\Omega_\mathrm{b} = 0.125$ are dimensionless constants specific to the EoS. For this gas EoS, the molar volume of the gas in **Equation 3** can be solved by simultaneously applying **Equations 1–5**.

Saffari and Zahedi[26] proposed a modified version of the cubic EoS, known as the corrected Peng–Robinson equation (CPR). Unlike the VDW equation, CPR introduces a temperature-dependent term α into the attraction parameter a, making it a function of temperature rather than a constant. This modification significantly improves predictions of vapor pressure and liquid density. Furthermore, by incorporating the acentric factor to account for molecular polarity differences, CPR achieves markedly higher accuracy in describing vapor–liquid equilibrium compared to VDW. As a result, it

has become a widely adopted basis for many industrial calculations. The general form of the CPR equation is as follows:

$$P=\frac{\mathrm{R}T_c}{(V\text{-b})}-\frac{\mathrm{a}\alpha(T_c)}{V^2+2V\mathrm{b}-\mathrm{b}^2} \tag{6}$$

$$T_r=\frac{T_c}{\mathrm{T_{cr}}} \tag{7}$$

$$\alpha(T_c)=(1+\mathrm{m}[(1-\sqrt{(T_r)})]^2 \tag{8}$$

$$\mathrm{m}=\begin{cases}0.37464+1.54226\omega-0.26992\omega^2 & \omega\le 0.49\\ 0.379642+1.487503\omega+0.164423\omega^2 & \\ +0.016666\omega^3 & \omega>0.49\end{cases} \tag{9}$$

where $\alpha(T_c)$ is a dimensionless temperature-dependent correction factor introduced to improve vapor pressure predictions, T_r is the reduced temperature, and ω is the acentric factor.

In contrast to such EoS, Hekayati *et al.*[27] proposed a more advanced computational approach. Instead of modifying the form of **Equation 6**, this method identifies new, more precise α functions for different gases to replace the generic α function. The specific forms are as follows, for CO_2:

$$\alpha(T_c)=\mathrm{A_1}+\ln(P_r)(\mathrm{A_2}+\mathrm{A_3}\ln(T_r)-\mathrm{A_4}\ln(T_r^2)-\mathrm{A_5}\sin(\mathrm{A_6}\ln(P_r^2)-\mathrm{A_7}\sin(\ln(T_r)) \tag{10}$$

where

$$P_r=\frac{P_c}{\mathrm{P_{cr}}} \tag{11}$$

For CH_4 and H_2, α can be written as:

$$\alpha(T_c)=\exp\left(\mathrm{B_1}T_r+\mathrm{B_2}\ln(T_r)+\mathrm{B_3}\left(1-\sqrt{T_r}\right)\right) \tag{12}$$

where $\mathrm{A_1}=1.0010$, $\mathrm{A_2}=0.0524$, $\mathrm{A_3}=0.2315$, $\mathrm{A_4}=0.1286$, $\mathrm{A_5}=0.3258$, $\mathrm{A_6}=0.0704$, $\mathrm{A_7}=0.9461$, $\mathrm{B_1}=0.039$, $\mathrm{B_2}=0.0473$, and $\mathrm{B_3}=0.8514$. It is important to note that, in order to distinguish between the two computational methods, the algorithm is classified as follows: if $\alpha(T_r)$ in **Equation 6** adopts the form given in **Equation 9**, the method is referred to as the CPR algorithm; if $\alpha(T_r)$ is determined by solving **Equations 11** and **12** simultaneously, the method is termed the MPR algorithm. By solving the above system of equations, the molar volume of the target gas can be obtained. The mass density of the gas is then given by:

$$\rho_g=\frac{\mathrm{M}}{V} \tag{13}$$

where M is the molar mass and V represents the molar volume of the gas, obtained by solving **Equations 1–5** simultaneously.

Based on the physical parameters of the three gases listed in Table 1 and the NIST Chemistry WebBook,[28] the mass density variation of the gases with depth can be calculated using the three different methods described above. The results are presented in Figure 1, which also allows for a comparison of the accuracy among these methods.

To calculate the variation of gas velocity with depth, the bulk modulus of the gas must also be determined. For acoustic waves with frequencies below approximately 1 GHz, a more physically reasonable approximation is the adiabatic compression model. This model assumes that the entropy of the gas remains essentially constant during compression.[29] The relationship between the isentropic bulk modulus and the isothermal bulk modulus is given by:

$$\mathrm{C_S}=\frac{\mathrm{G}}{\gamma} \tag{14}$$

where $\mathrm{C_s}$ represents the isentropic bulk modulus, G denotes the isothermal bulk modulus, and γ is the adiabatic index (heat capacity ratio), which primarily depends on temperature and pressure.[30] For the VDW algorithm, **Equation 3** yields:

$$K_g=\frac{\gamma}{\mathrm{G}}=\gamma\left\{\frac{V\mathrm{R}T_C}{(V\text{-b})^2}-\left(\frac{2\mathrm{a}}{V^2}\right)\right\} \tag{15}$$

For the CPR and MPR algorithms, **Equation 6** yields:

$$K_g=\frac{\gamma}{G}=\gamma\left\{\frac{V\mathrm{R}T_C}{(V\text{-b})^2}-V\left(\frac{2\mathrm{a}\alpha(V+\mathrm{b})}{V^2+2V\mathrm{b}-\mathrm{b}^2}\right)^2\right\} \tag{16}$$

After calculating K_g, the velocity and related acoustic expressions for the gas can be determined.[31] The velocity formula is given by:

$$V_g=\sqrt{\frac{K_g}{\rho_g}} \tag{17}$$

Using the velocity calculation method (**Equation 17**), the velocity curves for the three gases under the three EoS can be obtained, as shown in Figures 2–4.

For the three gases considered, their key physical properties are listed in Table 1.

Table 1. Critical properties, molar mass, and acentric factor of the three gases

Substance	T_{cr} (K)	P_{cr} (MPa)	V_{cr} (cm^3/mol)	Molar mass (g/mol)	ϖ
CO_2	304.12	7.37	94.07	44.010	0.225
CH_4	190.56	4.56	98.60	16.043	0.011
H_2	33.25	1.30	65.00	2.016	−0.2202

Abbreviations: CH_4: Methane; CO_2: Carbon dioxide; H_2: Hydrogen.

As shown in Figures 1–4, the analysis reveals that, in terms of gas density variation with depth, the mass density of CO_2 increases rapidly around 800 m before the growth rate slows down, whereas the densities of CH_4 and H_2 exhibit a steadily rising trend with overall stable growth. Regarding velocity, the velocity of CO_2 first decreases and then increases with depth. The velocity of CH_4 also shows a slight initial decrease followed by an increase, while the velocity of H_2 rises continuously and remains the highest among the three gases. Furthermore, by examining the velocity trends of the three gases, it can be observed that the CO_2 velocity profile exhibits a distinct change around 800 m. This is because CO_2 transitions into a supercritical state within this depth range, where its phase exists between gaseous and liquid states, resulting in unstable properties. Consequently, its density increases rapidly, while its velocity shows an initial decline followed by an upward trend. This pattern can be more conveniently observed in Figure 6. Meanwhile, comparative analysis indicates that the MPR algorithm demonstrates higher accuracy and better agreement with the NIST data compared to the other two algorithms.

Figure 5 shows the comparative precision of the MPR algorithm against the alternatives. It can be observed that the agreement between calculated and reference data for CO_2 and H_2 is highest when using the MPR method. For the density parameter of CH_4, the CPR algorithm yields relatively more accurate results. However, in terms of velocity prediction, the MPR algorithm exhibits the highest accuracy, showing near-perfect alignment with the NIST data. Therefore, given that the MPR algorithm achieves the highest computational accuracy for both density and velocity parameters across the three gases, it will be uniformly adopted for calculating the thermodynamic properties of gases in all subsequent analyses, ensuring both computational consistency and reliability.

Additionally, in the computational process, the specific heat ratio γ plays multiple critical roles in thermodynamic properties and influences the variation of gas velocity curves. To assess its impact on the calculation results, the specific heat ratio γ for the three gases is plotted, as shown in Figures 6–8.

As shown in Figures 6–8, the observed trend where the velocity of CO_2 initially decreases and then increases around a depth of 800 m can be attributed to variations in its heat capacity ratio. These changes indicate that CO_2 reaches its critical state at this depth, resulting in the characteristic velocity profile. Similarly, variations in the heat capacity ratios of CH_4 and H_2 also influence their respective velocity trends and the calculation of their bulk moduli.

Regarding the viscosity properties of gases, the Lohrenz–Bray–Clark model[32] was employed to model and calculate the viscosities of the three gases. The principal calculation procedure is as follows:

$$\left[(\eta_g-\eta_0)\xi+10^{-4}\right]^{0.25}=\sum_{j=0}^{4}a_j\left(\frac{\rho_g}{\rho_{cr}}\right) \tag{18}$$

$$\xi=T_{cr}^{1/6}M^{-1/2}P_{cr}^{-2/3} \tag{19}$$

$$\eta_0=\begin{cases}34\cdot10^{-5}T_r^{0.94}/\xi & T_r\le1.5\\ 17.78\cdot10^{-5}(4.58T_r-1.67)^{5/8}/\xi & T_r>1.5\end{cases} \tag{20}$$

$$\rho_{cr}=\frac{M}{V_{cr}} \tag{21}$$

where $a_0=0.10230$, $a_1=0.023364$, $a_2=0.058533$, $a_3=-0.040758$, and $a_4=0.0093324$. The results of these calculations are shown in Figure 9.

As shown in Figure 9, while minor differences exist between the Lohrenz–Bray–Clark model calculations and the NIST dataset, the overall agreement remains strong. In terms of viscosity variation with depth, the viscosities of all three gases increase as depth rises, with CO_2 exhibiting the fastest growth rate. Around 1 km depth, its rate of increase reaches a maximum and subsequently levels off.

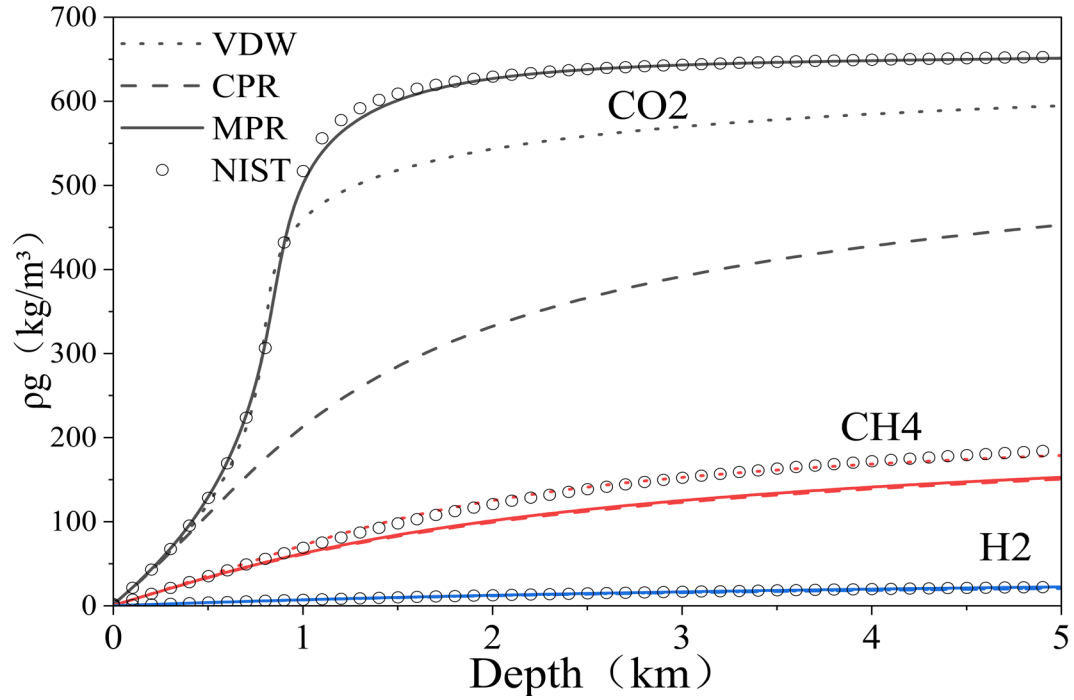

Figure 1. Graph of mass density versus depth for three gases under three equations of state. The solid lines represent the values calculated by the equations of state, whereas the circles indicate the reference data obtained from the NIST Chemistry WebBook for comparison.
Abbreviations: CH_4: Methane; CO_2: Carbon dioxide; CPR: Corrected Peng–Robinson; H_2: Hydrogen; MPR: Modified Peng–Robinson; NIST: National Institute of Standards and Technology; VDW: Van der Waals.

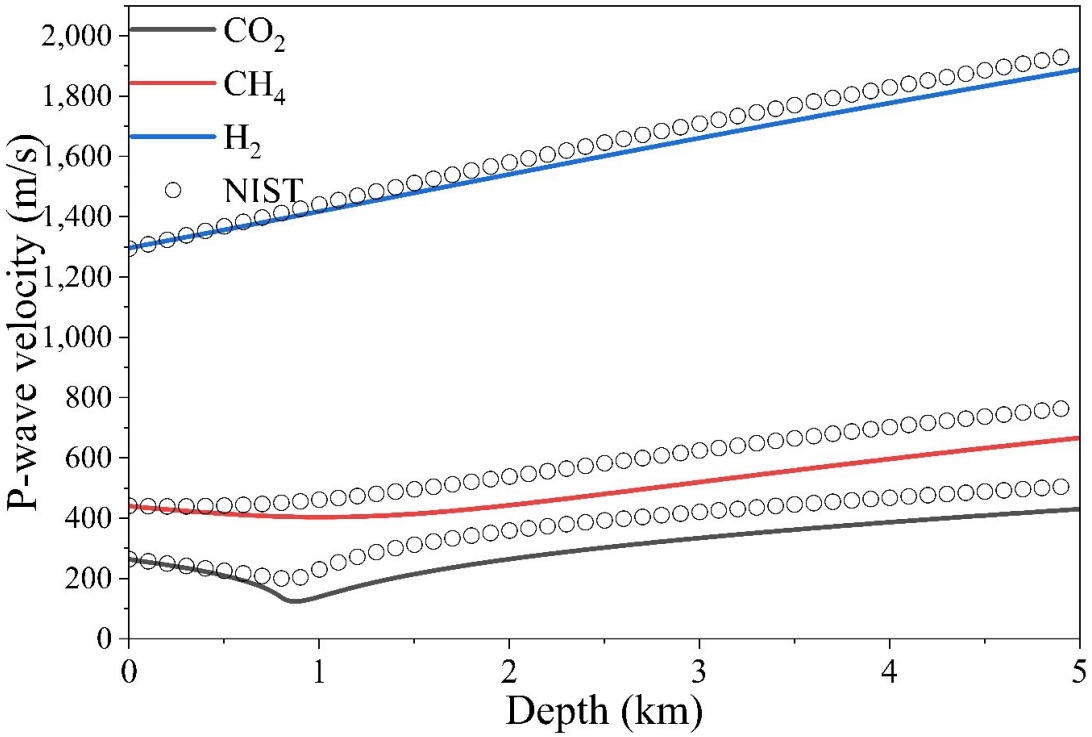

Figure 2. Graph of acoustic velocity versus depth for three gases under the van der Waals equation of state. The solid lines represent the values calculated by the equations of state, whereas the circles indicate the reference data obtained from the NIST Chemistry WebBook for comparison.
Abbreviations: CH_4: Methane; CO_2: Carbon dioxide; H_2: Hydrogen; NIST: National Institute of Standards and Technology.

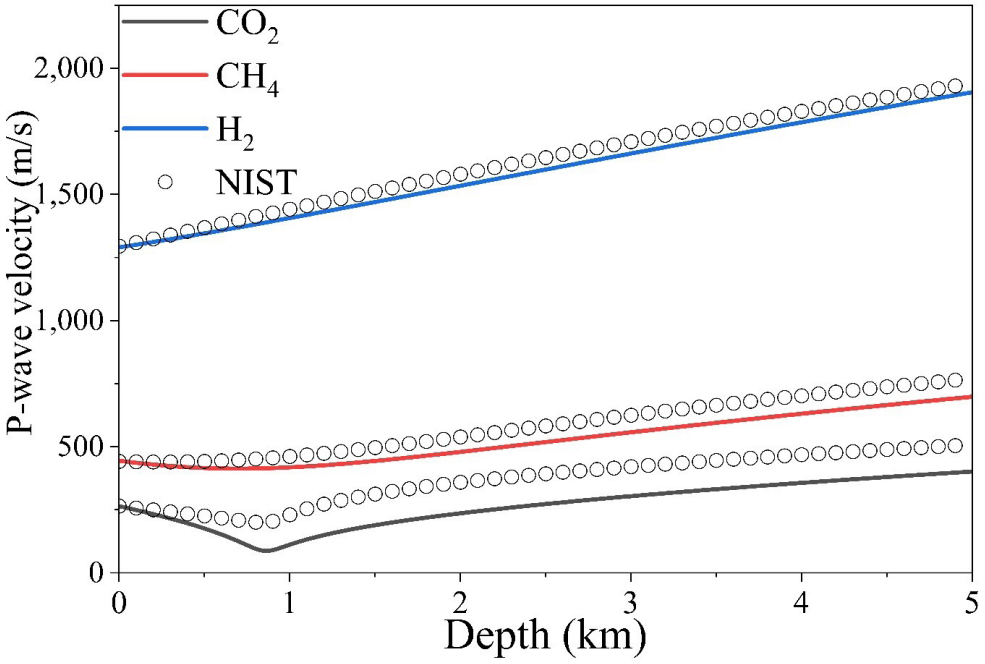

Figure 3. Graph of acoustic velocity versus depth for three gases under the corrected Peng–Robinson equation of state. The solid lines represent the values calculated by the equations of state, whereas the circles indicate the reference data obtained from the NIST Chemistry WebBook for comparison. Abbreviations: CH_4: Methane; CO_2: Carbon dioxide; H_2: Hydrogen; NIST: National Institute of Standards and Technology.

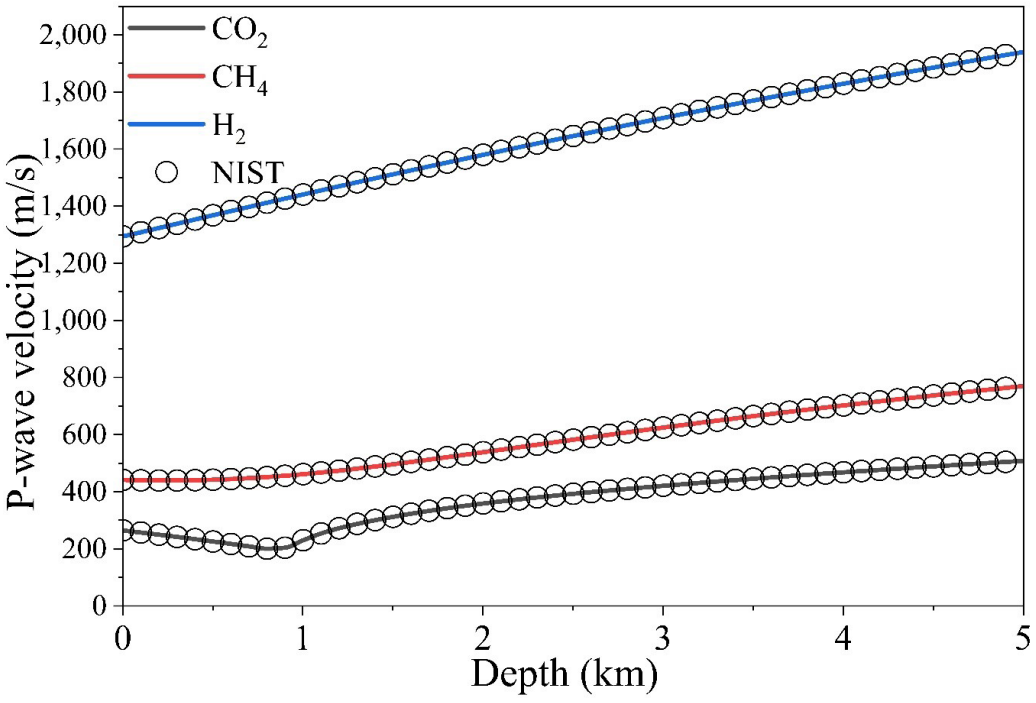

Figure 4. Graph of acoustic velocity versus depth for three gases under the modified Peng–Robinson equation of state. The solid lines represent the values calculated by the equations of state, whereas the circles indicate the reference data obtained from the NIST Chemistry WebBook for comparison. Abbreviations: CH_4: Methane; CO_2: Carbon dioxide; H_2: Hydrogen; NIST: National Institute of Standards and Technology.

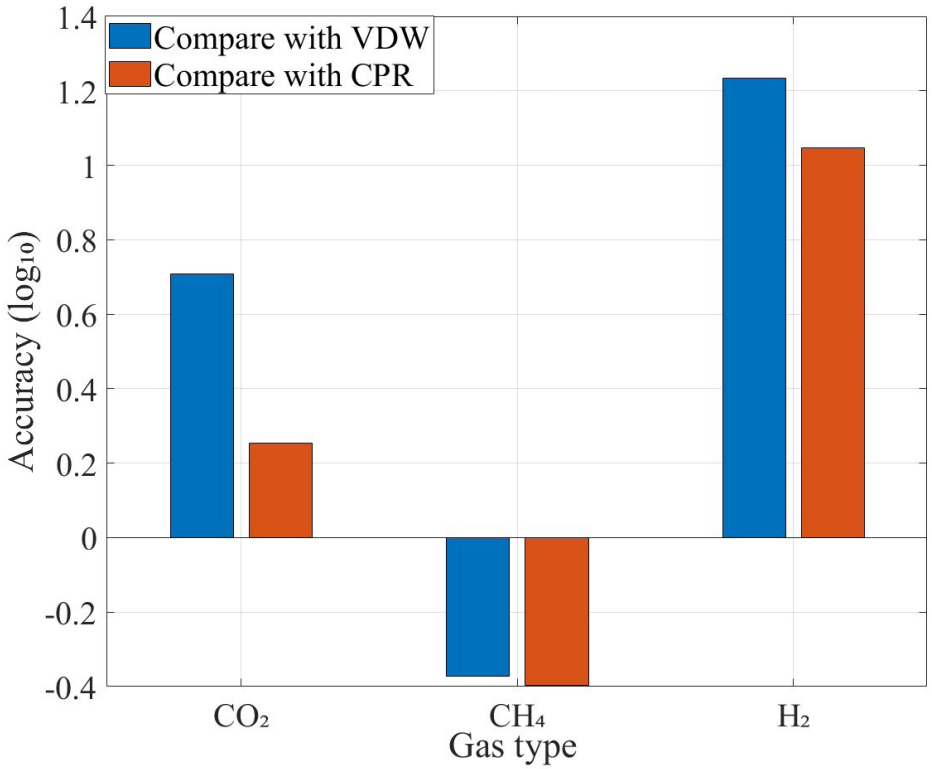

Figure 5. Accuracy of the modified Peng–Robinson algorithm compared to the other two algorithms
Abbreviations: CH_4: Methane; CO_2: Carbon dioxide; CPR: Corrected Peng–Robinson; H_2: Hydrogen; VDW: Van der Waals.

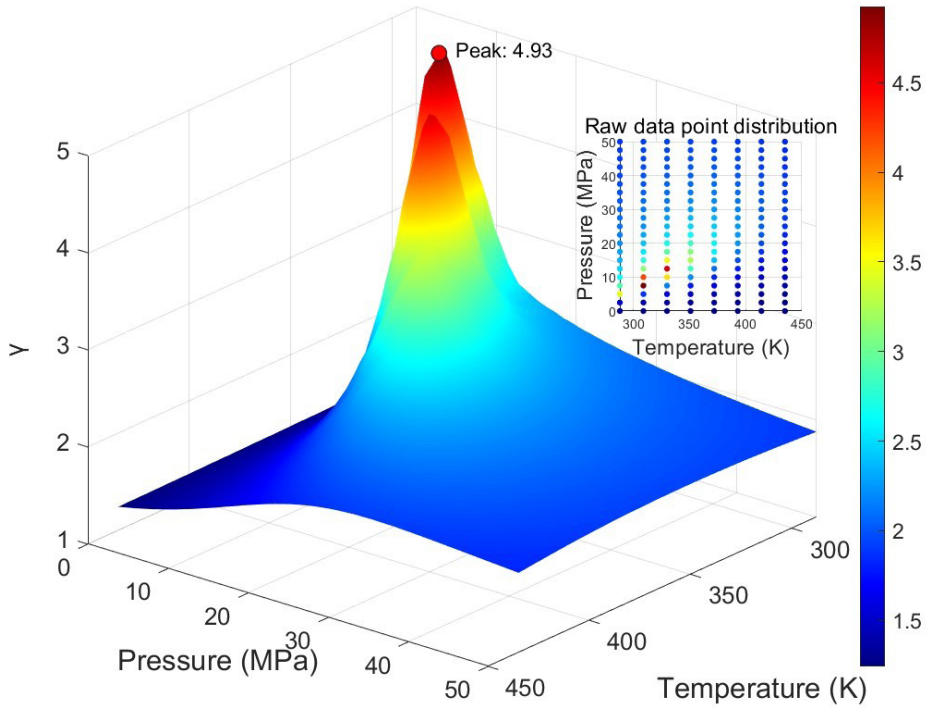

Figure 6. Surface plot of the specific heat ratio distribution for carbon dioxide

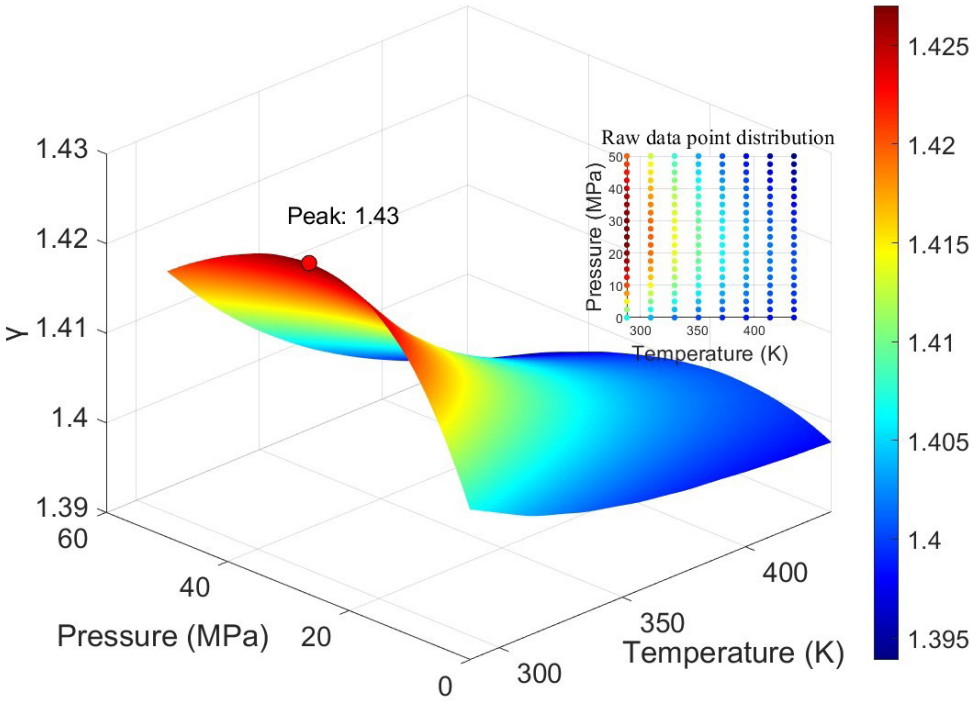

Figure 7. Surface plot of the specific heat ratio distribution for methane

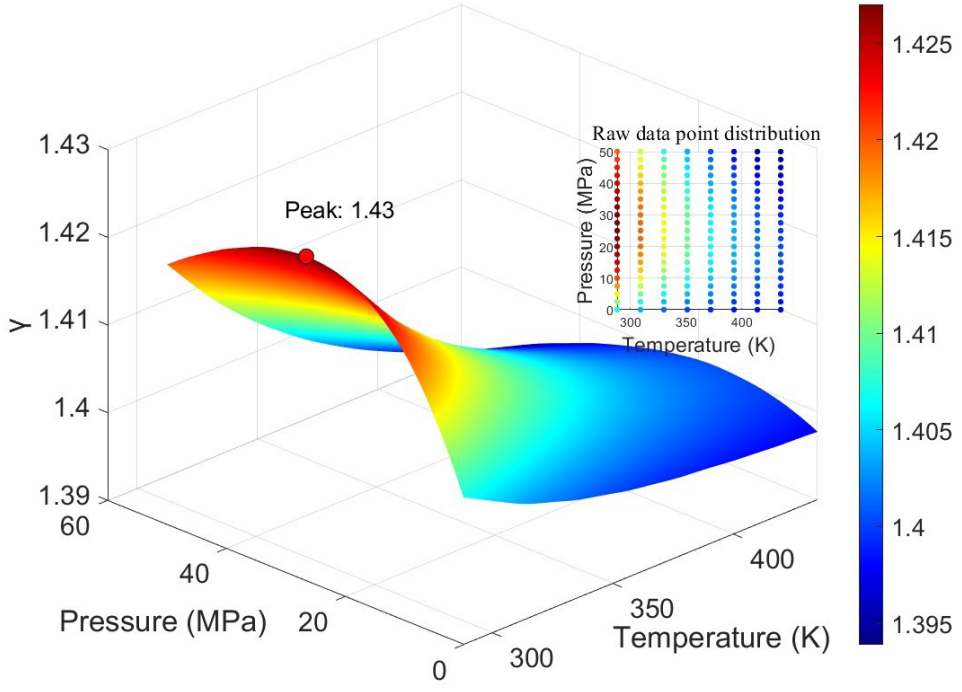

Figure 8. Surface plot of the specific heat ratio distribution for hydrogen

In comparison, CH_4 and H_2 show slower viscosity growth. At a depth of 5 km, the viscosity values of the three gases, ranked from highest to lowest, are: CO_2, CH_4, and H_2.

3. The properties of brine

The calculation of brine properties is also related to temperature and pressure. Following the Batzle–Wang[6] model and considering the compressional wave velocity, density, and viscosity of brine under different temperature–pressure conditions, the brine density formula can be expressed as:

$$\rho_b = \rho_w + S\{0.668 + 0.445 + 10^{-6}[300p - 2400pS + T_c(80 + 3T_c - 3300S - 13p + 47pS)]\} \quad (22)$$

where,

$$\rho_w = 1 + 10^{-6}(-80T_c - 3.3T_c^2 + 0.00175T_c^3 + 489p - 2T_cp + 0.016T_c^2p - 1.3\times10^{-5}T_c^3p - 0.333p^2 - 0.002T_cp^2) \quad (23)$$

where S is the mass fraction of sodium chloride (ppm/1,000,000). In this study, S = 50,000 ppm.

The brine velocity is given by:

$$V_b = V_w + \mathrm{S}(1170 - 9.6T_c + 0.055T_c^2 - 8.5\times10^{-5}T_c^3 + 2.6p - 0.0029T_cp - 0.0476p^2) + \mathrm{S}^{1.5}(780 - 10p + 0.16p^2) - 1820\mathrm{S}^2 \quad (24)$$

where V_w is the velocity of pure water, calculated as:

$$V_w = \sum_{i=0}^{4}\sum_{j=0}^{3}\mathrm{w}_{ij}T_c^ip^j \quad (25)$$

and w_{ij} are provided in Table 2.

The bulk modulus of brine is:

$$K_b = \rho_bV_b^2 \quad (26)$$

and the viscosity of brine is:

$$\eta_g = 0.1 + 0.333\mathrm{S} + (1.65 + 91.9\mathrm{S}^3)\exp\left\{-\left[0.42(\mathrm{S}^{0.8} - 0.17)^2 + 0.045\right]\mathrm{T}_c^{0.8}\right\} \quad (27)$$

Figure 10 shows the density and P-wave velocity of brine. The figure illustrates that the P-wave velocity curve exhibits a characteristic, non-monotonic, and complex trend, which can be divided into three distinct segments:

(i) Shallow rapid-increase segment (0–1,000 m): Within this interval, as depth increases, the effect of lithostatic pressure dominates. The rising pressure reduces the volume of the brine and significantly increases its bulk modulus, leading to a rapid rise in acoustic velocity. Although temperature also increases with depth—which would typically reduce velocity in the shallow section—the rate of increase from pressure effects far exceeds that from temperature effects.

(ii) Mid-depth transitional-decline segment (1,000–3,000 m): The curve peaks at approximately 1,000 m depth, then turns and begins a gradual decline. This indicates that as depth continues to increase, the velocity-reducing effect of rising temperature strengthens and gradually counteracts—even surpasses—the velocity-enhancing effect of pressure.

(iii) Deep gradual-recovery segment (3,000–5,000 m): Beyond about 3,000 m depth, the curve slowly rises again. This occurs because, under high-temperature and high-pressure conditions, the physical properties of the brine change. At such extreme pressures, the compressibility of water becomes low, and the enhancing effect of pressure reasserts itself significantly, driving a slow recovery in velocity despite the high temperatures.

Table 2. Coefficients for brine property calculation

$\mathrm{w}_{00} = 1{,}402.85$	$\mathrm{w}_{02} = 3.437\times10^{-3}$
$\mathrm{w}_{10} = 4.871$	$\mathrm{w}_{12} = 1.739\times10^{-4}$
$\mathrm{w}_{20} = -0.04783$	$\mathrm{w}_{22} = -2.135\times10^{-6}$
$\mathrm{w}_{30} = 1.487\times10^{-4}$	$\mathrm{w}_{32} = -1.455\times10^{-8}$
$\mathrm{w}_{40} = 2.197\times10^{-7}$	$\mathrm{w}_{42} = 5.230\times10^{-11}$
$\mathrm{w}_{01} = 1.524$	$\mathrm{w}_{03} = -1.197\times10^{-5}$
$\mathrm{w}_{11} = -0.0111$	$\mathrm{w}_{13} = -1.628\times10^{-6}$
$\mathrm{w}_{21} = 2.747\times10^{-4}$	$\mathrm{w}_{23} = 1.237\times10^{-8}$
$\mathrm{w}_{31} = -6.503\times10^{-7}$	$\mathrm{w}_{33} = 1.327\times10^{-10}$
$\mathrm{w}_{41} = 7.987\times10^{-10}$	$\mathrm{w}_{42} = 4.614\times10^{-13}$

Meanwhile, the blue density ρ_b curve shows a continuous yet gradually slowing decline. As depth increases, the sustained rise in temperature causes the brine to expand thermally, increasing its volume and thus decreasing its bulk density. Although increasing pressure compresses the water and would act to increase density, over the entire 0–5,000 m interval, the effect of the rising geothermal gradient leads to a monotonic decrease in

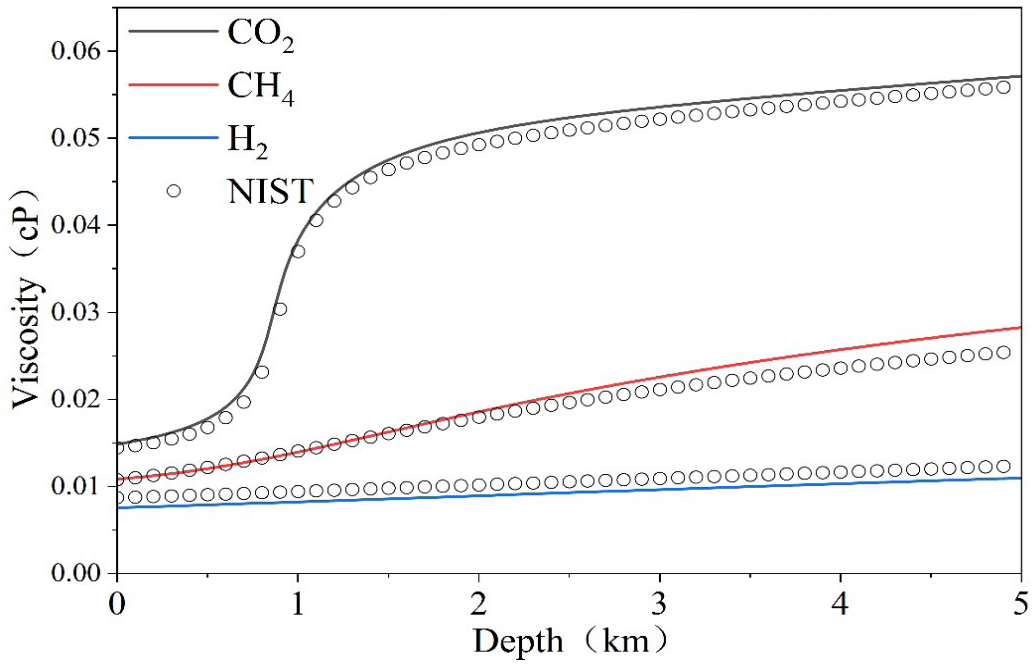

Figure 9. Plot of viscosity variation with depth for the three gases under the Lohrenz–Bray–Clark equation. Black circles denote the reference data obtained from the NIST Chemistry WebBook.
Abbreviations: CH_4: Methane; CO_2: Carbon dioxide; H_2: Hydrogen; NIST: National Institute of Standards and Technology.

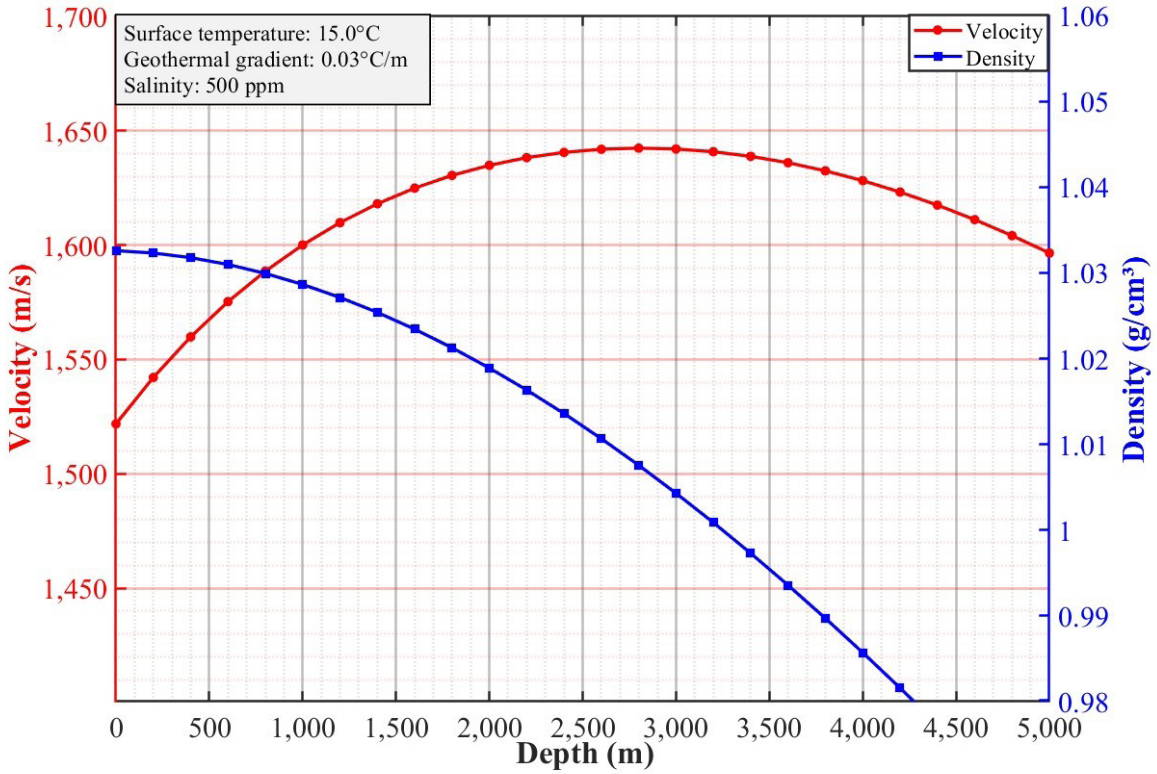

Figure 10. Density and P-wave velocity of brine as functions of depth

density. The slowing rate of decline with depth is due to the partially offsetting influence of pressure on density.

In summary, the two curves clearly demonstrate that with increasing depth, the P-wave velocity of the brine shows an overall rising trend while its density exhibits a falling trend—the two parameters vary inversely.

4. Effective fluid model

By considering the mineral composition of reservoir rocks and the characteristics of their pore microstructure, and based on the effective medium assumption, seismic rock physics modeling methods can be effectively applied to calculate their elastic parameters.[33] Through the calculations and analyses presented above, the modeled characteristics and systems for gases and brine have been established. These properties now need to be integrated with the rock matrix to obtain the elastic characteristics of the fluid-bearing rock model. Currently, various theories exist to describe the frequency-dependent dispersion and attenuation of seismic waves in fluid-saturated rocks.

For an effective fluid model, the key parameters are the respective bulk moduli and saturations, namely S_g (gas saturation) and S_b (brine saturation), which satisfy the following equation:

$$S_g + S_b = 1, \tag{28}$$

and the density of the gas–liquid mixture can be calculated as:

$$\rho_f = S_g \rho_g + S_b \rho_b \tag{29}$$

Next, the relationship of the bulk modulus for the gas–brine mixture can be determined using Wood's[8] equation:

$$K_w = \left(S_g K_g^{-1} + S_b K_b^{-1} \right)^{-1} \tag{30}$$

where K_g and K_b represent the bulk moduli of the gas and the brine, respectively.

Due to the influence of pore fluids, the propagation velocities of compressional waves in the same rock can differ significantly across frequency bands, which is manifested as velocity dispersion in multiscale seismic data.[34] In fluid-bearing rocks where gas, water, or mixed fluids coexist without mutual mixing, pressure differences near the gas–water interfaces become pronounced under wave excitation, inducing vigorous fluid motion. Such motion occurs extensively inside the rock; consequently, the superposition of local fluid flow across numerous discontinuous interfaces within a unit volume of rock can lead to substantial attenuation.

To simulate the inelastic behavior of rocks, this study adopts the patchy saturation model proposed by the Johnson model as the primary framework for analyzing the waveresponse characteristics of the rock-physics model. The results obtained from this model will be compared with those from the White model to discuss their differences and provide recommendations for model selection. Secondly, regarding the frequency-dependent characteristics of this study, since the dominant frequency range for seismic exploration is 10–60 Hz, with the advantageous band being 20–40 Hz, the frequency is set to f = 30 Hz for the analysis. The model developed in this work allows for obtaining responses at various frequencies by simply changing the value of f. Using 30 Hz here is solely intended to clearly illustrate and highlight the computational differences between the Johnson and White models at a specific frequency, thereby enabling a better understanding and analysis of the proposed rock-physics modeling.

The analysis was conducted at a frequency of f = 30 Hz, focusing on how compressional-wave velocity and attenuation factors vary under two distinct patch geometries: concentriccircle patches and fractal patches. In the concentriccircle configuration—which can be visualized as "brinecoated gas patches," where an outer layer of brine encloses an inner gas core—the outer brine radius is set to R = 30 cm. The saturations of the liquid (brine) and gas are denoted as S_g and S_b, respectively. When fluids are not fully mixed within the pore volume but instead distributed in patchy form, the high-frequency effective bulk modulus tends to be higher than the value predicted by the Wood model.

Following the approach of Picotti *et al.*,[35] two key parameters describe these patchy systems: the size factor T and the surfacetovolume ratio (S/V). In this study, the same size factor T was used for both fractal and concentric-circle patches. By increasing the S/V parameter by a factor of 10, the originally regular spherical patches are transformed into rough, irregular geometries. This modification allows the mixed fluid to be incorporated into the rock pores, enabling subsequent calculations of wave velocity and attenuation.

According to the Johnson model, the equivalent bulk modulus of rocks is calculated at the low- and high-frequency limits. For intermediate frequencies between these limits, a closed-form analytical expression is provided for approximation.

The bulk modulus of the saturated rock at low frequencies

can be computed using the Gassmann equations,[36] which are expressed as:

$$K_g\left(K_f\right)=\mathrm{K_m}+a^2\mathrm{M}\left(\mathrm{K_f}\right) \tag{31}$$

$$\alpha=1-\frac{\mathrm{K_m}}{\mathrm{K_s}} \tag{32}$$

$$M\left(K_f\right)=\left(\frac{\alpha\text{-}\phi}{\mathrm{K_s}}+\frac{\phi}{K_f}\right)^{-1} \tag{33}$$

where K_f represents the bulk modulus of the fluid within the pores.

For a gas–brine mixture, the shear modulus K_f can take the value of either K_W or K_B, depending on the distribution of the two-phase fluid in the pore space. $\mathrm{K_m}$ is the bulk modulus of the dry rock matrix, ϕ denotes the rock porosity, and $\mathrm{K_s}$ stands for the bulk modulus of the rock mineral grains. Substituting these parameters into the Johnson model yields the bulk modulus under low-frequency conditions as:

$$K_{gw}=K_g\left(K_w\right) \tag{34}$$

In this case, the computed value corresponds to substituting the bulk modulus of the mixed fluid calculated using the Wood model into **Equation 30**. Dutta and Ode[37] derived and validated this approach based on classical Biot theory. The predicted bulk modulus corresponds to the scenario in which the two-phase fluid in the rock is in a fully relaxed state, resulting in the softest effective state of the rock and the lowest seismic-wave propagation velocity. Hence, this value is regarded as the lower bound for seismic-wave velocities in partially saturated rocks.

Under highfrequency conditions, pore pressure is nonuniform across the whole medium but can be considered constant within each fluid phase. In this case, the effective bulk modulus can be calculated using the Hill equation[38] for bulk modulus, expressed as:

$$K_{gh}=\left(\frac{S_g}{K_g\left(K_g\right)+4/3\mu_m)}+\frac{S_b}{K_g\left(K_b\right)+4/3\mu_m}\right)^{-1}-4/3\mu_m \tag{35}$$

where, μ_{m} denotes the shear modulus of the dry rock. For practical purposes, the shear modulus of the fluid-saturated rock can be taken as equal to that of the dry rock. $K_g\left(K_g\right)$ and $K_g\left(K_b\right)$ represent the results obtained from **Equation 30** by substituting the bulk modulus of the pore fluid with that of the gas and the brine, respectively. Substituting the calculated K_{gw} and K_{gh} into the expression for the bulk modulus at intermediate frequencies, the equation based on Pride's[39] simple branch function is given as:

$$K\left(w\right)=K_{gh}-\frac{K_{gh}-K_{gw}}{1-\xi+\xi\sqrt{1-i\omega\tau/\xi^2}} \tag{36}$$

where i denotes the imaginary unit, ξ represents the shape parameter (a broader transition region corresponds to $\xi<1$, while a narrower one corresponds to $\xi>1$), and τ is the frequency-scale parameter. Both ξ and τ can be calculated with S/V and T. For S/V, the calculation method is as follows:

$$\frac{S}{V}=3\times\frac{a^2}{\mathrm{b}^3} \tag{37}$$

$$a=b\times S_g^{1/3} \tag{38}$$

where b is the outer brine layer radius of 30 cm. The formula for calculating T is:

$$\begin{aligned}T=\frac{K_{GW}\phi^2}{30\kappa b^3}\{&\left[3\eta_2g_2^2+5\left(\eta_1-\eta_2\right)g_1g_2-3\eta_1g_1^2\right]a^5\\&-15\eta_2g_2(g_2-g_1)a^3b^2\\&+5g_2\left[3\eta_2g_2-\left(2\eta_1-\eta_2\right)g_1\right]a^2b^3-3\eta_2g_2^2b^5\}\end{aligned} \tag{39}$$

where

$$g_j=\frac{\left(1\text{-Km/Ks}\right)\left(1/\mathrm{K_W}\text{-}1/\mathrm{K}f_j\right)}{1\text{-Km/Ks-}\phi\mathrm{Km/Ks+}\phi\mathrm{Km/K_W}},\ \mathrm{j}=1,2 \tag{40}$$

Subsequently, the P-wave modulus is:

$$E\left(\omega\right)=K\left(\omega\right)+4/3\mu_m \tag{41}$$

the P-wave velocity is:

$$V_c=\sqrt{\frac{K\left(\omega\right)+4/3\mu_m}{\rho}} \tag{42}$$

the final phase velocity is:

$$V_p=\left[\mathrm{Re}\left(\frac{1}{V_c}\right)\right]^{-1} \tag{43}$$

and the attenuation factor is calculated as:

$$Q = \frac{\mathrm{Re}\left(V_c^2\right)}{\mathrm{Im}\left(V_c^2\right)} \tag{44}$$

where Re and Im represent the real and imaginary parts, respectively, of the result calculated from **Equation 41**. Based on the data provided by Gei *et al.*,[40] this study employs parameters of Utsira-type sand at depths of 800 m and 3,000 m for simulation calculations, with the relevant properties of the gases and rocks provided in Table 3. The resulting plots of V_p and Q are shown in Figure 11.

Table 3. Properties of the three gases, the rock, and brine

Properties	Depth	
	800 m	3,000 m
Physical conditions	P = 8.1 MPa P_c = 18.2 MPa T_c = 39 °C	P = 30.1 MPa P_c = 67.8 MPa T_c = 105 °C
Sediment	ϕ = 0.29 K_m = 1.39 GPa μ_m = 0.83 GPa κ = 0.41 d	ϕ = 0.17 K_m = 8.75 GPa μ_m = 5.23 GPa κ = 0.06 d
Brine	K_b = 2.6 GPa ρ_b = 1,030 kg/m^3 η_b = 0.8 mPa·s	K_b = 2.7 GPa ρ_b = 1,004 kg/m^3 η_b = 0.35 mPa·s
CO_2	K_g = 9.97 MPa ρ_g = 310 kg/m^3 η_g = 25.25 μPa·s	K_g = 115.7 MPa ρ_g = 644 kg/m^3 η_g = 53.72 μPa·s
CH_4	K_g = 11.37 MPa ρ_g = 56 kg/m^3 η_g = 13.13 μPa·s	K_g = 59.17 MPa ρ_g = 152 kg/m^3 η_g = 21.67 μPa·s
H_2	K_g = 11.98 MPa ρ_g = 6 kg/m^3 η_g = 8.08 μPa·s	K_g = 48.9 MPa ρ_g = 17 kg/m^3 η_g = 9.62 μPa·s

Abbreviations: CH_4: Methane; CO_2: Carbon dioxide; H_2: Hydrogen.

In Figure 11A and 11C, the P-wave velocity exhibits an increasing trend with rising brine saturation. This occurs because the compressibility of the liquid brine phase is significantly lower than that of the gaseous phase. As brine saturation increases, the effective bulk modulus of the rock increases, leading to higher Pwave velocity. In contrast, the presence of gas tends to "soften" the rock and reduce wave velocity.

Specifically, regarding different gases, it can be observed that the P-wave velocity of brine containing CO_2 is higher than that of brines containing the other two gases. Its "hookshaped" curve also approaches a more linear, gradual variation. Furthermore, from the perspective of patch geometry, the P-wave velocity for spherical patches is generally higher than that for fractal patches. At a depth of 3,000 m, the Pwave velocities of rocks containing the three gases with the same brine follow the order $CO_2 > CH_4 > H_2$. This difference is even more pronounced for fractal patches.

Under higher confining pressure at 3,000 m depth, the rock frame becomes denser, resulting in an overall higher P-wave velocity compared to the 800 m depth. However, the relative amplitude of fluidsubstitution effects may be reduced, likely due to decreased pore compressibility under high pressure.

Figure 11B and 11D illustrate the variation of attenuation factors with brine saturation. Attenuation peaks typically occur within the partial-saturation range, which is dominated by wave-induced fluid flow mechanisms. In the figure, the spherical gas bubbles of CO_2 and H_2 may lead to relatively narrow attenuation peaks at moderate saturations, as uniform bubble geometries promote local fluid flow. In contrast, the fractal geometry of CH_4 may broaden the attenuation peak or shift its position, because the fractal structure enhances pore-scale heterogeneity, triggering more complex fluid motion.

A comparison of depths shows that the attenuation values at 3,000 m are lower than those at 800 m. This is because the high-pressure environment suppresses the relative motion of pore fluids, thereby reducing energy dissipation. The frequency is fixed at 30 Hz (within the seismic frequency band), which ensures that the attenuation mechanism is dominated by macroscopic fluid flow rather than highfrequency scattering.

This analysis reveals how gas morphology (geometry) and depth jointly regulate acoustic parameters, providing insights for interpreting seismic responses in partially saturated reservoirs under varying burial conditions.

5. Model validation and comparative analysis: Johnson and White model prediction differences

To more intuitively characterize fluid behavior in deep geological environments and highlight the differences between modeling approaches, we further calculated the compressional wave velocity and attenuation factor using the improved White model by Dutta and Ode.[34] A comparison with the Johnson model is shown in Figure 12.

As shown in Figure 12, a more intuitive comparison

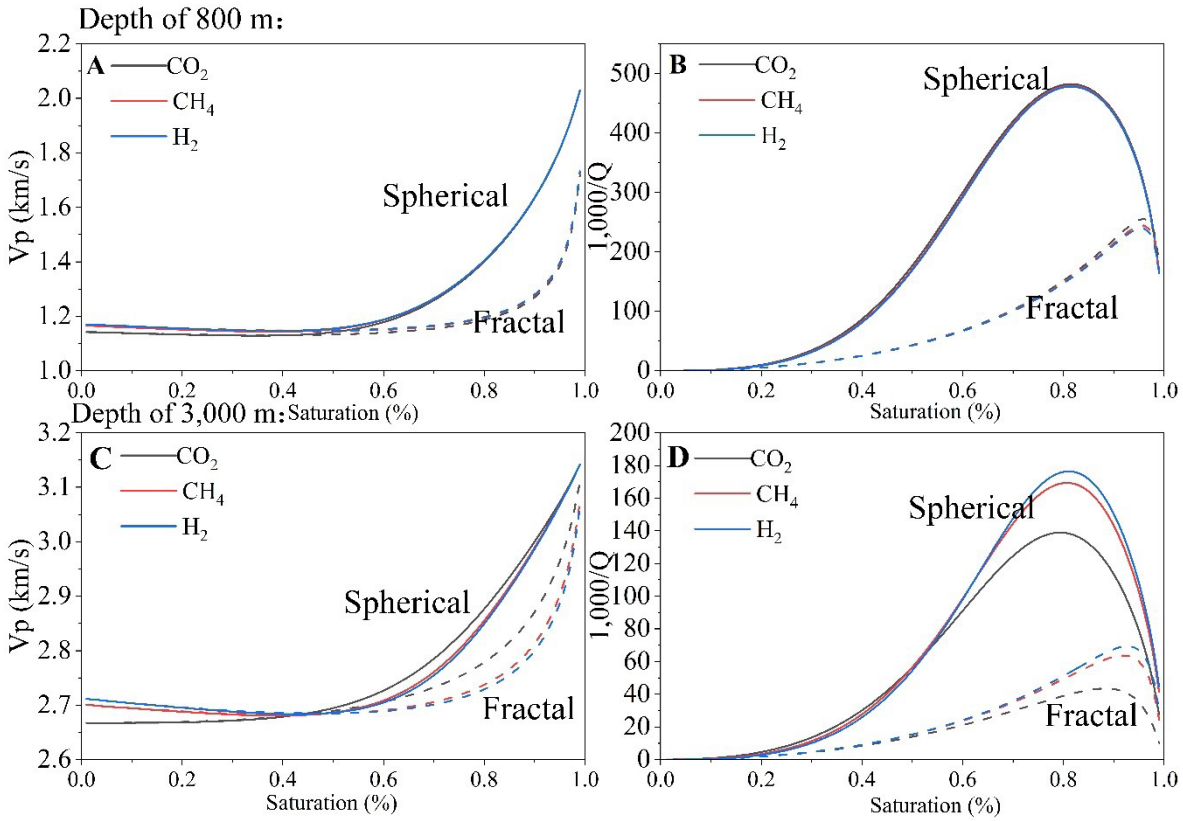

Figure 11. Variation of Vp and attenuation factor of wet rock versus saturation at depths of 800 m and 3,000 m. (A) Vp and (B) attenuation factor at 800 m; (C) Vp and (D) attenuation factor at 3,000 m.
Abbreviations: CH_4: Methane; CO_2: Carbon dioxide; H_2: Hydrogen; Vp: P-wave velocity.

reveals that both the Johnson and White models predict essentially the same trend for P-wave velocity—monotonically increasing with rising brine saturation. This indicates that, for elastic properties such as seismic velocity, the macroscopic averaging effects of the two models are similar. For P-wave velocity, regardless of whether the geometry is spherical or fractal patches, an inflection point occurs at approximately 50% brine saturation, beyond which the velocity increases markedly. Among the three gases, CO_2 exhibits the highest velocity, followed by CH_4 and H_2. This difference is primarily governed by the mass of the gas, with heavier gases generally producing higher velocities than lighter ones.

In terms of the attenuation factor, which characterizes energy dissipation, the attenuation peak predicted by the White model is lower than that of the Johnson model. Furthermore, the White model yields a broader, more symmetric attenuation peak in fractal patches, centered around 50% saturation. In contrast, the Johnson model produces a sharper, narrower attenuation peak whose position is shifted. To clarify the distinctions between the two models more explicitly, CO_2—which exhibits the most pronounced differences—was selected for separate plotting and further analysis.

The critical point of CO_2 (304.12 K, 7.38 MPa) lies within the depth range of this study. At a depth of 800 m, it exists in a gaseous or near-critical state, while at 3,000 m, it is in a supercritical state. This significant phase change leads to drastic variations in its acoustic properties, with clear differences observed in compressional wave velocity and attenuation factor.

The differences between the two models are more clearly illustrated in Figure 13. The White model predicts a broad, symmetric attenuation peak located approximately near 50% saturation. In contrast, the attenuation peak predicted by the Johnson model is sharper and narrower. This is because, in the Johnson model, the mechanism is primarily wave-field–induced squirt flow, where fluid is injected from soft pores into adjacent stiff pores due to wave compression.[41] Furthermore, the peak position is shifted—

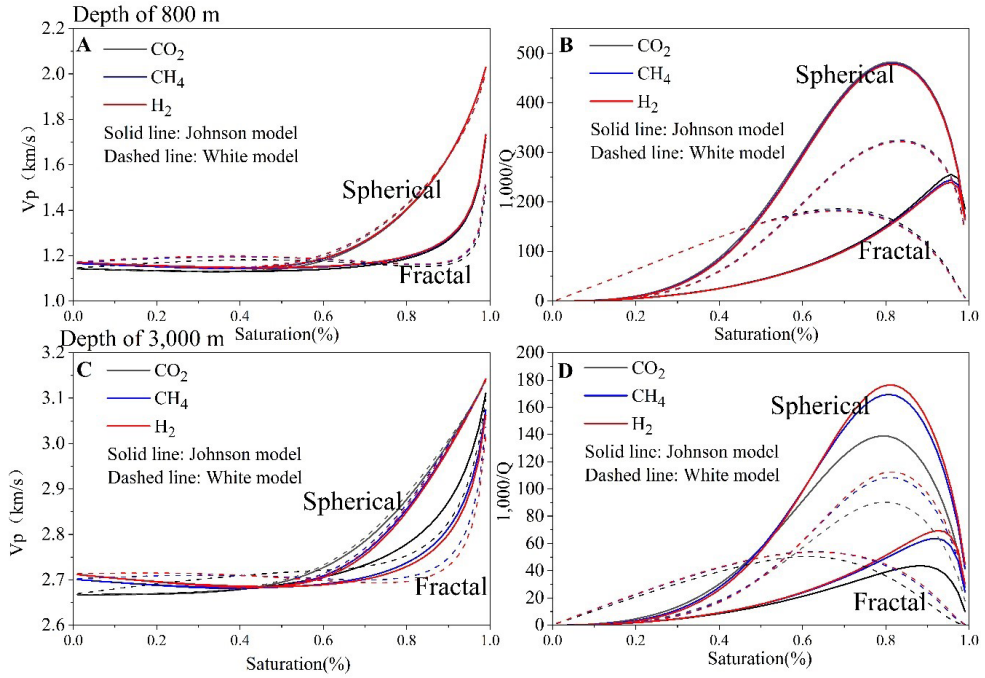

Figure 12. Variations of Vp and the attenuation factor with saturation for gas–brine mixtures of the three gases under the Johnson and White models at depths of 800 m and 3,000 m. (A) Vp and (B) attenuation factor at 800 m. (C) Vp and (D) attenuation factor at 3,000 m.
Abbreviations: CH_4: Methane; CO_2: Carbon dioxide; H_2: Hydrogen; Vp: P-wave velocity.

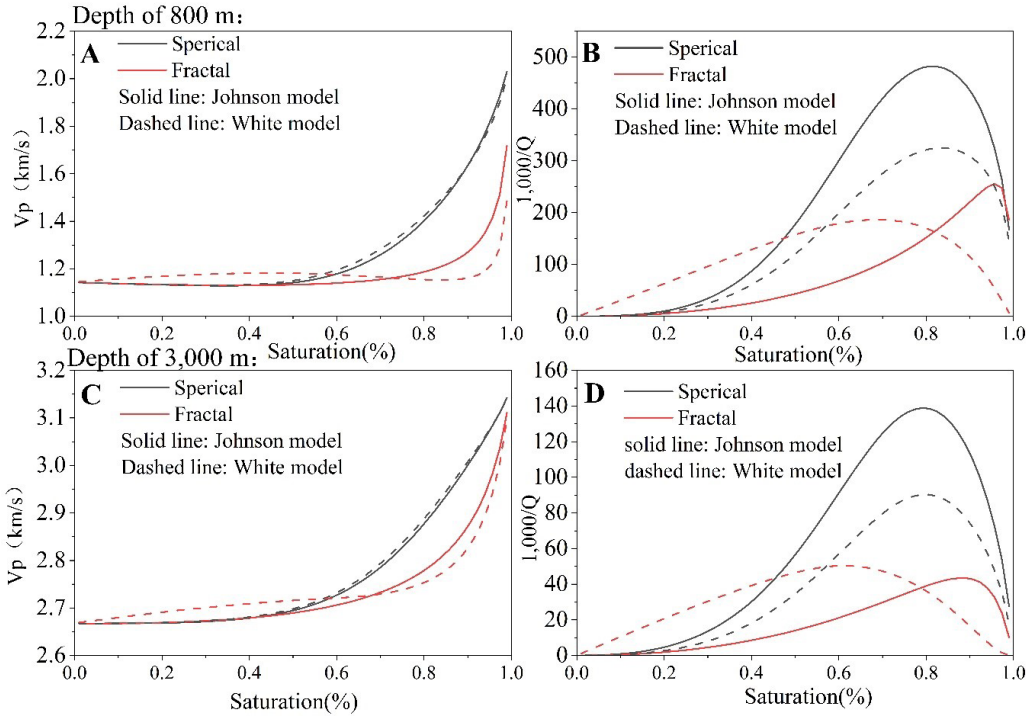

Figure 13. Comparative plots of carbon dioxide under the Johnson and White models. (A) Vp and (B) attenuation factor for rocks containing carbon dioxide–brine mixture at 800 m. (C) Vp and (D) attenuation factor at 3,000 m.
Abbreviation: Vp: P-wave velocity.

particularly evident in the fractal patch model—due to wave-induced fluid flow at the mesoscopic scale, which operates at a scale larger than pore sizes but smaller than the wavelength.[42] In the White model, attenuation arises from macroscopic fluid flow driven by pressure gradients between differently saturated fluid patches, induced by the wave field. This flow occurs over a large scale with a broad distribution of relaxation times, resulting in a broad attenuation peak. The peak occurs at intermediate saturations because at this point, both gas and water phases are continuous, allowing for the highest efficiency of pressure diffusion.

In terms of P-wave velocity, the predicted values from the two models are generally consistent. However, in the Johnson model, the influence of heterogeneous fluid distribution on the effective bulk modulus of the rock is directly coupled into the frame elastic modulus. Its squirt-flow mechanism not only enhances attenuation but also contributes additional stiffness, leading to a higher estimated overall rock stiffness in partially saturated states and therefore relatively higher predicted wave velocities. In contrast, the macroscopic flow mechanism in the White model primarily affects wave velocity through fluid substitution and global pressure relaxation, while its description of the hardening effect on the effective modulus of the frame itself is relatively weaker. Consequently, its predictions are usually lower than those of the Johnson model, which accounts for both microscopic and macroscopic stiffening mechanisms.[43]

A comparison of Figure 13B and 13D indicates that attenuation predicted by both models decreases markedly under high-pressure conditions. This occurs because high confining pressure compresses the soft pores in the rock, significantly suppressing microscopic squirt-flow activity, which relies on the existence of such soft pores. Consequently, the attenuation predicted by the Johnson model drops substantially under high-pressure conditions. Meanwhile, although pressure diffusion between macroscopic patches is also influenced by changes in fluid compressibility, the mechanism itself is less sensitive to pore closure than squirt flow. Therefore, under deep high-pressure conditions, the relative importance of microscopic flow mechanisms declines, while the contribution of macroscopic flow mechanisms increases, leading to a convergence of the predictions from the two models. This provides an important boundary condition for the applicability of the models in seismic interpretation of deep reservoirs.

In summary, this section systematically analyzes the differences and underlying mechanisms between the Johnson and White models in predicting compressional wave velocity V_p and attenuation factor Q in sandstone reservoirs saturated with CO_2-, CH_4-, and H_2-bearing fluids, through theoretical comparison and numerical simulation. It must be clearly noted that the specific numerical conclusions and comparative analyses presented here are primarily based on the sandstone matrix parameters and the defined patch morphology given in Table 3. The applicability of the two models is also influenced by the inherent physical mechanism differences of the models themselves, the reservoir conditions, and the fluid properties. In practical monitoring of fluids in underground reservoirs, the optimal model selection should be based on a comprehensive understanding of the target reservoir's lithology, pore structure, temperature–pressure conditions, and fluid phase state, and should be calibrated and validated using actual data (e.g., well logs, core experiments, and seismic data). This study provides a quantitative analysis framework for understanding the behavioral differences of the two models under various conditions, serving as a theoretical reference for selecting or improving rock physics models based on specific application scenarios.

6. Conclusion

This study proposes a methodology for constructing a frequency-dependent rock physics model that incorporates fluid thermodynamic parameters, aimed at investigating the behavior and state of fluids in deep geological storage and energy-storage environments. The research primarily focuses on three gases—CO_2, CH_4, and H_2—taking into account not only the variations in their elastic parameters and viscosity under different temperature and pressure conditions but also the changes in brine properties with temperature and pressure. By combining these, the parameter variations of fluids when filling rock pores are obtained, allowing for a more accurate description of the physical characteristics and flow behavior of fluids in reservoirs at different depths, thereby better aligning with realistic subsurface fluid states.

Furthermore, through an in-depth analysis of patch saturation effects in this frequency-dependent rock physics model with integrated fluid thermodynamic parameters, the study demonstrates how different unsaturated-patch prediction models can be applied to analyze the inelastic properties of the investigated reservoirs. This provides a critical theoretical foundation and quantitative tools for the identification and monitoring of underground storage of CO_2, CH_4, and H_2. It should be noted that the findings of this study are based on simulation calculations conducted in relatively ideal, porous sandstone reservoirs, without extensive consideration of complex pore structures or

special lithologies. Therefore, future work should be expanded to incorporate more complex rock-pore-structure models and anisotropy factors. Additionally, as this study relies on simulation results, it lacks certain conditions and factors present in real systems and can only serve as a theoretical reference. Subsequent research should aim to validate and apply the model by integrating actual well logs, core analysis, and seismic data, optimizing the study from practical perspectives to enrich the findings. Finally, the research can be extended to include more comprehensive seismic-attribute analyses, such as shear waves and anisotropy, with the goal of constructing a more comprehensive fluid identification and monitoring index system.

Acknowledgments

None.

Funding

This work was supported by the National Key R&D Program of China (Grant No.: 2024YFB4007100), the National Major Science and Technology Projects of China (Grant No.: 2024ZD1004300), the National Natural Science Foundation of China (Grant No.: 42304133 and 42574175) and the Key Project from the Hubei Research Center for Basic Disciplines of Earth Sciences (Grant No.: HRCES-202401).

Conflict of interest

Guangtan Huang is an Editorial Board Member of this journal, but was not in any way involved in the editorial and peer-review process conducted for this paper, directly or indirectly. The authors declare there is no conflict of interest.

Author contributions

Conceptualization: Guangtan Huang
Formal analysis: Lujia Ma
Investigation: Zhennan Yu, Haiyu Li, Mingliao Wu
Methodology: Lujia Ma
Writing–original draft: Lujia Ma
Writing–review & editing: Lujia Ma

Availability of data

Some of the data used in this study are available from the NIST Chemistry WebBook (https://webbook.nist.gov/chemistry).

References

1. Ledley TS, Sundquist ET, Schwartz SE, Hall DK, Fellows JD, Killeen TL. Climate change and greenhouse gases. *Eos Trans AGU*. 1999;80(39):453-458.

   doi: 10.1029/99EO00325

2. Ni Z, Li YY, Chen XX, Yu D. Change in soil greenhouse gas fluxes with tidal pattern in a mangrove forest in Jiulong River Estuary in summer. *J Appl Oceanogr*. 2026;45(1):100-106. [In Chinese].

   doi: 10.3969/j.issn.2095-4972.20240911001

3. Yang CH, Wang GB, Shi XL. Demands and challenges of large-scale salt cavern hydrogen storage in China. *Rock Soil Mech*. 2024;45(1):1-19.

   doi: 10.16285/j.rsm.2023.1785

4. Miocic J, Heinemann N, Edlmann K, Scafidi J, Molaei F, Alcalde J. Underground hydrogen storage: a review. *Geol Soc Lond Spec Publ*. 2023;528(1):73-86.

   doi: 10.1144/SP528-2022-88

5. Biot MA. Theory of propagation of elastic waves in a fluid-saturated porous solid. II. Higher frequency range. *J Acoust Soc Am*. 1956;28(2):179-191.

   doi: 10.1121/1.1908241

6. Batzle ML, Wang Z. Seismic properties of pore fluids. *Geophysics*. 1992;57(11):1396-1408.

   doi: 10.1190/1.1443207

7. Murphy WF. Acoustic measures of partial gas saturation in tight sandstones. *J Geophys Res*. 1984;89(B13):11549-11559.

   doi: 10.1029/JB089iB13p11549

8. Wood A. *A Textbook of Sound*. New York, NY, USA: Macmillan; 1955.

9. White JE. Computed seismic speeds and attenuation in rocks with partial gas saturation. *Geophysics*. 1975;40(2):224-232.

   doi: 10.1190/1.1440520

10. Johnson DL. Theory of frequency dependent acoustics in patchy-saturated porous media. *J Acoust Soc Am*. 2001;110(2):682-694.

    doi: 10.1121/1.1381021

11. Picotti S, Carcione JM, Gei D, Rossi G, Santos JE. Seismic modeling to monitor CO2 geological storage: the Atzbach-Schwanenstadt gas field. *J Geophys Res*. 2012;117(B6):B06103.

    doi: 10.1029/2011JB008540

12. Carcione JM, Picotti S, Gei D, Rossi G. Physics and seismic modeling for monitoring CO2 storage. *Pure Appl Geophys*. 2006;163(1):175-207.

    doi: 10.1007/s00024-005-0002-1

13. Wang Z, Cates ME, Langan RT. Seismic monitoring of a CO2 flood in a carbonate reservoir; a rock physics study. *Geophysics*. 1998;63(5):1604-1617.

    doi: 10.1190/1.1444457

14. Oldenburg CM. Carbon dioxide as cushion gas for natural gas storage. *Energy Fuels*. 2003;17(1):240-260.

doi: 10.1021/ef020162b

15. Xue Z, Ohsumi T. Seismic wave monitoring of CO2 migration in water-saturated porous sandstone. *Explor Geophys*. 2004;35(1):25-32.

doi: 10.1071/EG04025

16. Melideo D, Baraldi D. Erratum to "CFD analysis of fast filling strategies for hydrogen tanks and their effects on key-parameters" [Int J Hydrogen Energy 40 (2015) 735–745]. *Int J Hydrogen Energy*. 2015;40(18):6260-6268.

doi: 10.1016/j.ijhydene.2015.02.125

17. Carcione JM, Gei D, Picotti S, *et al*. Porosity and permeability of the overburden from wireline logs: a case study from offshore Malaysia. *Geomech Geophys Geo-Energy Geo-Resour*. 2020;6(1):48.

doi: 10.1007/s40948-020-00172-y

18. Heinemann N, Alcalde J, Miocic JM, *et al*. Enabling large-scale hydrogen storage in porous media – the scientific challenges. *Energy Environ Sci*. 2021;14(2):853-864.

doi: 10.1039/D0EE03536J

19. Ali M, Isah A, Yekeen N, *et al*. Recent progress in underground hydrogen storage. *Energy Environ Sci*. 2025;18(12):5740-5810.

doi: 10.1039/D4EE04564E

20. Alajmi M, Gei D, Carcione JM, Qadrouh AN, Santos J, Ba J. Methodology to monitor the seismic response to injected carbon dioxide. *Acta Geophys*. 2024;72(2):1343-1353.

doi: 10.1007/s11600-023-01199-x

21. Creasy N, Huang L, Gasperikova E, Harbert W, Bratton T, Zhou Q. CO2 rock physics modeling for reliable monitoring of geologic carbon storage. *Commun Earth Environ*. 2024;5(1):246.

doi: 10.1038/s43247-024-01493-6

22. Dupuy B, Romdhane A, Eliasson P, Yan H. Combined geophysical and rock physics workflow for quantitative CO2 monitoring. *Int J Greenhouse Gas Control*. 2021;106:103217.

doi: 10.1016/j.ijggc.2020.103217

23. van der Waals JD. *Over de Continuïteit van Den Gas- En Vloeistoftoestand*. Sijthoff; 1873.

24. Ba J, Carcione JM, Cao H, Du QZ, Yuan ZY, Lu MH. Velocity dispersion and attenuation of P waves in partially-saturated rocks: Wave propagation equations in double-porosity medium. *Chin J Geophys*. 2012;55(1):219-231.

doi: 10.6038/j.issn.0001-5733.2012.01.021

25. Poling BE, Prausnitz JM, O'Connell JP. *The Properties of Gases and Liquids*. 5th ed. McGraw-Hill; 2001.

26. Saffari H. A new alpha-function for the Peng-Robinson equation of state: application to natural gas. *Chin J Chem Eng*. 2013;21(10):1155-1161.

doi: 10.1016/S1004-9541(13)60581-9

27. Hekayati J, Roosta A, Javanmardi J. Volumetric properties of supercritical carbon dioxide from volume-translated and modified Peng-Robinson equations of state. *Korean J Chem Eng*. 2016;33(11):3231-3244.

doi: 10.1007/s11814-016-0176-5

28. NIST Office of Data and Informatics. NIST Chemistry WebBook, SRD 69. Updated March 2025.

doi: 10.18434/T4D303

29. Morse PM, Ingard KU. *Theoretical Acoustics*. Princeton University Press; 1986.

30. Schappert K, Pelster R. Requirements to determine the average pore size of nanoporous media using ultrasound. *ACS Omega*. 2018;3(12):18906-18910.

doi: 10.1021/acsomega.8b03091

31. Span R, Wagner W. A new equation of state for carbon dioxide covering the fluid region from the triple-point temperature to 1100 K at pressures up to 800 MPa. *J Phys Chem Ref Data*. 1996;25(6):1509-1596.

doi: 10.1063/1.555991

32. Lohrenz J, Bray BG, Clark CR. Calculating viscosities of reservoir fluids from their compositions. *J Pet Technol*. 1964;16(10):1171-1176.

doi: 10.2118/915-PA

33. Yin XY, Ma ZQ, Zong ZY, Shang S. Review of fracture prediction driven by the seismic rock physics theory (II): Fracture prediction from five-dimensional seismic data. *Geophys Prospect Pet*. 2022;61(3):373-391.

doi: 10.3969/j.issn.1000-1441.2022.03.001

34. Sams MS, Neep JP, Worthington MH, King MS. The measurement of velocity dispersion and frequency-dependent intrinsic attenuation in sedimentary rocks. *Geophysics*. 1997;62(5):1456-1464.

doi: 10.1190/1.1444249

35. Stefano P. A viscoelastic representation of wave attenuation in porous media. *Comput Geosci*. 2010;36(1):44-53.

doi: 10.1016/j.cageo.2009.07.003

36. Naturforschende Gesellschaft in Zürich. *Mittheilungen Der Naturforschende Gesellschaft in Zürich*. In Commission bei S. Höhr; 1847.

37. Dutta NC, Ode H. Attenuation and dispersion of compressional waves in fluid-filled porous rocks with partial gas saturation (White Model); Part I, Biot theory. *Geophysics*. 1979;44(11):1777-1788.

doi: 10.1190/1.1440938

38. Hill R. Theory of mechanical properties of fibre-strengthened materials: I. Elastic behaviour. *J Mech Phys Solids*. 1964;12(4):199-212.

doi: 10.1016/0022-5096(64)90019-5

39. Pride SR. Drag forces of porous-medium acoustics. *Phys Rev B*. 1993;47(9):4964-4978.

doi: 10.1103/PhysRevB.47.4964

40. Gei D, Carcione JM, Picotti S. Acoustics for seismic monitoring H2 storage in saline aquifers. A comparative study with the CO2 and CH4 cases. *Research Square*. Preprint posted online February 8, 2024.

doi: 10.21203/rs.3.rs-3896786/v1

41. Alkhimenkov Y. Simulating squirt flow in realistic rock models using graphical processing units (GPUs). *Geophys J Int*. 2024;238(1):272-289.

doi: 10.1093/gji/ggae152

42. Pride SR, Berryman JG, Harris JM. Seismic attenuation due to wave-induced flow. *J Geophys Res*. 2004;109(B1):B01201.

doi: 10.1029/2003JB002639

43. Liu X, Greenhalgh S, Zhou B. Scattering of plane transverse waves by spherical inclusions in a poroelastic medium. *Geophys J Int*. 2009;176(3):938-950.

doi: 10.1111/j.1365-246X.2008.04026.x

ACCSCIENCE PUBLISHING

Journal of Seismic Exploration

ARTICLE

Three-dimensional high-order total variation regularized acoustic impedance inversion for thin coal seam thickness prediction in the Yushe East Area, China

Yinping Dong[1,2], Youyi Shen[1,2], Zhongbin Tian[3,4], Wei Wei[1,2], Xiaodong Yang[1,2], Yaju Hao[5], and Peng Zhang[5]*

[1]Key Laboratory of Monitoring and Protection of Natural Resources in Mining Cities, Ministry of Natural Resources, Jinzhong, Shanxi, China

[2]Coal Geological Geophysical Exploration Surveying and Mapping Institute of Shanxi Province Co., Ltd., Jinzhong, Shanxi, China

[3]Shanxi Provincial Geological Prospecting Bureau, Taiyuan, Shanxi, China

[4]School of Resources and Geosciences, China University of Mining and Technology, Xuzhou, Jiangsu, China.

[5]School of Geophysics and Space Exploration, East China University of Technology, Nanchang, Jiangxi, China

(This article belongs to the *Special Issue: Geophysical Inversion and Intelligent Prediction Technologies for Complex Hydrocarbon Reservoirs*)

***Corresponding author:**
Peng Zhang
(zp296495@ecut.edu.cn)

Citation: Dong Y, Shen Y, Tian Z, *et al*. Three-dimensional high-order total variation regularized acoustic impedance inversion for thin coal seam thickness prediction in the Yushe East Area, China. *J Seismic Explor.* 2026;35(3):026120050. doi: 10.36922/JSE026120050

Received: March 20, 2026

Revised: April 14, 2026

Accepted: April 16, 2026

Published online: May 20, 2026

Copyright: © 2026 Author(s). This is an Open-Access article distributed under the terms of the Creative Commons Attribution License, permitting distribution, and reproduction in any medium, provided the original work is properly cited.

Publisher's Note: AccScience Publishing remains neutral with regard to jurisdictional claims in published maps and institutional affiliations.

Abstract

Conventional three-dimensional (3D) impedance inversion methods exhibit poor lateral continuity during the inversion of thin coal seams, making it difficult to effectively preserve the lateral structural characteristics of the coal seams, which in turn affects the accurate prediction of the thickness and extent of thin coal seams. To address this issue, we propose a 3D high-order total variation (TV) regularized impedance inversion method. This method introduces high-order TV regularization constraints in both the inline and crossline directions to enhance the spatial continuity of the inversion results. The inversion objective function is solved in the frequency domain using the split-Bregman method, thereby improving computational efficiency for large-scale 3D matrix operations compared to time-domain approaches. The test results of the 3D overthrust model show that the 3D high-order TV constraint can effectively improve the transverse continuity and structural retention ability of the inversion results. The practical application results on the 3D seismic data of Yushe East Exploration Area in Shanxi Province show that, compared to the model-based inversion method in STRATA, the proposed method achieves higher vertical resolution and better lateral continuity, and can clearly depict the low-impedance characteristics of the No. 15 coal seam. Based on this, the error between the predicted coal seam thickness and the well-logging interpretation thickness is less than 8.8%, indicating that the proposed method maintains good stability and predictive capability even under limited well-control conditions.

Keywords: Acoustic impedance inversion; Three-dimensional total variation regularization; High-order difference operator; Coal seam thickness prediction; Lateral continuity

1. Introduction

Thin coal seams are important targets in coalbed methane exploration and coal mining, and accurate prediction of their thickness and lateral distribution is essential for reservoir evaluation and safe production. With the growing demand for mine safety and production efficiency, coal geophysics has become increasingly important for thin-seam identification and characterization.[1] Coal seams usually exhibit relatively low acoustic impedance compared to surrounding rocks, making seismic impedance inversion an effective tool for predicting coal seams. However, due to the limited bandwidth of seismic data and the thin thickness of coal seams, conventional inversion methods often suffer from low vertical resolution and poor lateral continuity, making it difficult to accurately describe the spatial distribution of thin coal seams.[2–4]

At present, the acoustic impedance inversion method widely used in engineering practice mainly includes the model-based inversion method and the constrained sparse pulse inversion method. Cook and Schneider[5] first proposed the model-based acoustic impedance inversion, which provides low-frequency background and structural trends by introducing an initial impedance model, thereby ensuring inversion stability. However, in three-dimensional (3D) seismic data processing, this method is usually implemented in a trace-by-trace or line-by-line manner, and the lateral continuity of the inversion results strongly depends on the quality of the initial model. When the number of wells is limited or the initial model is inaccurate, the inversion results are prone to strong model-controlled characteristics.[6–8] Model-based inversion has been widely applied in thin interbedded coal seam prediction, but its resolution remains limited under thin-layer conditions.[9]

To reduce the dependence on the initial model, constrained sparse spike inversion methods have been proposed. By imposing sparsity constraints on the reflection coefficients, these methods improve vertical resolution and are more suitable for thin-layer target characterization.[10,11] Sparse spike inversion has been successfully applied in reservoir prediction and thin-layer identification[12], and related methods have also been combined with machine learning techniques to further enhance reservoir characterization capability.[13,14] These approaches have been widely implemented in commercial software such as STRATA and JASON.[15,16] In studies of coal seam thickness prediction and fine reservoir characterization, geostatistical inversion methods have also been widely applied.[17,18] By introducing geostatistical constraints, such as random simulation and variogram models, these methods integrate both seismic and well data during inversion and generate multiple impedance realizations that satisfy statistical characteristics, thereby improving the reliability of reservoir parameter prediction. In coal seam thickness prediction, geostatistical inversion can effectively describe spatial variations between wells. However, this type of method usually requires a sufficient number of wells for statistical modeling. When well control is sparse or seismic resolution is limited, prediction uncertainty increases significantly, and the computational cost is relatively high, which limits its efficiency in large-scale 3D data applications. In addition, other inversion techniques, such as MGI inversion, have also been applied to coal seam thickness prediction and have shown certain advantages under complex geological conditions.[19]

In addition, to improve lateral continuity, some studies have introduced spatial smoothing or other regularization constraints into the inversion process.[20–22] Structurally constrained inversion can enhance the spatial stability of inversion results by incorporating geological structure information.[23] Total variation (TV) regularization, originally developed in the field of image processing[24], has been widely used in seismic inversion for its ability to preserve structural edges while suppressing noise. Nonlinear multichannel impedance inversion based on TV regularization has been shown to improve spatial stability and reduce inversion artifacts.[25] However, conventional first-order TV regularization tends to introduce the so-called "staircase effect," which may oversimplify smoothly varying geological features. Previous studies in both image processing and geophysical inversion have shown that high-order TV regularization can effectively alleviate this effect by penalizing higher-order derivatives, thereby better preserving smooth variations while maintaining structural boundaries.[26–28] Despite these improvements, most existing TV-based inversion methods are still implemented within a line-by-line framework, and the effect of true 3D spatial constraints is limited. As a result, the problem of poor lateral continuity remains, making it difficult to meet the requirements for fine characterization of thin coal seams.[29,30] Recent studies have shown that improving the lateral stability of inversion is particularly important for thin coal-seam detection and thickness prediction under complex geological conditions.[31]

The research target of this paper is the No. 15 coal seam in the Yushe East exploration area, Shanxi Province, with an average thickness of approximately 4.5 m. The lateral development of this coal seam is relatively stable, but the number of wells is limited, necessitating accurate characterization of the spatial variation in coal seam thickness. Therefore, high requirements are imposed on the lateral continuity and vertical resolution of the inversion results. To address these challenges, this paper

proposes a 3D acoustic impedance inversion method based on high-order TV regularization. Unlike conventional approaches that perform inversion in a trace-by-trace or line-by-line manner, the proposed method directly imposes 3D spatial constraints across the full data volume, enabling simultaneous use of inter-trace correlations in both the inline and crossline directions. This method constructs a 3D high-order TV regularization constraint and integrates it into the inversion framework to enhance lateral continuity. The proposed method is validated using both synthetic models and field data and is compared to conventional impedance inversion methods. The results demonstrate that the proposed method provides clear improvements in lateral continuity and vertical resolution for thin coal-seam inversion.

2. Methodology

2.1. Model-constrained acoustic impedance inversion

The 3D seismic data s can be represented as a 3D convolutional form of wavelet w with the reflectivity volume R (**Equation 1**):

$$\boldsymbol{s}(x,y,t)=\boldsymbol{w}*\boldsymbol{R} \tag{1}$$

where $*$ represents the 3D convolution operation.

Under the assumption of horizontally layered media, when the variation of acoustic impedance Z between adjacent sample points is smaller than the absolute impedance value, the reflectivity R can be approximated in the form of the adjacent impedance difference. By introducing the logarithmic acoustic impedance, a linear relationship between the reflectivity and the logarithmic impedance can be established as follows (**Equation 2**):

$$\boldsymbol{R}_{i,j}=\frac{\boldsymbol{Z}_{i+1,j}-\boldsymbol{Z}_{i,j}}{\boldsymbol{Z}_{i+1,j}+\boldsymbol{Z}_{i,j}}\approx\frac{1}{2}(\ln\boldsymbol{Z}_{i+1,j}-\ln\boldsymbol{Z}_{i,j}) \tag{2}$$

The relationship between the seismic data s and the logarithmic impedance can be expressed as a convolutional model with a first-order vertical difference operator applied to the log-impedance (**Equation 3**):

$$\boldsymbol{s}=\boldsymbol{WD}\ln\boldsymbol{Z}+\boldsymbol{n} \tag{3}$$

where s denotes the seismic data, W is the wavelet convolution matrix constructed from the seismic wavelet w, D is the first-order vertical difference operator, and n represents the noise. In practical applications, the most commonly used regularization is the Tikhonov regularization. Accordingly, the objective function of model-based acoustic impedance inversion can be written as **Equation 4**:

$$J(\boldsymbol{Z})=\frac{1}{2}\left\|\boldsymbol{s}_{obs}-\boldsymbol{WD}\widetilde{\boldsymbol{Z}}\right\|_F^2+\lambda\left\|\boldsymbol{T}(\widetilde{\boldsymbol{Z}}-\widetilde{\boldsymbol{Z}}_0)\right\|_2^2 \tag{4}$$

where $\|\bullet\|_F$ represents the Frobenius norm of the matrix; s_{obs} represents the observed seismic data; $\tilde{z}$ represents the logarithmic impedance, defined as $\widetilde{\boldsymbol{Z}}=\ln\boldsymbol{Z}$; λ is the regularization parameter; T is the Tikhonov matrix, usually taken as the first-order difference matrix. This method essentially applies an L_2-norm constraint to impose an overall smoothing effect on the impedance model, which can weaken the boundary characteristics of geological bodies. Moreover, the lateral continuity of the inversion result strongly depends on the accuracy of the initial model. When the initial model is low-frequency, the method cannot obtain high-resolution inversion results, which limits its application to 3D fine reservoir prediction.

2.2. Three-dimensional high-order total variation regularization model

Thin-layer reservoirs such as coal seams are usually characterized by thin vertical thickness and stable lateral continuity. Therefore, in 3D acoustic impedance inversion, it is necessary to explicitly introduce spatial constraints in the lateral directions to enhance the lateral continuity of the inversion results. Conventional TV regularization imposes constraints using first-order differences in both vertical and horizontal directions. However, the first-order difference often contains amplitude-variation information of the seismic data. As shown in Figure 1B, the first-order TV model tends to suppress these variations, which may lead to the well-known staircase effect in the inversion result. Figure 1C shows the second-order difference profile. The second-order difference reflects the rate of change in amplitude rather than the amplitude itself, and it mainly appears as random noise in the profile, without containing the primary amplitude information of the seismic data. Therefore, in this study, a second-order difference operator is introduced in the lateral directions to construct the TV regularization term, thereby enhancing lateral continuity while preserving structural boundaries.

For 3D seismic data $u(x, y, t)$, there are three forms of second-order difference in the x–y plane: second-order difference along the x direction $\boldsymbol{u}_{xx}=\nabla_{xx}\otimes\boldsymbol{u}$, second-order difference along the y direction $\boldsymbol{u}_{yy}=\nabla_{yy}\otimes\boldsymbol{u}$, and mixed difference along the x–y direction $\boldsymbol{u}_{xy}=\boldsymbol{u}_{yx}=\nabla_{xy}\otimes\boldsymbol{u}$, as shown in Figure 2.

By combining the above operators, a set of high-order lateral difference operators is constructed, enabling a more accurate representation of inter-trace correlations

in the 3D seismic volume. The combined operators can be expressed as **Equation 5**:

$$\begin{cases} \Psi_1 = \nabla_{xx} + \nabla_{yy} \\ \Psi_2 = \nabla_{xx} - \nabla_{yy} \\ \Psi_3 = 2 \bullet \nabla_{xy} \end{cases} \quad (5)$$

where Ψ_1, Ψ_2 and Ψ_3 are the newly combined 3D difference operators. Assuming the size of the 3D seismic data is 10 × 10 × 10, Figure 3 shows the construction diagram of Ψ_1, Ψ_2 and Ψ_3.

Therefore, the 3D higher-order TV regularization constraint term can be expressed as **Equation 6**:

$$TV(\boldsymbol{u}) = \sum_{m=1}^{3} \left\| \Psi_m * (\boldsymbol{WD}\widetilde{\boldsymbol{Z}}) \right\|_2 = \sum \sqrt{(\Psi_1 * \boldsymbol{u})^2 + (\Psi_2 * \boldsymbol{u})^2 + (\Psi_3 * \boldsymbol{u})^2} \quad (6)$$

2.3. Objective function and solution method for three-dimensional acoustic impedance inversion

Under the 3D high-order TV regularization constraint, the objective function shown in **Equation 4** becomes **Equation 7**:

$$J(\widetilde{\boldsymbol{Z}}) = \frac{1}{2} \left\| s_{obs} - \boldsymbol{WD}\widetilde{\boldsymbol{Z}} \right\|_F^2 + \alpha \left\| (\widetilde{\boldsymbol{Z}} - \widetilde{\boldsymbol{Z}}_0) \right\|_2^2 + \beta \sum_{m=1}^{3} \left\| \Psi_m * (\boldsymbol{WD}\widetilde{\boldsymbol{Z}}) \right\|_2 \quad (7)$$

where the regularization parameters α and β control the balance between data fidelity and the strength of the high-order TV constraint. In this study, these parameters were determined empirically through a series of trial-and-error tests on a subset of the data to achieve an optimal trade-off between inversion accuracy and spatial continuity. Specifically, multiple combinations of α and β were evaluated, and the final values were selected based on quantitative metrics and visual inspection of the residuals. In general, a larger β enhances lateral smoothness but may lead to over-smoothing, whereas a smaller β may result in insufficient noise suppression.

The objective function in **Equation 7** involves 3D convolution operations, making it difficult to solve using traditional gradient-based optimization methods. Therefore, the split-Bregman method was employed to solve the inversion problem. For large 3D seismic datasets, solving the objective function in the time domain can be computationally expensive. To address this issue, the objective function is transformed into the frequency domain (**Equation 8**):

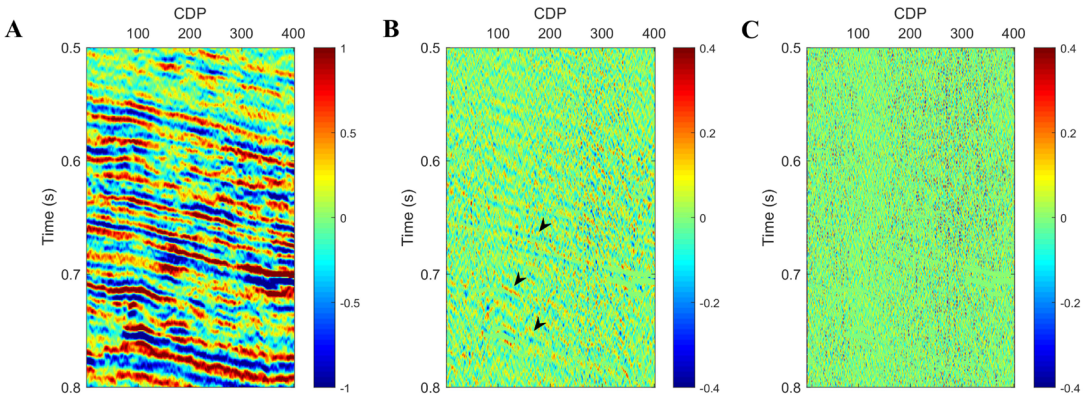

Figure 1. Seismic data and difference profiles. (A) Noisy seismic data. (B) First-order difference profile. (C) Second-order difference profile.

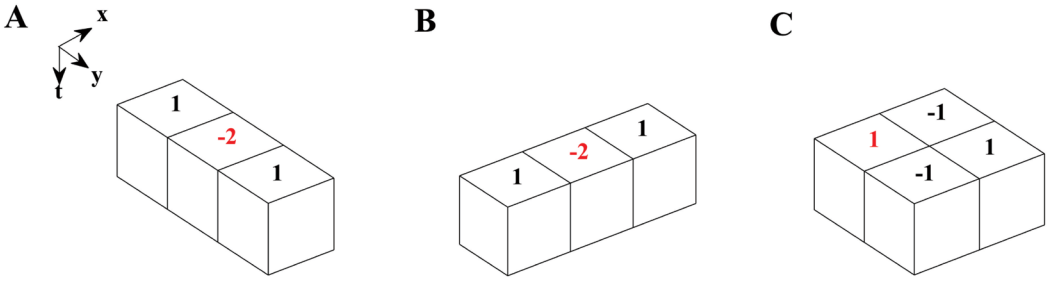

Figure 2. Three second-order difference operators on the *x*-*y* plane. (A) ∇_{xx}. (B) ∇_{yy}. (C) ∇_{xy}.

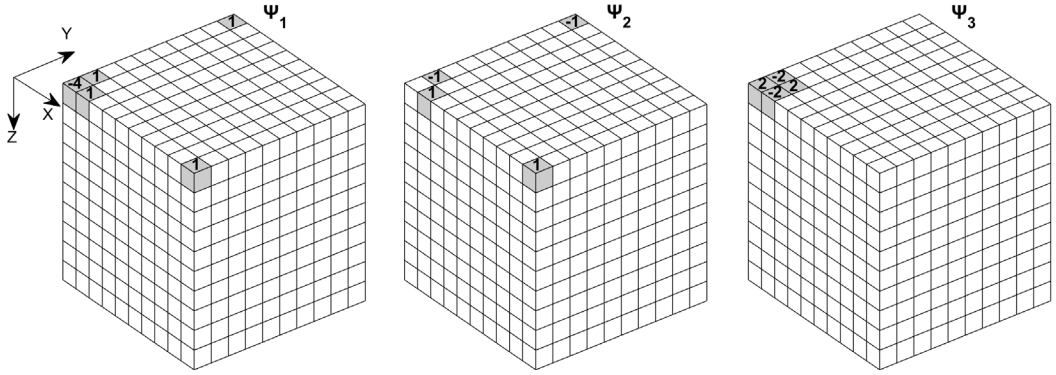

Figure 3. Schematic diagram of the construction of three combination operators

$$J(\hat{\tilde{\boldsymbol{Z}}})=\frac{1}{2}\left\|\hat{\boldsymbol{S}}-\hat{\boldsymbol{W}}\bullet\hat{\boldsymbol{D}}\bullet\hat{\tilde{\boldsymbol{Z}}}\right\|_F^2+\alpha\left\|(\hat{\tilde{\boldsymbol{Z}}}-\hat{\tilde{\boldsymbol{Z}}}_0)\right\|_2^2+\beta\sum_{m=1}^{3}\left\|\hat{\boldsymbol{\Psi}}_m\bullet(\hat{\boldsymbol{W}}\bullet\hat{\boldsymbol{D}}\bullet\hat{\tilde{\boldsymbol{Z}}})\right\|_2 \quad (8)$$

The variables marked with "$\hat{\circ}$" represent their own 3D Fourier transform results, and "$\bullet$" represents the dot product operation between 3D matrices. Within the split-Bregman framework, **Equation 8** can be split into the following problems (**Equations 9–11**):

$$\hat{\tilde{\boldsymbol{Z}}}^{k+1}=\min_{r}\left[\begin{array}{l}\frac{1}{2}\left\|\hat{\boldsymbol{S}}-\hat{\boldsymbol{W}}\bullet\hat{\boldsymbol{D}}\bullet\hat{\tilde{\boldsymbol{Z}}}\right\|_F^2+\frac{\alpha}{2}\left\|\hat{\tilde{\boldsymbol{Z}}}-\hat{\tilde{\boldsymbol{Z}}}_0\right\|_2^2\\+\frac{\beta}{2}\left\|\hat{\boldsymbol{d}}_m^k-\hat{\boldsymbol{\Psi}}_m\bullet\hat{\boldsymbol{W}}\bullet\hat{\boldsymbol{D}}\bullet\hat{\tilde{\boldsymbol{Z}}}-\hat{\boldsymbol{b}}_m^k\right\|_2^2\end{array}\right] \quad (9)$$

$$\hat{\boldsymbol{d}}_m^{k+1}=\min_{d_m}\left[\lambda\left\|\hat{\boldsymbol{d}}_1,\hat{\boldsymbol{d}}_2,\hat{\boldsymbol{d}}_3\right\|_2+\frac{\beta}{2}\sum_{m=1}^{3}\left\|\hat{\boldsymbol{d}}_m^k-\hat{\boldsymbol{\Psi}}_m\bullet\hat{\boldsymbol{W}}\bullet\hat{\boldsymbol{D}}\bullet\hat{\tilde{\boldsymbol{Z}}}-\hat{\boldsymbol{b}}_m^k\right\|_F^2\right] \quad (10)$$

$$\hat{\boldsymbol{b}}_m^{k+1}=\hat{\boldsymbol{b}}_m^k-\left[\hat{\boldsymbol{d}}_m^{k+1}-\hat{\boldsymbol{\Psi}}_m\bullet\hat{\boldsymbol{W}}\bullet\hat{\boldsymbol{D}}\bullet\hat{\tilde{\boldsymbol{Z}}}^{k+1}\right] \quad (11)$$

where d and b are intermediate variables; k is the number of iterations. Taking the derivative of **Equation 9** and setting it to 0, we can simplify to obtain (**Equation 12**):

$$\boldsymbol{Z}^k=\exp\left(IFFT_{3D}\left[\frac{\alpha\hat{\tilde{\boldsymbol{Z}}}_0+\hat{\tilde{\boldsymbol{W}}}\bullet\hat{\tilde{\boldsymbol{D}}}\bullet\hat{\boldsymbol{S}}+\beta\hat{\tilde{\boldsymbol{W}}}\bullet\hat{\tilde{\boldsymbol{D}}}\bullet\sum_m\{\hat{\tilde{\boldsymbol{\Psi}}}_m\bullet(\hat{\boldsymbol{d}}_m^k-\hat{\boldsymbol{b}}_m^k)\}}{\hat{\tilde{\boldsymbol{W}}}\bullet\hat{\boldsymbol{W}}\bullet\hat{\tilde{\boldsymbol{D}}}\bullet\hat{\boldsymbol{D}}+\alpha\boldsymbol{I}+\beta\hat{\tilde{\boldsymbol{W}}}\bullet\hat{\boldsymbol{W}}\bullet\sum_m(\hat{\tilde{\boldsymbol{\Psi}}}_m\bullet\hat{\boldsymbol{\Psi}}_m)}\right]\right) \quad (12)$$

where Z represents the desired acoustic impedance inversion result, "exp" represents the exponential operation; $IFFT_{3D}$ represents the 3D inverse Fourier transform operation; and I is an all-1 matrix. **Equation 10** can be solved using the soft threshold constraint function (**Equation 13**):

$$\hat{\boldsymbol{d}}_m^{k+1}=FFT_{3D}\left(\max(1-\frac{\lambda/\beta}{\boldsymbol{s}^k},0)\bullet[\boldsymbol{\Psi}_m*\boldsymbol{WD}\tilde{\boldsymbol{Z}}^{k+1}+\boldsymbol{b}_m^k]\right) \quad (13)$$

where $\boldsymbol{s}^k=\sqrt{\sum_{m=1}^{3}\left(\boldsymbol{\Psi}_m*(\boldsymbol{WD}\tilde{\boldsymbol{Z}}^{k+1})+\boldsymbol{b}_m^k\right)^2}$.

3. Algorithm verification

To evaluate the effectiveness of the proposed method, a 3D overthrust model was constructed for algorithm testing (Figure 4A). The model exhibited clear horizontal structural changes and local fracture and thin-layer characteristics, which could be used to test the inversion method's ability to portray spatial continuity under complex structural conditions. The original impedance model was smoothed using a low-pass filter to generate the initial low-frequency model required for inversion (Figure 4B). The corresponding 3D synthetic seismic record was generated using a convolution model, and 20% Gaussian random noise was added to the seismic record to simulate noise interference in the actual data. The obtained seismic data is shown in Figure 5. To analyze the impact of different dimensional constraints on the inversion results, we used the one-dimensional trace-by-trace inversion method, the two-dimensional line-by-line inversion method, and the proposed method. Among them, the one-dimensional trace-by-trace inversion method only introduced L_1-norm constraints in the time direction, and each trace was independent of each other and did not contain any horizontal constraint information; the two-dimensional line-by-line inversion method inverted on a single measurement line, and introduced horizontal second-order TV regularization constraints in the line direction, so as to enhance the continuity of the inline direction, but there remained no mutual constraints between different measurement lines.

Figure 6 shows the acoustic impedance inversion results of the three methods and the corresponding residual profile comparison. From the inversion results, the one-dimensional trace-by-trace inversion (Figure 6A) showed clear "string-shaped" characteristics horizontally, with large amplitude variations between traces, reflecting strong randomness. This is due to the lack of horizontal constraints in the independent solution of each trace inversion, which prevents effective suppression of noise and inversion errors in space.

The two-dimensional line-by-line inversion (Figure 6C) showed improved continuity along the main inline direction compared to the one-dimensional approach, indicating that introducing lateral constraints along the line direction enhanced inversion stability. However, significant "vertical streaks" remain in the crossline direction, demonstrating that line-by-line inversion can only ensure continuity along a single direction and is insufficient to preserve 3D spatial consistency.

In contrast, the proposed method produced results (Figure 6E) that more closely match the true model. Within the overthrust structural region, impedance interfaces maintained good lateral continuity, structural boundaries were clear, and the overall inversion result was smoother and more stable. This improvement is attributed to the high-order TV regularization applied simultaneously in both horizontal directions, which effectively exploits the spatial correlation between traces and significantly suppresses the lateral propagation of random noise and inversion errors.

Examining the original impedance model in Figure 4A, an obvious fault structure was evident at the position indicated by the black arrow. Both the one-dimensional and two-dimensional inversion methods failed to accurately recover the spatial position and boundary geometry of this

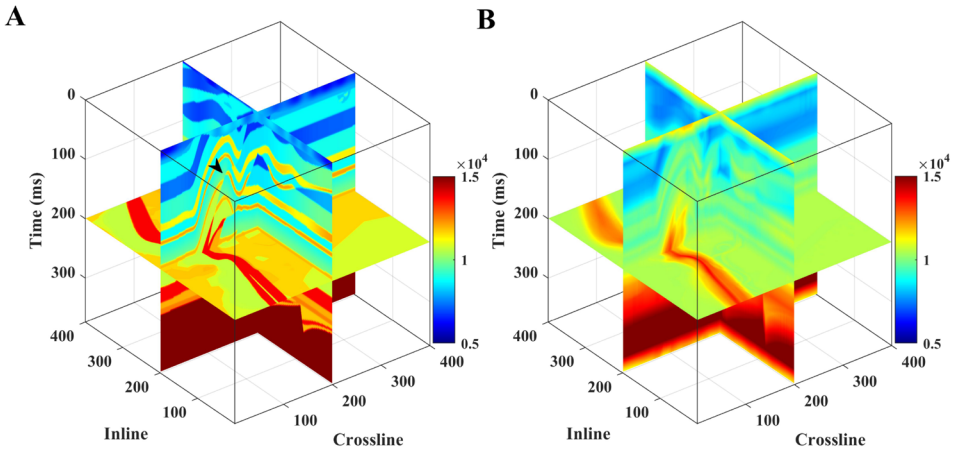

Figure 4. The overthrust model. (A) Three-dimensional overthrust impedance model. (B) Smoothed initial impedance model.

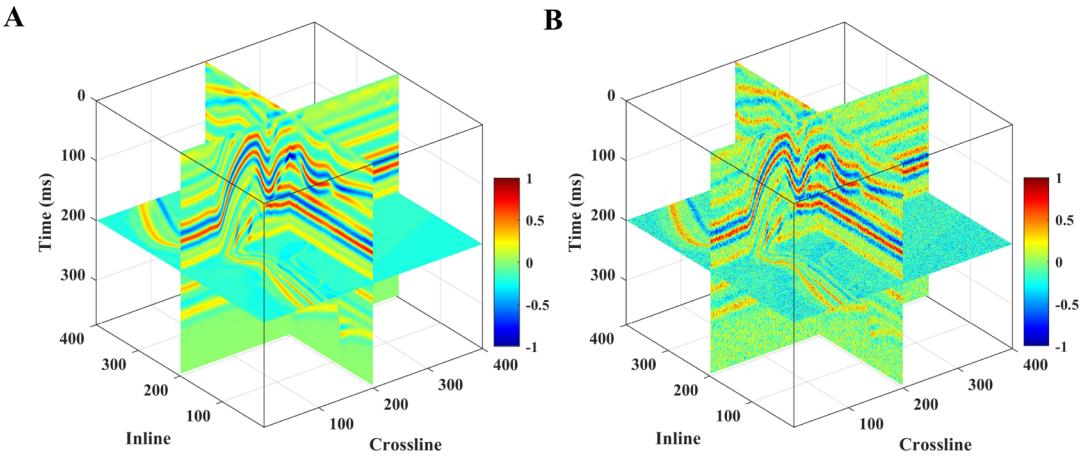

Figure 5. The seismic data. (A) Noise-free seismic data. (B) Noisy seismic data.

structure, showing varying degrees of displacement and blurring near the fault. In contrast, the proposed method reconstructed the fault geometry with high fidelity, and the fault position closely matched the true model, demonstrating the clear advantage of incorporating 3D spatial constraints in complex structural characterization.

Analysis of the residual profile further confirmed these observations. The residuals of the one- and two-dimensional inversions (Figure 6B and 6D) showed clear layered reflections and boundary features, indicating that the inversion results do not fully fit the seismic data. Moreover, the residuals exhibited lateral striping, reflecting strong spatial inconsistencies during inversion. In comparison, the residual section of the proposed method (Figure 6F) contained almost no continuous reflection features, indicating that the 3D high-order TV regularization can maintain data fitting accuracy while substantially improving the stability and spatial consistency of the inversion results.

In addition, the root mean square error (RMSE) and the correlation coefficient (CC) for different methods were compared to provide a quantitative assessment of their performance. The RMSE and CC are defined as **Equation 14**:

$$\mathrm{RMSE} = \sqrt{\frac{1}{N \times M \times P}\left\| Z^{inv} - Z^{true} \right\|_2^2},$$
$$\mathrm{CC} = \frac{\left| Z^{inv} - \bar{Z}^{inv} \right|_1 \cdot \left| Z^{true} - \bar{Z}^{true} \right|_1}{\sqrt{\left\| Z^{inv} - \bar{Z}^{inv} \right\|_2^2 \cdot \left\| Z^{true} - \bar{Z}^{true} \right\|_2^2}} \tag{14}$$

where Z_i^{inv} and Z_i^{true} denote the inverted and true impedance values, respectively; $\bar{Z}^{inv}$ and $\bar{Z}^{true}$ represent their corresponding mean values; N, M, and P denote the number of sampling points, traces, and inlines of the 3D seismic data, respectively. A smaller RMSE indicates that the inversion result is closer to the true impedance, whereas the CC ranges from −1 to 1, with values closer to 1 indicating a higher similarity between the inverted and true impedance.

As shown in Table 1, the proposed method yields the lowest RMSE and the highest CC, demonstrating superior inversion accuracy and better consistency with the reference data compared to other methods.

4. Practical applications

4.1. Overview of the study area

The study area is located in the eastern part of Yushe County, Jinzhong City, Shanxi Province, within the central-western portion of the Yushe East exploration block in the northeastern Qinshui Basin.[32] The 3D seismic data used in this study cover an area of approximately 10 km^2. The area lies in the western foothills of the Taihang Mountains and is characterized by eroded, dissected mid-mountain terrain with pronounced topographic relief and well-developed valleys. The overall topography is higher in the central region and lower on both sides, with elevations ranging from 1,220 to 1,380 m and a relative relief of about 150 m. The surface is predominantly bedrock, locally overlain by thin loess layers. Such complex terrain can affect the quality of seismic data and the lateral continuity of inversion results, placing higher demands on the stability of acoustic impedance inversion methods.

Structurally, the study area lies within the gentle fold belt of the Qinshui Basin, dominated by northeast-trending strata with relatively low dip angles and minor faulting. The overall structural conditions are relatively stable, favoring the preservation and lateral continuity of coal seams. The basin interior is characterized by short-axis folds and predominantly small-scale normal faults, indicating weak overall deformation. The stratigraphic sequence in the area is relatively complete, comprising, from bottom to top, the Precambrian, Paleozoic, Mesozoic, and Cenozoic sediments, with the Carboniferous–Permian coal-bearing strata being the main target. These coal-bearing units consist primarily of interbedded sandstones, mudstones, and coal layers, representing a marine–continental transitional depositional system. Coal seams generally exhibit stable lateral continuity, although local variations in thickness are observed.

The target layer for this study is the No. 15 coal seam, which is laterally continuous across the area but exhibits

Table 1. Comparison of quantitative indicators for different inversion results

Indicator	One-dimensional trace-by-trace method	Two-dimensional line-by-line method	The proposed method
CC	0.9731	0.9802	0.9980
RMSE	628.8129	538.2387	170.1518

Abbreviations: CC: Correlation coefficient; RMSE: Root mean square error.

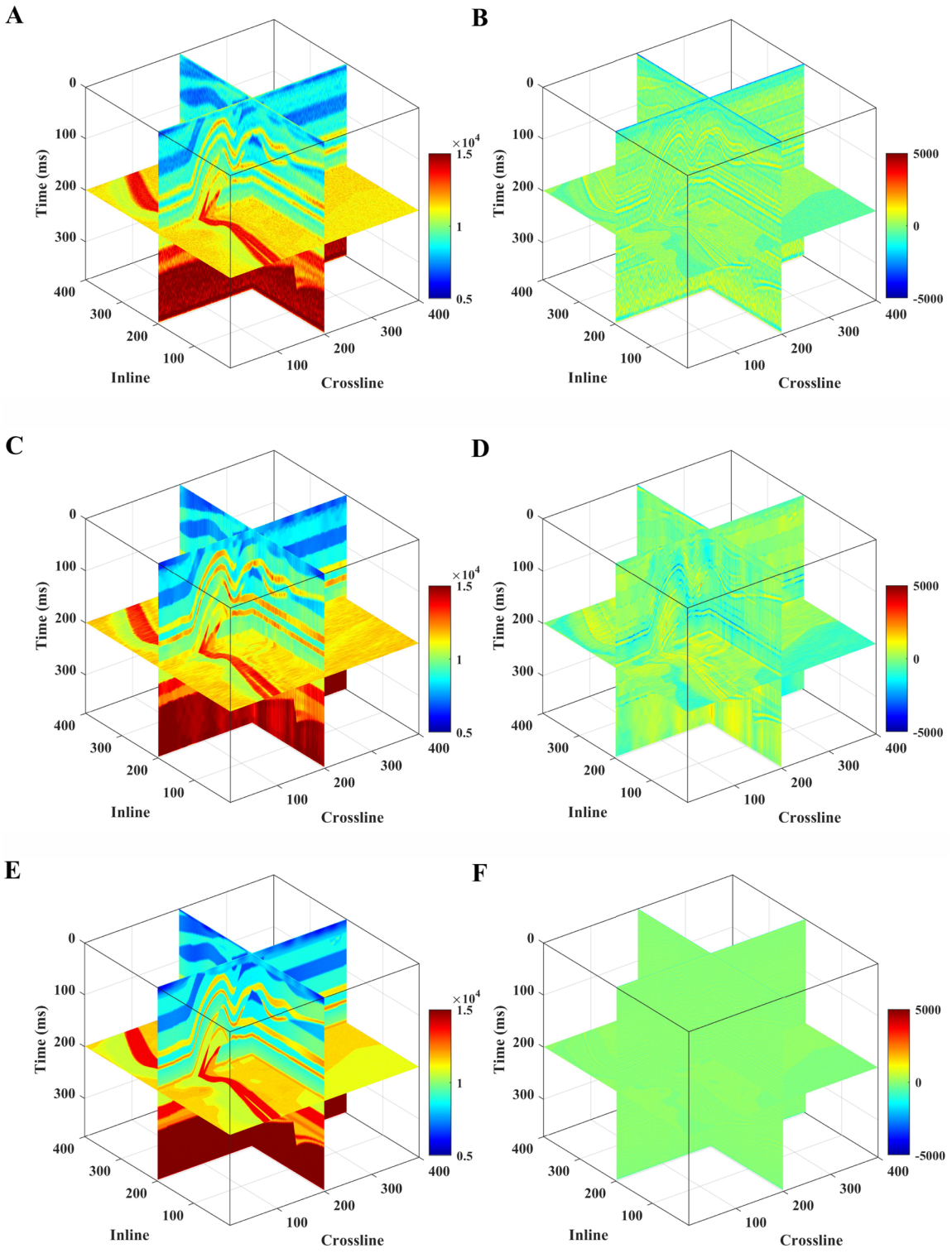

Figure 6. Inversion results and residual profiles of each method

some heterogeneity due to sedimentary and structural influences. The seam is relatively thin in the vertical direction, placing high demands on the lateral stability and vertical resolution of seismic inversion results. Given the limited well control in the study area, accurately characterizing lateral variations in coal thickness is challenging based solely on wells. Therefore, high-resolution 3D acoustic impedance inversion using seismic data is necessary to improve the reliability of coal seam spatial distribution predictions.

4.2. Rock physical characteristics

To analyze the petrophysical characteristics of the target coal seam, a cross-plot analysis of well-log data was performed. The results (Figure 7) indicate that the target coal seam (black) exhibited distinct rock-physics properties compared to the surrounding strata (purple). According to the cross-plot analysis, the coal seam was characterized by relatively low P-wave velocity, low density, and low acoustic impedance. Specifically, the P-wave velocity is generally less than 2,400 m/s, the density is less than 1.5 g/cm^3, and the acoustic impedance is less than 5,000 (m/s)·(g/cc). These features clearly distinguish the coal seam from the surrounding rocks and provide a reliable basis for identifying it using impedance inversion.

4.3. Analysis of acoustic impedance inversion results

To evaluate the practical performance of the proposed method, we use a model-based multi-channel acoustic impedance inversion module implemented in commercial software STRATA (7.1, CGG GeoSoftware, France) as a reference. The 3D seismic data are shown in Figure 8A. Acoustic impedance curves were first calculated from well-log data. Low-pass filtering was then applied to the well-derived impedance curves to extract the low-frequency trend. Subsequently, horizon-constrained inter-well interpolation was performed to construct a 3D low-frequency acoustic impedance model (Figure 8B).

Figure 9 compares 3D inversion results obtained from the two methods. Black arrows indicate the target No.15 coal seam. Overall, STRATA inversion results exhibit relatively low vertical resolution. Consequently, the top and bottom interfaces of the coal seam appeared ambiguous, and recovery of high-frequency components was limited. In contrast, the proposed method significantly enhanced vertical resolution. Interlayer interfaces became clearer, while thin-layer structures were delineated more accurately. Moreover, detailed variations of reservoir properties were better represented.

Figure 10 shows the inversion profile at inline #295, which passes through the well location. Impedance values derived from STRATA inversion were generally overestimated, and the target coal seam showed poor lateral continuity. Noticeable smoothing also appeared in thin-layer zones near the well. As a result, sensitivity to local high- and low-impedance variations remained limited, leading to inaccurate delineation of reservoir boundaries. In comparison, inversion results produced by the proposed method matched well-log curves more closely. High-frequency impedance variations near well-controlled locations were effectively recovered. Furthermore, coal seam interfaces appeared clearer, and both vertical resolution and lateral continuity were substantially improved.

For further comparison, inversion results at inline #485 were examined. This line lies far from the well location, and inversion constraints mainly relied on seismic data and the low-frequency model (Figure 11). Under this condition, STRATA inversion was strongly dominated

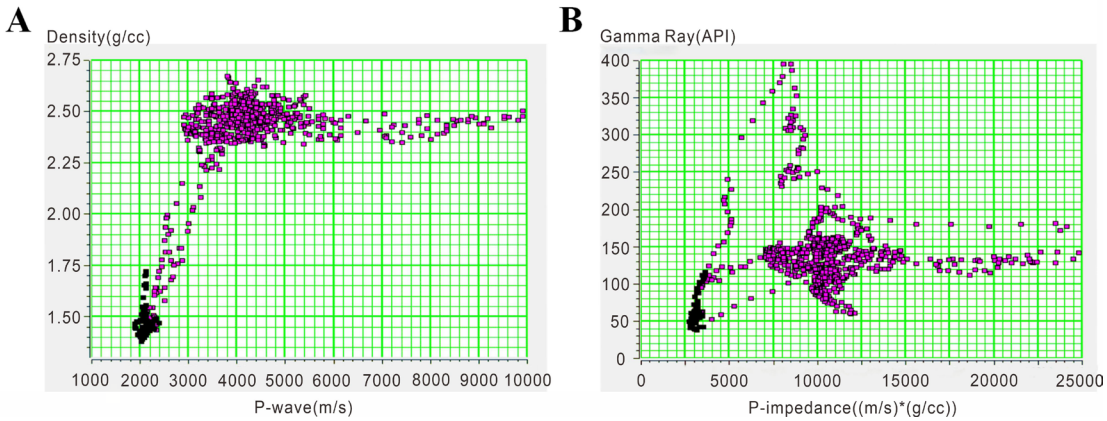

Figure 7. Cross-plot analysis. (A) Density-P wave. (B) Gamma-Impedance.

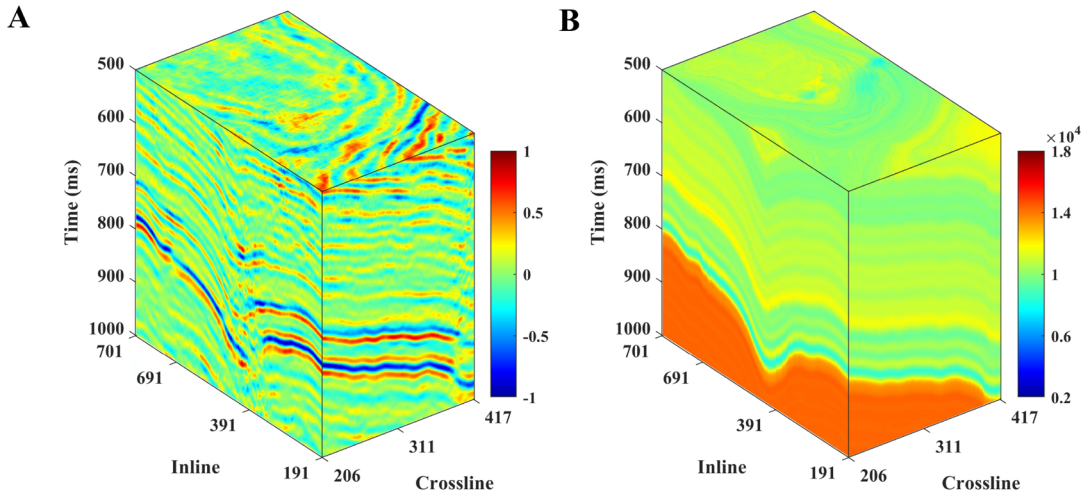

Figure 8. The field data. (A) Three-dimensional field seismic data. (B) Low-frequency impedance model.

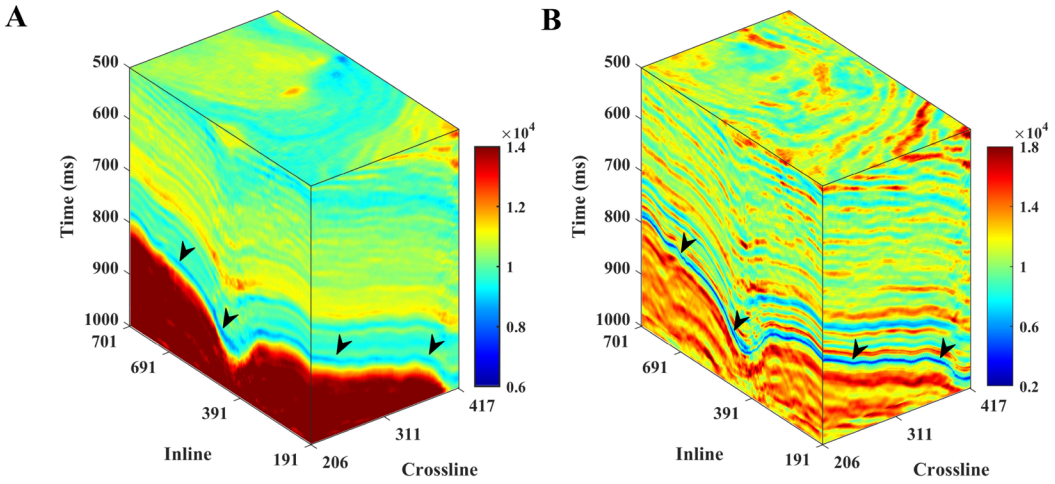

Figure 9. Comparison of inversion results. (A) Result from STRATA inversion. (B) Result from the proposed method.

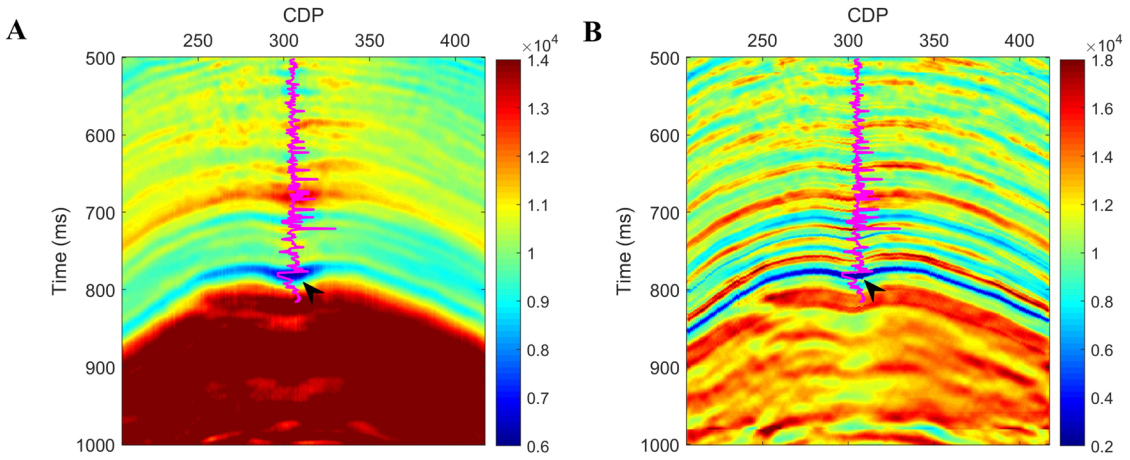

Figure 10. Inversion profile at inline #295. (A) Result from STRATA inversion. (B) Result from the proposed method.

by the low-frequency model. Consequently, structural smoothing became evident, impedance interfaces showed poor continuity, thin-layer features remained unclear, and contrasts between high- and low-impedance zones were weak. These limitations hindered the accurate characterization of the coal seam and adjacent strata. In contrast, the proposed method successfully recovered the low-impedance anomaly associated with the target coal seam. Coal seam interfaces were delineated with good lateral continuity, and predicted results agreed with regional geological understanding. These observations demonstrate that the proposed method maintained stable performance and reliable predictive capability even under weakly constrained conditions.

4.4. Coal seam thickness prediction

Preliminary cross-plot analysis indicated that the acoustic impedance of the target coal seam was lower than 5,000 (m/s)·(g/cm^3). However, the STRATA inversion results generally show higher impedance values, with notable discrepancies relative to the coal-seam impedance inferred from well-log data. This mismatch obscured the low-impedance characteristics of the coal seam, making it difficult to accurately identify the roof and floor interfaces and, consequently, to reliably estimate coal seam thickness.

Figure 12 presents the coal seam thickness prediction results obtained using the two methods. The proposed method yielded a relatively stable thickness distribution within the target area, with values mainly ranging from 3 m to 6.5 m. Relatively thick and laterally continuous coal seams were developed in the northwestern and southern parts of the study area, which were favorable for coalbed methane exploitation. In contrast, the thickness predicted by the STRATA inversion was generally underestimated and showed poor lateral continuity, making it difficult to effectively identify the stable distribution of the coal seam.

Table 2 compares the predicted coal seam thicknesses at five wells with those interpreted from well logs. The results obtained by the proposed method agreed well with the logging interpretations, with absolute errors less than 0.5 m. In addition, the predicted coal seam thickness away from the well locations varied smoothly without unreasonable abrupt changes.

The dominant frequency of the seismic data used in this study was approximately 35 Hz. No explicit spectral broadening or resolution enhancement processing was applied beyond standard preprocessing procedures. Based on this frequency, the theoretical vertical resolution of seismic data was approximately 8 m. It should be noted that the high accuracy of thickness prediction (errors < 0.5 m) does not rely solely on intrinsic seismic resolution, but also on the integration of well constraints and high-order TV regularization, which enhances the continuity and stability of the inversion results. As a result, the proposed method provided reliable thickness estimates even for thin coal seams.

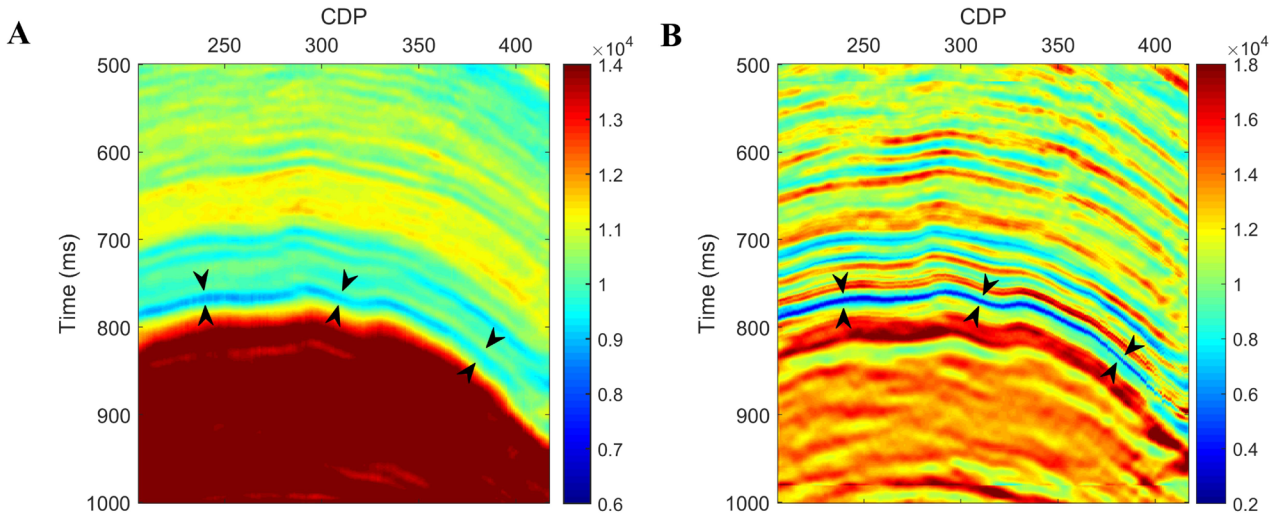

Figure 11. Inversion profile at inline #485. (A) Result from STRATA inversion. (B) Result from the proposed method.

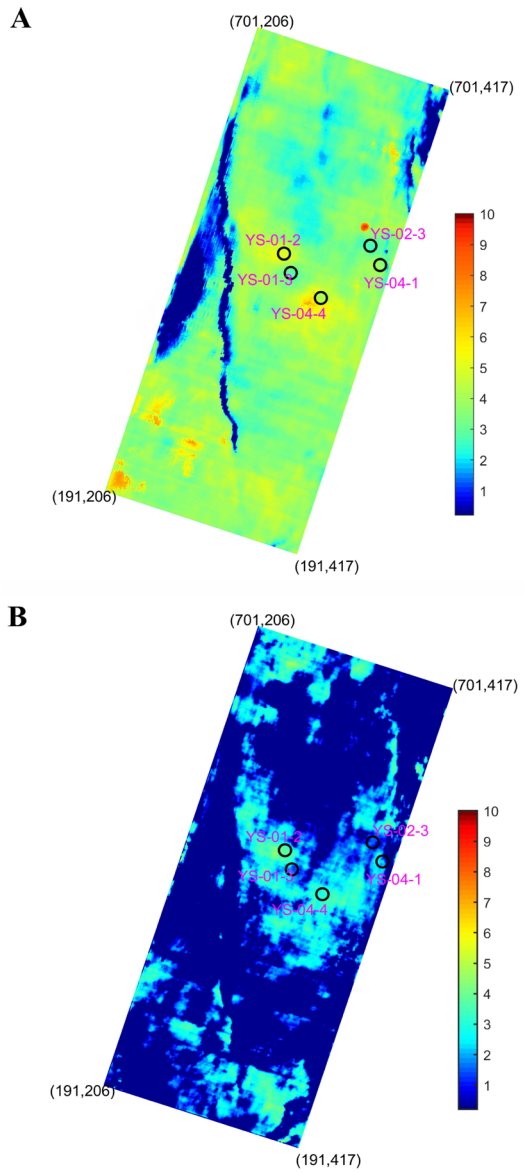

Figure 12. Predicted thickness of the target coal seam. (A) The proposed method; (B) STRATA inversion.

5. Discussion

The proposed method applies high-order TV constraints simultaneously in both the inline and crossline directions, allowing direct inversion of the entire 3D seismic volume without trace-by-trace or line-by-line processing. This strategy strengthens the spatial correlation within the seismic cube and improves the lateral stability of the inversion results. The high-order difference operator preserves structural boundaries while maintaining strong robustness to noise. In addition, the method shows reduced dependence on the initial model, enabling more reliable impedance estimation under limited well constraints. These characteristics are consistent with the requirements for predicting thin coal seam thickness.

Although the proposed 3D high-order TV-regularized inversion method shows clear advantages in improving lateral continuity and vertical resolution, several limitations should be noted. First, the inversion result is sensitive to the selection of regularization parameters. The weights of the high-order TV constraint and the data misfit term (α and β) need to be determined through empirical testing. In general, larger regularization parameters promote smoothness but can lead to over-smoothing, whereas smaller values preserve fine-scale features but can introduce noise. In practice, parameter selection is performed stepwise. Specifically, α, which controls data fidelity, is first adjusted to ensure that the reconstructed data match the observed seismic data with an acceptable residual level. Then, β, which controls the strength of the high-order TV constraint, is gradually increased to improve lateral continuity while monitoring the preservation of structural details. The optimal parameter combination is selected by jointly considering quantitative metrics (e.g., RMSE and CC) and visual assessment of inversion results.

Second, the introduction of 3D spatial constraints increases the computational complexity of the inversion process. Compared to conventional trace-by-trace or line-by-line inversion methods, the proposed method requires solving the objective function over the entire 3-D seismic volume. Although the split-Bregman algorithm and frequency-domain solution are used to improve computational efficiency, the computational cost remains higher, especially for large-scale 3D seismic datasets.

Third, the high-order TV regularization enhances lateral continuity by suppressing rapid spatial variations, which may otherwise lead to excessive smoothing in areas with complex geological structures, such as fault zones or strongly heterogeneous strata. In these cases, small-scale structural details may be partially weakened, and additional structural constraints or adaptive regularization strategies may be required.

Future work should focus on developing adaptive regularization-parameter selection methods that incorporate structural or geological constraints and combine intelligent inversion techniques to further enhance the method's applicability to complex reservoirs and thin-layer prediction problems.

6. Conclusion

To overcome poor lateral continuity and strong dependence on initial models in conventional impedance inversion for

Table 2. Comparison of log-interpreted and predicted thicknesses of the target coal seam

Well	Well logging interpretation thickness (m)	Predicted thickness (m)		Absolute error (m)	Percentage of relative error
		STRATA	The proposed method		
YS01-2	4.21	3.762	4.258	0.048	1.14%
YS01-3	4.22	2.153	4.319	0.099	2.35%
YS02-3	4.15	1.765	3.955	−0.195	4.70%
YS04-1	5.28	2.688	4.816	−0.464	8.79%
YS04-4	4.62	3.216	4.425	−0.195	4.22%

3D seismic data, a 3D impedance inversion method based on high-order TV regularization is proposed. High-order difference operators were introduced in both horizontal directions to construct spatial TV constraints, allowing global regularization of the entire seismic volume and better utilization of trace-to-trace correlations. Synthetic tests showed that the proposed method significantly improved lateral continuity while preserving structural boundaries and accurately recovered impedance in structurally complex areas, demonstrating the effectiveness of 3D spatial constraints.

Application to 3D seismic data from the Yushe East exploration area, compared to model-based inversion in STRATA, the proposed method provided higher vertical resolution, better lateral continuity, and more clearly revealed the low-impedance characteristics of the No. 15 coal seam. Coal seam thickness prediction based on the inversion results shows a stable distribution, with errors less than 0.5 m compared to well interpretations, even in areas far from wells. The results indicate that the proposed method can achieve reliable characterization of thin coal seams. It is particularly effective in scenarios with limited well control and relatively high noise levels, where enhanced spatial continuity and noise suppression are critical for improving inversion stability and thin-layer prediction accuracy.

Acknowledgments

None.

Funding

This study was supported by the Shanxi Provincial Natural Science Foundation Youth Project (202303021212369), the National Natural Science Foundation of China (Grant No. 42004114), and the Jiangxi Province Natural Science Foundation (Grant Nos. 20242BAB25191 and 20252BAC220017).

Conflict of interest

Yaju Hao is an Early Career Editorial Board Member of this journal, but was not in any way involved in the editorial and peer-review process conducted for this paper, directly or indirectly. The authors declare no potential conflict of interest.

Author contributions

Conceptualization: Yinping Dong, Peng Zhang
Formal analysis: Xiaodong Yang
Investigation: Youyi Shen, Zhongbin Tian
Methodology: Wei Wei, Peng Zhang
Writing–original draft: Yinping Dong
Writing–review & editing: Yaju Hao, Peng Zhang

Availability of data

Data are available from the corresponding author upon reasonable request.

References

1. Gochioco LM, Gochioco JR, Ruev F, Coal geophysics expands with growing global demands for mine safety and productivity. *Lead Edge*. 2012;31(3):308-314.

   doi: 10.1190/1.3694898

2. Xing WJ, Cao SY, Chen SY, Sun YG, Post-stack P-acoustic impedance inversion based on spectral inversion. *Geophys Geochem Explor.* 2023;47(2):429-437. [In Chinese]

   doi: 10.11720/wtyht.2023.1222

3. Yang Y, Lei Y, Wang Q, *et al.* Reservoir thickness prediction method of lacustrine carbonate based on two-dimension scattering transformation. *Chin J Geophys.* 2024;67(4):1601-1612. [In Chinese]

   doi: 10.6038/cjg2023Q0974

4. Bao L, Zhang J, Zhang C, Guo R, Wei X, Jiang Z, A reliable Bayesian neural network for the prediction of reservoir thickness with quantified uncertainty. *Comput Geosci*.

2023;178:105409.

doi: 10.1016/j.cageo.2023.105409

5. Cook DA, Schneider WA, Generalized linear inversion of reflection seismic data. *Geophysics*. 1983;48(6):665–676.

doi: 10.1190/1.1441497

6. Bao L, Zhang J, Zhang C, Guo R, Wei X, Jiang Z, A reliable Bayesian neural network for the prediction of reservoir thickness with quantified uncertainty. *Comput Geosci.* 2023;178:105409.

doi: 10.1016/j.cageo.2023.105409

7. Li HW, Li FY, Qi QH, Yang T, Prediction of CBM enrichment area based on seismic multi-attribute analysis in Jiergalangtu depression. *Pet Geol Oilfield Dev Daqing*. 2020;39(4):135-142. [In Chinese]

doi: 10.19597/j.issn.1000-3754.201908001

8. Sun XJ, Application of 3D seismic integrated interpretation technique in thin coal zone. *Coal Geol Explor.* 2018;46(S1): 56-59. [In Chinese]

doi: 10.3969/j.issn.1001-1986.2018.S1.012

9. Wang M, Liu Y, Zou G, Teng D, She J, Application of model-based acoustic impedance inversion in the prediction of thin interbedded coal seams: a case study in the Yuwang colliery, Yunnan Province. *Explor Geophys.* 2023;54(4):407-415.

doi: 10.1080/08123985.2022.2155514

10. Wang LQ, Application of sparse pulse inversion in coal thickness inversion using high-density 3D seismic data. *Coal Econ Res.* 2024;44(S1):166-171. [In Chinese]

doi: 10.13202/j.cnki.cer.2024.s1.037

11. Zhang CL, Application of constrained sparse pulse inversion in coal seam thickness prediction. *Coal Geol China*. 2022;34(9):68-72. [In Chinese]

12. Helgesen J, Magnus I, Prosser S, *et al.* Comparison of constrained sparse spike and stochastic inversion for porosity prediction at Kristin Field. *Lead Edge*. 2000;19(4):400-407.

doi: 10.1190/1.1438620

13. Huang Z, Li X, Chen J, Jiang L, Chen Y F, Huang Y, Research on seismic performance prediction of CFST latticed column–composite box girder joint based on machine learning. *Constr Build Mater.* 2025;460:139811.

doi: 10.1016/j.conbuildmat.2024.139811

14. Kushwaha PK, Maurya SP, Singh NP, Use of maximum likelihood sparse spike inversion and probabilistic neural network for reservoir characterization: A study from F-3 block, the Netherlands. *J Pet Explor Prod Technol.* 2020;10(2):829-845.

doi: 10.1007/s13202-019-00805-3

15. He LJ, Xiong R, Lei HF, Cheng C, Application of Jason-constrained sparse pulse inversion in Maoxing area, Daqing. *J Chongqing Univ Sci Technol.* 2009;11(2):43–45. [In Chinese]

doi: 10.19406/j.cnki.cqkjxyxbzkb.2009.02.014

16. Wang ZQ, *Study on sparse spike deconvolution and impedance inversion*. Master's thesis, China University of Petroleum (Beijing); 2018. [In Chinese]

doi: 10.27643/d.cnki.gsybu.2018.001091

17. Zhang Y, Yin YS, Qin ZY, Application of geostatistical inversion in thin sandstone reservoir prediction. *Fault-Block Oil Gas Field*. 2015;022(5):565–569.

doi: 10.6056/dkyqt201505005

18. He B, Yan H, Identification of thin coal seam based on geostatistical inversion. *China Coal*. 2024;50(S1):336-342. [In Chinese]

doi: 10.19880/j.cnki.ccm.2024.S1.050

19. Sun P, Li XF, Zhang F, Zhang BQ, Jia XC, Jiang HY, Application of MGI inversion technology in coal seam thickness prediction. In: Lin J (Ed.), Proceedings of the International Field Exploration and Development Conference. Springer Series in Geomechanics and Geoengineering. Singapore: Springer, 2024;131-140.

doi: 10.1007/978-981-97-0268-8_11

20. Zhang R, Sen MK, Srinivasan S, Multitrace basis pursuit inversion with spatial regularization. *J Geophys Eng.* 2013;10:1-6.

doi: 10.1088/1742-2132/10/3/035012

21. Yuan S Y, Wang SX, Luo CM, He YX, Simultaneous multitrace impedance inversion with transform-domain sparsity promotion. *Geophysics*. 2015;80(2):R71–R80.

doi: 10.1190/geo2014-0065.1

22. Hamid H, Pidlisecky A, Structurally constrained impedance inversion. *Interpretation*. 2016;4(4):T577–T589.

doi: 10.1190/INT-2016-0049.1

23. Hamid H, Pidlisecky A, Lines L, Prestack structurally constrained impedance inversion. *Geophysics*. 2018;83(2):R89–R103.

doi: 10.1190/geo2016-0703.1

24. Rudin LI, Osher S, Fatemi E, Nonlinear total variation based noise removal algorithms. *Phys D Nonlinear Phenom.* 1992;60(1):259–268.

doi: 10.1016/0167-2789(92)90242-F

25. Gholami A, Nonlinear multichannel impedance inversion by total-variation regularization. *Geophysics*. 2015;80(5):R217–R224.

doi: 10.1190/geo2015-0004.1

26. Zhang P, Hao Y, Zhu Y, Zhang H, Yin D, Tian X, Random noise suppression method in prestack NMO domain based

on high-order TV regularization. *Oil Geophys Prospect.* 2024;59(1):70-79. [In Chinese]

doi: 10.13810/j.cnki.issn.1000-7210.2024.01.006

27. Hao Y, Zhang P, Wen X, Zhang H, Zhu B, Dai Y, 3D reflectivity inversion method based on TV regularization of lateral second-order derivatives. *Oil Geophys Prospect.* 2023;58(3):680-689. [In Chinese]

doi: 10.13810/j.cnki.issn.1000-7210.2023.03.021

28. Lefkimmiatis S, Bourquard A, Unser M, Hessian-based norm regularization for image restoration with biomedical applications. *IEEE Trans Image Process.* 2012;21(3):983-995.

doi: 10.1109/TIP.2011.2168232

29. Tang G, Li H, Liang B, Zhang X, Liu Y, Spatially structured regularization multichannel sparse pulse deconvolution. *Pet. Sci. Bull.* 2024;9(6):911–920.

doi: 10.3969/j.issn.2096-1693.2024.06.070

30. Li W, Yue D, Wu S, *et al.* Thickness prediction for high-resolution stratigraphic interpretation by fusing seismic attributes of target and neighboring zones with an SVR algorithm. *Mar Pet Geol.* 2020;113:104153.

doi: 10.1016/j.marpetgeo.2019.104153

31. Seelam NK, Kumar T, Dhubia S, Rao GS, Pal SK, Enhancing thin coal seam detection in eastern Indian coalfields using ICWT-decon-based seismic attributes and acoustic impedance inversion. *Minerals*. 2024;14(9):920.

doi: 10.3390/min14090920

32. Jalal A, Liu D, Cai Y, *et al.* Controlling factors of gas content in coal reservoirs of Block 105, Mabi area, southern Qinshui Basin. *Energies*. 2026;19(6):1395.

doi: 10.3390/en19061395

ACCSCIENCE PUBLISHING

Journal of Seismic Exploration

ARTICLE

Coupled acoustic-elastic finite element modeling of underwater sound propagation

Youngjae Shin[1], Won-Ki Kim[2], Eunpyo Lim[3], Youngseok Lee[3], Jaehwan Oh[3], Dawoon Lee[4], and Ho Seuk Bae[4]*

[1]Department of Geology, Gyeongsang National University, Jinju, Republic of Korea

[2]Department of Earth & Environmental Sciences, Chungbuk National University, Cheongju, Republic of Korea

[3]Oceanographic Division, Sekwang Engineering Consultants Co., Ltd., Seoul, Republic of Korea

[4]5th R&D Institute, Agency for Defense Development, Changwon, Republic of Korea

Abstract

Underwater sound propagation modeling is fundamental to sonar design and marine exploration. The parabolic equation (PE) method has been the dominant tool, but carries inherent limitations: the one-way approximation neglects backscattered energy, acoustic-only implementations ignore shear-wave conversion at the fluid-solid interface, and range-marching discretization approximates irregular bathymetry as a staircase boundary. These limitations become significant at low frequencies (below 200 Hz), where acoustic wavelengths reach 7.5–30 m and a substantial fraction of energy penetrates into the elastic seabed, exciting both compressional and shear waves. This study develops a two-dimensional frequency-domain finite element model coupling the Helmholtz equation in the water column with the Navier equation in the elastic seabed, with pressure and normal displacement continuity enforced at the fluid-solid interface. Irregular bathymetry is represented by a terrain-following curvilinear mesh via transfinite interpolation, eliminating staircase errors. A perfectly matched layer truncates open boundaries. Validation against RAMGEO for a Pekeris waveguide yields a mean absolute error of 1.8 dB (mean bias –0.17 dB). In a lossless comparison, mean |ΔTL| between acoustic-only and coupled models is approximately 6 dB, nearly independent of frequency across 50–200 Hz. Under realistic attenuation, mean |ΔTL| ranges from 0.8 dB (soft sediment) to 5.1 dB (hard bottom), with local maxima exceeding 10 dB at interference nulls. Staircase meshes yield displacement errors of 53–116% and pressure errors of 23–24% versus the curvilinear solution. The proposed model provides a rigorous forward engine for accurate transmission loss prediction in complex shallow-water environments.

Keywords: Finite element method; Acoustic-elastic coupling; Transmission loss; Underwater sound propagation; Curvilinear mesh

***Corresponding author:**
Ho Seuk Bae
(belfre@add.re.kr)

Citation: Shin Y, Kim W-K, Lim E, *et al*. Coupled acoustic-elastic finite element modeling of underwater sound propagation. *J Seismic Explor*. 2026;35(3):026100045. doi: 10.36922/JSE026100045

Received: March 3, 2026

Revised: April 17, 2026

Accepted: April 23, 2026

Published online: May 20, 2026

Copyright: © 2026 Author(s). This is an Open-Access article distributed under the terms of the Creative Commons Attribution License, permitting distribution, and reproduction in any medium, provided the original work is properly cited.

Publisher's Note: AccScience Publishing remains neutral with regard to jurisdictional claims in published maps and institutional affiliations.

1. Introduction

Underwater sound propagation modeling is fundamental to sonar system design, marine exploration, underwater communications, and geoacoustic inversion.[1-3] The dominant computational paradigm is the parabolic equation (PE) method, which approximates

the full wave equation by a forward-marching one-way factorization. The split-step Padé algorithm of Collins,[4] implemented in the range-dependent acoustic model (RAM), provides an excellent balance of efficiency and accuracy for range-dependent environments. For stratified environments, KRAKEN[5] and the acousto-elastic model of Westwood *et al.*[6] offer accurate solutions; Collins and Westwood[7,8] extended PE to elastic seabeds in RAMGEO, which serves as the benchmark reference here.

However, the PE-based approach carries inherent physical and numerical limitations in low-frequency, shallow-water environments. At frequencies below approximately 200 Hz, acoustic wavelengths in the water column reach 7.5–30 m, and a substantial fraction of acoustic energy penetrates into the seabed.[1,9] The seabed becomes an active part of the propagation domain:[9,10] energy entering the elastic sediment propagates as both compressional (P) and shear (S) waves, interacts with sub-seabed layer interfaces, and can re-radiate back into the water column, modifying the interference pattern and transmission loss (TL) by several decibels.[9,10] These sub-seabed interactions are governed by the full elastic Navier equation[11-13] and cannot be captured by the one-way PE approximation, which neglects backscattered contributions from the seabed interior. Recent extensions such as the coupled-mode PE of Kozitskiy[14] partially address seabed elasticity within the PE framework but retain the fundamental one-way limitation.

Furthermore, at low frequencies where acoustic energy penetrates deeply into the seabed, the elastic properties of the seabed—particularly the shear-wave velocity V_S—become decisive for accurate TL prediction. At the fluid-solid interface, incident compressional waves undergo P-to-S mode conversion, diverting a fraction of the incident energy into shear waves in the sediment.[9,10] The magnitude of this energy partition depends on the impedance contrast and the P-wave critical angle $\theta_{cP} = \sin^{-1}\left(c_f / V_P\right)$; for soft sediments with V_S = 200–400 m/s, the mode-conversion effect can alter TL by 1–6 dB on average, with local maxima exceeding 10 dB at interference nulls.[9] Acoustic-only models, which treat the seabed as a fluid half-space with V_S = 0, are structurally incapable of representing this shear-wave energy loss and the associated phase shift in the reflection coefficient that modifies the multipath interference pattern throughout the water column. Consequently, for rigorous underwater acoustic analysis—and especially for geoacoustic inversion where V_S is itself an inversion target—a fully coupled acoustic-elastic formulation is essential.[15-17] This requirement is directly analogous to the need for elastic forward models in seismic full-waveform inversion (FWI), where multiparameter recovery demands accurate representation of both P and S wave physics.[13]

A separate but equally important limitation concerns the representation of irregular seabed topography. PE-based methods discretize water depth as flat steps, resulting in a staircase approximation that introduces artificial diffraction at step corners and incorrect reflection coefficients due to the distorted local normal direction.[11,12] Regular-grid finite-difference methods (FDM) share this limitation. Liu *et al.*[18] developed a 3D finite-difference Helmholtz model with perfectly matched layer (PML) for topographic effects, and Li *et al.*[19] coupled acoustic and elastic domains across an irregular seabed using a meshless generalized finite-difference method; however, neither employed a terrain-following structured finite element method (FEM) mesh. In exploration seismology, terrain-following curvilinear meshes generated via transfinite interpolation (TFI)[20,21] have long been the standard remedy for irregular topography, but this approach has seldom been applied to underwater acoustic modeling.

The FEM, a mature tool in exploration geophysics,[13,22,23] addresses all three limitations naturally. Frequency-domain FEM solves the complete Helmholtz equation without the one-way approximation, while the elastic Navier equation is solved simultaneously with acoustic-elastic coupling enforced at the fluid-solid interface as natural boundary conditions.[23,24] In ocean acoustics, FEM and the spectral element method (SEM) have been applied by Komatitsch and Tromp,[25] Bottero *et al.*,[26] Cristini and Komatitsch,[27] Isakson and Chotiros,[28] Vendhan *et al.*,[29] Zhou and Luo,[30] Gui *et al.*,[31] He *et al.*,[32] and Wang *et al.*[33] Zhang *et al.*[34] applied SEM to normal-mode computation in layered waveguides, Xu *et al.*[35] combined FEM with physics-informed neural networks, and Tu *et al.*[36] developed a Chebyshev–Tau spectral method for coupled-mode propagation. Absorbing boundaries are handled by the PML.[37-40] Table 1 shows that each prior study addresses only a subset of these capabilities; the present work addresses all three limitations within a single 2D frequency-domain FEM framework.

The present study addresses this gap by developing a 2D frequency-domain FEM model that fully couples the Helmholtz equation in the water column with the Navier equation in the elastic seabed, enforcing pressure continuity and normal displacement continuity at the fluid-solid interface as natural boundary conditions within a unified weak formulation. Irregular bathymetry is represented by a terrain-following curvilinear mesh generated via the TFI of Gordon and Hall,[20] an established technique in structured grid generation,[21,38,41] eliminating staircase errors at the geometrical level. Outgoing waves

Table 1. Comparison of selected FEM/SEM studies in ocean acoustics.

Study	Method	Domain	A-E coupling	Curvilinear mesh	Benchmark validation
Isakson & Chotiros[28]	FEM (freq.)	Acoustic	No	No	Yes (OASES)
Bottero *et al.*[26]	SEM (time)	Acoustic+Elastic	Yes	Unstructured	No (qualitative)
Cristini & Komatitsch[27]	SEM (time)	Acoustic +Elastic	Yes	Unstructured	Yes (analytic)
Zhou & Luo[30]	FEM (freq.)	Acoustic	No	No	Yes (ASA wedge)
He *et al.*[32]	FEM+ESM	Acoustic	No	No	Yes (KRAKEN)
Li *et al.*[19]	GFDM (freq.)	Acoustic +Elastic	Yes	Meshless	Yes (analytic)
Present study	FEM (freq.)	Acoustic +Elastic	Yes	Yes (TFI)	Yes (RAMGEO)

Notes: KRAKEN is a normal-mode ocean acoustic propagation model; RAMGEO is a range-dependent acoustic propagation model with geoacoustic bottom interaction.
Abbreviations: ASA wedge: Acoustical Society of America benchmark wedge; ESM: Equivalent source method; FEM: Finite element method; GFDM: Generalized finite-difference method; OASES: Ocean Acoustics and Seismic Exploration Synthesis; SEM: Spectral element method; TFI: Transfinite interpolation.

are absorbed by a PML.[34,35,39] The resulting sparse linear system is solved with the PARDISO direct solver.[40] The FEM model is systematically validated against RAMGEO,[7,8] and the TL difference (ΔTL) between the fully coupled and acoustic-only models is quantified. Sensitivity analyses are conducted over frequency (50, 100, 200 Hz) and seabed shear-wave velocity (soft, medium, and hard seabed types), and a case study comparing staircase and curvilinear mesh representations across three irregular bathymetric profiles completes the numerical investigation. The coupled solver thus serves a dual purpose: it provides a benchmark-quality forward solution for underwater acoustic propagation over elastic seabeds, and it highlights the practical consequences of the coupled physics that exploration-seismic FWI codes must likewise capture.[15,16] Because multiparameter FWI requires elastic wave modeling to resolve P- and S-velocity structures simultaneously, the accurate elastic forward model developed here plays the same role in geoacoustic inversion[15,16] as the FWI forward engine does in subsurface velocity estimation.[13]

The key contributions of this study are:

- A unified 2D frequency-domain FEM formulation that couples the Helmholtz equation in the water column with the Navier equation in the elastic seabed, capturing P-to-S mode conversion and two-way wave propagation without the one-way approximation of PE methods.
- A terrain-following curvilinear mesh based on TFI that eliminates staircase bathymetric errors, with quantified improvement over staircase representations for three benchmark topographies.
- Systematic parametric analysis across frequency (50–200 Hz) and seabed type (soft, medium, hard), validated against the RAMGEO benchmark and supplemented by a mesh convergence study.

The remainder of this paper is organized as follows: Section 2 presents the governing equations, acoustic-elastic coupling conditions, FEM weak formulation, and curvilinear mesh generation. Section 3 presents six numerical experiments assessing model accuracy and parametric sensitivity. Section 4 discusses the physical interpretation of the results and limitations. Section 5 states the conclusions.

2. Theory and methods

This section presents the mathematical foundation of the 2D frequency-domain finite element model for coupled acoustic-elastic underwater sound propagation. As

discussed in the introduction section, at the low frequencies of interest (50–200 Hz) acoustic energy penetrates deeply into the seabed, where it propagates as both compressional and shear waves governed by the elastic wave equation. Accurate modeling of this sub-seabed response requires solving the full wave equations in both the water column and the elastic seabed simultaneously. Accordingly, the water column is treated as an inviscid ideal fluid governed by the Helmholtz equation, while the seabed is treated as an isotropic elastic solid governed by the frequency-domain Navier equation—the same equations that underpin seismic wave modeling in exploration geophysics.[13] The solutions in the two domains are linked through physically consistent coupling conditions at the fluid-solid interface that enforce pressure continuity and normal displacement continuity. Galerkin finite element discretization together with isoparametric curvilinear coordinate transformation leads to a coupled sparse linear system. Outgoing waves at artificial boundaries are absorbed by a PML, and irregular bathymetry is represented by a terrain-following curvilinear mesh based on TFI,[20] eliminating the staircase errors inherent in PE and FDM methods.

2.1. Acoustic governing equation

2.1.1. Helmholtz equation

The fundamental equation governing underwater sound propagation is the wave equation for acoustic pressure $p(\mathbf{x},t)$. In an inviscid, irrotational fluid, pressure perturbations satisfy:

$$\frac{1}{c_f^2(\mathbf{x})}\frac{\partial^2 p}{\partial t^2}-\nabla^2 p = s(\mathbf{x},t) \tag{1}$$

where $c_f(\mathbf{x})$ is the spatially varying sound speed, $s(\mathbf{x},t)$ is the source function, and $\nabla^2 = \partial^2/\partial x^2 + \partial^2/\partial z^2$ is the 2D Laplacian. The spatial dependence of c_f accommodates realistic ocean sound-speed profiles.

Assuming a time-harmonic source $e^{-i\omega t}$ and applying the Fourier transform, the time-domain wave **Equation 1** reduces to the frequency-domain Helmholtz equation, widely used in frequency-domain seismic modeling:[13]

$$\nabla^2 p(\mathbf{x},\omega)+k_f^2(\mathbf{x})\,p(\mathbf{x},\omega) = -S(\mathbf{x},\omega) \tag{2}$$

where $p(\mathbf{x},\omega)$ is the complex acoustic pressure amplitude, $k_f(\mathbf{x})=\omega/c_f(\mathbf{x})$ is the wavenumber, $\omega=2\pi f$ is the angular frequency, and $S(\mathbf{x},\omega)$ is the source spectrum. For a point source, $S(\mathbf{x},\omega)=\delta(\mathbf{x}-\mathbf{x}_s)$, whose 2D free-space Green's function is the zero-order Hankel function of the first kind, $p_{\text{inc}}(r)=(i/4)H_0^{(1)}(k_f r)$.

In **Equation 2**, the term $\nabla^2 p$ describes spatial diffusion of the pressure field, while $k_f^2 p$ represents the restoring character of wave propagation; the balance between these two terms determines the wave propagation pattern. Transmission loss (TL) at a receiver location is defined relative to the pressure p_0 at a reference distance $r_0 = 1$ m:

$$\text{TL} = -20\log_{10}\left|\frac{p(\mathbf{x})}{p_0}\right| \quad [\text{dB}] \tag{3}$$

2.1.2. Advantages of the frequency-domain formulation

Three principal advantages motivate the frequency-domain Helmholtz **Equation 2** over a time-domain formulation. First, solving a single linear system per frequency eliminates time-stepping costs. Second, boundary conditions such as the PML (Section 2.4.3) are naturally expressed in the frequency domain.[13] Third, the LU factorization of the global stiffness matrix is computed once per frequency and reused for all right-hand sides,[13] a key efficiency for geoacoustic inversion. **Equation 2** is solved independently at each target frequency.

2.2. Elastic governing equation

2.2.1. Frequency-domain Navier equation

Elastic wave propagation in the seabed (sediment and basement rock) is governed by linear elasticity theory—the same physical foundation underlying seismic exploration modeling. The equation of motion for the displacement vector $\mathbf{u}=(u_x,u_z)^T$, derived from Newton's second law and the divergence of the Cauchy stress tensor, becomes under the time-harmonic assumption $e^{-i\omega t}$:

$$-\omega^2\rho_s(\mathbf{x})\,\mathbf{u}(\mathbf{x},\omega) = \nabla\cdot\boldsymbol{\sigma}(\mathbf{x},\omega) \tag{4}$$

where $\rho_s(\mathbf{x})$ is the spatially varying density and $\boldsymbol{\sigma}$ is the Cauchy stress tensor. The left-hand side of **Equation 4** represents the inertia force $-\omega^2\rho_s\mathbf{u}$, and the right-hand side $\nabla\cdot\boldsymbol{\sigma}$ is the elastic restoring force arising from spatial gradients in internal stress. The balance between these two forces determines elastic wave propagation. Expanding by component for an isotropic elastic medium, the x- and z-direction equations of motion are:

$$(\lambda+2\mu)\frac{\partial^2 u_x}{\partial x^2}+\mu\frac{\partial^2 u_x}{\partial z^2}+(\lambda+\mu)\frac{\partial^2 u_z}{\partial x\partial z}+\omega^2\rho_s u_x = 0 \tag{5}$$

$$(\lambda+2\mu)\frac{\partial^2 u_z}{\partial z^2}+\mu\frac{\partial^2 u_z}{\partial x^2}+(\lambda+\mu)\frac{\partial^2 u_x}{\partial x\partial z}+\omega^2\rho_s u_z = 0 \tag{6}$$

2.2.2. Stress-strain relationship (Hooke's Law)

For an isotropic linearly elastic solid, the stress tensor **σ** and strain tensor **ε** are related by the generalized Hooke's law:

$$\sigma_{ij} = \lambda \delta_{ij} \varepsilon_{kk} + 2\mu \varepsilon_{ij} \tag{7}$$

where λ and μ are the Lamé constants and δ_{ij} is the Kronecker delta. The strain tensor is defined as the symmetric gradient of the displacement:

$$\varepsilon_{ij} = \frac{1}{2}\left(\frac{\partial u_i}{\partial x_j} + \frac{\partial u_j}{\partial x_i} \right) \tag{8}$$

Under 2D plane-strain conditions, the stress components are explicitly:

$$\sigma_{xx} = \left(\lambda + 2\mu\right)\frac{\partial u_x}{\partial x} + \lambda \frac{\partial u_z}{\partial z} \tag{9a}$$

$$\sigma_{zz} = \lambda \frac{\partial u_x}{\partial x} + \left(\lambda + 2\mu\right)\frac{\partial u_z}{\partial z} \tag{9b}$$

$$\sigma_{xz} = \mu\left(\frac{\partial u_x}{\partial z} + \frac{\partial u_z}{\partial x} \right) \tag{9c}$$

Equation 9a shows that the horizontal normal stress σ_{xx} depends primarily on the horizontal strain $\partial u_x/\partial x$, weighted by the P-wave modulus $\lambda + 2\mu$, with a volumetric coupling through λ. Similarly, σ_{zz} in **Equation 9b** is governed by the vertical strain. The shear stress σ_{xz} in **Equation 9c** is proportional to the shear modulus μ alone, confirming that shear stresses vanish in a fluid ($\mu = 0$).

2.2.3. Relationship between elastic wave velocities and Lamé constants

Because the Lamé constants are not directly measurable, it is convenient to express them in terms of the compressional wave velocity V_P, shear-wave velocity V_S, and density ρ_s:

$$V_P = \sqrt{\frac{\lambda + 2\mu}{\rho_s}},\ V_S = \sqrt{\frac{\mu}{\rho_s}} \tag{10}$$

V_P is determined by the bulk modulus $\lambda + 2\mu$ and density, while V_S depends solely on the shear modulus μ. The Lamé constants are recovered from the specified material properties as:

$$\mu = \rho_s V_S^2,\ \lambda = \rho_s\left(V_P^2 - 2V_S^2\right) \tag{11}$$

In the fluid (water column), shear stresses cannot be sustained, so $\mu = 0$ and shear waves do not exist. This is the fundamental physical distinction between the water column and the elastic seabed, and it necessitates separate governing equations for the two domains. Wave attenuation is incorporated by treating the Lamé constants as complex-valued quantities. Under the $e^{-i\omega t}$ time-harmonic convention, attenuation requires a negative imaginary part, so the complex velocities are defined as $V_P^* = V_P\left(1 - i/\left(2Q_P\right)\right)$ and $V_S^* = V_S\left(1 - i/\left(2Q_S\right)\right)$; substituting these into **Equation 11** naturally introduces frequency-domain attenuation parameterized by the quality factors Q_P and Q_S.[1]

2.3. Acoustic-elastic coupling conditions

At the interface Γ_{fs} between the acoustic fluid domain Ω_f and the elastic solid domain Ω_s, three physically required coupling conditions must be enforced.[1,9] We adopt the $e^{-i\omega t}$ time-harmonic convention throughout, with acoustic pressure defined as positive in compression (*i.e.*, $p > 0$ corresponds to a compressive state). The Cauchy stress **σ** follows the standard solid-mechanics sign convention (tension positive). Let $\hat{\mathbf{n}}$ denote the unit outward normal from the fluid domain directed into the solid domain. The fluid particle displacement is related to the pressure gradient through the linearized momentum equation $\rho_f \omega^2 \mathbf{u}^f = \nabla p$, which gives the normal component $u_n^f = \left(1/\rho_f \omega^2\right)\partial p/\partial n$.

Condition 1: Normal stress continuity. The normal stress must be continuous across the fluid-solid interface. Since an ideal fluid sustains no tangential stress, the normal traction on the fluid side equals the acoustic pressure *p*. The force balance condition is:

$$\boldsymbol{\sigma} \cdot \hat{\mathbf{n}}\,|_{\Omega_s} = -p\hat{\mathbf{n}}\,|_{\Omega_f} \quad \text{on } \Gamma_{fs} \tag{12}$$

That is, the acoustic pressure on the fluid side equals in magnitude, and is opposite in sign to the normal compressive stress on the solid side.

Condition 2: Normal displacement continuity. The interface must remain in contact, so the normal displacement is continuous. In the frequency domain, the normal displacement of the fluid particle is obtained from the momentum equation $\rho_f \omega^2 u_n^f = \partial p/\partial n$, giving:

$$\mathbf{u} \cdot \hat{\mathbf{n}}\,|_{\Omega_s} = -\frac{1}{\rho_f \omega^2}\frac{\partial p}{\partial n}|_{\Omega_f} \quad \text{on } \Gamma_{fs} \tag{13}$$

Condition 3: Zero shear traction. An ideal fluid cannot transmit shear stresses, so the tangential traction component on the solid side of the interface must vanish:

$$\left[\boldsymbol{\sigma}\cdot\hat{\mathbf{n}}-\left(\boldsymbol{\sigma}\cdot\hat{\mathbf{n}}\cdot\hat{\mathbf{n}}\right)\hat{\mathbf{n}}\right]|_{\Omega_s}=0 \ \text{ on } \Gamma_{fs} \tag{14}$$

Because the fluid traction vector is purely normal (an ideal fluid sustains no shear stress), the tangential traction on the solid side of the interface is zero by construction; thus condition (14) is enforced naturally together with the normal traction continuity (12). All three conditions are incorporated as natural boundary conditions in the surface integral terms of the weak formulation.

In the discrete FEM implementation, the fluid-solid interface is a conforming interface: the mesh nodes along the interface are shared between the acoustic and elastic domains, and each interface node carries both a pressure degree of freedom (DOF) from the acoustic side and two displacement DOFs (u_x, u_z) from the elastic side. Condition (13) enters the acoustic weak form through the boundary integral (16), which couples each pressure DOF at an interface node to the normal displacement DOFs at the same node via a 1D edge mass matrix. Condition (12) enters the elastic weak form through the boundary integral (18), which couples each displacement DOF to the pressure DOF at the same node. The resulting coupling matrix C_{fs} in equation (22) is assembled element-by-element along the interface edges using the same shape functions employed for the domain integrals, ensuring consistency. Because both coupling terms arise naturally from the surface integrals in the weak formulation, no penalty parameters or Lagrange multipliers are required, and the coupling is enforced to the same order of accuracy as the underlying finite element discretization.

2.4. Finite element formulation

2.4.1. Weak formulation

The full computational domain consists of the fluid region Ω_f, the solid region Ω_s, their shared interface Γ_{fs}, and the absorbing PML layer Ω_{PML} (Figure 1).

Acoustic domain weak form. Multiplying **Equation 2** by a test function $q \in H^1(\Omega_f)$, integrating over Ω_f, and applying Green's first identity (integration by parts) yields:

$$\int_{\Omega_f}\nabla q\cdot\nabla p\,d\Omega-k_f^2\int_{\Omega_f}q\,p\,d\Omega-\int_{\partial\Omega_f}q\frac{\partial p}{\partial n}d\Gamma=\int_{\Omega_f}q\,S\,d\Omega \tag{15}$$

The first term on the left represents spatial diffusion via the pressure gradient inner product; the second term represents wave propagation via the wavenumber. The boundary integral $\int_{\partial\Omega_f}q(\partial p/\partial n)d\Gamma$ is handled according to the boundary type. At the coupling interface Γ_{fs}, substituting condition (13) gives:

$$\int_{\Gamma_{fs}}q\frac{\partial p}{\partial n}d\Gamma=-\rho_f\omega^2\int_{\Gamma_{fs}}q\left(\mathbf{u}\cdot\hat{\mathbf{n}}\right)d\Gamma \tag{16}$$

This term expresses the physical action of the solid normal displacement as a pressure source in the acoustic domain.

Elastic domain weak form. Taking the inner product of **Equation 4** with a vector test function $\mathbf{v}\in[H^1(\Omega_s)]^2$, integrating over Ω_s, and applying Green's first identity yields:

$$\int_{\Omega_s}\boldsymbol{\sigma}(\mathbf{u}):\boldsymbol{\varepsilon}(\mathbf{v})d\Omega-\omega^2\int_{\Omega_s}\rho_s\mathbf{u}\cdot\mathbf{v}\,d\Omega=\int_{\partial\Omega_s}(\boldsymbol{\sigma}\cdot\hat{\mathbf{n}})\cdot\mathbf{v}\,d\Gamma \tag{17}$$

The first term on the left is the internal elastic energy; the second is the inertia term. At the coupling interface Γ_{fs}, substituting condition (12) gives:

$$\int_{\Gamma_{fs}}(\boldsymbol{\sigma}\cdot\hat{\mathbf{n}})\cdot\mathbf{v}\,d\Gamma=-\int_{\Gamma_{fs}}p(\mathbf{v}\cdot\mathbf{n})d\Gamma \tag{18}$$

This term expresses the physical action of the acoustic pressure as a normal load on the elastic boundary. The coupled weak system is formed by combining **Equations 15–18**, with unknowns comprising the fluid pressure p and solid displacements (u_x, u_z).

2.4.2. Discretization and matrix assembly

The Galerkin method is adopted, so that the trial and test function spaces are identical. The computational domain is partitioned into isoparametric quadrilateral elements, within each of which the unknowns are approximated by nodal basis functions. Nine-node biquadratic Lagrange elements (Q9) are employed. In the reference coordinates $(\xi,\eta)\in[-1,1]^2$, the shape functions are tensor products of 1D quadratic Lagrange polynomials:

$$N_I(\xi,\eta)=L_i(\xi)L_j(\eta),\ I=3(j-1)+i,\ i,j\in\{1,2,3\} \tag{19}$$

where the 1D Lagrange basis functions are:

$$L_1(\xi)=\frac{\xi(\xi-1)}{2},\ L_2(\xi)=1-\xi^2,\ L_3(\xi)=\frac{\xi(\xi+1)}{2} \tag{20}$$

Q9 elements are chosen because, for the same number of nodes per wavelength, the numerical dispersion error is substantially lower than for bilinear Q4 elements. Since numerical dispersion (the pollution error) worsens with increasing frequency in Helmholtz problems, higher-order elements are essential.[22] Approximating the pressure and

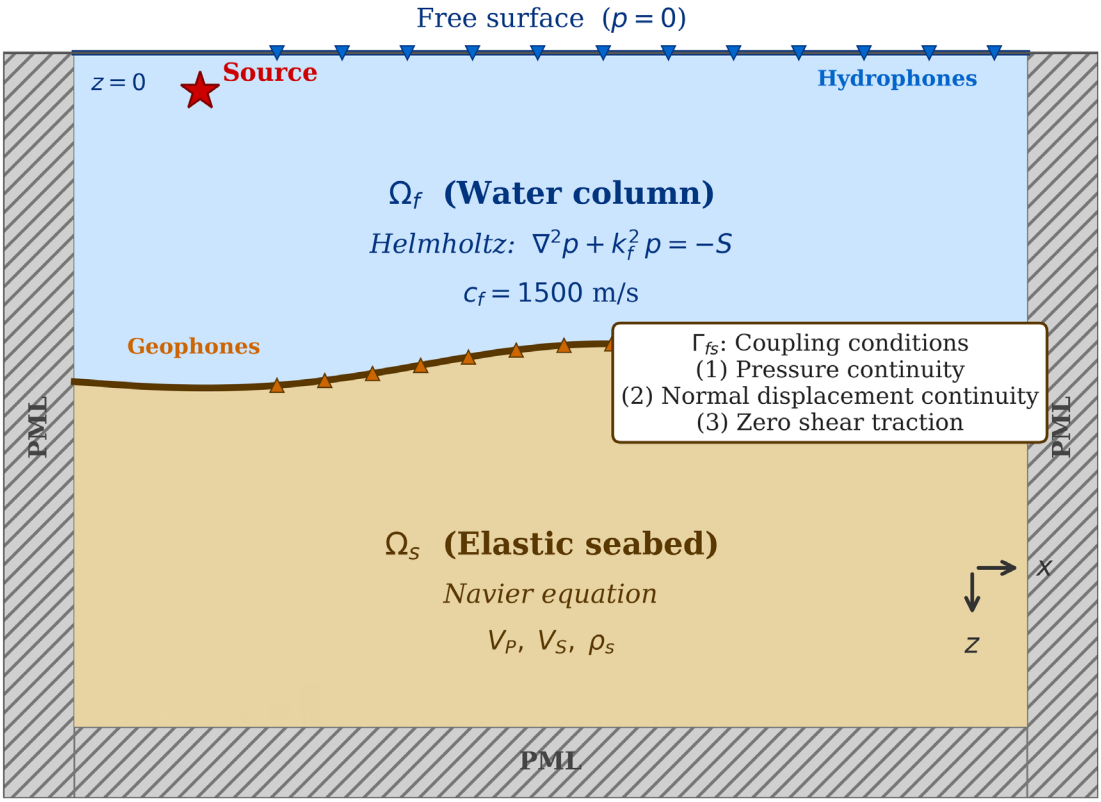

Figure 1. Schematic of the 2D computational domain showing the acoustic fluid domain (Ω_f), elastic solid domain (Ω_s), fluid-solid interface (Γ_{fs}), perfectly matched layer (PML), and boundary conditions. The point source is located at depth z_s in the water column.

displacements within each element by the shape functions:

$$p^h(\mathbf{x}) = \sum_{I=1}^{9} N_I(\mathbf{x})\hat{p}_I, \quad u_k^h(\mathbf{x}) = \sum_{I=1}^{9} N_I(\mathbf{x})\hat{u}_{k,I} \quad (k = x, z) \tag{21}$$

and substituting into the weak formulation and assembling over all elements yields the coupled block linear algebraic system:

$$\begin{pmatrix} \mathbf{K}_f - \omega^2 \mathbf{M}_f & \rho_f \omega^2 \mathbf{C}_{fs}^T \\ \mathbf{C}_{fs} & \mathbf{K}_s - \omega^2 \mathbf{M}_s \end{pmatrix} \begin{pmatrix} \hat{\mathbf{p}} \\ \hat{\mathbf{u}} \end{pmatrix} = \begin{pmatrix} \mathbf{f}_p \\ 0 \end{pmatrix} \tag{22}$$

The individual block matrices are defined as:

$$[\mathbf{K}_f]_{ij} = \int_{\Omega_f} \nabla N_i \cdot \nabla N_j \, d\Omega, \quad [\mathbf{M}_f]_{ij} = \int_{\Omega_f} \frac{1}{c_f^2(\mathbf{x})} N_i N_j \, d\Omega \tag{23}$$

$$[\mathbf{K}_s]_{IJ} = \int_{\Omega_s} \mathbf{B}_I^T \mathbf{D} \mathbf{B}_J \, d\Omega, \quad [\mathbf{M}_s]_{IJ} = \int_{\Omega_s} \rho_s \mathbf{N}_I^T \mathbf{N}_J \, d\Omega \tag{24}$$

$$[\mathbf{C}_{fs}]_{i,(J,k)} = \int_{\Gamma_{fs}} N_i \, \mathbf{N}_J n_k \, d\Gamma \tag{25}$$

where $\mathbf{B}$ is the strain-displacement matrix, $\mathbf{D}$ is the elastic constitutive matrix assembled from the Lamé constants, $\hat{\mathbf{p}}$ and $\hat{\mathbf{u}}$ are the nodal degree-of-freedom vectors for pressure and displacement respectively, and $\mathbf{f}_p$ is the acoustic source load vector. In $\mathbf{M}_f$, the factor $1/c_f^2(\mathbf{x})$ is retained inside the integral to accommodate spatially varying sound speed. The coupling matrix $\mathbf{C}_{fs}$ appears in the off-diagonal blocks of system (22) as $\rho_f \omega^2 \mathbf{C}_{fs}^T$ in the (1,2) position and $\mathbf{C}_{fs}$ in the (2,1) position, yielding an unsymmetric structure. This unsymmetry arises because the acoustic pressure and elastic displacement unknowns have different physical dimensions, and it correctly represents bidirectional energy transfer between the fluid

and solid.[23,24] Numerical integration employs a 3 × 3 Gauss-Legendre quadrature rule per element.

The global matrix in system (22) is a large sparse complex matrix, which is solved efficiently by the PARDISO direct sparse solver based on LU factorization.[40,42] For multiple sources at the same frequency, the factorization is reused for all right-hand sides.

2.4.3. Absorbing boundary condition: PML

To suppress reflections of outgoing waves at the artificial boundaries of the computational domain, a PML[34] is applied, implemented via complex coordinate stretching.[35,36,39,43] The stretching function in the direction ξ (x or z) is:

$$\tilde{\xi} = \xi + \frac{1}{i\omega}\int_0^{\xi}\sigma(\xi')d\xi',\ s_{\xi}(\xi) = 1 + \frac{\sigma(\xi)}{i\omega} \tag{26}$$

where $\sigma(\xi) \geq 0$ is a damping function that increases gradually within the PML. A quadratic profile $\sigma(\xi) = \sigma_{\max}(\xi / d_{\mathrm{PML}})^2$ is adopted, where d_{PML} is the PML thickness, set to $2\lambda_f$ ($\lambda_f = c_f / f$, the acoustic wavelength in water). The maximum damping coefficient is chosen to achieve a target theoretical reflection coefficient R_0 at normal incidence:[35]

$$\sigma_{\max} = \frac{3c_f}{2d_{\mathrm{PML}}}\ln\left(\frac{1}{R_0}\right) \tag{27}$$

with $R_0 = 10^{-4}$ (i.e., 80 dB attenuation) $\lambda_f = 15d_{\mathrm{PML}} = 30\sigma_{\max} \approx 690^{-1}$. The PML is applied to all four sides of the computational domain except the free surface ($z = 0$), where the Dirichlet condition $p = 0$ is imposed. In the elastic domain, the same complex coordinate stretching is applied to the Navier equation by replacing partial derivatives $\partial / \partial\xi$ with $(1/s_{\xi})\partial / \partial\xi$, ensuring consistent PML treatment across the fluid-solid interface.[36] Inside the PML, the spatial differential operators in both the Helmholtz and Navier equations are replaced by stretched-coordinate derivatives, and the PML element matrices are assembled within the same weak-form framework as the acoustic and elastic domains.

2.5. Curvilinear mesh

2.5.1. TFI-based mesh generation

To represent irregular seabed topography accurately, a terrain-following curvilinear mesh is employed. The mapping between physical coordinates (x,z) and computational coordinates (ξ,η) is defined by the TFI method of Gordon and Hall.[20] Here, $\xi \in [0,1]$ is the horizontal computational coordinate and $\eta \in [0,1]$ is the vertical coordinate running from the sea surface to the seabed.

In the simplest case of a flat sea surface at $z = 0$ and a bathymetric profile $z_b(x)$, the TFI mapping reduces to a unidirectional linear blending along the vertical coordinate:

$$z(x,\eta) = (1-\eta)\cdot 0 + \eta \cdot z_b(x) = \eta\, z_b(x) \tag{28}$$

This is a special case of the general TFI framework,[20] in which the top boundary is flat and the mapping simplifies to a single projector. Despite its simplicity, this mapping deforms the uniform computational grid (ξ,η) to conform precisely to the seabed geometry.[21] The elastic solid region below the seabed is generated by an analogous vertical blending between the seabed and the bottom boundary of the computational domain.

2.5.2. Jacobian coordinate transformation

To evaluate FEM integrals on curvilinear elements, physical-domain integrals are transformed to computational-domain integrals. The Jacobian matrix is:

$$\mathbf{J} = \begin{pmatrix} \partial x/\partial\xi & \partial x/\partial\eta \\ \partial z/\partial\xi & \partial z/\partial\eta \end{pmatrix} \tag{29}$$

Physical-domain partial derivatives are obtained by the chain rule as:

$$\begin{pmatrix} \partial/\partial x \\ \partial/\partial z \end{pmatrix} = \mathbf{J}^{-1}\begin{pmatrix} \partial/\partial\xi \\ \partial/\partial\eta \end{pmatrix} \tag{30}$$

and the area element transforms as $d\Omega = |\det\mathbf{J}|\, d\xi\, d\eta$. A 3×3 Gauss-Legendre quadrature rule is applied for numerical integration within each element.

2.5.3. Comparison with staircase mesh

In conventional PE-based methods and regular-grid FEM, irregular bathymetry is approximated by a staircase boundary. This approximation generates artificial diffraction at step corners and introduces errors in the local normal direction of the seabed, distorting the reflection coefficient. For a sloping seabed inclined at angle θ, the vertical positional error of the staircase approximation is proportional to the grid spacing Δz, manifesting as phase errors in reflected pressure. The terrain-following curvilinear mesh eliminates these geometric errors by aligning element edges with the physical boundary. The TFI approach adopted here [20] is an established mesh-generation technique; its effectiveness in reducing staircase-induced errors in the present context is quantified in Section 3.6.

3. Numerical examples

The performance of the proposed FEM model for coupled acoustic-elastic underwater sound propagation is assessed through six numerical examples. Section 3.1 validates the FEM code against RAMGEO in a range-independent environment with a flat seabed. Section 3.2 presents a mesh convergence study to verify the numerical reliability of the adopted mesh resolution rule. Section 3.3 quantifies the TL difference between the acoustic-only and acoustic-elastic coupled models. Sections 3.4 and 3.5 present systematic sensitivity analyses with respect to frequency and seabed shear-wave velocity, respectively. Section 3.6 provides a case study comparing staircase and curvilinear meshes across three irregular bathymetric profiles. In all examples, the PML thickness is set to twice the acoustic wavelength ($2\lambda_f$) at the analysis frequency, and the element size satisfies $h \le \lambda_f / 8$.[22] In the elastic domain, the shear wavelength $\lambda_S = V_S / f$ can be considerably shorter than the acoustic wavelength. For Q9 biquadratic elements; however, the effective number of points per wavelength is approximately twice that of linear elements due to the mid-side and center nodes. For example, at 200 Hz with $V_S = 200$ m/s (the most demanding case), $\lambda_S = 1.0$ m and $h = 0.94$ m, yielding approximately three Q9 nodes per shear wavelength (equivalent to ~6 sampling points per λ_S), which satisfies the minimum resolution requirement for second-order elements.[22]

3.1. FEM model validation: Comparison with RAMGEO

3.1.1. Model configuration

The accuracy of the proposed FEM code is validated by comparing transmission loss against RAMGEO (elastic PE) in a range-independent environment with a flat horizontal seabed. RAMGEO is based on the energy-conserving higher-order PE of Collins[7] and serves as an established benchmark for underwater sound propagation with elastic seabed representation.[1,8]

The test environment is configured as follows: water depth 200 m, point source at approximately 101 m depth (grid index 112 with grid spacing $h = 0.9$ m; grid dimensions $n_x = 11114$, $n_z = 557$, corresponding to a total grid extent of 10 km including PML regions), and frequency 100 Hz. TL is analyzed over the range of 0–5 km. Water column properties are $c_f = 1{,}500$ m/s and $\rho_f = 1{,}000$ kg/m^3. The elastic seabed half-space is assigned $V_P = 1{,}800$ m/s, $V_S = 400$ m/s, $\rho_s = 1{,}800$ kg/m^3, consistent with a medium-stiffness sandy sediment in the geoacoustic classification of Hamilton.[10] In Sections 3.1–3.4, no intrinsic attenuation is applied ($Q_P = Q_S = \infty$, *i.e.*, lossless), in order to isolate the effect of acoustic-elastic coupling from material absorption; attenuation is introduced in Section 3.5 to investigate its combined influence with shear-wave velocity. The receiver array is placed at the same depth as the source (approximately 101 m), and TL is computed from **Equation 3**.

3.1.2. Results and analysis

Figure 2 shows the TL comparison at approximately 101 m receiver depth over the range 0–5 km. The FEM and RAMGEO TL curves reproduce the positions and amplitudes of the multipath interference peaks (TL minima) and troughs (TL maxima) throughout the entire range. The raw MAE of 5.0 dB reflects phase-shift sensitivity at interference nulls, documented in PE-FEM comparisons.[1] Running-average smoothing (100 m) yields MAE = 1.8 dB with mean bias of −0.17 dB, confirming that the envelope structure is accurately reproduced. The small discrepancy observed at ranges below 500 m (up to 1.2 dB) is attributed to the difference between RAMGEO's PE starting-field approximation and the Green's function-based source representation used in the FEM.[1] These results confirm that the proposed FEM correctly reproduces multipath interference in coupled acoustic-elastic waveguides.

3.2. Mesh convergence study

To verify the numerical reliability of the adopted $\lambda/8$ mesh resolution rule, a quantitative mesh convergence study is performed. The same lossless Pekeris waveguide environment as Section 3.1 is used, with TL computed at 100 Hz for five mesh resolutions: $\lambda/4$, $\lambda/6$, $\lambda/8$, $\lambda/10$, and $\lambda/12$ elements per minimum acoustic wavelength ($\lambda_{min} = c_{min}/f = 1450/100 = 14.5$ m, where $c_{min} = 1450$ m/s is adopted as a conservative design value for mesh sizing, slightly below the nominal water-column speed $c_f = 1500$ m/s of Section 3.1, to provide margin against potential sound-speed decrease toward the seabed; the nominal wavelength $\lambda = c_f/f = 15.0$ m at the same frequency is used for the frequency sensitivity analysis). A reference solution at $\lambda/16$ resolution ($h = 0.9$ m $\approx \lambda_{min}/16$, $N \approx 6.4 \times 10^6$ DOFs) is used for comparison.

Table 2 summarizes the grid parameters and the smoothed TL error at approximately 100 m receiver depth over the range 0.5–9.5 km. TL curves are smoothed with a 50 m moving average (approximately 3.4λ) to suppress the sensitivity of point-wise error metrics to minor shifts in interference null positions, which is a well-known artifact in waveguide TL comparisons.[1] Figure 3 shows the smoothed TL comparison at approximately 100 m depth for four mesh resolutions.

The RMS error decreases monotonically from 12.3 dB at $\lambda/4$ to 3.9 dB at $\lambda/12$, confirming mesh convergence. The

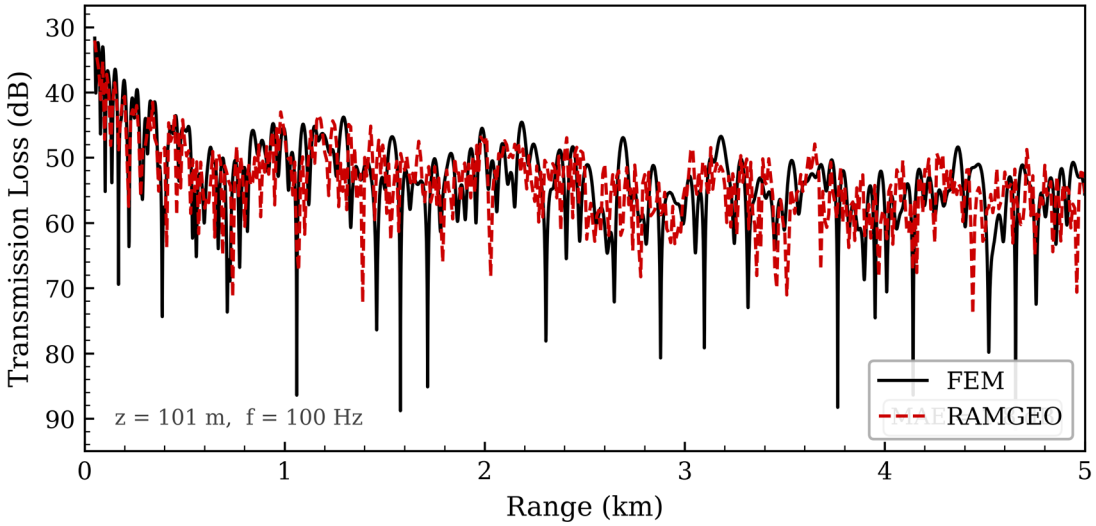

Figure 2. Transmission loss comparison between the FEM acoustic-elastic coupled model (solid black) and RAMGEO (dashed red) at approximately 101 m receiver depth over range 0–5 km in a range-independent Pekeris waveguide at 100 Hz. RAMGEO is a fully range-dependent parabolic-equation acoustic propagation model for fluid seabeds.
Abbreviation: FEM: Finite element method.

Table 2. Mesh convergence results at 100 Hz (acoustic mode) for five resolutions ranging from λ/4 to λ/12, compared against a λ/16 reference solution.

Resolution (λ/h)	h (m)	Grid (nx × nz)	DOFs	RMS error (dB)	MAE (dB)
λ/4	3.63	2760 × 139	445,200	12.3	10.9
λ/6	2.42	4139 × 208	952,812	9.6	8.3
λ/8	1.81	5518 × 277	1,650,726	5.6	4.6
λ/10	1.45	6898 × 347	2,546,246	4.7	3.8
λ/12	1.21	8277 × 416	3,626,212	3.9	2.9

convergence rate is approximately $O(h^{1.1})$, which is below the theoretical $O(h^{p+1})$ rate (where p is the polynomial order) expected for biquadratic Q9 elements applied to smooth problems. This reduced rate is attributed to three factors: (i) the impedance discontinuity at the fluid-solid interface reduces the solution regularity below the H^{p+1} assumption underlying optimal convergence estimates, (ii) the Helmholtz pollution effect—the well-known degradation of FEM accuracy with increasing wavenumber k—introduces a resolution-dependent phase error that persists even at moderately fine meshes,[22] and (iii) the logarithmic (dB) scale of TL amplifies relative errors near interference nulls. A pronounced error reduction occurs between λ/6 (9.6 dB) and λ/8 (5.6 dB), confirming that λ/8 represents the practical threshold for acceptable accuracy. The λ/8 MAE of 4.6 dB is comparable to the 5.0 dB raw MAE observed in the FEM-RAMGEO validation (Section 3.1), indicating that the discretization error at λ/8 is of the same order as the inherent methodological difference between FEM and PE.

3.3. Comparison of acoustic-only and coupled acoustic-elastic models

3.3.1. Model configuration

To quantify the influence of seabed elastic properties on transmission loss, the acoustic-only and coupled models are compared in the same environment. The acoustic-only model treats the seabed as an ideal fluid half-space,

ignoring shear-wave transmission ($V_S = 0$), while the coupled model fully accounts for elastic seabed properties. The configuration is identical to Section 3.1. The TL difference $\Delta TL = TL_{coupled} - TL_{acoustic}$ is computed over the 2D range-depth space. Positive ΔTL indicates greater attenuation in the coupled model, reflecting additional acoustic energy loss due to P-to-S mode conversion at the fluid-solid interface.

3.3.2. Results and analysis

Figure 4 compares the TL curves of the acoustic-elastic coupled model (solid) and the acoustic-only model (dashed) at three receiver depths: 50 m, 101 m, and 150 m. The acoustic-only model consistently underestimates TL relative to the coupled model across all depths and ranges, confirming that neglecting shear-wave interactions in the seabed leads to a systematic bias. The mean absolute TL difference ($|\Delta TL|$) is 5.89 dB at 50 m, 5.97 dB at 101 m, and 5.59 dB at 150 m. Note that these values are obtained under the lossless assumption ($Q_P = Q_S = \infty$); under attenuation (Section 3.5), mean $|\Delta TL|$ is reduced but persists throughout the water column.

At ranges below 1 km, direct-path energy dominates and the elastic seabed effect is comparatively small. At ranges of 1–5 km, the number of bottom reflections increases and the cumulative energy loss from P-to-S mode conversion grows progressively, so ΔTL increases with range. At the mid-water depth (101 m), where the source is located, the $|\Delta TL|$ is largest (5.97 dB), consistent with the stronger bottom interaction of ray paths near the source depth. Near the surface (50 m) and closer to the seabed (150 m), the slightly lower $|\Delta TL|$ values reflect the different modal excitation patterns at each depth.[1] These results indicate that acoustic-only models may underestimate TL by approximately 5–6 dB on average under lossless conditions.

3.4. Frequency sensitivity analysis

3.4.1. Model configuration

To investigate the influence of frequency on the acoustic-elastic coupling effect and the numerical properties of the FEM, the coupled FEM model is compared with the acoustic-only FEM model at three frequencies: 50, 100, and 200 Hz. All other settings follow Section 3.1. To isolate the physical frequency dependence of $|\Delta TL|$ from numerical discretization effects, a single computational grid (h = 0.9 m, ~10.4 million DOF) is used for all three frequencies. This resolution satisfies $h \le \lambda / 8$ at the highest frequency (200 Hz, $\lambda = 7.5$ m) and oversamples the lower frequencies. Computational parameters are summarized in Table 3.

3.4.2. Results and analysis

Figure 5 compares TL curves at approximately 101 m receiver depth for the three frequencies from the acoustic-elastic coupled FEM model (solid lines) and the acoustic-only FEM model (dashed lines). At 50 Hz, the long wavelength yields a wide spatial period of the interference pattern (approximately 200–300 m), and the greater penetration depth into the seabed distributes the elastic coupling effect over a broad range. At 100 Hz, the interference pattern is distinct and ΔTL is most clearly

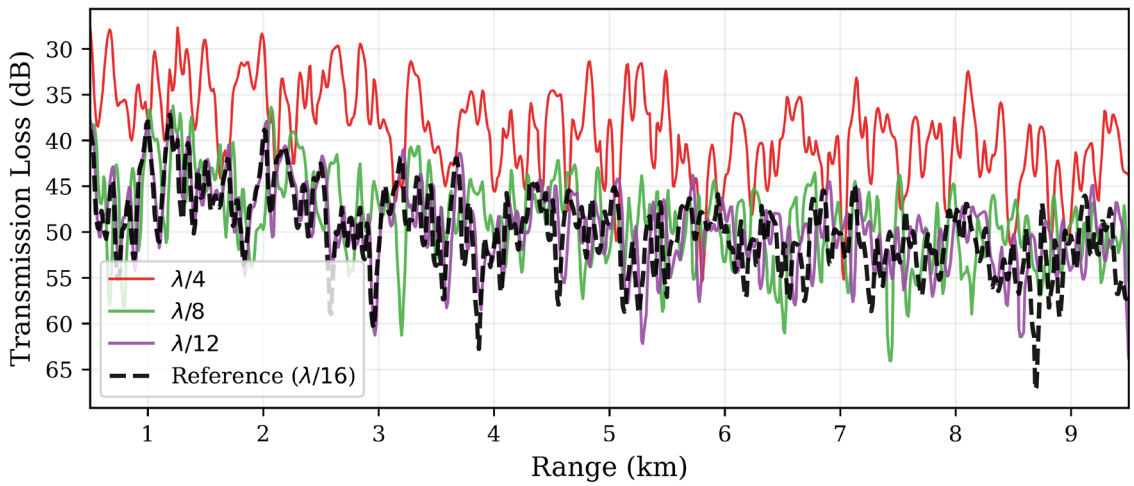

Figure 3. Smoothed transmission loss at 100 m depth for four mesh resolutions at 100 Hz in the lossless Pekeris waveguide: λ/4, λ/8, λ/12, and reference (λ/16). The λ/8 solution closely follows the reference, confirming numerical convergence.

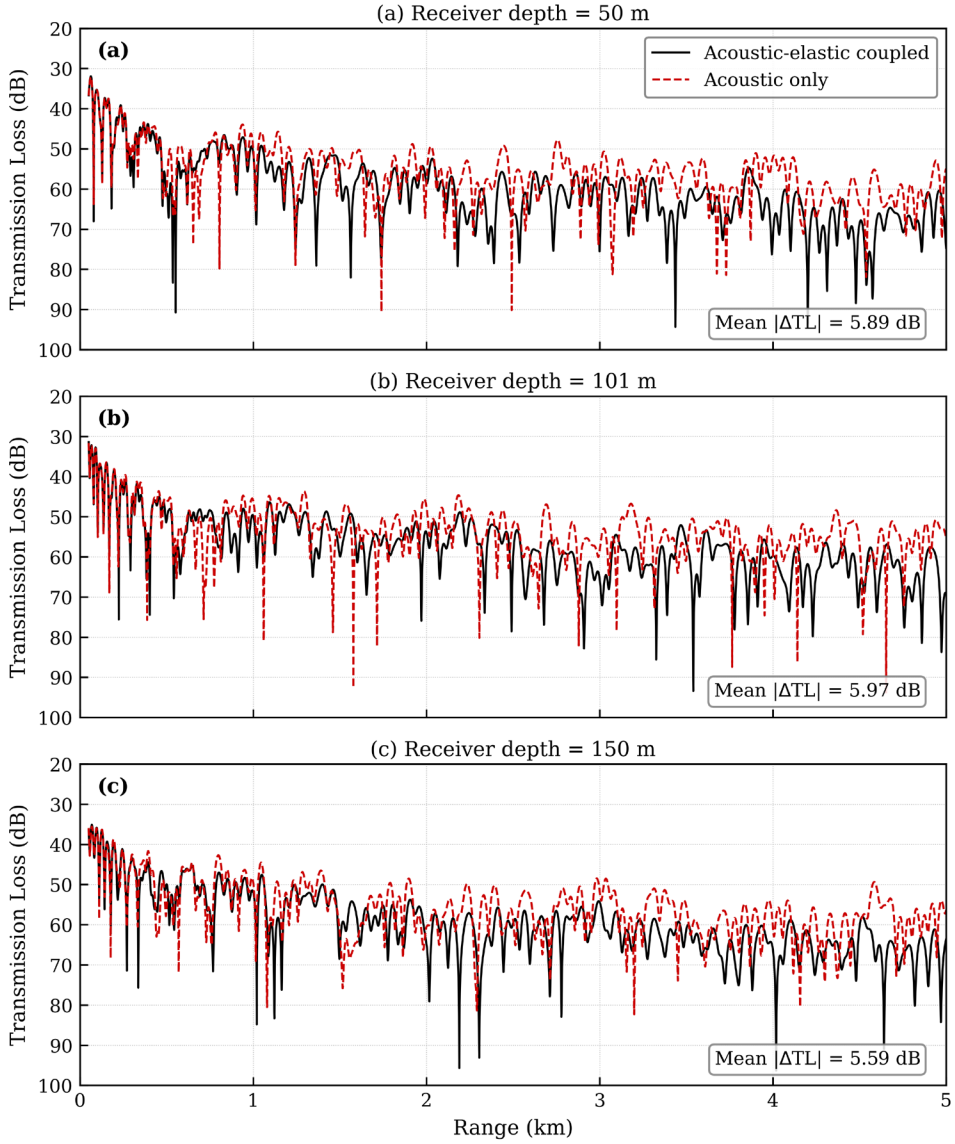

Figure 4. Transmission loss comparison between coupled (solid) and acoustic-only (dashed) models at three receiver depths: (a) 50 m, (b) 101 m, and (c) 150 m over range 0–5 km at 100 Hz

Table 3. Computational parameters of the FEM model at three analysis frequencies.

Frequency (Hz)	Wavelength λ (m)	h (m)	DOF	Computation time (s)
50	30.0	0.9	~10,400,000	~10
100	15.0	0.9	~10,400,000	~10
200	7.5	0.9	~10,400,000	~10

Abbreviations: DOF: Degrees of freedom; FEM: Finite element method; h_{max} : maximum element size.

resolved. At 200 Hz, the interference pattern becomes considerably more complex, with shorter spatial periods (50–80 m) and larger peak-to-trough amplitudes in the TL curves.

The mean |ΔTL| between the coupled and acoustic-only FEM models is approximately 5.6 dB at 50 Hz, 6.0 dB at 100 Hz, and 6.0 dB at 200 Hz. These values reflect the consistent sensitivity of the 200 m water column to P-to-S mode conversion across the tested frequency range.

Because the same discretization is used at all three frequencies, computation time is nearly constant (~10 s per frequency) and the observed |ΔTL| variation is attributable to wave physics, not grid resolution. The range-averaged |ΔTL| is nearly constant (5.6–6.0 dB); range-resolved variations are discussed in Section 4.

3.5. Shear-wave velocity sensitivity analysis

3.5.1. Model configuration

To quantify the effect of seabed shear-wave velocity (V_S) on transmission loss, three seabed types are defined following the geoacoustic classification of Hamilton.[10] Material properties for each type are listed in Table 4. The quality factors Q_P and Q_S are derived from Hamilton's reported compressional-wave attenuation coefficients k_P (dB/m/kHz) via $Q_P = 27{,}272 / (k_P \times V_P)$,[10] with $Q_S \approx 0.5$–$0.6\, Q_P$ following established marine sediment models. The analysis frequency is 100 Hz; all other settings follow Section 3.1.

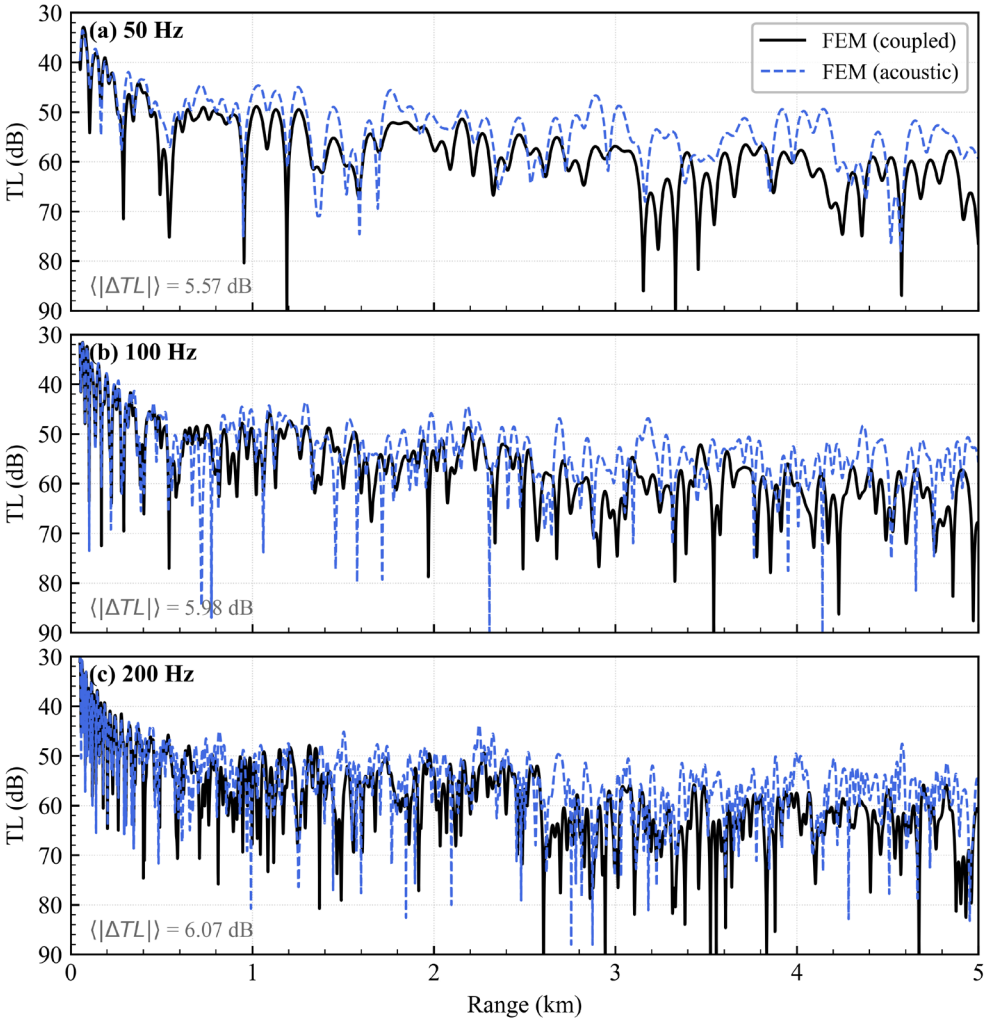

Figure 5. Frequency sensitivity analysis: Coupled (solid) and acoustic-only (dashed) FEM models at (a) 50 Hz, (b) 100 Hz, and (c) 200 Hz at approximately 101 m receiver depth
Abbreviation: FEM: Finite element method.

Table 4. Geoacoustic parameters for three seabed types used in the shear-wave velocity sensitivity analysis.

Seabed type	V_P (m/s)	V_S (m/s)	ρ_S (kg/m³)	Q_P	Q_S
Soft sediment	1,550	200	1,400	50	30
Medium sediment	1,800	400	1,800	100	60
Hard bottom	3,000	800	2,500	300	150

Notes: Classification follows Hamilton.[10] Q_P and Q_S: quality factors for compressional and shear waves.

3.5.2. Results and analysis

Figure 6 compares the coupled and acoustic-only model TL at approximately 101 m receiver depth for the three seabed types.

The spatial average of $|\Delta TL|$ for the soft sediment ($V_S = 200$ m/s) is approximately 0.8 dB, for the medium sediment ($V_S = 400$ m/s) approximately 1.8 dB, and for the hard bottom ($V_S = 800$ m/s) approximately 5.1 dB. Note that these $|\Delta TL|$ values differ from the medium-sediment result in Section 3.3 (mean $|\Delta TL|$ of approximately 5.97 dB at 101 m depth). This difference arises primarily because Sections 3.1–3.4 use a lossless seabed ($Q_P = Q_S = \infty$) to isolate the coupling effect, whereas Section 3.5 introduces intrinsic attenuation ($Q_P = 100$, $Q_S = 60$ for medium sediment; Table 4), which damps the shear waves in the seabed and reduces the net $|\Delta TL|$. Furthermore, all geoacoustic parameters (V_P, ρ_S, Q_P, Q_S) vary simultaneously across the three seabed types (Table 4), so the reported $|\Delta TL|$ values reflect the combined influence of all material properties, not V_S alone.

These results quantitatively confirm that geoacoustic seabed properties are decisive for accurate TL prediction. The increasing $|\Delta TL|$ from soft to hard seabed is driven by the growing impedance contrast (Section 4). For the soft sediment ($Z_s / Z_f \approx 1.4$), the impedance contrast is small, yielding modest coupling. For the hard bottom ($Z_s / Z_f \approx 5.0$), the large impedance contrast introduces a pronounced phase shift in the reflection coefficient—particularly near the P-wave critical angle $\theta_{cP} = \sin^{-1}\left(c_f / V_P\right) \approx 30^\circ$—producing the largest $|\Delta TL|$.[1,9]

The variation in $|\Delta TL|$ across the three seabed types demonstrates the strong sensitivity of the coupled model to seabed properties, with practical implications for model selection. The coupled model's sensitivity to V_s confirms that it possesses the parametric sensitivity required to serve as a forward model for geoacoustic inversion of seabed shear-wave velocity—analogous to the role of the elastic wave equation in seismic FWI.[13] These results provide a practical guideline for selecting model complexity: for environments where errors of 1–2 dB are intolerable, or where V_s estimation is an inversion objective, an acoustic-elastic coupled formulation is indispensable.

3.6. Case study: Staircase vs. curvilinear mesh

3.6.1. Model configuration

Three representative irregular bathymetric profiles are considered to compare the numerical accuracy of staircase and curvilinear meshes:

- **Downslope**: water depth increases linearly from 790 m to approximately 980 m over 0–3.98 km (slope gradient 5%).
- **Anticline**: a Gaussian bathymetric high centered at approximately 2 km, with depth rising from a mean of 790 m to 690 m at the apex (amplitude 100 m).
- **Syncline**: a Gaussian bathymetric low centered at approximately 2 km, with depth dropping from a mean of 790 m to 890 m at the trough (amplitude 100 m).

The domain is discretized on a 399×399 grid with spacing $h = 10$ m. This spacing corresponds to approximately 3 elements per acoustic wavelength at the highest frequency (200 Hz, $\lambda_f = 7.5$ m), which is coarser than the $h \le \lambda / 8$ criterion used in the TL experiments of Sections 3.1–3.5. However, since the objective of this case study is to compare the *relative* difference between staircase and curvilinear mesh solutions; the identical grid ensures observed differences are attributable solely to boundary representation. The analysis covers 50–200 Hz with medium sediment properties (Table 4).

3.6.2. Results and analysis

Figure 7 presents the velocity model and broadband seismograms for each of the three bathymetric profiles. For each case, the left panel shows the velocity model with the true seabed boundary (solid black line) and the staircase approximation (dashed red line) overlaid. The remaining columns display three wavefield components—horizontal displacement u_x, vertical displacement u_z, and pressure p—obtained by inverse Fourier transform of the frequency-domain elastic solutions over 50–200 Hz.

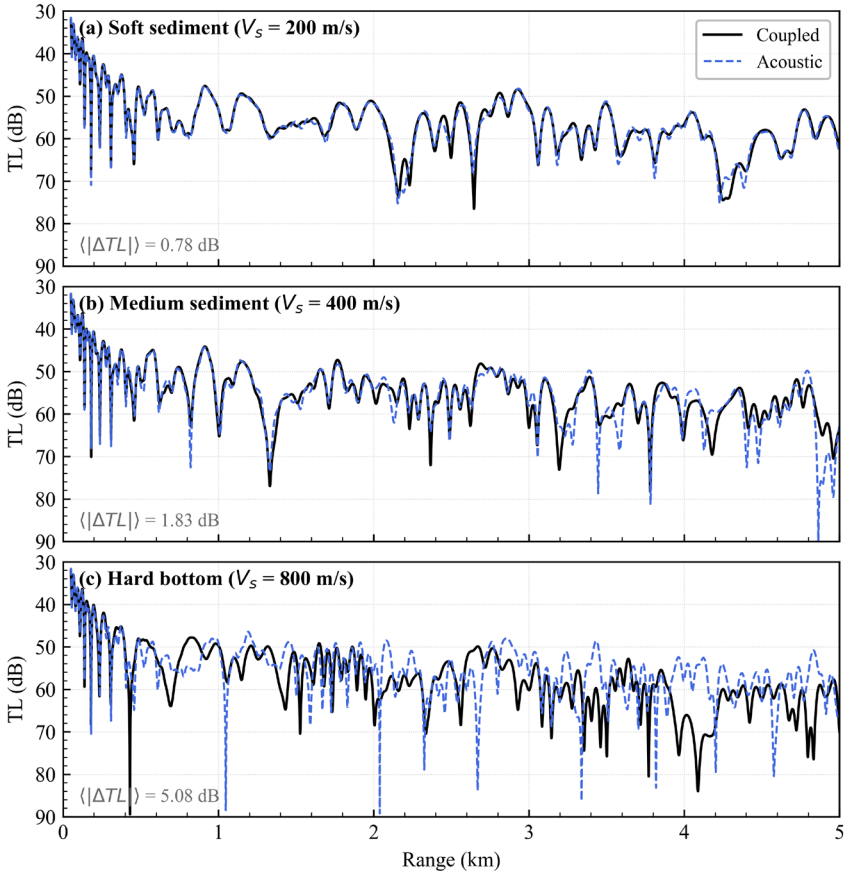

Figure 6. Shear-wave velocity sensitivity: Coupled (solid) vs. acoustic-only (dashed) FEM models for (a) soft sediment (V_S = 200 m/s), (b) medium sediment (V_S = 400 m/s) and (c) hard bottom (V_S = 800 m/s) at approximately 101 m receiver depth (100 Hz)
Abbreviations: FEM: Finite element method; TL: Transmission loss.

For each component, the staircase mesh result (top) is compared against the curvilinear mesh result (bottom).

Table 5 summarizes the relative difference between the staircase and curvilinear solutions for all three wavefield components, measured by the L_2 norm $\| \mathbf{u}_{\text{stair}} - \mathbf{u}_{\text{curv}} \|_2 / \| \mathbf{u}_{\text{curv}} \|_2$. The displacement components (u_x, u_z) show substantially larger differences (53–116%) than pressure (23–24%), as the displacement field depends directly on traction boundary accuracy. Among the three profiles, the anticline and syncline exhibit the largest u_z discrepancies (98% and 116%), consistent with their stronger seabed curvature.

The physical origin of the staircase mesh error is twofold, as discussed in Section 2: artificial diffraction at step corners generates numerically spurious diffracted waves, and incorrect local normal directions at step faces introduce errors in the traction boundary conditions. Because the displacement field depends directly on the tangential traction continuity at the fluid-solid interface, the displacement components u_x and u_z are affected more severely than the scalar pressure. The approximately 2–5 times greater sensitivity of the displacement components (Table 5) confirms that terrain-following meshing is essential for accurate elastic wavefield prediction at irregular seabeds.

Table 5. Relative L_2 difference (%) between staircase and curvilinear mesh solutions for three wavefield components across the three bathymetric profiles.

Profile	u_x (%)	u_z (%)	p (%)
Downslope	78.7	84.8	24.4
Anticline	53.0	98.0	23.4
Syncline	63.4	115.5	24.2

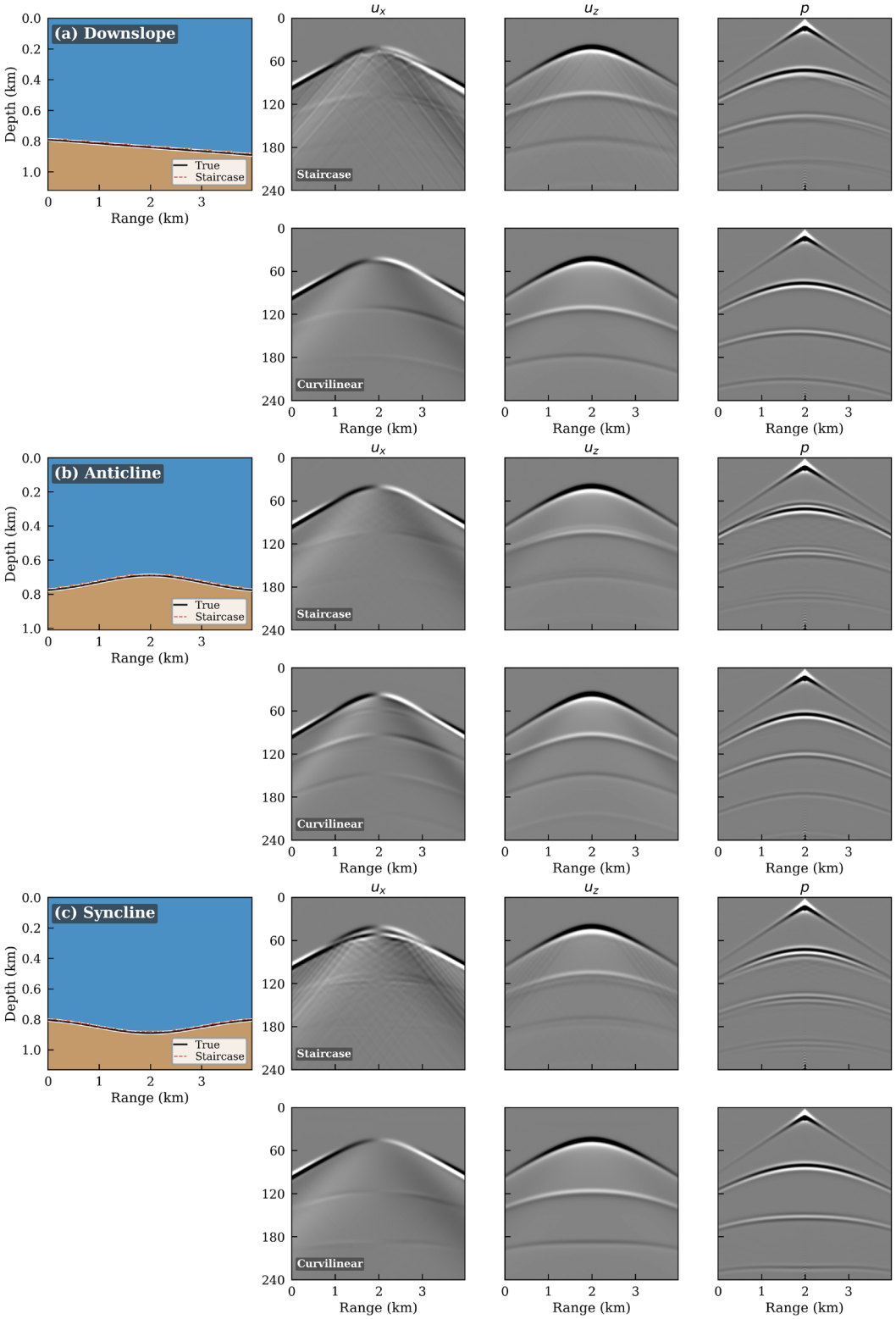

Figure 7. Staircase vs. curvilinear mesh comparison for three bathymetric profiles: (a) Downslope, (b) anticline, and (c) syncline. Left column: Velocity model with true seabed (solid black) and staircase approximation (dashed red). Remaining columns: Broadband seismograms of u_x, u_z, and p components (50–200 Hz), with staircase mesh (top) and curvilinear mesh (bottom) for each profile.

4. Discussion

The following subsections interpret the numerical results in terms of the underlying wave physics and assess the practical applicability of the proposed FEM model.

4.1. Physical interpretation of acoustic-elastic coupling effects

The numerical examples demonstrate that the acoustic-elastic coupled model differs from the acoustic-only model by a spatially averaged |ΔTL| that varies systematically with seabed type, reaching approximately 5.1 dB for the hard bottom ($V_S = 800$ m/s), 1.8 dB for the medium sediment ($V_S = 400$ m/s), and 0.8 dB for the soft sediment ($V_S = 200$ m/s), with local maxima exceeding 10 dB at interference nulls. These differences originate from two distinct physical mechanisms at the water-seabed interface.

The first mechanism is direct energy loss via P-to-S mode conversion. When a compressional wave impinges on the elastic seabed, a fraction of the incident energy is converted into shear waves in the sediment, which is captured by the coupled model but entirely absent from the acoustic-only model. The second, and often dominant, mechanism is the modification of the plane-wave reflection coefficient phase by the presence of shear rigidity ($\mu = \rho_s V_S^2$). Even when shear-wave energy conversion is modest, the phase of the reflected wave changes relative to the fluid-only case, shifting the positions and amplitudes of the multipath interference pattern in the water column and thereby producing large |ΔTL| at interference nulls.[1,9]

The observed trend—|ΔTL| increasing from soft to hard seabed—is explained by this phase-shift mechanism rather than by mode-conversion energy loss alone. It should be noted that V_P, ρ_s, and Q also vary across the three seabed types (Table 4), so the reported |ΔTL| values reflect the combined effect of all geoacoustic parameters, not V_S in isolation. For the soft sediment ($V_P = 1{,}550$ m/s, $V_S = 200$ m/s), the compressional impedance contrast with water is small ($Z_s / Z_f \approx 1.4$), so the reflection coefficient differs only modestly between the elastic and fluid models, and |ΔTL| remains below 1 dB. For the hard bottom ($V_P = 3{,}000$ m/s, $V_S = 800$ m/s), the large impedance contrast ($Z_s / Z_f \approx 5.0$) and the emergence of a P-wave critical angle at $\theta_{cP} = \sin^{-1}\left(c_f / V_P\right) \approx 30^\circ$ cause a pronounced phase jump in the reflection coefficient near the critical angle. This phase jump shifts the positions of constructive and destructive interference, producing the largest |ΔTL| of 5.1 dB. The systematic dependence of |ΔTL| on seabed type observed in Figure 6 is thus primarily governed by the impedance contrast and the associated reflection-coefficient phase behavior, rather than by the absolute magnitude of shear-wave energy conversion.

The frequency sensitivity analysis (Section 3.4) reveals that the range-averaged |ΔTL| remains approximately constant across frequencies: 5.6 dB at 50 Hz, 6.0 dB at 100 Hz, and 6.0 dB at 200 Hz. This near-frequency-independence is primarily governed by the plane-wave reflection coefficient at the fluid–solid interface. The Zoeppritz equations yield reflection and transmission coefficients that depend on incidence angle and material properties, but not on frequency;[1] consequently, the energy partition per bottom reflection is the same at all frequencies for a given seabed type and grazing angle. In a modal waveguide, although the number of propagating modes and their angular distribution are frequency-dependent, the range-averaged |ΔTL| is approximately preserved across the 50–200 Hz band. The residual frequency dependence appears in range-resolved results: at 50 Hz, fewer propagating modes at steeper grazing angles produce |ΔTL| of 14.3 dB at 10 km; at 200 Hz, the broader modal distribution yields 8.7 dB, averaging out over the full propagation range. The operating frequency therefore does not strongly affect the mean coupling magnitude, though the spatial distribution of ΔTL varies with frequency.

Taken together, these results directly address the second limitation identified in the introduction section—the neglect of shear-wave effects in acoustic-only FEM models. The practical implications for model selection can be summarized as follows. In shallow-water continental shelf environments where V_S exceeds approximately 400 m/s, acoustic-elastic coupled modeling is essential; for medium sediments ($V_S \approx 400$ m/s), the mean |ΔTL| of 1.8 dB makes coupled modeling recommended for quantitative TL prediction; only for soft sediments ($V_S \lesssim 200$ m/s) can a simpler acoustic-only formulation be considered, and even then only when the associated errors can be tolerated. For geoacoustic inversion aimed at estimating V_S, a coupled forward model is indispensable regardless of substrate type, since even the soft-sediment |ΔTL| of 0.8 dB exceeds typical inversion sensitivity thresholds.[9,10,15,16]

4.2. Performance and applicability of the curvilinear mesh

The case study in Section 3.6 demonstrates that the staircase mesh introduces pressure errors of 23–24% and displacement errors of 53–116% relative to the curvilinear mesh (Table 5), confirming that terrain-following meshing substantially improves waveform prediction accuracy in irregular-bathymetry environments.

Two distinct mechanisms contribute to staircase mesh errors. First, artificial diffraction at step corners generates spurious scattered waves absent from the true solution at a smooth seabed, perturbing the pressure waveform and

shifting peak and trough positions. Second, the normal direction is forced to be vertical or horizontal at each step face, yielding incorrect reflection coefficients at the wrong incidence angle.[21]

The TFI-based curvilinear mesh[20] eliminates staircase errors by aligning element boundaries with the physical seabed. The linear TFI mapping adopted here generates the interior mesh by algebraic interpolation between the sea surface and the seabed profile. The mapping is effective for bathymetric slopes below approximately 30°; at greater slopes, the Jacobian determinant of the isoparametric mapping can approach zero at integration points, leading to ill-conditioned stiffness matrices—an important constraint for environments with steep submarine canyons or escarpments. For such cases, elliptic PDE-based mesh smoothing[21] or fully unstructured triangular meshes provide more robust alternatives.

4.3. Comparison with RAMGEO and methodological differences

The FEM methodology adopted here draws on established techniques from seismic wave modeling. The frequency-domain approach, the use of sparse direct solvers via LU factorization, and the coupling of acoustic and elastic domains all derive from the computational seismology tradition.[13,23] The present work demonstrates that these tools transfer directly and effectively to the underwater acoustic problem.

The validation in Section 3.1 shows FEM-RAMGEO agreement with a running-average MAE of 1.8 dB (mean bias −0.17 dB) in a range-independent horizontally stratified environment. The residual discrepancy arises primarily from three methodological differences. First, PE is inherently a one-way propagation method that neglects backscattering, whereas FEM fully resolves two-way wave propagation—a capability well established in computational seismology, where backscattering from impedance contrasts is routinely handled.[13] In horizontal stratification, backscattering is weak and the effect of this difference is small; however, in range-dependent environments with strong impedance contrasts or irregular topography, backscattering contributions may become significant, and FEM's two-way treatment would then provide a meaningful accuracy advantage. Second, RAMGEO solves the elastic wave equation within the one-way PE framework,[8] which inherently restricts backscattering and wide-angle propagation, while the present FEM solves the full Navier equation without directional constraints and therefore captures all elastic wave phenomena without approximation. Third, the finite-order Padé approximation underlying the PE formulation introduces phase errors at wide propagation angles, and these errors accumulate at higher frequencies.

PE-based methods retain superior computational efficiency—roughly 20–30 times shorter runtime than the present FEM for equivalent geometries—making them preferred for long-range (tens to hundreds of kilometers) and real-time operational applications. The present FEM model is particularly suited to short-to-medium range propagation (1–10 km), complex irregular seabed environments, and geoacoustic forward modeling, where two-way propagation, complete elastic treatment, and bathymetric conformity provide the most decisive accuracy benefits.

4.4. Connection to geoacoustic full-waveform inversion

The sensitivity of the coupled FEM forward model to seabed parameters (V_P, V_S, ρ_s, Q) demonstrated in Sections 3.3–3.5 has direct implications for geoacoustic inversion[17]—the underwater acoustic analogue of seismic full-waveform inversion (FWI),[13] where an accurate forward model directly constrains inversion accuracy and convergence.[15,16]

Both problems share a common mathematical structure in the frequency domain: the sparse system matrix is factorized once per frequency and reused for multiple source positions via back-substitution, a strategy central to the efficiency of frequency-domain seismic FWI.[13] The present results confirm that the FEM model possesses sufficient parametric sensitivity to V_S (mean $|\Delta TL|$ ranging from 0.8 to 5.1 dB across seabed types) to serve as such a forward engine for geoacoustic inversion.

4.5. Computational efficiency and practical considerations

The FEM model developed in this study employs the actual grid dimensions of $n_x = 11114$ and $n_z = 557$ nodes at grid spacing $h = 0.9$ m for the 200 m water depth configuration at 100 Hz. Using the PARDISO direct solver on an Intel Core i9-13900K workstation (8 threads, 64 GB RAM), the total computation time per frequency—including matrix assembly, LU factorization, and back-substitution—is approximately 10 seconds per frequency (Table 3), which is roughly 20–30 times slower than RAMGEO under equivalent conditions. However, the frequency-domain FEM formulation offers important practical advantages in multi-source and multi-receiver scenarios: the LU factorization of the system matrix is computed only once per frequency and reused for all source positions via back-substitution, and the responses at all receiver locations are obtained simultaneously from a single matrix solve.[13] Multi-

frequency analyses can be parallelized straightforwardly across frequency channels.

The cost difference reflects fundamentally different algorithmic structures: RAMGEO uses range-marching at O(N_z z × N_r r) cost, while FEM factorizes a global sparse matrix at O($N^{3/2}$) cost via PARDISO, with 2–4 GB LU factor storage as the primary practical constraint. Scalability to larger problems can be addressed through iterative Krylov-subspace solvers (*e.g.*, the generalized minimal residual method, GMRES, with domain-decomposition preconditioners), distributed-memory parallelization via the finite element tearing and interconnecting (FETI) method, or GPU-accelerated sparse matrix-vector products. Alternative high-order schemes such as the discontinuous Galerkin method on unstructured meshes[44] offer comparable geometrical flexibility but at higher computational cost per degree of freedom.

4.6. Modeling assumptions, limitations, and future works

The present model relies on two simplifying constitutive assumptions. First, the water column is modeled as an inviscid fluid, neglecting volume attenuation. At the frequencies considered here (50–200 Hz), the absorption coefficient of seawater is on the order of 10^{-3} dB/m,[45] corresponding to a cumulative loss of less than 10 dB over the 10 km propagation range—small compared to spreading and bottom-interaction losses. The inviscid approximation is therefore well justified for the present frequency range and propagation distances. At frequencies above 1 kHz, where seawater absorption increases quadratically, a complex bulk modulus would be required to represent volume attenuation.

Second, the seabed is modeled as an isotropic, linearly elastic solid. Real marine sediments are often transversely isotropic (VTI) due to horizontal layering and compaction-induced fabric, and exhibit viscoelastic attenuation that is poorly described by the Kelvin–Voigt model implicit in many FEM formulations. The isotropic assumption is adequate for demonstrating the methodology and quantifying the first-order effect of shear-wave conversion, but extension to VTI elasticity or constant-Q viscoelasticity[46] would be necessary for quantitative geoacoustic inversion in environments with strong anisotropy or high intrinsic attenuation.

The present study is restricted to 2D; real ocean environments include azimuth-dependent 3D effects, as demonstrated by recent 3D finite-difference models for ocean acoustic propagation.[18] Horizontal refraction and 3D scattering by complex seabed topography can play significant roles in certain environments, and 2D models cannot fully reproduce these phenomena. The present model also assumes a single seabed layer, whereas real seabeds typically consist of multiple sediment layers with distinct impedance contrasts, requiring additional interfacial coupling conditions. Sound-speed profile gradients in the water column, sea-surface roughness, and seabed roughness are additional physical effects that should be progressively incorporated in future model extensions.

The demonstrated sensitivity of the forward model to seabed parameters (Section 3.5) also suggests potential for future application as a forward engine in geoacoustic parameter estimation. Future work will extend the present FEM model to implement acoustic-elastic coupled full-waveform inversion (FWI), enabling simultaneous recovery of seabed geoacoustic parameters (V_P, V_S, ρ, Q) from field-measured acoustic propagation data. Application of the model to field data from the seas surrounding the Korean Peninsula, including the East Sea and the Yellow Sea, where complex bathymetry and variable sediment cover coexist, will provide an important test of the method's practical applicability.[47]

5. Conclusion

A two-dimensional frequency-domain acoustic-elastic coupled FEM model was developed and validated through six numerical examples. The main findings are as follows.

First, in a range-independent 200 m deep Pekeris waveguide environment, the proposed FEM acoustic-elastic coupled model agrees with RAMGEO with a 100 m running-average MAE of 1.8 dB and a mean bias of −0.17 dB, confirming that the amplitude envelope of multipath interference is accurately reproduced. The approach of coupling the Helmholtz equation for the acoustic domain with the Navier equation for the elastic domain within a single weak-form framework, and imposing fluid-solid interface conditions as natural boundary conditions, is shown to be numerically effective and consistent.

Second, a mesh convergence study confirms that the λ/8 resolution rule provides adequate numerical accuracy, with the RMS TL error decreasing monotonically from 12.3 dB at λ/4 to 3.9 dB at λ/12 relative to a λ/16 reference solution.

Third, quantitative comparison of the coupled and acoustic-only models reveals that the mean |ΔTL| at approximately 101 m receiver depth is approximately 0.8 dB for soft sediment ($V_S = 200$ m/s), 1.8 dB for medium sediment ($V_S = 400$ m/s), and 5.1 dB for hard bottom ($V_S = 800$ m/s), with local maxima exceeding 10 dB at interference nulls. The strong dependence on seabed type confirms that acoustic-elastic coupled modeling is essential

for accurate TL prediction in environments with variable seabed stiffness, and that the model possesses sufficient parametric sensitivity to serve as a forward engine for geoacoustic inversion of V_S.

Fourth, frequency sensitivity analysis at 50, 100, and 200 Hz yields mean |ΔTL| values of approximately 5.6 dB, 6.0 dB, and 6.0 dB respectively between the coupled and acoustic-only FEM models, confirming that the elastic coupling effect persists consistently across the tested frequency range for the 200 m waveguide configuration.

Fifth, across three irregular seabed profiles—downslope, anticline, and syncline—the staircase mesh introduces pressure differences of 23–24% and displacement errors of 53–116% compared to the curvilinear mesh, confirming that terrain-following meshing substantially improves waveform prediction accuracy in irregular-bathymetry environments.

The proposed FEM framework overcomes three fundamental limitations of existing PE and FDM methods—the one-way propagation approximation, staircase bathymetric representation, and neglect of shear-wave effects—within a single unified formulation. Future work will extend to 3D configurations, multilayer seabeds, and geoacoustic full-waveform inversion validated against field data.

Acknowledgments

None.

Funding

This work was supported by the Agency for Defense Development by the Korean Government (UE240520DD).

Conflict of interest

The authors declare they have no competing interests.

Author contributions

Conceptualization: Youngjae Shin, Ho Seuk Bae
Formal analysis: Youngjae Shin
Funding acquisition: Ho Seuk Bae
Investigation: Eunpyo Lim, Youngseok Lee, Jaehwan Oh
Methodology: Youngjae Shin, Won-Ki Kim
Project administration: Ho Seuk Bae
Resources: Dawoon Lee, Ho Seuk Bae
Software: Youngjae Shin
Supervision: Ho Seuk Bae
Validation: Youngjae Shin, Won-Ki Kim
Writing–original draft: Youngjae Shin
Writing–review & editing: Youngjae Shin, Won-Ki Kim, Ho Seuk Bae

Availability of data

The data and FEM code supporting the findings of this study are available from the corresponding author (Ho Seuk Bae) upon reasonable request.

Further disclosure

AI writing tools (Claude, Anthropic) were used for literature search assistance and language polishing. All scientific content, experimental design, numerical implementation, and conclusions were conceived, directed, and verified by the authors.

References

1. Jensen FB, Kuperman WA, Porter MB, Schmidt H. *Computational Ocean Acoustics*. 2nd ed. New York, NY: Springer; 2011.

   doi: 10.1007/978-1-4419-8678-8

2. Hovem JM. *Marine Acoustics: The Physics of Sound in Underwater Environments*. Los Altos, CA: Peninsula Publishing; 2010.

3. Etter PC. *Underwater Acoustic Modeling and Simulation*. 5th ed. Boca Raton, FL: CRC Press; 2018.

   doi: 10.1201/9781315166346

4. Collins MD. A split-step Padé solution for the parabolic equation method. *J Acoust Soc Am*. 1993;93(4):1736-1742.

   doi: 10.1121/1.406739

5. Porter MB, Reiss EL. A numerical method for ocean-acoustic normal modes. *J Acoust Soc Am*. 1984;76(1):244-252.

   doi: 10.1121/1.391101

6. Westwood EK, Tindle CT, Chapman NR. A normal mode model for acousto-elastic ocean environments. *J Acoust Soc Am*. 1996;100(6):3631-3645.

   doi: 10.1121/1.417226

7. Collins MD. A higher-order parabolic equation for wave propagation in an ocean overlying an elastic bottom. *J Acoust Soc Am*. 1989;86(4):1459-1464.

   doi: 10.1121/1.398706

8. Collins MD, Westwood EK. A higher-order energy-conserving parabolic equation for range-dependent ocean depth, sound speed, and density. *J Acoust Soc Am*. 1991;89(3):1068-1075.

   doi: 10.1121/1.400526

9. Schmidt H, Jensen FB. A full wave solution for propagation in multilayered viscoelastic media with application to Gaussian beam reflection at fluid-solid interfaces. *J Acoust Soc Am*. 1985;77(3):813-825.

   doi: 10.1121/1.392050

10. Hamilton EL. Geoacoustic modeling of the sea floor. *J Acoust Soc Am*. 1980;68(5):1313-1340.

doi: 10.1121/1.385100

11. Virieux J. P-SV wave propagation in heterogeneous media: Velocity-stress finite-difference method. *Geophysics*. 1986;51(4):889-901.

doi: 10.1190/1.1442147

12. Levander AR. Fourth-order finite-difference P-SV seismograms. *Geophysics*. 1988;53(11):1425-1436.

doi: 10.1190/1.1442422

13. Pratt RG. Seismic waveform inversion in the frequency domain, Part 1: Theory and verification in a physical scale model. *Geophysics*. 1999;64(3):888-901.

doi: 10.1190/1.1444597

14. Kozitskiy S. Coupled-mode parabolic equations for the modeling of sound propagation in a shallow-water waveguide with weak elastic bottom. *J Mar Sci Eng*. 2022;10(10):1355.

doi: 10.3390/jmse10101355

15. Dosso SE, Dettmer J. Bayesian matched-field geoacoustic inversion. *Inverse Probl*. 2011;27(5):055009.

doi: 10.1088/0266-5611/27/5/055009

16. Gerstoft P. Inversion of seismoacoustic data using genetic algorithms and a posteriori probability distributions. *J Acoust Soc Am*. 1994;95(2):770-782.

doi: 10.1121/1.408387

17. Sonnemann T, Dettmer J, Holland CW, Dosso SE. Meso-scale seabed quantification with geoacoustic inversion. *Commun Eng*. 2024;3:60.

doi: 10.1038/s44172-024-00204-5

18. Liu W, Zhang L, Wang W, *et al*. A three-dimensional finite difference model for ocean acoustic propagation and benchmarking for topographic effects. *J Acoust Soc Am*. 2021;150(2):1140-1156.

doi: 10.1121/10.0005853

19. Li Q, Wu G, Jia Z, Duan P. Full-waveform inversion in acoustic-elastic coupled media with irregular seafloor based on the generalized finite-difference method. *Geophysics*. 2023;88(2):T83-T100.

doi: 10.1190/geo2022-0408.1

20. Gordon WJ, Hall CA. Construction of curvilinear co-ordinate systems and applications to mesh generation. *Int J Numer Methods Eng*. 1973;7(4):461-477.

doi: 10.1002/nme.1620070405

21. Thompson JF, Warsi ZUA, Mastin CW. *Numerical Grid Generation: Foundations and Applications*. Amsterdam, Netherlands: North-Holland; 1985.

22. Ihlenburg F. *Finite Element Analysis of Acoustic Scattering*. New York, NY: Springer; 1998.

doi: 10.1007/b98828

23. Zienkiewicz OC, Taylor RL. *The Finite Element Method, Vol. 1: The Basis*. 5th ed. Oxford, UK: Butterworth-Heinemann; 2000.

24. Atalla N, Sgard F. *Finite Element and Boundary Methods in Structural Acoustics and Vibration*. Boca Raton, FL: CRC Press; 2015.

doi: 10.1201/b18366

25. Komatitsch D, Tromp J. Introduction to the spectral element method for three-dimensional seismic wave propagation. *Geophys J Int*. 1999;139(3):806-822.

doi: 10.1046/j.1365-246x.1999.00967.x

26. Bottero A, Cristini P, Komatitsch D, Asch M. An axisymmetric time-domain spectral-element method for full-wave simulations: Application to ocean acoustics. *J Acoust Soc Am*. 2016;140(5):3520-3530.

doi: 10.1121/1.4965964

27. Cristini P, Komatitsch D. Some illustrative examples of the use of a spectral-element method in ocean acoustics. *J Acoust Soc Am*. 2012;131(3):EL229-EL235.

doi: 10.1121/1.3682459

28. Isakson MJ, Chotiros NP. Finite element modeling of reverberation and transmission loss in shallow water waveguides with rough boundaries. *J Acoust Soc Am*. 2011;129(3):1273-1279.

doi: 10.1121/1.3531810

29. Vendhan CP, Diwan GC, Bhattacharyya SK. Finite-element modeling of depth and range dependent acoustic propagation in oceanic waveguides. *J Acoust Soc Am*. 2010;127(6):3319-3326.

doi: 10.1121/1.3392440

30. Zhou YQ, Luo WY. A finite element model for underwater sound propagation in 2-D environment. *J Mar Sci Eng*. 2021;9(9):956.

doi: 10.3390/jmse9090956

31. Gui Q, Zhang GY, Chai YB, Li W. A finite element method with cover functions for underwater acoustic propagation problems. *Ocean Eng*. 2022;243:110174.

doi: 10.1016/j.oceaneng.2021.110174

32. He T, Wang B, Mo S, Fang E. Predicting range-dependent underwater sound propagation from structural sources in shallow water using coupled finite element/equivalent source computations. *Ocean Eng*. 2023;272:113904.

doi: 10.1016/j.oceaneng.2023.113904

33. Wang Y, Tu H, Xu G, Gao D. A review of the application of spectral methods in computational ocean acoustics. *Phys Fluids*. 2023;35(12):121301.

doi: 10.1063/5.0176116

34. Zhang Y, Tu H, Wang Y, Xu G, Gao D. A normal mode model based on the spectral element method for simulating horizontally layered acoustic waveguides. *J Mar Sci Eng*. 2024;12(9):1499.

doi: 10.3390/jmse12091499

35. Xu W, Fu Z, Xu W, Xue MA, Rashed YF, Zheng J. FEM-PIKFNN for underwater acoustic propagation induced by structural vibrations in different ocean environments. *Comput Math Appl*. 2024;166:46-54.

doi: 10.1016/j.camwa.2024.09.007

36. Tu H, Wang Y, Yang C, Liu W, Wang X. A Chebyshev-Tau spectral method for coupled modes of underwater sound propagation in range-dependent ocean environments. *Phys Fluids*. 2023;35(3):037113.

doi: 10.1063/5.0138012

37. Bérenger JP. A perfectly matched layer for the absorption of electromagnetic waves. *J Comput Phys*. 1994;114(2):185-200.

doi: 10.1006/jcph.1994.1159

38. Collino F, Tsogka C. Application of the perfectly matched absorbing layer model to the linear elastodynamic problem in anisotropic heterogeneous media. *Geophysics*. 2001;66(1):294-307.

doi: 10.1190/1.1444908

39. Komatitsch D, Martin R. An unsplit convolutional perfectly matched layer improved at grazing incidence for the seismic wave equation. *Geophysics*. 2007;72(5):SM155-SM167.

doi: 10.1190/1.2757586

40. Pled F, Desceliers C. Review and recent developments on the perfectly matched layer (PML) method for the numerical modeling and simulation of elastic wave propagation in unbounded domains. *Arch Comput Methods Eng*. 2022;29:471-518.

doi: 10.1007/s11831-021-09581-y

41. Liseikin VD. *Grid Generation Methods*. 2nd ed. Dordrecht, Netherlands: Springer; 2010.

doi: 10.1007/978-90-481-2912-6

42. Schenk O, Gärtner K. Solving unsymmetric sparse systems of linear equations with PARDISO. *Future Gener Comput Syst*. 2004;20(3):475-487.

doi: 10.1016/j.future.2003.07.011

43. Chew WC, Weedon WH. A 3D perfectly matched medium from modified Maxwell's equations with stretched coordinates. *Microw Opt Technol Lett*. 1994;7(13):599-604.

doi: 10.1002/mop.4650071304

44. Käser M, Dumbser M. An arbitrary high-order discontinuous Galerkin method for elastic waves on unstructured meshes I: The two-dimensional isotropic case with external source terms. *Geophys J Int*. 2006;166(2):855-877.

doi: 10.1111/j.1365-246X.2006.03051.x

45. Francois RE, Garrison GR. Sound absorption based on ocean measurements. Part II: Boric acid contribution and equation for total absorption. *J Acoust Soc Am*. 1982;72(6):1879-1890.

doi: 10.1121/1.388673

46. Blanch JO, Robertsson JOA, Symes WW. Modeling of a constant Q: Methodology and algorithm for an efficient and optimally inexpensive viscoelastic technique. *Geophysics*. 1995;60(1):176-184.

doi: 10.1190/1.1443744

47. Jung Y, Lee K. Observation of the relationship between ocean bathymetry and acoustic bearing-time record patterns acquired during a reverberation experiment in the southwestern continental margin of the Ulleung Basin, Korea. *J Mar Sci Eng*. 2021;9(11):1259.

doi: 10.3390/jmse9111259

ACCSCIENCE PUBLISHING

Journal of Seismic Exploration

ARTICLE

Fault prediction method for coalfields based on an SVD–ResCBAM–U-Net framework

Guangui Zou[1,2], Jingwen Xue[1], Zeming Wang[1]*, Xiaopeng Jin[1], and Chengyang Han[1]

[1]College of Geoscience and Surveying Engineering, China University of Mining and Technology, Beijing, China

[2]State Key Laboratory for Fine Exploration and Intelligent Development of Coal Resources, China University of Mining and Technology, Beijing, China

Abstract

Accurate fault prediction in coalfield seismic data is important for geological interpretation and the safe and efficient exploitation of coal resources. However, conventional fault interpretation methods and shallow machine-learning approaches usually rely on manually extracted seismic attributes. They often show limited robustness to noise and insufficient capability in characterizing fault continuity, boundary features, and small faults in structurally complex areas. To overcome these limitations, a fault prediction method based on the singular value decomposition–residual convolutional block attention module–U-Net (SVD–ResCBAM–U-Net) framework is proposed. First, SVD was used to denoise the seismic data and improve its quality. Then, residual blocks and a convolutional block attention module were incorporated into the U-Net architecture to enhance fault-related feature extraction and improve prediction performance. Experimental results show that the proposed SVD–ResCBAM–U-Net achieved the best performance among all compared models, with a global accuracy of 0.9556, a mean intersection over union of 0.6241, and a mean boundary F1-score of 0.6796. These results clearly demonstrate the proposed method's advantages in fault continuity, boundary delineation, and small-fault prediction, underscoring its effectiveness for fault prediction in coalfield seismic data under complex geological conditions.

Keywords: Seismic interpretation; U-Net; Fault prediction; Singular value decomposition; Coal mine

***Corresponding author:**
Zeming Wang
(cumtbwzm@163.com)

Citation: Zou G, Xue J, Wang Z, Jin X, Han C. Fault prediction method for coalfields based on an SVD–ResCBAM–U-Net framework. *J Seismic Explor*. 2026;35(3):026090040. doi: 10.36922/JSE026090040

Received: March 1, 2026

Revised: April 22, 2026

Accepted: April 24, 2026

Published online: May 21, 2026

Copyright: © 2026 Author(s). This is an Open-Access article distributed under the terms of the Creative Commons Attribution License, permitting distribution, and reproduction in any medium, provided the original work is properly cited.

Publisher's Note: AccScience Publishing remains neutral with regard to jurisdictional claims in published maps and institutional affiliations.

1. Introduction

Coal plays a critical role in the national energy security strategy. Safe and effective extraction is important for ensuring the safety of the national electricity supply and promoting sustainable economic growth.[1] Nevertheless, complicated geological formations, especially faults, often interrupt the continuity of coal seams. These structures are the primary geological factors that cause hazardous events, including water inrush[2,3] and gas outbursts.[4-6] Three-dimensional (3D) seismic technology has become the primary tool for detecting faults in coalfields due to its wide coverage and high detection accuracy.[7] Faults usually appear as discontinuities, distortions, or abnormal

attenuation of seismic reflection events in seismic profiles.[8] Manual profile-by-profile interpretation is not only time-consuming and labor-intensive but also prone to missing subtle responses associated with small faults. Technological advancements have advanced fault interpretation methods and led to a variety of seismic attributes based on discontinuity characteristics of reflected seismic events, including coherence,[9,10] curvature,[11,12] and variance,[13] and more recently, hybrid discontinuity attributes.[14] The methodologies have been enhanced, which has given birth to many wave features. However, human factors can lead to incorrect fault identification or omission. To reduce the influence of human bias, researchers have applied machine learning algorithms, including artificial neural networks,[15,16] support vector machines,[17-19] and random forests,[20-22] to build intelligent recognition models based on multi-attribute fusion. More recently, hybrid approaches that combine machine learning with seismic structural attributes have also been used to automate the extraction and mapping of complex fault systems.[23,24] Although these methods have improved the efficiency and objectivity of fault interpretation, their performance still depends heavily on manually selected or constructed seismic attributes. Moreover, most methods rely on pointwise estimates and ignore the spatial distribution and structural patterns of faults. Therefore, when dealing with low-signal-to-noise geological data, attribute-based methods remain vulnerable to noise, making small faults difficult to identify.

Deep learning has made significant advances in seismic data processing and interpretation by enabling automatic feature extraction. It has been widely used in tasks such as seismic event detection,[25,26] inversion,[27,28] and fault recognition.[29-31] Xiong *et al.*[32] trained a pixel-wise classification convolutional neural network using field seismic data and achieved automatic fault detection and mapping in seismic data cubes. Nevertheless, this sliding-window-based method is computationally expensive. To address this limitation, Wu *et al.*[33] presented a lightweight U-Net model for end-to-end fault segmentation on synthetic seismic records, demonstrating that fault identification can be formulated as a semantic segmentation problem. Since the introduction of U-Net by Ronneberger *et al.*[34] in 2015, researchers have continued to refine its architecture for more effective application to complex seismic data. For example, Yang *et al.*[35] proposed U-Net++, which improves the fusion of shallow and deep features through a dense connection strategy. Similarly, the WNet model proposed by Yan *et al.*[36] improves feature propagation between network layers by introducing an additional expansion path to the decoder. In addition, Cui *et al.*[37] introduced MS-U-Net to reduce spatial information loss during down-sampling by combining multi-level encoder features through skip connections. To alleviate gradient vanishing during training, Gao *et al.*[38] integrated a residual learning mechanism into the U-Net architecture. Finally, to address the limitation of non-adaptive feature selection in the conventional U-Net, Sun *et al.*[39] incorporated attention mechanisms into the model, thereby improving the representation of fault features.

However, the use of attention mechanisms in U-N*et al*one cannot fully overcome noise interference in feature learning, nor can it completely address the gradient vanishing problem in deep network training for complex coalfield seismic data. Therefore, we propose a coalfield fault prediction method based on a singular value decomposition–residual convolutional block attention module–U-Net (SVD–ResCBAM–U-Net) framework. Previous studies have shown that SVD is effective in separating useful seismic signals from random noise.[40,41] In this study, SVD is used during preprocessing to denoise the seismic data, thereby improving the signal-to-noise ratio of the network input by integrating residual blocks and the convolutional block attention module (CBAM) into the encoder. The model improves fault-feature extraction and enhances deep feature propagation. This strategy combines signal enhancement with network optimization and provides an effective solution for fault prediction in coalfield seismic data.

2. Denoising analysis of seismic profiles using singular value decomposition

2.1. Synthetic seismic data

To evaluate the effectiveness of SVD for seismic profile denoising, a fault-forward model was built to simulate noise characteristics observed in real seismic data. The model was designed to ensure that the simulated data closely resemble actual subsurface geologic conditions, as it was based on the characteristics of the roadway-exposed geological profiles. As shown in Figure 1, the model consists of seven layers arranged from top to bottom: the 1# sandstone layer, 1# coal seam, 2# sandstone layer, 2# coal seam, 3# sandstone layer, 3# coal seam, and 4# sandstone layer. The P-wave velocity and density of the sandstone layers were set to 3,000 m/s and 2.7 g/cm^3, respectively, whereas those of the coal seams were set to 2,000 m/s and 1.5 g/cm^3, respectively. To better reflect realistic seismic acquisition conditions, the trace spacing was set to 5 m, and the source wavelet was selected as a Ricker wavelet with a dominant frequency of 60 Hz.

To assess denoising performance across different noise levels, the synthetic data were contaminated with random noise at 20%, 50%, and 70%. The resulting seismic profiles are shown in Figure 2.

2.2. Principle of singular value decomposition-based noise attenuation

A two-dimensional (2D) seismic profile can also be represented by a data matrix X of size $m \times n$, where m is the number of time samples, and n is the number of seismic traces. After applying SVD to the matrix X, we obtain:

$$X = U\Sigma V^T = \sum_{i=1}^{r} \sigma_i u_i v_i^T \tag{1}$$

Here, the singular values satisfy, $\sigma_1 \geq \sigma_2 \geq \cdots \sigma_r \geq 0$, where $r = rank(X)$. u_i and v_i denote the left and right singular vectors, respectively. Because seismic reflections usually exhibit strong lateral continuity, most of their energy is concentrated in a few leading singular values and their corresponding singular vectors. In contrast, random noise, which is incoherent in both space and time, tends to be distributed among smaller singular values corresponding to higher-order modes. The best rank-k approximation, according to the Eckart–Young theorem,[42] can be constructed from the k largest singular values and their corresponding singular vectors as follows:

$$\hat{X}_k = \sum_{i=1}^{k} \sigma_i u_i v_i^T \tag{2}$$

where, $k \ll r$ represents the number of retained singular values, meaning that only the first k singular components contributing most to the total energy are used for seismic data reconstruction. This process preserves the main seismic reflection signals while suppressing higher-order components to reduce the noise. In practice, k is usually selected based on the cumulative energy ratio or the inflection point of the singular value spectrum, such that:

$$\frac{\sum_{i=1}^{k} \sigma_i^2}{\sum_{i=1}^{r} \sigma_i^2} \geq \eta \tag{3}$$

where, η denotes a predefined energy threshold, typically set between 90% and 98% according to the requirements of seismic data processing.

2.3. Analysis of singular value decomposition denoising

To evaluate the effectiveness of SVD-based noise suppression, three groups of seismic profiles with varying noise levels were compared, as shown in Figure 2. The reconstruction rank of each dataset was determined using the energy-thresholding approach, with cumulative singular-value energy retention levels of 99%, 97%, and 90%, respectively. The seismic sections before and after SVD processing are shown in Figure 3.

The results show that SVD effectively suppresses background noise, resulting in smoother texture patterns in the seismic profiles. At a noise level of 20%, seismic responses near small faults are weak in the original profile, whereas event discontinuities become clearer after SVD processing. At a noise level of 50%, the reflection events

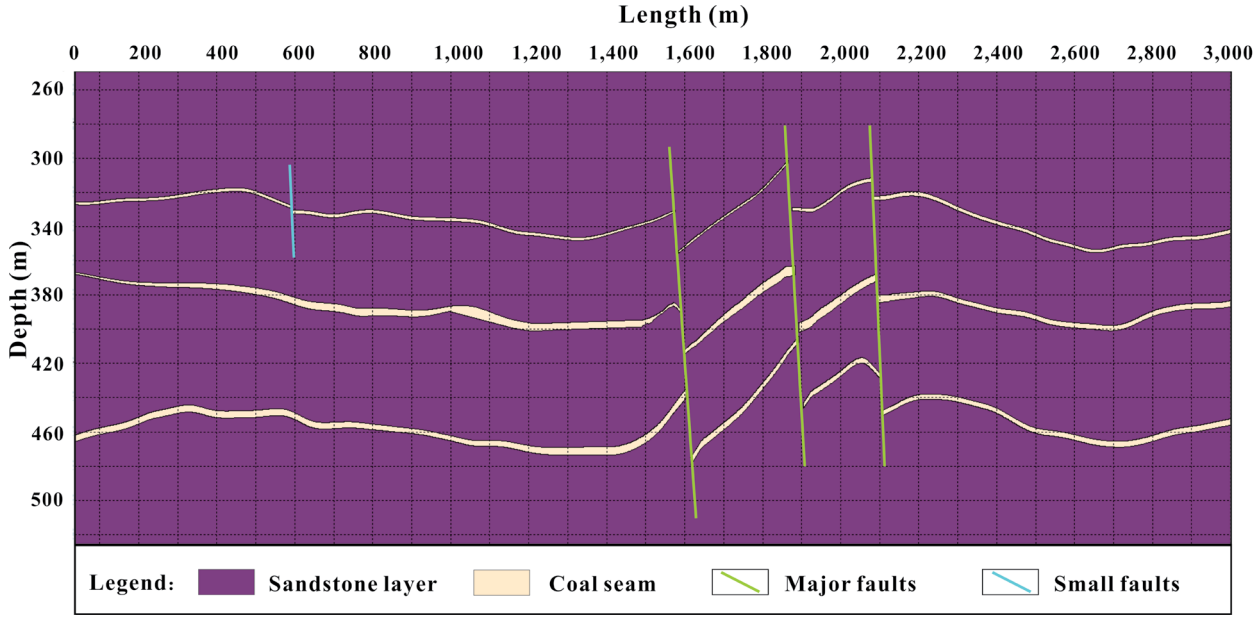

Figure 1. Seismic fault model with one small fault and three large faults

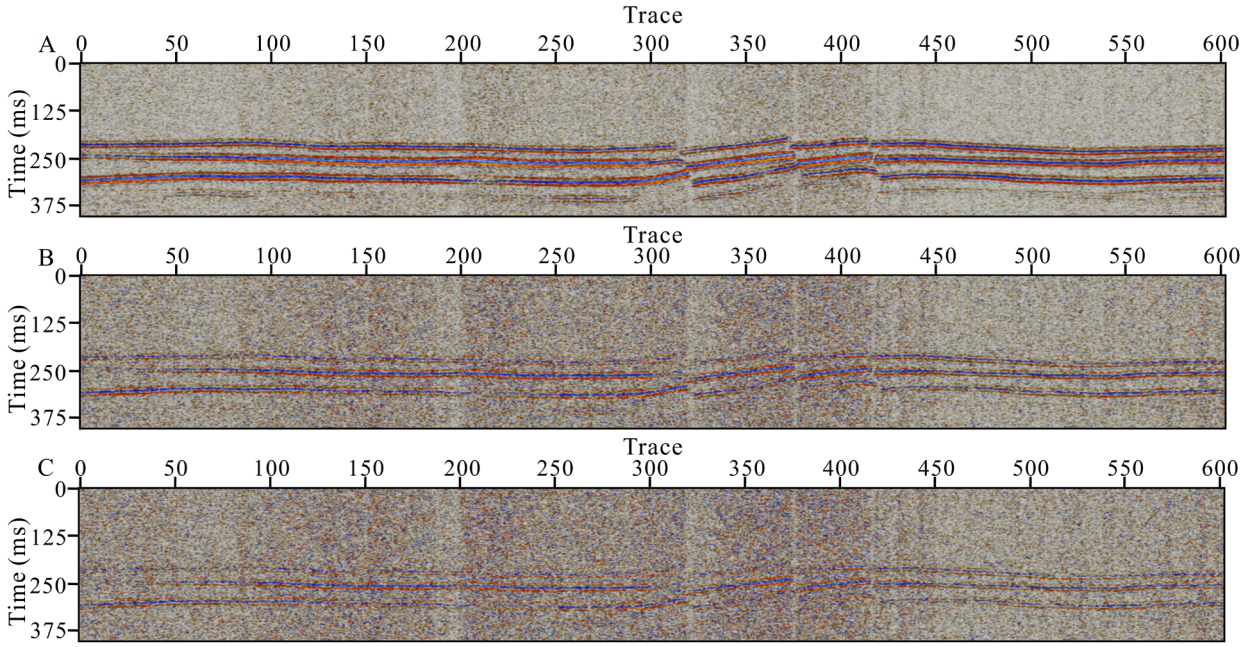

Figure 2. Noisy seismic profiles of the model under different noise levels: (A) seismic profile with 20% noise, (B) seismic profile with 50% noise, (C) seismic profile with 70% noise

become blurred in the original seismic profile. SVD processing significantly reduces random noise, clarifies seismic events, and better delineates the locations of large faults. Even at a noise level of 70%, SVD still preserves the main structural morphology, allowing seismic signals to remain distinguishable.

In summary, SVD shows stable denoising performance under different noise levels. It improves the quality of seismic images and provides a more reliable basis for subsequent analysis by suppressing random noise while preserving important reflection information.

3. Framework of the proposed singular value decomposition–residual convolutional block attention module–U-Net

The SVD-based denoising analysis of artificial seismic data indicates that this method can be successfully used to reduce noise and enhance phase and amplitude contrast, thus yielding high-SNR outputs in fault delineation. Since SVD is a dimensionality-reduction filter based on linear algebra, it cannot directly describe the spatial distribution and the complex geometric structure of fault systems. However, this paper presents the SVD–ResCBAM–U-Net framework, which integrates SVD preprocessing with deep learning algorithms and introduces attention mechanisms and residual structures. The overall workflow of the proposed SVD–ResCBAM–U-Net fault prediction framework is shown in Figure 4. In this framework, data augmentation is first used to enlarge the sample space and enhance data diversity. After SVD denoising of the seismic profiles, the dataset was divided into training, validation, and test sets. The training set was used to train the ResCBAM–U-Net network, the validation set was used for model evaluation and hyperparameter tuning, and the test set was used to compare the prediction results with manual interpretation and to further examine the generalization capability of the proposed method.

3.1. Residual convolutional block attention module–U-Net network architecture

The proposed ResCBAM–U-Net is based on the classical U-Net architecture, a widely used fully convolutional network for semantic segmentation.[43] It adopts an encoder-decoder structure with skip connections, where the encoder extracts hierarchical features and the decoder progressively restores spatial resolution. The skip connections help fuse shallow and deep features, thereby improving pixel-level fault prediction.

In seismology, faults are usually expressed as reflector breaks or stratigraphic offsets. Seismic data often have a low signal-to-noise ratio and exhibit complex texture due to the complexity of the deep subsurface. Therefore, the seismic signature of small faults is often weak and can be easily obscured by noise. The conventional U-Net performs

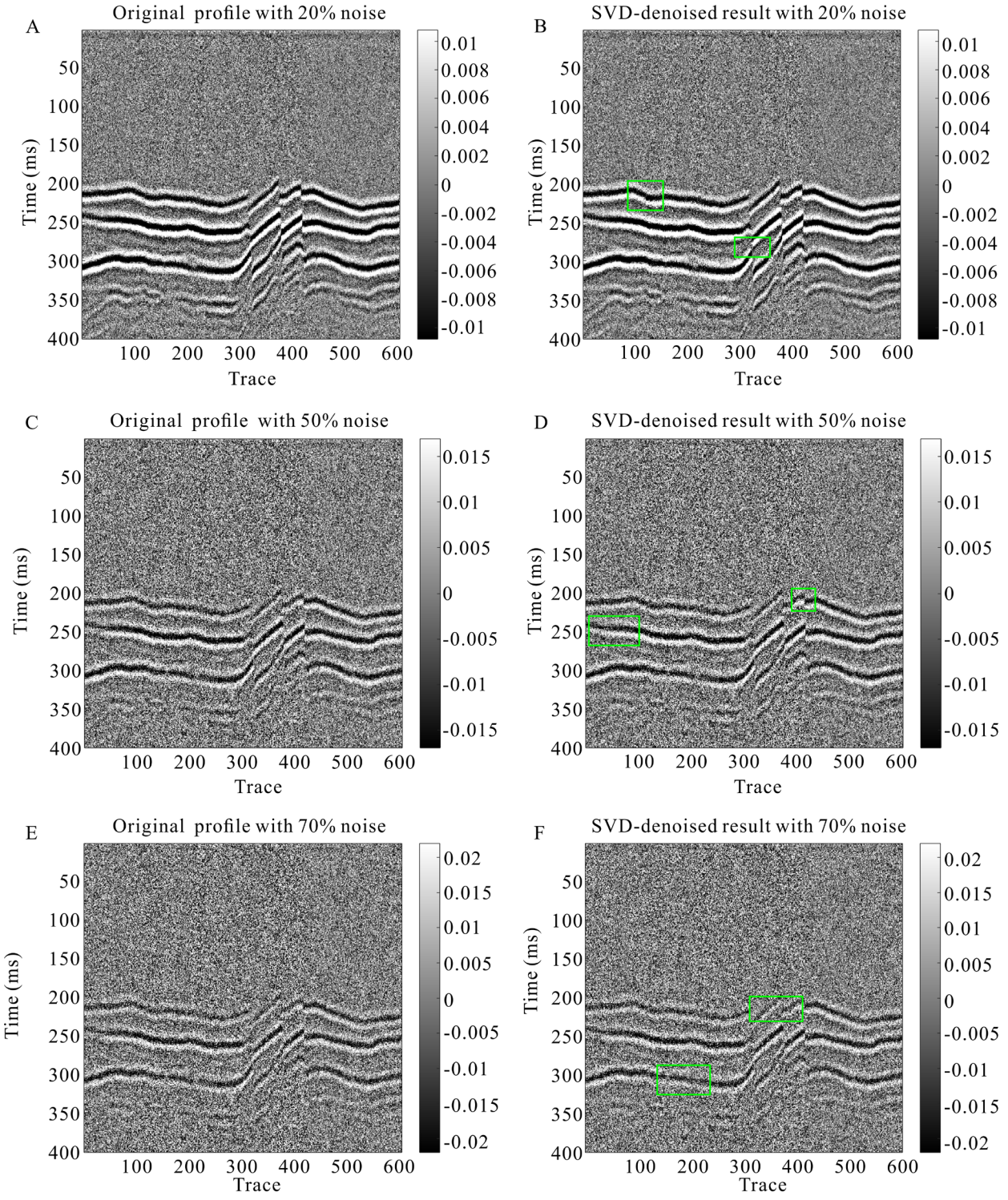

Figure 3. Comparison of seismic profile before and after singular value decomposition (SVD) denoising under different noise levels. For each noise level, the left panel shows the original noisy seismic profile and the right panel shows the corresponding SVD-denoised result. Specifically, (A) original profile with 20% random noise, (B) SVD-denoised result with 20% random noise, (C) original profile with 50% random noise, (D) SVD-denoised result with 50% random noise, (E) original profile with 70% random noise, and (F) SVD-denoised result with 70% random noise.

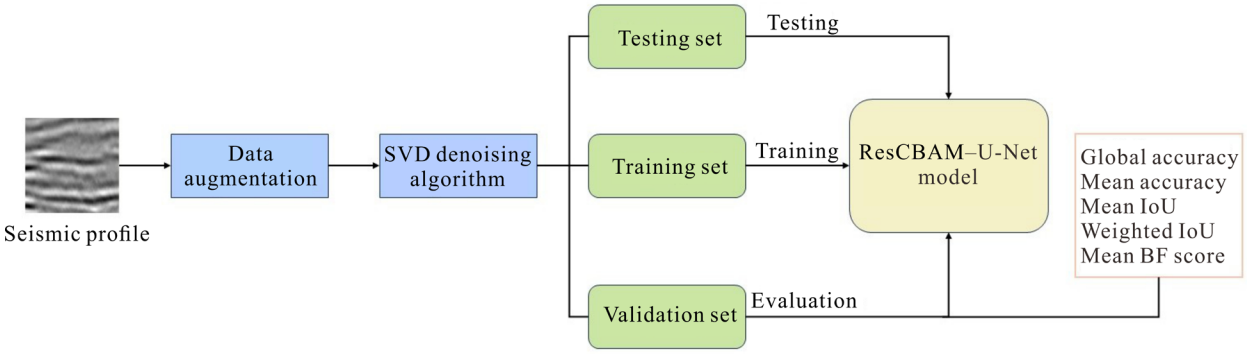

Figure 4. Framework of the singular value decomposition–residual convolutional block attention module–U-Net for fault identification
Abbreviations: BF: Boundary F1-score; IoU: Intersection over union; ResCBAM–U-Net: Residual convolutional block attention module–U-Net; SVD: Singular value decomposition.

convolutional operations without distinguishing between fault and background pixels. The lack of an adaptive feature-selection mechanism makes the model vulnerable to noise, resulting in false detections or discontinuous fault predictions. To capture global semantic information, the depth of the network needs to be increased, but standard U-Net models often suffer from gradient vanishing or feature degradation during deep training. Simple feature concatenations alone are insufficient to exploit the multi-scale residual information required to characterize complex geological structures. To address these limitations, this study proposes the ResCBAM–U-Net model (Figure 5). The U-Net encoder was enhanced by incorporating CBAM into the residual convolutional architecture. This design uses attention mechanisms to improve the learning of subtle fault signals, while residual connections help alleviate the gradient-vanishing problem. Together, these improvements promote stable convergence during deep network training.

3.2. Principle of the improved module

3.2.1. Residual learning mechanism

Deep network architectures are commonly used to represent the global semantic characteristics of faults in seismic data. Nevertheless, increasing network depth leads to repeated non-linear transformations. This phenomenon frequently causes gradient vanishing during backpropagation, which prevents effective parameter updating and optimization in deeper layers.[44,45]

To address gradient degradation, this study incorporates an additional residual learning module into the U-Net architecture. Unlike the direct mapping used in conventional networks, the residual structure introduces an identity shortcut connection. This mechanism allows the input to bypass the transformation layers and be added elementwise to the output of the residual path. The final output of the residual unit can be mathematically expressed as follows:

$$H(x) = \sigma(F(x) + x) \tag{4}$$

where $F(x)$ denotes the residual mapping function in the proposed ResCBAM–U-Net architecture, which consists of convolutional layers combined with attention modules, and $\sigma(\bullet)$ denotes the rectified linear unit (ReLU) activation function. The residual connection unit is shown in Figure 6.

During backpropagation, the gradient of the loss function l with respect to the input x can be expressed as:

$$\frac{\partial l}{\partial x} = \frac{\partial l}{\partial H(x)} \cdot \frac{\partial H(x)}{\partial x} = \frac{\partial l}{\partial H(x)} \left(\frac{\partial F(x)}{\partial x} + 1 \right) \tag{5}$$

In this expression, the constant term 1 corresponds to the identity shortcut connection of the residual unit. This means that even when the gradient of the residual mapping function tends to 0, gradient information can still be directly propagated to shallower layers through this identity term. As a result, this mechanism helps alleviate the vanishing gradient problem during deep network training.

3.2.2. Convolutional block attention module-based feature enhancement mechanism

In coalfield seismic sections, continuous stratigraphic reflections and complex background noise typically appear as strong amplitude responses. In contrast, fault signals are typically characterized by small displacements or breaks in low-energy seismic events. Standard convolution operations treat all regions of an image equally and cannot

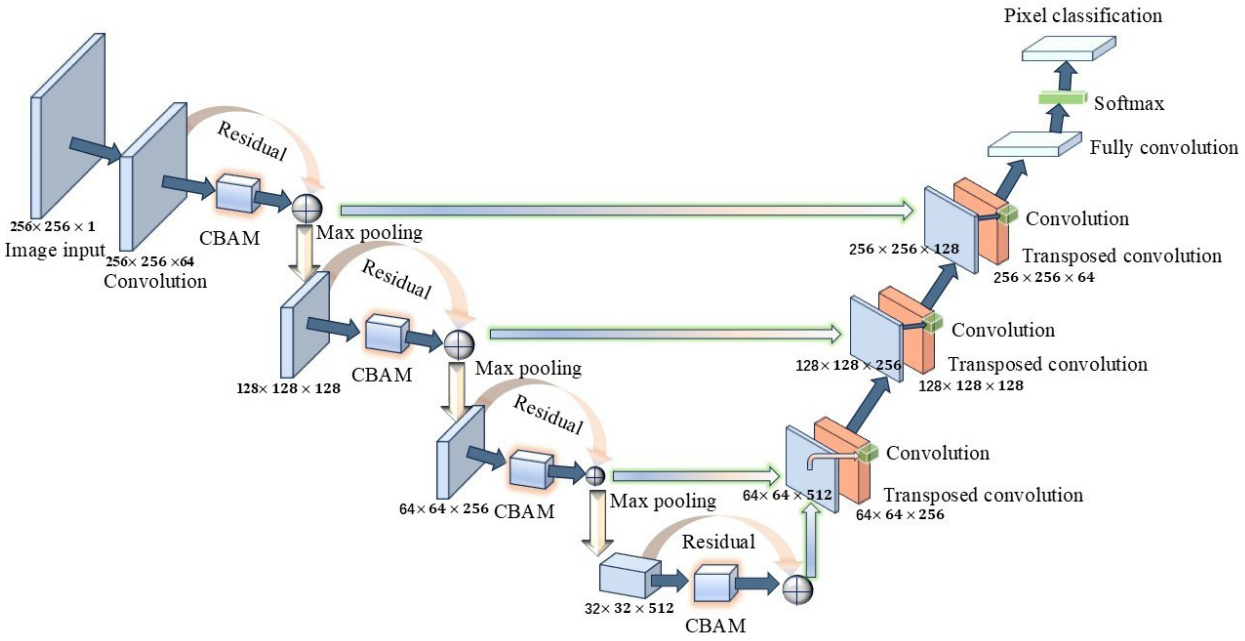

Figure 5. Architecture of the Residual convolutional block attention module–U-Net network
Abbreviation: CBAM: Convolutional block attention module.

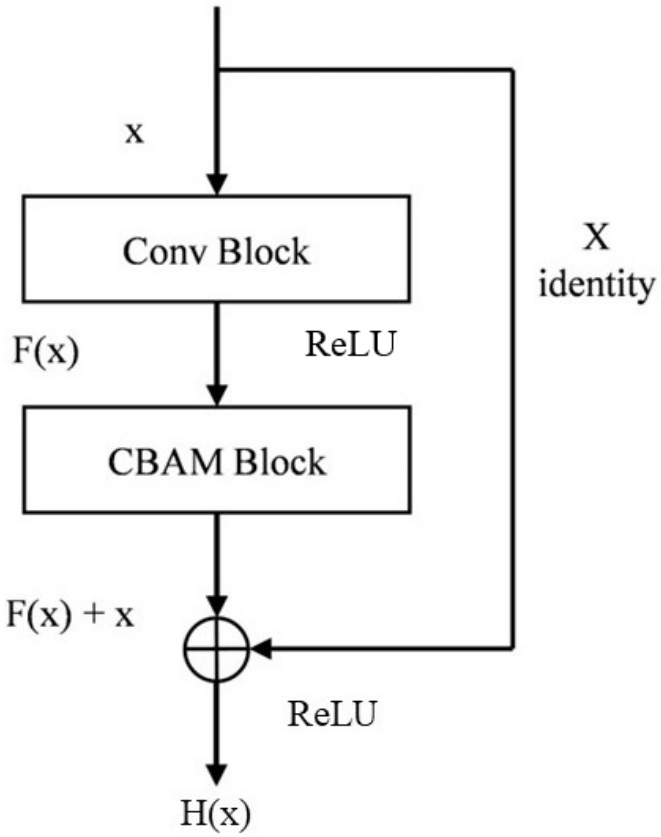

Figure 6. Residual connection unit

adaptively suppress background interference. Therefore, such subtle fault features can be easily obscured by high-energy reflectors.[46] To address this problem, the study introduces the CBAM into the U-Net decoder. This module improves the model's sensitivity to weak fault signals by recalibrating feature weights across both the channel and spatial dimensions.

As shown in Figure 7, CBAM consists of two submodules: the channel attention module and the spatial attention module. These two modules are connected in serial to enhance feature representation. The input feature is denoted as $F \in R^{C\times H\times W}$. F is first processed by the channel attention module to emphasize important feature channels, producing the intermediate feature F'. Then, F' is fed into the spatial attention module to locate fault structures in the spatial domain, yielding the final refined feature F''.

The channel attention module performs global average pooling and global max pooling on the input feature map F in parallel. This operation aggregates spatial information to produce two complementary channel descriptors that capture global contextual information and local texture details, respectively. These descriptors are then fed into a shared multi-layer perceptron, followed by a sigmoid activation function to obtain the channel attention map $M_C(F)$. The resulting attention map is then used to multiply element-wise with input features, completing the first stage of feature recalibration in the channel dimension. This process can be formulated as follows:

$$M_C(F) = \sigma(\mathrm{MLP}(\mathrm{AvgPool}(F)) + \mathrm{MLP}(\mathrm{MaxPool}(F))) \tag{6}$$

$$F' = M_c(F) \otimes F \tag{7}$$

After the initial feature refinement by the channel attention module, the spatial attention module further localizes important features in the spatial domain. The channel-refined feature map F' is processed by average pooling and max pooling along the channel dimension, generating 2D spatial descriptors. These descriptors are concatenated and then convolved with a 7 × 7 kernel to integrate spatial information, followed by a sigmoid activation function to produce the spatial attention map $M_S(F')$. This map reflects the spatial distribution of fault-related features across the seismic profile. To obtain the final output feature, an element–wise product between $M_S(F')$ and F' is performed as follows:

$$M_S(F') = \sigma(f^{7\times7}([\mathrm{AvgPool}(F'); \mathrm{MaxPool}(F')])) \tag{8}$$

$$F'' = M_s(F') \otimes F' \tag{9}$$

Through these cascaded operations, the ResCBAM–U-Net architecture can suppress background noise and significantly enhance the representation of fault-zone features. Therefore, this approach improves the accuracy of fault prediction in complex geological settings.

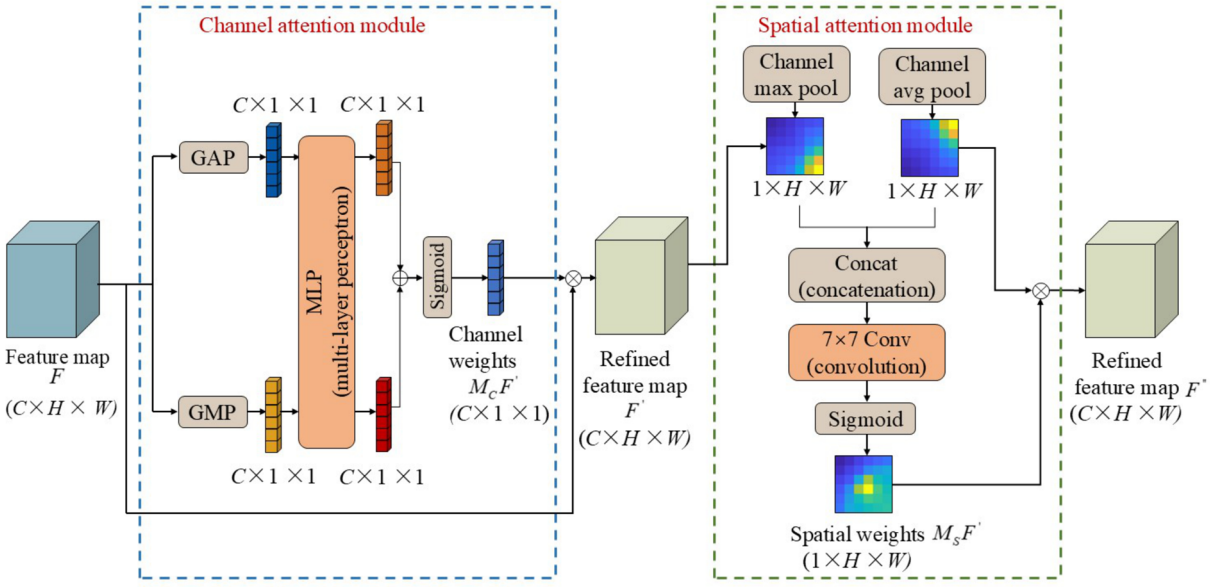

Figure 7. Schematic diagram of the convolutional block attention module structure
Abbreviations: GAP: Global average pooling; GMP: Global max pooling.

3.3. Evaluation metrics

In a field seismic profile, faults usually appear as linear features with complex morphology. In contrast to continuous stratigraphic reflections, faults occupy only a very small proportion of the pixels, leading to severe class imbalance. Therefore, this study uses a set of evaluation metrics to assess model performance. The first category introduces pixel-level metrics to evaluate the model's segmentation performance. These metrics include global accuracy (GA), mean accuracy (MA), mean intersection over union (MIoU), and weighted intersection over union (WIoU). The second category consists of the boundary F1 score, namely the mean BF-score, which is a boundary-distance-based metric used to evaluate the accuracy of fault-boundary extraction.

In this study, fault pixels are treated as positive samples, whereas non-fault areas are treated as negative samples. The corresponding confusion matrix is shown in Table 1. In this matrix, true positive denotes fault pixels correctly classified as faults; true negative denotes non-fault pixels correctly classified as non-fault; false positive denotes non-fault pixels incorrectly classified as faults; and false negative denotes fault pixels incorrectly classified as non-fault. GA is the ratio of correctly classified pixels to the total number of pixels. MA is calculated as the arithmetic mean of the class-wise accuracies and reflects the model's sensitivity to the minority class, namely faults. MIoU reflects the overlap between the predicted fault regions and the ground-truth labels, whereas WIoU evaluates the overall segmentation performance under class imbalance. The corresponding equations are given in **Equations 10–13**.

$$GA = \frac{TP + TN}{TP + TN + FP + FN} \tag{10}$$

$$MA = \frac{1}{2}\left(\frac{TP}{TP + FN} + \frac{TN}{TN + FP}\right) \tag{11}$$

$$MIoU = \frac{1}{2}\left(\frac{TP}{TP + FN + FP} + \frac{TN}{TN + FP + FN}\right) \tag{12}$$

$$WIoU = \frac{TP + FN}{TP + TN + FP + FN} \cdot \frac{TP}{TP + FP + FN} + \frac{TN + FP}{TP + TN + FP + FN} \cdot \frac{TN}{TN + FN + FP} \tag{13}$$

The boundary F1 evaluates the accuracy of fault-boundary extraction on the matching of boundary pixels.[47] It can be formulated as follows:

$$Mean\ BF\ Score = \frac{2 \times P_B \times R_B}{P_B + R_B} \tag{14}$$

where, P_B represents the boundary precision, i.e., the proportion of predicted boundary pixels that are correctly aligned with the ground truth. Similarly, R_B denotes boundary recall, which is the proportion of ground-truth boundary pixels that are correctly identified. Pixel correspondence is determined using a predefined distance threshold.

Table 1. Confusion matrix for the fault identification

Class	Fault	Non-fault
Fault	True positive	False negative
Non-fault	False positive	True negative

4. Field data examples and analysis

4.1. Dataset construction

The seismic dataset used in this study was acquired from an operating coalfield in Henan province, China. The survey area is located at the southern margin of the North China Block, where tectonic activity is controlled by a thrust belt, resulting in a high density of faults with diverse morphologies. These structural features are mainly represented by nearly East–West-tending normal faults. The Carboniferous–Permian coal-bearing strata, particularly the No. 2 and No. 4 seams, show a significant acoustic impedance contrast with the surrounding roof and floor rocks, thereby generating strong seismic reflection interfaces. However, large thickness variations in the No. 2 coal seam, combined with local folding, cause highly disrupted seismic events near fault-break zones. Furthermore, compressive-torsional deformation in the southeastern part of the study area results in the superposition of minor faults, stratigraphic distortion, and diffraction interference. These complex geological conditions pose significant challenges for traditional structural interpretation.

The 3D seismic data volume used in this study consists of 641 inlines and 641 crosslines, with a 2-way travel time of 300–600ms. From this volume, 2D seismic profiles were extracted in the inline and crossline directions, resulting

in 256 seismic slices. The corresponding fault labels were generated from manual interpretation of the complete seismic profiles and then mapped onto the cropped samples to ensure a consistent input image size for the deep learning model. Representative examples of the fault prediction dataset are shown in Figure 8.

In the interpretation stage, it was noted that the number of fault samples is much lower than that of non-fault samples in the seismic profile, which can lead to class imbalance during model training. To counteract such influence, this paper proposes a data augmentation approach using geometric transformation. Some of the methods are: random rotations between + 5 and −5° to simulate deviation angles caused by acquisition error and processing artifact; random horizontal inversion to increase the diversity of samples; random scaling with factors of 0.9–1.1 to mimic different spatial resolutions; and random horizontal and vertical displacement by +5 and −5°, respectively, to simulate positional changes. During these augmentation operations, the corresponding fault-label images were transformed synchronously with the seismic images using the same parameters. This ensured pixel-level alignment between the seismic sections and labels. After these augmentation steps, a final dataset of 828 samples was formed. Out of this dataset, 76 samples were chosen at random as an independent test set to measure the generalization ability of the model. The other 752 samples were then divided into 676 training samples and 76 validation samples to enable training of models and hyperparameter optimization.

4.2. Network model construction

After data augmentation and dataset partitioning, a deep learning model for fault identification was constructed. First, the preprocessed seismic sections were denoised using

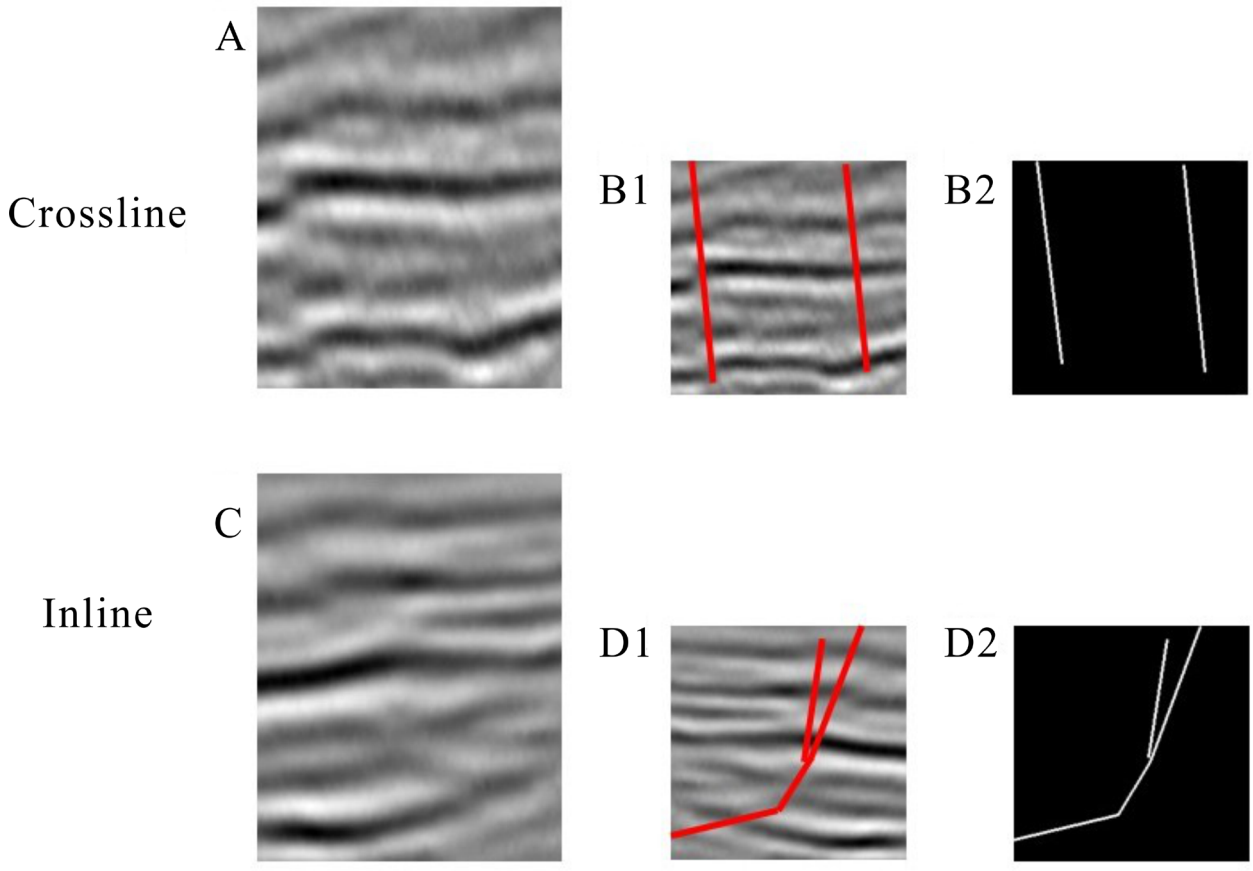

Figure 8. Schematic diagram of dataset construction for fault identification. (A) Original seismic profile in the crossline direction; (B1) cropped seismic image in the crossline direction with interpreted fault traces marked in red; (B2) corresponding fault label; (C) original seismic profile in the inline direction; (D1) cropped seismic image in the inline direction with interpreted fault traces marked in red; (D2) corresponding fault label. The fault labels were generated based on manual interpretation of the complete seismic profiles and then projected onto the cropped samples.

SVD. The economy-sized SVD was then used to decompose the seismic section matrix to achieve computational efficiency and stability in the denoising process, and the first r singular values along with their corresponding singular vectors were retained to obtain a low-rank approximation. We determined the reconstruction rank r for real seismic data using the cumulative singular-value energy criterion. The cumulative energy threshold was set to 90%, based on the SVD denoising analysis under different noise conditions presented in Section 2. This threshold helps reduce random noise. Meanwhile, effective seismic reflection information can be retained. The resulting seismic sections were normalized (amplitude scaled to the range of [0, 1]) and then fed into the ResCBAM–U-Net model.

After SVD denoising and normalization, the normalized seismic profiles were put into the ResCBAM–U-Net model to extract deep features and identify faults. In the training process, Adam optimizer was used to dynamically optimize the network parameters with an initial learning rate of 1.0×10^{-4}, a batch size of 16, and 200 training epochs. Each encoder stage in the network architecture has two convolutional layers. Linear convolutional features are normalized on a batch and processed by the ReLU activation function and then passed on to the CBAM attention module, where adaptive responses to features occur both in channels and spatially. The CBAM module output is then element–wise summed with the main-branch feature via a residual connection. The combination of features is max-pooled, decreasing the spatial resolution of the feature maps and reducing computational cost. Transposed convolution is used during decoding to gradually recover the spatial resolution of the feature maps. High-level features of the encoder at the same scale are connected with the current decoder features via skip connections to perform feature fusion. Following feature extraction, a convolutional layer is applied to the multi-channel features to produce a single-channel prediction map, and a sigmoid activation function is applied to obtain pixel-wise fault probabilities. To alleviate the class imbalance between fault and non-fault pixels in seismic profiles, a weighted binary cross-entropy loss function was adopted to quantify the discrepancy between predicted probabilities and ground-truth labels. The class weights were determined with reference to the pixel distribution in the dataset, where non-fault and fault pixels accounted for 97.34% and 2.66%, respectively. Accordingly, the weights for the fault and non-fault categories were set to 0.9 and 0.1, respectively. This was intended to enhance the learning of minority fault pixels while avoiding unstable training. As shown in Figure 9, training and validation losses decrease steadily with increasing number of epochs. The rate of decline declines after about 50 epochs, and after about 100 epochs, the loss stabilizes near 0.1 and converges. The validation loss is consistently close to the training loss, and therefore, the suggested network successfully alleviates the problem of overfitting and has a good generalization capability.

The quantitative results on the validation set indicate a clear performance hierarchy among the compared models, and the proposed SVD–ResCBAM–U-Net achieves the best overall performance for fault prediction. As shown in Table 2, the proposed model attains the highest GA (0.9556), MA (0.8565), MioU (0.6241), WIoU (0.9386), and mean BF-Score (0.6796), indicating advantages in suppressing false detections, reducing missed fault response, preserving fault continuity, and improving boundary delineation. In addition, the confusion matrix of the proposed model (Figure 10) further confirms its reliable classification performance on fault and non-fault pixels. By contrast, the baseline U-Net performs the worst, with an MIoU of 0.5038 and a mean BF score of 0.4152, indicating strong background interference, poor structural continuity, and inadequate delineation of fault boundaries. Introducing SVD preprocessing improves U-Net performance. SVD–U-Net increases GA from 0.8883 to 0.9376 and mean BF-score from 0.4125 to 0.5504, showing that denoising helps suppress background noise. However, its MIoU remains limited at 0.5716, suggesting that denoising alone cannot fully compensate for the lack of effective fault-feature representation. ResCBAM–U-Net further improves the results by introducing residual learning and attention mechanisms, achieving a mean BF score of 0.6589 and an MioU of 0.6090, which indicates stronger capability in boundary refinement and structural continuity modeling. To further evaluate the contribution of CBAM under SVD preprocessing, SVD–residual (Res)–U-Net was introduced as an ablation model. SVD–Res–U-N*et al*so showed good performance, but its results were consistently lower than those of the proposed SVD–ResCBAM–U-Net across all evaluation metrics. This comparison demonstrates that integrating CBAM yields additional gains in fault-feature discrimination and boundary delineation. Overall, the combination of SVD denoising, residual learning, and attention enhancement enables the proposed model to achieve the most balanced and robust performance among all compared methods.

To summarize, SVD preprocessing and the feature-enhancement mechanisms in ResCBAM–U-Net work together effectively. Their integration reduces false detections and missed fault responses while improving fault localization, boundary delineation, and structural continuity.

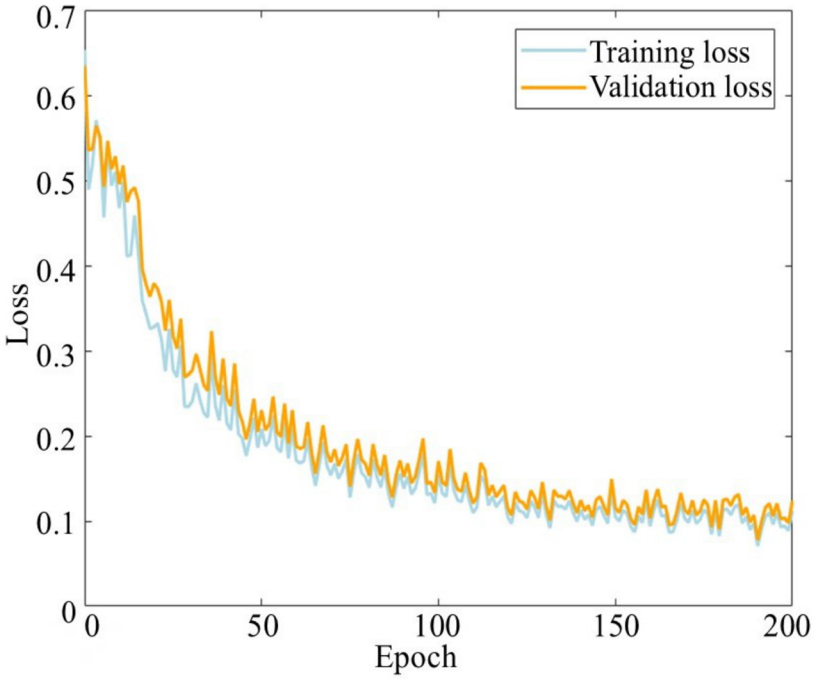

Figure 9. Loss curves of the training and validation set as a function of the number of epochs

		Predicted	
		Fault	Non-fault
Actual	Fault	0.7523	0.2477
	Non-fault	0.0393	0.9607

Figure 10. Normalized confusion matrix of the proposed Singular value decomposition–residual convolutional block attention module–U-Net model for fault and non-fault classification

4.3. Analysis of prediction results

The fault prediction results for representative samples from the test set in the study area are presented in Figure 11. Four representative cases were selected for visualization and comparative analysis. Figure 11A shows the original seismic profiles with manually interpreted fault traces marked in red. Figure 11B–F shows the prediction results of U-Net, SVD–U-Net, ResCBAM–U-Net, SVD–Res–U-Net, and the proposed SVD–ResCBAM–U-Net model, respectively. The prediction results of the proposed model are highly consistent with the manually interpreted fault traces in terms of fault contours, orientations, and geometric characteristics.

The prediction output of the proposed SVD–ResCBAM–U-Net model shows a significantly clean background, structurally continuous fault shapes, and clear-cut boundaries between seismic profiles, as shown in Figure 11F. Adjacent faults in even intensely faulted areas or those that are structurally complicated still have a clear separation between them and do not falsely merge together. Moreover, regarding the location of small faults in the study area, the SVD–ResCBAM–U-Net model demonstrates strong detection capability; it can successfully locate these small features without compromising continuity. The baseline U-Net model (Figure 11B), on the other hand, predicts artificially expanded fault zones with bad structural continuity, and areas with minor faults are virtually absent from the response. With the addition of SVD preprocessing (Figure 11C), background interference in the prediction result is greatly reduced, and the fault responses become narrower than those of the U-Net

Table 2. Evaluation metrics of different models on the validation set

Model	GA	MA	MIoU	WIoU	Mean BF score
U-Net	0.8883	0.7731	0.5038	0.8685	0.4125
SVD-U-Net	0.9376	0.7974	0.5716	0.9183	0.5504
ResCBAM–U-Net	0.9497	0.8479	0.6090	0.9318	0.6598
SVD–Res–U-Net	0.9479	0.8487	0.6097	0.9217	0.61642
SVD–ResCBAM–UNet	0.9556	0.8565	0.6241	0.9386	0.6796

Abbreviations: BF: BF: Boundary F1-score; GA: Global accuracy; MA: Mean accuracy; MioU: mean intersection over union; ResCBAM–U-Net: Residual convolutional block attention module–U-Net; SVD-U-Net: Singular value decomposition–U-Net; SVD–Res–U-Net: Singular value decomposition–residual–U-Net; SVD–ResCBAM–UNet: Singular value decomposition–residual convolutional block attention module–U-Net; WIoU: Weighted intersection over union.

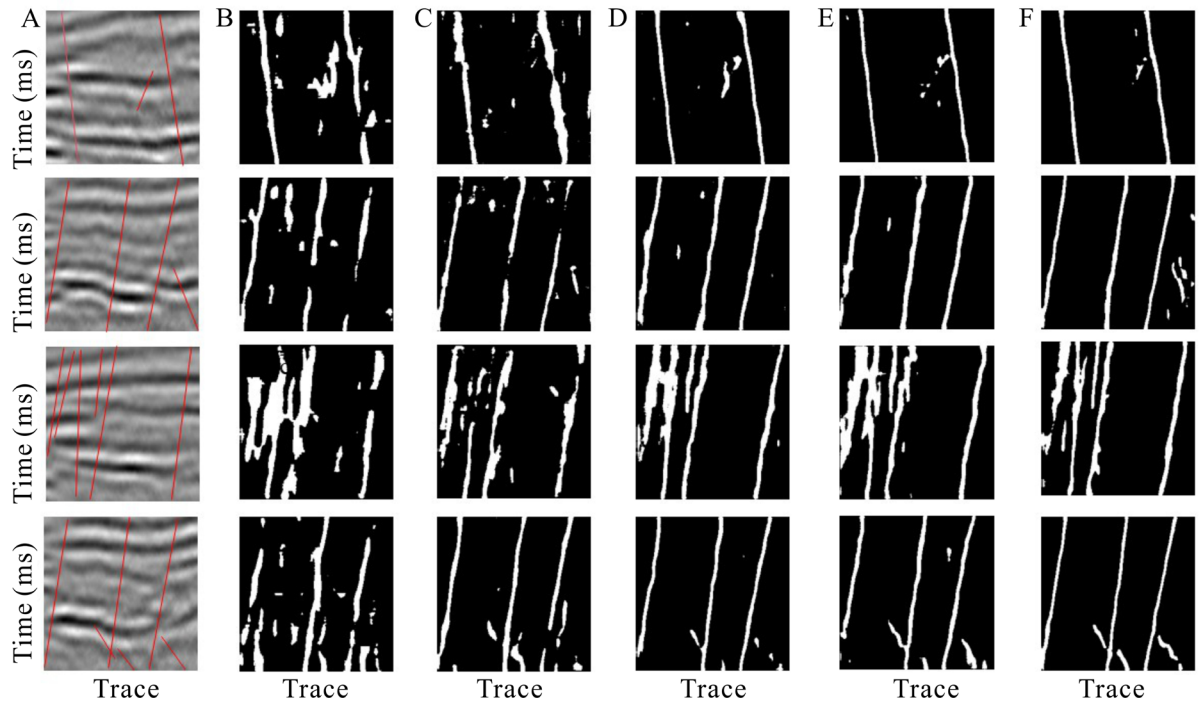

Figure 11. Comparison of fault prediction results on representative samples from the test set in the study area. (A) Original seismic profiles with manually interpreted fault traces marked by red lines; (B) prediction results of U-Net; (C) prediction results of SVD–U-Net; (D) prediction results of ResCBAM–U-Net; (E) prediction results of SVD–Res–U-Net, and (F) prediction results of the proposed SVD–ResCBAM–U-Net model. In the binary prediction maps, white indicates fault pixels and black indicates non-fault pixels.

model. Nevertheless, local fragmentation and missing segments remain visible, consistent with the overall validation performance reported in Table 2. In addition, the small faults predicted by SVD–U-Net mostly appear as scattered rather than coherent structural patterns.

The SVD–ResCBAM–U-Net model provides an absolute performance reference in seismic fault detection, going beyond the constraints of other architectures by using a highly integrated, two-step improvement approach. It is superior because of a specific functional synergy: whereas the SVD acts as a background filter, i.e., cleanses stochastic noise to reveal the major reflection plane, ResCBAM module functions as a refined architectural eye. Not only does the network map data, but the fusion of residual learning and dual-domain attention processes also actively strengthens the representation of weak fault signatures, which can easily be missed during regular processing. The new design is able to strike an unusual compromise between geological interpretation, which preserves the strict structural integrity of large-scale fault systems, and reduces the threshold for detecting the most obscure small faults by several orders of magnitude.

5. Conclusion

This study proposes an SVD–ResCBAM–U-Net framework for fault prediction by combining SVD-based denoising with an improved U-Net architecture. The effectiveness of the proposed method was verified using seismic data from a coal mine in Henan province, China. By introducing SVD during preprocessing, background noise in the seismic profiles was effectively suppressed, thereby improving the representation of fault-related seismic signals. In the network design, residual connections and CBAM were incorporated into the conventional U-Net framework. This design improves the extraction of discriminative deep features related to fault structures. The combination of SVD-based denoising, residual learning, and attention enhancement helps preserve fault continuity and produces clearer fault boundaries, especially in structurally complex or densely faulted areas. In particular, the proposed method shows clear advantages in detecting small faults and improves the structural consistency of the prediction results.

However, despite the effectiveness of the proposed SVD–ResCBAM–U-Net architecture in reducing false fault detections and improving the identification of small faults, some limitations still remain. First, the current study is based on 2D seismic sections and does not fully exploit the spatial continuity information in 3D seismic volumes. Thus, there is still room for improvement in characterizing 3D fault assemblages in complex structural areas. Second, the model was mainly validated on an independent test set from the study area, and its generalization ability under different mining areas, geological conditions, and data qualities remains to be further assessed. Future work will extend the method to 3D seismic volumes and validate it using data from more mining areas.

Acknowledgments

None.

Funding

This work was supported by the National Key Research and Development Program of China (Grant number 2023YFB3211002), the National Natural Science Foundation of China (Grant number 42274165), and the 2025 Undergraduate Education and Teaching Reform and Research Program (Grant number J25ZD03).

Conflict of interest

The authors declare that they have no known competing financial interests or personal relationships that could have appeared to influence the work reported in this paper.

Author contributions

Conceptualization: Guangui Zou, Jingwen Xue, Zeming Wang
Formal analysis: Jingwen Xue, Zeming Wang, Xiaopeng Jin
Investigation: Xiaopeng Jin, Chengyang Han
Methodology: Zeming Wang, Jingwen Xue, Chengyang Han
Writing–original draft: Guangui Zou
Writing–review & editing: Jingwen Xue, Zeming Wang

Availability of data

Data supporting the findings of this study are available from the corresponding author upon reasonable request.

References

1. Wang H, Zhang D. Examining the interplay between fossil fuel mining, sustainable growth, and economic prosperity. *Resour Policy*. 2023;87:104324.

   doi: 10.1016/j.resourpol.2023.104324

2. Odintsov E, Zhao Z, Gusev V, *et al*. Integrated physical and numerical assessment of the formation of water-conducting fracture zones in deep ore mines with structural faults. *Mining*. 2026;6(1):10.

   doi: 10.3390/mining6010010

3. Zhu G, Wang S, Zhang W, *et al*. Research on the mechanism and evolution law of delayed water inrush caused by fault activation with mining. *Water*. 2023;15(24):4209.

doi: 10.3390/w15244209

4. Wang C, Ge C, Zhou B, *et al*. Dynamic damage law of coals under stress paths for disaster inoculation and its influence mechanism on outburst risk level. *Nat Resour Res*. 2026;35(2):1317-1347.

   doi: 10.1007/s11053-025-10585-9

5. Yan J, Feng X, Guo Y, *et al*. Discussion on the main control effect of geological structures on coal and gas outburst. *ACS Omega*. 2023;8(1):835-845.

   doi: 10.1021/acsomega.2c06200

6. Wang H, Wang L, Cheng Y, *et al*. Characteristics and dominant controlling factors of gas outburst in Huaibei coalfield and its countermeasures. *Int J Min Sci Technol*. 2013;23(4):591-596.

   doi: 10.1016/j.ijmst.2013.07.019

7. Zhou B, Hatherly P, Sun W. Enhancing the detection of small coal structures by seismic diffraction imaging. *Int J Coal Geol*. 2017;178:1-12.

   doi: 10.1016/j.coal.2017.04.010

8. Gou R, Song D, He X, *et al*. Microseismic response characteristics and stress anomaly zoning in deep outburst-prone coal seams with multi-concealed structures: A case study. *J Appl Geophys*. 2025;242:105932.

   doi: 10.1016/j.jappgeo.2025.105932

9. Bahorich MS, Haskell NL, Nissen SE, *et al*. Stratigraphic and structural interpretation with 3-D coherence. In: *SEG Technical Program Expanded Abstracts*. Houston, TX: Society of Exploration Geophysicists; 1995:97-100.

   doi: 10.1190/1.1887435

10. Marfurt KJ, Kirlin RL, Farmer SL, *et al*. 3-D seismic attributes using a semblance-based coherency algorithm. *Geophysics*. 1998;63(4):1150-1165.

    doi: 10.1190/1.1444415

11. Gao D. Integrating 3D seismic curvature and curvature gradient attributes for fracture characterization: Methodologies and interpretational implications. *Geophysics*. 2013;78(2):O21-O31.

    doi: 10.1190/geo2012-0190.1

12. Cao L, Yao Y, Liu D, *et al*. Application of seismic curvature attributes in the delineation of coal texture and deformation in Zhengzhuang field, southern Qinshui Basin. *AAPG Bull*. 2020;104(5):1143-1166.

    doi: 10.1306/12031918208

13. Jingbin C, Zhonghong W, Ping C, *et al*. The application of seismic attribute analysis technique in coal field exploration. *Interpretation*. 2016;4(1):SB13-SB21.

    doi: 10.1190/INT-2015-0090.1

14. Khan M, Bery AA, Bashir Y, *et al*. Automated fault network extraction in complex tectonic regimes: A hybrid machine learning and structural attributes approach. *Appl Comput Geosci*. 2025;27:100264.

    doi: 10.1016/j.acags.2025.100264

15. Gui Z, Zhang J, Zhang Y, *et al*. Characterization of fault-karst reservoirs based on deep learning and attribute fusion. *Acta Geophys*. 2024;73(2):1335-1347.

    doi: 10.1007/s11600-024-01420-5

16. Yasin Q, Majdański M, Sohail GM, *et al*. Fault and fracture network characterization using seismic data: a study based on neural network models assessment. *Geomech Geophys Geo-Energy Geo-Resour*. 2022;8(2):41.

    doi: 10.1007/s40948-022-00352-y

17. Zou G, Ren K, Sun Z, *et al*. Fault interpretation using a support vector machine: A study based on 3D seismic mapping of the Zhaozhuang coal mine in the Qinshui Basin, China. *J Appl Geophys*. 2019;171:103870.

    doi: 10.1016/j.jappgeo.2019.103870

18. Ren K, Zou G, Peng S, *et al*. Fault identification based on the kernel principal component analysis-genetic particle swarm optimization-support vector machine algorithm for seismic attributes in the Sihe Coal Mine, Qinshui Basin, China. *Interpretation*. 2023;11(1):T59-T73.

    doi: 10.1190/INT-2022-0039.1

19. Han C, Zou G, Yeh HG, *et al*. Intelligent fault prediction with wavelet-SVM fusion in coal mine. *Comput Geosci*. 2025;194:105744.

    doi: 10.1016/j.cageo.2024.105744

20. Li D, Peng S, Lu Y, *et al*. Seismic structure interpretation based on machine learning: A case study in coal mining. *Interpretation*. 2019;7(3):SE69-SE79.

    doi: 10.1190/INT-2018-0208.1

21. Tsinidis G, Pitilakis K. Improved R-F relations for the transversal seismic analysis of rectangular tunnels. *Soil Dyn Earthq Eng*. 2018;107:48-65.

    doi: 10.1016/j.soildyn.2018.01.004

22. Jang J, So BD, Yuen DA. A machine learning algorithm with random forest for recognizing hidden control factors from seismic fault distribution. *Geosci J*. 2023;27(1):113-126.

    doi: 10.1007/s12303-022-0029-7

23. Khan MK, Bashir Y, Dossary S, *et al*. Machine learning and seismic structural attributes hybrid approach to map complex fault system. In: *Second EAGE Subsurface Intelligence Workshop*. The Netherlands: European Association of Geoscientists & Engineers; 2022:1-5.

    doi: 10.3997/2214-4609.2022616010

24. Imran QS, Siddiqui NA, Latiff AA, *et al*. Automated fault detection and extraction under gas chimneys using hybrid

discontinuity attributes. *Appl Sci*. 2021;11(16):7218.

doi: 10.3390/app11167218

25. Pham N, Fomel S, Dunlap D. Automatic channel detection using deep learning. *Interpretation*. 2019;7(3):SE43-SE50.

doi: 10.1190/INT-2018-0202.1

26. Ross ZE, Meier M, Hauksson E, *et al*. Generalized seismic phase detection with deep learning. *Bull Seismol Soc Am*. 2018;108(5A):2894-2901.

doi: 10.1785/0120180080

27. Feng R. Estimation of reservoir porosity based on seismic inversion results using deep learning methods. *J Nat Gas Sci Eng*. 2020;77:103270.

doi: 10.1016/j.jngse.2020.103270

28. Azizzadeh Mehmandost Olya B, Mohebian R, Moradzadeh A. A new approach for seismic inversion with GAN algorithm. *J Seism Explor*. 2024;33:1-36.

doi: 10.36922/JSE024450003.t

29. Li S, Yang C, Sun H, *et al*. Seismic fault detection using an encoder–decoder convolutional neural network with a small training set. *J Geophys Eng*. 2019;16(1):175-189.

doi: 10.1093/jge/gxy015

30. Zou G, Liu H, Ren K, *et al*. Automatic recognition of faults in mining areas based on convolutional neural network. *Energies*. 2022;15(10):3758.

doi: 10.3390/en15103758

31. Wang J, Niu C, Wang Y, *et al*. Fault identification and enhancement using residual U-Net: Application to field seismic data. *J Seism Explor*. 2026;35(1):025360067.

doi: 10.36922/JSE025360067

32. Xiong W, Ji X, Ma Y, *et al*. Seismic fault detection with convolutional neural network. *Geophysics*. 2018;83(5):O97-O103.

doi: 10.1190/geo2017-0666.1

33. Wu X, Liang L, Shi Y, *et al*. FaultSeg3D: Using synthetic data sets to train an end-to-end convolutional neural network for 3D seismic fault segmentation. *Geophysics*. 2019;84(3):IM35-IM45.

doi: 10.1190/geo2018-0646.1

34. Ronneberger O, Fischer P, Brox T. U-Net: convolutional networks for biomedical image segmentation. *arXiv*. Preprint posted online 2015.

doi: 10.48550/arXiv.1505.04597

35. Yang D, Cai Y, Hu G, *et al*. Seismic fault detection based on 3D Unet++ model. In: *SEG International Exposition and Annual Meeting*. OnePetro; 2020:1631-1635.

doi: 10.1190/segam2020-3426516.1

36. Yan B, Qian L, Zhao J, *et al*. Fault Identification Based on W-Net in 3-D Seismic Images. *IEEE Geosci Remote Sens Lett*. 2024;21:1-5.

doi: 10.1109/LGRS.2024.3404505

37. Cui L, Huang Y, Niu Y, *et al*. MS-Unet: A multi-scale feature fusion U-Net for 3D seismic fault detection. *Processes*. 2025;13(7):1976.

doi: 10.3390/pr13071976

38. Gao K, Huang L, Zheng Y. Fault detection on seismic structural images using a Nested Residual U-Net. *IEEE Trans Geosci Remote Sens*. 2022;60:1-15.

doi: 10.1109/TGRS.2021.3073840

39. Sun Q, Wang X, Ni H, *et al*. Fault identification of U-Net based on enhanced feature fusion and attention mechanism. *Electronics*. 2023;12(12):2562.

doi: 10.3390/electronics12122562

40. Bekara M, Van Der Baan M. Local singular value decomposition for signal enhancement of seismic data. *Geophysics*. 2007;72(2):V59-V65.

doi: 10.1190/1.2435967

41. Freire SLM, Ulrych TJ. Application of singular value decomposition to vertical seismic profiling. *Geophysics*. 1988;53(6):778-785.

doi: 10.1190/1.1442513

42. Eckart C, Young G. The approximation of one matrix by another of lower rank. *Psychometrika*. 1936;1(3):211-218.

doi: 10.1007/BF02288367

43. Siddique N, Sidike P, Elkin CP, *et al*. U-net and its variants for medical image segmentation: A review of theory and applications. *IEEE Access*. 2021;9:82031-82057.

doi: 10.1109/ACCESS.2021.3086020

44. Bengio Y, Simard P, Frasconi P. Learning long-term dependencies with gradient descent is difficult. *IEEE Trans Neural Netw*. 1994;5(2):157-166.

doi: 10.1109/72.279181

45. Hochreiter S. The vanishing gradient problem during learning recurrent neural nets and problem solutions. *Int J Uncertain Fuzziness Knowl Based Syst*. 1998;6(2):107-116.

doi: 10.1142/S0218488598000094

46. Chen M, Cao H, Jia L. AG-Net3D: embedding attention gate into U-Net for 3D seismic data fault detection. *IEEE Access*. 2025;13:139267-139274.

doi: 10.1109/ACCESS.2025.3596339

47. Perazzi F, Pont-Tuset J, McWilliams B, *et al*. A benchmark dataset and evaluation methodology for video object segmentation. In: *Proceedings of the IEEE Conference on Computer Vision and Pattern Recognition*. IEEE; 2016:724-732.

doi: 10.1109/CVPR.2016.85

ACCSCIENCE PUBLISHING

Journal of Seismic Exploration

ARTICLE

Influence of filling characteristics on rock physical properties of deep carbonate reservoirs based on digital rock modeling

Siqi Ji[1,2], Wei Cheng[1,2,3]*, Hui Shen[1,2,4], Wei-Hua Liu[1,2,5], and Dechao Han[1,2]

[1]SINOPEC Geophysical Research Institute, SINOPEC Corp., Nanjing, Jiangsu, China

[2]SINOPEC Key Laboratory of Rock Physics and Seismic Modeling, SINOPEC Geophysical Research Institute, SINOPEC Corp., Nanjing, Jiangsu, China

[3]Department of Geological Sciences and Engineering, School of Earth Sciences and Engineering, Hohai University, Nanjing, Jiangsu, China

[4]Department of Geophysical Prospecting, School of Geophysics and Information Engineering, China University of Petroleum-Beijing, Beijing, China

[5]Department of Geophysics, School of Geophysics and Information Technology, China University of Geosciences-Beijing, Beijing, China

(This article belongs to the *Special Issue: Seismic Wave Propagation Theories and Reservoir Characterization Technologies for Complex Anisotropic Media*)

***Corresponding author:**
Wei Cheng
(chengw.swty@sinopec.com)

Citation: Ji S, Cheng W, Shen H, Liu W-H, Han D. Influence of filling characteristics on rock physical properties of deep carbonate reservoirs based on digital rock modeling. *J Seismic Explor*. 2026;35(3):026090038. doi: 10.36922/JSE026090038

Received: February 25, 2026

Revised: April 7, 2026

Accepted: April 15, 2026

Published online: May 22, 2026

Copyright: © 2026 Author(s). This is an Open-Access article distributed under the terms of the Creative Commons Attribution License, permitting distribution, and reproduction in any medium, provided the original work is properly cited.

Publisher's Note: AccScience Publishing remains neutral with regard to jurisdictional claims in published maps and institutional affiliations.

Abstract

Deep carbonate reservoirs are rich in oil and gas resources and are important targets for exploration. This study focuses on the Maokou Formation carbonate reservoir in the Sichuan Basin, which exhibits significant heterogeneity, complex karst characteristics, and filling phenomena. Due to the limited number of carbonate samples with representative filling characteristics and the difficulty of characterizing different types of fillings with similar densities using high-precision X-ray computed tomography, the rock physical properties of carbonate rocks with different filling minerals in the Maokou Formation reservoir are unclear. This makes it difficult to establish a system for the reservoir's physical properties and fluid-sensitive parameters. This study integrates thin-section and image analyses to statistically characterize the filling minerals and proposes two approaches for constructing 3D digital rock models that incorporate karst and filling features of the Maokou Formation reservoir. Additionally, accurate P-wave velocity (Vp) and S-wave velocity (Vs) for different types of fillings were obtained using rock-physics experiments, providing precise input parameters for digital rock simulations. Several typical samples were selected to conduct acoustic experiments under varying confining pressures to measure Vp and Vs. This study analyzed the elastic properties of the rock under different mineral-filling proportions, filling orientations, and fluid-filling characteristics in the Maokou Formation carbonate reservoir, providing support for the extraction of the reservoir's physical properties and fluid-sensitive parameters, as well as for quantitative reservoir prediction.

Keywords: Deep carbonate reservoirs; Filling characteristics; Digital rock; Rock-physics experiment; Numerical simulation

1. Introduction

Carbonate strata host abundant oil and gas resources globally, representing a significant target for hydrocarbon exploration and a viable pathway for China's energy transition. In recent years, advancements in exploration technologies have progressively extended carbonate exploration into deep and ultra-deep formations. According to drilling engineering standards, formations with burial depths exceeding 4,500 m are classified as deep, while those deeper than 6,000 m are considered ultra-deep.[1,2] Over the past two decades, several large and medium-sized carbonate oil and gas fields have been discovered in the Sichuan, Tarim, and Ordos Basins.[3] Notable examples include the Upper Permian–Lower Triassic reef and shoal carbonate gas fields in Puguang, Yuanba, and Longgang in the Sichuan Basin,[4] as well as the Sinian–Lower Cambrian reef and shoal carbonate gas field in Anyue.[5] In addition, recent discoveries in the Permian Maokou and Qixia formations of the Sichuan Basin have revealed carbonate reservoirs modified by fracture-fluid interaction.[6]

Since the initial gas detection in the Middle Permian Maokou Formation in the Sichuan Basin in 1957, significant exploration efforts have focused on two main reservoir types: weathering crust karst reservoirs formed at the top of the Maokou Formation due to the Dongwu Movement, and structure-fracture reservoirs closely associated with the evolution of paleo-uplifts. These efforts have led to the discovery of a series of karst-fracture carbonate gas reservoirs.[7,8] Since 2000, discoveries in the northern and southeastern Sichuan regions have revealed a new type of hydrothermal dolomite reservoir within the Maokou Formation.[9-11] Starting in 2015, comprehensive geological investigations have been conducted on Maokou Formation reservoirs in northwestern Sichuan. These studies indicated the development of platform-margin reef–shoal reservoirs, and subsequent drilling has confirmed their presence. Several wells have since been drilled in the Qijiang and Yuanba areas targeting the Maokou Formation. The results indicate that the reef–shoal matrix at the platform margin is generally tight, and the effective reservoir type is primarily dissolution-enhanced shoal facies formed through superimposed karstification. Petrographic observations reveal that weathering crust karstification is well developed in the area, with abundant dissolution fractures and caverns. However, these features are often heavily filled with calcite, algal debris, etc., resulting in poor preservation of effective cavities and unclear rock-physics properties of carbonate rocks.[12]

Rock-physics experiments are the most direct method for obtaining rock properties.[13-15] While traditional petrophysical experiments have long been considered the most direct and effective research approach, acquiring typical samples from wells remains challenging. Due to limitations in both the quantity and quality of rock samples, it is difficult to study variations in individual filling factors. In recent years, the rapid development of digital rock physics has provided a new approach for rock property analysis.[16-22] Digital rock physics involves the use of mathematical methods, computational technology, and high-resolution imaging to construct digital models under specific geological constraints.[23-26] These models are then analyzed through numerical simulations to derive equivalent physical parameters. In practice, digital rock physics has made significant advancements in the calculation of electrical properties,[27-28] elastic properties,[29-30] and permeability properties,[31-32] among others.

The construction of digital rock models is a crucial method for studying the petrophysical filling characteristics of the Maokou Formation reservoir in the Sichuan Basin. An accurate digital rock model serves as the foundation for numerical simulations and petrophysical analysis. Digital rock technology employs mathematical modeling, computer image processing, and high-resolution computed tomography (CT) imaging to digitally represent rock samples and subsequently use numerical simulations to derive rock properties. Among these, high-precision X-ray CT scanning of real drilled rock samples is the most commonly used modeling technique.[33-34] The digital rock 3D image is reconstructed from a large number of X-ray projections taken from various angles. The reconstruction is a grayscale image where the brightness corresponds to the CT value of the material within the sample.[35] Another method for obtaining 3D images of rock microstructure involves stochastic modeling techniques, sometimes referred to as 2D-to-3D reconstruction.[36-37] The core idea of this approach is to estimate the statistical properties of rock samples by analyzing two-dimensional images, such as those obtained through scanning electron microscopy. The advantage of this method is its ability to generate a large number of digitized samples with similar microstructural characteristics. However, the resulting images cannot fully represent real rock samples, limiting their application. In recent years, with the continuous advancement of computer hardware and software and the development of artificial intelligence, neural networks have emerged in the field of digital rock modeling and have shown promising applications.[38-43] However, current generative networks based on unsupervised learning methods still face challenges in considering the actual rock structures, making it difficult to construct digital models that accurately represent the complex internal filling structures of real rocks.

The rock samples from the Maokou Formation reveal complex karst and filling structures at the surface and within the rock. Through density measurements, the densities of different fillings can be determined, and these densities are found to be very similar. However, CT scanning faces challenges in distinguishing rock structures with similar densities. This is primarily due to the imaging principle of CT, which relies on differences in X-ray absorption between materials. When mineral densities are close together, the difference in CT values (which reflect the linear attenuation coefficient) may be smaller than the device's resolution threshold, leading to insufficient grayscale contrast. Additionally, partial-volume effects (polyphase mixing within a single voxel) and noise interference (such as quantum noise and beam-hardening artifacts) further obscure boundary information. Conventional image segmentation algorithms, such as thresholding methods, struggle to accurately separate pore and mineral phases under low-contrast conditions. This issue is especially pronounced when the mineral particle size approaches or falls below the scan resolution (micron level), significantly reducing discrimination ability. Therefore, it is challenging to accurately segment filling assemblages with similar densities using gray values alone. As a result, constructing a numerical rock filling model of the Maokou Formation using CT scanning becomes difficult. The relevant CT scan experimental tests are described in detail in Section 2. In this study, by collecting and analyzing rock surface and thin-section data from actual sampling in the Sichuan Basin, the proportion and structure of different fillings were quantified. These statistical results were then integrated with a numerical modeling approach to propose two methods for constructing 3D digital rock models that consider karst and filling characteristics for the Maokou Formation reservoir. Subsequently, the elastic properties of the rock were calculated using numerical simulations. This method allows digital rock modeling to fully incorporate the filling structure and proportion of the real rock, enabling precise control over the components of the filling model. This, in turn, facilitates a deeper study of how different filling characteristics impact the reservoir.

2. Modeling approaches

2.1. Digital rock modeling based on computed tomography

High-resolution CT scanning is one of the most widely employed and essential techniques for constructing digital rock models. It is extensively used in studies of rock porosity and pore structure due to its ability to precisely capture the internal microstructure of rock samples. In this study, CT scans were conducted on rock samples with complex filling structures from the Sichuan Basin at varying resolutions. The resulting images and analyses are shown in Figure 1.

This study selected typical samples, MK1 and MK2, obtained from wells for CT scanning modeling research. The MK1 sample measured 125 mm in length and 100 mm in diameter, containing a large amount of ellipsoidal calcite

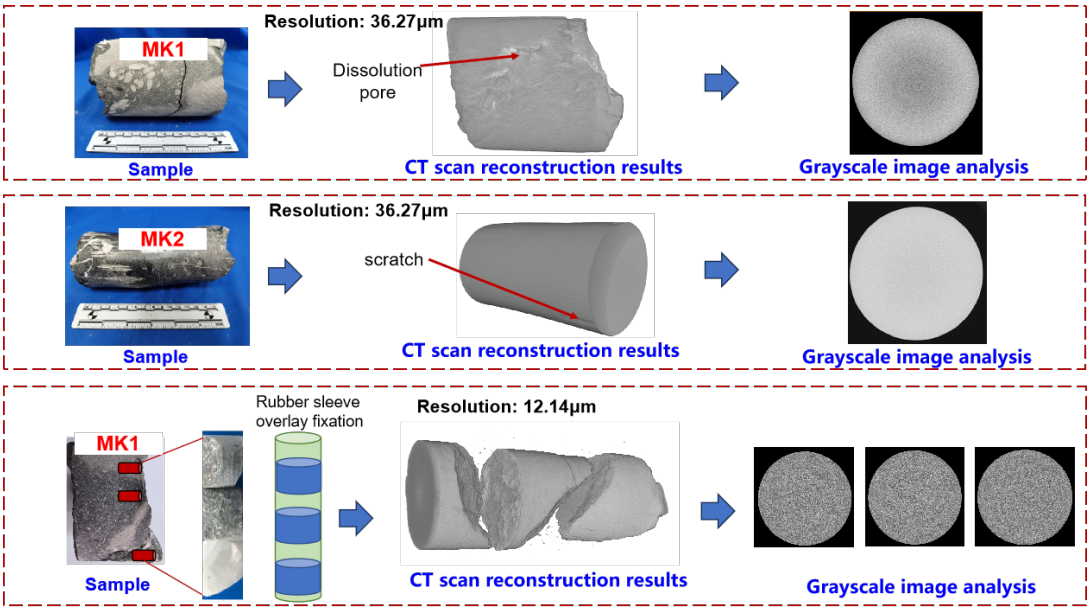

Figure 1. Computed tomography (CT) scanning modeling. Results of CT scanning modeling and grayscale analysis of rocks from the Sichuan Basin at different resolutions.

filling material and elongated algal debris filling strips. The MK2 sample measures 165 mm in length and 65.06 mm in diameter, with a large amount of banded calcite filling material. As illustrated in Figure 1, at a resolution of 36.27 μm, CT scans of full-diameter rock samples MK1 and MK2, which feature complex filling structures, indicate that distinguishing different types of fillings based on grayscale values is challenging. To address this, a smaller section of the MK1 sample was drilled, spliced, and secured using a rubber sleeve, then subjected to a high-resolution CT scan at 12.14 μm. However, the high-resolution results still failed to differentiate filling structures effectively using grayscale segmentation methods. This limitation arises from the principle of CT scanning, which relies on variations in X-ray absorption rates to differentiate materials. The similar densities of different filling materials result in minimal differences in X-ray absorption rates, leading to low grayscale contrast. These findings highlight the inadequacy of conventional CT scanning techniques for modeling rocks with complex filling structures, underscoring the need to explore alternative research methodologies.

2.2. Method 1: Digital rock modeling based on mineral filling information fusion

Constructing an equivalent three-dimensional (3D) digital rock model based on rock surface characteristic analysis is a feasible and effective modeling approach. The overall workflow is divided into four main steps. First, high-resolution images of the rock surface are acquired by focusing a high-precision camera on the center of the rock sample. Second, binary image segmentation is performed. This involves a series of preprocessing techniques (such as denoising, smoothing, and edge enhancement) to improve grayscale contrast, followed by threshold segmentation to distinguish different mineral components. In the third step, structural parameters of the segmented filling features are statistically analyzed. These include measurements of area, Feret diameter (i.e., maximum diameter), aspect ratio, and spatial proportion of each isolated filling region, thereby providing a quantitative foundation for digital rock reconstruction. Finally, based on the extracted surface filling information, an equivalent 3D digital rock model is constructed, and the elastic properties of the rock are evaluated through numerical simulations.

In this study, a typical carbonate rock sample, MK3, from the Maokou Formation in the Sichuan Basin, was selected as the example. The MK3 sample was a plunger sample obtained by drilling, and its experimentally measured porosity was 0.9%. The detailed information of the sample can be found in Table 1. The modeling process for the first three steps is illustrated in Figure 2. By rotating the same sample by 90° and capturing images at each interval, a complete 360° coverage of the surface information of the plunger sample was achieved. After obtaining the rock images, they underwent preprocessing and segmentation. Subsequently, statistical analysis was conducted based on the aspect ratio and Feret diameter of the different segmented features.

The types and structural characteristics of the 15 most volumetrically significant filling components are summarized in Table 2. An equivalent 3D digital rock model can then be constructed based on multiple parameters, including the distribution of aspect ratios and corresponding Feret diameters of the identified features.

Table 1. Basic physical property information of typical samples

Sample	Length (mm)	Diameter (mm)	Density (g/cm^3)	Porosity (%)	Permeability (mD)
MK3	47.33	25.22	2.66	0.90	0.000322
MK4	56.01	25.19	2.62	2.33	0.009010
MK5	48.50	25.22	2.67	0.66	0.000218
MK6	28.97	25.13	2.62	2.01	0.001120
MK7	52.31	25.28	2.67	2.92	0.014800

The digital rock model construction process for the MK3 sample is illustrated in Figure 3. This study used ImageJ (VERSION, National Institutes of Health, United States) for structural information extraction and statistics, and the open-source Python library Puma for equivalent 3D digital rock model reconstruction. Equivalent models with different aspect ratios were built for the filling materials, and these models were then combined to form a statistically representative equivalent 3D digital rock model. In the samples shown in Figure 3, for calcite filling, structures with aspect ratios of 0.875, 0.625, and 0.125 account for 2.47%, 8.9%, and 11.26% of the volume, respectively. For algal debris filling, structures with aspect ratios of 0.125, 0.625, and 0.875 account for 8.55%, 9.85%, and 9.23% of the volume, respectively. The calcite filling is shown in gray and white, while the algal debris filling is shown in blue. The final digital rock model is obtained by combining the six models. The overall calcite filling ratio is 22.64%, and the algal debris filling ratio is 27.63%.

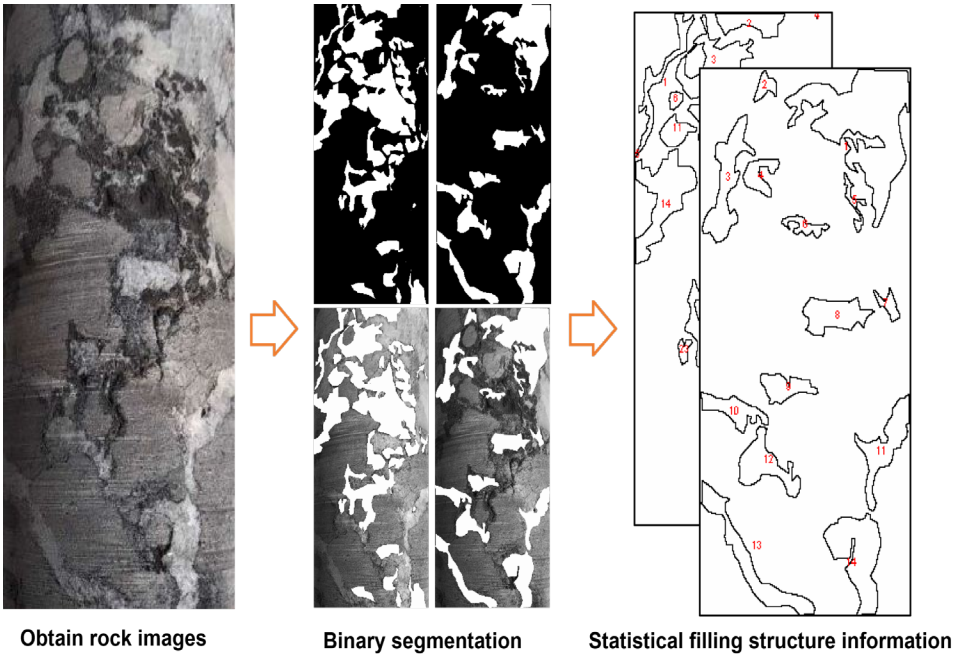

Figure 2. Workflow of rock image processing

Table 2. Main filling and structural information of typical samples

Filling material	Feret diameters (pixel)	Area (pixel)	Proportion (%)	Aspect ratio
Calcite	307.519	35,616	9.893261	0.625
Algal debris	186.724	13,958	4.048552	0.718
Algal debris	206.693	12,198	3.538060	0.395
Algal debris	203.961	12,069	3.500643	0.669
Calcite	242.074	9,082	2.522759	0.294
Algal debris	165.012	8,054	2.336083	0.698
Calcite	137.906	6,493	1.803598	0.793
Algal debris	150.841	6,267	1.817759	0.455
Algal debris	132.201	4,877	1.414586	0.860
Algal debris	153.587	3,392	0.983858	0.257
Calcite	107.815	3,177	0.882494	0.421
Algal debris	108.241	3,159	0.916276	0.881
Algal debris	101.597	2,811	0.815337	0.544
Algal debris	104.547	2,737	0.793874	0.443
Algal debris	85.615	2,707	0.785172	0.783

After conducting representative volume element analysis on multiple sample models, we set the digital rock grid to 200 × 200 × 200, ensuring grid sensitivity while maximizing computational efficiency. To further verify whether the rock-filling information collection was sufficient, additional rock sectioning experiments were conducted to obtain more detailed internal structural information. This also enabled the exploration of methods for jointly constructing digital rocks using information from multiple thin sections.

2.3. Method 2: Digital rock modeling based on rock-section reconstruction

This section introduces an alternative method for studying rock-filling materials that involves sequentially slicing rock samples to obtain layer-by-layer filling information, followed by the construction of a digital rock model. This approach has both advantages and limitations. The primary advantage is that it allows for more accurate calculation of the filling structure and proportion within the rock's internal space, especially when CT scanning methods are unable to achieve this level of precision. As a result, a more accurate digital model of the filling can be constructed. However, the main limitation is that this method is irreversible, and the sequential cutting process can damage the rock, leading to the loss of potentially valuable and representative samples.

The rock sample MK6 selected for this study is shown

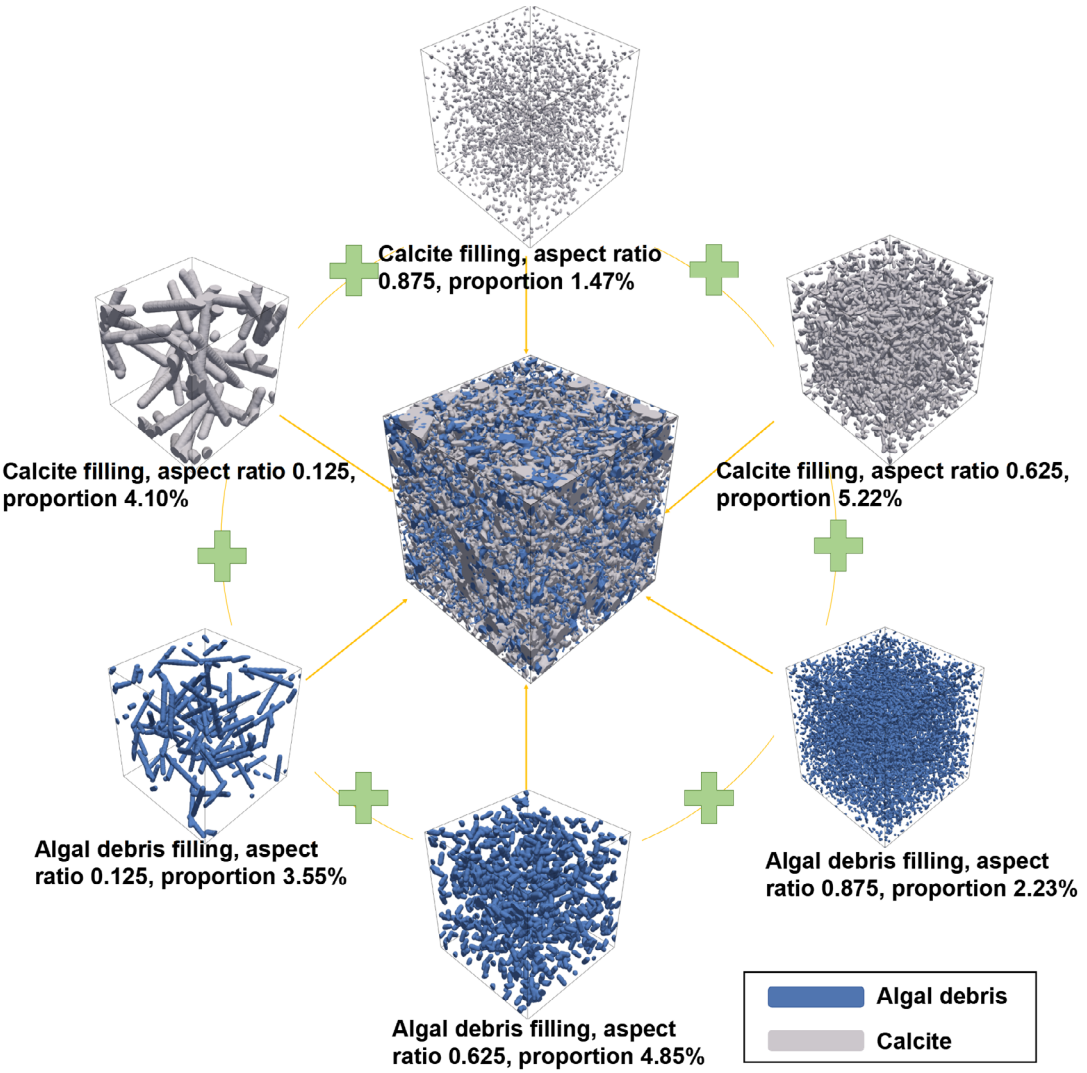

Figure 3. Construction of the digital rock model

in Figure 4, with a density of 2.62 g/cm^3, porosity of 2.01%, and permeability of 0.001120 mD. The white regions represent calcite band fillings, the darker areas correspond to algal debris, and the remaining portions represent the rock matrix.

The MK6 sample was cut from top to bottom, with the filling structure at the upper end being more complex. In regions with abundant mineral infill structures, the slice thickness was controlled to 2–3 mm, whereas in regions with insufficient infill structures, the slices were made thicker or left unprocessed. The subsequent construction of the digital rock model was also carried out strictly in accordance with this cutting ratio. To further ensure the representativeness of the slices, efforts were made to preserve the complete mineral infill structure within a single slice whenever possible, thereby enabling the digital rock model to more accurately reflect the actual rock fabric. This adaptive cutting approach is designed to capture as much detailed and complete filling structure information as possible, providing a solid foundation for the subsequent construction of digital rock models.

The MK6 model construction process is illustrated in Figure 5. After cutting the entire rock into 8 sections, 17 slices containing internal filling structures were obtained. First, filtering and denoising were applied to the slices at different positions to suppress image noise. Next, accurate three-phase image segmentation was performed, dividing the images into calcite filling (white), matrix (gray), and algal debris filling (black) based on grayscale values. Finally, a 3D digital rock model with spatially correlated filling structures was constructed by progressively interpolating the contours of the 17 slices. Based on component

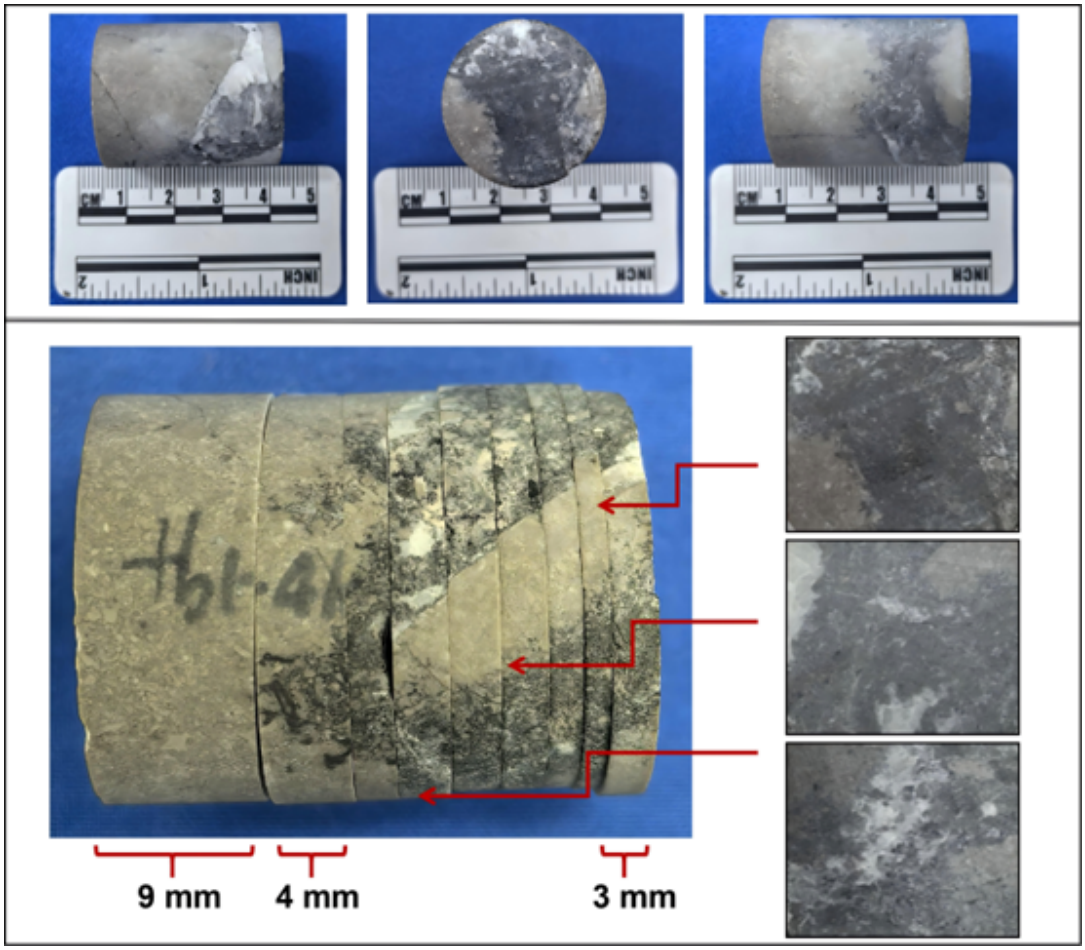

Figure 4. Investigation of typical fill structure in the rock (MK6) section

statistics, the resulting model consisted of 66.82% matrix, 5.81% calcite filling, and 27.37% algal debris filling. The numerical simulation results of the two digital rock modeling methods and the comparative verification with rock-physics experiments are detailed in the next section.

3. Numerical simulation

3.1. Method for obtaining numerical simulation parameters

The first step in the workflow of digital rock physics is to construct a digital rock model, and the second step is to perform numerical simulation on it to obtain the corresponding rock properties. This study employed a multi-component static elastic parameter simulation method based on the finite element method for numerical simulation work. After calculating the stress and strain values of rocks through finite element analysis, the longitudinal and transverse wave velocities or other elastic moduli were calculated based on the generalized Hooke's law for isotropic media. Static finite element numerical simulation requires the elastic moduli (bulk modulus K, shear modulus μ, etc.) of different mineral components in the rock as simulation parameters; therefore, accurate parameter selection is crucial for ensuring the reliability of numerical simulation results.

The full-diameter rock obtained from the well in the Sichuan Basin was cut to obtain internal sections, and thin sections were prepared for analysis. The results are shown in Figure 6. The black region in the upper part of the rock generally exhibits a calcareous structure with algal cementation, primarily composed of mud-microcrystalline calcite and rich in algae. Small algal pellets and algal aggregates are formed between detrital fragments, which is described in this paper as algal detritus filling. The middle section of the rock is almost entirely composed of calcite based on mineral composition and has undergone weak recrystallization, which is referred to in this paper as the matrix. The white strip at the lower end of the rock

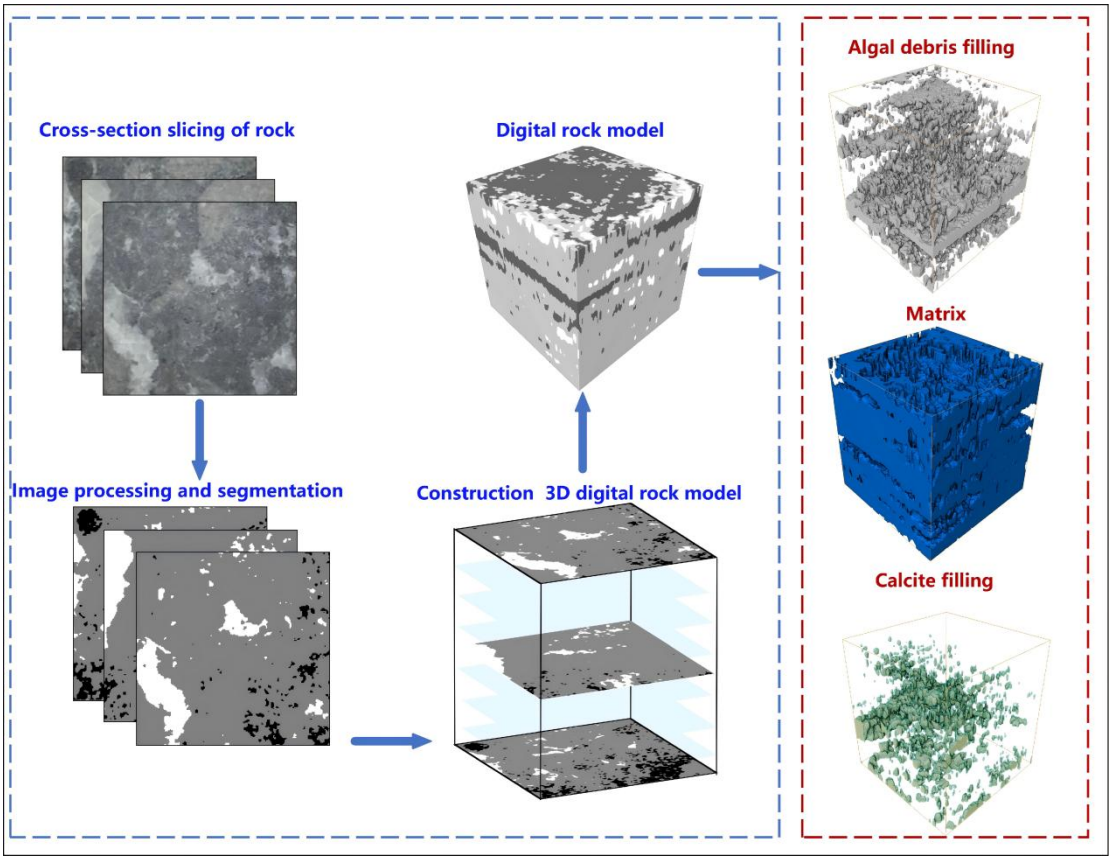

Figure 5. Model construction process for the MK6 sample

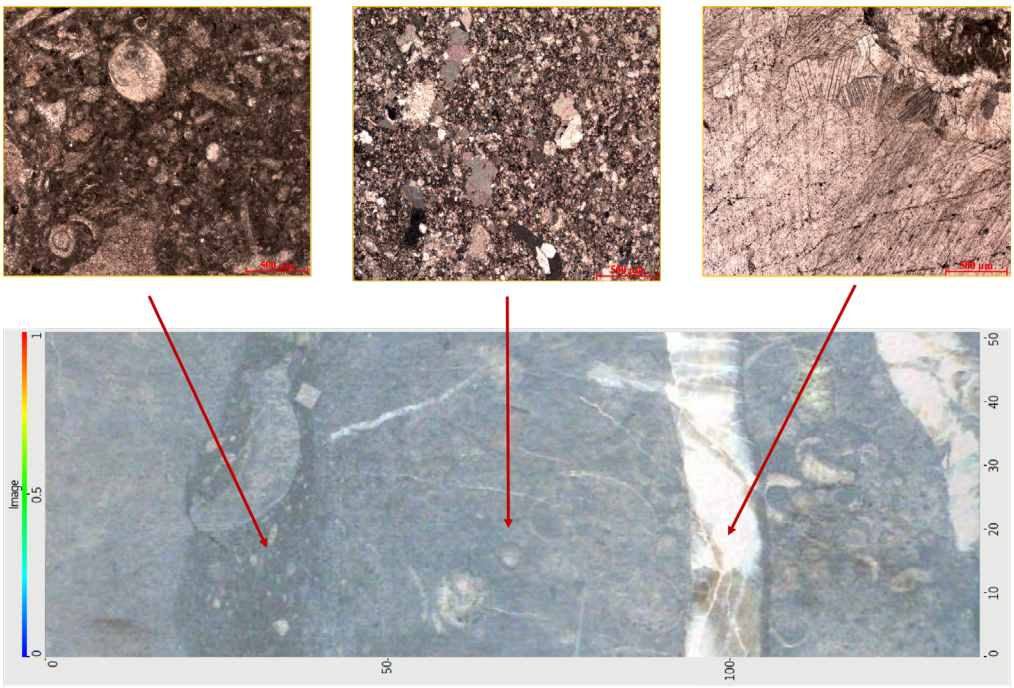

Figure 6. Rock thin sections. Analysis of thin sections of different components in the rock plane.

primarily consists of mud-microcrystalline calcite, with some algal sandstone detritus, and bright calcite fills the fractures in the rock, which is described as calcite filling in this paper.

The filling minerals and characteristics of the Maokou Formation are complex, and accurate elastic moduli of minerals can ensure the accuracy of numerical simulation calculations. In this study, a high-resolution rock-physics multi-parameter field rapid-scanning experimental system was applied to directly measure the elastic moduli of various components under normal pressure by scanning the rock plane. This provides accurate simulation parameters for digital rock numerical simulation. The test results are shown in Figure 7.

Figure 7A shows a full-diameter rock sample from the Sichuan Basin, comprising continuous calcite filling bands and a large number of algal debris filling areas. The calcite filling is off-white, the algal debris filling is off-black, and the matrix is gray. The test was conducted from top to bottom according to the red vertical line, and the results are displayed in Figure 7B and 7C. Accurate acoustic velocities of calcite filling, algal debris filling, and matrix were then obtained and subsequently converted into elastic moduli to derive simulation parameters based on experimental test results (Table 3).

The elastic moduli measured in this experiment were used as digital rock simulation parameters. It should be noted that these elastic parameters corresponded to the dry frames of matrix, calcite mineral, and algal debris fillings.

Table 3. Bulk modulus and shear modulus of the main filling materials in typical samples

Filling material type	Matrix	Calcite	Algal debris
Bulk modulus (GPa)	53.4	39.4	48
Shear modulus (GPa)	28.7	19	22.5

3.2. Method 1 reliability verification

In this paper, the MK3 sample was selected for analysis,

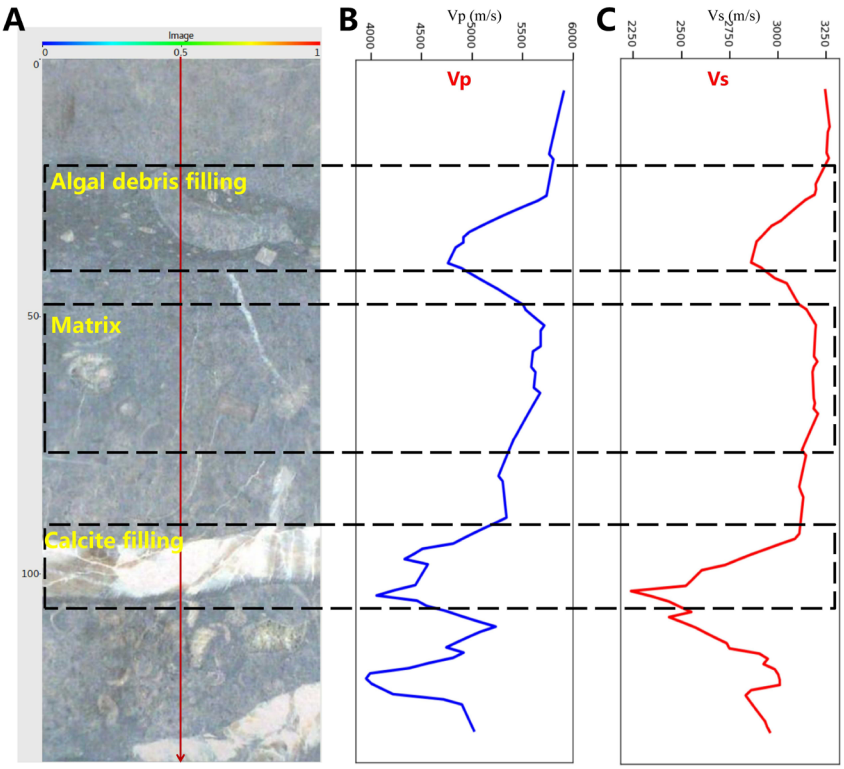

Figure 7. Fill material velocity analysis. Velocity scanning of the entire rock and velocity analysis of the fill material and matrix. (A) Full-diameter rock sample from the Sichuan Basin. (B) P-wave velocity (Vp). (C) S-wave velocity (Vs).

modeling, and numerical simulation, and the simulation results were compared with the experimental results under different pressures. The pressure-dependent ultrasonic velocities were calculated using:

$$V = \frac{L}{t} \tag{1}$$

where L is the effective propagation distance through the rock specimen, and t is the corresponding wave travel time. Since the specimen geometry remained unchanged during each measurement stage and the dimensional variation induced by confining pressure was much smaller than the travel-time variation, the uncertainty in wave velocity was considered to be dominated primarily by the travel-time determination. Among the various potential error sources, first-arrival identification was found to be the dominant contributor, especially at low confining pressures where microcrack closure was incomplete, and the received waveform was relatively less stable.

As shown in Figure 8, the uncertainty ranges were significantly smaller than the overall increase in wave velocity induced by confining pressure. This indicates that the observed growth of both Vp and Vs with increasing confining pressure is well above the measurement uncertainty and therefore reflects a real physical response of the rock. In particular, the increase in wave velocity at lower confining pressures was more pronounced, which is consistent with the progressive closure of pre-existing pores and microcracks. At higher confining pressures, the rate of increase became smaller, while the uncertainty remained relatively limited, suggesting that the measured trends are stable and statistically meaningful over the full pressure range. Overall, the uncertainty analysis confirms that the experimental ultrasonic velocity data are sufficiently reliable for interpreting the pressure-dependent acoustic response of the tested rock specimens.

The simulation results are shown in Figure 9A and 9B. The blue dots represent the P- and S-wave velocities under 15–105 MPa pressure, and the red dots represent the P- and S-wave velocities obtained by digital rock simulation. The numerical simulation represents the rock elastic parameters at normal temperature and pressure; therefore, the experimental velocities were lower than those measured at 15 MPa (it is expected that the experimental velocities measured under confining pressure are higher than those under atmospheric conditions). To validate the numerical results, the experimental data were extrapolated to 0 MPa using linear regression analysis. At 0 MPa, the relative errors for Vp and Vs were 0.34% and 0.47%, respectively.

$$Relative\ error\,(\%) = \frac{|Experimental\ value - Simulated\ value|}{Experimental\ value} \tag{2}$$

These results demonstrate excellent agreement between the numerical simulation and experimental measurements, thereby validating the accuracy of the digital rock-physics approach.

Furthermore, MK4 and MK5 samples were selected for the same experiments and simulation tests. The results are shown in Figure 9C–F. The simulation results demonstrate that the digital rock model construction results matched well with the experimental results. When the experimental data were extrapolated to 0 MPa, the relative errors between simulated and experimental values were 0.31% and 0.85% for Vp and Vs of MK4, respectively, and 0.38% and 0.47% for those of MK5, respectively. These quantitative comparisons demonstrate that the digital rock model construction methodology exhibits consistent accuracy and reliability across different rock samples. The detailed information of the three samples used for verification is shown in Table 1.

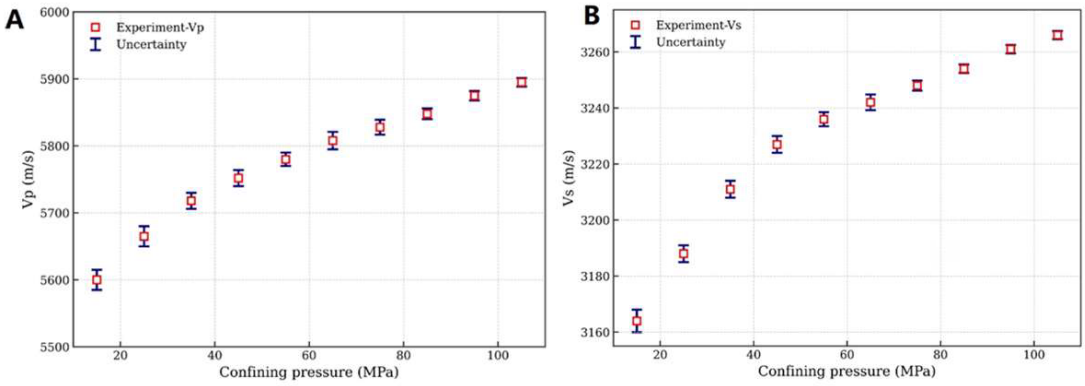

Figure 8. Uncertainty analysis of acoustic testing under variable confining pressure for the MK3 sample. (A) P-wave velocity (Vp). (B) S-wave velocity (Vs).

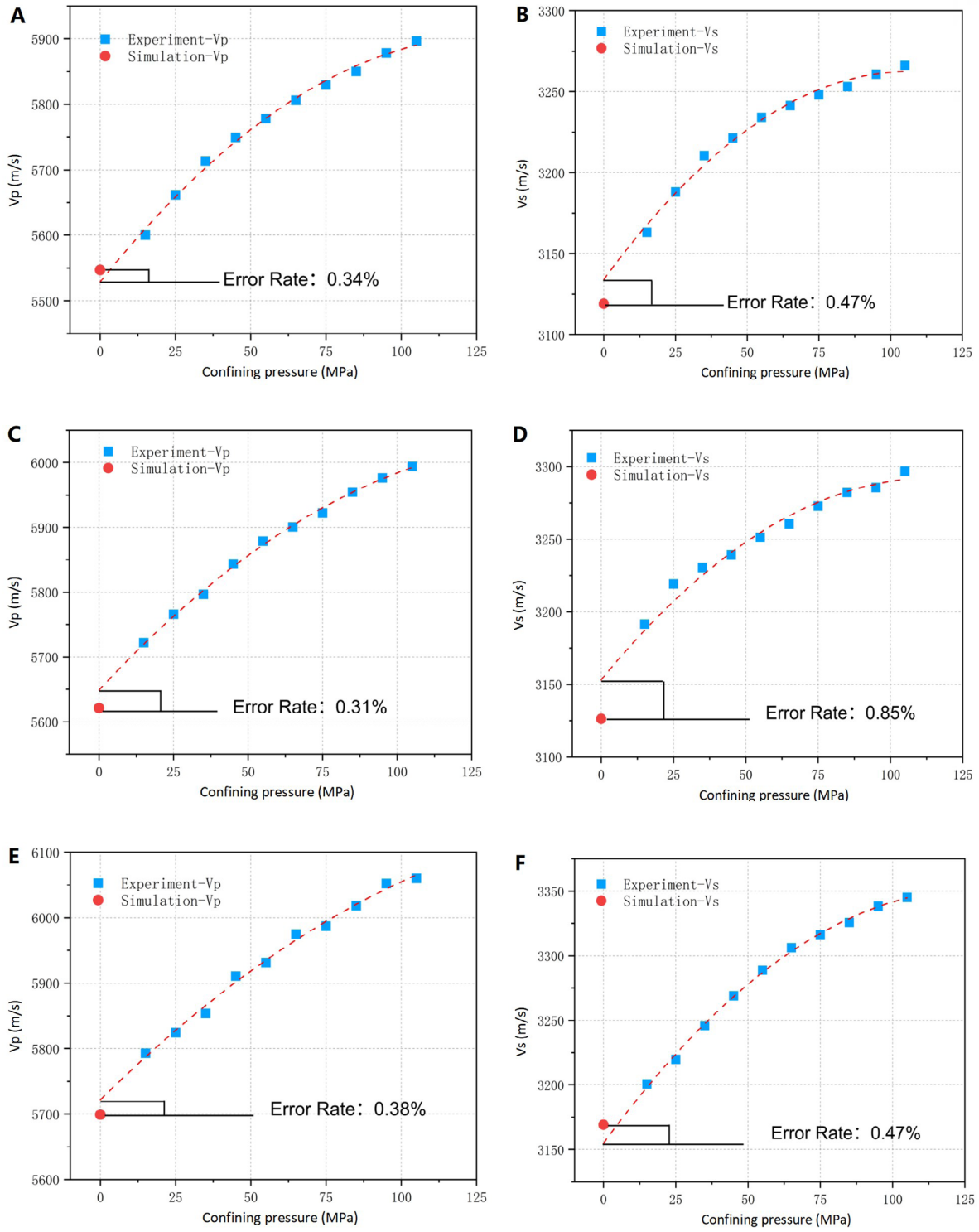

Figure 9. Experimental and simulation results of typical samples. (A) P-wave velocity (Vp) of MK3. (B) S-wave velocity (Vs) of MK3. (C) Vp of MK4. (D) Vs of MK4. (E) Vp of MK5. (F) Vs of MK5.

3.3. Method 2 reliability verification

In this study, sample MK6 was selected for experimental measurements and numerical simulations to validate the reliability of Method 2. The experimental and numerical simulation results are shown in Figure 10. The blue circles represent the experimental test results under a confining pressure of 15–105 MPa, the green squares represent the simulation results of the 3D model obtained using the model construction method described in Method 1, the red stars represent the results from the sequential slicing method introduced in this section, and the red dashed line represents the fitting line for the experimental data. Digital rock models constructed using Method 1 exhibited relative errors of 1.5% (Vp) and 0.81% (Vs) when validated against experimental measurements at 0 MPa confining pressure. Models developed using Method 2 demonstrated significantly higher accuracy, with corresponding errors reduced to 1.1% and 0.45%. Therefore, the model constructed using the method presented in this section better aligns with the actual rock filling structure and filling ratio, making the resulting 3D digital rock model more representative of the real situation. Consequently, the reliability of the numerical simulation results is slightly enhanced. The experimental and simulation results of different methods are shown in Table 4.

In summary, the method of cutting rock samples to examine their internal filling materials and structures is feasible. Compared to the surface-based modeling approach described in Method 1, Method 2 offers higher accuracy and provides a more precise depiction of the filling ratio and structural details within the rock. Additionally, the numerical simulation results of this model are closer to the experimental predictions. However, this method has irreversible destructive effects on the rocks and requires significant labor costs, making it challenging for large-scale studies and for quickly obtaining relevant insights through rock physics to guide oil and gas exploration.

In summary, while both methods achieved similar accuracy, Method 1 offers the significant advantage of being non-destructive, thus representing a more valuable approach for rock-filling material characterization.

4. Application

4.1. Analysis of rock physical characteristics with different mineral filling ratios

Based on the above modeling and simulation methods, a digital rock model with variable calcite content was constructed to explore the influence of different filling ratios. The calcite mineral filling content varied from 2% to 42% (Figure 11), while the algal debris filling content was kept constant at 4%. An increase in calcite content was accommodated by a corresponding decrease in matrix content. The elastic characteristics at different calcite mineral filling contents were explored using static finite element simulation, and the results are shown in Figure 12.

The simulation results show that an increase in calcite content decreased bulk modulus, shear modulus, Vp, Vs, and P-wave impedance, while increasing the Vp/Vs ratio. This trend may be attributed to the input calcite filling material, which includes partially filled pores, resulting in experimentally measured elastic moduli being lower than the corresponding matrix moduli.

4.2. Analysis of rock physical characteristics in different mineral filling directions

The karst characteristics of the Maokou Formation reservoir in the Qijiang area are complex, mainly including surface karst zones (mineral randomly fillings), vertical

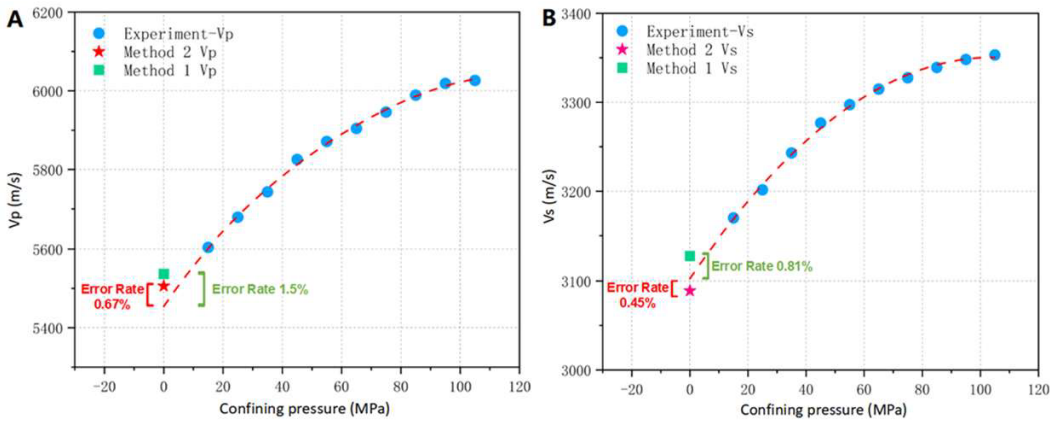

Figure 10. Comparison of experimental and simulation results for the MK6 sample. (A) P-wave velocity (Vp). (B) S-wave velocity (Vs).

Table 4. Comparison of different modeling methods and experiments

Digital rock modeling conditions	Method 1	Method 2	Rock-physics Experiment
Whether to damage the rock sample	No	Yes	No
Proportion of calcite filling material (%)	9.27	10.19	-
Proportion of algal debris filling material (%)	24.73	29.68	-
Vp obtained from numerical simulation (m/s)	5,537	5,501	-
Vs obtained from numerical simulation (m/s)	3,128	3,089	-
Vp under normal pressure (fitted through experiments) (m/s)	-	-	5,454
Vs under normal pressure (fitted through experiments) (m/s)	-	-	3,102

Abbreviations: Vp: P-wave velocity; Vs: S-wave velocity.

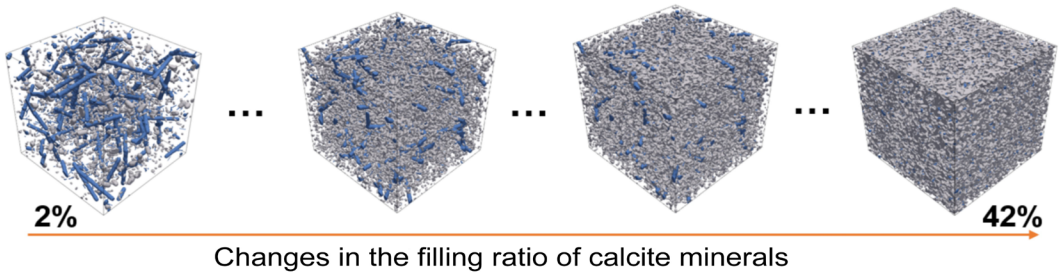

Figure 11. Schematic diagram illustrating variations in calcite filling proportion

seepage zones (mineral vertically oriented fillings), and horizontal subsurface flow zones (mineral horizontally oriented fillings). By maintaining constant filling mineral types, contents, and geometric shapes while exclusively varying the orientation of mineral fillings as a monotonic variable, we investigated the influence of filling orientation on the elastic properties of carbonate rocks. This approach establishes quantitative relationships between karst features and elastic behavior in the reservoir. All calcite filling models were updated to represent vertical and horizontal filling configurations, and numerical simulations were carried out. The results were compared with the corresponding Voigt model (theoretical upper bound) and Reuss model (theoretical lower bound).

To predict the equivalent elastic modulus of mineral particle mixtures using theoretical methods, it is necessary to know: (i) the volume content, (ii) the elastic modulus, and (iii) the geometric distribution of each component. The Voigt model, which represents the theoretical upper bound, assumes uniform strain across all components. The equivalent elastic modulus for N components can be expressed as:

$$M_v = \sum_{i=1}^{N} f_i M_i \tag{3}$$

where f_i is the volume fraction of the i-th component, and M_i is the elastic modulus of the i-th component.

The Reuss model provides the theoretical lower bound for the equivalent elastic modulus:

$$\frac{1}{M_R} = \sum_{i=1}^{N} \frac{f_i}{M_R} \tag{4}$$

For any rock, given the volume content of each component, the equivalent modulus falls between the Voigt upper bound and the Reuss lower bound. Based on the above modeling methods, horizontal and vertical filling models with the same volume content as the samples were constructed, and numerical simulation methods were applied for calculation. The calculation results are shown in Figure 13.

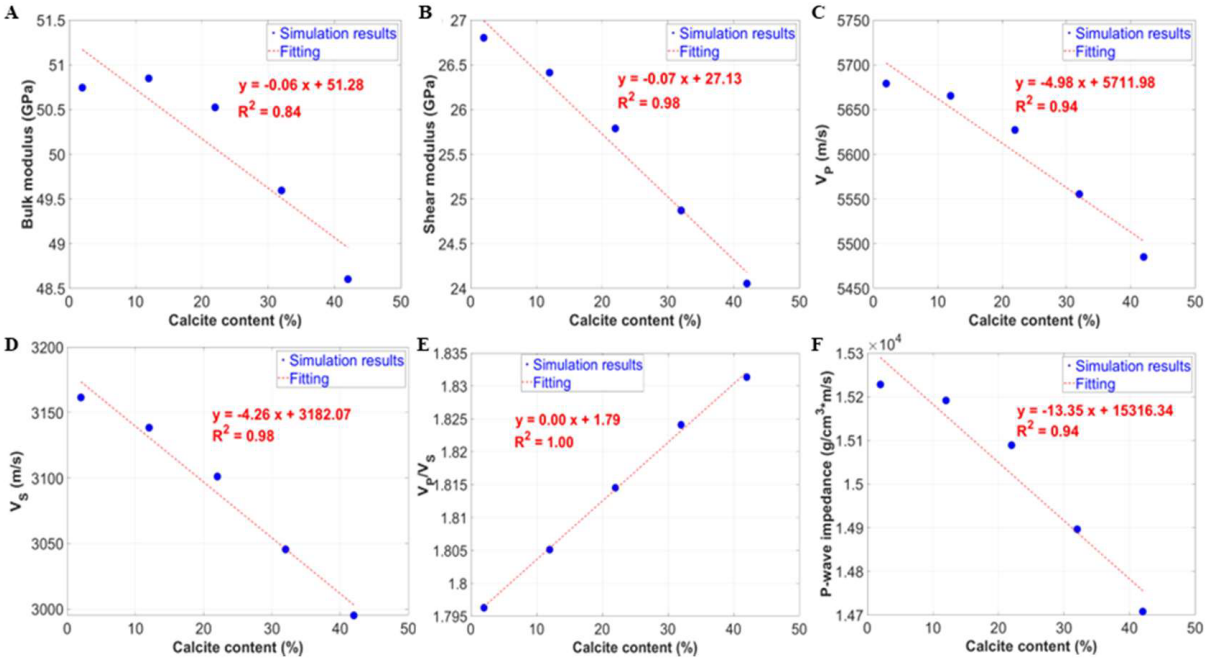

Figure 12. Studies on the content of dolomite and its elastic properties. (A) Bulk modulus. (B) Shear modulus. (C) P-wave velocity (Vp). (D) S-wave velocity (Vs). (E) Vp/Vs. (F) P-wave impedance.

The digital rock simulations for vertically oriented mineral fillings exhibited Vp and Vs that closely matched the Voigt model predictions, whereas the horizontally filled counterparts aligned with the Reuss model results. Notably, simulations revealed moderately higher wave velocities for mineral vertically oriented fillings compared to horizontal configurations. At 40% calcite filling content, the normalized differences were 1.54% for Vp and 0.91% for Vs.

$$Normalized\ difference(\%) = \frac{|V_vertical - V_horizontal|}{V_vertical} \quad (5)$$

Consequently, mineral-filling orientation exerted a measurable though limited influence (<2%) on both Vp and Vs in carbonate rocks. In addition, both orientations displayed systematically decreasing Vp and Vs with increasing calcite content, revealing a strong linear correlation. The study of different mineral filling orientations can provide robust support for characterizing and understanding karst reservoir features.

4.3. Analysis of rock physical characteristics filled with different fluids

We have shown that while the orientation of calcite fillings influenced Vp and Vs in carbonate rocks, the magnitude of the influences remained below 2%. Therefore, we used the Hill average to represent the overall elastic modulus of the model framework. The Hill average is expressed as follows:

$$M_{VRH} = \frac{M_V + M_R}{2} \quad (6)$$

where M_V is the Voigt upper bound, M_R is the Reuss lower bound, and M_{VRH} is the Hill average modulus. Where M can represent any elastic modulus, in this paper, M refers to both the bulk modulus and shear modulus.

To investigate the variation of rock elastic modulus with fluid saturation in the Maokou Formation of the Sichuan Basin, a representative sample (MK7) from this area (calcite filling 13.4%, algal debris filling 12.2%) was selected for digital rock modeling. Following the derivation of the dry-frame elastic moduli via the Hill model, we simulated Vp and Vs under brine saturation at variable water saturations (0, 0.25, 0.5, 0.75, 1) for both vertically and horizontally oriented pore systems.

Simulation results in Figure 14 demonstrate that Vp for vertically oriented mineral fillings exceeded those of horizontal configurations. This directional dependence aligns with the Voigt (upper bound) and Reuss (lower bound) theoretical models. Vp exhibited progressive enhancement with increasing water saturation, displaying a near-linear relationship. The variation in the simulation results for the vertical distribution of pores was slightly

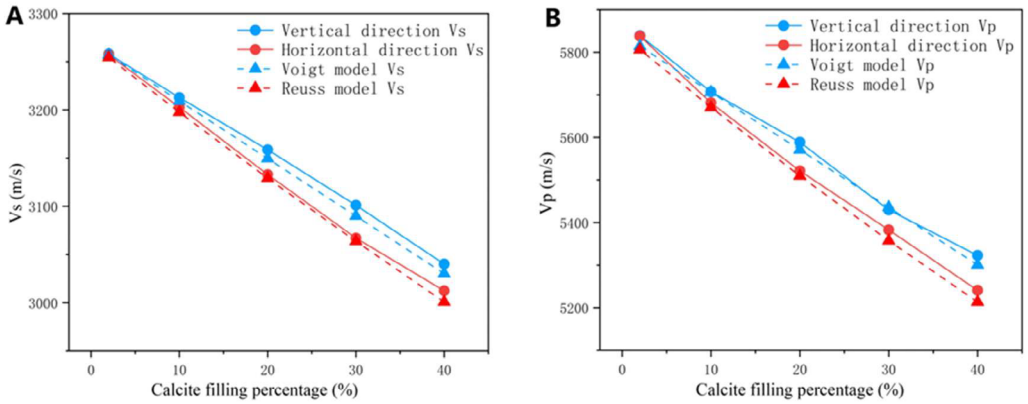

Figure 13. Comparison of the theoretical model and simulation results. (A) P-wave velocity (Vp). (B) S-wave velocity (Vs).

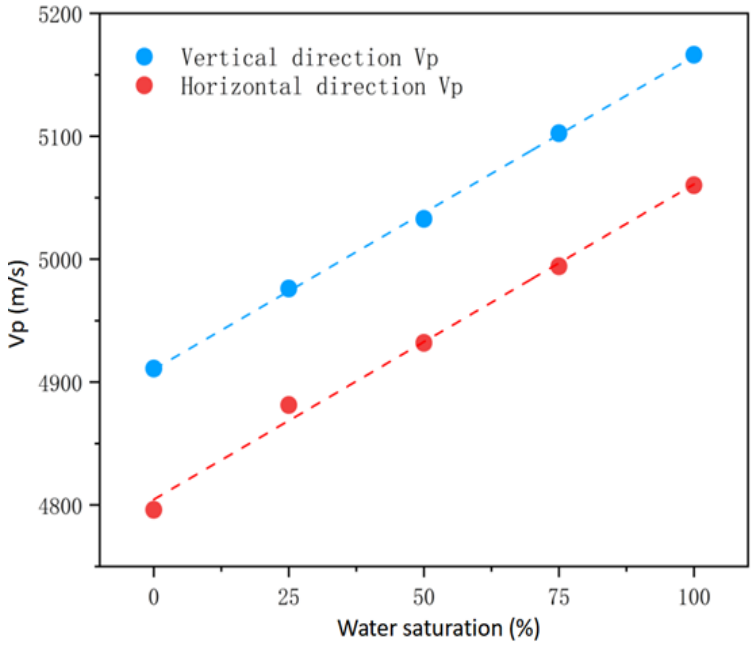

Figure 14. Simulation of P-wave velocities at different fluid saturations

lower than that for the horizontal distribution. It is important to note that water saturation has a negligible effect on Vs; hence, those results are not displayed. This study demonstrates that fluid types within pores exert a substantially greater influence on elastic properties than pore orientation in the Maokou Formation carbonate rocks.

5. Conclusion

This study focuses on the Maokou Formation carbonate reservoir in the Sichuan Basin, characterized by significant heterogeneity, complex karst features, and pronounced filling. The physical properties of carbonate rocks with different filling minerals, mineral proportions, and filling types in the Maokou Formation reservoir are unclear. By integrating thin-section petrography with advanced imaging analysis, we quantitatively determined the mineral compositions, volumetric proportions, and geometric configurations of pore-filling materials in rock samples. Two distinct methodologies for constructing 3D digital rock models that incorporate karst and filling characteristics were developed: Method 1 (mineral filling information fusion) and Method 2 (rock section reconstruction). The reliability of the two methods was verified using experimental data, and Method 2 offers

higher accuracy and a more precise depiction of the filling ratio and structural details within the rock. However, this method has irreversible, destructive effects on the rocks. Based on the proposed digital rock technology, this study analyzed the elastic properties of the rock under different mineral filling proportions, filling orientations, and different fluid filling characteristics. The simulation results show that an increase in calcite content decreased the bulk modulus, shear modulus, Vp, Vs, and P-wave impedance, while increasing the Vp/Vs ratio. Moreover, the digital rock simulations for vertically oriented mineral fillings exhibited Vp and Vs that closely match Voigt model predictions, whereas those for horizontally filled counterparts align with Reuss model results. In addition, this study demonstrates that fluid types within pores exert a substantially greater influence on elastic properties than pore orientation in the Maokou Formation carbonate rocks.

Nevertheless, several limitations remain, including the limited number of representative sections and the overly simplified representation of pore-fracture-filling geometries in the digital models. Future work should incorporate a broader sample base and more realistic pore-system characterization, and establish links between digitally derived elastic properties and well-log and seismic responses to support the fine-scale characterization of deep carbonate reservoirs.

Acknowledgments

None.

Funding

This research was financially supported by the Project from SINOPEC Science and Technology Department (Grant No. P24170) and the Joint Funds Key Support Project of the National Natural Science Foundation of China (Grant No. U24B2020) and Natural Science Foundation of Jiangsu Province (BK20220995).

Conflict of interest

All authors are employees of SINOPEC Corp.; however, they were not involved in any activities that could constitute a conflict of interest in relation to this study.

Author contributions

Conceptualization: Wei Cheng, Wei-Hua Liu
Formal analysis: Dechao Han
Investigation: Hui Shen
Methodology: Siqi Ji
Writing–original draft: Siqi Ji
Writing–review & editing: Siqi Ji

Ethics approval and consent to participate

Not applicable.

Consent for publication

Not applicable.

Availability of data

Data are available from the corresponding author upon reasonable request.

References

1. Ma Y, Cai X, Yun L, *et al*. Practice and theoretical and technical progress in exploration and development of Shunbei ultra-deep carbonate oil and gas field, Tarim Basin, NW China. *Pet Explor Dev*. 2022;49(1):1-20.

   doi: 10.1016/S1876-3804(22)60001-6

2. He ZL, Ma YS, Zhu DY, *et al*. Theoretical and technological progress and research direction of deep and ultra-deep carbonate reservoirs. *Oil Gas Geol*. 2021;42(3):533-546. [In Chinese].

   doi: 10.11743/ogg20210301

3. Ma Y, Cai X, Zhao P, Luo Y, Zhang X. Distribution and further exploration of the large-medium sized gas fields in Sichuan Basin. *Acta Pet Sin*. 2010;31(3):347-354. [In Chinese].

   doi: 10.7623/syxb201003001

4. Ma Y, Li M, Cai X, *et al*. Mechanisms and exploitation of deep marine petroleum accumulations in China: advances, technological bottlenecks and basic scientific problems. *Oil Gas Geol*. 2020;41(4):655-672,683. [In Chinese].

   doi: 10.11743/ogg20200401

5. Ma Y, Guo X, Guo T, *et al*. The Puguang gas field: new giant discovery in the mature Sichuan Basin, southwest China. *AAPG Bull*. 2007;91(5):627-643.

   doi: 10.1306/11030606062

6. Zhao W, Hu S, Wang Z, Zhang S, Wang T. Petroleum geological conditions and exploration importance of Proterozoic to Cambrian in China. *Pet Explor Dev*. 2018;45(1):1-14.

   doi: 10.1016/S1876-3804(18)30001-6

7. Hu A, Pan L, Hao Y, Shen A, Gu M. Origin, Characteristics and Distribution of Dolostone Reservoir in Qixia Formation and Maokou Formation, Sichuan Basin, China. *Mar Orig Pet Geol*. 2018;23(2):39-52. [In Chinese].

8. Song J, Wang J, Liu S, *et al*. Types, composition and diagenetic evolution of authigenic clay minerals in argillaceous limestone of sepiolite-bearing strata: a case study of Mao-1 Member of Middle Permian Maokou Formation, eastern Sichuan Basin, SW China. *Pet Explor Dev*. 2024;51(2):351-363.

doi: 10.1016/S1876-3804(24)60028-5

9. Zhang H, Yang Z, Li Z, *et al*. Discovery of volcanic matter in the Upper Maokou Formation of the Wumengshan area: Evidence of early activity of the Emeishan mantle plume. *Geol Bull China*. 2024;43(7):1207-1220. [In Chinese].

   doi: 10.12097/gbc.2023.07.002

10. Xiao Q, Yuan H, Chen S, *et al*. Analysis of dolomite genesis in the Maokou Formation, northern slope area of central Sichuan, China: petrologic, in situ geochemical, and chronological evidence. *Nat Gas Geosci*. 2024;35(7):1160-1186. [In Chinese].

    doi: 10.11764/j.issn.1672-1926.2023.12.004

11. He J, Lian Z, Luo W, *et al*. Characteristics and main controlling factors of intra-platform shoal thin-layer dolomite reservoirs: a case study of Middle Permian Qixia Formation in Gaoshiti–Moxi area of Sichuan Basin, SW China. *Pet Explor Dev*. 2024;51(1):69-80.

    doi: 10.1016/S1876-3804(24)60006-6

12. Li S, Li Z, Zhang L, Li Y, Meng X, Wang H. Hydrocarbon accumulation conditions and exploration targets of the Triassic subsalt ultra-deep sequences in the western Sichuan Depression, Sichuan Basin. *Oil Gas Geol*. 2023;44(6):1555-1567.

    doi: 10.11743/ogg20230617

13. Ahmed N, Khalid P, Anwar A. Rock physics modeling to assess the impact of spatial distribution pattern of pore fluid and clay contents on acoustic signatures of partially-saturated reservoirs. *Acta Geod Geophys*. 2016;51:1-13.

    doi: 10.1007/s40328-015-0101-0

14. Correa JL, Grana D, Crepaldi JLS. Rock-physics-guided petrophysical seismic AVO inversion using the Levenberg-Marquardt algorithm. *Geophysics*. 2025;90(4):M85-M97.

    doi: 10.1190/geo2024-0631.1

15. Ahmed N, Weibull W, Grana D, Bhakta T. Constrained nonlinear amplitude-variation-with-offset inversion for reservoir dynamic changes estimation from time-lapse seismic data. *Geophysics*. 2024;89(1):1-16.

    doi: 10.1190/geo2022-0750.1

16. Xu P, Tang S, Sun C, Liang J, Li T, Shi Q. Development characteristics and paleogeomorphology restoration of karsts in Middle Permian Maokou Formation, Gaoshiti-Moxi area, central Sichuan Basin. *Nat Gas Explor Dev*. 2023;46(4):35-46. [In Chinese].

    doi: 10.12055/gaskk.issn.1673-3177.2023.04.004

17. Derzhi N, Sisk C, Kalam Z. Application of Digital Rock Physics for Geophysical Rock Properties. In: *Proceedings of the 12th International Congress of the Brazilian Geophysical Society & EXPOGEF*; August 15-18, 2011; Rio de Janeiro, Brazil.

    doi: 10.1190/sbgf2011-304

18. Andrä H, Combaret N, Dvorkin J, *et al*. Digital rock physics benchmarks—Part I: Imaging and segmentation. *Comput Geosci*. 2013;50:25-32.

    doi: 10.1016/j.cageo.2012.06.007

19. Andrä H, Combaret N, Dvorkin J, *et al*. Digital rock physics benchmarks—Part II: Computing effective properties. *Comput Geosci*. 2013;50(1):33-43.

    doi: 10.1016/j.cageo.2012.09.008

20. Nan Z, Tan M, Li J, *et al*. Numerical simulation, response analysis, and physical experiment of induction logging in an inclined fractured formation. *IEEE Trans Geosci Remote Sens*. 2022;60:1-11.

    doi: 10.1109/TGRS.2021.3056133

21. Tan M, Wang K, Zou Y, *et al*. Nuclear magnetic resonance simulations of nano-scale cores and microscopic mechanisms of oil shale. *Fuel*. 2019;256:115843.

    doi: 10.1016/j.fuel.2019.115843

22. Wang Z, Ding X, Liu J, Yun L. Numerical simulations on compression behaviors of the laminated shale based on the digital image technology and the discrete element method. *Sci Rep*. 2024;14:15890.

    doi: 10.1038/s41598-024-66333-1

23. Wang Z, Cao G, Liu J, Yun L. Prediction of the anisotropic effective moduli of shales based on the Mori-Tanaka model and the digital core technique. *Pure Appl Geophys*. 2023;180:2981-2998.

    doi: 10.1007/s00024-023-03298-8

24. Liu N, Fu L. Elastic characteristics of digital cores from Longmaxi shale using lattice spring models. *Commun Comput Phys*. 2020;28(1):518-538.

    doi: 10.4208/cicp.OA-2018-0085

25. Deng J, Zhou H, Wang H, Zhao G, Wang SX. The influence of pore structure in reservoir sandstone on dispersion properties of elastic waves. *Chin J Geophys*. 2015;58(9):3389-3400. [In Chinese].

    doi: 10.6038/cjg20150931

26. Idowu NA. *Pore-Scale Modeling: Stochastic Network Generation and Modeling of Rate Effects in Waterflooding*. Dissertation. London: Imperial College London; 2009.

27. Saxena N, Dietderich J, Alpak FO, *et al*. Estimating electrical cementation and saturation exponents using digital rock physics. *J Pet Sci Eng*. 2021;198:108198.

    doi: 10.1016/j.petrol.2020.108198

28. Kong Q, Zhou C, Li C, Hu F. Numerical simulation method of digital core electrical property and its development orientations. *China Pet Explor*. 2015;20(1):69-77. [In Chinese].

doi: 10.3969/j.issn.1672-7703.2015.01.008

29. Yin XY, Qin QP, Zong ZY. Simulation of elastic parameters based on the finite difference method in digital rock physics. *Chin J Geophys*. 2016;59(10):3883-3890. [In Chinese].

doi: 10.6038/cjg20161031

30. Sun J, Gao J, Jiang Y, *et al*. Resistivity and relative permittivity imaging for oil-based mud: a method and numerical simulation. *J Pet Sci Eng*. 2016;147:24-33.

doi: 10.1016/j.petrol.2016.04.042

31. Silva AA, Lima Neto IA, Misságia RM, *et al*. Artificial neural networks to support petrographic classification of carbonate-siliciclastic rocks using well logs and textural information. *J Appl Geophys*. 2015;117:118-125.

doi: 10.1016/j.jappgeo.2015.03.027

32. Chen H, Innanen KA. Estimation of fracture weaknesses and integrated attenuation factors from azimuthal variations in seismic amplitudes. *Geophysics*. 2018;83(6):R711-R723.

doi: 10.1190/geo2018-0199.1

33. Dunsmuir JH, Ferguson SR, D'Amico KL, *et al*. X-ray microtomography: a new tool for the characterization of porous media. In *Proceedings of the SPE Annual Technical Conference and Exhibition*; October 6-9, 1991; Dallas, TX.

doi: 10.2118/22860-MS

34. Arns CH, Knackstedt MA, Pinczewski WV, *et al*. Virtual permeametry on microtomographic images. *J Pet Sci Eng*. 2004;45(1-2):41-46.

doi: 10.1016/j.petrol.2004.05.001

35. Mees F, Swennen R, Van Geet M, *et al*. Applications of X-ray computed tomography in the geosciences. In: *Applications of X-ray Computed Tomography in the Geosciences*. London: Geological Society, Special Publications; 2003:1-6.

doi: 10.1144/GSL.SP.2003.215.01.01

36. Liang Z, Ioannidis MA, Chatzis I. Permeability and electrical conductivity of porous media from 3D stochastic replicas of the microstructure. *Chem Eng Sci*. 2000;55(22):5247-5262.

doi: 10.1016/S0009-2509(00)00142-1

37. Keehm Y. *Computational Rock Physics: Transport Properties in Porous Media and Applications*. Dissertation. Stanford, CA: Stanford University; 2003.

38. Mosser L, Dubrule O, Blunt MJ. Reconstruction of three-dimensional porous media using generative adversarial neural networks. *Phys Rev E*. 2017;96(4):043309.

doi: 10.1103/physreve.96.043309

39. You N, Li YE, Cheng A. 3D carbonate digital rock reconstruction using progressive growing GAN. *J Geophys Res Solid Earth*. 2021;126(5):e2021JB021687.

doi: 10.1029/2021JB021687

40. Hou Z, Cao D, Ji S, *et al*. Enhancing digital rock image resolution with a GAN constrained by prior and perceptual information. *Comput Geosci*. 2021;157:104939.

doi: 10.1016/j.cageo.2021.104939

41. Pang M, Ba J, Carcione JM, *et al*. Structural and elastic properties of carbonate rocks with different pore types based on digital and theoretical rock physics. *J Geophys Res Solid Earth*. 2025;130(3):e2024JB030538.

doi: 10.1029/2024JB030538

42. Zhao L, Zhu X, Zhao X, *et al*. Deep carbonate reservoir characterization using multiseismic attributes: a comparison of unsupervised machine-learning approaches. *Geophysics*. 2024;89(2):B65-B82.

doi: 10.1190/geo2023-0199.1

43. Wang Y, Zhao L, Quintal B, Geng J. Characterizing broad-band seismic dispersion and attenuation in carbonates with fractures and cavities: a numerical approach. *Geophys J Int*. 2024;240(3):1404-1425.

doi: 10.1093/gji/ggaf452

ACCSCIENCE PUBLISHING

Journal of Seismic Exploration

ARTICLE

An integrated approach of wavefield reconstruction and jointly constrained velocity modeling for seismic imaging in the complex foothill belt

Lan-hua Wang, Wei-wei Duan*, Hai-feng Wang, and Xiao-nan Wang

Research and Development Center of Science and Technology, SINOPEC Geophysical Corporation, Nanjing, Jiangsu, China

Abstract

Seismic imaging in complex foothill belts remains a classic and persistent challenge due to intense near-surface lateral velocity variations and steeply dipping, fractured subsurface structures. These conditions collectively induce severe wavefield distortion, drastically low signal-to-noise ratio (SNR), and significant difficulties in velocity model building. To address the pervasive problems of low SNR and poor image registration in such highly heterogeneous areas, this paper proposes an integrated methodological framework. First, a quasi-three-dimensional (3D) static correction technique based on wave equation continuation is introduced, which fundamentally eliminates time shifts and phase distortions by back-propagating the seismic wavefield to a unified datum plane. Second, an anti-aliasing, fidelity-preserving denoising technique is developed, leveraging the synchrosqueezed curvelet transform to achieve precise signal–noise separation within a super-resolution time–frequency domain, thereby effectively preserving low-frequency components and steep-dip reflections. Finally, a multi-line traveltime-constrained tomographic velocity modeling technique is established. This method constructs a quasi-3D velocity volume and performs an inversion constrained by traveltime closure errors at line intersections, yielding a spatially consistent, high-precision velocity model. Applications in the western Liaoning Jinyang Basin (China) and a salt dome region in Kazakhstan demonstrate that this integrated approach significantly enhances the SNR, event continuity, and structural positioning accuracy of seismic sections, confirming its effectiveness and general applicability for high-precision imaging in "dually complex" geological settings.

Keywords: Complex foothill belts; High-precision imaging; Wave equation continuation static correction; Anti-aliasing denoising; Multi-line joint tomography; Western Liaoning Jinyang Basin

***Corresponding author:**
Wei-wei Duan
(duanww.osgc@sinopec.com)

Citation: Wang L, Duan W, Wang H, Wang X. An integrated approach of wavefield reconstruction and jointly constrained velocity modeling for seismic imaging in the complex foothill belt. *J Seismic Explor.* 2026;35(3):025520135. doi: 10.36922/JSE025520135

Received: December 26, 2025

Revised: March 6, 2026

Accepted: April 13, 2026

Published online: May 26, 2026

Copyright: © 2026 Author(s). This is an Open-Access article distributed under the terms of the Creative Commons Attribution License, permitting distribution, and reproduction in any medium, provided the original work is properly cited.

Publisher's Note: AccScience Publishing remains neutral with regard to jurisdictional claims in published maps and institutional affiliations.

1. Introduction

Complex foothill belts represent a critical yet challenging frontier for hydrocarbon exploration, where the quality of seismic imaging directly dictates the accuracy of structural interpretation and the success of exploration decisions. These areas are

typically characterized by a "dual-complexity" geological setting,[1-5] featuring a complex overburden with rugged surface topography and drastically variable near-surface velocity structures, underlain by steeply dipping and intensely fractured subsurface formations. This dual complexity severely disturbs seismic wave propagation, giving rise to three intertwined fundamental challenges: First, the complex near-surface induces severe non-stationary time shifts and phase distortions in the seismic wavefield, rendering traditional static correction methods based on uniform or vertical-ray assumptions (e.g., elevation, refraction statics) fundamentally inadequate.[6] Second, intense scattered noise, side-scattered energy, and linear interference severely alias with effective signals in the time–space–frequency domain.[7] Conventional denoising techniques struggle to suppress such noise without damaging the high-frequency and weak signal components that are crucial for imaging steep dips and subtle structures.[8] Third, strong lateral velocity variations in the subsurface invalidate conventional velocity analysis and migration methods predicated on horizontal layer assumptions. Furthermore, tomographic inversion constrained only by data from a single two-dimensional (2D) seismic line suffers from severe non-uniqueness due to limited aperture and the lack of lateral constraints, leading to significant mis-ties at line intersections and distorted structural images in final depth volumes. These factors are deeply coupled, collectively resulting in blurred final seismic images, inaccurate fault positioning, and ultimately constraining the detailed characterization and evaluation of hydrocarbon reservoirs.[9]

In recent years, scholars worldwide have conducted extensive research on the imaging challenges in "dually complex" areas, proposing numerous methodological improvements. In the realm of static correction, tomographic static correction techniques have, to some extent, enhanced correction effectiveness in complex terrains by inverting near-surface velocity models.[10-19] Regarding noise suppression, various transform-domain denoising techniques (e.g., in the f-x, wavelet, and curvelet domains) have been continuously developed, aiming to improve the signal-to-noise (SNR).[20-22] For velocity model building, high-precision techniques such as full-waveform inversion (FWI) have demonstrated significant potential.[23-25] However, existing research predominantly focuses on the localized optimization of individual technical steps or on application attempts within specific work areas.[15-22] The prevalent approach treats wavefield reconstruction, signal fidelity preservation, and velocity modeling as isolated steps in a sequential processing pipeline, overlooking the fundamental issue of error propagation and mutual constraint between these stages. For instance, inaccurate static corrections introduce residual distortions into the data, compromising the accuracy of subsequent velocity analysis. Similarly, crude denoising can attenuate valid signals, particularly low-frequency information, thereby reducing the resolution of tomographic inversion for deeper slowness perturbations.[26,27] Consequently, isolated techniques targeting individual problems often yield limited effectiveness in "dually complex" regions and struggle to fundamentally resolve the imaging bottleneck.

The key to solving this problem lies in developing a systematic technical framework. This framework must not only achieve methodological breakthroughs at each individual stage but, more crucially, must emphasize the organic integration and iterative constraints among wavefield reconstruction, signal fidelity preservation, and high-precision velocity modeling. The goal is to form a closed-loop optimized processing-imaging workflow. Based on this premise, this paper proposes and validates an integrated methodology that combines physics-driven wave-equation-based wavefield reconstruction, mathematics-driven anti-aliasing signal fidelity processing, and data-driven multi-information jointly constrained velocity modeling. The innovation of this work is manifested not only in the individual advancements of the three core technologies but, more significantly, in the construction of a logically coherent, tightly interlinked collaborative technical framework. The following sections elaborate in detail on the principles, implementation specifics, and intrinsic connections of each technology. Subsequently, through systematic application and quantitative efficacy analysis in two geologically distinct yet similarly challenging "dually complex" areas—the western Liaoning Jinyang Basin in China (a compressional thrust belt) and a salt dome region in Kazakhstan (a salt dome complex)—and the intrinsic connections of each technology. Subsequently, through systematic application and quantitative efficacy analysis in two geologically distinct evolutions of this methodology, aiming to provide an innovative technical solution with a solid theoretical foundation and demonstrable practical efficacy for high-precision seismic imaging in analogous complex exploration regions worldwide.

2. Methodology

The integrated methodological framework proposed in this paper constitutes a systematic engineering project characterized by progressive layers and mutual feedback. The core of this framework lies in sequentially purifying the initial wavefield using wave-equation-based wavefield reconstruction, extracting the effective signal via high-fidelity denoising, and ultimately achieving precise imaging via multi-information-constrained velocity modeling.

These three components work synergistically to jointly overcome the challenges posed by "dual complexity."

2.1. Quasi-three-dimensional static correction technique based on wave equation continuation

Conventional static correction methods, including elevation correction, refraction statics, and even the widely used first-arrival tomography statics, are physically based on vertical-ray or straight-ray assumptions.[11,12] These assumptions provide a valid approximation when near-surface velocities vary gently laterally. However, in complex foothill belts, near-surface velocities often change drastically over short distances, with anomalies such as high-velocity conglomerate outcrops and low-velocity weathered layers that significantly bend seismic wave propagation paths. Under these conditions, ray-based correction methods fail to accurately describe true wave propagation. Consequently, significant non-surface-consistent residual moveout and waveform distortions remain within the corrected common-shot or common-receiver gathers. These residual errors are directly carried into stacked sections, leading to blurred events, reduced resolution, and systematic bias in subsequent velocity analysis.[13,28,29]

To fundamentally address this issue, this study departed from the traditional ray-theoretical approximation and returned to wave theory itself, adopting a static correction method based on wave equation wavefield continuation. The physical essence of this method was to transform the static correction problem into a mathematical-physical problem of wavefield back-propagation.[30,31] Its core concept could be stated as follows: treating the seismic wavefield u (x_{surf}, t) recorded at the surface—already perturbed by the complex near-surface—as the boundary condition, and utilizing a detailed near-surface velocity model $v(x)$ obtained through methods like first-arrival traveltime tomography, we solved the wave equation in reverse time to back-propagate the wavefield until it was "retrieved" to a smooth, unified datum level z_{ref}. For the 2D case, the governing equation is the acoustic wave equation (**Equation 1**):

$$\frac{\partial^2 u}{\partial x^2}+\frac{\partial^2 u}{\partial z^2}=\frac{1}{v^2(x)}\frac{\partial^2 u}{\partial t^2} \quad (1)$$

Here, u represents the wavefield value, x and z denote the horizontal and vertical spatial coordinates, respectively, and t denotes time. The key technical challenge in implementing this reverse propagation was selecting a stable numerical algorithm. This study employed the frequency–space-domain finite-difference method for the solution. In the specific implementation, we adopted a high-order (e.g., 25-point) difference operator to improve dispersion relation accuracy and implemented parallel computation using the Message Passing Interface across different frequency components, thereby significantly improving computational efficiency. This method transformed the wave equation into the Helmholtz equation in the frequency domain, thereby avoiding the complex treatment of time-reversal boundary conditions required in time-domain finite-difference schemes. It offered higher computational efficiency and numerical stability. In the specific implementation, a system of linear equations with complex coefficients was solved independently for each frequency component. The wavefield on the datum was ultimately obtained via inverse Fourier transform.

However, applying the traditional 2D wave equation continuation directly to multiple independently acquired 2D seismic lines led to non-closing static corrections between lines and inconsistent processing results. To address this, this study innovatively introduced a "quasi-three-dimensional (3D)" processing strategy. The technical workflow comprised the following steps: (i) Unified data preparation and first-arrival picking: All source and receiver point coordinates, along with the seismic data from every 2D line within the survey area, were integrated into a unified planar coordinate system. The first-arrival times across the entire area were then picked with high precision using an automated process supplemented by interactive quality control. (ii) Joint tomographic inversion: Using all the picked first-arrival times as input, a cross-line joint tomographic inversion was performed. This yielded a spatially continuous and consistent 3D near-surface velocity model, including the top interface of any high-velocity layers. (iii) Wave equation continuation correction: Using this 3D velocity model as input, for each individual 2D line, the corresponding source wavefield and receiver wavefield were separately continued from the surface to a unified intermediate reference datum, and then further to the final processing datum, based on **Equation 1**. This process was not a simple vertical time shift but a physics-based wavefield reconstruction. It accurately compensated for the time shifts, amplitude changes, and phase distortions incurred by wave propagation through the complex near-surface medium. The output gathered possessed higher fidelity and improved surface consistency, establishing a crucial, high-quality data foundation for all subsequent processing stages.

2.2. Anti-aliasing fidelity-preserving denoising technique based on synchrosqueezed curvelet transform

The seismic data after wavefield reconstruction still contained substantial scattered noise from subsurface

heterogeneities, side-interference from topography, and cultural linear noise. These noises severely aliased with the effective signals—particularly steep-dip reflections and low-frequency components—in the time, space, and frequency domains.[20-22] Conventional denoising methods, such as f-x domain predictive filtering based on stationarity assumptions or wavelet transform thresholding within fixed time windows, are fundamentally limited by insufficient time–frequency resolution (constrained by the Heisenberg uncertainty principle) and a limited ability to capture directional anisotropic features. When suppressing noise, these methods often produce a "smearing" effect in the time–frequency domain, failing to clearly distinguish between signal ridges and noise energy. Consequently, the denoising process is either incomplete or causes excessive damage to valid signals, especially high-frequency components and events with specific dip directions. Moreover, in 2D seismic lines with insufficient spatial sampling, spatial aliasing further distorts the morphology of both noise and signal, making conventional approaches particularly inadequate for such scenarios.

To address the challenges mentioned above, this study proposed an anti-aliasing, fidelity-preserving denoising algorithm that integrates the curvelet and synchrosqueezing transforms (SSTs). The innovation of this method was the construction of a joint sparse time–frequency domain with ultra-high resolution. The core procedure began by applying the curvelet transform to the noisy seismic data $s(t)$. The curvelet transform represented a breakthrough in second-generation wavelet theory; its basis functions possessed elliptical support regions that vary with scale, offering extremely high directional sensitivity and anisotropy in the 2D spatial domain. This enabled an optimally sparse representation of signals exhibiting curve-like singularities, such as seismic events. After the transformation, the signal energy became highly concentrated into a small number of curvelet coefficients $C(a, \theta, b)$ with distinct directional signatures, whereas the coefficients corresponding to random noise exhibited smaller magnitudes and a scattered distribution. This step achieved a preliminary sparse separation of the signal based on its spatial geometric structure.

However, traditional denoising via simple thresholding of curvelet coefficients still yielded a relatively coarse resolution in the time–frequency plane. To address this, we introduced the SST. SST was an advanced time–frequency reassignment technique whose core idea is to "compress" and focus the blurred time–frequency spectrum obtained from conventional continuous wavelet transforms (or short-time Fourier transforms). Specifically, within our method, for each scale and directional slice of the curvelet coefficients, we computed the phase-derivative-based instantaneous frequency $\omega(a_k, t)$. The coefficient energy was then reassigned to its true instantaneous frequency location according to the following expression (**Equation 2**):

$$T(\omega_c, t) = \frac{1}{\Delta\omega} \sum_{a_k : |\omega(a_k, t) - \omega_c| \le \Delta\omega/2} C(a_k, \theta, b) a_k^{-3/2} \Delta a_k \quad (2)$$

In this equation, where $T(\omega_c, t)$ represents the energy density at the reassigned time–frequency point with central frequency ω_c and time t,[32] $\omega(a_k, t)$ represents the instantaneous frequency corresponding to scale a_k and time t, ω_c is the target frequency center, and $\Delta\omega$ is the frequency bin width. Through this transformation, the effective signal manifested as continuous, energy-concentrated ridges in the time–frequency plane, whereas the noise energy was distributed diffusely. This resulted in a markedly enhanced separability between the two. Building upon this clarified time–frequency spectrum $T(\omega, t)$, an adaptive thresholding algorithm based on energy clustering and local statistics was employed to accurately identify and separate the signal and noise components. Finally, only the time–frequency components identified as signal underwent the inverse SST and the inverse curvelet transform, reconstructing the denoised, high-fidelity data $\hat{s}(t)$.

The advantage of this method was the effective synergy between the sparsity of the curvelet transform, which provided a preliminary separation of the signal based on its spatial geometric structure, and the SST's precise subsample-level localization in the time–frequency domain. This combined strategy theoretically mitigated aliasing noise and, in practice, maximally preserved steep-dip reflections and weak low-frequency signals. Consequently, it provided a crucial guarantee for data preprocessing in support of subsequent high-precision velocity modeling and migration imaging.

2.3. Multi-line traveltime jointly constrained tomographic velocity modeling technique

After obtaining high-SNR, high-fidelity seismic gathers, building a high-precision velocity model was the final, critical step toward accurate depth-migration imaging. In complex structural areas, using data from a single 2D seismic line for tomographic inversion is a common industry practice, yet it suffers from inherent flaws: ray paths are confined to the line's vertical plane, providing extremely weak constraints on lateral variations in the model. This results in a severe non-uniqueness problem for the inversion, yielding velocity models that are laterally discontinuous, unstable, and geologically implausible.

A direct consequence is that, after performing depth migration separately using velocity models derived from different 2D lines, significant mismatches occur in the imaged horizons at their intersections. This prevents the formation of a unified 3D structural understanding and severely compromises confidence in interpretation.[23-25]

Inspired by the use of omnidirectional information to constrain velocity models in 3D seismic exploration, this study proposed a multi-line traveltime jointly constrained tomographic velocity modeling technique. Its core idea was to treat multiple 2D seismic lines with a given network density as an integrated whole. A unified "quasi-3D" spatial grid was established, within which a holistic tomographic inversion was performed. The most powerful physical constraint for this approach stemmed from the principle of traveltime consistency in 3D space: in a true, continuous subsurface velocity field $v(x, y, z)$, all rays that pass through the same subsurface reflection or scattering point p—regardless of which line they originate from or their incident azimuth—should, in theory, have a unique traveltime from the surface to that point.

Therefore, the observed traveltime closure error $\boldsymbol{\Delta t}_{closure}$ at the intersections of 2D seismic lines was not a random error but a direct quantitative measure of the systematic deviation between the current velocity model m (typically parameterized as slowness perturbation) and the true velocity structure. We formalized this consistency constraint and incorporated it as a mandatory term in the inversion objective function.

In terms of technical implementation, the initial velocity functions from individual 2D lines were first fused through spatial interpolation to construct an initial 3D velocity volume $v_0(x)$. Subsequently, based on ray tracing or wave-equation forward modeling, the theoretical traveltime closure errors for rays arriving from different azimuths at all line intersections were calculated. To integrate this consistency constraint into the inversion, an extended objective function $J(m)$ was constructed (**Equation 3**):

$$J(m) = W_d(t_{obs} - t_{cal}(m))^2 + \lambda L\Delta t_{closure}(m)^2 + \in Rm^2 \quad (3)$$

In this equation, m represents the slowness perturbation parameters to be inverted. The first term is the data misfit term, which drives the predicted traveltime t_{cal} to approximate the observed traveltime t_{obs} (W_d denotes the data weighting matrix). The second term constitutes the core innovative constraint of this method. It quantifies and minimizes the traveltime inconsistency at multi-line intersections through the closure error operator L, with the weighting coefficient λ controlling the strength of this constraint. The third term is the model regularization term (R is the regularization operator, and ϵ is its weight), employed to ensure the stability and geological plausibility of the solution. An iterative algorithm (e.g., the conjugate gradient method) was adopted to solve this objective function, simultaneously updating the 3D velocity volume until both the data residuals and the inter-line closure errors were jointly minimized. Ultimately, velocity profiles for each 2D line were extracted from the spatially consistent, high-precision 3D velocity volume obtained upon convergence of the inversion, for use in depth-migration imaging.

By introducing multi-line traveltime consistency as a strong lateral constraint, this method significantly reduced the non-uniqueness of the velocity inversion. The constructed velocity model exhibited improved lateral continuity and clearer geological meaning. Compared to conventional single-line independent tomographic inversion or velocity modeling without lateral constraints, this method reduced the average imaging mis-tie at line intersections by more than 60% (Table 1), significantly enhancing the reliability of 2D structural interpretation. Practical applications demonstrated that this technique effectively solved the imaging tie problem for 2D survey networks in complex structural areas, notably enhancing imaging positioning accuracy for steeply dipping strata and complex fault systems.

3. Case studies and efficacy analysis

3.1. Application in the complex foothill belt of the Western Liaoning Jinyang Basin

The foothill belt of the western Liaoning Jinyang Basin is a product of intense compressional forces during the Yanshanian period. The surface is characterized by a rugged bedrock mountain range with drastic lateral variations in near-surface velocity. Subsurface geology involves multiple sets of steeply dipping to overturned strata and a complex thrust fault system, indicating extremely intense structural deformation. This area represents a classic compressional-type "dually complex" exploration region. Prior to applying our methodology, seismic data from this area exhibited low SNR, poor continuity of reflection events, and ambiguous structural geometries.

Following the application of the integrated technical workflow proposed in this paper, the imaging quality was systematically improved. Firstly, the static correction technique based on wave equation continuation effectively eliminated wavefield distortions caused by severe lateral velocity variations. As shown in Figure 1, compared to the result from conventional tomographic static correction (Figure 1A), the stacked section after wavefield

reconstruction (Figure 1B) exhibited significantly enhanced continuity of deep reflection events, more focused energy, and clearer, sharper fault terminations. Secondly, the synchrosqueezed curvelet transform denoising technique preserved the dynamic characteristics of the effective signal while strongly suppressing low-frequency surface waves and scattered noise. A comparison between the denoised result (Figure 2B) and the original data (Figure 2A) for the seismic line revealed that previously noise-masked weak reflection events had become visible, and the data SNR was substantially increased. To quantitatively evaluate the advantages of the proposed technical system, we compared data quality between the conventional and proposed workflows. As shown in Table 1, the proposed method achieved significant improvements across all key metrics. Figure 3 displays the spectral analysis comparison before and after denoising for this area, demonstrating that while effectively suppressing noise, our method maximally preserved low-frequency components below 15 Hz and weak signal energy, which was critical for subsequent velocity inversion and depth imaging. Finally, the velocity model obtained from the multi-line traveltime jointly constrained tomographic inversion exhibited a lateral variation pattern with clearer geological significance. The depth-migration imaging result driven by this high-precision velocity model (Figure 4B) demonstrates, in contrast to the legacy result, more accurate structural positioning for the line, sharper delineation of steeply dipping strata, complex fault systems, and high-velocity anomaly boundaries, resulting in a more geologically reasonable overall structural framework.

3.2. Validation and generalization in a salt dome region in Kazakhstan

To evaluate the methodological framework's general applicability, it was applied to a geologically distinct salt-dome structural region in Kazakhstan. This area is characterized by the plastic flow of a massive salt layer as its core feature, resulting in highly irregular salt body geometries with steeply dipping flanks, and is thus classified as a diapiric-type "dually complex" region. The primary imaging challenges were the severe velocity contrasts at the salt flanks, which caused significant wavefield penetration shadows and turning-wave interference, and the extremely weak sub-salt signals, which resulted in extremely low SNR.

The application results demonstrate that this technical system was equally suitable for complex salt tectonic regions. The wavefield continuation static correction technique effectively restored the wavefield distorted by sharp velocity contrasts at the salt flanks (Figure 5), laying the foundation for accurate imaging. The fidelity-preserving denoising technique enhanced the weak reflection signals within and beneath the salt, improving event continuity (Figure 6). The final depth-migration section shown in Figure 7 revealed significantly improved imaging of the salt dome's geometry, internal structure, and contact relationships with the surrounding rock, yielding richer structural detail. Figure 8 shows the spectral analysis comparison for this area, further confirming that the proposed method consistently preserved low-frequency signals below 15 Hz across different geological settings, thereby ensuring the reliability of subsequent imaging. The success of this case not only yields direct production benefits but also compellingly demonstrates, from an academic standpoint, that the integrated methodological framework proposed in this paper is not merely a customized solution for a specific geological type. Rooted in the core principles of physics, mathematics, and data consistency, it can effectively address the "dually complex" imaging challenges arising from different genetic origins (e.g., compressional vs. ductile) and diverse manifestations (e.g., faulting vs. salt structures). This attests to its genuine methodological generality and technical robustness.

3.3. Comprehensive comparative analysis of application effects in two areas

To comprehensively evaluate the applicability of the proposed method across different types of "dually complex" geological conditions, Table 1 summarizes quantitative comparison metrics for the application effects in the two areas.

As shown in Table 1, the proposed method achieved significant improvements in imaging quality in both areas with distinctly different geological backgrounds. In the compressional thrust belt of the Western Liaoning Jinyang Basin, the SNR was increased by 6.7 dB, and the mis-tie at intersections was reduced by 18 ms. In the salt tectonic region of Kazakhstan, the SNR was increased by 6.7 dB, and the mis-tie at intersections was reduced by 23 ms. These results fully validate that the proposed method was not only suitable for specific types of complex structures but also exhibited excellent geological universality and technical robustness, providing a high-quality imaging foundation for subsequent structural interpretation and reservoir prediction.

4. Discussion

The technical framework proposed in this paper constitutes an organically integrated system characterized by logical progression and synergistic enhancement. Its systemic value far exceeds the simple sum of its individual component technologies, marking a methodological evolution from "discrete processing" to "collaborative inversion."

Table 1. Quantitative comparison of the application effects of the proposed method in two complex areas

Area	Geological type	Metric	Conventional method	Proposed method	Improvement
Western Liaoning Jinyang Basin	Compressional thrust belt	SNR (dB)	8.5	15.2	+6.7 dB
		Mis-tie at intersections (ms)	24	6	−18 ms
A salt dome region in Kazakhstan	Salt tectonic type	SNR (dB)	6.8	13.5	+6.7 dB
		Mis-tie at intersections (ms)	32	9	−23 ms

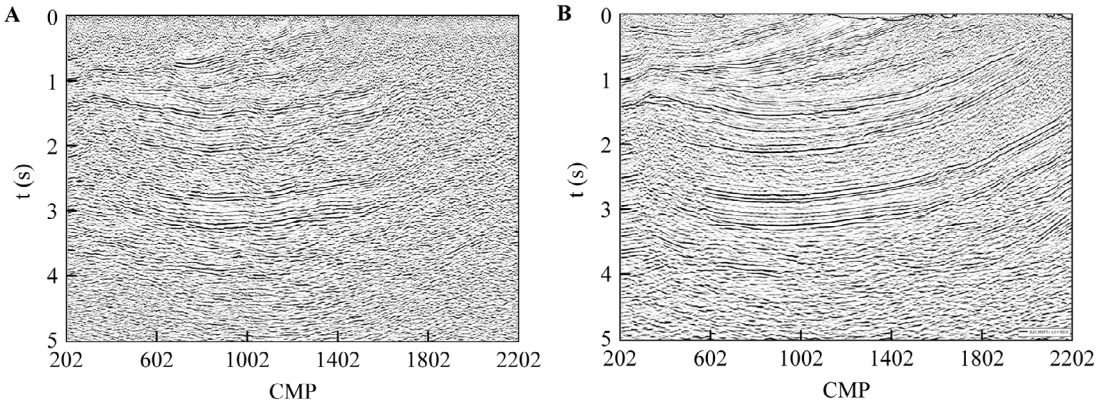

Figure 1. Processed sections from the Jinyang Basin using (A) conventional tomography static correction and (B) wavefield continuation static correction methods
Abbreviation: CMP: Common midpoint.

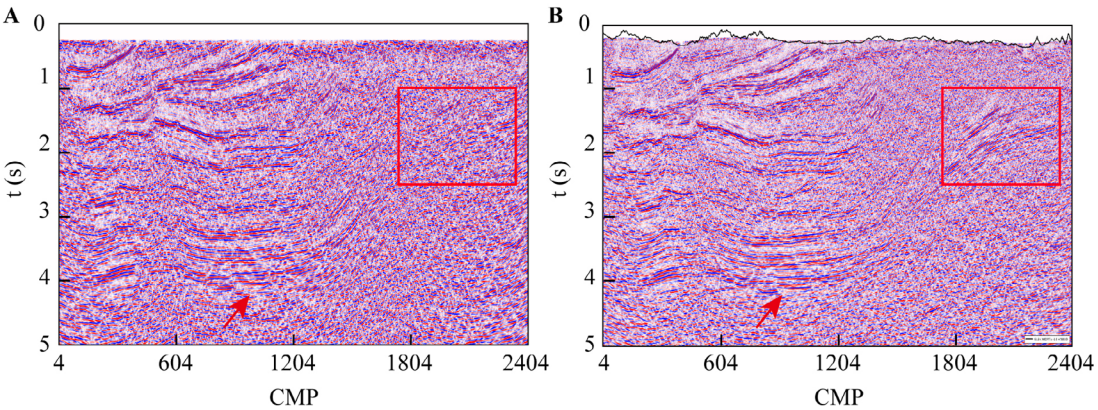

Figure 2. Processed sections from the Jinyang Basin using (A) conventional noise suppression and (B) anti-aliasing fidelity-preserving noise suppression methods
Abbreviation: CMP: Common midpoint.

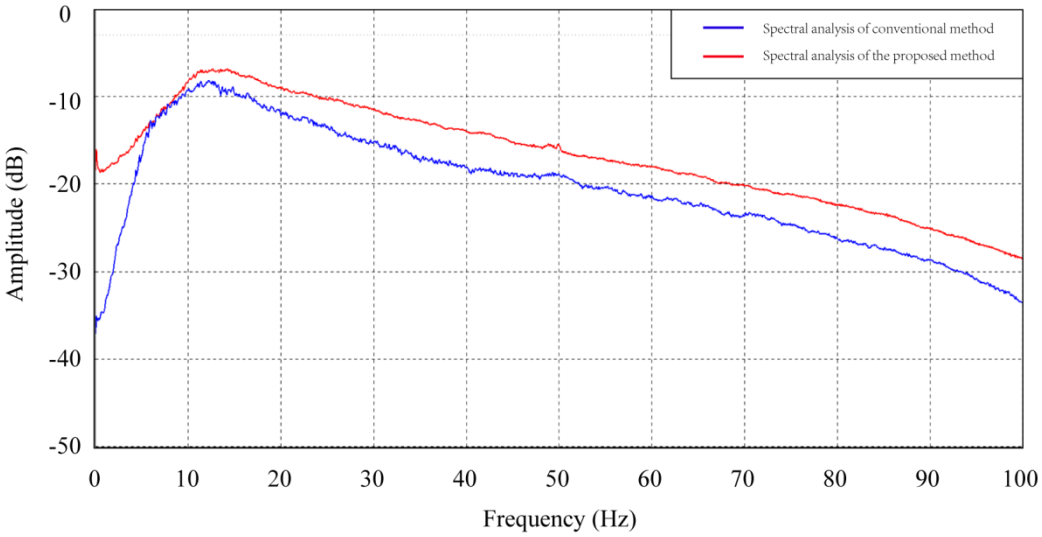

Figure 3. Amplitude spectra of the denoised data: conventional method vs. proposed method in the Jinyang Basin

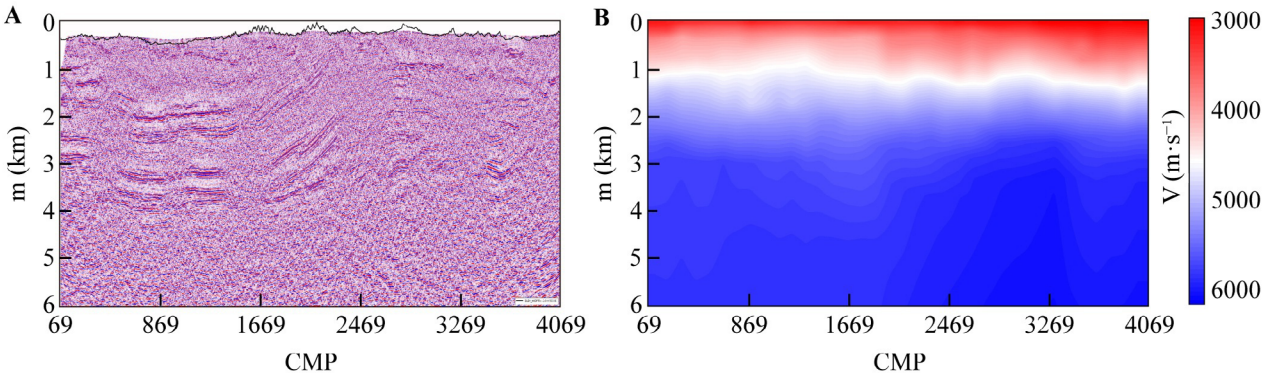

Figure 4. Processed section (A) and corresponding velocity model (B) from the application of multi-line jointly constrained tomography velocity modeling technology in the Jinyang Basin
Abbreviation: CMP: Common midpoint.

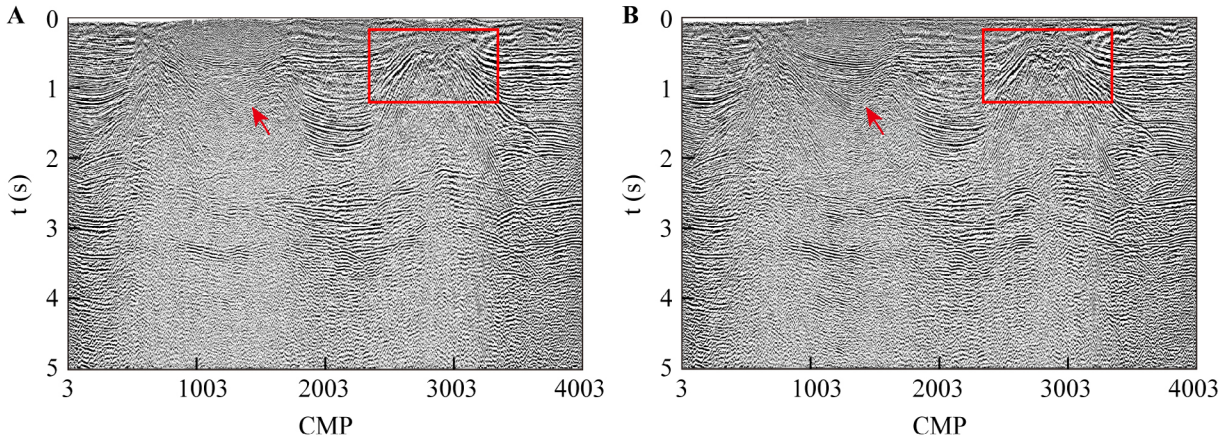

Figure 5. Processed sections using (A) conventional tomography static correction and (B) wavefield continuation static correction methods
Abbreviation: CMP: Common midpoint.

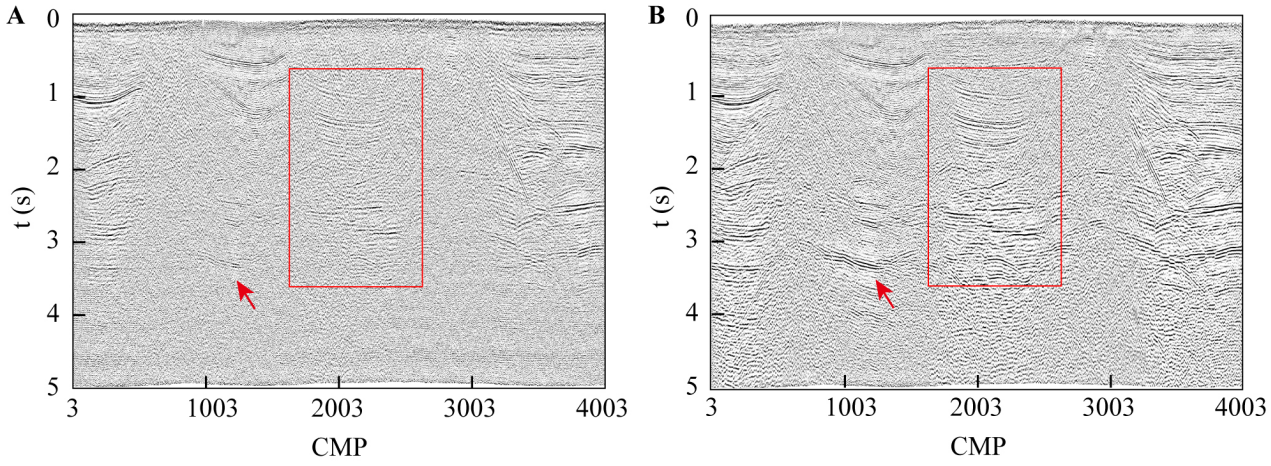

Figure 6. Processed sections using (A) conventional noise suppression and (B) anti-aliasing fidelity-preserving noise suppression methods
Abbreviation: CMP: Common midpoint.

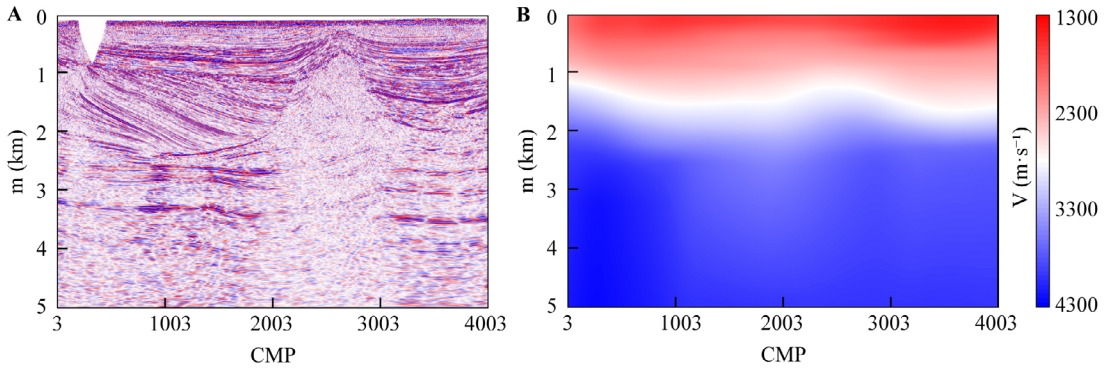

Figure 7. Processed section (A) and corresponding velocity model (B) from the application of multi-line jointly constrained tomography velocity modeling technology in an area
Abbreviation: CMP: Common midpoint.

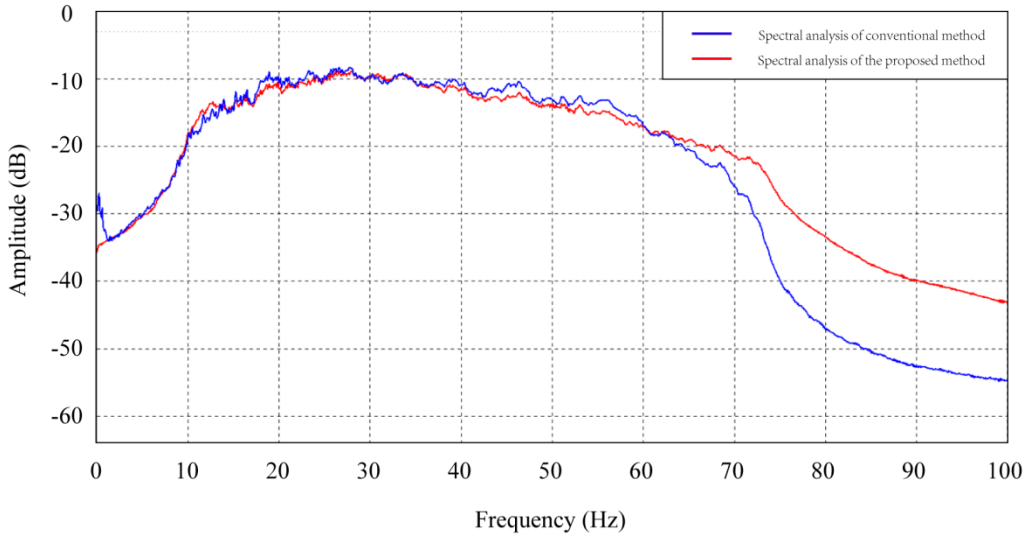

Figure 8. Amplitude spectra of the denoised data: conventional method vs. proposed method in the salt dome region of Kazakhstan

4.1. Technological synergy and systemic logic

This system adheres to a core logic of "physical reconstruction → mathematical purification → data synergy." The static correction based on wave-equation continuation accomplishes a paradigm shift from empirical correction to physical reconstruction, establishing a high-fidelity data foundation. Denoising via the synchrosqueezed curvelet transform achieves a leap from "noise suppression" to "precision signal extraction," ensuring the integrity of signals, particularly weak ones. The multi-line jointly constrained tomographic modeling leverages the inherent spatial relationships within the data itself, upgrading from "single-line independent inversion" to "networked collaborative constraint." These three components are interlinked, with the output of one stage serving as high-quality input to the next. This creates a positive, closed-loop process in which errors are progressively suppressed, and information fidelity is propagated, thereby systematically overcoming the coupled challenges of "dually complex" imaging.

4.2. Advantages, limitations, and future prospects

The comprehensive advantages of this method were validated through its applications: it delivered high imaging precision, significantly improving SNR, event continuity, and structural positioning accuracy; it fundamentally resolved the spatial closure problem inherent to 2D survey network imaging; it demonstrated good generalizability and robustness across complex areas of different origins, such as compressional foothill belts and ductile salt domes; and its implementation based on existing 2D seismic lines offered notable practicality. However, this study also acknowledges certain limitations: the computational cost of wave-equation continuation is relatively high; under our current parallel implementation (using 200 CPU cores), processing a 50 km 2D line (4 GB of data) takes approximately eight hours. For large-scale 3D surveys with hundreds of lines, computation time can reach weeks, posing a challenge for industrial adoption. constraints based on ray traveltimes have limited resolution for small-scale anomalies (e.g., small fault blocks, fractures, and cavities); and the influence of anisotropy has not been considered. Future work should focus on: developing more efficient algorithms (e.g., phase-screen methods) to reduce computational costs; transitioning towards full-waveform joint inversion to enhance resolution; and incorporating anisotropy parameters (e.g., vertical or tilted transverse isotropy medium assumptions) into the inversion framework, which would require replacing the current acoustic wave equation (**Equation 1**) with an appropriate anisotropic wave equation, aiming to achieve more accurate "geological transparency" modeling.

5. Conclusion

Focusing on the challenges of seismic imaging in complex foothill belts, this study, through methodological innovation and integration, drew the following key conclusions:

(i) An effective high-precision imaging technical system was established. Integrating innovative techniques—wave-equation static correction, anti-aliasing fidelity-preserving denoising, and multi-line joint tomographic velocity modeling—constituted a systematic solution for addressing geological conditions characterized by "dual complexity."

(ii) The imaging quality of real seismic data was significantly improved. The application in the western Liaoning Jinyang Basin demonstrated that this technical suite fundamentally enhances data quality. The resulting imaging profiles exhibited clear structural frameworks, accurate fault positioning, and well-defined event characteristics, thereby resolving long-standing imaging blurriness in this region. Spectral analysis of this case study (Figure 3) confirmed that the proposed method preserved low-frequency signals, which were essential for accurate velocity inversion and depth imaging.

(iii) The general applicability and robustness of the methodological principles were validated. The application in a salt dome region of Kazakhstan proved the good adaptability of this methodological system to complex exploration areas of different origins (e.g., foothill belts and salt tectonic regions), indicating broad prospects for its wider application. Spectral analysis from this region (Figure 8) further supported the consistency of low-frequency signal preservation across diverse geological settings.

(iv) A clear technical development pathway was outlined. This integrated framework established a foundation for future technological evolution. Subsequent work can involve deeper integration with techniques such as FWI and anisotropy modeling, aiming to achieve a transition from precise structural imaging to the quantitative prediction of reservoir parameters.

Acknowledgments

The authors thank Fu Ting and Zhao Sisi for providing the figures, and also thank the processing team of the Research and Development Center of Science and Technology, SINOPEC Geophysical Corporation, for their technical support and helpful discussions.

Funding

This work was supported by the SINOPEC Group-

level Scientific Research Project (Grant No. JP24092, "Quantitative Analysis of Acquisition Geometry Attributes Based on Depth-Domain Imaging").

Conflict of interest

The authors declare no conflicts of interest.

Author contributions

Conceptualization: Lan-hua Wang
Formal analysis: Wei-wei Duan
Investigation: Xiao-nan Wang
Methodology: Wei-wei Duan, Hai-feng Wang
Writing–original draft: Lan-hua Wang
Writing–review & editing: Lan-hua Wang, Hai-feng Wang

Availability of data

Data are available from the corresponding author upon reasonable request.

References

1. Li J, Li G, Diao Y, Feng R, Du J, Wu S. Fuza shandi shen du yu di zhen cheng xiang chu li fang fa—yi Longmenshan shan qian dai Haitangpu fuza gou zao qu wei li [Depth-domain seismic imaging processing method for complex mountain areas: A case study of Haitangpu complex tectonic zone of Longmenshan piedmont belt]. *Geophysical Prospecting for Petroleum.* 2024;63(3):578-588. [In Chinese].

   doi: 10.12431/issn.1000-1441.2024.63.03.006

2. Wang H, Xu R, Feng B, Wu J. Fuza dibiao tanqu dizhen kantan de renshi ji dizhen shuju chengxiang chuli de guandian [Understanding of seismic exploration and viewpoint of seismic data imaging processing in a complex surface exploration area]. *Geophysical Prospecting for Petroleum.* 2023;62(5):789-805. [In Chinese].

   doi: 10.12431/issn.1000-1441.2023.62.05.001

3. Di Z, Xie J, Gu Y, Song Z, Huo H. Ji yu die qian pian yi cheng xiang de gao mi du guan ce xi tong fen xi ping jia fang fa—yi Zhunanshan qian dai kuai wei li [Analysis and evaluation method for high-density geometry based on prestack migration imaging—A case study in the piedmont zone of southern Junggar basin]. *Geophysical Prospecting for Petroleum.* 2022;61(5):771-781. [In Chinese].

   doi: 10.3969/j.issn.1000-1441.2022.05.002

4. Liu D, Liu Z, Jiang B. Mian xiang fuza shanqian dai de shen du yu di zhen cheng xiang chu li yan jiu [The processing workflow of depth domain imaging facing the complex piedmont belt]. *Geophysical Prospecting for Petroleum.* 2016;55(1):49-59. [In Chinese].

   doi: 10.3969/j.issn.1000-1441.2016.01.007

5. Zhao H, Li W, Wu Y, *et al.* Acquisition parameters and sensitivity analysis affecting the seismic imaging quality of the complex piedmont zone. *Appl Geophys*. 2023;20(4):351-363.

   doi: 10.1007/s11770-023-1004-4

6. Taner MT, Koehler F. Surface consistent corrections. *Geophysics*. 1981;46(1):17-22.

   doi: 10.1190/1.1441133

7. Zhang W, Yang L, Si W, Liu H. Seismic wave simulation of a complex foothill belt. *J Geophys Eng*. 2020;17(5):893-905.

   doi: 10.1093/jge/gxaa038

8. Peng HX. Nanfang shanqian dai B qu dizhen sudu jianmo ji pianyi chengxiang [Velocity model building and migration imaging in a foothill belt area]. *Oil Geophys Prospect*. 2013;48(4):526-530. [In Chinese].

9. Duan Y, Chen Y, Huang F, Liu C, Cheng Y, Zhang H. Fuza shanqian dai die qian shen du pian yi cheng xiang guan jian ji shu yan jiu—yi Talimu Pendi Keping nan diqu wei li [Key technologies for pre-stack depth migration imaging of complex piedmontz zones: A case study of Kepingnan area in Tarim Basin]. *Oil Geophysical Prospecting.* 2025;60(6):1463-1472. [In Chinese].

   doi: 10.13810/j.cnki.issn.1000-7210.20250047

10. Wang Y, Shang X, Zhao S, Teng H, Yan Y, Zhu X. Shanqian dai lian he ceng xi fan yan di zhen cheng xiang [Joint tomography for foothills seismic imaging]. *Oil Geophysical Prospecting.* 2021;56(4):782-791. [In Chinese].

    doi: 10.13810/j.cnki.issn.1000-7210.2021.04.011

11. Wang R, Zhang W, Ning Y, Zhao W, Yang X, Zhu S. Zhe she jing zheng jiao zheng yu ceng xi jing zheng jiao zheng ji shu zai E'erduosi pendi beibu shaxing youkuang di zhen kan tan zhong de ying yong fen xi [Application analysis of refraction static correction and tomographic static correction techniques in seismic exploration for sandstone-type uranium deposits in the northern Ordos Basin]. *Miner Resour Geol.* 2023;37(6):1258-1263. [In Chinese].

    doi: 10.19856/j.cnki.issn.1001-5663.2023.06.014

12. Cui XF, Xu L, Chen LK. Wave equation wavefield continuation static correction for seismic data on complex near surface. *Pet Explor Dev*. 2006;33(1):1240.

13. Li J, Li Q, Yang G, Zhi M. Ji yu VTI jie zhi de di zhen chu bo ceng xi jing zheng jiao zheng fang fa [Tomography static corrections by seismic first break based on VTI media]. *J China Coal Soc*. 2026;51(5):1−11. [In Chinese].

    doi: 10.13225/j.cnki.jccs.2025.0272

14. Liu M, Xiong D, Wen X, Chen H, Zhao H, Qian Z. Gao jie you xian fen cha bo chang yan xu jing zheng jiao zheng ji shu shi yan ji ying yong [Experiment and application of high-order finite-difference wavefield continuation static correction technology]. *Energy Environ Prot*. 2018;40(4):124-129,133.

[In Chinese].

doi: 10.19389/j.cnki.1003-0506.2018.04.026

15. Cui Q, Pan S, Han Z. Bo chang yan xu jing zheng jiao zheng zai fuza di biao qu de ying yong ji fen xi [Application and analysis of wave field continuation static correction in area with complex surface]. *Sci Technol Eng*. 2016;16(15):36-40,53. [In Chinese].

doi: 10.3969/j.issn.1671-1815.2016.15.006

16. McMechan GA. Seismic tomography in boreholes. *Geophys J R Astron Soc*. 1983;74(2):601-612.

doi: 10.1111/j.1365-246X.1983.tb01891.x

17. Daily W. Underground oil-shale retort monitoring using geotomograph. *Explor Geophys*. 1984;15(3):1701-1711.

doi: 10.1071/EG984194b

18. Somerstein SF, Berg M, Chang D, *et al*. Radio-frequency geotomography for remotely probing the interiors of operating mini-and commercial-sized oil-shale retorts. *Geophysics*. 1984;49(8):1288-1300.

doi: 10.1190/1.1441756

19. Marsden D. Static corrections—a review, Part 1. *Leading Edge*. 1993;12(1):43-49.

doi: 10.1190/1.1436912

20. Li W, Liu Y, Chen Y, *et al*. Fuza dibiao san she gan rao bo jiao du yu xiang liang fen jie qu zao [Removing the complex near-surface scattered wave via an angle-domain vector resolution method]. *Geophysical Prospecting for Petroleum*. 2021;60(4):565-573. [In Chinese].

doi: 10.3969/j.issn.1000-1441.2021.04.005

21. Xu Y, Liu C, Lyu Q, Shao W, Xu C, Mu J. Duo yu lian he qu zao ji shu zai Tazhong Aoxi xi di xin zao bi shu ju chu li zhong de ying yong [Application of multi-domain composite denoising technology for the processing of Ordovician low SNR seismic data in Tazhong Area]. *Geophysical Prospecting for Petroleum*. 2015;54(2):172-179,196. [In Chinese].

doi: 10.3969/j.issn.1000-1441.2015.02.008

22. Zhang A, Zhao J, Zhao N, Kang X, Guo C. Jiehe zhangliang kongjian yu daoyi jingbao de gaoguangpu yingxiang qu zao qu hundie [Hyperspectral image denoising and antialiasing based on tensor space and reciprocal cell]. *Infrared Laser Eng*. 2018;47(10):1026002. [In Chinese].

doi: 10.3788/IRLA201847.1026002

23. Su Y, Xi Y, Wang X, Xiao Y. Zhunnan Hutubi diqu fuza gou zao su du jian mo ji ying yong [Complex structural velocity modeling and application in the Hutubi area of Zhunnan]. *Xinjiang Geol*. 2024;42(4):661-666. [In Chinese].

24. Liu M, Chen L, Niu H, Zhao X, Li Y. Ji yu quan bo xing fan yan yu zou shi ceng xi de fen bu gao jing du su du jian mo ji shu ji qi zai Weizhou you tian fu za gou zao cheng xiang zhong de ying yong [Step-by-step high-precision velocity modeling technique based on full waveform inversion and traveltime tomography and its application in complex structure imaging of Weizhou Oilfield]. *J Trop Oceanogr*. 2025;44(2):178-186. [In Chinese].

doi: 10.11978/2024078

25. Peng G, Gu X, Duan W, Gong T, Zhao R, Wang Q. Zhen di biao su du jian mo ji shu zai fuza shan di di zhen zi liao cheng xiang zhong de ying yong [Application of true surface velocity modeling technology in seismic data imaging in complex mountainous areas]. *Xinjiang Pet Geol*. 2024;45(2):244-252. [In Chinese].

doi: 10.7657/XJPG20240214

26. Sheriff RE, Geldart LP. *Exploration Seismology*. 2nd ed. Cambridge, UK: Cambridge University Press; 1995:1-31.

27. Yilmaz O. *Seismic Data Analysis: Processing, Inversion, and Interpretation of Seismic Data*. 2nd ed. Tulsa, OK: Society of Exploration Geophysicists; 2001:324-395.

28. Tannich JD. Liquid removal from hydraulically fractured gas wells. *J Pet Technol*. 1975;27(11):1309-1317.

doi: 10.2118/5113-PA

29. Buckley SE, Leverett MC. Mechanism of fluid displacement in sands. *Trans AIME*. 1942;146(1):107-116.

doi: 10.2118/942107-G

30. Barone A, Vassiliou A. 2D/3D Kirchhoff-based wavefield continuation. Paper presented at: *SEG International Exposition and Annual Meeting;* October 14-19, 2018; Anaheim, CA. Society of Exploration Geophysicists; 2018:4382-4386.

doi: 10.1190/segam2018-2998625.1

31. Bevc D. Flooding the topography: wave-equation datuming of land data with rugged acquisition topography. *Geophysics*. 1997;62(5):1558-1569.

doi: 10.1190/1.1444258

32. Daubechies I, Lu J, Wu HT. Synchrosqueezed wavelet transforms: an empirical mode decomposition-like tool. *Appl Comput Harmon Anal*. 2011;30(2):243-261.

doi: 10.1016/j.acha.2010.08.002

ACCSCIENCE PUBLISHING

Journal of Seismic Exploration

ARTICLE

Processing four-dimensional vertical seismic profiling in the CO2CRC Otway Stage 4 Project

Alina Almukhametova*, Konstantin Tertyshnikov, Nikita Beloborodov, Olivia Collet, Boris Gurevich, Roman Isaenkov, Mustafa Al Marzooq, Pavel Shashkin, Mikhail Vorobev, and Roman Pevzner

School of Earth and Planetary Sciences, Centre for Exploration Geophysics, Curtin University, Perth, Western Australia, Australia

Abstract

Long-term containment assurance is critical for regulatory approval and public acceptance of geological carbon dioxide (CO_2) storage, placing strict requirements on the repeatability and robustness of time-lapse seismic monitoring over multi-year operational periods. Multi-well vertical seismic profiling (VSP) using distributed acoustic sensing (DAS) offers a compact, repeatable monitoring option; however, long-term deployments can be compromised by non-geological changes, such as altered surface optical routing, interrogator artifacts, or fiber integrity loss. The CO2CRC Otway Stage 4 Project provides a relevant test case because non-repeatable acquisition conditions occurred between the baseline and monitor surveys. This study presents the processing and initial evaluation of a four-dimensional (4D) VSP dataset acquired in February 2025, following the injection of approximately 10 kt of CO_2-rich gas into the Paaratte Formation (~1,500 m depth) via the CRC-3 injector. Processing was adapted from the previous Otway DAS-VSP monitoring workflow, with cross-vintage comparability improved through well-specific channel alignment, including correction for time-varying channel shifts. The workflow further included cross-equalization and Wiener matching to reduce residual source–signature differences and improve repeatability, wavefield separation, and in-house Kirchhoff migration. Time-lapse analysis of migrated volumes and root mean square difference attributes computed over the injection interval shows coherent anomalies at CRC-4 and CRC-5 that are geometrically consistent with the Stage 4 injection interval, although no usable 4D data were available from the injector well CRC-3. CRC-6 exhibits no coherent anomaly. An anomaly near CRC-7 is spatially separated from the injector and is likely due to the continued evolution of CO_2 plumes from previous Otway injections. These results demonstrate that multi-well 4D DAS-VSP can provide robust qualitative detection and delineation of plume-related seismic anomalies under substantial acquisition non-repeatability, strengthening conformance monitoring workflows for long-term CO_2 storage.

Keywords: Four-dimensional vertical seismic profiling; Distributed acoustic sensing; Carbon dioxide storage

***Corresponding author:**
Alina Almukhametova (alina.almukhametova@postgrad.curtin.edu.au)

Citation: Almukhametova A, Tertyshnikov K, Beloborodov N, *et al*. Processing four-dimensional vertical seismic profiling in the CO2CRC Otway Stage 4 Project. *J Seismic Explor.* 2026;35(3):026040015. doi: 10.36922/JSE026040015

Received: January 25, 2026

Revised: April 4, 2026

Accepted: April 16, 2026

Published online: May 26, 2026

Copyright: © 2026 Author(s). This is an Open-Access article distributed under the terms of the Creative Commons Attribution License, permitting distribution, and reproduction in any medium, provided the original work is properly cited.

Publisher's Note: AccScience Publishing remains neutral with regard to jurisdictional claims in published maps and institutional affiliations.

1. Introduction

Climate change remains one of the key global challenges requiring integrated solutions in the energy and industrial sectors. The latest international assessments identify carbon capture and storage as a necessary component of large-scale decarbonization pathways for achieving net-zero emissions.[1,2] Deep saline aquifers offer the largest theoretical storage capacity among geological options; however, demonstration of long-term containment is required to secure regulatory approval and public acceptance.[3] Therefore, effective carbon dioxide (CO_2) injection monitoring is essential for tracking plume evolution and detecting potential leakage.

Time-lapse (four-dimensional [4D]) seismic imaging is widely regarded as an effective tool for detailed characterization of the CO_2 plume evolution and containment.[4] Time-lapse seismic has been successfully used in numerous saline aquifer storage projects, demonstrating the ability of repeated seismic surveys to track plume dynamics. Vertical seismic profiling (VSP) with fiber-optic distributed acoustic sensing (DAS) enables frequent and repeatable seismic monitoring around wells, providing a robust approach for CO_2 storage applications.[5-7] Using DAS in VSP surveys replaces discrete downhole geophones with a permanently installed optical fiber that is interrogated to measure axial strain or strain-rate along the well at meter-scale spacing, yielding densely sampled VSP gathers with a small operational footprint and excellent repeatability.[8,9] Compared with surface 4D seismic, DAS-VSP offers receiver-side repeatability because the permanently installed fiber remains fixed in the borehole, and the downhole receiver geometry places measurements closer to the reservoir, supporting high-resolution imaging around the wells and reducing the operational footprint. In contrast, surface seismic provides broader areal coverage and is therefore advantageous for regional plume tracking, but it typically requires a larger acquisition footprint and is more exposed to survey-to-survey variations in near-surface and receiver conditions. Compared with repeated retrievable borehole-geophone deployments and large-footprint surface 4D seismic, DAS-VSP is a more cost-effective and less disruptive monitoring option that can be repeated without well intervention and has been demonstrated in walkaway and three-dimensional (3D) VSP acquisition geometries.

The CO2CRC Otway International Test Centre (OITC) in Victoria, Australia, offers a unique testbed for exploring and improving carbon capture and storage monitoring methods.[10] OITC has been used for a series of CO_2 injection and monitoring experiments to observe plume movement. The studied interval at OITC is part of the Late Cretaceous Paaratte Formation of the Sherbrook Group in the onshore Otway Basin. At the site, the interval of interest lies at approximately 1,500 m depth and comprises sandstone, siltstone, and mudstone, including cemented and carbonate-cemented intervals. The two studied parasequences are interpreted as coastal-to-shallow-marine deposits and comprise delta-front, distal mouthbar, proximal mouthbar, and distributary-channel facies.[11] Exploring CO_2 storage in the Paaratte Formation began in the Stage 2C Otway Project with the injection of 15 kt of CO_2-rich gas (a mixture of supercritical 80 mol% CO_2 and 20 mol% methane, produced from the nearby Buttress gas field) through the CRC-2 well. This injection was monitored using 4D surface seismic with a buried geophone array and conventional surface seismic sources.[12,13] During the next experiment, the Otway Stage 3 Project, 4D surface seismic was replaced with multi-well 4D DAS-VSP surveys, which were conducted before and after 12.5 kt (out of a total of 15 kt) of CO_2-rich gas was injected via CRC-3 well, resulting in high-quality time-lapse seismic datasets.[14] The current experiment, the Otway Stage 4 Project, includes 10 kt of CO_2-rich gas injected 50 m above the Stage 3 interval from November 2024 to January 2025 using the same CRC-3 well, followed by a multi-well 4D DAS-VSP survey acquired in February 2025.

Stage 3 results demonstrated high-quality imaging and repeatability of multi-well 4D DAS-VSP for monitoring CO_2 migration in the Paaratte Formation. However, long-term deployment introduces practical challenges that can directly affect time-lapse consistency, and Stage 4 differs from Stage 3 in both the injection interval and acquisition conditions. In particular, changes in surface optical routing, interrogator behavior, and fiber integrity can compromise baseline–monitor comparability and must be accounted for prior to time-lapse analysis. This study presents the processing and initial evaluation of the Stage 4 time-lapse dataset relative to the Stage 3 baseline. The objectives are to determine whether reliable time-lapse response can be recovered under non-equivalent DAS channel–depth mapping and acquisition artifacts between vintages, and to characterize the geometry and extent of the Stage 4 seismic anomaly associated with the shallower injection interval. This supports long-term containment and conformance monitoring at the OITC.

2. Methodology

2.1. Data acquisition

As part of the Stage 4 monitoring and verification program, a time-lapse 3D VSP monitor dataset was acquired. Under the Otway project's established time-lapse survey identifiers that distinguish individual acquisition vintages across

multiple injection projects, this monitor survey is called M9. In Stage 2C, the program comprised a baseline survey and monitor surveys M1, M2, and M3 acquired during the injection, followed by post-injection monitor surveys M4 and M5.[15] In Stage 3, the 4D VSP program included M6, M7, and M8 surveys acquired during injection.[8] M8 also serves as a baseline for Stage 4, while M9 is the monitor. Figure 1 illustrates the M9 survey acquisition layout, along with interpreted CO_2 plume contours from previous stages.

The survey was acquired after the injection of approximately 10 kt of CO_2-rich gas into a saline aquifer via the near-vertical injection well CRC-3 into the Paaratte Formation at approximately 1,500 m depth (approximately 50 m shallower than in the Stage 3 injection).

The plan for the M9 survey was to use 4,185 point locations to match the M8 survey from Stage 3, which served as the baseline survey for Stage 4. In total, 4,044 shot points were acquired, as some planned source shot points had to be skipped during the survey due to the presence of certain farming crops or inaccessibility. The survey employed two 26,000-lb INOVA UniVib vibrators. Each shot used a single 24 s linear sweep from 6 to 150 Hz at 70% of the vibrator's rated maximum force of 26,000 lbf (115 kN). The sweep was tapered with 0.5-s cosine ramps and followed by a 3-s listen time. Shot points were spaced at 15 m along source lines separated by approximately 100 m, replicating the M8 Stage 3 acquisition geometry.

The 4D VSP dataset was acquired using six wells instrumented with fiber-optic DAS arrays: CRC-3, CRC-4, CRC-5, CRC-6, CRC-7, and CRC-8. Data acquisition used a DAS system connected to optical fibers installed in the wells. The full DAS system configuration is summarized in Table 1. Multiple interrogators were deployed during the survey; however, this study focuses on data from the Silixa iDAS-v3 Carina units, as baseline data (M8) are only available for these instruments.

The processed data were recorded on individual fiber-optic receiver arrays in each well, comprising the

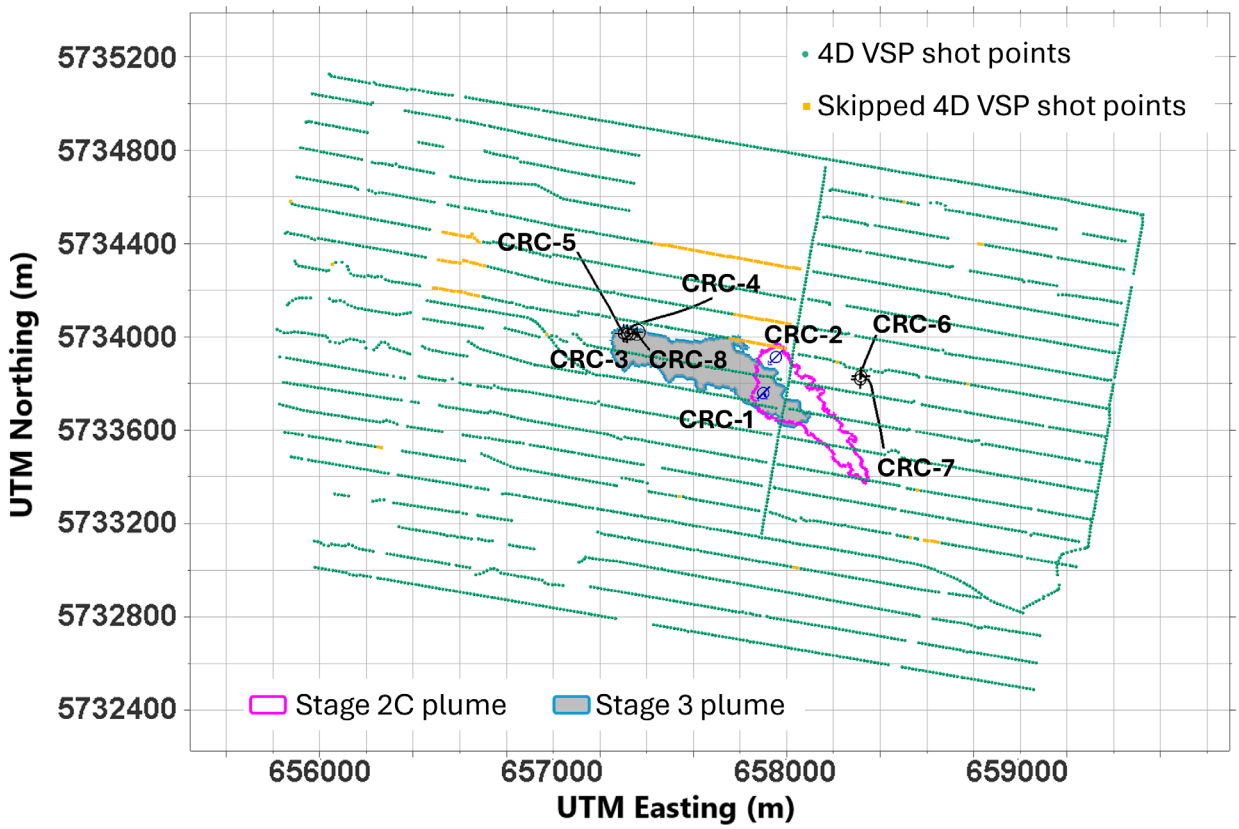

Figure 1. Acquisition geometry for the Stage 4 time-lapse 3D VSP (M9 Seismic Survey) at the Otway site, showing the surface projections of the well locations (black solid lines), 4D VSP shot points (green circles), and skipped shot points (orange squares), as well as previously interpreted extents of the Stage 2C (magenta line) and Stage 3 (blue line, grey filled area) CO_2 plume in the Paaratte Formation.
Abbreviations: 3D: Three-dimensional; 4D: Four-dimensional; CO_2: Carbon dioxide; UTM: Universal Transverse Mercator; VSP: Vertical seismic profiling.

engineered constellation fiber (CF) (Silixa Ltd, United Kingdom) with enhanced backscattering. All downhole fiber sections used in this 4D VSP study were permanently installed behind casing and cemented in the wells. The unit iDAS-v3 P06 was connected to a single-mode fiber (SMF) on the cable in the CRC-4 well, spliced to the CF core at the bottom of the CRC-4 well, and then to the CF core on the cable cemented in the CRC-3 well. The iDAS-v3 P08 unit was connected to four fiber sections: an SMF section, followed by a CF section in the CRC-7 well, and then a CF and an SMF section in the CRC-6 well. The iDAS-v3 P22 unit was connected to SMF and CF sections in the CRC-5 well, followed by a horizontal section of a Silixa-branded helically wound cable buried in a shallow trench. The total fibre length per unit was less than 6 km. As in M8, the acquisition was done with a 10 m gauge length, a 5 m pulse length, a 16 kHz pulse repetition frequency, and 1 m channel spacing. All recording systems were synchronized and triggered via radio links through the Sercel 428 system (Sercel, United States) installed on-site. Data from DAS interrogators were continuously acquired, and shot gathers were extracted from the global positioning system time on the Sercel 428 system, which was used to launch the signal excitation.

2.2. Rerouting of surface cables

Between Stage 3 and Stage 4 projects (i.e., between the M8 and M9 surveys), all fiber-optic surface cables from the wells to the acquisition cabin were rerouted, resulting in a different optical path compared with the Stage 3 layout. This rerouting affected the mapping between DAS channels and physical locations along the wells. In addition, the P06 unit experienced a recording issue that manifested as a random temporal channel shift during acquisition. Figure 2 shows the root mean square (RMS) amplitudes for the M8 and M9 surveys recorded by the iDAS-v3 units; the red arrows mark the beginning of the fiber after the interrogators in M8.

To restore consistency and enable a valid comparison of the datasets, a uniform shift was applied to each channel within each well (for iDAS-v3 P06, this was combined with a temporal shift correction). The shift values differed between wells and were determined by manually aligning recognizable features between the M8 and M9 surveys. To align M9 with M8, 1–16 channels were subtracted from the M9 channel numbers, depending on the well. The random temporal shift observed in the P06 interrogator was corrected by adding approximately 25 channels.

2.3. Constellation fiber damage in CRC-3

During the reperforation of CRC-3, the CF cable was damaged. The inflowing fluid caused fiber degradation, rendering it practically unusable for seismic monitoring. Figure 3 illustrates a comparison of 4D VSP data acquired during M8 and M9 surveys in CRC-3 and CRC-4. CRC-4 fiber data showed consistent data quality across the time axis; in contrast, CRC-3 data showed a broad band of channels losing integrity, as evidenced by noisy, incoherent traces across a range of channel numbers. Although the first arrival remained visible in the affected interval, the increased noise floor prevents identification of weaker coherent events. Consequently, CRC-3 CF data from M9

Table 1. List of distributed acoustic sensing interrogators and system configuration

Interrogator	Vendor	Connected Well 1	Connected Well 2	Connected Well 3
iDAS-MG	Silixa	CRC-8 (SMF↓↑)	-	-
iDAS-v3 P06	Silixa	CRC-4 (SMF↓ CF↑)	CRC-3 (CF↓)	-
iDAS-v3 P22	Silixa	CRC-5 (SMF↓ CF↑)	HWC (CF)	-
iDAS-v3 P08	Silixa	CRC-7 (SMF↓ CF↑)	CRC-6 (CF↓ SMF↑)	-
OptoDAS	ASN	CRC-8 (SMF↓↑)	CRC-4 (SMF↓↑)	CRC-3 (SMF↓↑)
Treble+	Terra15	CRC-8 (SMF↓)	-	-

Note: Arrows indicate the downgoing and upgoing segments of the borehole optical path.
Abbreviations: CF: Constellation fiber; DAS: Distributed acoustic sensing; HWC: Helically wound cable; SMF: Single-mode fiber.

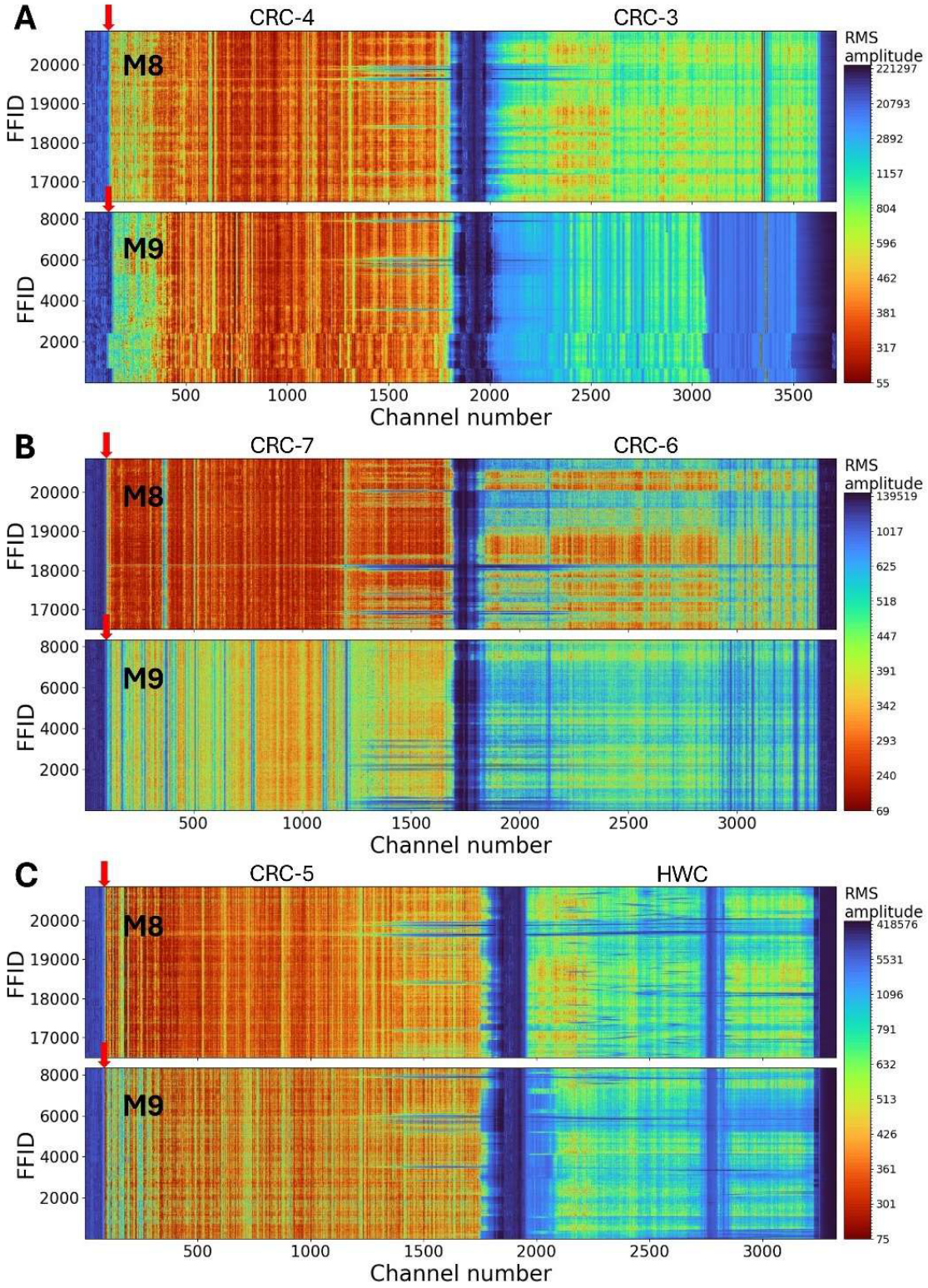

Figure 2. Root mean square (RMS) amplitudes of the Silixa iDAS-v3 Carina units. The red arrows indicate the beginning of the fiber after the interrogators on M8. (A) iDAS-v3 P06. (B) iDAS-v3 P08. (C) iDAS-v3 P22.

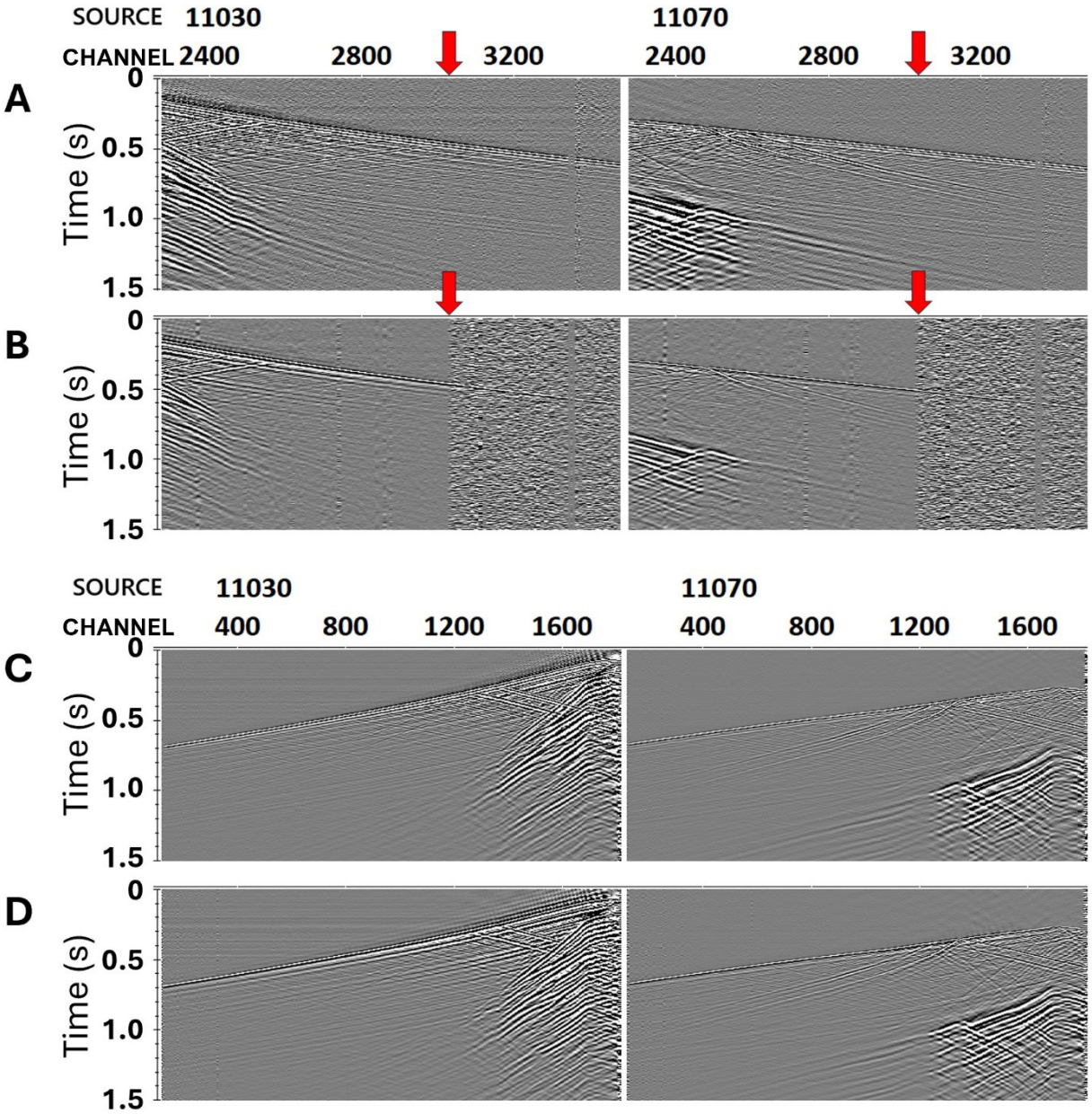

Figure 3. Four-dimensional (4D) vertical seismic profiling (VSP) data from survey vintages M8 and M9 in wells CRC-3 and CRC-4. Panels show CRC-3: (A) M8, (B) M9; CRC-4: (C) M8, (D) M9. Red arrows mark the fiber section in CRC-3 damaged by inflowing fluid, which caused progressive darkening along the fiber path and loss of signal over the affected channel range in M9. The first arrival remains visible in this interval; however, the increased noise floor prevents identification of weaker coherent events. In CRC-4, consistent data quality and comparable numbers of functional channels are observed across survey vintages. The first 1.5 s of the 3 s records are displayed.

were not used in the 4D VSP analysis.

2.4. Data processing

Time-lapse processing for Stage 4 was adapted from the DAS-VSP workflow established for Stage 3 (Figure 4), with M8 used as the baseline and M9 as the monitor survey. Each well was treated as an independent dataset throughout the processing sequence.

Field data were acquired in the native iDAS-v3 technical data management streaming format and subsequently converted to SEG-Y. Shot locations were taken from the differential global positioning system measurements.

Along each well, DAS channel depths were tied to known cable markers, and noisy or dead channels were removed. For Stage 3 vintages, traces were stacked in 5 m depth intervals and then correlated with the source sweep. For the Stage 4 M8–M9 pair, the order was reversed: correlation with the pilot sweep was performed first, followed by channel alignment and then stacking in 5 m depth bins. This change of order was required because rerouting the surface cable between M8 and M9 (and the iDAS-v3 P06 interrogator recording issue) altered the channel-depth mapping, necessitating well-specific channel shifts to restore consistent geometry. Channel alignment, therefore, was performed on the correlated data at native channel sampling before 5 m stacking, to ensure each depth bin represented the same physical interval in M8 and M9, rather than combining misaligned depths. Both M8 and M9 were processed using this same revised workflow before time-lapse comparison. Therefore, the modified order does not introduce a vintage-dependent processing inconsistency, but instead ensures that corresponding depth bins represent the same physical interval in both surveys. The resulting M9 seismic fold at the level of the Paaratte Formation, summed over all wells, is shown in Figure 5.

After cross-equalization of the survey geometries, a two-dimensional spatial filter using a single-sample operator was applied to each shot gather across all traces to suppress coherent stripe-type noise attributed to DAS interrogator artifacts, followed by deterministic deconvolution. Direct-wave arrivals were flattened and stacked for each shot using traces recorded below 1,000 m depth to estimate the source wavelet. For a given shot position, wavelets derived from the contributing wells were averaged and scaled to a unit RMS amplitude.

The deconvolved data were then band-pass filtered with Ormsby operators (0–40–80–160 Hz and 5–10–90–180 Hz) to suppress the low-frequency ground roll and high-frequency noise. To further improve repeatability between vintages and reduce residual differences in the source signature, monitor (M9) datasets were subjected to Wiener matching filters. For each shot, direct P-wave segments were extracted from depths below 800 m within a window from −50 ms to 350 ms relative to the picked first break in every well. Traces without reliable first-break picks were excluded. The remaining traces were aligned on the first-break time and combined using a 30% trimmed mean to obtain representative baseline and monitor wavelets. This alpha-trim was used to preserve the coherent first-break wavelet while reducing contamination from outliers and residual upgoing-wave energy. A 150 ms Wiener filter was then designed for each shot by minimizing the RMS misfit between the baseline wavelet and the filtered monitor wavelet and was applied by convolution to the full deconvolved monitor shot record. The filter length was chosen to capture most of the filter energy, with longer filters producing no meaningful change in the output. An example of M8 and M9 shot gathers after deconvolution, together with their time-lapse differences before and after Wiener matching, is shown in Figure 6A–D. The corresponding 60-ms window normalized RMS sections in Figure 6E and 6F demonstrate the reduction in non-repeatable energy achieved by this step.

Wavefield separation was carried out in the frequency–wavenumber (F–K) domain. In the first pass, an F–K filter was applied to attenuate downgoing energy. A second F–K operation, applied after flattening the upgoing P-wave to P-wave reflections, suppressed residual upgoing P-wave to S-wave and S-waves. Geometric spreading was approximated by multiplying the data by t^2. Because the remaining S-wave energy was difficult to remove without damaging the target signal, data below the direct S-arrival were muted.

Before imaging, model-based static corrections were introduced. For each shot, direct-wave travel times were calculated using the one-dimensional isotropic velocity model derived from the zero-offset VSP in CRC-3. The misfit between these theoretical travel times and the picked first breaks was evaluated over depths below 1,400 m. Model-based statistics were then estimated independently for each vintage by taking the 33% trimmed mean of the misfit distribution for each shot and applying the resulting shift to the corresponding dataset. This procedure reduced systematic timing discrepancies between wells and vintages.

Imaging employed an in-house Kirchhoff migration based on the formulation of Dillon,[16] adapted for DAS by applying a $cos^2\theta$ weighting factor in the migration kernel, where θ is the angle between the receiver-side ray direction and the local fiber tangent at each DAS channel. This weighting accounts for the directional sensitivity of DAS receivers. The migration assumed straight-ray propagation and the actual well trajectories, with a central dip of 0° and an aperture of 15°. Data from each well were independently migrated onto a common 3D grid with a 7.5 × 7.5 m lateral bin size and a 1 m vertical sampling resolution.

3. Results

Time-lapse 3D DAS-VSP analysis of the M9 survey reveals coherent seismic anomalies associated with CO_2 injection within the Paaratte Formation. In a 3D VSP acquisition, shots were located at the surface, and the seismic wavefield was recorded on fiber-optic DAS arrays along the wells.



Figure 4. Processing workflow for Stage 3 DAS-VSP datasets. Reprinted with permission from Yurikov *et al.*[8] Copyright © 2022 Elsevier Ltd.
Abbreviations: 3D: Three-dimensional; DAS: Distributed acoustic sensing; F–K: Frequency–wavenumber; VSP: Vertical seismic profiling.

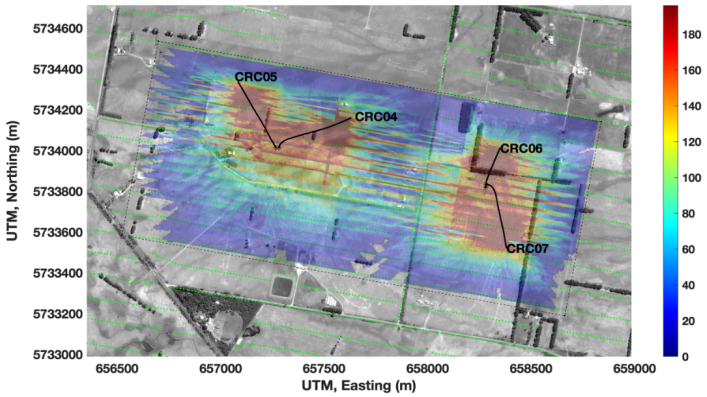

Figure 5. Seismic fold for the M9 survey computed for receiver spacing of 5 m and 7.5 × 7.5 m bin size, combined for all wells at the depth of Paaratte Formation
Abbreviation: UTM: Universal Transverse Mercator.

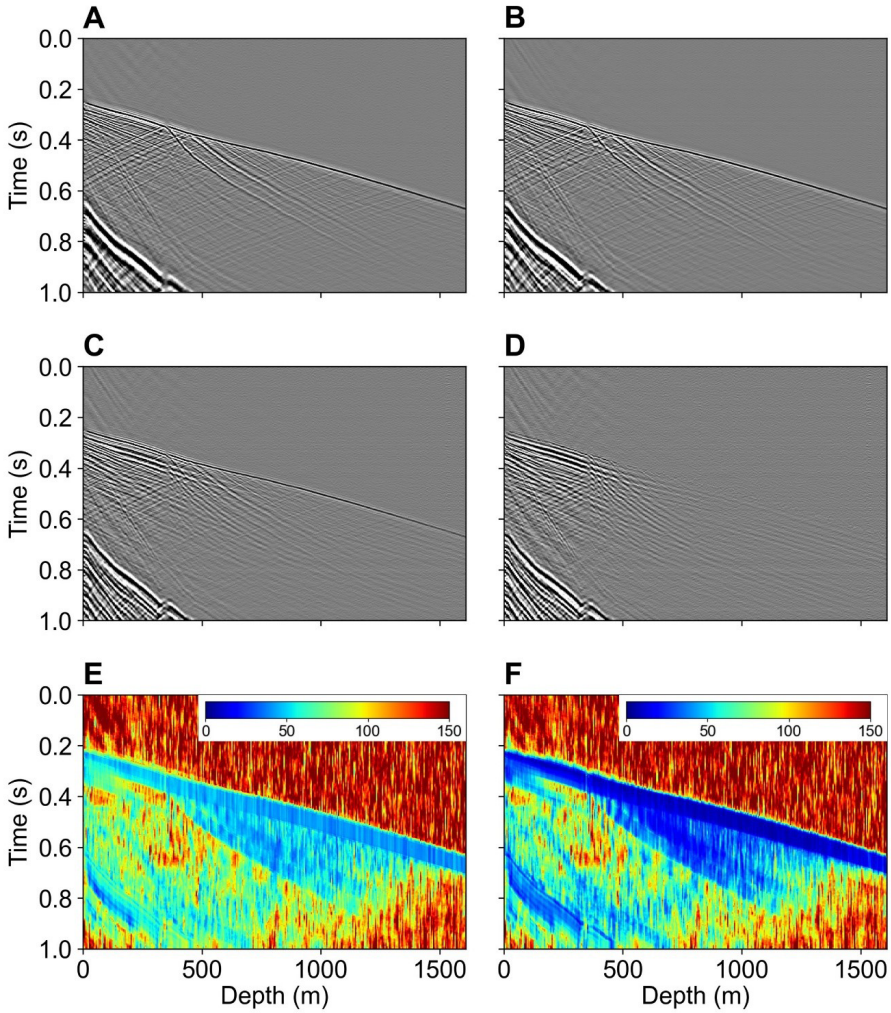

Figure 6. Example of (A) M8 and (B) M9 shot records after deconvolution from the same source location and receiver well, and their time-lapse difference (C) before and (D) after application of the Wiener matching filter. Panels (E) and (F) show the normalized root mean square (NRMS) (%) of the 60 ms window before and after Wiener filtering, respectively, demonstrating the reduction of non-repeatable noise and improved time-lapse repeatability along the primary reflection corridor.

Each well, therefore, provides an independent view of the subsurface that can be compared and correlated with images from the other wells.

Figure 7 presents a vertical cross-section through the migrated M9 3D DAS-VSP volumes for CRC-4, CRC-5, CRC-6 and CRC-7. The section displays continuous reflectors and high-quality seismic data at the depth of the Paaratte Formation, providing a suitable basis for identifying time-lapse amplitude anomalies at the Stage 4 injection interval.

Figure 8 illustrates the time-lapse difference (M9–M8) along the A–A' line intersecting the injector, extracted from the migrated volumes of M8 and M9, and highlights the seismic changes associated with CO_2 injection. Clear anomalies are visible at the depth of the Paaratte Formation near the CRC-4, CRC-5, and CRC-7 wells. Plan-view maps of the maximum RMS difference (M9–M8) over 1,400–1,500 m true vertical depth subsea, shown in Figure 9, further clarify the lateral extent and spatial distribution of these changes.

CRC-4 and CRC-5 anomalies are associated with the Stage 4 CO_2 injection, whose outlines are overlain on the RMS difference maps shown in Figure 9. In CRC-4, CO_2 plume contours were delineated from the RMS difference volume by thresholding to retain only voxels with high values (> 99.9th percentile); the visible areal extent was then manually outlined. The threshold was used as a statistical detection criterion rather than as a direct petrophysical cutoff, with the aim of isolating the strongest spatially coherent time-lapse response above the residual non-repeatable background. In CRC-5, the CO_2 plume outline was visually interpreted from the RMS difference map view between M8 and M9, corresponding to the horizon

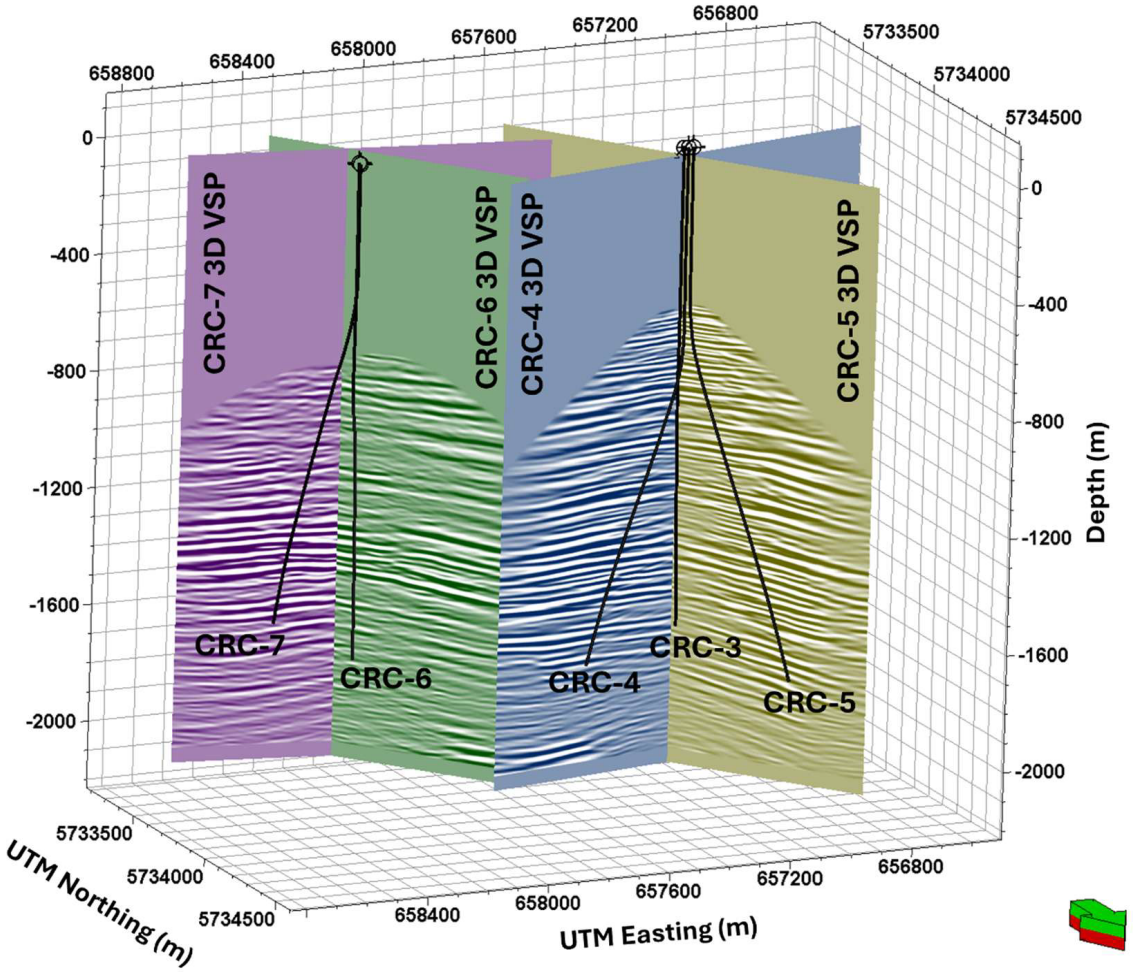

Figure 7. Cross-section of the migrated M9 3D DAS-VSP volumes from four wells: CRC-4 (blue), CRC-5 (yellow), CRC-6 (green), CRC-7 (purple)
Abbreviations: 3D: Three-dimensional; DAS: Distributed acoustic sensing; UTM: Universal Transverse Mercator; VSP: Vertical seismic profiling.

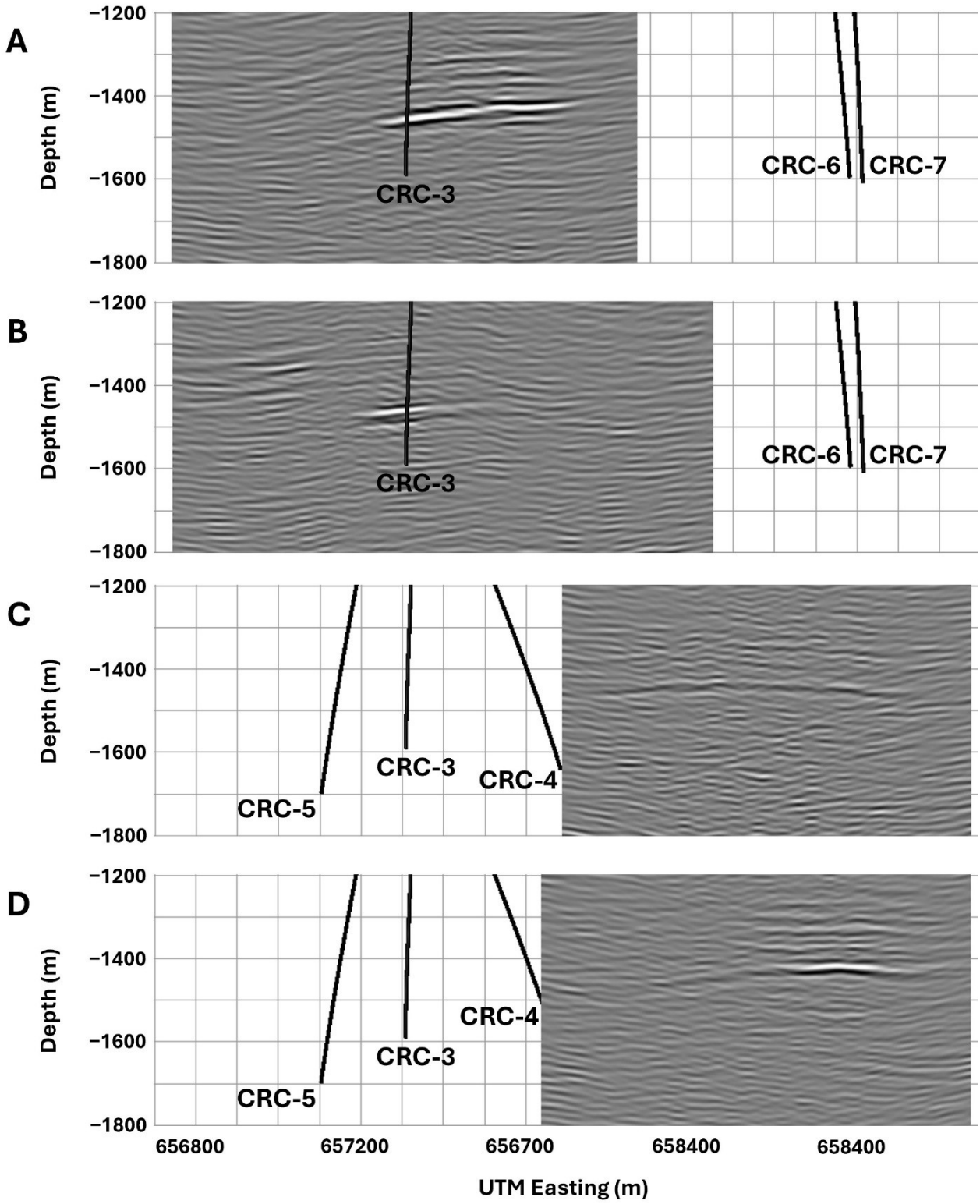

Figure 8. Time-lapse difference (M9 minus M8) vertical slices along line A–A' (see Figure 9 for line location), extracted from the 3D migrated DAS-VSP volumes for wells (A) CRC-4, (B) CRC-5, (C) CRC-6, and (D) CRC-7

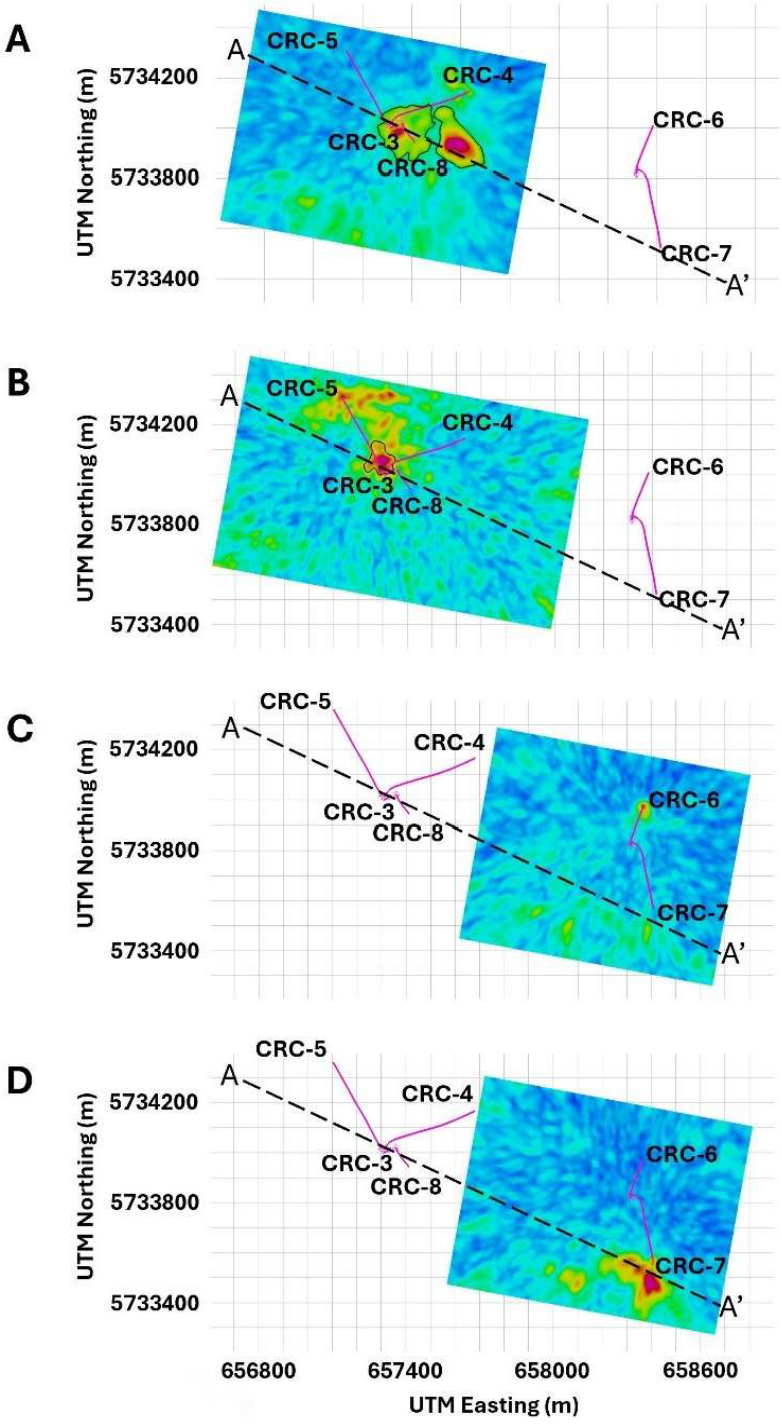

Figure 9. Plan-view maps of the maximum root mean square (RMS) difference between three-dimensional migrated data acquired at observation wells: (A) CRC-4, (B) CRC-5, (C) CRC-6, and (D) CRC-7 during M8 and M9 (M9–M8) over the representative depth interval 1,400 to 1,500 m true vertical depth subsea. Warm colors (pink, red, yellow) indicate stronger RMS differences likely associated with the presence of carbon dioxide, while cool colors (blue) denote minimal change. Pink lines indicate well trajectories. The black contours on the CRC-4 and CRC-5 maps mark the interpreted areal extent of the Stage 4 carbon dioxide plume. The black dashed line shows the position of line A–A' used in Figure 8.

of the strongest seismic response. These interpreted plume extents should be considered approximate rather than exact boundaries, with uncertainty arising from the threshold selection, manual outlining, migration resolution, and residual non-repeatable noise. CRC-6 data show no coherent anomaly. At CRC-7, the observed seismic anomaly is interpreted as related to a combination of CO_2 injected during Stage 2C and Stage 3, most likely due to subsequent migration of the plume into the area between surveys M8 and M9. This finding is consistent with published Stage 3 4D DAS-VSP results, which indicated that the newly injected CO_2 reached and remobilized a previous plume in the same formation.[8,17]

4. Discussion

Operationally, the M9 survey highlighted two acquisition risks: surface cable rerouting and downhole cable integrity. Rerouting of surface cables between M8 and M9 altered the mapping between DAS channels and physical depth; however, because the rerouting affected only the surface cable sections while the downhole fibers remained cemented in place, this effect was addressed using well-specific channel shifts as a first-order correction. This procedure restored practical cross-vintage comparability for time-lapse interpretation. In contrast, the fiber in CRC-3 was irreversibly damaged by fluid ingress during perforation, rendering the cemented cable segment unusable for 4D monitoring. This is an important precedent demonstrating that cables installed behind the casing can act as a leakage pathway if perforation and completion design do not explicitly protect the fiber. To reduce the likelihood of similar failures in future permanent installations, oriented perforation schemes or gravel-packed completions confined to defined azimuthal sectors are preferable to full 360° perforation around the wellbore.

Following the failure of the CRC-3 fiber, the SMF connected to the OptoDAS interrogator remained operational in that well. The absence of an OptoDAS baseline complicates direct inclusion of the CRC-3 Stage 4 response into the M8–M9 4D analysis, which is currently limited to the iDAS-v3 Carina data. Reconciling the OptoDAS CRC-3 measurements with the existing iDAS-v3 vintages through cross-calibration of instrument responses and noise characteristics is therefore an important topic for subsequent work, as it would restore the well as a central control point for future time-lapse surveys.

A key limitation of the present Stage 4 dataset is that no usable M8–M9 4D response is available from the injector well CRC-3 itself. Therefore, interpretation of the Stage 4 plume geometry relies on observations from neighboring wells, rather than on direct time-lapse constraints within the injector.

Multi-well DAS-VSP data were processed per well, consistent with the Stage 3 workflow. In a multi-well DAS geometry, each borehole acts as an independent VSP experiment with its own interrogator, fiber installation, noise characteristics, and illumination pattern. Processing wells separately allows geometry calibration, deconvolution, wavefield separation, and statics to be optimized for the local acquisition conditions, rather than forcing a single processing parameter set onto datasets with different directional sensitivities and amplitude responses. Comparison between wells is then performed at the interpretation stage, by aligning depth-registered sections and attribute maps, rather than by merging the data into a single processing flow.

From a reservoir engineering perspective, the current workflow provides qualitative yet operationally valuable information: a map of the plume outline obtained from the 4D DAS-VSP anomaly envelopes. This delineation already provides a critical consistency check for dynamic reservoir models and can be used to discriminate between scenarios with markedly different lateral plume spread or vertical migration. However, for rigorous history matching, a quantitative link between flow simulation variables and observed seismic attributes must be established. This will involve defining robust 4D observables that can be predicted from reservoir simulations and formulating misfit measures to assimilate these attributes into history-matching workflows. Developing and validating such quantitative integration strategies, including cross-calibration of different interrogator types and explicit treatment of multi-stage injection history, constitutes the next step towards fully exploiting multi-well DAS-VSP data for reservoir management and long-term conformance assessment at the Otway site and similar storage projects.

The observed time-lapse anomalies underline both the strengths and the limitations of the current monitoring configuration. At CRC-4 and CRC-5, the coherent RMS-difference anomalies at the Paaratte Formation depth are geometrically consistent with the Stage 4 injection interval and provide a clear qualitative outline of the new plume. The anomaly in the vicinity of CRC-7 is spatially separated from the current injector and, given its location, is most plausibly associated with the spreading of the Stage 2C and/or Stage 3 plume into that area between the two surveys rather than with the Stage 4 injection. This behavior emphasizes that the multi-well DAS-VSP system is sensitive to both legacy and recently injected CO_2, and that multiple injection stages need to be considered jointly when interpreting 4D responses.

At the same time, the CRC-7 response illustrates an

important limitation of time-lapse seismic for quantitative characterization. The seismic anomalies primarily reflect changes caused by free-phase CO_2, but seismic data alone cannot provide a reliable saturation estimate. Methods for deriving CO_2 saturation from seismic observations remain subject to significant uncertainty and require site-specific calibration.[18] Consequently, in the present study, 4D seismic is used qualitatively to detect and outline the CO_2 plume.

5. Conclusion

The M9 multi-well 3D DAS-VSP survey conducted during the Otway Stage 4 Project provided high-quality time-lapse data that are consistent and comparable with the M8 baseline using the adapted Stage 3 processing workflow. The resulting time-lapse images demonstrate that multi-well DAS-VSP monitoring enables reliable tracking of the CO_2 plume, thereby strengthening confidence in storage conformance and containment.

Time-lapse analysis reveals seismic anomalies around the CRC-4 and CRC-5 wells, which are spatially aligned with the Stage 4 CO_2 injection interval within the Paaratte Formation, indicating the presence and evolution of the plume. At CRC-7, the observed anomaly is interpreted as residual CO_2 from Stage 2C/3, highlighting the method's ability to capture both recent and legacy injection signals.

Surface cable rerouting effects were corrected by applying a uniform shift to all channels in the affected wells. In contrast, the damage in the CRC-3 fiber precludes its use for acquisition or time-lapse analysis. Overall, the M9 results confirm that permanent multi-well DAS-VSP offers a practical and effective technology for high-resolution time-lapse monitoring of CO_2 injection and storage.

Acknowledgments

The authors acknowledge CO2CRC and its members for their support in this project. The authors thank Michael Mondanos (Silixa, the LUNA company) for helping with the fibre-optic equipment, and Murray Hehir (Curtin University) and Peter Dumesny (GR Production Services) for invaluable help with all aspects of field operations.

Funding

This research was supported by CO2CRC Limited, its industry members and research partners, and by the Australian and Victorian Governments through various funding programs. The Curtin Reservoir Geophysical Consortium (CRGC) provided funding for the PhD research projects. The Otway Stage 4 program received funding from Low Emissions Technology Australia for the seismic monitoring project, RITE for the microbubble injection project, and from ExxonMobil, BP, BHP, and the Australian Federal Government for the GFV project.

Conflicts of interest

Boris Gurevich and Roman Pevzner are Editorial Board Members of this journal, but were not in any way involved in the editorial and peer-review process conducted for this paper, directly or indirectly. The authors declare no conflicts of interest.

Author contributions

Conceptualization: Roman Pevzner, Alina Almukhametova
Formal analysis: Alina Almukhametova, Roman Isaenkov, Roman Pevzner, Konstantin Tertyshnikov
Investigation: Konstantin Tertyshnikov, Nikita Beloborodov, Olivia Collet, Roman Isaenkov, Mustafa Al Marzooq, Pavel Shashkin, Mikhail Vorobev
Methodology: Alina Almukhametova, Roman Pevzner, Konstantin Tertyshnikov, Roman Isaenkov
Writing–original draft: Alina Almukhametova
Writing–review & editing: Alina Almukhametova, Boris Gurevich

Availability of data

Data are available on request to CO2CRC Ltd. (info@co2crc.com.au).

References

1. Calvin K, Dasgupta D, Krinner G, *et al*. IPCC, 2023: Climate Change 2023: Synthesis Report, Summary for Policymakers. In: *Climate Change 2023: Synthesis Report. Contribution of Working Groups I, II and III to the Sixth Assessment Report of the Intergovernmental Panel on Climate Change*. Geneva, Switzerland: IPCC; 2023:1-34.

   doi: 10.59327/IPCC/AR6-9789291691647.001

2. International Energy Agency. *Net Zero Roadmap: A Global Pathway to Keep the 1.5°C Goal in Reach—2023 Update*. International Energy Agency; 2023. Accessed January 23, 2026. https://www.iea.org/reports/net-zero-roadmap-a-global-pathway-to-keep-the-15-0c-goal-in-reach

3. Bachu S. CO2 storage in geological media: role, means, status and barriers to deployment. *Prog Energy Combust Sci*. 2008;34(2):254-273.

   doi: 10.1016/j.pecs.2007.10.001

4. Ringrose PS, Furre AK, Gilfillan SMV, *et al*. Storage of carbon dioxide in saline aquifers: physicochemical processes, key constraints, and scale-up potential. *Annu Rev Chem Biomol Eng*. 2021;12(1):471-494.

   doi: 10.1146/annurev-chembioeng-093020-091447

5. IEA Greenhouse Gas R&D Programme. Monitoring

Network Meeting Report. Technical Review 2023-TR05. IEA Greenhouse Gas R&D Programme; 2023. Accessed April 1, 2026. https://ieaghg.org/publications/monitoring-network-meeting-report/

6. Harvey S, Hopkins J, Kuehl H, O'Brien S, Mateeva A. Quest CCS facility: time-lapse seismic campaigns. *Int J Greenh Gas Control*. 2022;117:103665.

   doi: 10.1016/j.ijggc.2022.103665

7. Isaenkov R, Pevzner R, Glubokovskikh S, *et al*. An automated system for continuous monitoring of CO2 geosequestration using multi-well offset VSP with permanent seismic sources and receivers: Stage 3 of the CO2CRC Otway project. *Int J Greenh Gas Control*. 2021;108:103317.

   doi: 10.1016/j.ijggc.2021.103317

8. Yurikov A, Tertyshnikov K, Yavuz S, *et al*. Seismic monitoring of CO2 geosequestration using multi-well 4D DAS VSP: Stage 3 of the CO2CRC Otway project. *Int J Greenh Gas Control*. 2022;119:103726.

   doi: 10.1016/j.ijggc.2022.103726

9. Hopkins J, Mateeva A, Harvey S, Kiyashchenko D, Duan Y. Maturing DAS VSP as an onshore CCUS monitoring technology at the Quest CCS Facility. In: *Proceedings of the GeoConvention Conference*. September 13-15, 2021; Online.

10. Jenkins C, Barraclough P, Correa J, *et al*. Field tests of geological storage of CO2 at the Otway International Test Centre, Australia: trapping and monitoring the migrating plumes. *Geoenergy*. 2024;2(1):geoenergy2023-035.

    doi: 10.1144/geoenergy2023-035

11. Mishra A, Pajank L, Haese RR. High resolution characterization of lithological heterogeneity of the Paaratte Formation, Otway Basin (Australia), a coastal to shallow-marine deposit. *Geosciences*. 2019;9(6):278.

    doi: 10.3390/geosciences9060278

12. Pevzner R, Urosevic M, Popik D, *et al*. 4D surface seismic tracks small supercritical CO2 injection into the subsurface: CO2CRC Otway project. *Int J Greenh Gas Control*. 2017;63:150-157.

    doi: 10.1016/j.ijggc.2017.05.008

13. Watson M, Pevzner R, Dance T, *et al*. The Otway Stage 2C Project–End to end CO2 storage in a saline formation, comprising characterisation, injection and monitoring. In *Proceedings of the 14th Greenhouse Gas Control Technologies Conference (GHGT-14)*. October 21–25, 2018; Melbourne, Australia.

    doi: 10.2139/ssrn.3365633

14. Pevzner R, Isaenkov R, Yavuz S, *et al*. Seismic monitoring of a small CO2 injection using a multi-well DAS array: operations and initial results of Stage 3 of the CO2CRC Otway project. *Int J Greenh Gas Control*. 2021;110:103437.

    doi: 10.1016/j.ijggc.2021.103437

15. Popik S, Pevzner R, Tertyshnikov K, *et al*. 4D surface seismic monitoring the evolution of a small CO2 plume during and after injection: CO2CRC Otway Project study. *Explor Geophys*. 2020;51(5):570-580.

    doi: 10.1080/08123985.2020.1735934

16. Dillon PB. Vertical seismic profiling migration using the Kirchhoff integral. *Geophysics*. 1988;53(6):786-799.

    doi: 10.1190/1.1442514

17. Isaenkov R, Pevzner R, Glubokovskikh S, *et al*. Advanced time-lapse processing of continuous DAS VSP data for plume evolution monitoring: Stage 3 of the CO2CRC Otway project case study. *Int J Greenh Gas Control*. 2022;119:103716.

    doi: 10.1016/j.ijggc.2022.103716

18. Glubokovskikh S, Gurevich B, Shashkin P, *et al*. Near-Field Seismic Scattering Explains the Variation of DAS Amplitudes Inside a Leakage of Supercritical CO2. *Seismol Res Lett*. 2025;96(6):3718-3730.

    doi: 10.1785/0220240281

ACCSCIENCE PUBLISHING

Journal of Seismic Exploration

ARTICLE

Multi-constraint two-step intelligent prestack seismic inversion and its application: A case study in the Junggar Basin, Northwest China

Hongyan Qi[1,2], Zhenlin Wang[2,3], Wei Li[2]*, Tingming Tang[2], Juqin Yao[2], Gang Chen[2], and Qingyong Luo[1]

[1]Department of Geology, College of Geosciences, China University of Petroleum (Beijing), Beijing, China

[2]Well Logging Research Institute, Research Institute of Exploration and Development, Xinjiang Oilfield Company, PetroChina, Karamay, Xinjiang, China

[3]Department of Engineering Mechanics, College of Petroleum Engineering, China University of Petroleum (Beijing), Beijing, China

(This article belongs to the *Special Issue: Advanced Artificial Intelligence Theories and Methods for Seismic Exploration*)

Abstract

Prestack seismic inversion serves as a bridge connecting seismic observations to subsurface rock properties, enabling quantitative estimation of elastic parameters, such as P-wave velocity (V_p), S-wave velocity (V_s), and density (ρ), which provides direct evidence for reservoir prediction and fluid identification. However, simultaneously inverting V_p, V_s, and ρ from prestack data is a highly nonlinear and ill-posed problem. Traditional inversion methods often struggle to achieve an optimal balance among accuracy, stability, and physical consistency. In recent years, deep learning has offered new insights through its powerful nonlinear mapping capabilities. However, purely data-driven models rely heavily on large labeled datasets and often overlook physical laws, leading to inversion results that lack geological consistency. To overcome these limitations, this paper proposes a multi-constraint two-step intelligent prestack inversion method. First, near-angle seismic data were used to robustly invert P-wave impedance (I_p). Then, employing TransUNet as the core network, a multi-constraint joint loss function was constructed to systematically integrate four types of prior information: (i) seismic data matching to ensure consistency with observed data. (ii) Physical relationship constraints linking I_p, V_p, and ρ. (iii) Empirical statistical relationships from well logs to regularize the ill-posed ρ inversion. (iv) Well data fitting to realize the matching of inversion results at well locations. This achieved high-precision inversion of V_p, V_s and ρ under the dual guidance of data driving and physical mechanisms. Tests on the Marmousi 2 model and actual shale reservoir data from the Junggar Basin demonstrated that the proposed method significantly improved inversion accuracy, stability, and noise resistance for all three parameters, particularly ρ, validating its potential for practical applications.

Keywords: Prestack seismic inversion; Multiple constraints; TransUNet; Two-step method

***Corresponding author:**
Wei Li (iwei@petrochina.com.cn)

Citation: Qi H, Wang Z, Li W, *et al*. Multi-constraint two-step intelligent prestack seismic inversion and its application: A case study in the Junggar Basin, Northwest China. *J Seismic Explor*. 2026;35(3):026040013. doi: 10.36922/JSE026040013

Received: January 20, 2026

Revised: April 20, 2026

Accepted: April 20, 2026

Published online: May 28, 2026

Copyright: © 2026 Author(s). This is an Open-Access article distributed under the terms of the Creative Commons Attribution License, permitting distribution, and reproduction in any medium, provided the original work is properly cited.

Publisher's Note: AccScience Publishing remains neutral with regard to jurisdictional claims in published maps and institutional affiliations.

1. Introduction

Prestack seismic inversion serves as a critical bridge connecting seismic observations to subsurface rock properties. By analyzing and processing amplitude variations with incident angle in prestack gathers, this approach enables quantitative estimation of elastic parameters, such as P-wave velocity (V_p), S-wave velocity (V_s), and density (ρ), providing direct evidence for reservoir lithology identification, property prediction, and fluid detection. The accuracy of these parameters directly determines the reliability of subsequent reservoir modeling and hydrocarbon evaluation, making them core tasks in geophysical exploration.[1]

However, simultaneously inverting V_p, V_s, and ρ from prestack seismic data presents a highly nonlinear and ill-posed problem.[2,3] The challenges primarily arise from three aspects: firstly, the limited frequency band of seismic data and noise interference lead to significant non-uniqueness in inversion results;[4] secondly, ρ parameters are considerably less sensitive to seismic amplitudes compared to velocity parameters, particularly at small to medium incident angles, resulting in generally low inversion accuracy—a persistent challenge in the field of prestack inversion;[5,6] finally, the complex physical coupling relationships among these three parameters make it difficult for traditional methods to maintain this inherent consistency during the inversion process.

To address these challenges, geophysicists have developed a series of inversion theories and methods. Early deterministic inversion methods, such as linear inversions based on Zoeppritz approximations, including Aki and Richards[7] or Shuey[8] equations, offer high computational efficiency and good lateral continuity. However, their linearization assumptions limit their application accuracy in complex structures or under large incident angles.[9] To improve resolution, the Bayesian inversion framework, represented by sparse-spike inversion, has been widely adopted. By incorporating prior constraints such as the Cauchy,[10] Laplace,[11] or generalized Gaussian distribution,[12] it effectively highlights the sparse reflectivity characteristics of strata. While such approaches improve vertical resolution to some extent, they often struggle to quantify inversion uncertainty effectively and tend to become trapped in local optima. On the other hand, stochastic inversion methods, such as geostatistical inversion[13,14] and Markov Chain Monte Carlo approaches,[15] can provide high-resolution inversion results and uncertainty assessments. However, their substantial computational costs and strong dependence on well control limit their application in large-scale practical production.[16-19]

In recent years, artificial intelligence technologies, particularly deep learning, have opened new pathways for prestack inversion through their powerful nonlinear mapping capabilities.[20-22] By constructing deep neural networks such as convolutional neural networks (CNN),[23,24] recurrent neural networks,[25,26] and U-Net,[27] researchers can directly learn complex mappings from seismic data to elastic parameters. The TransUNet architecture, which integrates the global modeling capabilities of transformers,[28] has shown particular promise in capturing both local waveform details and global geological structural features from seismic data.[29] However, purely data-driven deep learning methods still face significant challenges. First, these methods rely heavily on large quantities of high-quality labeled data, whereas the limited number of wells in actual working areas often leads to network overfitting and insufficient generalization.[30] Second, purely data-driven models learn only from statistical correlations, making it difficult to ensure that inversion results comply with known physical laws and intrinsic parameter relationships, raising concerns about the physical consistency of results.[31,32]

To overcome these limitations, the concept of deeply integrating physical mechanisms with data-driven approaches has emerged.[33] Physics-informed neural networks incorporate wave equations or Zoeppritz-based approximations as physical constraints into loss functions, guiding networks to learn solutions that conform to physical laws and significantly improving the reliability and structural rationality of inversion results.[34,35] Biswas *et al.*[31] achieved promising results in unsupervised prestack inversion using physics-guided CNNs. These studies demonstrate that incorporating prior information is key to improving the generalization capability and robustness of deep learning methods.[36] Nevertheless, current methods still require further investigation in areas such as handling strong multi-parameter coupling, addressing fragmented information utilization, and systematically integrating multi-source information (physical laws, empirical statistics, well data, etc.).

It should be noted that although this study uses shale reservoirs as an application scenario and shale that exhibits significant anisotropic characteristics,[37] this work aims to provide a new, reliable solution to a fundamental reservoir characterization problem—improving inversion accuracy of conventional elastic parameters, particularly ρ. The shale example serves only to validate the proposed method's effectiveness. Therefore, this study is conducted under the assumption of isotropic media and has not incorporated anisotropic parameters.

In view of these considerations, we proposed a multi-constraint fusion-driven stepwise intelligent inversion method for prestack three-parameter inversion. This

method developed a dual closed-loop inversion workflow driven by well data while integrating physical laws and empirical statistical relationships. First, near-angle seismic data were used to robustly invert P-wave impedance (I_p). Then, using full-angle seismic data with TransUNet as the core network framework, a multi-constraint joint loss function was developed to systematically integrate four types of prior information: seismic data matching, physical relationship constraints, empirical statistical relationships, and well data fitting. This achieved prestack three-parameter inversion under dual guidance from data-driven constraints and physical mechanisms. Finally, through testing on the Marmousi 2 model and actual shale reservoir data from the Junggar Basin, the proposed method demonstrated superior performance in improving inversion accuracy, stability, and noise resistance for three parameters, especially ρ.

2. Materials and methods

2.1. Stepwise inversion workflow for prestack three parameters

This study developed an intelligent dual closed-loop workflow guided by well data and integrating physical and empirical constraints for accurate prestack three-parameter inversion. The overall architecture is shown in Figure 1. The workflow employed a two-step inversion strategy. In the first step, as indicated by the green arrows and boxes in the figure, near-angle seismic data were input into Inversion Model 1 to obtain I_p. In the second step, as indicated by the red arrows and boxes, full-angle seismic data were input into Inversion Models 1 and 2 to derive the final V_p, V_s, and ρ. The workflow primarily incorporated the following four constraint mechanisms:

(i) Seismic response matching constraint ($Loss_1$): This constraint minimized the difference between synthetic and actual seismic records, enabling closed-loop correction at the seismic response level. Synthetic seismograms were generated via forward modeling based on the Aki–Richards approximation and convolution model. Physically, it guaranteed that inverted parameters could accurately reconstruct field seismic records via reflectivity-wavelet convolution in forward modeling, which complied with seismic wave propagation laws. This constraint supplied effective information within the seismic frequency band, maintained regional consistency and lateral continuity, and served as the essential bridge between seismic observations and subsurface petrophysical properties. The corresponding objective function is defined as **Equation 1**:

$$Loss_1 = \frac{1}{XY}\sum_{i=1}^{X}\sum_{j=1}^{Y}\left\|\mathrm{S}(i,j)-\tilde{\mathrm{S}}(i,j)\right\|_2^2 \tag{1}$$

where S and $\tilde{S}$ are the actual and synthetic seismic records, respectively. X and Y are the number of samples in the horizontal and vertical directions, and i and j are the current horizontal and vertical sample indices.

(ii) Physical relationship constraint ($Loss_2$): Leveraging the stable and effective inversion of I_p, this constraint enforced the deterministic rock-physics relationship $I_p = V_p \cdot \rho$. By penalizing deviations from this relationship, the constraint avoided mathematically valid but physically contradictory combinations of V_p and ρ, mitigated the ill-posedness of the inversion, and ensured physical consistency among all inverted results. We introduced the following loss function as a constraint (**Equation 2**):

$$Loss_2 = \frac{1}{XY}\sum_{i=1}^{X}\sum_{j=1}^{Y}\left\|\tilde{I}_p(i,j)-\tilde{V}_p(i,j)\cdot\tilde{\rho}(i,j)\right\|_2^2 \tag{2}$$

where, $\tilde{I}_p$, $\tilde{V}_p$, and $\tilde{\rho}$ are the inverted I_p, V_p, and ρ, respectively.

(iii) Empirical formula constraint ($Loss_3$): Based on the statistical relationship between V_p and ρ from well logs, this loss function imposed a constraint on the ρ term, optimizing network parameters and enhancing the stability and reliability of ρ inversion. Although less rigorous than deterministic physical laws, it provided crucial statistical guidance on density inversion, which was notoriously insensitive to seismic amplitude variations, thereby regularizing the solution space and improving inversion stability. The updated objective function can be written as **Equation 3**:

$$Loss_3 = \frac{1}{XY}\sum_{i=1}^{X}\sum_{j=1}^{Y}\left\|\tilde{\rho}(i,j)-a\cdot(\tilde{V}_p(i,j))^b\right\|_2^2 \tag{3}$$

where a and b are empirical coefficients fitted from well data.

(iv) Well data fitting constraint ($Loss_4$): **Equation 4** minimizes the difference between the inverted results and the true values at the well locations, serving as a supervised learning signal. This ensured that the network's predictions at sparse but accurate control points matched true formation information, providing high-frequency constraints from well logs and preventing the inversion from drifting into

geologically implausible scenarios. The objective function is given by:

$$Loss_4 = \frac{1}{NM}\sum_{i=1}^{N}\sum_{j=1}^{M}\left\|\mathrm{m}(i,j)-\tilde{m}(i,j)\right\|_2^2 \quad (4)$$

where, N is the number of wells, M is the total number of samples in time for a single well, m and $\tilde{m}$ are the true and inverted three-parameter values at the well location, respectively.

In summary, this study developed a joint loss-function system that integrates multiple constraints (**Equation 5**). This system not only ensured spatial prediction rationality through seismic response matching but also enhanced inversion stability via physical and empirical constraints, and guaranteed reliability at well locations through well data fitting. The synergistic action of these constraints achieved deep integration between data-driven learning and physical mechanisms, resulting in a final prediction model with high accuracy, strong generalization, and good spatial continuity.

$$Loss_{total} = \alpha Loss_1 + \beta Loss_2 + \gamma Loss_3 + \eta Loss_4 \quad (5)$$

where, α, β, γ, and η are weight coefficients for $Loss_1$, $Loss_2$, $Loss_3$ and $Loss_4$, respectively. Since $Loss_1$ and $Loss_4$ represent the losses between the fitted actual data and the synthetic or inverted data, they possess clear physical meanings, making the minimization of these two terms highly reliable; accordingly, α and η are generally set to 1. In contrast, $Loss_2$ and $Loss_3$ are derived from inversion results or fitting relationships with relatively lower reliability, so β and γ are typically set between 0 and 0.5 and are manually adjusted based on the inversion performance to achieve optimal results. These coefficients are adjusted based on the quality and credibility of the seismic, inversion, and well log data. During training, the Adam optimizer iteratively updates the network parameters by minimizing the total loss function to achieve optimal prediction performance.

2.2. Network architecture

The aforementioned workflow primarily involves two inversion networks, both utilizing the TransUNet architecture. This architecture integrates the local feature-extraction capability of CNN with the global dependency modeling strength of the Transformer within a U-Net encoder–decoder framework. It aims to establish the complex nonlinear mapping between prestack seismic gathers and the three parameters. Figure 2 shows the network structure with an encoder and a decoder.

2.2.1. Encoder part

The encoder is responsible for extracting both local and global features from the input data, comprising CNN and transformer modules. The CNN module captures multi-scale waveform responses and structural features from seismic data by adjusting the dilation rates of convolutional layers to control the receptive field. The Transformer module performs global modeling of the input data using self-attention, capturing long-range dependencies in both vertical and horizontal directions. The core computation of self-attention is as follows:

For an input sequence $I \in \mathbb{R}^{L\times d_m}$ (sequence length L, feature dimension d_m), query (Q), key (K), and value (V) matrices are obtained via linear transformations ($Q = IW^Q$, $K = IW^K$, $V = IW^V$). Here, W^Q, W^K, and $W^V \in \mathbb{R}^{d_m\times d_k}$ are learnable weight matrices, and d_k is the projection dimension. The attention is then calculated as **Equation 6**:

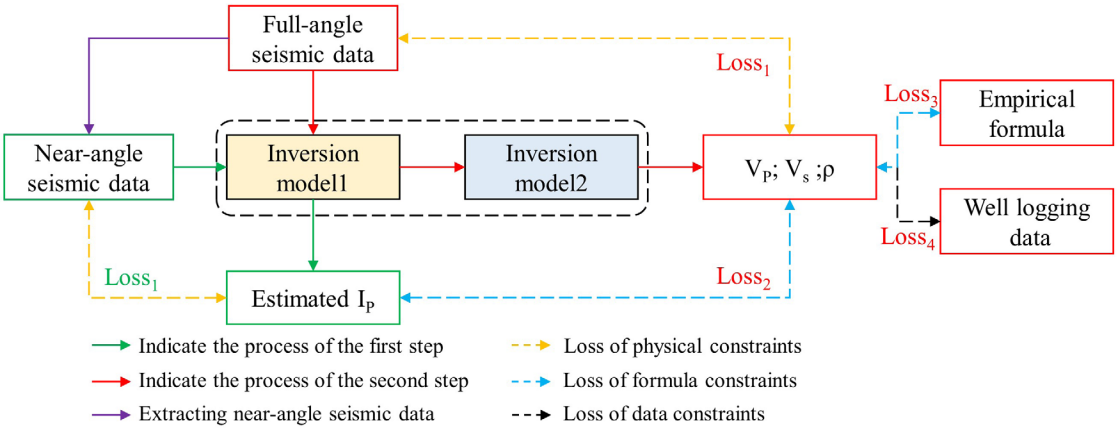

Figure 1. Stepwise inversion workflow for prestack three parameters

$$Attention(Q,K,V) = soft\max(\frac{QK^T}{\sqrt{d_k}})V \quad (6)$$

where, QK^T is used to compute the correlation scores between all positions, $\sqrt{d_k}$ is applied for scaling to prevent vanishing gradients, and the softmax function normalizes the scores so that each position can incorporate global information.

In implementation, the input data is first processed through six 3 × 3 convolutional layers to capture local patterns and details, thereby forming initial shallow features. These features are then linearly projected into a transformer encoder. Following the classical architecture, the encoder comprises multi-head self-attention layers, feed-forward network layers, layer normalization, and residual connections. To balance model expressiveness with computational efficiency, we configure the encoder with four attention heads, a hidden dimension of 512, and a depth of $n = 6$ transformer layers. Leveraging its multi-head self-attention mechanism, the network effectively captures vertical depositional patterns and lateral distributions, ultimately outputting deep features that incorporate long-range dependencies and global contextual information.

2.2.2. Decoder part

The decoder is designed to perform multi-scale feature fusion and restore spatial resolution from the deep feature representations. Through three successive upsampling stages, it progressively enlarges the spatial dimensions of the deep features. At each skip connection, the CNN-extracted shallow features are concatenated with the corresponding upsampled features across scales. A repeated sequence of convolution, upsampling, and feature concatenation operations gradually reconstructs the spatial architecture of the parameter volume, enabling precise localization of geological interfaces such as thin layers. Finally, a 1 × 1 convolutional layer maps and integrates the channels to produce the target parameter inversion result, matching the input data dimensions.

In summary, the TransUNet architecture, through its hybrid design and multi-scale feature fusion, provides core algorithmic support for high-precision elastic parameter inversion under complex geological conditions. Embedding this structure within the dual closed-loop system, combined with the progressive multi-constraint mechanism, establishes a solid technical foundation for elastic parameter inversion.

2.2.3. Evaluation of prediction results

We use the mean absolute error (MAE), root-mean-square error (RMSE), and correlation coefficient (R) as evaluation metrics for the three-parameter inversion results. MAE is the average of absolute differences between inverted and actual values. A smaller MAE indicates better inversion performance. Its value range is [0, +∞). This metric weights all errors equally and is relatively robust to outliers. The formula is shown in **Equation 7**:

$$MAE = \frac{1}{n}\sum_{i=1}^{n}|m_i - \tilde{m}_i| \quad (7)$$

An RMSE is the square root of the average of squared errors. Its value range is [0, +∞). A smaller RMSE indicates that the inverted values are closer to the true values. Since errors are squared values, RMSE is more sensitive to large errors, reflecting the impact of outliers. The formula is shown in **Equation 8**:

$$RMSE = \sqrt{\frac{1}{n}\sum_{i=1}^{n}(m_i - \tilde{m}_i)^2} \quad (8)$$

The R measures the linear correlation between two variables, ranging from [−1, 1]. The sign indicates the direction of the correlation, while the absolute value indicates the strength. An absolute value closer to 1 signifies stronger linear correlation, and closer to 0 signifies weaker correlation. The formula is shown in **Equation 9**:

$$R = \frac{1}{n}\frac{\sum_{i=1}^{n}(m_i - \mu_m)(\tilde{m}_i - \mu_{\tilde{m}})}{\sqrt{\sum_{i=1}^{n}(m_i - \mu_m)^2}\sqrt{\sum_{i=1}^{n}(\tilde{m}_i - \mu_{\tilde{m}})^2}} \quad (9)$$

In these formulas, m_i and $\tilde{m}_i$ represent the *i-th* actual and inverted values, respectively. n is the total number of samples. μ_m and $\mu_{\tilde{m}}$ are the means of the actual and inverted values, respectively.

3. Results

3.1. Prestack three-parameter inversion under noise-free conditions

Based on the Marmousi 2 model, this study used selected V_p, V_s, and ρ data to synthesize prestack seismic records at three incidence angles (10°, 20°, and 30°) using a Ricker wavelet with a dominant frequency of 30 Hz. Low-pass filtering was applied to the three-parameter data to construct corresponding low-frequency models. Ten traces were uniformly selected from the known three-parameter profiles as labels for subsequent data-driven tasks. Figure 3A–C displays the seismic data at the three angles. Figure 3D–F shows the known three-parameter profiles, with black solid lines indicating the positions of

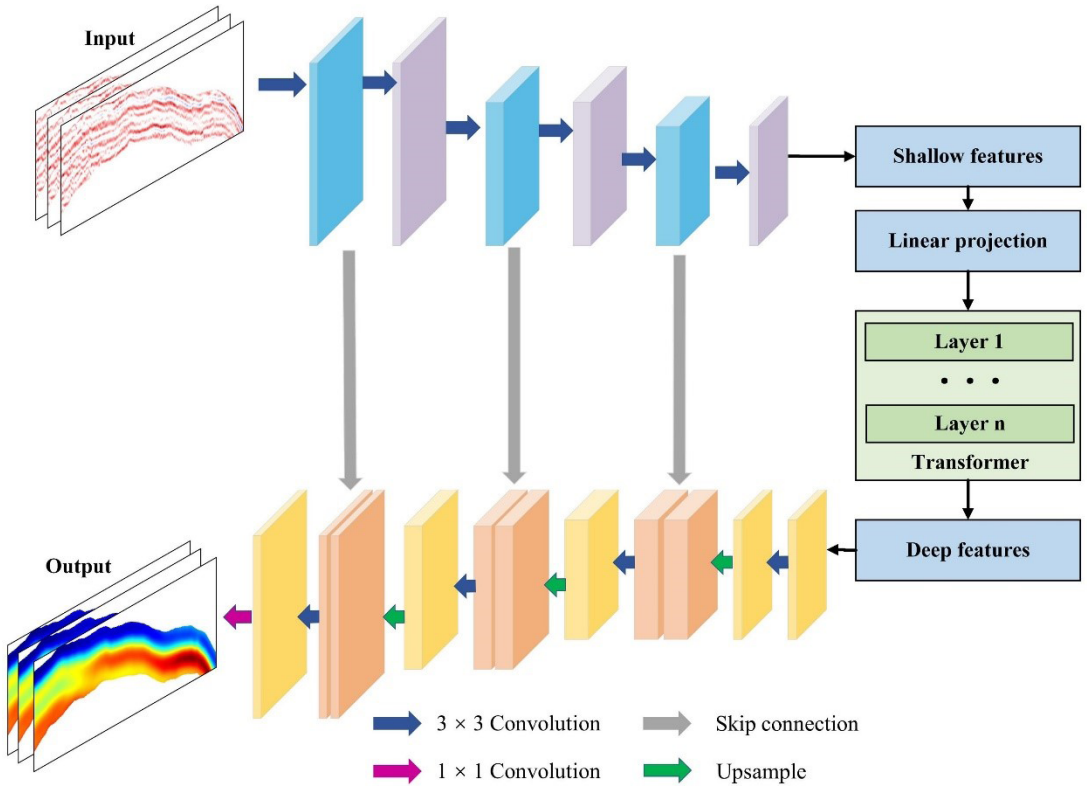

Figure 2. TransUNet network architecture. It comprises two primary components: an encoder and a decoder. The encoder is responsible for feature extraction, while the decoder performs feature fusion and restores the spatial resolution.

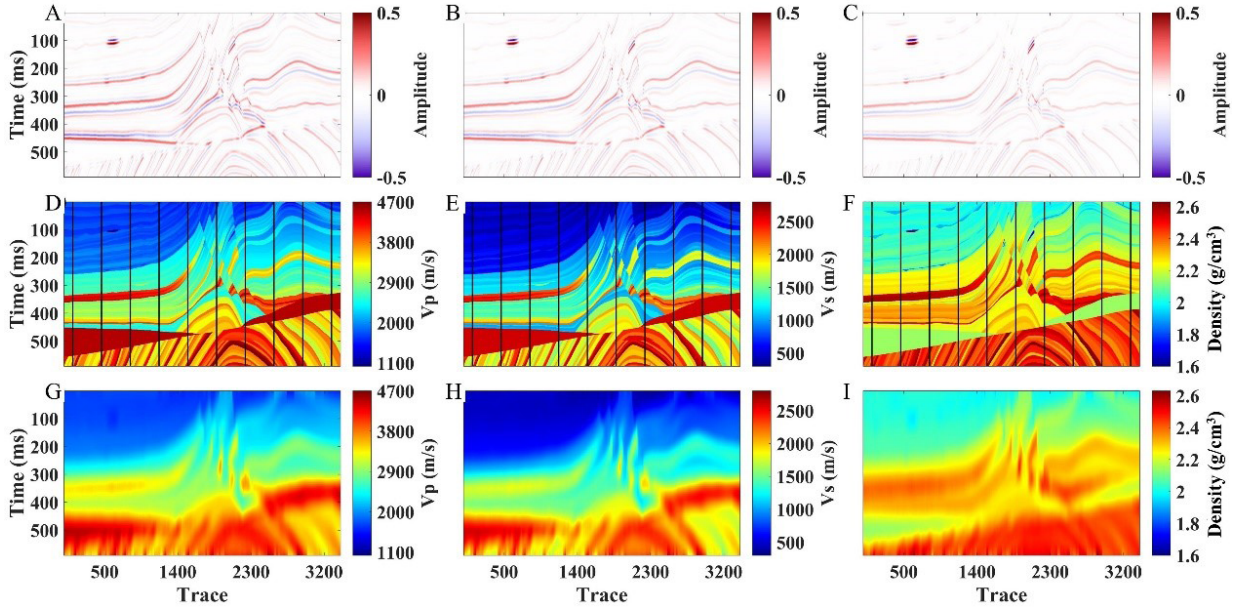

Figure 3. Seismic data, elastic parameters and the corresponding low-frequency models. The seismic data at (A) 10°, (B) 20°, and (C) 30°. The elastic parameters of (D) P-wave velocity, (E) S-wave velocity, and (F) density. The low-frequency models of (G) P-wave velocity, (H) S-wave velocity, and (I) density. The black solid lines indicating the positions of the uniformly selected ten pseudo-well traces. The low-frequency models are generated using a 10 Hz low-pass filter.

the uniformly selected 10 pseudo-well traces. Figure 3G–I presents the constructed low-frequency models for the three parameters, spanning 0–10 Hz.

Following the proposed workflow, two inversion models were trained using the synthetic three-angle seismic data, low-frequency models, pseudo-well data, and wavelets. The training epoch was set to 600 with a batch size of 128. The weights in the total loss function (α, β, γ, and η) were set to 1.0, 0.5, 0.5, and 1.0, respectively. The trained models were then used for inversion, with the outputs designated as proposed. For systematic comparison, an alternative intelligent method was designed. This method used a single inversion network directly from seismic data to the three parameters, without physical or empirical constraints, keeping all other settings identical. The corresponding inversion results were denoted as intelligent. Additionally, the results obtained using the direct inversion method with L_2-norm constraints were denoted as traditional for comparative analysis. During the aforementioned inversion process, the synthetic seismic data were generated through forward modeling using the Aki–Richards approximation and the convolution model. Correspondingly, the inversion was also performed using this approximation equation to ensure consistency in the forward modeling process. The objective function adopted in the traditional method is given by **Equation 10**:

$$J(m) = \arg\min \left\| S - Gm \right\|_2^2 + \lambda \left\| m - m_0 \right\|_2^2 \quad (10)$$

where S represents the observed seismic data, G denotes the forward modeling operator, m is the parameter to be inverted, m_0 is the low-frequency model corresponding to the inversion parameters, and λ is the regularization parameter. The generalized inverse method was used as the optimization algorithm.

The inversion results from the three methods are shown in Figure 4, and the absolute errors compared to the true models are shown in Figure 5. Figure 4 shows that all three methods can effectively invert the three-parameter profiles. Compared to the known profiles, the proposed method yielded better results, particularly in the areas marked by black rectangles and arrows. The error profiles in Figure 5 clearly show that the proposed method generally exhibited smaller errors. Differences among the three methods were more pronounced near the upper unconformity of the wedge-shaped body in the lower-left corner for both velocity profiles (red rectangle) and around the lens body in the upper-left corner for the ρ profile (red rectangle).

Figure 6 shows the inversion results for the 666th trace (a blind well). In Figure 6A–C, the black solid and dashed lines represent the true model and low-frequency model, respectively. The blue, green, and red solid lines represent results from the traditional, intelligent, and proposed methods, respectively. Purple boxes highlight key areas. For V_p and V_s (Figure 6A and 6B), the differences among the three methods were subtle, but within the purple boxes, the proposed method aligned more closely with the true values. For ρ (Figure 6C), the traditional method showed substantial oscillations and fluctuations, performing worse compared to the intelligent method.

Table 1 presents the evaluation metrics (MAE, RMSE, R) for the three inversion results against the true values. Lower MAE and RMSE, and a higher R, indicate better performance. Analysis showed that the proposed two-step constrained method maintained good accuracy for V_p and V_s inversion while significantly improving the ρ inversion results. Specifically, for V_p inversion, it reduced MAE by 38.2% compared to the traditional method and by 28.8% compared to the intelligent method. For V_s inversion, MAE was reduced by 38.1% and 28.4%, respectively. In ρ inversion, MAE decreases by 17.6% and 24.2%, respectively. Furthermore, the proposed method achieved substantially lower RMSE and higher R, particularly in ρ inversion, where R achieved 0.9771. These results demonstrate that the proposed approach not only improved inversion accuracy and stability but also enhanced the physical consistency among parameters.

Table 1. A comparison of the inverted results using the three inversion methods on the seismic data (noise-free)

Target parameter	Method	MAE	RMSE	*R*
V_p(m/s)	Tradition	80.5872	138.0611	0.9885
	Intelligence	69.9539	111.0208	0.9925
	Proposed	49.7904	79.6904	0.9961
V_s(m/s)	Tradition	70.0194	116.1000	0.9865
	Intelligence	60.5759	94.0233	0.9911
	Proposed	43.3690	69.9909	0.9950
ρ (g/cm^3)	Tradition	0.0289	0.0443	0.9654
	Intelligence	0.0314	0.0481	0.9595
	Proposed	0.0238	0.0366	0.9771

Abbreviations: MAE: Mean absolute error; RMSE: Root-mean-square error.

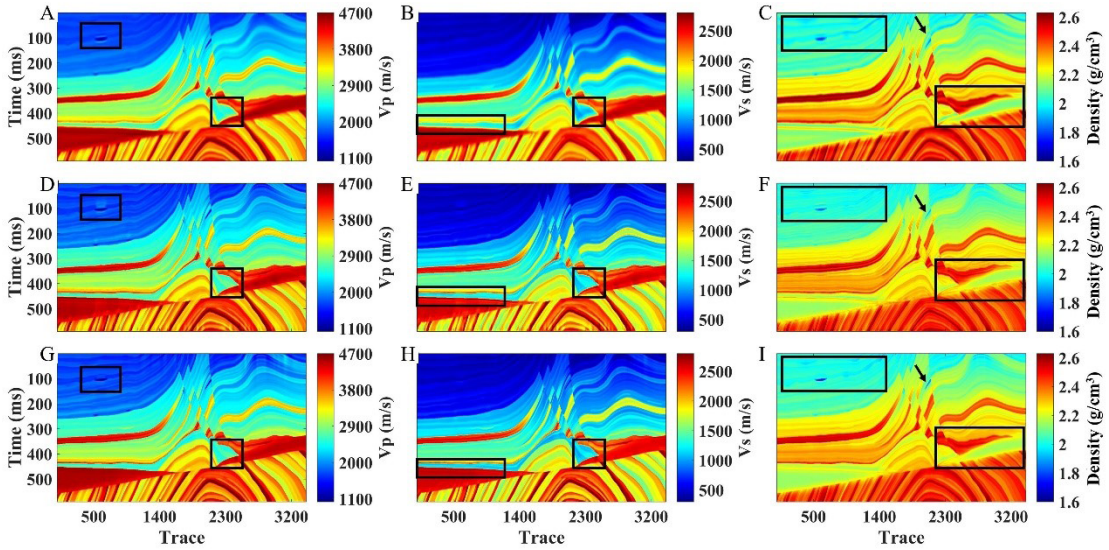

Figure 4. The inversion results of elastic parameters using three different methods. The predicted elastic parameters using the traditional method: (A) P-wave velocity, (B) S-wave velocity, and (C) density. The predicted elastic parameters using the intelligent method: (D) P-wave velocity, (E) S-wave velocity, and (F) density. The predicted elastic parameters using the proposed method: (G) P-wave velocity, (H) S-wave velocity, and (I) density.

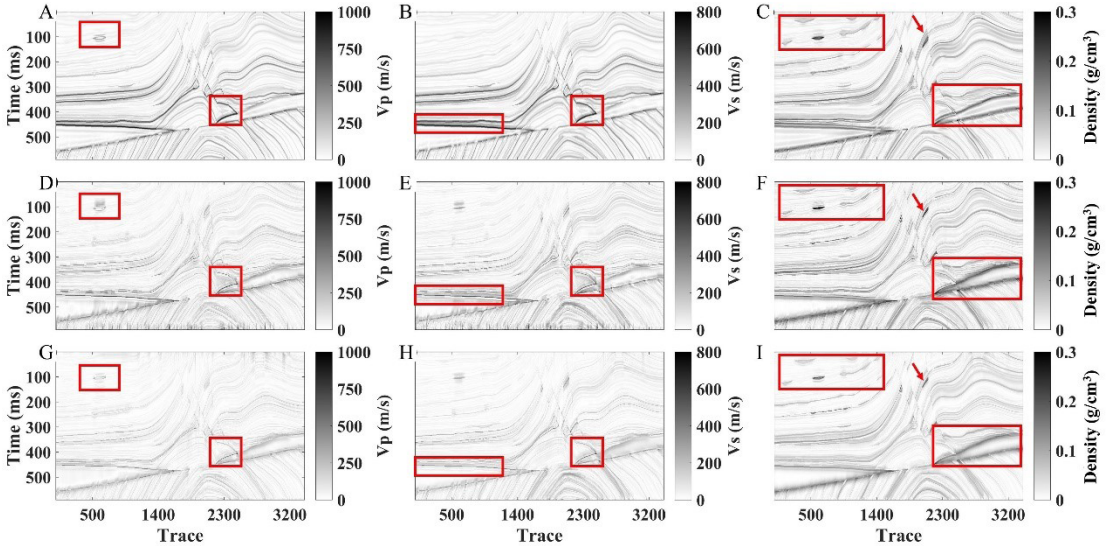

Figure 5. The absolute error between the inversion results from the three different methods and the true values. The absolute error using the traditional method: (A) P-wave velocity, (B) S-wave velocity, and (C) density. The absolute error using the intelligent method: (D) P-wave velocity, (E) S-wave velocity, and (F) density. The absolute error using the proposed method: (G) P-wave velocity, (H) S-wave velocity, and (I) density.

3.2. Prestack three-parameter inversion under noisy conditions

To test the robustness of the proposed method, 20% random Gaussian noise was added to the synthetic seismic data. The three methods were then applied to invert the noisy data. Figure 7 shows the inversion results, and Figure 8 shows the absolute errors. The layout is the same as Figures 4 and 5. All three methods exhibited some noise resistance, but the traditional method and intelligent method performed slightly worse, with visible noise in the inverted V_s and ρ profiles. Compared with the proposed method, the baseline method showed poorer overall results, with noticeable differences in the areas marked by black or red rectangles and arrows.

Figure 9 shows the results for the 666th trace with 20% noise. In Figure 9A–C, the black solid and dashed lines represent the true model and low-frequency model, respectively. The blue, green, and red solid lines represent results from the traditional, intelligent, and proposed methods, respectively. As observed, the inversion results

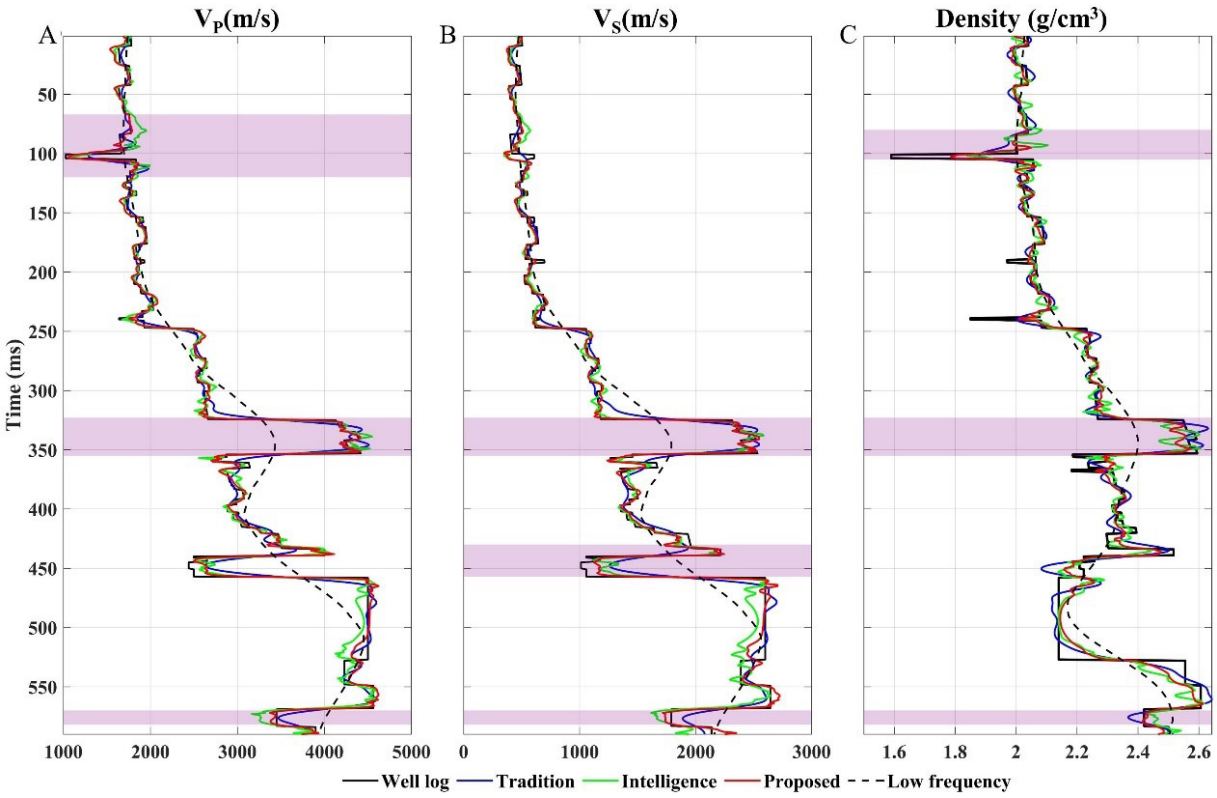

Figure 6. The inverted results of the 666th trace data (noise-free). (A) A comparison of the inverted (A) P-wave velocity, (B) S-wave velocity, and (C) density using the three inversion methods. The solid lines in black, blue, green, and red represent true data, results from the traditional, intelligent, and proposed methods, respectively, while the black dashed line represents the low-frequency model.

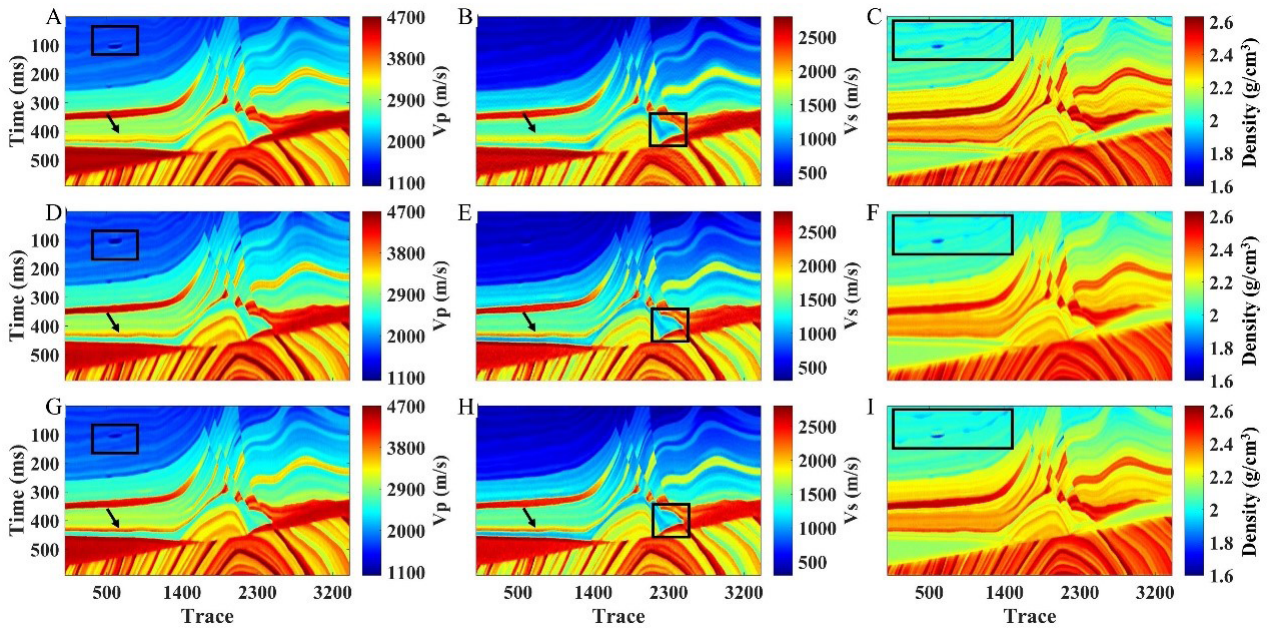

Figure 7. The inversion results of elastic parameters using three different methods (with 20% noise). The predicted elastic parameters using the traditional method: (A) P-wave velocity, (B) S-wave velocity, and (C) density. The predicted elastic parameters using the intelligent method: (D) P-wave velocity, (E) S-wave velocity, and (F) density. The predicted elastic parameters using the proposed method: (G) P-wave velocity, (H) S-wave velocity, and (I) density.

from all three methods degraded under noisy conditions relative to the noise-free case, exhibiting increased noise-induced fluctuations. This was particularly evident in the V_s and ρ inversion outcomes. However, within the region marked by the purple box in the figure, the results of our proposed method clearly align more closely with the true values. Moreover, the advantages of the proposed approach were more pronounced in the inversion of V_s and ρ.

Table 2 presents the evaluation metrics for the noisy case. The analysis indicated that noise degraded performance across all inversion methods. Nevertheless, the proposed method consistently demonstrated superior accuracy and robustness. Specifically, for V_p inversion, the proposed method achieved MAE reductions of 30.31% and 20.83% compared to traditional and intelligent methods, respectively, with RMSE decreasing by 30.53% and 20.47%, respectively. In V_s inversion, MAE was lowered by 41.40% and 19.90%, and RMSE by 40.66% and 20.12%, respectively. The ρ inversion showed the most substantial improvements, with MAE reduced by 33.95% and 22.19%, RMSE decreased by 29.00% and 22.20%, and R increased by 7.70% and 1.79% relative to the two baseline methods, respectively. These results affirm that the proposed method maintained higher overall accuracy and greater robustness compared to existing approaches.

Table 2. A comparison of the inverted results using the three inversion methods on the seismic data (with 20% noise)

Target parameter	Method	MAE	RMSE	R
V_p(m/s)	Tradition	102.7359	164.3678	0.9837
	Intelligence	90.4232	143.5943	0.9875
	Proposed	71.5926	114.2027	0.9922
V_s(m/s)	Tradition	101.0245	155.3812	0.9755
	Intelligence	73.9123	115.4408	0.9865
	Proposed	59.1995	92.2067	0.9915
ρ (g/cm^3)	Tradition	0.0377	0.0538	0.9050
	Intelligence	0.0320	0.0491	0.9576
	Proposed	0.0249	0.0382	0.9747

Abbreviations: MAE: Mean absolute error; RMSE: Root-mean-square error.

3.3. Application to real data

We applied the proposed method to real two-dimensional prestack three-angle seismic data from a shale reservoir in the Junggar Basin, China (5°, 12.5°, and 20°, shown in Figure 10A–C). The study area contains three wells (W1, W2, W3), covers 1,100 common depth points, and has a record length of 390 ms. The sampling interval was 2 ms. Only the target zone data were displayed. The reflection structure in this area showed relatively minor overall variations, but the lower middle part between wells W2 and W3 exhibited weaker reflection amplitudes. W1 and W3 were used as training wells, while W2 served as the blind well to validate the model's inversion performance.

Wavelet estimation and low-frequency model construction (Figure 10D–F) were performed based on the seismic data and well logs. The input data were normalized for network training. Model parameters and constraint weights were adjusted iteratively based on inversion results until satisfactory outcomes were achieved.

The inversion results of the three methods are presented in Figure 11. Figure 11A–C shows the three-parameter inversion results obtained using the traditional method, Figure 11D–F corresponds to those of the intelligent method, and Figure 11G–I displays the results of the proposed method. In each row, the V_p, V_s, and ρ are arranged from left to right. It can be observed that all three methods yielded reasonably good reconstructions of the V_p. However, noticeable differences were observed in the V_s and ρ profiles. For the V_s, the result of the traditional method closely resembled the low-frequency model, making it difficult to effectively distinguish the two sets of strata within the black rectangle in the figure. The intelligent method result exhibited noticeable noise, which also hindered clear identification of the strata. In contrast, the proposed method delivered a more accurate V_s inversion, showing good agreement with well log data. Regarding ρ inversion, the traditional method produced profiles with considerable fluctuations, corresponding to the darker-colored areas in the image. The intelligent method failed to adequately represent the reservoir within the black rectangle. On the other hand, the ρ inversion result from the proposed method was overall more stable compared to other methods, clearly revealing ρ variations and providing a better characterization of the reservoir features.

A comparison of the three inversion results at trace 526 is presented in Figure 12. In Figure 12A–C, the black solid and dashed lines represent the true model and low-frequency model, respectively. The blue, green, and red solid lines represent results from the traditional, intelligent, and proposed methods, respectively. In the region marked

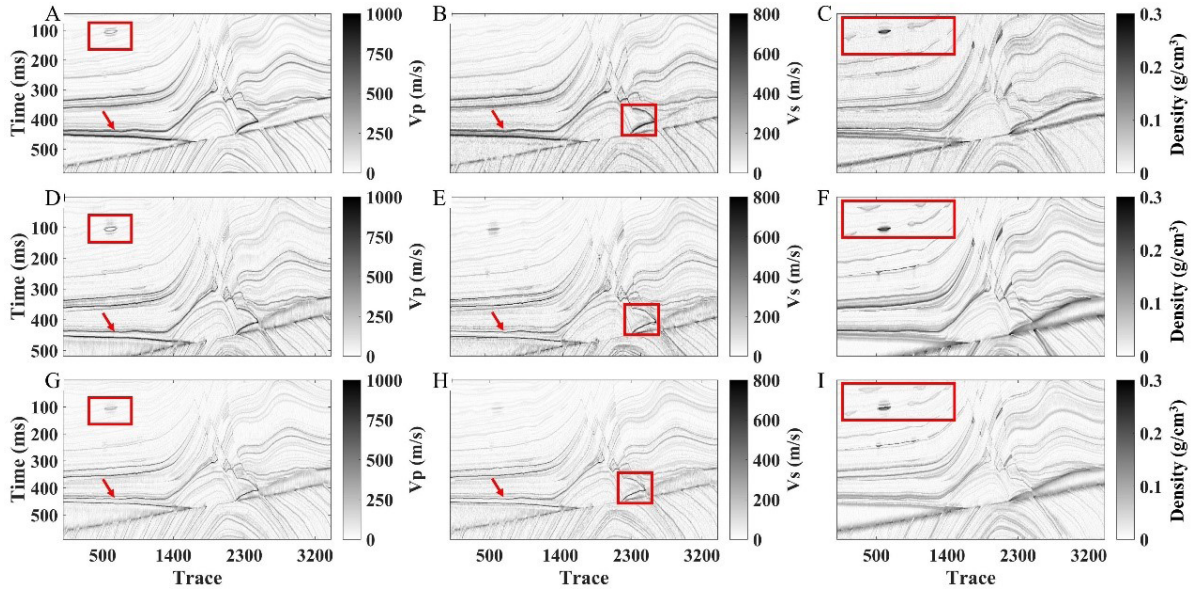

Figure 8. The absolute error between the inversion results from the three different methods and the true values (with 20% noise). The absolute error using the traditional method: (A) P-wave velocity, (B) S-wave velocity, and (C) density. The absolute error using the intelligent method: (D) P-wave velocity, (E) S-wave velocity, and (F) density. The absolute error using the proposed method: (G) P-wave velocity, (H) S-wave velocity, and (I) density.

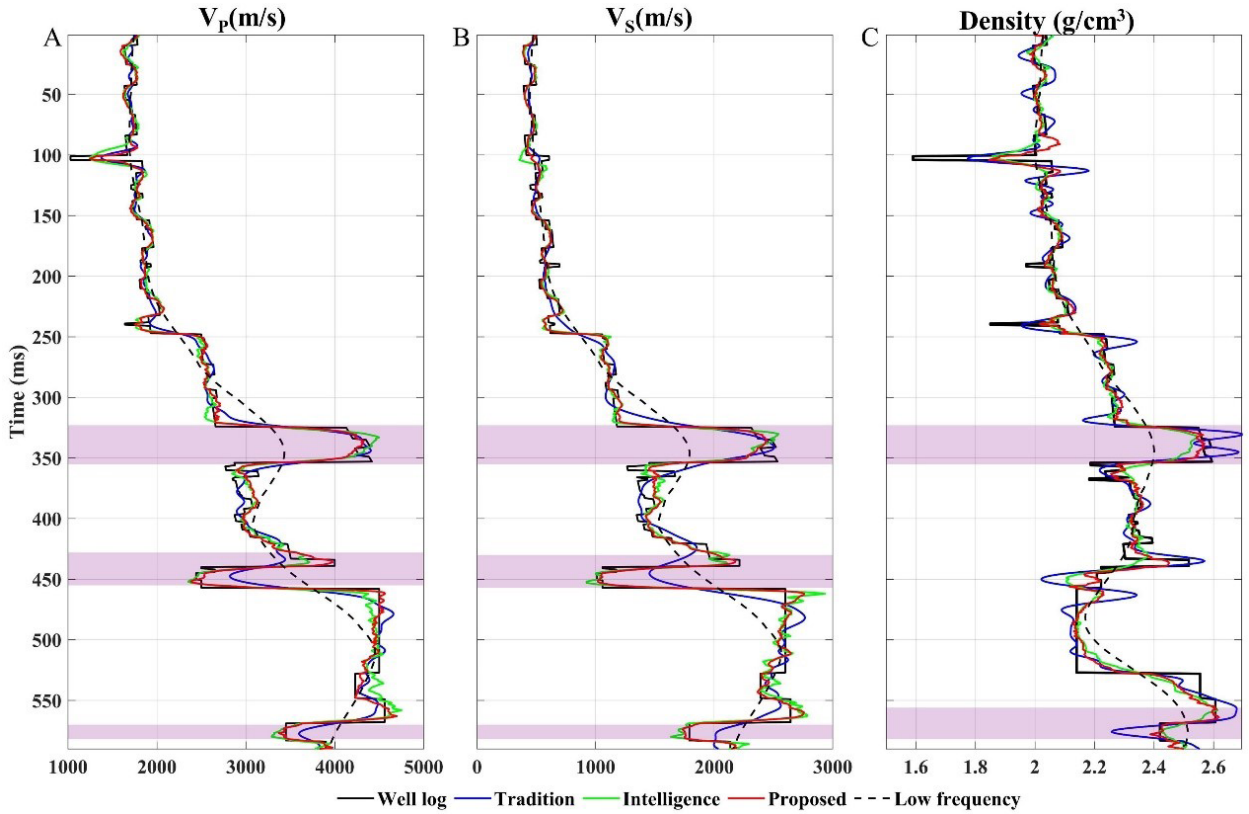

Figure 9. The inverted results of the 666th trace data (with 20% noise). A comparison of the inverted (A) P-wave velocity, (B) S-wave velocity, and (C) density using the three inversion methods. The solid lines in black, blue, green, and red represent the well log, the results from traditional, intelligent, and proposed methods, respectively, while the black dashed line represents the low-frequency model.

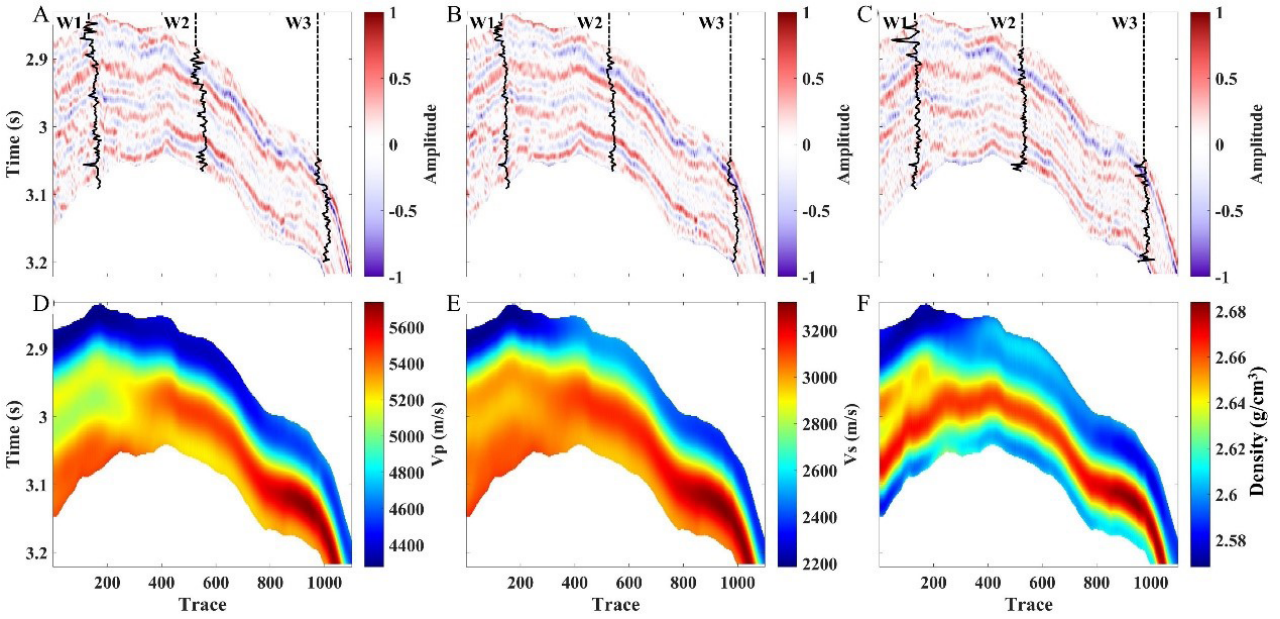

Figure 10. Seismic data and the corresponding low-frequency models. The seismic data at (A) 5°, (B) 12.5°, and (C) 20°. The low-frequency models of (D) P-wave velocity, (E) S-wave velocity, and (F) density. The black curve represents the well-log. The low-frequency models were generated using a 10 Hz low-pass filter.

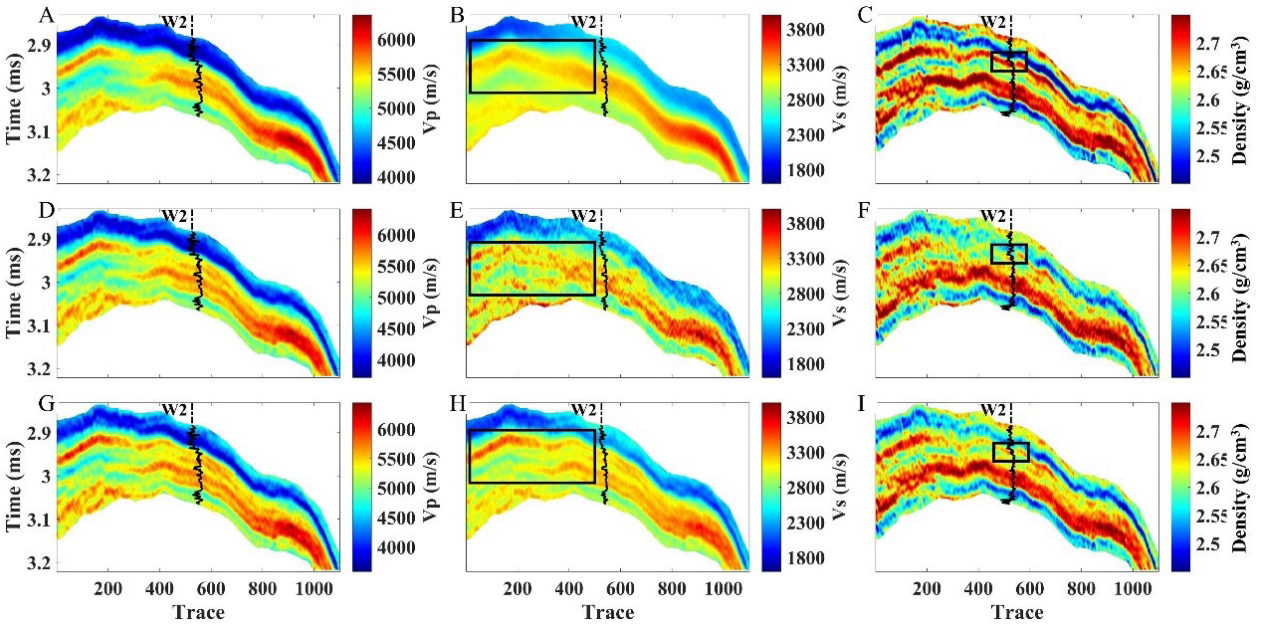

Figure 11. The inversion results of elastic parameters using three different methods on the actual seismic data. The predicted elastic parameters using the traditional method: (A) P-wave velocity, (B) S-wave velocity, and (C) density. The predicted elastic parameters using the intelligent method: (D) P-wave velocity, (E) S-wave velocity, and (F) density. The predicted elastic parameters using the proposed method: (G) P-wave velocity, (H) S-wave velocity, and (I) density. The black curve represents the well-log.

by the purple rectangle, the differences between the three methods were more clearly illustrated, with the red curve overall being closer to the black well log curve.

Table 3 presents the performance evaluation of three methods on the blind well. Overall, the proposed method achieved better accuracy and stability across all

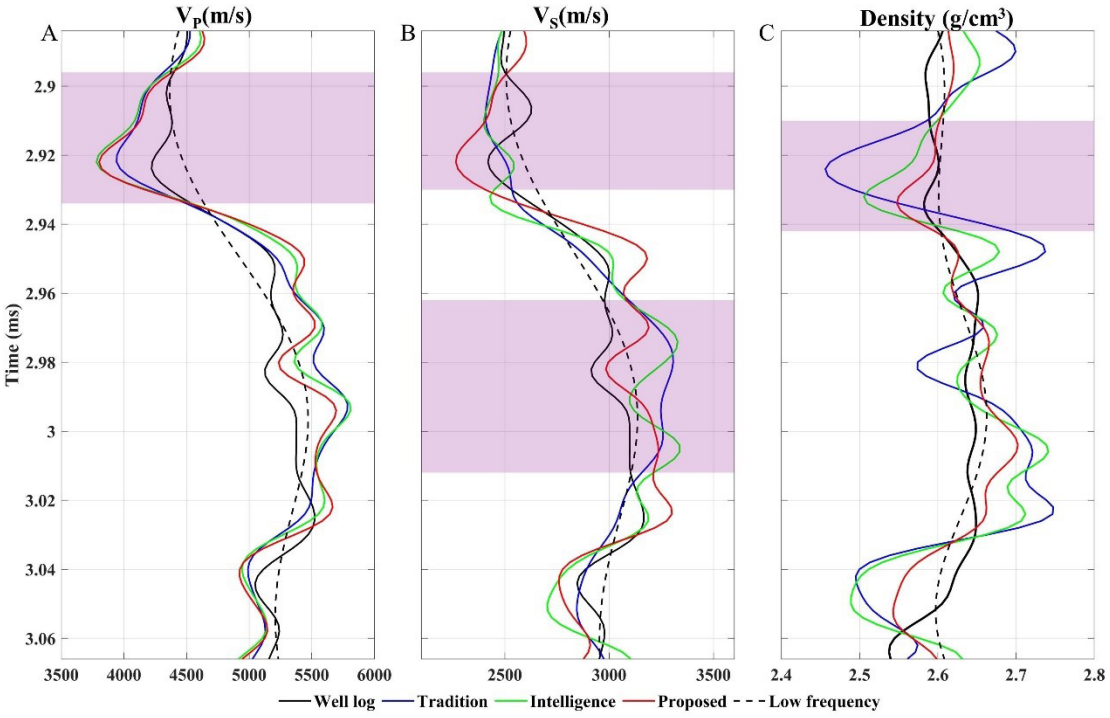

Figure 12. The inverted results of the 526th trace data. A comparison of the inverted (A) P-wave velocity, (B) S-wave velocity, and (C) density using the three inversion methods. The solid lines in black, blue, green, and red represent the well log, the results from the traditional, intelligent, and proposed methods, respectively, while the black dashed line represents the low-frequency model.

parameters. Specifically, for V_p inversion, compared to the traditional and intelligent methods, the proposed method reduced MAE by 5% and 17.03%, respectively, and lowered RMSE by 3.39% and 11.24%, while maintaining a higher R value. For V_s inversion, MAE decreased by 2.13% and 7.39%, and RMSE decreased by 16.31% and 19.89%, with further improvements in R value. In ρ inversion, the proposed method lowered MAE by 38.31% and 29.69%, reduced RMSE by 36.89% and 27.50%, and increased R by 11.24% and 36.47% compared to the two baseline methods, respectively. These results indicate that the proposed method achieved lower error and higher correlation across different inversion tasks, demonstrating overall superior performance compared to the other methods.

4. Discussion

The two-step intelligent inversion method driven by multi-constraint fusion proposed in this paper, through the construction of a multi-constraint joint loss function, effectively improved the inversion accuracy of V_p, V_s, and ρ. This study aims to provide a new solution to the fundamental problem of prestack three-parameter inversion, with its core innovation at the methodological level—namely, how to systematically integrate multi-source prior information to guide the learning process of intelligent networks. The shale reservoir was selected as the application scenario for method validation because shale oil and gas exploration demands high accuracy in reservoir parameter prediction, thereby fully testing the effectiveness of the proposed method.

Although the proposed method achieved satisfactory results in both synthetic-model and field-data tests, certain limitations remained. First, the weights of various terms in the multi-constraint joint loss function are currently determined mainly through empirical manual tuning, lacking an adaptive adjustment mechanism, which may affect the model's generalization capability under different data conditions. Second, although the multi-constraint fusion strategy alleviated inherent challenges such as parameter coupling to some extent, in practical applications, the accuracy of prestack three-parameter inversion still faces challenges due to factors such as the limited frequency band of seismic data, noise interference, and the low physical sensitivity of ρ parameters. Looking ahead, future studies should focus on the following works: first, introducing adaptive weighting strategies that leverage uncertainty estimation or attention mechanisms to dynamically balance the contributions of various loss function terms; second, extending the proposed method from isotropic media to more complex vertical transverse

isotropy or horizontal transverse isotropy media, conducting anisotropic parameter inversion research to address the practical demands of complex reservoirs such as shale.

Table 3. A comparison of the inverted results using the three inversion methods on the real data (blind well)

Target parameter	Method	MAE	RMSE	R
V_p(m/s)	Tradition	155.3665	199.7186	0.9368
	Intelligence	181.2970	217.3702	0.9376
	Proposed	150.3665	192.9521	0.9514
V_s(m/s)	Tradition	104.6960	135.6808	0.8798
	Intelligence	110.6391	141.7022	0.8854
	Proposed	102.4695	113.5337	0.9347
ρ (g/cm^3)	Tradition	0.0522	0.0656	0.5443
	Intelligence	0.0458	0.0571	0.4437
	Proposed	0.0322	0.0414	0.6055

Abbreviations: MAE: Mean absolute error; RMSE: Root-mean-square error.

5. Conclusion

To tackle the issues of non-uniqueness and parameter coupling in prestack three-parameter inversion, this study introduces a two-step intelligent inversion method based on multi-constraint fusion. The approach builds a dual closed-loop framework that integrates well log data with constraints from physical laws and empirical relationships. It uses a step-by-step strategy, first inverting I_p before estimating all three parameters. The TransUNet architecture is used to model both local features and global dependencies. Tests on synthetic and real data, with and without noise, showed that the proposed method improved the accuracy and stability of three-parameter inversion, especially for ρ, compared to traditional and intelligent methods without physical constraints, demonstrating strong robustness. In real data applications, the method also enhances the inversion of V_s and ρ while maintaining the accuracy of V_p results.

Acknowledgments

None.

Funding

This work was supported by the National Science and Technology Major Project (2025ZD1405001), the PetroChina Science and Technology Project (2023ZZ15YJ02), and the "Tianshan Talent" Program of Xinjiang Uygur Autonomous Region (2022TSYCJC0027).

Conflict of interest

The authors declare that they have no competing interests.

Author contributions

Conceptualization: Hongyan Qi, Zhenlin Wang
Formal analysis: Wei Li, Tingming Tang
Investigation: Juqin Yao
Methodology: Hongyan Qi, Zhenlin Wang, Wei Li
Validation: Tingming Tang, Juqin Yao
Visualization: Qingyong Luo, Gang Chen
Writing–original draft: Hongyan Qi, Zhenlin Wang
Writing–review & editing: Wei Li, Tingming Tang, Juqin Yao, Gang Chen, Qingyong Luo

Ethics approval and consent to participate

Not applicable.

Consent for publication

Not applicable.

Availability of data

The raw data of this study are available from the corresponding author upon reasonable request.

References

1. Zong Z, Yin X, Wu G. Geofluid Discrimination Incorporating Poroelasticity and Seismic Reflection Inversion. *Surv Geophys*. 2015;36(5):659-681.

   doi: 10.1007/s10712-015-9330-6

2. Tarantola A. *Inverse Problem Theory and Methods for Model Parameter Estimation*. Philadelphia, PA: Society for Industrial and Applied Mathematics; 2005.

   doi: 10.1137/1.9780898717921

3. Buland A, Omre H. Bayesian linearized AVO inversion. *Geophysics*. 2003;68(1):185-198.

   doi: 10.1190/1.1543206

4. Cooke DA, Schneider WA. Generalized linear inversion of reflection seismic data. *Geophysics*. 1983;48(6):665-676.

doi: 10.1190/1.1441497

5. Downton JE. *Seismic parameter estimation from AVO inversion*. Dissertation. Calgary, AB: University of Calgary; 2005.

6. Guo Q, Zhang HB, Han FL, *et al*. Prestack Seismic Inversion Based on Anisotropic Markov Random Field. *IEEE Trans Geosci Remote Sens*. 2018;56(2):1069-1079.

   doi: 10.1109/TGRS.2017.2758800

7. Aki K, Richards PG. *Quantitative Seismology: Theory and Methods*. San Francisco, CA: W.H. Freeman; 1980.

8. Shuey RT. A simplification of the Zoeppritz equations. *Geophysics*. 1985;50(4):609-614.

   doi: 10.1190/1.1441936

9. Zhi LX, Chen SQ, Li XY. Amplitude variation with angle inversion using the exact Zoeppritz equations - Theory and methodology. *Geophysics*. 2016;81(2):N1-N15.

   doi: 10.1190/geo2014-0582.1

10. Alemie W, Sacchi MD. High-resolution three-term AVO inversion by means of a Trivariate Cauchy probability distribution. *Geophysics*. 2011;76(3):420-424.

    doi: 10.1190/1.3554627

11. Theune U, Jensås IØ, Eidsvik J. Analysis of prior models for a blocky inversion of seismic AVA data. *Geophysics*. 2010;75(3):C25-C35.

    doi: 10.1190/1.3427538

12. Yuan M, Miao Z, Pan L, *et al*. Generalized Gaussian distribution-based prestack inversion: A case study of channel sands in the Lianggaoshan Formation, Sichuan Basin. *J Seism Explor*. 2026;35(1):200-220.

    doi: 10.36922/JSE025450105

13. Haas A, Dubrule O. Geostatistical inversion-a sequential method of stochastic reservoir modelling constrained by seismic data. *First Break*. 1994;12(11):561-569.

14. Azevedo L, Soares A. *Geostatistical Methods for Reservoir Geophysics*. Berlin, Germany: Springer; 2017.

15. Sen MK, Stoffa PL. Bayesian inference, Gibbs' sampler and uncertainty estimation in geophysical inversion. *Geophys Prospect*. 1996;44(2):313-350.

16. Francis A. Understanding stochastic inversion: part 1. *First Break*. 2006;24(11):69-77.

    doi: 10.3997/1365-2397.2006026

17. Srivastava RP, Sen MK. Stochastic inversion of prestack seismic data using fractal-based initial models. *Geophysics*. 2010;75(3):R47-R59.

    doi: 10.1190/1.3379322

18. Hamid H, Pidlisecky A. Multitrace impedance inversion with lateral constraints. *Geophysics*. 2015;80(6):M101-M111.

    doi: 10.1190/geo2014-0546.1

19. Li C, Liu G, Deng Y. Nonstationary phase-corrected full-waveform inversion with attenuation compensation in viscoacoustic medium. *J Geophys Eng*. 2022;19(4):724-738.

    doi: 10.1093/jge/gxac046

20. Zhang G, Wang Z, Chen Y. Deep learning for seismic lithology prediction. *Geophys J Int*. 2018;215(2):1368-1387.

    doi: 10.1093/gji/ggy344

21. Yang L, Fomel S, Wang S, *et al*. Denoising of distributed acoustic sensing data using supervised deep learning. *Geophysics*. 2023;88(1):WA91-WA104.

    doi: 10.1190/geo2022-0138.1

22. Gao Y, Zhao D, Li T, *et al*. Deep learning vertical resolution enhancement considering features of seismic data. *IEEE Trans Geosci Remote Sens*. 2023;61:1-13.

    doi: 10.1109/TGRS.2023.3234617

23. Das V, Pollack A, Wollner U, *et al*. Convolutional neural network for seismic impedance inversion. *Geophysics*. 2019;84(6):R869-R880.

    doi: 10.1190/geo2018-0838.1

24. Chen Y, Zhang G, Bai M, *et al*. Automatic waveform classification and arrival picking based on convolutional neural network. *Earth Space Sci*. 2019;6(7):1244-1261.

    doi: 10.1029/2018EA000466

25. Wu B, Meng D, Wang L, *et al*. Seismic impedance inversion using fully convolutional residual network and transfer learning. *IEEE Geosci Remote Sens Lett*. 2020;17(12):2140-2144.

    doi: 10.1109/LGRS.2019.2963106

26. Alfarraj M, AlRegib G. Semisupervised sequence modeling for elastic impedance inversion. *Interpretation*. 2019;7(3):SE237-SE249.

    doi: 10.1190/INT-2018-0250.1

27. Liu X, Wu B, Yang H. Multitask full attention U-Net for prestack seismic inversion. *IEEE Geosci Remote Sens Lett*. 2023;20:1-5.

    doi: 10.1109/LGRS.2023.3303698

28. Vaswani A, Shazeer N, Parmar N, *et al*. Attention is all you need. In: *Advances in Neural Information Processing Systems*. Vol 30. 2017:5998-6008.

29. Aleardi M, Salusti A. Elastic prestack inversion through Discrete Cosine Transform reparameterization and Convolutional Neural Networks. *Geophysics*. 2021;86(1):R129-R146.

    doi: 10.1190/geo2020-0313.1

30. Chen T, Zou B, Wang Y, *et al*. Prestack Seismic Inversion Driven by Priori Information Neural Network and Statistical

Characteristic. *IEEE Trans Geosci Remote Sens*. 2024;62:1-14.

doi: 10.1109/TGRS.2024.3394523

31. Biswas R, Sen MK, Das V, *et al*. Prestack and poststack inversion using a physics-guided convolutional neural network. *Interpretation*. 2019;7(3):SE161-SE174.

doi: 10.1190/INT-2018-0236.1

32. Wang S, Liu C, Song C, *et al*. Prestack AVO Inversion Based On Physics-constrained Deep Learning Method. *Appl Geophys*. 2025:1-19.

doi: 10.1007/s11770-025-1179-y

33. Karpatne A, Atluri G, Faghmous JH, *et al*. Theory-Guided Data Science: A New Paradigm for Scientific Discovery from Data. *IEEE Trans Knowl Data Eng*. 2017;29(10):2318-2331.

doi: 10.1109/TKDE.2017.2720168

34. Raissi M, Perdikaris P, Karniadakis GE. Physics-informed neural networks: a deep learning framework for solving forward and inverse problems involving nonlinear partial differential equations. *J Comput Phys*. 2019;378:686-707.

doi: 10.1016/j.jcp.2018.10.045

35. Liu Z, Zhang J, Chen Y, *et al*. From Physics Constraints to Trustworthy Bayesian Reasoning: Synergies of PINN, iPINN, and iBPINN in Prestack AVO Inversion. *IEEE Trans Geosci Remote Sens*. 2025;63:1-14.

doi: 10.1109/TGRS.2025.3636416

36. Zhang J, Zhao X, Chen Y, *et al*. Domain knowledge-guided data-driven prestack seismic inversion using deep learning. *Geophysics*. 2023;88(2):M31-M47.

doi: 10.1190/geo2021-0560.1

37. Zhao L, Zhu J, Qin X, *et al*. Joint geochemistry-rock physics modeling: Quantifying the effects of thermal maturity on the elastic and anisotropic properties of organic shale. *Earth-Sci Rev*. 2023;247:104627.

doi: 10.1016/j.earscirev.2023.104627

ACCSCIENCE PUBLISHING

Journal of Seismic Exploration

ARTICLE

Full-wavefield modeling using a decoupled viscoacoustic wave equation with vector-reflectivity

Fei Li[1], Zilong Ye[2]*, Jintao Liu[1], Jianping Huang[2], Mengmeng Wu[1], Mei Li[1], and Yanjiao Dong[2]

[1]Exploration and Development Research Institute, Changqing Oilfield Branch Company Ltd., PetroChina, Xi'an, Shanxi, China

[2]National Key Laboratory of Deep Oil and Gas, School of Geosciences, China University of Petroleum (East China), Qingdao, Shandong, China

Abstract

Conventional Q-compensated least-squares reverse time migration generally employs a linearized viscoacoustic modeling operator based on the first-order Born approximation, which simulates only primary reflections in synthetic data. As a result, it cannot properly match seismic data containing multiples, leading to prominent crosstalk artifacts and reduced image quality. To overcome this limitation, we started with the relaxation function of the generalized standard linearized solid model and derived a viscoacoustic wave equation with vector-reflectivity. This formulation enabled the simulation of full viscoacoustic wavefields that included both primary and multiple reflections, and it could be numerically solved using finite-difference algorithms. Numerical experiments demonstrated that the wavefields generated using the proposed vector-reflectivity equation were equivalent to those produced using the original variable-density viscoacoustic wave equation. To further investigate the attenuation characterizations, we decoupled the dissipation and dispersion effects in the viscoacoustic wave equation with vector-reflectivity and derived a corresponding decoupled formulation. Numerical experiments demonstrated that the decoupled viscoacoustic wave equation with vector-reflectivity accurately simulated both dissipation and phase-dispersion wavefields. Based on decoupled characteristics and full-wavefield simulation capabilities, the proposed formulation provides an effective linearized forward-modeling engine for Q-compensated least-squares reverse time migration.

Keywords: Attenuation; Generalized standard linearized solid; Vector-reflectivity; Forward modeling

***Corresponding author:**
Zilong Ye
(B23010050@s.upc.edu.cn)

Citation: Li F, Ye Z, Liu J, *et al*. Full-wavefield modeling using a decoupled viscoacoustic wave equation with vector-reflectivity. *J Seismic Explor*. 2026;35(3):026030004. doi: 10.36922/JSE026030004

Received: January 13, 2026

Revised: March 6, 2026

Accepted: March 20, 2026

Published online: May 29, 2026

Copyright: © 2026 Author(s). This is an Open-Access article distributed under the terms of the Creative Commons Attribution License, permitting distribution, and reproduction in any medium, provided the original work is properly cited.

Publisher's Note: AccScience Publishing remains neutral with regard to jurisdictional claims in published maps and institutional affiliations.

1. Introduction

The anelastic properties of subsurface media lead to the conversion of seismic wave energy into heat as waves propagate through attenuating media.[1] This intrinsic attenuation effect, quantified by the quality factor Q, is especially significant in hydrocarbon reservoirs and gas-bearing sandstones, causing both amplitude loss and phase distortion in the seismic wavefield, thereby degrading the quality of the seismic data.[2] When

numerical simulation methods for seismic wavefields neglect attenuation effects, significant discrepancies arise between synthetic and field data in both amplitude and phase, ultimately leading to imaging results characterized by weak amplitudes, mispositioned events, and reduced resolution. Therefore, it is essential to develop an accurate and efficient viscoacoustic wave equation incorporating intrinsic attenuation that simulates the attenuation effects on seismic wavefields.

In seismic exploration, scholars employ attenuation models to characterize constant-Q behavior within the seismic frequency band, thereby constructing various viscoacoustic wave equations with distinct characteristics. The constant-Q model,[3] capable of accurately characterizing attenuation behavior across the seismic exploration frequency band, has garnered increasing attention in recent years. Based on the constant-Q model, decoupled fractional Laplacians viscoacoustic wave equation with amplitude-loss and phase-dispersion terms have been developed and widely used in attenuating wavefield forward modeling,[4-9] Q-compensated reverse time migration (Q-RTM),[10,11] and Q-compensated least-squares reverse time migration (Q-LSRTM).[12-15] However, numerically solving the fractional Laplacian operators requires multiple Fourier transforms using the pseudo-spectral method at each time step, leading to prohibitive computational costs in three-dimensional applications and industrial-scale implementations.[16-18] Moreover, as a global algorithm, the pseudo-spectral method is difficult to scale to graphics processing unit-based parallel computing. Another numerical challenge is that the fractional Laplacian operator is a space-wavenumber mixed-domain operator. Direct implementation using the pseudo-spectral method introduces strong Gibbs phenomena, thereby impairing the accuracy of wavefield simulation.

Another commonly used attenuation model is the generalized standard linearized solid (GSLS) model.[19,20] Different from the constant-Q model, which is constructed through mathematical formulations, the GSLS model is built using physical components—springs and dashpots—as its fundamental elements. Viscoacoustic wave equations derived from this model can be efficiently solved using finite-difference methods, making them broadly applicable in seismic forward modeling and migration.[21-29] The GSLS model estimates constant-Q behavior by configuring multiple standard linear solid (SLS) relaxation parameters,[19,30] yielding time-domain wave equations with numerous, intricately related relaxation terms. Consequently, attenuation effects are implicitly represented through parameter relationships rather than explicitly appearing in the equations.[31,32] Theoretically, as the number of SLS models increases, the GSLS attenuation model provides a more accurate estimation of constant-Q behavior, enabling the derived viscoacoustic wave equations to better describe seismic wave propagation in attenuating media. However, this indiscriminate increase in the number of SLS models inevitably increases model complexity and substantially raises computational costs. Clearly, a judicious balance must be struck among parameter complexity, physical model accuracy, and computational efficiency.

Recently, a relaxation function containing an explicit Q factor and the viscoacoustic wave equation derived from it has attracted considerable attention in the research community.[31] The explicit appearance of the seismic quality factor Q in the viscoacoustic wave equation not only avoids the complexity associated with relaxation parameters but also facilitates the derivation of gradient formulas with respect to Q in both Q-LSRTM and Q Full Waveform Inversion. Beyond parameter complexity, conventional GSLS-based viscoacoustic wave equations face a fundamental limitation in their implementation for migration and inversion: the mathematical coupling between amplitude dissipation and phase dispersion. Bai *et al.*[22] eliminated the memory variable from the single-SLS viscoacoustic wave equation and isolated an amplitude loss term characterized by a pseudo-differential operator. However, the phase dispersion term was omitted in their formulation, resulting in a decoupled viscoacoustic wave equation that accounted only for amplitude loss and was incapable of simulating phase dispersion effects in attenuated wavefields. Li *et al.*[11] and Fathalian *et al.*[24] derived a decoupled viscoacoustic wave equation with amplitude-loss and phase-dispersion terms based on the single-SLS model. However, in these single-SLS decoupled viscoacoustic wave equations, the amplitude loss term took the form of a pseudo-differential operator, whose numerical implementation relies on the computationally expensive pseudo-spectral method. This not only hinders their extension to viscoelastic media but also limits their applicability in industrial production. Moreover, a single-SLS relaxation mechanism can only approximate constant-Q behavior over a relatively narrow seismic exploration frequency band. Consequently, the single-SLS decoupled viscoacoustic wave equations fail to achieve satisfactory numerical simulation performance in strongly attenuating regions. The migration process requires reversing the sign of the amplitude attenuation term in the decoupled viscoacoustic wave equation while maintaining the sign of the phase dispersion term, thereby constructing an attenuation-compensated viscoacoustic wave equation.[3,4] This inherent coupling in the GSLS viscoacoustic wave equation substantially limits their

applicability in both Q-compensated migration and inversion.

Q-compensated least-squares reverse time migration effectively mitigates attenuation effects, significantly enhancing deep-target illumination, improving resolution, and preserving amplitude fidelity.[5-7,33-36] However, conventional Q-LSRTM typically relies on linearized modeling operators constructed under the first-order Born approximation, which simulate only primary reflections. This creates a mismatch between synthetic records and actual seismic records that contain full-wavefield information, including multiples and converted waves. This data mismatch leads to slow iterative convergence and introduces crosstalk artifacts in the imaging results, primarily due to multiples. To obtain high-quality Q-LSRTM images, seismic data are usually preprocessed to suppress multiples,[37,38] thereby avoiding crosstalk artifacts in the final images. Nevertheless, accurate identification and effective separation of multiples remain technically challenging, particularly in complex geological structures. Consequently, there is a clear need to develop a novel linearized viscoacoustic wave equation that is both suitable for least-squares inversion and capable of accurately describing attenuation while simulating full-wavefield responses—including primaries and multiples.[39,40] Establishing such an equation would enable high-precision attenuation-compensated imaging directly from full-wavefield data, without relying on multiple suppression. This advancement would enhance the practicality, robustness, and ultimate imaging quality of Q-LSRTM.

Traditional seismic forward modeling typically considers only velocity parameters while neglecting the influence of density variations on wavefield amplitudes. This simplification introduces amplitude discrepancies between synthetic and observed data in least-squares inversion, with amplitude distortions becoming particularly pronounced in zones of strong lateral density contrast. In recent years, an acoustic wave equation with vector-reflectivity has been proposed that avoids explicit density parameters.[41-43] This approach enables full-wavefield forward modeling using only a velocity model and iteratively updated reflectivity images of least-squares inversion. Studies have shown that the wavefields simulated by this method achieve numerical accuracy comparable to those from variable density acoustic equations and effectively reproduce complex wavefield responses, including primaries and multiples.[41,44] Compared to linearized forward operators based on the first-order Born approximation, the vector-reflectivity equation can directly utilize the iteratively updated velocity and reflectivity models to accurately simulate full-wavefield data that includes multiple reflections. This results in improved kinematic and dynamic consistency between synthetic and observed records. Therefore, developing a viscoacoustic wave equation with vector-reflectivity promises several enhancements for Q-LSRTM: (i) more accurate amplitude information without requiring density parameters; (ii) effective suppression of imaging artifacts caused by multiple-related crosstalk; and (iii) accelerated convergence and enhanced inversion stability due to better data misfit reduction. This approach offers a promising technical pathway for high precision Q-LSRTM.

In this paper, we started from the relaxation function of the GSLS model and derived a variable-density viscoacoustic wave equation with explicitly expressed Q. Based on this formulation, we then introduced a vector-reflectivity representation and derived the viscoacoustic wave equation with vector-reflectivity that enables the simulation of viscoacoustic wavefields containing both primary reflections and multiples without explicit knowledge of density. Subsequently, we decoupled the amplitude dissipation and phase dispersion effects of the viscoacoustic wave equation with vector-reflectivity, thereby making it suitable for Q-LSRTM. Finally, the numerical experiments demonstrated the feasibility and effectiveness of the proposed approach.

2. Methods

2.1. Derivation of the viscoacoustic wave equation with vector-reflectivity

In attenuating media, stress is represented as the convolution of a relaxation function with the strain history of time. According to the GSLS model, the relaxation function $M(t)$ in attenuating media can be given as **Equation 1**.[20,32,45,46]

$$M(t) = M_0\left[1+\frac{1}{Q}\sum_{l=1}^{L} D_l \exp^{(-t/\tau_l)}\right]H(t) \tag{1}$$

where $M_0 = \rho v_{p0}^2$ denotes the relaxed modulus, t is the time variable, ρ is density, v_{p0} is the relaxed P-wave velocity, Q is the P-wave quality factor, $l \in [1, L]$ represents the number of relaxation mechanisms, and $H(t)$ is the step function. D_l and τ_l are the weights and decay times of lth relaxation mechanism, which are calculated by optimizing algorithm to approximate constant-Q effects over a preset seismic exploration frequency band. In this paper, we use L = 3, and the resulting parameters are defined in Table 1.[31,32]

Table 1. The coefficient of D_l and τ_1

Coefficients	Values
D_1	1.74278563
D_2	1.41221145
D_3	1.72183357
τ_1	0.00159180
τ_2	0.01450505
τ_3	0.14020500

Based on the relaxation function defined in **Equation 1**, combining the stress–strain relationship and the second Newton's law, the second-order variable-density viscoacoustic wave equation with the explicitly expressed Q is derived as **Equations 2** and **3**.[45]

$$\frac{\partial^2 p}{\partial t^2} = \rho v^2 \left[1 + \frac{1}{Q} \sum_{l=1}^{L} D_l \right] \nabla \cdot \frac{1}{\rho} \nabla p - \frac{1}{Q} \sum_{l=1}^{L} r_l \tag{2}$$

$$\frac{\partial r_l}{\partial t} = -\frac{1}{\tau_l} \left\{ r_l - D_l \rho v^2 \nabla \cdot \frac{1}{\rho} \nabla p \right\} \tag{3}$$

where r_l is the memory variable defined in lth SLS relaxation mechanism, and p is the pressure wavefield, v is the particle velocity. ∇ is the gradient operator and $\nabla \cdot$ is the divergence operator. The above variable-density viscoacoustic wave equation accurately captures the characteristics of the full seismic wavefields in attenuating media. Forward modeling using **Equation 1** requires three parameters as input: velocity, density, and Q. However, obtaining an accurate density field remains particularly challenging. By incorporating the impedance definition, we rewrite **Equations 2** and **3** into **Equations 4** and **5**:

$$\frac{\partial^2 p}{\partial t^2} = vz \left[1 + \frac{1}{Q} \sum_{l=1}^{L} D_l \right] \nabla \cdot \frac{v}{z} \nabla p - \frac{1}{Q} \sum_{l=1}^{L} r_l \tag{4}$$

$$\frac{\partial r_l}{\partial t} = -\frac{1}{\tau_l} \left\{ r_l - D_l z v \nabla \cdot \frac{v}{z} \nabla p \right\} \tag{5}$$

where $z = \rho v$ denotes the acoustic impedance. Using a simple mathematical divergence algorithm, the above velocity-impedance viscoacoustic wave equation can be further rewritten as **Equations 6** and **7**:

$$\frac{\partial^2 p}{\partial t^2} = \left(1 + \frac{1}{Q} \sum_{l=1}^{L} D_l \right) \left(v^2 \nabla^2 p + v \nabla v \cdot \nabla p + v^2 z \nabla \frac{1}{z} \cdot \nabla p \right) - \frac{1}{Q} \sum_{l=1}^{L} r_l \tag{6}$$

$$\frac{\partial r_l}{\partial t} = -\frac{1}{\tau_l} \left\{ r_l - D_l v^2 \nabla^2 p - D_l v \nabla v \cdot \nabla p - D_l v^2 z \nabla \frac{1}{z} \cdot \nabla p \right\} \tag{7}$$

Here, we define the vector-reflectivity **R** as the normalized rate of impedance change in each vector direction (**Equation 8**):[41]

$$\mathbf{R} = -\frac{1}{2} z \nabla \frac{1}{z} \tag{8}$$

Substituting **Equation 8** into **Equations 6** and **7**, we can obtain **Equations 9** and **10**:

$$\frac{\partial^2 p}{\partial t^2} = \left(1 + \frac{1}{Q} \sum_{l=1}^{L} D_l \right) \left(v^2 \nabla^2 p + v \nabla v \cdot \nabla p - 2 v^2 \mathbf{R} \cdot \nabla p \right) - \frac{1}{Q} \sum_{l=1}^{L} r_l \tag{9}$$

$$\frac{\partial r_l}{\partial t} = -\frac{1}{\tau_l} \left\{ r_l - D_l v^2 \nabla^2 p - D_l v \nabla v \cdot \nabla p + D_l 2 v^2 \mathbf{R} \cdot \nabla p \right\} \tag{10}$$

As a result, **Equations 9** and **10** are the derived viscoacoustic wave equations with vector-reflectivity. In this way, we can conduct forward modeling using **Equations 9** and **10** with velocity, Q, and impedance as input parameters. The impedance is usually estimated from the migrated images. In seismic exploration, imaging results are more readily obtainable than estimates of density parameters. Moreover, imaging results inherently contain information related to density. Compared to using constant or inaccurate density as input for forward modeling, using estimated imaging results as input is more reasonable, as it accounts for the influence of density on wavefield simulation. To be noted, **Equations 2**, **4,** and **9**, as well as **Equations 3**, **5,** and **10**, are mathematically equivalent, and no approximations are introduced in the derivation. Ignoring the influence of density, **Equations 9** and **10** reduce to the viscoacoustic wave equation with constant density. In Section 3, we demonstrate that the wavefield simulated by **Equations 9** and **10** is equivalent to that simulated in **Equations 2** and **3**.

2.2. Derivation of the decoupled viscoacoustic wave equation with vector-reflectivity

Although the viscoacoustic wave equation derived in Section 2.1 with vector-reflectivity accurately captures the feature of seismic waves propagating in attenuating media,

it couples dissipation and dispersion effects in memory variables, which are not readily used to implement Q-compensated migrations. To decouple the dissipation and dispersion effects, we now proceed to derive the decoupled form of **Equations 9** and **10**. Here, we first expand the gradient operator and rewrite the derived equation as **Equations 11** and **12**:

$$\frac{\partial^2 p}{\partial t^2}=\left(1+\frac{1}{Q}\sum_{l=1}^{L}D_l\right)[v^2\nabla^2 p+v\left(\partial_x v\cdot\partial_x p+\partial_z v\cdot\partial_z p\right)+v^2 z\left(\partial_x\frac{1}{z}\cdot\partial_x p+\partial_z\frac{1}{z}\cdot\partial_z p\right)]-\frac{1}{Q}\sum_{l=1}^{L}r_l \tag{11}$$

$$\frac{\partial r_l}{\partial t}=-\frac{1}{\tau_l}\{r_l-D_l v^2\nabla^2 p-D_l v\left(\partial_x v\cdot\partial_x p+\partial_z v\cdot\partial_z p\right)-D_l v^2 z(\partial_x\frac{1}{z}\cdot\partial_x p+\partial_z\frac{1}{z}\cdot\partial_z p)\} \tag{12}$$

The symbol ∂_i represents the directional derivative of the variable in i direction. We then apply the Fourier transform to **Equations 11** and **12** in the time domain to obtain the frequency-domain viscoacoustic wave equation with vector-reflectivity (**Equations 13** and **14**):

$$\omega^2 P=\left(1+\frac{1}{Q}\sum_{l=1}^{L}D_l\right)[v^2k^2P+v\left(k_x vk_x P+k_z vk_z P\right)+v^2 z\left(k_x\frac{1}{z}k_x P+k_z\frac{1}{z}k_z P\right)]+\frac{1}{Q}\sum_{l=1}^{L}\tilde{r}_l \tag{13}$$

$$i\omega\tilde{r}_l\tau_l=-\{\tilde{r}_l+D_l v^2k^2P+D_l v\left(k_x vk_x P+k_z vk_z P\right)+D_l v^2 z\left(k_x\frac{1}{z}k_x P+k_z\frac{1}{z}k_z P\right)\} \tag{14}$$

where ω denotes the angular frequency, P and $\tilde{r}_l$ are the frequency domain form of the time domain wavefield p and memory variables r_l, respectively. The memory variables in **Equation 14** can be expressed as

$$\tilde{r}_l=-\frac{1}{1+i\omega\tau_l}\{D_l v^2k^2P+D_l v\left(k_x vk_x P+k_z vk_z P\right)+D_l v^2 z(k_x\frac{1}{z}k_x P+k_z\frac{1}{z}k_z P)\} \tag{15}$$

Substituting **Equation 15** into **Equation 13** and eliminating the memory variables, we can obtain the dispersion relation of the viscoacoustic wave equation (**Equation 16**):

$$\begin{aligned}\omega^2 P=&\left(1+\frac{1}{Q}\sum_{l=1}^{L}D_l\right)[v^2k^2P+v\left(k_x vk_x P+k_z vk_z P\right)\\&+v^2 z(k_x\frac{1}{z}k_x P+k_z\frac{1}{z}k_z P)]\\&-\frac{1}{Q}\{\sum_{l=1}^{L}\frac{D_l}{1+\omega^2\tau_l^2}(v^2k^2P+v\left(k_x vk_x P+k_z vk_z P\right)\\&+v^2 z(k_x\frac{1}{z}k_x P+k_z\frac{1}{z}k_z P))\}\\&+\frac{i\omega\tau_l}{Q}\{\sum_{l=1}^{L}\frac{D_l}{1+\omega^2\tau_l^2}(v^2k^2P+\\&v\left(k_x vk_x P+k_z vk_z P\right)+v^2 z(k_x\frac{1}{z}k_x P+k_z\frac{1}{z}k_z P))\}\end{aligned} \tag{16}$$

Equation 16 is decomposed into two components: one containing only the real part controls phase dispersion, and the other containing only the imaginary part controls amplitude dissipation.[2,28] If we ignore the dissipation-dominated effects, namely, the imaginary part, the dispersion-dominated dispersion relation can be expressed as **Equation 17**:

$$\begin{aligned}\omega^2 P=&\left(1+\frac{1}{Q}\sum_{l=1}^{L}D_l\right)[v^2k^2P+v\left(k_x vk_x P+k_z vk_z P\right)\\&+v^2 z(k_x\frac{1}{z}k_x P+k_z\frac{1}{z}k_z P)]\\&-\frac{1}{Q}\{\sum_{l=1}^{L}\frac{D_l}{1+\omega^2\tau_l^2}(v^2k^2P+v\left(k_x vk_x P+k_z vk_z P\right)\\&+v^2 z(k_x\frac{1}{z}k_x P+k_z\frac{1}{z}k_z P))\}\end{aligned} \tag{17}$$

The frequency-related term $D_l/\left(1+\omega^2\tau_l^2\right)$ in **Equation 17**, transformed into the time-space domain, it becomes a space-wavenumber mixed domain operator, which cannot be solved using a finite-difference method. To effectively estimate this frequency-related term, we perform a polynomial fitting method. Moreover, to preserve the original intent of explicitly incorporating Q into the viscoacoustic wave equation, we select a polynomial $\sum_{l=1}^{L}D_l/\left[1+\sum_{n=0}^{N}\left(a_n Q^{-n}\right)\right]$ that includes Q to fit the term $\sum_{l=1}^{L}D_l/\left(1+\omega^2\tau_l^2\right)$, $n\in[0,N]$ is the degree of the polynomial. A higher polynomial order n yields a more accurate approximation, but at the cost of increased equation complexity and computational resources. In this study, we choose n = 1 for equation simplicity and computational cost. Thus, we make the following

approximation for Q > 10 and seismic frequency band [1, 125] Hz (**Equation 18**):[46]

$$\sum_{l=1}^{L}\frac{D_l}{1+\omega^2\tau_l^2}\approx\sum_{l=1}^{L}\frac{D_l}{1+1+1/Q} \tag{18}$$

By inserting the approximation **Equation 18** into **Equation 17** and transforming **Equation 17** into the time-space domain, **Equation 19** can be derived:

$$\begin{aligned}\frac{\partial^2 p}{\partial t^2}=&\left(1+\frac{1}{Q}\sum_{l=1}^{L}D_l-\frac{1}{Q}\sum_{l=1}^{L}D_l'\right)\\&\left[v^2\nabla^2 p+v\left(\partial_x v\cdot\partial_x p+\partial_z v\cdot\partial_z p\right)+v^2 z\left(\partial_x\frac{1}{z}\cdot\partial_x p+\partial_z\frac{1}{z}\cdot\partial_z p\right)\right]\end{aligned} \tag{19}$$

Applying **Equation 8** in **Equation 19**, we have the dispersion-dominated viscoacoustic wave equation with vector-reflectivity (**Equation 20**):

$$\begin{aligned}\frac{\partial^2 p}{\partial t^2}=&(1+\frac{1}{Q}\sum_{l=1}^{L}D_l-\frac{1}{Q}\sum_{l=1}^{L}D_l')\\&\left(v^2\nabla^2 p+v\nabla v\cdot\nabla p-2v^2\mathbf{R}\cdot\nabla p\right)\end{aligned} \tag{20}$$

where $D_l'=D_l/\left(2+1/Q\right)$. In **Equation 20**, the unit 1 in parentheses represents the acoustic wave effect, while the term $\frac{1}{Q}\sum_{l=1}^{L}D_l-\frac{1}{Q}\sum_{l=1}^{L}D'$ corresponds to dispersion components. According to Mu and Huang,[26] the dissipation-dominant term equals the full viscoacoustic term minus the dispersion-dominant term. Thus, the dissipation-dominated viscoacoustic wave equation with vector-reflectivity can be derived as **Equations 21** and **22**:

$$\frac{\partial^2 p}{\partial t^2}=\left(1+\frac{1}{Q}\sum_{l=1}^{L}D_l'\right)\left(v^2\nabla^2 p+v\nabla v\cdot\nabla p-2v^2\mathbf{R}\cdot\nabla p\right)-\frac{1}{Q}\sum_{l=1}^{L}r_l \tag{21}$$

$$\frac{\partial r_l}{\partial t}=-\frac{1}{\tau_l}\left\{r_l-D_l v^2\nabla^2 p-D_l v\nabla v\cdot\nabla p+D_l 2v^2\mathbf{R}\cdot\nabla p\right\} \tag{22}$$

Finally, the decoupled viscoacoustic wave equation with vector-reflectivity is derived. To unify the representation of viscoacoustic wave equations with vector-reflectivity with different characteristics using a single formulation, we adopt the following form (**Equations 23** and **24**):

$$\begin{aligned}\frac{\partial^2 p}{\partial t^2}=&\left[1+\kappa_1\left(\frac{1}{Q}\sum_{l=1}^{L}D_l-\frac{1}{Q}\sum_{l=1}^{L}D_l'\right)\right]\\&\left(v^2\nabla^2 p+v\nabla v\cdot\nabla p-2v^2\mathbf{R}\cdot\nabla p\right)\\&+\kappa_2\left[\frac{1}{Q}\sum_{l=1}^{L}D_l'\right]\left(v^2\nabla^2 p+v\nabla v\cdot\nabla p-2v^2\mathbf{R}\cdot\nabla p\right)\\&-\kappa_2\frac{1}{Q}\sum_{l=1}^{L}r_l\end{aligned} \tag{23}$$

$$\frac{\partial r_l}{\partial t}=-\frac{1}{\tau_l}\left\{r_l-D_l v^2\nabla^2 p-D_l v\nabla v\cdot\nabla p+D_l 2v^2\mathbf{R}\cdot\nabla p\right\} \tag{24}$$

where κ_1 and κ_2 are two dimensionless control parameters independent of the equation itself, and their values are restricted to the following four combinations: When $\kappa_1=1$ and $\kappa_2=1$, **Equation 23** degenerates into viscoacoustic wave **Equation 9** that describes the viscoacoustic wavefield; when $\kappa_1=1$ and $\kappa_2=0$, **Equation 23** becomes the dispersion-dominated viscoacoustic wave **Equation 20** that characterizes only phase dispersion effects of viscoacoustic wavefield; when $\kappa_1=0$ and $\kappa_2=1$, **Equation 23** becomes the dissipation-dominated viscoacoustic wave **Equation 21** that describes only amplitude loss effects of viscoacoustic wavefield; when $\kappa_1=1$ and $\kappa_2=-1$, the sign of dissipation term is reversed while the sign of phase dispersion term is unchanged, **Equation 23** becomes the attenuation-compensated viscoacoustic wave equation that characterizes the energy-compensated effects of viscoacoustic wavefield. Notably, all formulations derived from **Equation 23** remain amenable to numerical solution using the finite-difference method. Moreover, after incorporating an appropriate regularization operator,[46] the attenuation-compensated equation can also achieve stable propagation in the time domain and be solved using the finite-difference method.

Compared to previous decoupled viscoacoustic wave equations, the newly proposed formulation incorporates an explicit Q factor, facilitating the derivation of gradient formulas with respect to Q in subsequent inversion imaging. Moreover, the new equation includes vector-reflectivity, enabling accurate simulation of the full wavefield using velocity and estimated imaging results, thereby circumventing inaccuracies arising from the absence of density parameters in wavefield modeling.

3. Numerical example

In this section, we demonstrate that the newly derived decoupled viscoacoustic wave equation with vector-reflectivity effectively simulates dissipation and dispersion effects independently. We then present synthetic examples to validate that this equation reproduces wavefields equivalent to those generated by the variable-density viscoacoustic wave equation. Numerically, we employ a staggered-grid finite-difference scheme with tenth-order spatial accuracy and second-order temporal accuracy[47] to solve the viscoacoustic wave equation.

3.1. Decoupled dissipation- and dispersion-characteristics

To validate the decoupled characteristics of the dispersion-

dominated **Equation 20** and the dissipation-dominated **Equation 21** in the newly derived decoupled viscoacoustic wave equation with vector-reflectivity, we conducted forward modeling for a homogeneous model. The model had 401 × 401 grid points with 10 m spacing in both the x- and z-directions. We excited a Ricker wavelet with a dominant frequency of 25 Hz at the model center. Figure 1 presents wavefield snapshots simulated at 0.5 s using four distinct wave equations: the acoustic wave equation with vector-reflectivity (upper left), the dissipation-dominated equation (upper right), the dispersion-dominant equation (lower left), and the viscoacoustic wave equation with vector-reflectivity (lower right). When compared to the acoustic reference (upper left), the viscoacoustic wavefield (lower right) exhibited remarkable amplitude attenuation and a clear phase advance in the waveform. Notably, the dissipation-dominated wavefield (upper right) maintained wavefront alignment with the acoustic reference while reproducing amplitude loss consistent with the full viscoacoustic wavefield. Conversely, the dispersion-dominated wavefield (lower left) preserved the phase characteristics and wavefront geometry of the viscoacoustic wavefield without showing noticeable amplitude decay.

In addition, we conducted forward modeling for the same homogeneous model with Q = 40 and 15, respectively, using the four wavefield propagators above. A receiver was deployed 1 km from the source to record waveforms from different wavefields. Figure 2 shows the waveforms and the corresponding amplitude spectra. As the Q value decreased, the horizontal distance between the red and black curves increased, while their peak amplitudes remained essentially consistent. The red and blue curves maintained the same horizontal position. This indicates that the phase-dispersion-dominant wave equation primarily governs the velocity-dispersion behavior of viscoacoustic waves. The green curve consistently aligned horizontally with the black curve, yet its amplitude closely matched that of the blue curve. This indicates that the dissipation-dominant wave equation primarily governs the amplitude behavior of viscoacoustic waves. In the amplitude spectrum (Figure 2C and 2D), the dissipation-dominant term largely coincided with the full viscoacoustic term, and similarly, the phase dispersion-dominant term closely aligned with the acoustic term.

These results provide clear, direct evidence of the decoupling achieved in the proposed equations. The

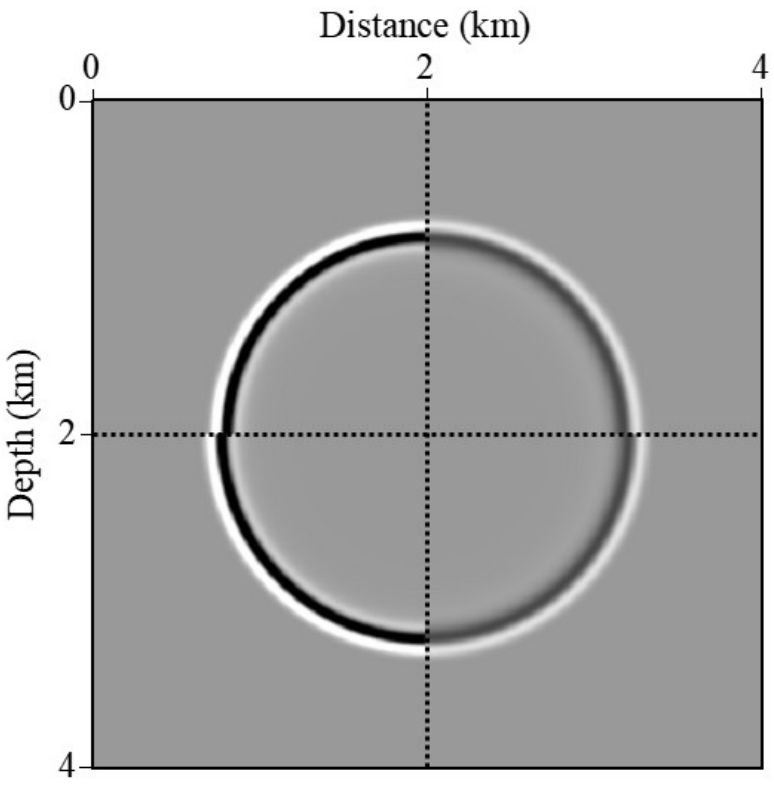

Figure 1. Wavefield snapshots simulated at 0.3 s using four distinct wave equations with vector-reflectivity: The acoustic (top left), the dissipation-dominated (top right), the dispersion-dominated lower left), and the viscoacoustic wave equation (lower right). The parameters of this homogeneous viscoacoustic model are: v_p = 2000 m/s, Q = 15, ρ = 2 g/cm^3.

dissipation-dominated equation independently captures amplitude effects, whereas the dispersion-dominated equation faithfully models velocity-dispersion effects. This explicit separation of physical effects not only confirms the theoretical validity of the decoupled formulation but also establishes a practical foundation for implementing amplitude compensation and phase correction in seismic imaging and inversion workflows.

3.2. Comparison with the variable-density viscoacoustic wave equation

The theoretical analysis in Section 3.1 demonstrated that the variable-density viscoacoustic wave equation and the viscoacoustic wave equation with vector-reflectivity are mathematically and physically equivalent. To evaluate the numerical simulation accuracy of the proposed viscoacoustic wave equation with vector-reflectivity, we conducted forward modeling using the complex modified Marmousi model, as shown in Figure 3. The modified Marmousi model was discretized into 801 × 561 grids with a uniform spacing of 12.5 m in both the x- and z-directions. The horizontal and vertical components of the vector-reflectivity were derived from **Equation 8**. A Ricker wavelet with a dominant frequency of 25 Hz was excited at the surface. Two receivers, positioned 2.0 km and 3.0 km from the source, respectively, were used to record the waveforms. The data were sampled at 0.8 ms intervals over a total recording time of 5.0 s. We adopted the variable-density viscoacoustic wave **Equation 2** from Guo *et al.*[45] as the reference solution, given its accurate representation of attenuation behavior.

Figure 4 displays the wavefield snapshots simulated at 2.8 s using the variable-density viscoacoustic wave equation and the viscoacoustic wave equation with vector-reflectivity. The reference result (Figure 4A) and the wavefield simulated by the proposed method (Figure 4B) exhibited nearly identical kinematic and dynamic characteristics. The residual between the two (Figure 4C) remained negligible, confirming the high fidelity of the proposed formulation. Both equations can accurately and stably simulate the wavefield in subsurface attenuating media. For a more detailed comparison, Figure 5 presents the recorded waveforms at the two receivers. We observed that the green curve and the red dashed curves were essentially coincident, regardless of the waveform recording location. The residual between the two curves was negligible relative to the waveform amplitude. The high consistency in both kinematic and dynamic features between the reference and proposed solutions demonstrates that the viscoacoustic wave equation with vector-reflectivity achieves numerical simulation accuracy essentially equivalent to that of the variable-density viscoacoustic wave equation. Furthermore, the single-shot records are shown in Figure 6. We observed that the deep reflection events in the shot records exhibit low energy and poor coherence, attributable to attenuation. The shot records simulated by the two methods were highly similar, with negligible residuals between them. This indicates that the wavefields generated throughout the numerical simulation process exhibit essentially identical kinematic and dynamic characteristics. However, due to grid discretization, large impedance contrasts lead to inaccuracies in reflectivity estimates, which in turn impair the accuracy of wavefield simulation at those locations.

Additionally, we employed a scaled version of the Society of Exploration Geophysicists Advanced Modeling model to further evaluate the simulation accuracy of the proposed viscoacoustic wave equation with vector-reflectivity. The model, shown in Figure 7, consisted of 876 × 751 grid points with uniform 10 m spacing in horizontal and vertical directions. A Ricker wavelet source with a dominant frequency of 25 Hz was excited at the surface at a horizontal position of 4.4 km. Data were recorded with a time sampling of 0.8 ms over 6.0 s.

Figure 8A and 8B displays wavefield snapshots simulated at 2.0 s computed using the reference variable-density viscoacoustic equation and the proposed vector-reflectivity viscoacoustic wave equation, respectively. The two snapshots exhibited excellent agreement, with only minor residuals, as shown in Figure 8C. Figure 9 presents a common-shot gather recorded by 876 receivers spaced at 10 m intervals. Figure 9A and 9B is essentially identical, yet their residual—shown in Figure 9C—contains a relatively strong reflection. This reflection originates from the first interface of the velocity and density model. We hypothesize that it results from excessively large density contrasts at the interface, leading to pronounced gradient discontinuities. A vertical trace extracted at 4.4 km from Figure 9 is plotted in Figure 10. Both the shot gather and the extracted trace demonstrated that results from the vector-reflectivity formulation closely matched those of the variable-density reference, confirming that the proposed wave equation accurately captures both kinematic behavior and attenuation effects in heterogeneous viscoacoustic media.

However, in practical seismic exploration, the reflectivity is typically estimated from stacked images obtained with small-offset data using the deconvolution imaging condition. This reflectivity is input only as the vertical reflectivity estimate, while the horizontal reflectivity estimate remains absent.

4. Discussion

In the previous sections, numerical forward-modeling

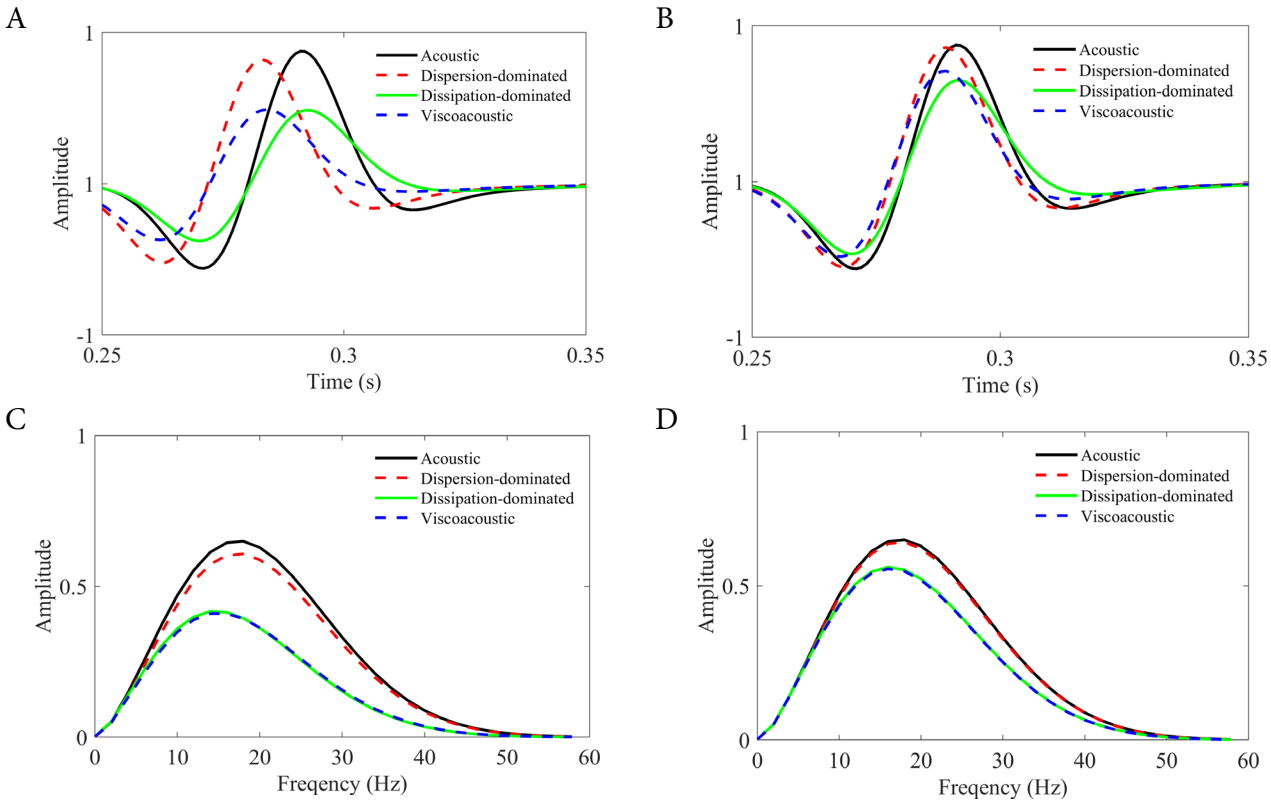

Figure 2. The waveforms recorded by the receiver are numerically simulated by the acoustic wave equation (black curve), dispersion-dominated equation (red dashed curve), dissipation-dominated equation (green curve), and viscoacoustic wave equation (blue dashed curve) with: (A) Q = 15, (B) Q = 40 in homogeneous media. (C) and (D) are the amplitude spectra of the waveforms in (A) and (B).

experiments confirmed that the viscoacoustic wave equation with vector-reflectivity and the variable-density viscoacoustic wave equation achieved comparable accuracy in simulating heterogeneous attenuating media. This demonstrates that the viscoacoustic wave equation with vector-reflectivity (**Equation 9**) can serve as a substitute for the variable-density viscoacoustic wave equation (**Equation 2**) as the wavefield propagation operator in both Q-RTM and Q-LSRTM. Given their identical simulation accuracy, the computational efficiency of the numerical solutions of the two equations must also be considered. Comparing **Equation 2** and **Equation 9**, **Equation 2** contains one gradient operator ∇p and one divergence operator $\nabla\cdot\left(\frac{1}{\rho}\nabla p\right)$. Whereas **Equation 9** includes two gradient operators ∇p and ∇v, and one divergence operator $\nabla\cdot(\nabla p)$. Theoretically, this implies that solving **Equation 9** requires additional computational resources to handle the extra gradient operator ∇v. Nevertheless, since **Equation 9** does not rely on accurate density parameters as input and can instead utilize estimated reflectivity images, it retains distinct advantages.

Since we decoupled the dissipation and phase dispersion effects of the viscoacoustic wave equation with vector-reflectivity (**Equation 9**), we can derive the corresponding attenuation-compensated viscoacoustic wave equation with vector-reflectivity ($\kappa_1 = 1$ and $\kappa_2 = -1$ in **Equation 24**) to implement Q-RTM. Yet, this appears to fall into a circular dilemma: numerically solving the equation requires reflectivity images as input, while the purpose of numerically solving the equation in Q-RTM is to obtain attenuation-compensated reflectivity images. However, this circular dependency can be resolved within the Q-LSRTM framework because least-squares inversion utilizes the updated reflectivity images as the input to the linearized viscoacoustic wave equation to compute the predicted data. Having derived the forward and migration operators within Q-LSRTM, we now turn to the linearized forward operator.

The linearized viscoacoustic wave equation derived under the first-order Born approximation is widely used in Q-LSRTM. However, this linearized operator only generates primary reflections and inherently excludes full-wavefield information such as multiples. To highlight the advantages

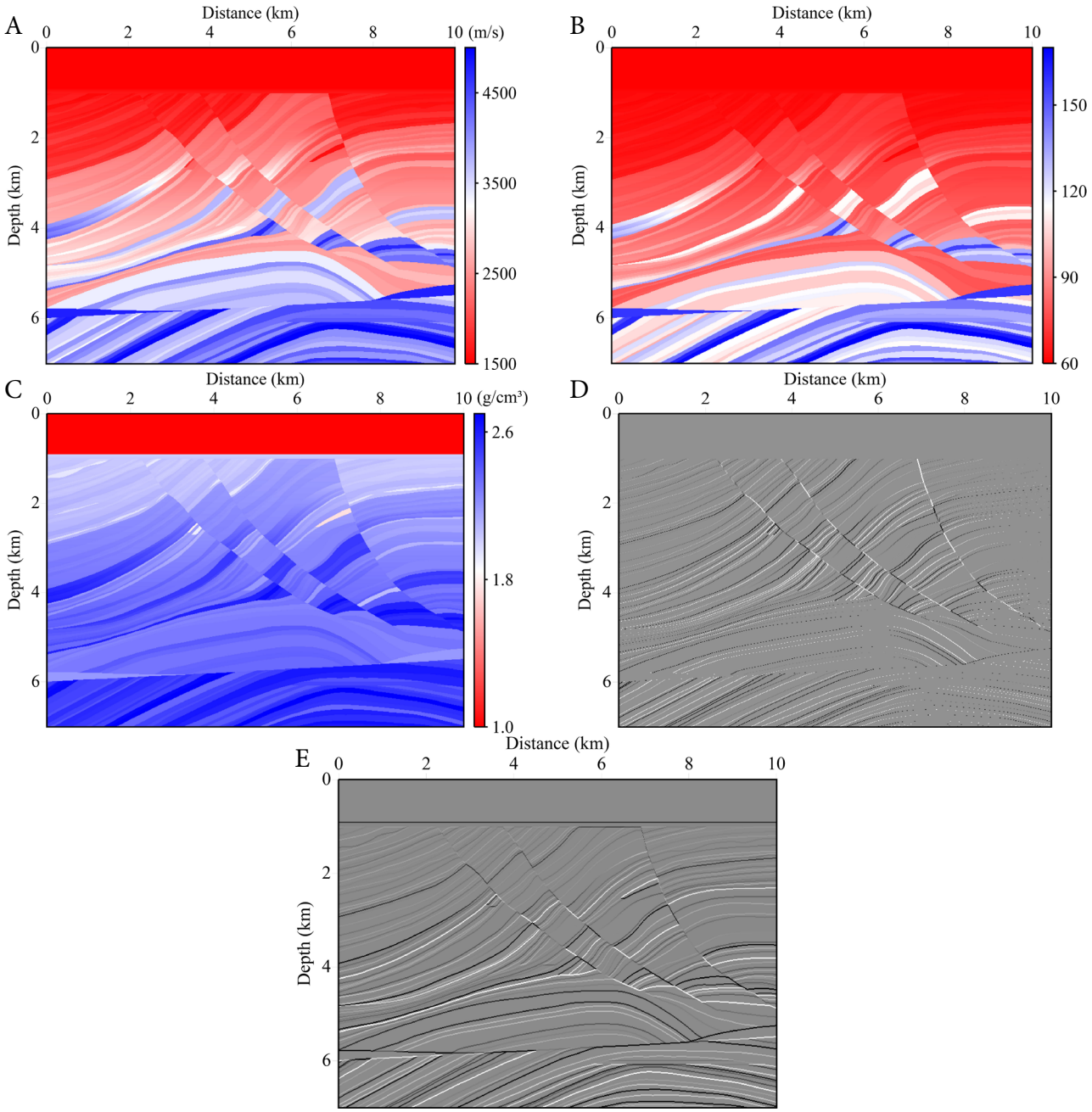

Figure 3. The modified Marmousi model. (A) P-wave velocity v_p. (B) P–wave quality factor Q. (C) Density ρ. (D) and (E) Horizontal and vertical components of the vector-reflectivity.

of the proposed vector-reflectivity viscoacoustic wave equation over the first-order Born linearized operator, we conducted forward modeling using a constant-velocity, variable-density model. Figure 11 illustrates the model parameters: constant velocity, constant Q, variable density, and the vector-reflectivity components in the horizontal and vertical directions. Reflectivity and the associated wavefields originate solely from density variations. A Ricker wavelet with a dominant frequency of 25 Hz was excited at the surface at a horizontal position of 1.5 km. Modeling experiments were performed using three distinct equations: the variable-density viscoacoustic wave equation (full-wavefield reference), the proposed vector-reflectivity viscoacoustic wave equation, and the variable-density linearized viscoacoustic wave equation based on the first-order Born approximation.

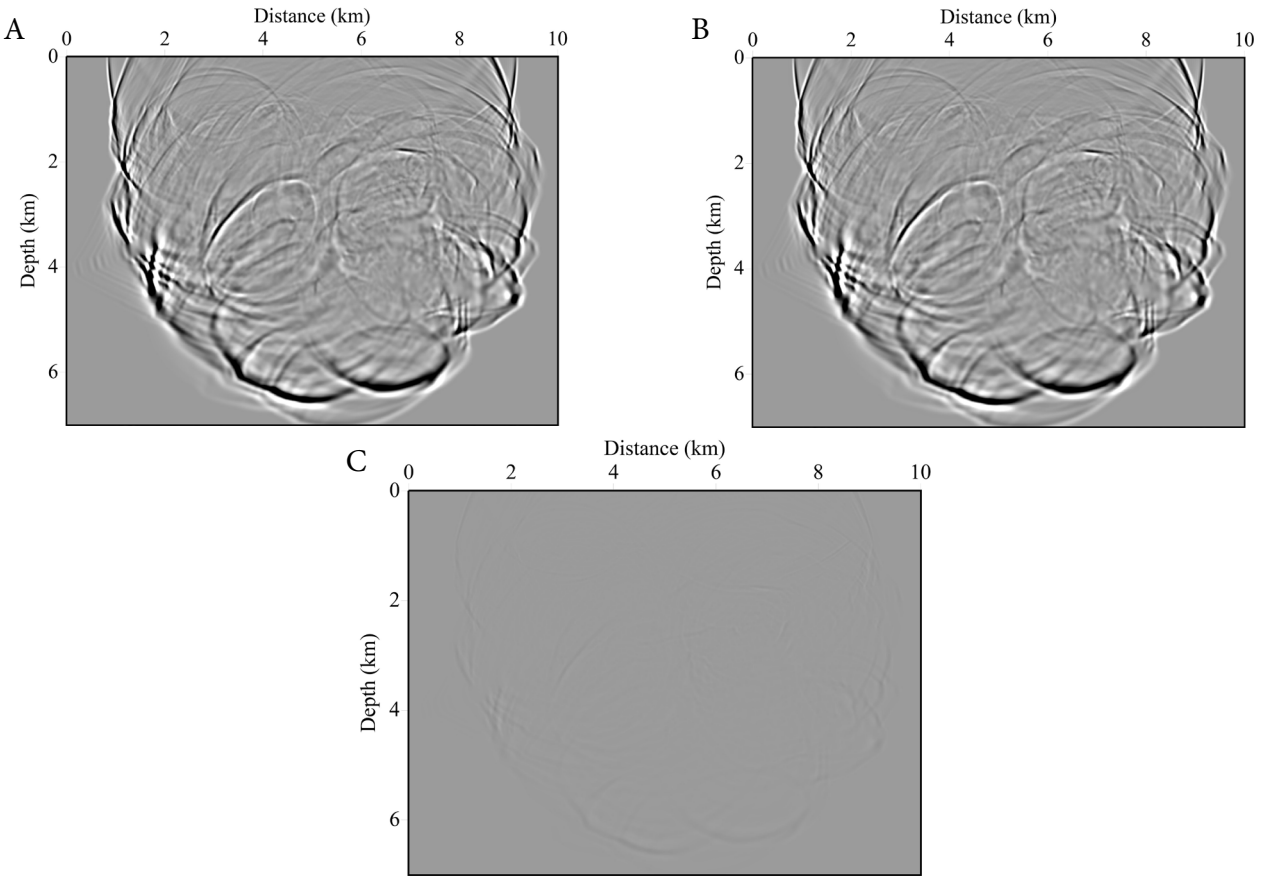

Figure 4. Wavefield snapshots of the modified Marmousi model simulated at 2.8 s using (A) variable-density viscoacoustic wave equation and (B) viscoacoustic wave equation with vector-reflectivity. (C) The residual of (A) and (B). The same color scale was used for all subplots.

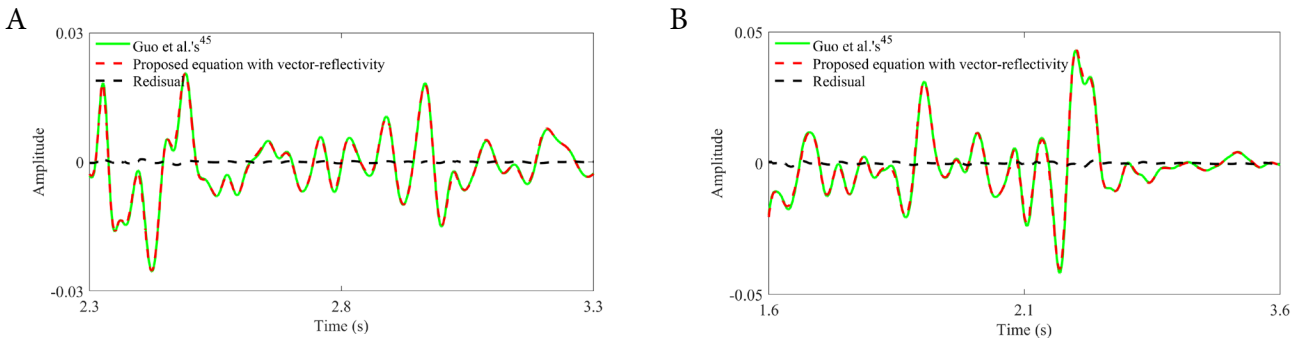

Figure 5. The recorded waveforms located (A) 2.0 km and (B) 3.0 km from the source, simulated using the viscoacoustic wave equation of Guo *et al.*[45] (green curves) and the viscoacoustic wave equation with vector-reflectivity (red dashed curves). The black dashed curves are the residual between the green curves and the red dashed curves.

The corresponding synthetic shot records are shown in Figure 12. The first four reflection events in the seismograms arose from density contrasts, while the two later events marked by black arrows corresponded to internal multiples. The record generated using the variable-density viscoacoustic wave equation (Figure 12A) served as the full-wavefield reference. Comparison between Figure 12A and 12B revealed that the vector-reflectivity equation correctly simulated internal multiples, whereas the linearized equation (Figure 11C) failed to model these events. This demonstrates that the proposed vector-reflectivity viscoacoustic wave equation can

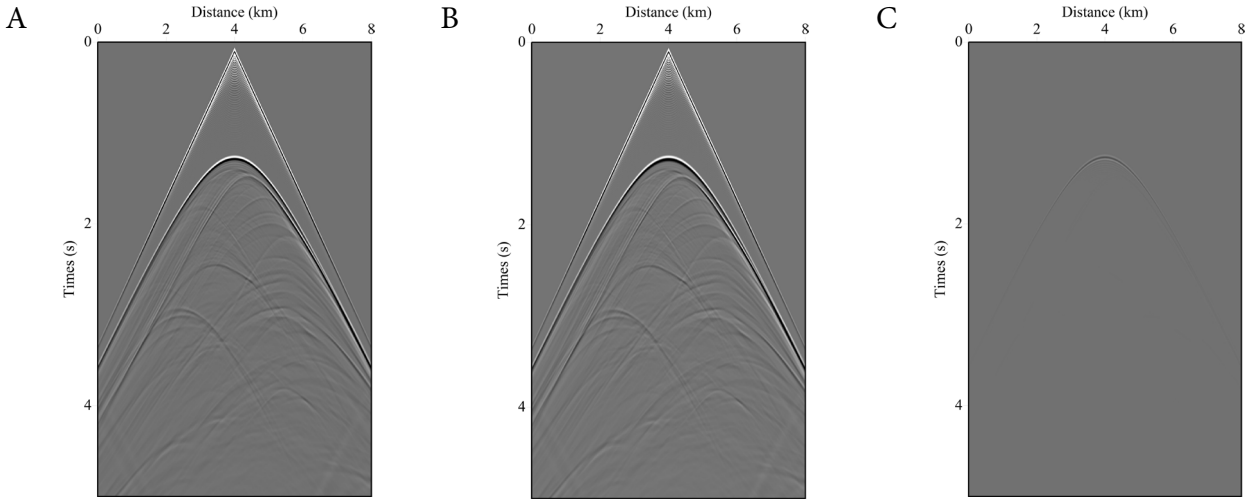

Figure 6. Shot gathers of the modified Marmousi model simulated using (A) the viscoacoustic wave equation with vector-reflectivity and (B) the variable-density viscoacoustic wave equation. (C) The residual of (A) and (B). The same color scale was used for all subplots.

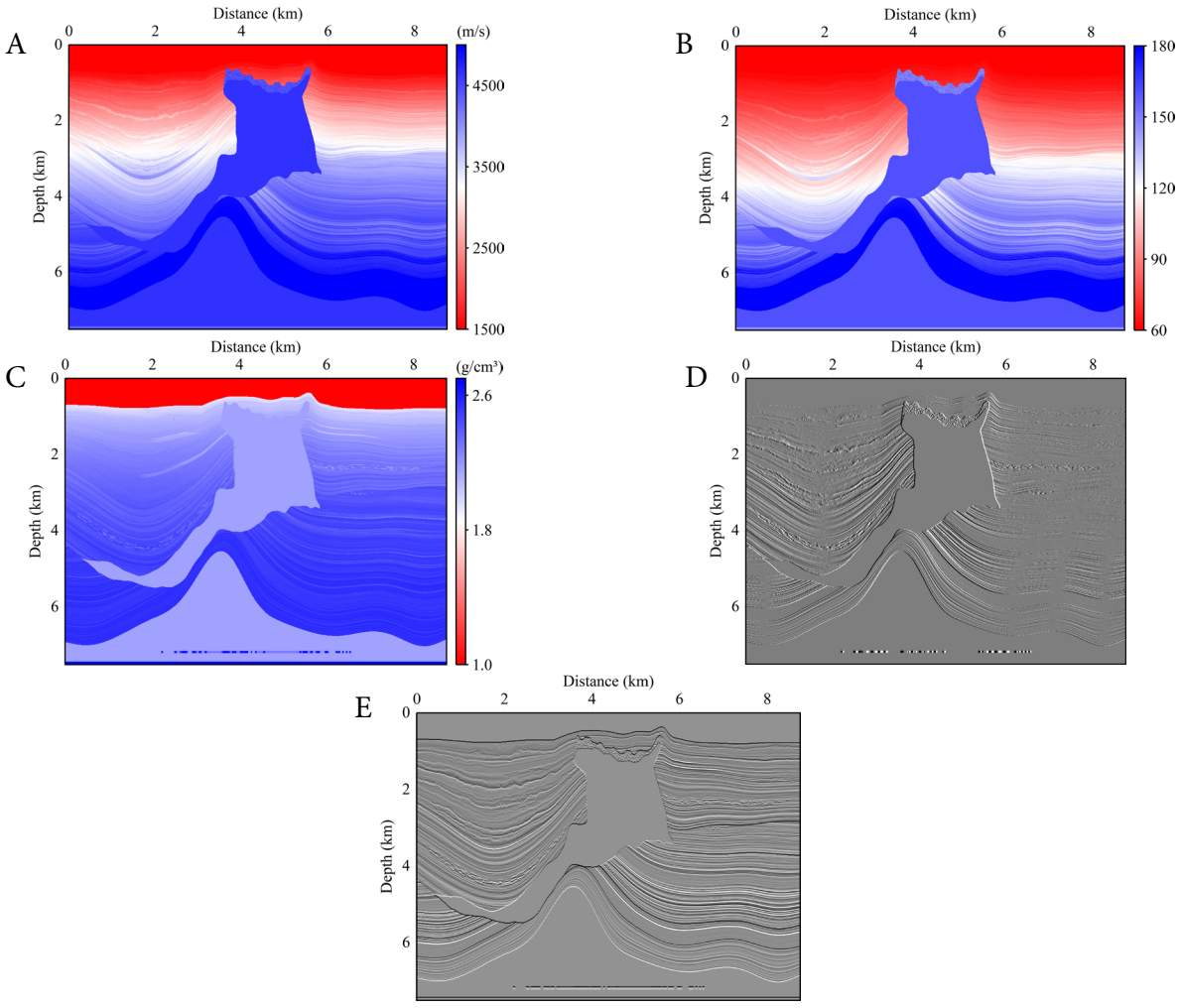

Figure 7. The modified Society of Exploration Geophysicists Advanced Modeling model with a grid point of 876 × 751 and a grid spacing of 10 m. (A) P-wave velocity v_p. (B) P-wave quality factor Q. (C) Density ρ. (D) and (E) Horizontal and vertical components of the vector-reflectivity.

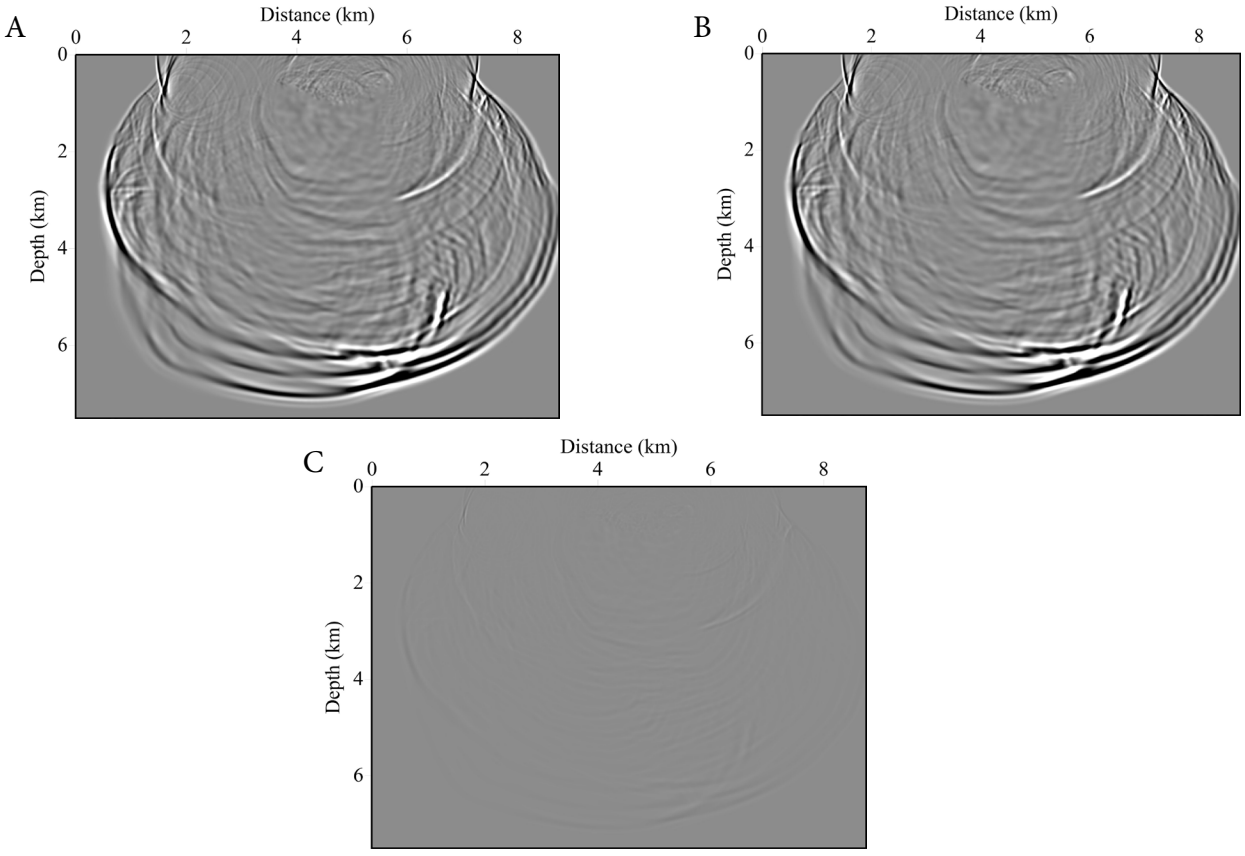

Figure 8. Wavefield snapshots of the modified Society of Exploration Geophysicists Advanced Modeling model simulated at 2.0 s using (A) variable-density viscoacoustic wave equation and (B) viscoacoustic wave equation with vector-reflectivity. (C) The residual of (A) and (B). The same color scale was used for all subplots.

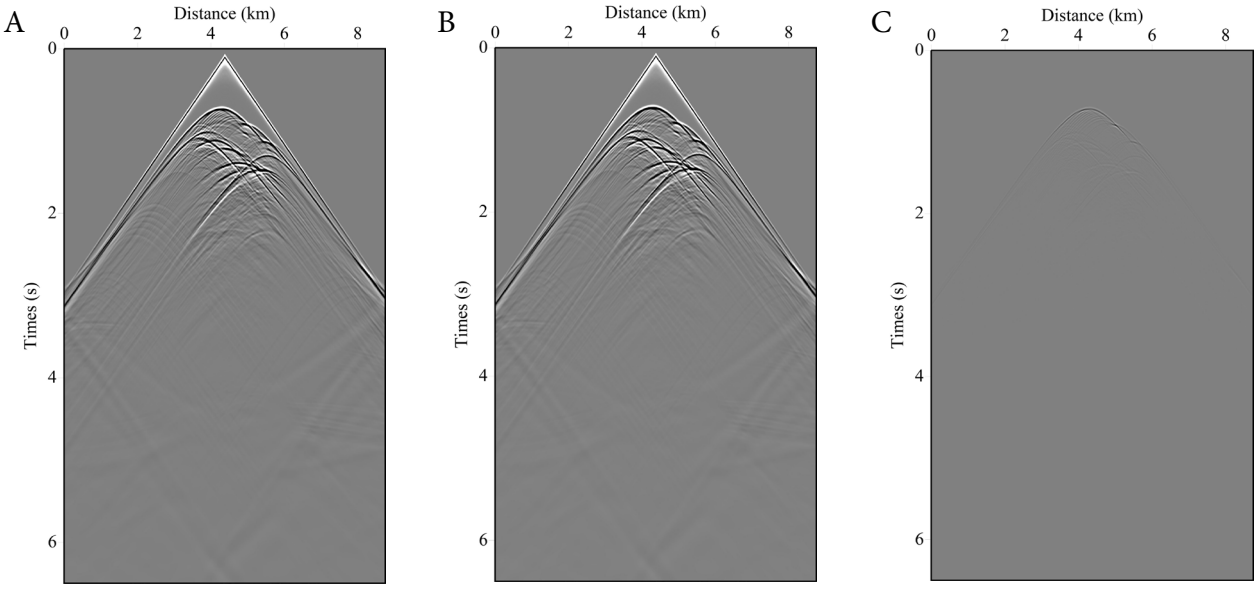

Figure 9. Shot gathers of the modified Society of Exploration Geophysicists Advanced Modeling model simulated using (A) the viscoacoustic wave equation with vector-reflectivity and (B) the variable-density viscoacoustic wave equation. (C) The residual of (A) and (B). The same color scale was used for all subplots.

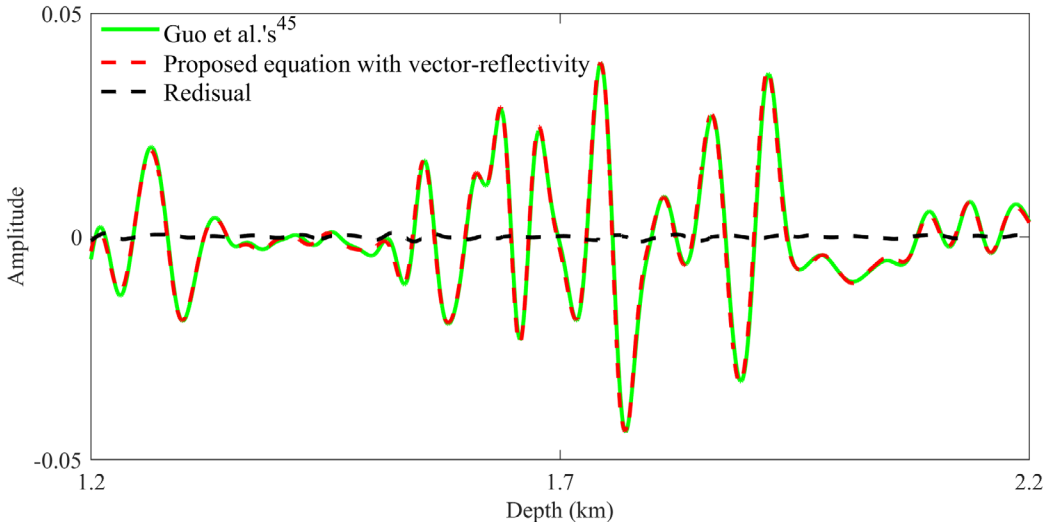

Figure 10. Vertical trace extracted at 4.4 km in horizontal distance from **Figure 9**. Notes: Green curves: viscoacoustic wave equation of Guo *et al.*;[45] Red dashed curves: viscoacoustic wave equation with vector-reflectivity; Black dashed curves: residual between green curves and red dashed curves.

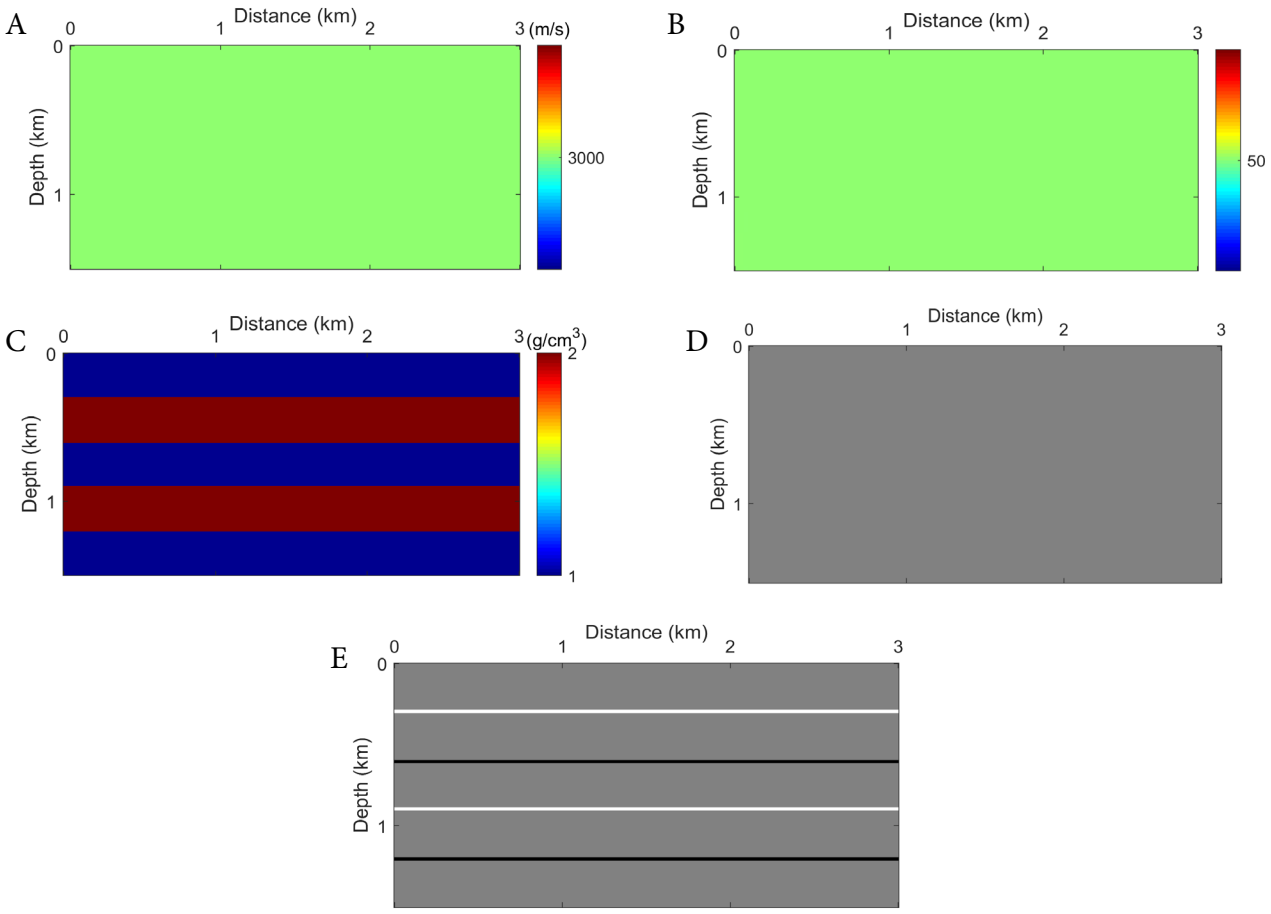

Figure 11. The constant-velocity, variable-density model with a grid point of 301 × 151 and a grid spacing of 10 m. (A) P-wave velocity v_p. (B) P-wave quality factor Q. (C) Density ρ. (D) and (E) Horizontal and vertical components of the vector-reflectivity.

effectively replace the first-order Born linearized operator in Q-LSRTM, as the simulated multiples can be matched with those in the field data and subsequently eliminated through subtraction.[44]

5. Conclusion

This study presents a viscoacoustic wave equation with a vector-reflectivity forward-modeling framework to overcome the limitations of conventional Q-LSRTM. Compared to the forward operators in conventional Q-LSRTM, the viscoacoustic wave equation with vector-reflectivity accurately simulated the full-wavefield without requiring explicit density parameters. Moreover, the proposed equation explicitly incorporates the Q factor, thereby avoiding the need for complex relaxation-time parameters. We further derived a decoupled formulation in which dissipation and dispersion effects were treated separately, serving as the migration operator to accelerate convergence in Q-LSRTM. Compared to the linearized viscoacoustic operator derived from the first-order Born approximation, the proposed viscoacoustic wave equation with vector-reflectivity accurately described attenuation effects and simulated full-wavefield responses—including both primaries and multiples. Numerical experiments demonstrated that the proposed formulation is mathematically equivalent to the original variable-density viscoacoustic wave equation. Future work should focus on applying this decoupled vector-reflectivity viscoacoustic wave equation to Q-LSRTM to effectively suppress crosstalk artifacts and produce high-resolution seismic images in attenuating media.

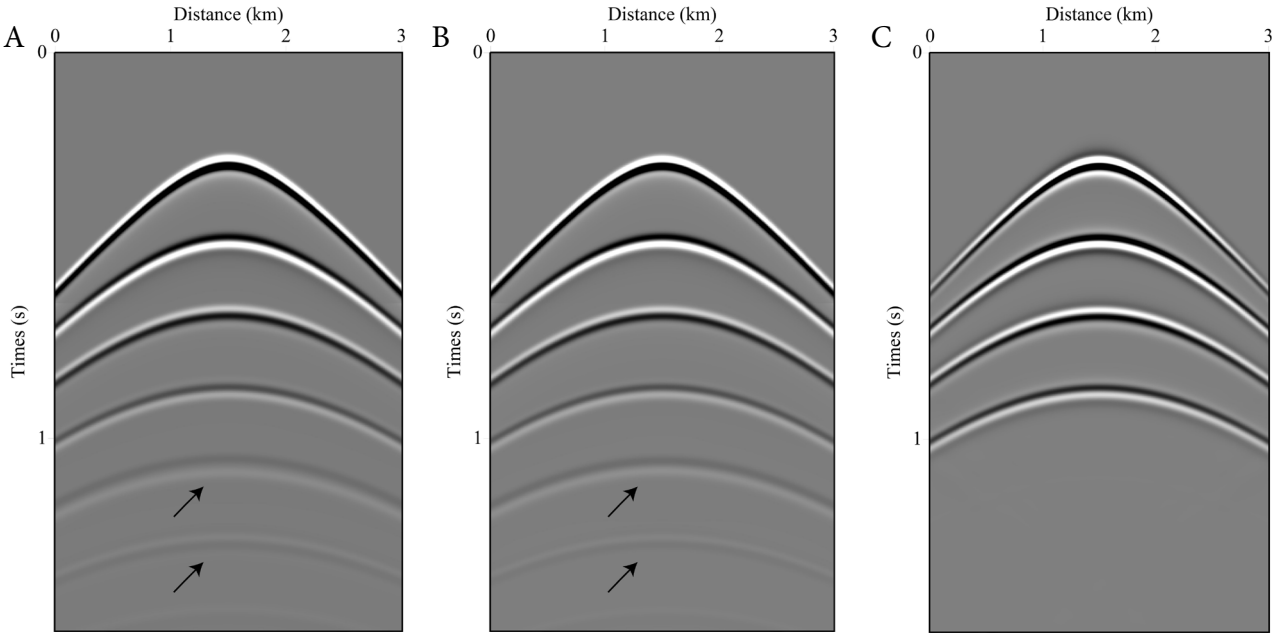

Figure 12. Shot gathers of the constant-velocity, variable-density simulated using (A) the variable-density viscoacoustic wave equation, (B) the viscoacoustic wave equation with vector-reflectivity, and (C) the linearized variable-density viscoacoustic wave equation. The same color scale was used for all subplots.

Acknowledgments

None.

Funding

This study is supported by the National Natural Science Foundation of China (Grant No. 42374164) and the High Precision Imaging Study of Small-scale and High-angle Structures in the Western Ordos Basin (Grant No. 2024D2ZZ01).

Conflict of interest

The authors declare they have no competing interests.

Author contributions

Conceptualization: Fei Li, Zilong Ye
Formal analysis: Fei Li, Jintao Liu
Investigation: Mengmeng Wu, Mei Li, Yanjiao Dong
Methodology: Jintao Liu, Mengmeng Wu
Writing–original draft: Fei Li
Writing–review & editing: Fei Li, Zilong Ye, Jianping Huang

Availability of data

All data are available upon reasonable request from the corresponding authors.

References

1. Claerbout JF. *Earth Soundings Analysis: Processing Versus Inversion*. Boston, MA: Blackwell Scientific Publications; 1992.
2. Aki K, Richards PG. *Quantitative Seismology: Theory and Methods*. San Francisco, CA: W.H. Freeman; 1980.
3. Kjartansson E. Constant Q-wave propagation and attenuation. *J Geophys Res Solid Earth*. 1979;84(B9):4737-4748.

   doi: 10.1029/JB084iB09p04737
4. Zhu T, Harris JM. Modelling acoustic wave propagation in heterogeneous attenuating media using decoupled fractional Laplacians. *Geophysics*. 2014;79(3):T105-T116.

   doi: 10.1190/geo2013-0245.1
5. Chen H, Zhou H, Li Q, Wang Y. Two efficient modelling schemes for fractional Laplacian viscoacoustic wave equation. *Geophysics*. 2016;81(5):T233-T249.

   doi: 10.1190/geo2015-0660.1
6. Yang JD, Zhu HJ. A time-domain complex-valued wave equation for modelling visco-acoustic wave propagation. *Geophys J Int*. 2018;215(2):1064-1079.

   doi: 10.1093/gji/ggy323
7. Mu X, Huang J, Wen L, Zhuang S. Modelling viscoacoustic wave propagation using a new spatial variable-order fractional Laplacian wave equation. *Geophysics*. 2021;86(6):T487-T507.

   doi: 10.1190/geo2020-0610.1
8. Mu X, Huang J, Li Z, Liu Y, Su L, Liu J. Attenuation Compensation and Anisotropy Correction in Reverse Time Migration for Attenuating Tilted Transversely Isotropic Media. *Surv Geophys*. 2022;43(3):737-773.

   doi: 10.1007/s10712-022-09707-2
9. Mao Q, Huang JP, Mu XR, Yang JD, Zhang YJ. Accurate simulations of pure-viscoacoustic wave propagation in tilted transversely isotropic media. *Pet Sci*. 2024;21(2):866-884.

   doi: 10.1016/j.petsci.2023.11.005
10. Zhang Y, Zhang P, Zhang HZ. Compensating for visco-acoustic effects in reverse-time migration. In: *SEG Technical Program Expanded Abstracts 2010*. 80th SEG Annual International Meeting; October 17-22, 2010; Denver, CO. Society of Exploration Geophysicists; 2010:3160-3164.

    doi: 10.1190/1.3513503
11. Li Q, Fu LY, Zhou H, Wei W, Hou WT. Effective Q-compensated reverse time migration using new decoupled fractional Laplacian viscoacoustic wave equation. *Geophysics*. 2019;84(2):S57-S69.

    doi: 10.1190/geo2017-0748.1
12. Zhu T, Harris JM, Biondi B. Q-compensated reverse-time migration. *Geophysics*. 2014;79(3):S77-S87.

    doi: 10.1190/geo2013-0344.1
13. Dutta G, Schuster GT. Attenuation compensation for least-squares reverse time migration using the viscoacoustic-wave equation. *Geophysics*. 2014;79(6):S251-S262.

    doi: 10.1190/geo2013-0414.1
14. Sun J, Fomel S, Zhu T, Hu J. Q-compensated least-squares reverse time migration using low-rank one-step wave extrapolation. *Geophysics*. 2016;81(4):S271-S279.

    doi: 10.1190/geo2015-0520.1
15. Liu W, Shi Y, Wang N, Wang W, Fang J. Source-independent Q-compensated viscoacoustic least-squares reverse time migration. *Geophysics*. 2024;89(5):S361-S377.

    doi: 10.1190/geo2023-0639.1
16. Carcione JM. A generalization of the Fourier pseudospectral method. *Geophysics*. 2010;75(6):A53-A56.

    doi: 10.1190/1.3509472
17. Fomel S, Ying L, Song X. Seismic wave extrapolation using low-rank symbol approximation. *Geophys Prospect*. 2013;61(3):526-536.

    doi: 10.1111/j.1365-2478.2012.01064.x
18. Zhang Y, Liu Y, Xu SG. Arbitrary-order Taylor series expansion-based viscoacoustic wavefield simulation in 3D vertical transversely isotropic media. *Geophys Prospect*. 2020;68(8):2379-2399.

    doi: 10.1111/1365-2478.12999
19. Liu HP, Anderson DL, Kanamori H. Velocity dispersion due to anelasticity: Implication for seismology and mantle composition. *Geophys J Int*. 1976;47(1):41-58.

    doi: 10.1111/j.1365-246X.1976.tb01261.x
20. Carcione JM. *Wave Fields in Real Media: Theory and Numerical Simulation of Wave Propagation in Anisotropic, Anelastic, Porous and Electromagnetic Media*. 2nd ed. Amsterdam, Netherlands: Elsevier; 2007.
21. Robertsson JO, Blanch JO, Symes WW. Viscoelastic finite difference modelling. *Geophysics*. 1994;59(9):1444-1456.

    doi: 10.1190/1.1443701
22. Bai JY, Chen GQ, Yingst D, Leveille J. Attenuation compensation in viscoacoustic reverse time migration. In: *SEG Technical Program Expanded Abstracts 2013*. 83rd SEG Annual International Meeting; September 22-27, 2013; Houston, TX. Society of Exploration Geophysicists; 2013:3825-3830.

doi: 10.1190/segam2013-1252.1

23. Li Q, Zhou H, Zhang QC, Chen HM, Sheng SB. Efficient reverse time migration based on fractional Laplacian viscoacoustic wave equation. *Geophys J Int*. 2016;204(1):488-504.

doi: 10.1093/gji/ggv456

24. Fathalian A, Trad DO, Innanen KA. An approach for attenuation compensating multidimensional constant-Q viscoacoustic reverse time migration. *Geophysics*. 2020;85(1):S33-S46.

doi: 10.1190/geo2019-0107.1

25. Hao Q, Greenhalgh S. Nearly constant Q models of the generalized standard linear solid type and the corresponding wave equations. *Geophysics*. 2021;86(4):T239-T260.

doi: 10.1190/geo2020-0548.1

26. Mu XR, Huang JP. A simple and high-efficient viscoacoustic reverse time migration calculated by finite difference. *Geophysics*. 2023;88(6):S213-S223.

doi: 10.1190/geo2022-0762.1

27. Huang JD, Yang DH, He XJ. Discontinuous Galerkin method for solving viscoacoustic wave equations with amplitude dissipation and phase dispersion separation in isotropic and anisotropic media. *Geophys J Int*. 2023;235(3):2339-2360.

doi: 10.1093/gji/ggad369

28. Ye Z, Huang JP, Mu XR, Mao Q. Multidimensional Q-compensated reverse time migration using a high-efficient decoupled viscoacoustic wave equation. *Geophys Prospect*. 2024;72(6):2109-2122.

doi: 10.1111/1365-2478.13501

29. Mao Q, Huang JP, Shen Y. Efficient Q-compensated reverse time migration using a new decoupled viscoacoustic wave equation based on the generalized standard linear solid. *Geophysics*. 2025;90(5):S145-S160.

doi: 10.1190/geo2024-0767.1

30. Blanch JO, Robertsson JO, Symes WW. Modelling of a constant Q; Methodology and algorithm for an efficient and optimally inexpensive viscoelastic technique. *Geophysics*. 1995;60(1):176-184.

doi: 10.1190/1.1443744

31. Fichtner A, Driel MV. Models and Frechet kernels for frequency-(in)dependent Q. *Geophys J Int*. 2014;198(3):1878-1889.

doi: 10.1093/gji/ggu228

32. Guo P, McMechan GA. Compensating Q effects in viscoelastic media by adjoint-based least-squares reverse time migration. *Geophysics*. 2018;83(2):S151-S172.

doi: 10.1190/geo2017-0235.1

33. Mu XR, Alkhalifah T, Huang JP. Attenuation-compensated viscoelastic reverse time migration with finite-difference operators. *Geophysics*. 2025;90(3):S41-S54.

doi: 10.1190/geo2024-0295.1

34. Ding Y, Li ZC, Zhang K, Sang YY. Wavefield reconstructed least-square reverse time migration based on stable pure qP-wave equation in tilted transversely isotropic media. *J Seism Explor*. 2022;31(3):279-303.

35. Gao GC, Huang JP, Li ZC. Least-squares reverse time migration of pure qP-wave in anisotropic media using low-rank finite-difference. *J Seism Explor*. 2021;30(2):121-146.

36. Ke X, Shi Y, Wang WH. An efficient wavefield simulation and reconstruction method for least-squares reverse time migration. *J Seism Explor*. 2018;27(2):183-200.

37. Zuberi MAH, Alkhalifah T. Generalized internal multiple imaging (GIMI) using feynman-like diagrams. *Geophys J Int*. 2014;197(3):1582-1592.

doi: 10.1093/gji/ggt527

38. Alkhalifah T, Guo Q. Subsurface wavefields based on the generalized internal multiple imaging. *Geophys J Int*. 2019;219(2):1212-1224.

doi: 10.1093/gji/ggz340

39. Berkhout AJG. Review paper: An outlook on the future of seismic imaging, Part I: Forward and reverse modelling. *Geophys Prospect*. 2014;62(5):911-930.

doi: 10.1111/1365-2478.12161

40. Berkhout AJG. Review paper: An outlook on the future of seismic imaging, Part II: Full-wavefield migration. *Geophys Prospect*. 2014;62(5):931-949.

doi: 10.1111/1365-2478.12154

41. Whitmore ND, Ramos-Martinez J, Yang Y, Valenciano A. Full Wavefield Modelling with Vector-reflectivity. In: *Proceedings of the EAGE 2020 Annual Conference & Exhibition Online*; December 8-11, 2020; online. European Association of Geoscientists & Engineers; 2020.

doi: 10.3997/2214-4609.202010332

42. Yang Y, Ramos-Martinez J, Whitmore D, Huang G, Chemingui N. Simultaneous velocity and reflectivity inversion: FWI+LSRTM. In: *Proceedings of the 82nd EAGE Annual Conference & Exhibition*. European Association of Geoscientists & Engineers; October 18-21, 2021; Amsterdam, Netherlands.

doi: 10.3997/2214-4609.202113278

43. Bai J, Yilmaz O. Joint full-waveform inversion for velocity and vector reflectivity. In: *Proceedings of the 86th EAGE Annual Conference & Exhibition*. European Association of Geoscientists & Engineers; June 2-5, 2025; Toulouse, France.

doi: 10.3997/2214-4609.202510839

44. Wu H, Lu S, Dong X, Deng X, Gao R. Least-Squares Full-

Wavefield Reverse Time Migration Using a Modelling Engine With Vector-reflectivity. *IEEE Trans Geosci Remote Sens*. 2023;61:590112.

doi: 10.1109/TGRS.2023.3234902

45. Guo P, Guan H, Nammour R, Duquet B, McMechan GA. A stable Q compensation approach for adjoint seismic imaging by pseudodifferential scaling. In: *Proceedings of the SEG Technical Program Expanded Abstracts 2017*. 87th SEG Annual International Meeting; September 24-29, 2017; Houston, TX. Society of Exploration Geophysicists; 2017:4566-4571.

doi: 10.1190/segam2017-17747338.1

46. Mao Q, Huang JP. High-Efficiency Viscoacoustic Least-Squares Reverse Time Migration With Q-Compensated Gradient Using Nearly Constant Q Model. *IEEE Trans Geosci Remote Sens*. 2025;63:5802917.

doi: 10.1109/TGRS.2025.3600301

47. Virieux J. SH-wave propagation in heterogeneous media: Velocity-stress finite-difference method. *Geophysics*. 1984;49(11):1933-1942.

doi: 10.1190/1.1441605

ACCSCIENCE PUBLISHING

Journal of Seismic Exploration

ARTICLE

Hierarchical division encoder–decoder network for distributed acoustic sensing-vertical seismic profile noise suppression

Li Han[1], Dongyan Wang[1]*, and Hang Yu[2]

[1]Department of Land and Resources, College of Earth Sciences, Jilin University, Changchun, Jilin, China

[2]Department of Communication Engineering, College of Electrical Engineering, Northeast Electric Power University, Jilin, China

(This article belongs to the *Special Issue: Advanced Artificial Intelligence Theories and Methods for Seismic Exploration*)

Abstract

In recent years, traditional geophones for well seismic data acquisition have progressively been replaced by distributed acoustic sensing (DAS), a novel technique. The primary attributes of DAS are its extensive well coverage and robust adaptability to challenging acquisition situations. Unlike conventional geophones, vertical seismic profile (VSP) data obtained using DAS exhibit lower signal-to-noise ratios (SNRs) and more complex noise types. These complex and energetic perturbations pose challenges for further data analysis. Contemporary methods for mitigating noise in DAS-VSP data sometimes fail to yield complete and precise information, leading to inferior denoising quality and diminished signal recovery. We propose a hierarchical division encoder–decoder network utilizing a convolutional neural network to address this issue. This network employs spatial attention techniques for systematic reconstruction and facilitates hierarchical feature extraction according to information scale. Our methodology provides superior noise reduction capabilities while preserving signal integrity. It achieves this by comprehensively addressing features at all scales. Additionally, we generated the required training set by combining synthetic data with real noise, as no publicly available training sets are available for DAS-VSP data. The trained denoising network processes and analyzes both synthetic and real recordings. The experimental results demonstrate the efficacy of this technique in eliminating various types of DAS-VSP noise while preserving signal amplitude integrity and ensuring continuity of signal recovery.

Keywords: Hierarchical division; Noise suppression; Convolutional neural network; Signal-to-noise ratio; Attention mechanism

***Corresponding author:**
Dongyan Wang
(447998390@qq.com)

Citation: Han L, Wang D, Yu H. Hierarchical division encoder–decoder network for distributed acoustic sensing-vertical seismic profile noise suppression. *J Seismic Explor.* 2026;35(3):025440099. doi: 10.36922/JSE025440099

Received: October 31, 2025

Revised: January 17, 2026

Accepted: May 4, 2026

Published online: June 11, 2026

Copyright: © 2026 Author(s). This is an Open-Access article distributed under the terms of the Creative Commons Attribution License, permitting distribution, and reproduction in any medium, provided the original work is properly cited.

Publisher's Note: AccScience Publishing remains neutral with regard to jurisdictional claims in published maps and institutional affiliations.

1. Introduction

Seismic exploration is advancing into deeper, more complex geological settings as surface resources are exhausted.[1-3] This depletion results from the extensive extraction of oil and other material resources. The seismic wave reflected from deep depths is

significantly attenuated by wave propagation phenomena such as geometrical spreading and attenuation, as well as the gradual deterioration of the acquisition environment, making it nearly inaudible amid ambient noise.[4] The effective signal is considerably disrupted by overlapping interference from multiple sources. The reliability of seismic data is therefore compromised. It is imperative to use more effective acquisition technology. The technology of distributed acoustic sensing (DAS), which uses optical fiber as the sensing medium rather than an electric geophone, has advanced steadily.[5,6] By extracting and demodulating interferometric signals generated by phase fluctuations of Rayleigh scattered light, DAS enables the quantitative analysis of vibration signals within a specific frequency range.[7–9] DAS exhibits superior sensitivity in detecting weaker signals compared to conventional detectors, demonstrates enhanced resistance to electromagnetic interference, is straightforward to install, and is more cost-effective. DAS has applications in border security, reservoir monitoring, and vertical seismic profiling (VSP), owing to its acquisition and economic advantages.[10,11]

The VSP approach provides interlayer velocity data, which are crucial for transforming seismic records from the time domain to the depth domain.[12] A geophone is utilized within the wellbore, accompanied by a surface source positioned adjacent to the well for vertical borehole measurements. Substituting conventional detectors with DAS can enhance the sampling density of borehole seismic data in VSP. Nonetheless, numerous obstacles emerge in the implementation of DAS. Noise removal is especially challenging. In DAS-acquired seismic data, signal amplitudes are much weaker than noise amplitudes. Furthermore, with DAS-VSP data, the predominant noise is generated by the device itself, whereas in geophone data, the majority of noise is derived from external sources. The noise composition of DAS-VSP data is intricate, encompassing inherent instrument noise—such as fading noise, time-varying optical noise, and horizontal noise—as well as externally generated stochastic noise. Thus, the signal-to-noise ratio (SNR) of DAS-VSP data is inferior to that of traditional geophone data owing to elevated noise levels and more complex noise attributes.[13,14]

Contemporary research on DAS in borehole VSP primarily focuses on two areas: data gathering and data processing.[15–17] Modifying the seismic source type and improving fiber-optic installation help mitigate noise during the acquisition phase. This method has a limited impact when confronted with aliasing noise that overlaps the frequency range of effective signals. A multitude of denoising methods have been developed for processing seismic data. The work mainly focuses on data processing. For example, diffusion models have been applied to denoise DAS-VSP data, effectively suppressing "zigzag" noise.[18] U-Net network architectures have been used to remove coupling noise, demonstrating strong signal recovery capabilities.[19] In addition, multitask deep learning models have been proposed to simultaneously perform denoising, interpolation, and wavefield separation, improving data quality.[20–24]

Initial denoising methods, including band-pass filtering, median filtering, and Wiener filtering, exploited the frequency differences between signals and noise to mitigate noise in seismic data.[25,26] These techniques are widely used due to their simplicity; however, their effectiveness on non-stationary seismic data is limited. Time-frequency analysis methodologies have been used for denoising, such as the S-transform and time-frequency peak filtering. These methods differentiate noise components by analyzing the distinct properties of signals and noise in both temporal and frequency domains. The efficacy of time-frequency analysis is significantly influenced by parameter selection, and manual adjustments may result in inadequate differentiation between signal and noise. Multi-scale decomposition techniques aim to denoise seismic data by removing intrinsic mode functions (IMFs) linked to noise. Notable instances include empirical mode decomposition (EMD)[27,28], variational mode decomposition[29,30], and ensemble empirical mode decomposition.[31,32] Nonetheless, considerable aliasing between signals and noise may result in their simultaneous presence within the same IMF. Consequently, maintaining or discarding a component may introduce residual noise or degrade the signal. Sparsity-based methods, such as the wavelet transform (WT), also draw attention in seismic data processing. WT transforms seismic data into a sparse representation and then applies thresholding to eliminate noise. While WT can effectively reduce noise, its efficacy is limited by subjective parameter selection and the absence of directional guidance in thresholding. Conventional denoising techniques for complex noise in DAS-VSP data, each based on different concepts, have inherent limitations.[33] Consequently, the development of more effective noise-reduction methodologies is essential.

Deep learning has become a significant research focus in recent years. They have shown substantial advancements in image processing, computer vision, speech recognition, and related fields.[34–37] Convolutional neural networks (CNNs) have been effectively applied in various seismic exploration tasks, including fault identification, seismic inversion, and seismic data denoising.[38–41] In seismic denoising, CNNs differentiate signals from noise efficiently by establishing a nonlinear mapping between the target signal and the

contaminated data. Traditional network architectures include supervised feedforward convolutional denoising networks (DnCNNs)[42] and unsupervised generative adversarial networks (GANs).[43,44] Deep learning techniques outperform conventional denoising algorithms by utilizing diverse hyperparameters to independently extract abstract information, facilitating more efficient sparse representations. Nevertheless, challenges remain. Noise reduction performance for complex DAS-VSP data may be insufficient, and using a single-scale convolution kernel in DnCNN can lead to the loss of essential information. GANs can reduce reliance on extensive training datasets by employing an adversarial framework. This framework directs the generative model to produce data consistent with the actual distribution. However, instability and convergence issues render GAN training challenging. Consequently, an ongoing investigation into more efficient network architectures is essential.

We propose a hierarchical division encoder–decoder network (HDEN) to efficiently distinguish signals from noise in DAS-VSP data. In the initial phase, convolution with a large kernel extracts fundamental features throughout the encoding process. The large kernel's extensive receptive field enhances global feature extraction, but considerably increases computational cost. HDEN employs asymmetric convolution to reduce computational expenses while preserving global feature extraction. A multi-scale method is used to enhance global features and capture more detailed information. During the decoding phase, an attention mechanism integrates diverse local features from the encoding phase and progressively refines them across multiple scales. Finally, deconvolution reconstructs the data. Due to the lack of a standardized training dataset for DAS-VSP data, we generated synthetic data using forward modeling. Environmental noise was then isolated and combined with the synthetic data to form the training set.

The rest of the manuscript comprises the following sections. In Section 2, we introduce the design principle and network structure of HDEN. In Section 3, the construction of the training dataset, which includes both the signal set and the noise set, is discussed. In Sections 4 and 5, the processing results for synthetic and field DAS data are presented to investigate denoising performance. Finally, Section 6 concludes the main findings of this study.

2. Methods

2.1. Principle of denoising

Generally, the seismic data, including DAS data, always suffer from additive noise. Thus, the expression of DAS-VSP data can be formulated as follows (**Equation 1**):

$$r = p + n \tag{1}$$

where p represents the clean DAS-VSP signal, while n denotes the noise component. The denoising process aims to establish a mapping relationship between noisy data r and pure signal p by simulating function F through a trained network, thereby effectively removing various types of noise, as follows (**Equation 2**):

$$p \approx F\left(r; w, b\right) \tag{2}$$

where w represents the weight parameters, and b represents the bias parameters. The primary objective of training is to optimize and adjust these two network parameters to remove noise while preserving signal integrity as much as possible. We guided the update of network parameters by minimizing the following loss function (**Equation 3**):

$$l\left(w,b\right) = \frac{1}{2T}\sum_{k=1}^{T}\left\| F\left(r_k; w, b\right) - p_k \right\|^2 \tag{3}$$

The denoising result of the training data r_k is represented by $F\left(r_k; w, b\right)$, while p_k represents the corresponding clean signal of r_k. Additionally, T denotes the number of training samples. During each iteration, we utilized T samples to update the network parameters and ultimately optimize them.

2.2. Structure of the denoising network

The network architecture of HDEN is depicted in Figure 1A and consists of four main components: input, encoder, decoder, and output. The input unit comprises a 7 × 7 convolution with a stride of 2. This layer reduces the resolution of seismic records to accelerate data processing and enhance the extraction of high-level abstract features. Unlike conventional downsampling, the input unit preserves relative quality while decreasing recorded resolution. The encoder employs a hierarchical feature coding approach guided by feedforward signals. This facilitates multi-level feature extraction and precise information encoding across scales. The decoder integrates features from every encoder level using the embedded attention mechanism. During the output phase, the decoder's features are processed by upsampling and convolution to restore resolution and channel count in the seismic record. The encoder and decoder are the fundamental components of HDEN, and their architectures will be elaborated upon subsequently.

2.2.1. Encoder

In the encoder, asymmetric convolution is applied to improve resource efficiency and reduce computational

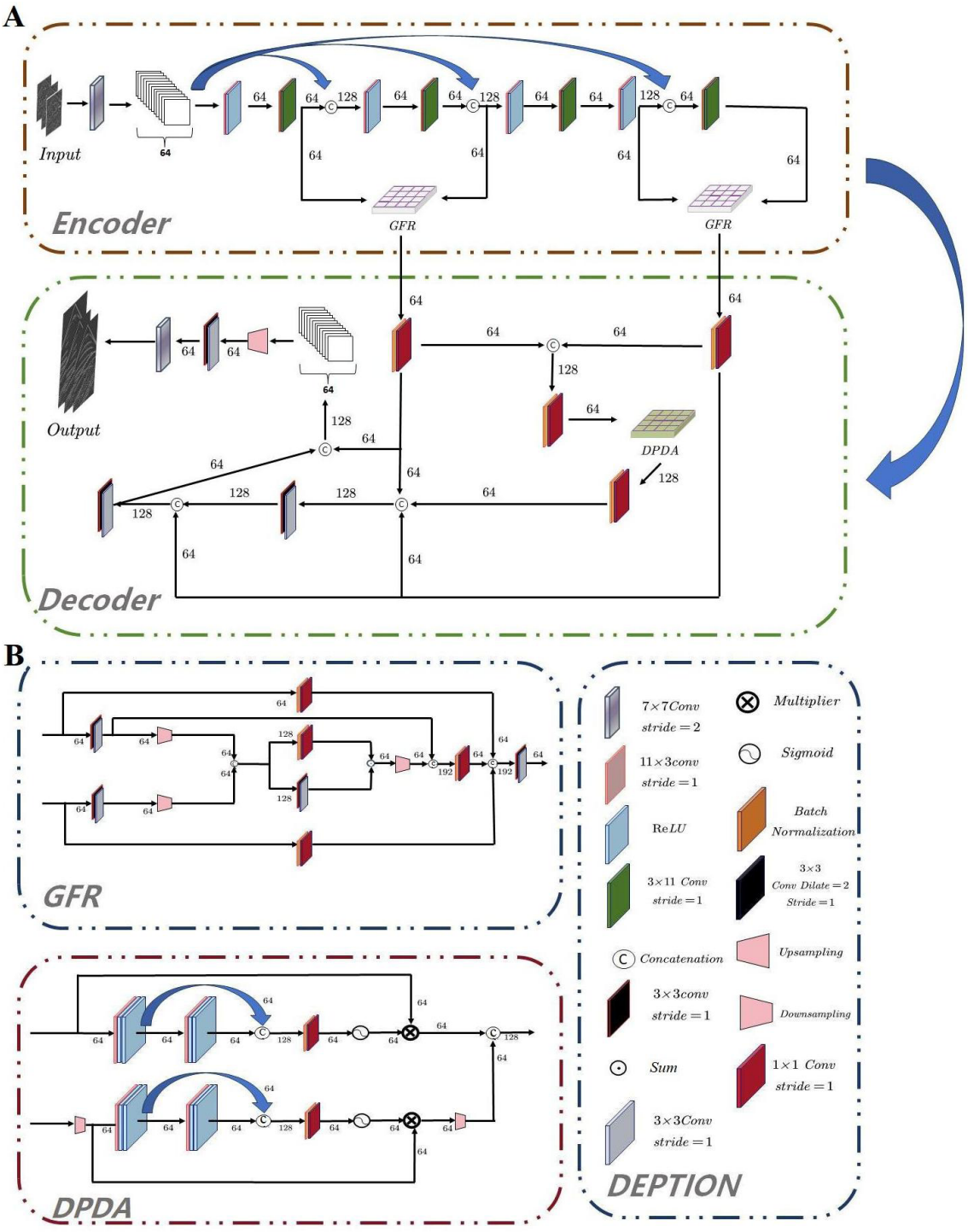

Figure 1. Hierarchical division encoder–decoder network architecture. (A) The overall structure. (B) The structure of the main network components. Abbreviations: DPDA: Dual-path dense attention; GFR: Global feature refinement; ReLU: Rectified linear unit.

burden.[45] The encoder predominantly uses a feedforward methodology to transmit information, thereby enhancing its capacity to extract novel features. Following global feature extraction, the global feature refinement (GFR) module partitions the global information obtained via asymmetric convolutions into multiple scales. This allows detailed local information to be refined across diverse scales. The GFR module effectively leverages both global and local information across hierarchical levels, thereby enhancing feature extraction precision.

2.2.2. Global feature refinement module

The GFR module achieves precise information segmentation by integrating skip connections with multi-scale feature extraction, as shown in Figure 1B. In the multi-scale component, two input datasets at different levels undergo independent 3 × 3 convolutions and are then downsampled to produce scales distinct from the original input. The two paths are combined and processed using standard and dilated convolutions to enhance multi-scale partitioning. After obtaining multi-scale features, the feature map is restored via upsampling to maintain its dimensions. Extracting features from a reduced feature map can lead to information loss, particularly for smaller targets and intricate details. Skip connections are employed to integrate features after upsampling, enabling effective feature fusion. This approach preserves specific information, minimizes information loss, and enhances network expressiveness. Input and output data are combined through skip connections to retain information from the original scale. Finally, the GFR module performs splicing between its input and output, preserving spatial integrity while improving both accuracy and robustness.

2.2.3. Decoder

The decoder features an expansion architecture distinct from the encoder, facilitating gradual recovery of data details and spatial dimensions while maintaining precise feature extraction via interconnections. It comprises two phases: fusion and restoration. In the fusion phase, encoder outputs at all levels are processed by the dual-path dense attention (DPDA) module, enabling selective emphasis on pertinent features. The decoder begins by obtaining the encoder's output through a 3 × 3 convolution. The resulting feature maps are concatenated and then processed by the DPDA module following channel adjustment. To ensure that the attention mechanism preserves critical information, the pre-concatenated data is integrated into the attention output, maintaining the original feature distributions. During the restoration phase, a 3×3 deconvolution reconstructs the recovered features. Skip connections systematically combine the encoder's output with the deconvolution, ensuring accurate feature recovery.

2.2.4. Dual-path dense attention module

The attention mechanism replicates human visual and cognitive processes, enabling the network to focus on critical information and thereby improving model performance and generalization.[46] Common attention mechanisms in CNNs include channel attention and spatial attention.[47,48] The channel attention mechanism selectively emphasizes important channels by evaluating their significance and assigning higher weights.[49] The spatial attention mechanism follows a similar principle, enhancing adaptive learning of attention weights across regions to highlight significant areas.[50] In this work, the spatial attention mechanism is implemented via the DPDA module, as shown in Figure 1B. The DPDA module generates two multi-scale pathways via downsampling and applies identical attention operations to each pathway independently, preventing interference across scales and enabling more precise focus on key regions. Additionally, dense connections integrate outputs from all convolutions to produce a spatial attention feature map via 1 × 1 convolution. After applying a Sigmoid function, the feature map is multiplied by the pathway input, thereby integrating both paths to focus on critical information.

3. Construction of training set

The effectiveness of deep learning techniques is directly associated with the quality and generalizability of the training data. The validity of the HDEN model depends on both its intrinsic structure and the reliability of the dataset. The training dataset in this study comprises two components: a pure DAS signal dataset and a pure DAS noise dataset. Direct acquisition of pure DAS signals is impractical due to inevitable noise in real-world measurements. To address this, the pure DAS signal dataset is generated from noise-free forward modeling data, while the pure DAS noise dataset is obtained from field DAS recordings.

3.1. Pure distributed acoustic sensing signal set

Recently, some studies have employed seismic wavelets with different fundamental frequencies and propagation velocities to generate the synthetic records.[2] However, signals produced this way are overly simplistic and do not reflect field data characteristics. Consequently, models trained on such analog signals perform poorly at retrieving weak reflection signals.[51,52] In contrast, we used a forward modeling method based on the wave equations to generate synthetic records, aiming to improve denoising accuracy. We used wave equations to simulate wavefield propagation and obtain synthetic records. Meanwhile,

the wave equation was activated by Ricker wavelets with fundamental frequencies ranging from 20 to 90 Hz. Furthermore, we used the finite difference method to solve the wave equation. Using the supplied stratigraphic profile data, we constructed a forward model that accurately represents the characteristics and structures of the strata. Finite difference equations are applied to solve the acoustic wave equation, effectively simulating seismic wave propagation through the geological layers. Based on prevailing conditions, 100 velocity models were generated by varying the thickness and density of the formations. Various wavelets with different center frequencies were used as inputs to the acoustic wave equation, producing 200 synthetic records. The detailed parameters for forward modeling are listed in Table 1. Parameters such as wavelet frequency and formation density were selected to span a wide range, enhancing data generalization and improving the model's denoising effectiveness. Figure 2 illustrates a representative forward model. Figure 2A shows a model with six distinct strata, each exhibiting an increasing wave velocity profile to simulate realistic stratigraphic conditions (1,500 m/s, 1,800 m/s, 2,200 m/s, 2,700 m/s, 3,300 m/s, and 4,000 m/s). The leftmost black vertical line indicates the DAS underground receiving line, while the red triangle 500 m away denotes the simulated source. The clean record in Figure 2B is generated by the forward model shown in Figure 2A. Using a sliding window technique, 18,159 clean DAS signal sets (64 × 64) were randomly extracted from the 200 synthetic records.

3.2. Pure distributed acoustic sensing noise set

Noise in DAS-VSP data arises from both environmental factors and inherent device interference, leading to a wide spectrum of DAS noise types. Interactions among these various noise types further increase the complexity of DAS-VSP noise. Consequently, noise generated solely through artificial simulation lacks precision and realism. To validate the pure DAS noise set, a diverse collection of typical noise segments—including fading, horizontal, and optical noise—was extracted from authentic DAS recordings without artificial stimulation sources. Combining multiple noise types enhances the neural network's ability to distinguish signals from noise. Here, we used noise data before the first arrival to construct the noise dataset, which contains only noise and no weak signals. Therefore, the denoising performance of the trained models can be further improved. On this basis, using a 64 × 64 sliding window, a total of 25,680 segments were extracted to create the pure DAS noise dataset.

3.3. Training process and training environment

During the training phase, we randomly selected one or more noise segments from the designated pure DAS noise set, then randomly extract a signal segment from the clean DAS signal set. To enhance training effectiveness, a random scaling factor between 0.3 and 3 is applied to the noise segments, which are then superimposed onto the signal segment, producing noisy records with varying SNRs. This process is iteratively repeated to generate 10,000 noisy records for network training, with the corresponding clean signal segments serving as network labels. The network is trained using mini-batch stochastic gradient descent to minimize the loss function, aiming to denoise DAS-VSP data so that the output closely matches the clean signals.

Experiments were conducted in MATLAB (2017b, MathWorks, USA) on a machine with an Intel(R) Core(TM) i5-9300H CPU at 2.40 GHz and an NVIDIA GeForce GTX 1050 GPU. The training batch size was set to 32, and training was performed over 60 epochs. The ADAM optimizer was used for network optimization. The learning rate was initially set to 10^{-4} and gradually decreased during training to 10^{-7}. Figure 3 shows the training and validation losses for HDEN. It is noted that all the losses are converged to small values, indicating the effectiveness of the training dataset and strategy.

4. Processing and analysis of the synthetic record

We employed HDEN to analyze synthetic recordings to assess its ability to distinguish signals from noise and examine the results. Synthetic records were generated similarly to the training set: clean DAS data were first generated by forward modeling and then combined with field noise. Figure 4A depicts the forward model used to generate the synthetic record, while Figure 4B shows the corresponding clean record after excitation. Figure 4C presents the noise record obtained from field data,

Table 1. Physical parameters of the forward model

Parameters	Specification
Wavelet	Ricker, single, and double
Central frequency (Hz)	20–90
Wave velocity (m/s)	1,000–5,000
Density (kg/m^3)	1,565–2,500
Interval (m)	1
Sampling frequency (Hz)	2,000

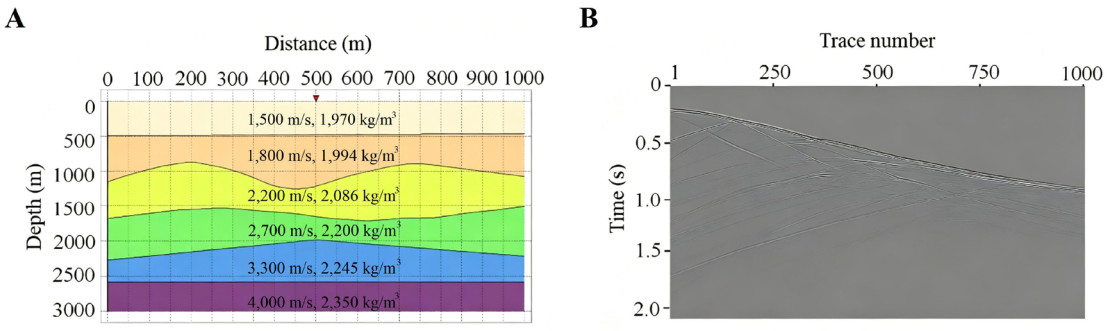

Figure 2. Construction of the pure synthetic record. (A) Stratigraphic model with velocity and density information; (B) The synthetic record.

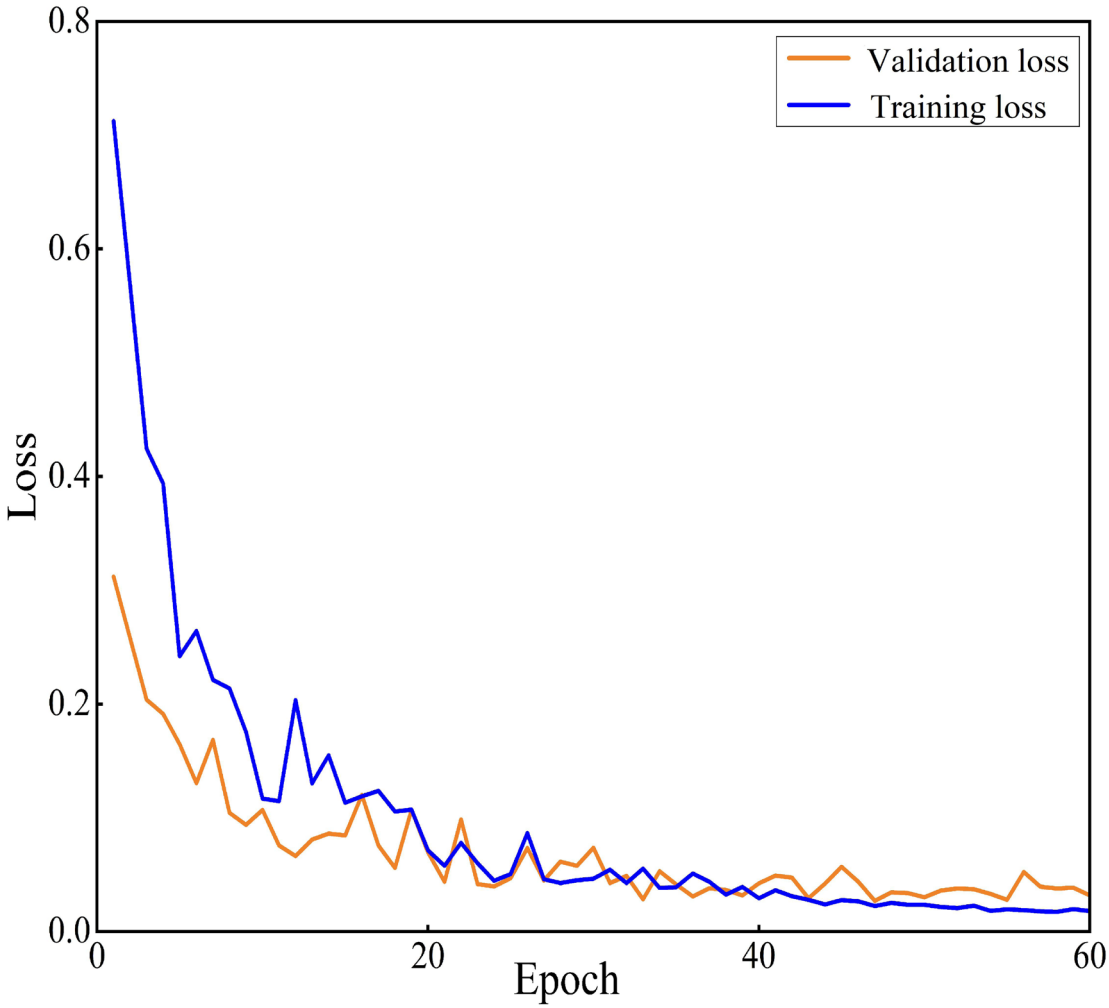

Figure 3. The training and validation losses for the hierarchical division encoder–decoder network

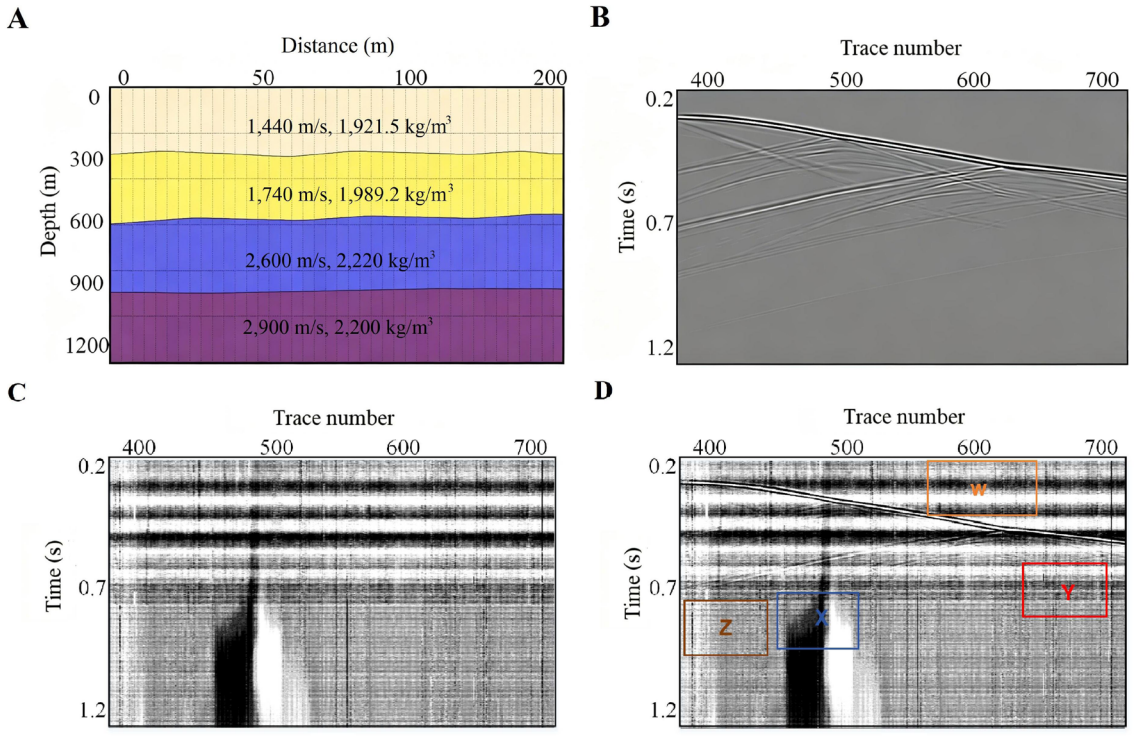

Figure 4. Noisy synthetic record. (A) Forward model. (B) Pure synthetic record. (C) Field noise record. (D) Noisy record (signal-to-noise ratio = −5 dB).

calibrated to match the actual noise distribution, including typical DAS-VSP noise types such as horizontal noise in box W, time-varying optical noise in box W, and fading noise in box Y. Figure 4D illustrates a synthetic test record produced by overlaying the clean and noisy records, resulting in an SNR of −5 dB. In this record, the overall signal is largely obscured by background noise, with only strong signals clearly visible, whereas the weak signal in box Z is difficult to discern due to substantial interference. We performed qualitative and quantitative evaluations of HDEN's denoising performance and compared the results with those obtained using singular value decomposition (SVD), WT, and DnCNN. To ensure the validity and fairness of the experiments, DnCNN and HDEN were trained under identical conditions.

4.1. Qualitative analysis

4.1.1. Analysis of denoising results

Figure 5 illustrates the denoising and local amplification results of SVD, WT, DnCNN, and HDEN. The SVD results in Figure 5B show poor noise reduction performance, with residual horizontal, fading, and time-varying optical noise. Signal recovery is effective only for high-energy signals. Amplification analysis in regions affected by time-varying optical noise reveals that multiple noise types hinder the retrieval of weak signals. The WT results in Figure 5C exhibit the lowest denoising effectiveness, primarily addressing random noise while performing poorly against other noise categories; even prominent reflected signals are difficult to discern due to substantial residual noise. Figure 5D presents the outputs of DnCNN, showing a relatively clear background with significant noise suppression. However, DnCNN is inadequate in removing time-varying optical noise, as residual noise remains visible in the magnified image. Most signals can be reconstructed, preserving overall integrity, though some fine details are lost. Compared to traditional methods, deep learning improves both signal recovery and noise suppression, but the simple architecture of fully convolutional networks, such as DnCNN, limits feature extraction. In contrast, HDEN, also shown in Figure 5E, outperforms the other methods by effectively suppressing nearly all types of noise, including intense time-varying optical noise. Amplification results indicate that weak reflection signals can be fully and continuously restored, a feat not achieved using other techniques. These results confirm HDEN's superior denoising performance.

4.1.2. Analysis of amplitude retention characteristics

Figure 6 displays the filtered noise, evaluated to determine the effectiveness of each method in preserving signal

amplitude and validating DAS-VSP signal restoration. Figure 6A shows the original noise record, while Figures 6B–6E present the filtered results obtained using SVD, WT, DnCNN, and HDEN. Compared to the original noise, the SVD (Figure 6B) output revealed residual signals that became increasingly apparent when magnified in certain regions, indicating inadequate noise suppression. WT (Figure 6C) demonstrated limited denoising capability, effectively targeting random noise but failing to reduce other noise types, which complicated the identification of even prominent reflected signals. DnCNN (Figure 6D) achieved significant noise reduction and preserved signal amplitude relatively well; however, residual signal leakage remained, highlighting its limitations in fully recovering weak signals. In contrast, HDEN (Figure 6E) employed a specialized encoder–decoder framework to effectively remove nearly all types of noise, including substantial time-varying optical noise. The filtered and amplified results show negligible residual signals, confirming that the original amplitude is largely preserved. Consequently, HDEN provided comprehensive restoration of formation data and outperformed the other methods in both amplitude preservation and denoising effectiveness.

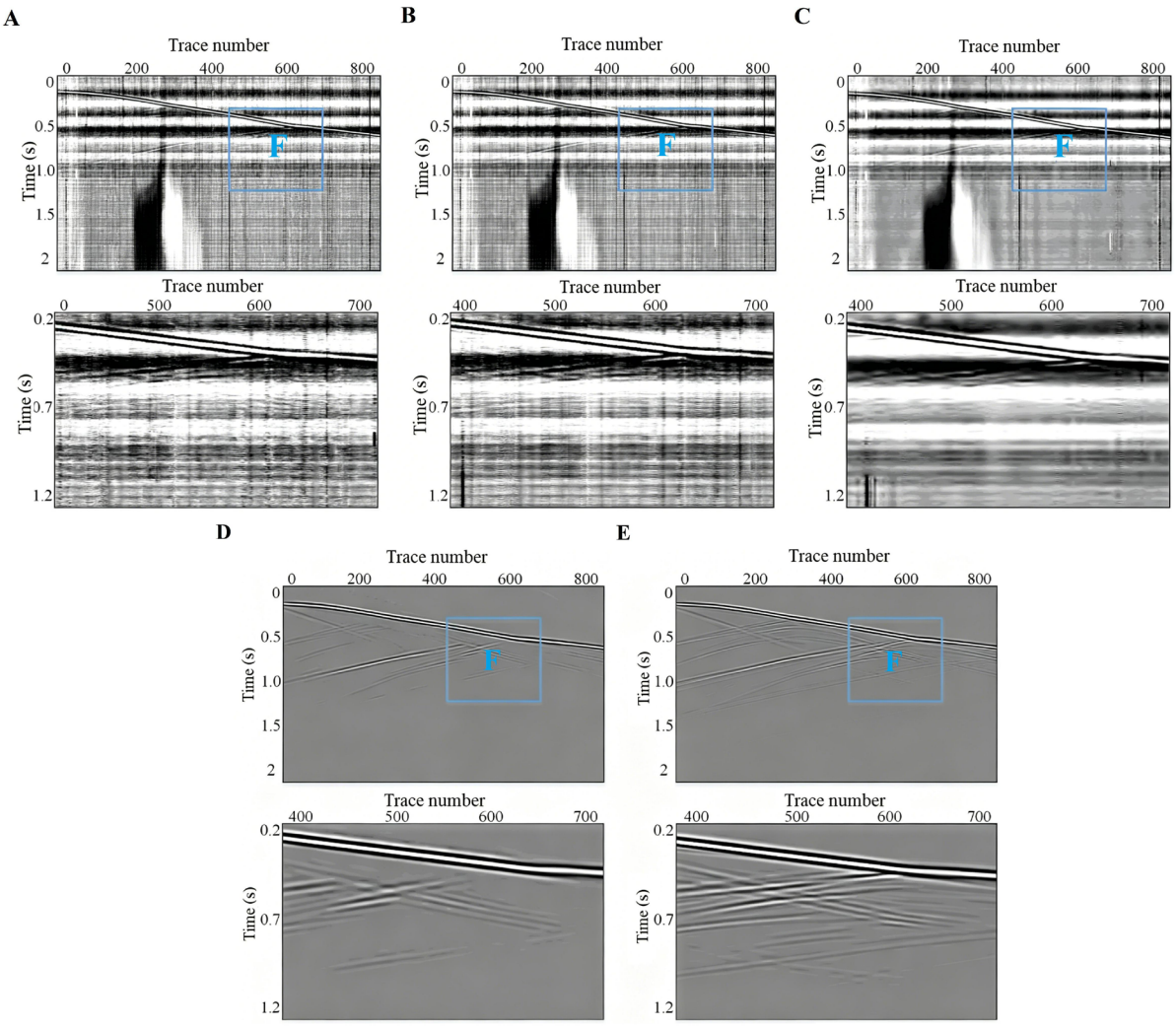

Figure 5. Denoising results of different methods. (A) Synthetic record and local magnification. (B)–(E) Denoising results (top subfigures) and local magnification (bottom subfigures) obtained using singular value decomposition, wavelet transform, convolutional denoising network, and hierarchical division encoder–decoder network. The boxed region magnifies the key detail to show the algorithm's noise suppression effect.

4.1.3. Frequency–wavenumber spectrum analysis

To comprehensively assess HDEN's denoising efficacy, we perform a comparison ofcompared frequency–wavenumber (F–K) spectrograms across several methods to elucidate frequency-domain behavior. Figure 7A shows the F–K spectrograms of the clean signal and noise. Figure 7B presents the denoised result and filtered noise after SVD processing. The SVD results are inadequate as residual noise remained, and both signal continuity and amplitude fidelity were compromised. Figure 7C displays the WT results, showing the least effective noise reduction and the greatest deviation from the pure recordings in the frequency domain. The denoising performance of DnCNN was slightly improved, as shown in Figure 7D. DnCNN efficiently removed most noise; however, residual frequency-domain components associated with noise persisted. Figure 7E presents the F–K spectrum of HDEN. Both the denoised output and the filtered noise closely resembled the F–K spectrum of the clean records. This comparison demonstrates that HDEN achieved superior denoising and better preserved signal integrity compared to other methods.

4.2. Quantitative analysis

4.2.1. Signal-to-noise ratio and root mean square error

A full and objective assessment of the denoising efficacy of various approaches necessitates more than a qualitative analysis alone. Consequently, we utilized two quantitative metrics: SNR^2 and root mean square error (RMSE).[19] The definitions of SNR and RMSE are shown in **Equations 4** and **5**:

$$SNR = 10lg\left(\frac{\sum_{i=1}^{x}\sum_{j=1}^{y}S_{(i,j)}^2}{\sum_{i=1}^{x}\sum_{j=1}^{y}\left(N_{(i,j)}-S_{(i,j)}\right)^2}\right) \quad (4)$$

$$RMSE = \sqrt{\frac{1}{xy}\sum_{i=1}^{x}\sum_{j=1}^{y}\left(N_{(i,j)}-S_{(i,j)}\right)^2} \quad (5)$$

where the symbol S signifies the signal, whereas the other symbol N represents noise. Furthermore, the symbols i and j correspond to the dimensions of the data, and the symbols x and y correspond to the length and width of the signal, respectively. We applied these measures to the results from SVD, WT, DnCNN, and HDEN for different SNR levels. The resultant SNR and RMSE are displayed in Table 2. At 0 dB, SVD yields less than 1 dB of SNR improvement, while WT shows a significant improvement beyond 2 dB. Nonetheless, both methods are constrained by specific restrictions. The implementation of DnCNN improved SNR by around 13 dB, demonstrating the superior denoising efficacy of deep learning compared to conventional methods. Of the four approaches, HDEN demonstrated the greatest SNR enhancement, nearly 17 dB. The SNR of the processed findings declined progressively as the original record's SNR decreased. The performance of WT was markedly diminished under low-SNR conditions, whereas SVD and DnCNN maintained some noise-suppression efficacy. The previously indicated methods, however, do not sufficiently meet the criteria for the further processing of DAS-VSP data. The HDEN approach demonstrated considerable benefits in low SNR records, delivering an approximate 25 dB SNR enhancement even at −10 dB. HDEN's resilience enabled it to reliably produce superior denoising results across diverse SNR conditions.

4.2.2. Analysis on computational efficiency

In deep learning applications, the time required for training and testing is an important consideration. Table 3 presents the training and testing durations and the average SNR improvement for HDEN and the comparative approaches. SVD and WT reduced computational burden, as they

Table 2. Comparison of SNR and RMSE

Synthetic record/dB	SVD		WT		DnCNN		HDEN	
	SNR/dB	RMSE	SNR/dB	RMSE	SNR/dB	RMSE	SNR/dB	RMSE
0	0.9678	0.6471	2.1711	0.5634	12.8600	0.1646	16.8926	0.1053
−2	0.7192	0.6659	0.2038	0.7067	12.2583	0.1764	16.4430	0.1088
−4	0.4016	0.6907	−1.7683	0.8868	11.4172	0.1943	16.5735	0.1114
−6	−0.2013	0.7404	−3.7426	1.1131	10.2311	0.2228	15.4429	0.1262
−8	−0.9473	0.8068	−5.7249	1.3984	8.5656	0.2698	15.0434	0.1301
−10	−1.8501	0.8952	−7.7117	1.7578	6.3872	0.3468	14.6438	0.1340

Abbreviations: DnCNN: Convolutional denoising network; HDEN: Hierarchical division encoder–decoder network; RMSE: Root mean square error; SNR: Signal-to-noise ratio; SVD: Singular value decomposition; WT: Wavelet transform.

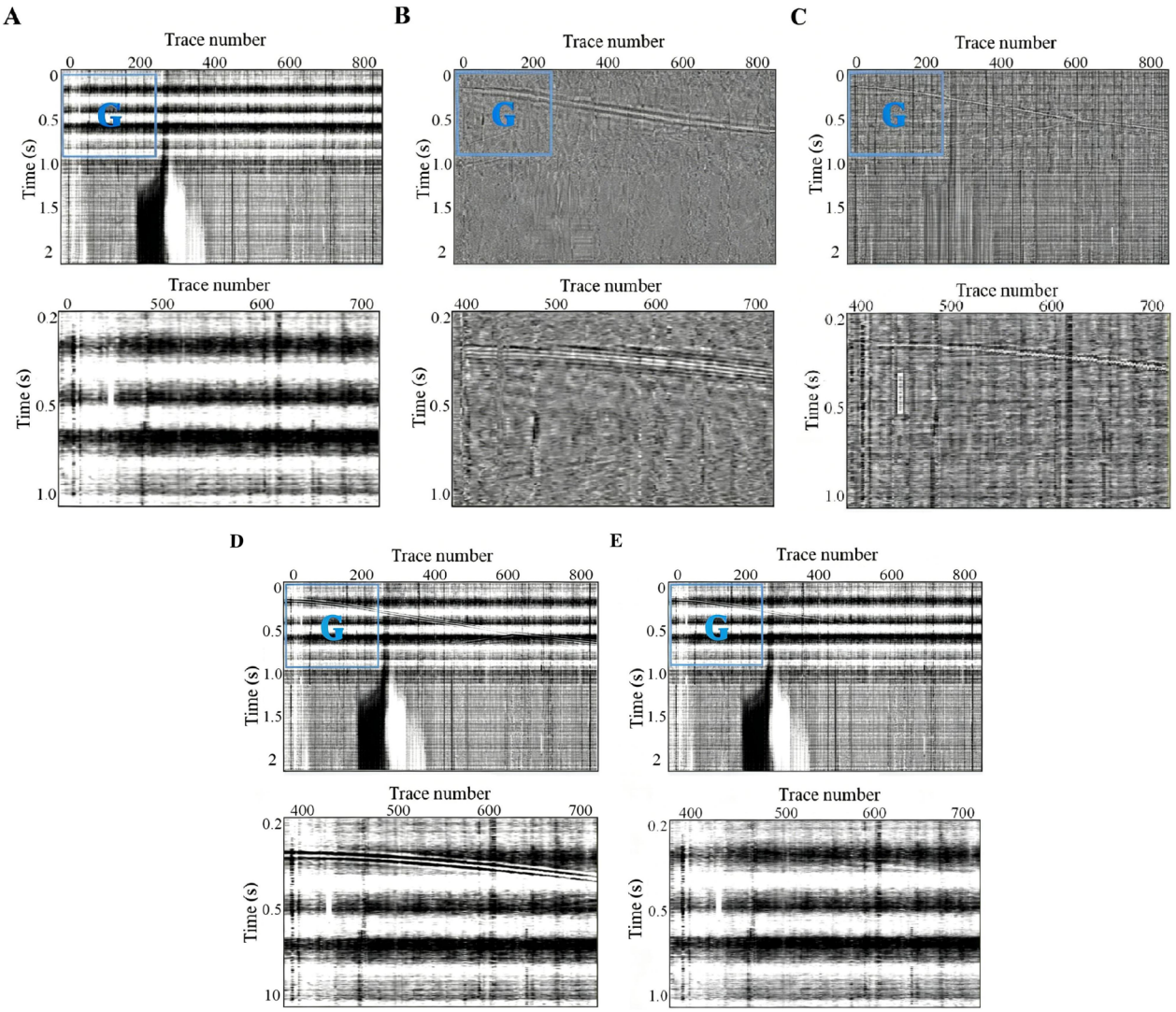

Figure 6. The filtered noise of different methods. (A) Pure noise record and local magnification. (B)–(E) The filtered noise (top subfigures) and local magnification (bottom subfigures) obtained using singular value decomposition, wavelet transform, convolutional denoising network, and hierarchical division encoder–decoder network. The boxed region magnifies another key detail, showing residual signals in the filtered result.

Table 3. The computational cost and improved SNR of different methods

Original record/dB	SVD	WT	DnCNN	HDEN
Processing time (s)	0.37	0.48	1.39	1.50
Training time (hour)	–	–	4.67	6.02
Averaged improved SNR (dB)	4.84	2.20	15.11	20.89

Abbreviations: DnCNN: Convolutional denoising network; HDEN: Hierarchical division encoder–decoder network; SNR: Signal-to-noise ratio; SVD: Singular value decomposition; WT: Wavelet transform.

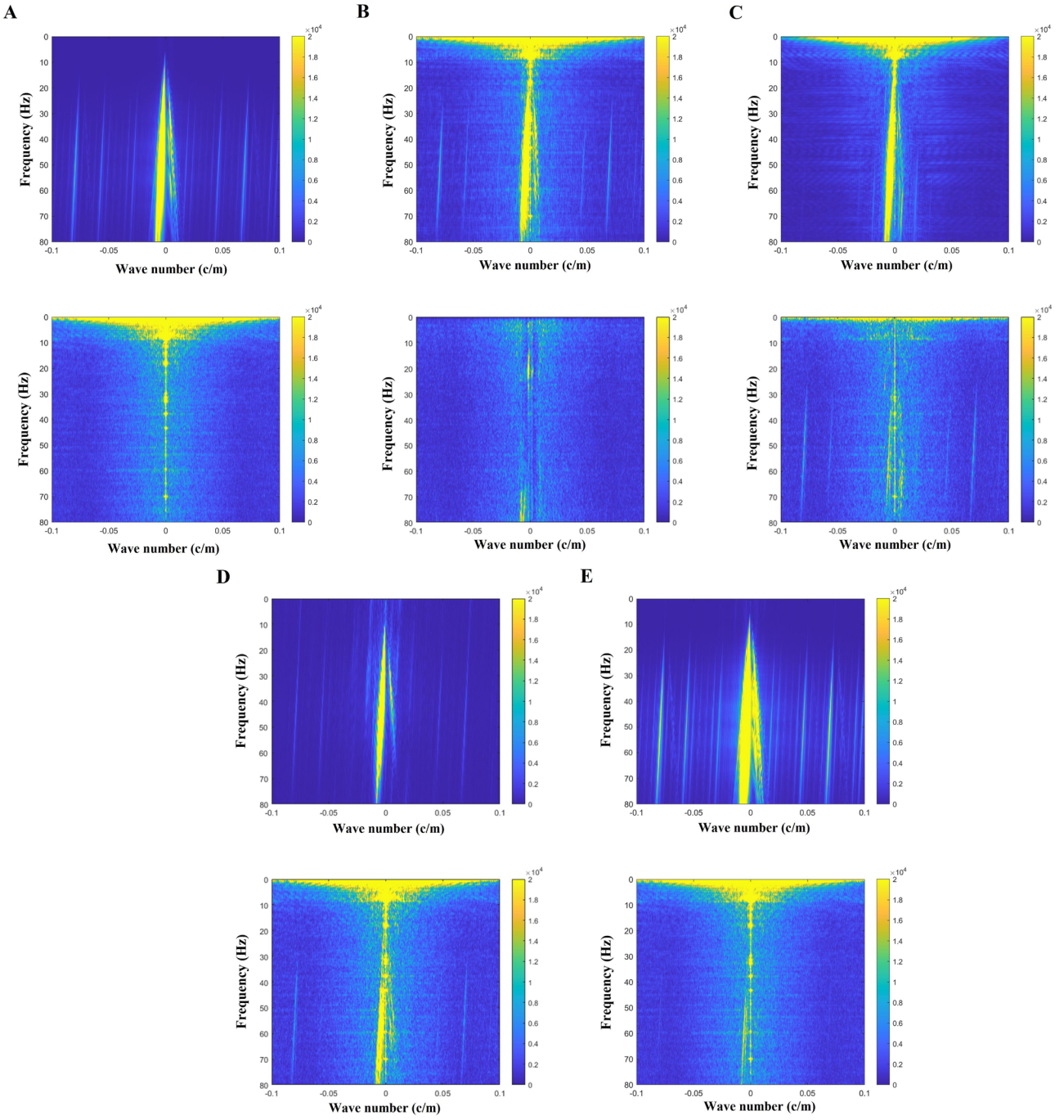

Figure 7. Frequency–wavenumber (F–K) spectra for different denoised results; (A) F–K results for pure signals and noise. (B)–(E) F–K results for recovered records (top subfigures) and removed noise (bottom subfigures) obtained using singular value decomposition, wavelet transform, convolutional denoising network, and hierarchical division encoder–decoder network.

did not require network training. While these methods enabled faster processing, their average SNR enhancement was insufficient to obtain high-quality DAS-VSP data. Both DnCNN and HDEN require considerable training time, with DnCNN being slightly faster. Nonetheless, deep learning techniques achieve substantially higher average SNR improvements than conventional methods, with HDEN achieving the largest enhancement, exceeding 20 dB on average. Given this significant gain in SNR and the rapid testing speed following a single training session, the time expenditure of deep learning approaches is justified. Consequently, HDEN offers significant advantages for efficiently and effectively processing DAS-VSP data.

5. Processing and analysis of the field records

Merely assessing denoising efficiency on synthetic data is inadequate for evaluating HDEN's efficacy in real-world scenarios. Consequently, we evaluated HDEN using DAS-VSP data collected in field conditions. Field recordings exhibit more complex signals and noise than synthetic data, necessitating a greater degree of signal-to-noise differentiation for efficient denoising. Acquiring clean signals in practical environments is difficult, rendering quantitative assessment impractical; hence, our comparisons are confined to qualitative evaluation.

5.1. Denoising results from field records

The field record utilized for testing is depicted in Figure 8A. The quality of the seismic data needs further improvement, as characterized by multiple noise types—such as random noise, time-varying optical noise, fading noise, and coupling noise—that obscure the signal and impede detection. Figure 8B illustrates the results from HDEN processing, demonstrating significant noise reduction. To enhance the demonstration of denoising efficacy, we magnified the areas impacted by time-varying optical noise (box M) and coupling noise (box N). Figure 9 presents expanded views: Figure 9A illustrates the original records, Figure 9B depicts the denoised findings, and Figure 9C exhibits the filtered noise. The results demonstrate a significant improvement in recording quality, with improved continuity and clarity of previously distorted reflected signals. These data indicate that HDEN effectively manages low-energy transmissions and those with considerable noise interference.

5.2. Generalization analysis

To assess HDEN's denoising efficacy, we performed comparison analyses utilizing identical approaches on synthetic data. Figure 10A presents the outcomes of SVD. While some noise reduction is evident, the presence of residual noise and signal deterioration suggests that SVD is inadequate for successful denoising. Figure 10B illustrates the results for WT, which predominantly mitigates minor random noise but demonstrates limited overall efficacy. The deep learning methodology, illustrated by DnCNN, demonstrated significant efficacy in field-record processing, achieving high-quality recordings while minimizing noise, as shown in Figure 10C. Nonetheless, DnCNN is inadequate at recovering signals that are significantly affected by noise. Figure 10D demonstrates that HDEN surpasses these approaches, offering enhanced noise reduction and signal retention.

The area of box P is enlarged to improve visibility, as illustrated in Figure 11A–11D. SVD and WT were hindered by residual noise problems, complicating signal detection. While DnCNN mitigated noise to a certain degree, the extent of signal reconstruction in the denoised results and the signal leakage in the filtered results indicate that it failed to meet the requirement for subsequent data interpretation. The comparison of the magnified findings

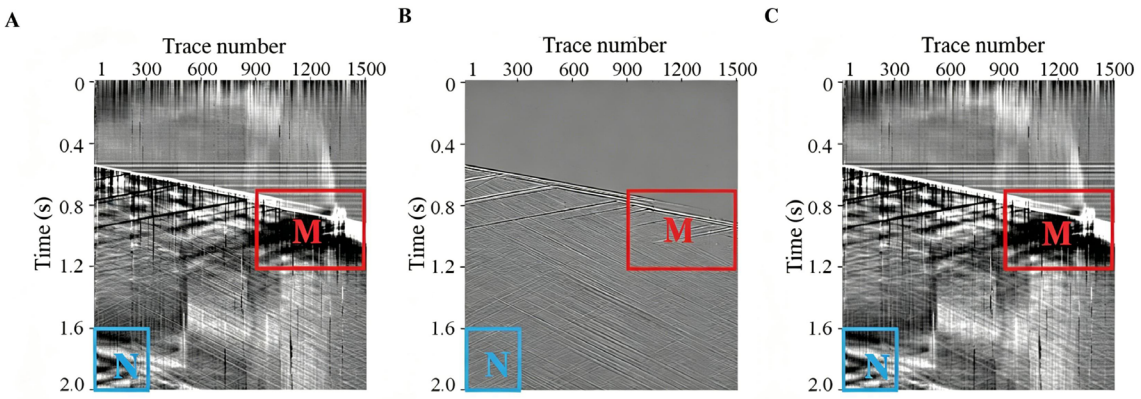

Figure 8. Processing result of the field record obtained using the hierarchical division encoder–decoder network. (A) Field record. (B) Denoising result. (C) Filtered noise. The red box highlights the severely noise-polluted region, while the blue box shows the weak signal area with mixed noise.

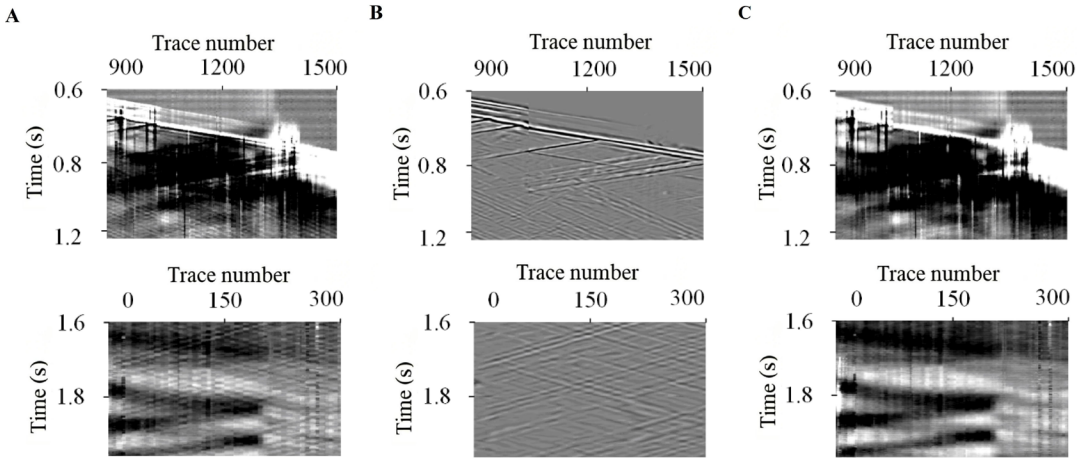

Figure 9. Local magnification result of the field record. (A) Magnified field noisy record of the area circled by boxes M and N shown in Figure 8. (B)–(C) Processing results and filtered noise (top: box M; bottom: box N) obtained using the hierarchical division encoder–decoder network.

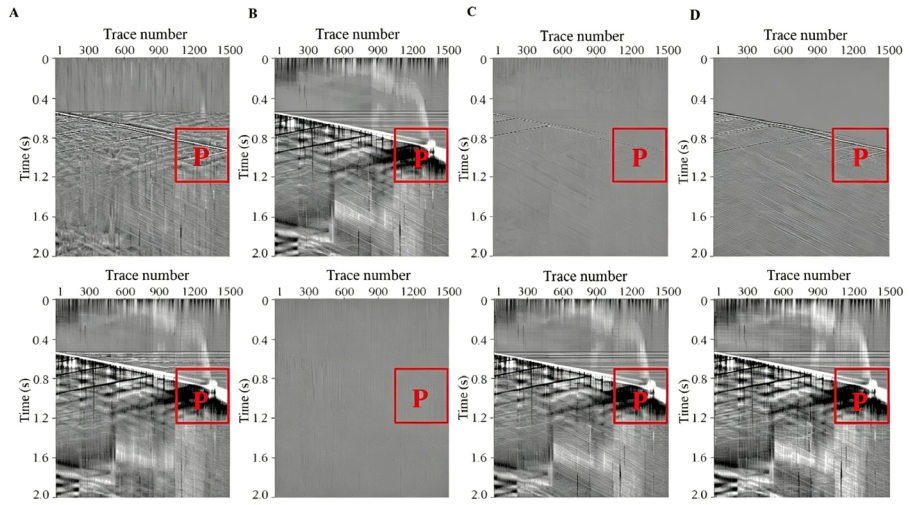

Figure 10. Comparison results for the processing of a field record. Denoising results (top subplots) and filtered noise (bottom subplots) for (A) singular value decomposition, (B) wavelet transform, (C) convolutional denoising network, and (D) hierarchical division encoder–decoder network, respectively.

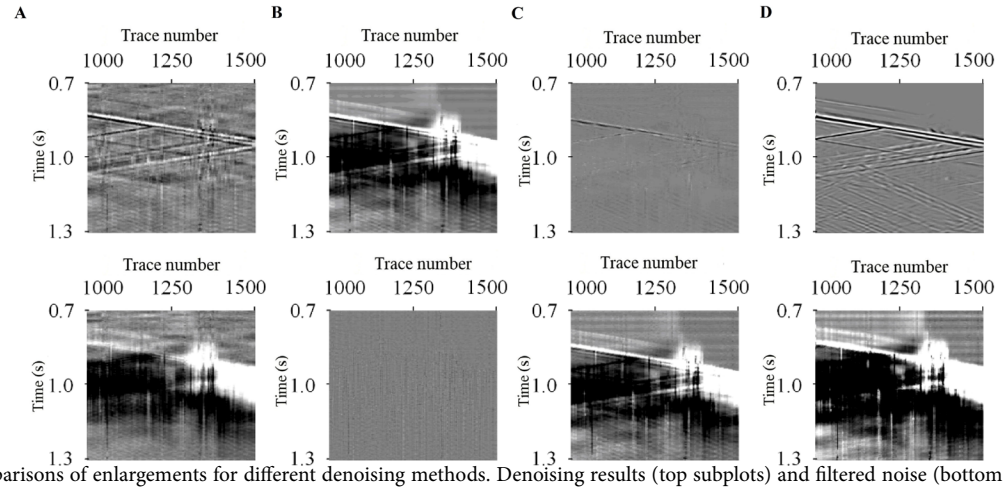

Figure 11. Comparisons of enlargements for different denoising methods. Denoising results (top subplots) and filtered noise (bottom subplots) for (A) singular value decomposition, (B) wavelet transform, (C) convolutional denoising network, and (D) hierarchical division encoder–decoder network, respectively.

further corroborates HDEN's outstanding denoising efficacy.

6. Conclusion

This study presents an HDEN for the effective separation of signal and noise in DAS-VSP data. HDEN first partitions information at a global scale and then processes it locally using the GFR module. This global-to-local approach ensures effective feature aggregation across all levels. The GFR module employs a multi-scale strategy to extract hierarchical features, enhancing feature representation. Furthermore, HDEN integrates a decoder with a spatial attention mechanism and skip connections, improving denoising performance and facilitating the integration of shallow and deep features.

The HDEN and several comparative methods were applied to both synthetic and field DAS data for performance evaluation. Qualitative analysis showed that HDEN effectively suppressed noise, recovered events masked by strong interference, and reduced signal leakage. Quantitative evaluation indicated that HDEN achieved the greatest SNR improvement across a range of SNR levels. These results demonstrate that HDEN enhanced the acquisition of high-quality DAS-VSP data, supporting more accurate seismic interpretation. In conclusion, HDEN exhibits substantial potential for broader applications in DAS-VSP data processing.

Acknowledgments

None.

Funding

None.

Conflict of interest

The authors declare they have no competing interests.

Author contributions

Conceptualization: Li Han
Formal analysis: Li Han
Investigation: Dongyan Wang
Methodology: Li Han, Dongyan Wang
Software: Dongyan Wang, Hang Yu
Visualization: Hang Yu
Writing–original draft: Li Han
Writing–review & editing: Dongyan Wang

Availability of data

Data are not openly available and are available upon reasonable request from the corresponding author.

References

1. Wang Q, Zhang Y, Xie Z, *et al.* The Advancement and Challenges of Seismic Techniques for Ultra-Deep Carbonate Reservoir Exploitation in the Tarim Basin of Northwestern China. *Energies*. 2022;15(20):7653.

   doi: 10.3390/en15207653

2. Dong XT, Li Y, Yang BJ. Desert low-frequency noise suppression by using adaptive DnCNNs based on the determination of high-order statistic. *Geophys J Int.* 2019;219(2):1281-1299.

   doi: 10.1093/gji/ggz363

3. Wang Z, Fan Z, Chen X, *et al.* Global oil and gas development situation, trends and enlightenment in 2023. *Pet Explor Dev*. 2024;51(6):1536-1555.

   doi: 10.1016/S1876-3804(25)60558-1

4. Zhu Q, Huang H, Wei X, *et al.* Fu Za You Qi Cang Chu Ceng Heng Xiang Yu Ce [Lateral prediction of complex oil and gas reservoirs]. *Oil Geophysical Prospecting.* 2003;38(004):405-408. [In Chinese]

   doi: 10.3321/j.issn:1000-7210.2003.04.013

5. Wang Z, Lu B, Ye Q, Cai H. Recent Progress in Distributed Fiber Acoustic Sensing with Φ-OTDR. *Sensors*. 2020;20(22):6594.

   doi: 10.3390/s20226594

6. Rashid A, Tackie-Otoo BN, Abdul Latiff AH, *et al.* Research Advances on Distributed Acoustic Sensing Technology for Seismology. *Photonics*. 2025;12(3):196.

   doi: 10.3390/photonics12030196

7. Liu Z, Gong H, Wu Y, *et al.* Xiang Gan Guang Shi Yu Fan She Yi Ji Shu Yu Ying Yong [Principle and Application of the C-OTDR]. *Study Opt Commun.* 2022;48(5):43-48,65. [In Chinese]

   doi: 10.13756/j.gtxyj.2022.05.008

8. Wang L, Xie X, Yao M, *et al.* Fen Bu Shi Guang Xian Sheng Bo Chuan Gan Ji Qi Jin Zhan Yan Jiu [Distributed Optical Fiber Acoustic Wave Sensing and Its Progress]. *Study Opt Commun.* 2025;51(5):240100-01. [In Chinese]

   doi: 10.13756/j.gtxyj.2025.240100

9. Zhang Z, Alajami M, Alkhalifah T. Wave-equation dispersion spectrum inversion for near-surface characterization using fiber-optics acquisition. *Geophys J Int.* 2020;222(2):907-918.

   doi: 10.1093/gji/ggaa211

10. Isaenkov R, Tertyshnikov K, Yurikov A, *et al.* Effect of Source Mispositioning on the Repeatability of 4D Vertical Seismic Profiling Acquired with Distributed Acoustic Sensors. *Sensors*. 2022;22(24):9742.

    doi: 10.3390/s22249742

11. Mad Zahir MH, Abdul Aziz KM, Ghazali AR, *et al.* Effectiveness of Fiber Optic Distributed Acoustic Sensing (DAS) in Vertical Seismic Profiling (VSP) Field Survey. *Appl Sci*. 2023;13(8):5002.

    doi: 10.3390/app13085002

12. Zhang S, Wang J, Yang Z. Walkaway VSP Chu Li Ji Shu Ji Ying Yong [The processing technology and application of The Walkaway VSP]. *Proc SPIE.* 2017;52(2):1-6. [In Chinese]

    doi: 10.13810/j.cnki.issn.1000-7210.2017.S2.001

13. Lin RB, Zeng XF, Song ZH, *et al.* Fen Bu Shi Guang Xian Sheng Bo Chuan Gan Xi Tong Zai Jin Di Biao Cheng Xiang Zhong De Ying Yong 2: Bei Jing Zao Sheng Cheng Xiang [Distributed acoustic sensing for imaging shallow structure II: Ambient noise tomography]. *Chinese J Geophys*. 2020;63(4):1622-1629. [In Chinese]

    doi: 10.6038/cjg2020N0272

14. Saad OM, Ravasi M, Alkhalifah T. Noise attenuation in distributed acoustic sensing data using a guided unsupervised deep learning network. *Geophysics*. 2025;89(6):V573-V587.

    doi: 10.1190/GEO2024-0109.1

15. Yu G, Chen YZ, Wu J, *et al.* 3D-VSP Survey Using a DAS System and Downhole Geophone Array in Southwest China. In: Proceedings of 81st EAGE Conference and Exhibition. London, UK; 2019:1-5.

    doi: 10.3997/2214-4609.201901252

16. Yu G, Xiong JL, Wu JJ, *et al.* Enhanced surface seismic data processing using simultaneous acquired DAS-VSP data. *First Break*. 2020;38(6):29-36.

    doi: 10.3997/1365-2397.fb2020039

17. Chavarria A, Minto C, Karrenbach M, *et al.* Offshore DASVSP Applications and Long-Range Distributed Fiber Optic Sensing. In: *First EAGE Workshop on Fibre Optic Sensing*. European Association of Geoscientists & Engineers; 2020;2020:1-5.

    doi: 10.3997/2214-4609.202030018

18. Zhu D, Fu L, Kazei V, Li W. Diffusion Model for DAS-VSP Data Denoising. *Sensors*. 2023;23(20):8619.

    doi: 10.3390/s23208619

19. Zhong T, Cheng M, Dong X, Li Y, Wu N. Seismic random noise suppression by using deep residual U-Net. *J Petrol Sci Eng.* 2022;209:109901.

    doi: 10.1016/j.petrol.2021.109901

20. Gu X, Collet O, Tertyshnikov K, Pevzner R. Removing Instrumental Noise in Distributed Acoustic Sensing Data: A Comparison Between Two Deep Learning Approaches. *Remote Sens*. 2024;16(22):4150.

    doi: 10.3390/rs16224150

21. Harsuko R, Alkhalifah T. Optimizing a transformer-based network for a deep-learning seismic processing workflow. *Geophysics*. 2024;89(4):V347-V359.

    doi: 10.1190/GEO2023-0403.1

22. Lou Y, Wang Y, Zhang X, *et al.* Seismic Reflector Dip Integrated Spatial–Spectral UFormer for Fault Detection. *IEEE Trans Geosci Remote Sens*. 2025;63:1-15.

    doi: 10.1109/TGRS.2025.3526814

23. Lou Y, Zhang X, Wang Y, *et al.* Unconformity-Enhanced Hierarchical Context Fusion Network for Seismic Facies Classification. *IEEE Trans Geosci Remote Sens*. 2025;63:1-12.

    doi: 10.1109/TGRS.2025.3563362

24. Lou Y, Wang Y, Chen Y, *et al.* Automatic Seismic Fault Interpretation With the Aid of Data-, Physics-, and Math-Assisted Synthetic Data Generation. *IEEE Trans Geosci Remote Sens*. 2024;62:1-15.

    doi: 10.1109/TGRS.2024.3402739

25. Zhou X, Qiao L. Di Zhen Kan Tan Zhong De Chang Jian Di Zhen Gan Rao Bo Ji Ya Zhi Fang Fa [Common seismic interference waves and suppression methods in seismic exploration]. *West China Explor Eng*. 2008;20(11):138-141. [In Chinese]

    doi: 10.3969/j.issn.1004-5716.2008.11.048

26. Tang S, Lin J. Xiao Bo Bian Huan Yu Zhong Zhi Lü Bo Xiang Jie He Tu Xiang Qu Zao Fang Fa [Image denoising with combination of wavelet transform and median filtering]. *J Harbin Inst Technol.* 2008;40(8):1334-1336. [In Chinese]

    doi: 10.3321/j.issn:0367-6234.2008.08.034

27. Bekara M, van der Baan M. Random and coherent noise attenuation by empirical mode decomposition. *Geophysics*. 2009;74(5):V89-V98.

    doi: 10.1190/1.3157244

28. Wang W, Yang G. Ji Yu EMD Yu ICA De Di Zhen Xin Hao Qu Zao Ji Shu Yan Jiu [Research on Seismic Signal Denoising Technology Based on EMD and ICA]. *Geophys Prospect Pet*. 2012;51(1):19-29. [In Chinese]

    doi: 10.3969/j.issn.1000-1441.2012.01.003

29. Yao Z, Li W, Zhu J, Hao L, Xing M. Seismic random noise separation and suppression based on improved variational mode decomposition via grey wolf optimization. *PLoS ONE*. 2025;20(9):e0330988.

    doi: 10.1371/journal.pone.0330988

30. Nie R, Xu H, Zhao Y. Lian He VMD He Shearlet Bian Huan De Qu Zao Fang Fa Yan Jiu [Research on Denoising Methods by Combining VMD and Shearlet Transform]. *Chin J Eng Geophys.* 2024;21(1):176-186. [In Chinese]

    doi: 10.3969/j.issn.1672-7940.2024.01.018

31. Han, J, van der Baan M. Microseismic and seismic denoising via ensemble empirical mode decomposition and adaptive thresholding. *Geophysics*. 2015;80(6):KS69–KS80.

    doi: 10.1190/GEO2014-0423.1

32. Li X, Yang K, Liu W, *et al.* Ji Yu Gai Jin De EEMD Shi Xian Di Zhen Xin Hao Qu Zao [Seismic Signal De-noising Based on Improved EEMD]. *Chin J Eng Geophys.* 2014;11(4):431-435. [In Chinese]

    doi: 10.3969/j.issn.1672-7940.2014.04.001

33. Tang HH, Cheng SJ, Li WQ, *et al.* An EDCC-EMD analysis-based network for DAS VSP data denoising in frequency domain. *Pet Sci.* 2025;22(5):1929-1945.

    doi: 10.1016/j.petsci.2025.03.006

34. Kong Q, Wu F, Fan B. Ji Yu Shen Du Xue Xi De Tu Xiang Pi Pei: Fang Fa Ying Yong Yu Tiao Zhan [Image Matching in Deep Learning Era: Methods, Applications and Challenges]. *Chin J Comput*. 2024;47(7):1485-1520. [In Chinese]

    doi: 10.11897/SP.J.1016.2024.01485

35. Li H, Liu F, Yang SY, *et al.* Ji Yu Shen Du Zhi Cheng Zhi Xue Xi Wang Luo De Yao Gan Tu Xiang Rong He [Remote sensing image fusion based on deep support value learning networks]. *Chin J Comput*. 2016;39(8):1583-1596. [In Chinese]

    doi: 10.11897/SP.J.1016.2016.01583

36. Lou Y, Zhang X, Liu N, *et al.* Seismic Unconformity Estimation via ECA-UNet plus plus With Physical Knowledge Constrained Synthetic Data. *IEEE Trans Geosci Remote Sens.* 2024;62:5933414.

    doi: 10.1109/TGRS.2024.3481448

37. Saad OM, Ravasi M, Alkhalifah T. Self-supervised multi-stage deep learning network for seismic data denoising. *Artif Intell Geosci.* 2025;6(1):100123.

    doi: 10.1016/j.aiig.2025.100123

38. Han W, Zhou Y, Chi Y. Ji Yu Shen Du Xue Xi Juan Ji Shen Jing Wang Luo De Di Zhen Shu Ju Sui Ji Zao Sheng Qu Chu [Deep learning convolutional neural networks for random noise attenuation in seismic data]. *Geophys Prospect Pet.* 2018;57(6):862-869,877. [In Chinese]

    doi: 10.3969/j.issn.1000-1441.2018.06.008

39. Liu S, Birnie C, Alkhalifah T. Trace-wise coherent noise suppression via a self-supervised blind-trace deep-learning scheme. *Geophysics*. 2023;88(6): V459-V472.

    doi: 10.1190/GEO2022-0371.1

40. Wang Y, Lou Y, Liu N, *et al.* Seismic Fault Delineation and Parameter Interpretation Using Dual U-Shaped Domain Fusion-Net. *IEEE Trans Geosci Remote Sens.* 2025;63:1-15.

    doi: 10.1109/TGRS.2025.3612429

41. Izzatullah M, Alkhalifah, T, Romero J. Posterior sampling with convolutional neural network-based plug-and-play regularization with applications to poststack seismic inversion. *Geophysics.* 2024;89(2):R137-R153.

    doi: 10.1190/geo2023-0035.1

42. Zhang K, Zuo W, Chen Y, *et al.* Beyond a Gaussian Denoiser: Residual Learning of Deep CNN for Image Denoising. *IEEE Trans Image Process.* 2017;26(7):3142-3155.

    doi: 10.1109/TIP.2017.2662206

43. Lehtinen J, Munkberg J, Hasselgren J, *et al.* Noise2noise: Learning image restoration without clean data. *arXiv*. 2018.

    doi: 10.48550/arXiv.1803.04189

44. Abedi MM, Pardo D, Alkhalifah T. Semi-blind-trace algorithm for self-supervised attenuation of trace-wise coherent noise. *Geophys Prospect.* 2024;72(3):965-977.

    doi: 10.1111/1365-2478.13448

45. Ding X, Zhang X, Han J, *et al.* Scaling Up Your Kernels to 31×31: Revisiting Large Kernel Design in CNNs. In: Proceedings of 2022 IEEE/CVF Conference on Computer Vision and Pattern Recognition (CVPR). New Orleans, LA, USA: IEEE; 2022:11953-11965.

    doi: 10.1109/CVPR52688.2022.01166

46. Liu JW, Liu JW, Luo XL. Shen Du Xue Xi Zhong Zhu Yi Li Ji Zhi Yan Jiu Jin Zhan [Research progress in attention mechanism in deep learning]. *Chin J Eng.* 2021;43(11):1499-1511. [In Chinese]

    doi: 10.13374/j.issn2095-9389.2021.01.30.005

47. Woo S, Park J, Lee JY, Kweon IS. CBAM: Convolutional block attention module. In: Ferrari V, Hebert M, Sminchisescu C, Weiss Y, (eds). *Computer Vision – ECCV 2018;* ECCV 2018; Lecture Notes in Computer Science (LNIP, volume 11211). Springer International Publishing; 2018;11211:3-19.

    doi: 10.1007/978-3-030-01234-2_1

48. Ren H, Wang X. Zhu Yi Li Ji Zhi Zong Shu [Review of attention mechanism]. *J Comput Appl.* 2021;41(S1):1-6. [In Chinese] Available from: https://cnki.com.cn/Article/CJFDTotal-JSJY2021S1002.html

49. Hu J, Shen L, Sun G. Squeeze-and-excitation networks. In: Proceedings of 2018 IEEE/CVF Conference on Computer Vision and Pattern Recognition. Salt Lake City, UT, USA: IEEE; 2018:7132-7141.

    doi: 10.1109/CVPR.2018.00745

50. Chen Y, Li W, Sakaridis C, *et al.* Domain Adaptive Faster R-CNN for Object Detection in the Wild. In: Proceedings of IEEE/CVF Conference on Computer Vision and Pattern Recognition. Salt Lake City, UT, USA: IEEE; 2018:3339-3348.

    doi: 10.1109/CVPR.2018.00352

51. Liu B, Yue J, Zuo Z, *et al.* Unsupervised deep learning for random noise attenuation of seismic data. *IEEE Geosci Remote Sens Lett*. 2022;19:1-5.

doi: 10.1109/LGRS.2021.3057631

52. Roncoroni G, Fortini C, Bortolussi L, Bienati N, Pipan M. Synthetic seismic data generation with deep learning. *J Appl Geophy*. 2021;190:104347.

doi: 10.1016/j.jappgeo.2021.104347

ACCSCIENCE PUBLISHING

Journal of Seismic Exploration

ARTICLE

CT-UNet: Curvelet transform-based component-wise deep learning framework for seismic trace interpolation

Jiyun Yu[1], Young Kim[2], and Daeung Yoon[1]*

[1]Department of Energy and Resources Engineering, Chonnam National University, Gwangju, Republic of Korea

[2]YK Geophysics, Seoul, Republic of Korea

Abstract

Seismic data may suffer from missing traces due to economic and environmental constraints as well as equipment malfunctions, where regular gaps caused by receiver or streamer spacing and irregular gaps resulting from topographic limitations occur simultaneously. Such missing data degrade the reliability of subsequent processing and interpretation, making accurate interpolation essential. High-resolution reconstruction requires balanced recovery of broadband components spanning low to high frequencies; however, existing deep learning-based interpolation methods exhibit degraded performance in certain spectral regions. In this study, we propose the curvelet transform (CT)-UNet, a deep learning interpolation method that leverages CT-based frequency- and directional-component separation to improve reconstruction balance across frequency bands, particularly under high-rate, regular undersampling conditions. The proposed method applies the uniform discrete CT (UDCT) to decompose input data into low-frequency and high-frequency components with multi-resolution and directional characteristics, trains specialized U-Net models for each component, and reconstructs the final result through inverse transformation. Performance was evaluated on synthetic data (Society of Exploration Geophysicists/European Association of Geoscientists and Engineers Salt Model) and field data (Mobil Amplitude Versus Offset Viking Graben Line 12) by comparing to f–x interpolation, Constrained Diffusion-Driven Deep Image Prior, a standard U-Net, a parameter-matched U-Net-Wide, and the wavelet-based wavelet transform-UNet. An exploratory experiment on irregular missing and a structural compatibility analysis of the UDCT level configuration were also conducted. Results show that CT-UNet improves reconstruction quality across the tested missing conditions, with the clearest gains observed under high-rate regular undersampling and the 70% irregular missing scenario. Shot-level analysis further supports its advantage in challenging cases, particularly for synthetic 80%, field 75%, field 80%, and 70% irregular missing conditions. The advantage is especially pronounced in recovering curvature-varying, conflicting-dip events, while structural similarity is generally maintained at a level comparable to or higher than that of the baseline methods.

Keywords: Seismic data interpolation; Curvelet transform; Deep learning; U-Net; Uniform discrete curvelet transform; Missing trace reconstruction

***Corresponding author:**
Daeung Yoon
(duyoon@jnu.ac.kr)

Citation: Yu J, Kim Y, Yoon D. CT-UNet: Curvelet transform-based component-wise deep learning framework for seismic trace interpolation. *J Seismic Explor.* 2026;35(3):026120048. doi: 10.36922/JSE026120048

Received: March 16, 2026

Revised: May 27, 2026

Accepted: May 27, 2026

Published online: June 15, 2026

Copyright: © 2026 Author(s). This is an Open-Access article distributed under the terms of the Creative Commons Attribution License, permitting distribution, and reproduction in any medium, provided the original work is properly cited.

Publisher's Note: AccScience Publishing remains neutral with regard to jurisdictional claims in published maps and institutional affiliations.

1. Introduction

Seismic data may suffer from missing traces due to economic and environmental constraints, as well as equipment and mechanical malfunctions, where regular gaps caused by receiver or streamer spacing and irregular gaps resulting from topographic limitations or instrument failures occur simultaneously. Such missing data not only degrade the reliability of subsequent processing (e.g., noise suppression, multiple removal, velocity analysis, and migration) and interpretation, but their recovery through additional surveys demands considerable time and cost, making accurate interpolation at the data processing stage essential.

Conventional seismic data interpolation methods include f–x interpolation and Projection Onto Convex Sets (POCS). f–x interpolation estimates missing traces by exploiting the predictability of signals in the frequency–space domain and offers the advantages of relative simplicity and computational efficiency.[1] However, in zones where complex dip components coexist or non-stationarity is strong, the assumptions underlying the prediction model are weakened, potentially leading to residual and artifact problems. POCS iteratively updates the solution through projections based on sparsity or constraint sets, providing stable reconstruction even under irregular missing conditions,[2] but it suffers from increased computational cost and difficulty in guaranteeing uniform recovery across the full spectral bandwidth.

In recent years, deep learning-based interpolation methods capable of effectively modeling complex geological structures and non-stationarity through data-driven learning have been actively investigated. Convolutional neural network (CNN) and U-Net[3] architectures have become representative approaches for seismic interpolation, demonstrating strength in recovering missing traces through multi-scale feature extraction and skip connections.[4-10] More recently, Mukherjee *et al.*[11] demonstrated the practical applicability of a three-dimensional (3D) U-Net framework for predicting missing traces in structurally complex field settings. Generative adversarial network (GAN)-based approaches preserve high-frequency fine structures through adversarial training with a discriminator,[12,13] and transformer-based models have shown promising results in interpolation by leveraging global contextual information.[14] Research on applying diffusion models[15] to seismic interpolation has also been actively progressing.[16-19] Diffusion models learn the distribution of training data through a progressive denoising process and offer the advantage of flexible reconstruction for diverse missing patterns. Although these methods achieve higher reconstruction accuracy than conventional techniques, the difficulty of a single network simultaneously satisfying all frequency and dip components results in spectral bias or residuals in certain regions.

To mitigate these limitations, various strategies for directly controlling spectral characteristics have been introduced. These include approaches that add Fourier loss or frequency-domain constraints to prevent excessive smoothing of high-frequency components (HFs),[20] dual-domain architectures that simultaneously incorporate time–frequency information,[21] and spectral constraint-based training strategies that directly control spectral energy distribution and phase coherence.[21,22] However, these approaches also tend to concentrate performance on bands that are relatively easier to learn, rather than fully guaranteeing balance across the entire bandwidth.

As an alternative approach, methods have been proposed that decompose signals into multi-resolution or subband representations and reconstruct each component with individual networks. The wavelet transform (WT), with its strength in time–frequency localization, has been widely used to separate and reconstruct scale-specific features of seismic signals.[23-26] However, wavelets have limited directional representation, and when dip or curvilinear reflection events are complex, residuals may persist in certain directional components.[27] This necessitates a transform-based design capable of simultaneously and precisely representing both directionality and scale.

The curvelet transform[28] has already demonstrated its effectiveness in seismic data recovery. Herrmann and Hennenfent[29] showed that seismic missing-trace recovery is achievable through curvelet-based sparsity-promoting optimization, providing empirical evidence that the sparse representation capability of curvelets is well-suited for seismic interpolation. However, such optimization-based approaches incur high computational costs due to iterative operations and are sensitive to hyperparameters, with limited generalization to complex geological structures.[30] In this study, we combine the representational power of curvelets with data-driven deep learning rather than iterative optimization, simultaneously pursuing inference efficiency and reconstruction quality.

More recently, coordinate-based implicit neural representations (INRs) have emerged as a continuous-representation alternative for seismic data reconstruction. Sitzmann *et al.*[31] introduced sinusoidal representation networks (SIRENs), which use periodic activation functions to overcome the spectral bias of conventional multilayer perceptrons (MLPs) and represent complex signals at fine detail. Building on this foundation, Gao *et al.*[32] proposed Neural Implicit Representations for Five-Dimensional

(5D) Seismic Data Interpolation, a coordinate-based MLP for self-supervised 5D seismic interpolation that infers missing trace amplitudes directly from spatio-temporal coordinates. SIREN-based approaches have also been applied to unsupervised single-gather seismic interpolation, demonstrating robust reconstruction under regular missing rates of up to 75%.[33] INR-based methods offer flexibility across diverse missing patterns and do not require large labeled training datasets; however, they typically rely on per-instance optimization at inference time and face challenges in generalization to large-scale datasets.

In this study, we propose the CT-UNet framework, which integrates the curvelet transform into deep learning-based interpolation. The curvelet transform retains the multi-resolution characteristics of wavelets while explicitly providing directionality and anisotropy, enabling efficient representation of reflection events with curvilinear and dipping structures.[28] Although the contourlet,[34] a similar directional multi-resolution transform, has been proposed, the UDCT provides a uniform sampling lattice that is more suitable for integration with CNNs. CT-UNet decomposes input seismic data into multi-scale and directional components using the UDCT, interpolates each component with dedicated U-Net models, and reconstructs the final result across the full bandwidth through inverse transformation.

Unlike generic multi-network approaches, the design of CT-UNet is structurally motivated by the 2-lattice decimation property of the UDCT, which naturally partitions the high-frequency subbands into groups with distinct spatial sampling structures, enabling component-wise learning aligned with the transform's inherent decomposition. The main contributions of this paper are as follows: (i) We propose the CT-UNet pipeline, which decomposes seismic data into multi-scale and directional components via the UDCT, reconstructs each component with dedicated U-Net models, and synthesizes the final result through inverse transformation. (ii) We demonstrate that the proposed method is particularly effective in recovering curvature-varying (conflicting-dip) events, where conventional single-network approaches tend to fail, through reduction of residuals in specific frequency and dip components, improving reconstruction quality compared to conventional deep learning interpolation using a single network without component separation. (iii) Through comparison with WT-based methods, we verify the advantages that the directional and anisotropic representation of the curvelet transform provides for seismic event reconstruction. (iv) We exploratorily examine the characteristics of CT-UNet under irregular missing scenarios and confirm the validity of the selected configuration through a structural compatibility analysis of the UDCT level settings.

2. Methods

2.1. Curvelet transform-UNet

The CT-UNet is a framework that takes two-dimensional seismic data containing missing traces as input, performs multi-resolution and multi-directional decomposition based on the UDCT, interpolates each decomposed component with dedicated U-Net models, and reconstructs a coherent section in the original domain via inverse transformation (Figure 1).

Applying the UDCT forward transform to the input data decomposes it into a low-frequency component (LF) and high-frequency directional components (HF_V, HF_H), where each component is fed into an independent U-Net interpolation model for component-wise prediction. The predicted components are then synthesized through the UDCT inverse transform to produce the final interpolation result (Figure 1A). Figure 1B illustrates the schematic of the UDCT forward and inverse transform processes.

In conventional original-domain interpolation, a single model must simultaneously recover both the low-frequency background and the high-frequency detailed reflection events, leading to imbalanced reconstruction quality across frequency bands and directions. In contrast, CT-UNet reformulates the reconstruction problem component-by-component using the scale and directional separation provided by the UDCT, and learns tailored to the statistical characteristics of each component, thereby aiming for stable interpolation across the full bandwidth.

2.2. Uniform discrete curvelet transform forward transform

Given seismic data X, CT-UNet first applies the UDCT forward transform operator C(·) to compute a set of subband coefficients decomposed into multiple scales and directions (**Equation 1**).

$$\{C_{j,k}\} = C(X) \tag{1}$$

where $\{C_{j,k}\}$ is the set of UDCT coefficients, j is the scale (resolution) index, and k is the directional index.

The UDCT forward transform consists of two stages. First, in the multi-resolution filter bank stage, analysis filters $F_0(z)$ through $F_N(z)$ are applied to the input signal to decompose the frequency bands by scale, and downsampling generates data at each scale (Figure 2A).

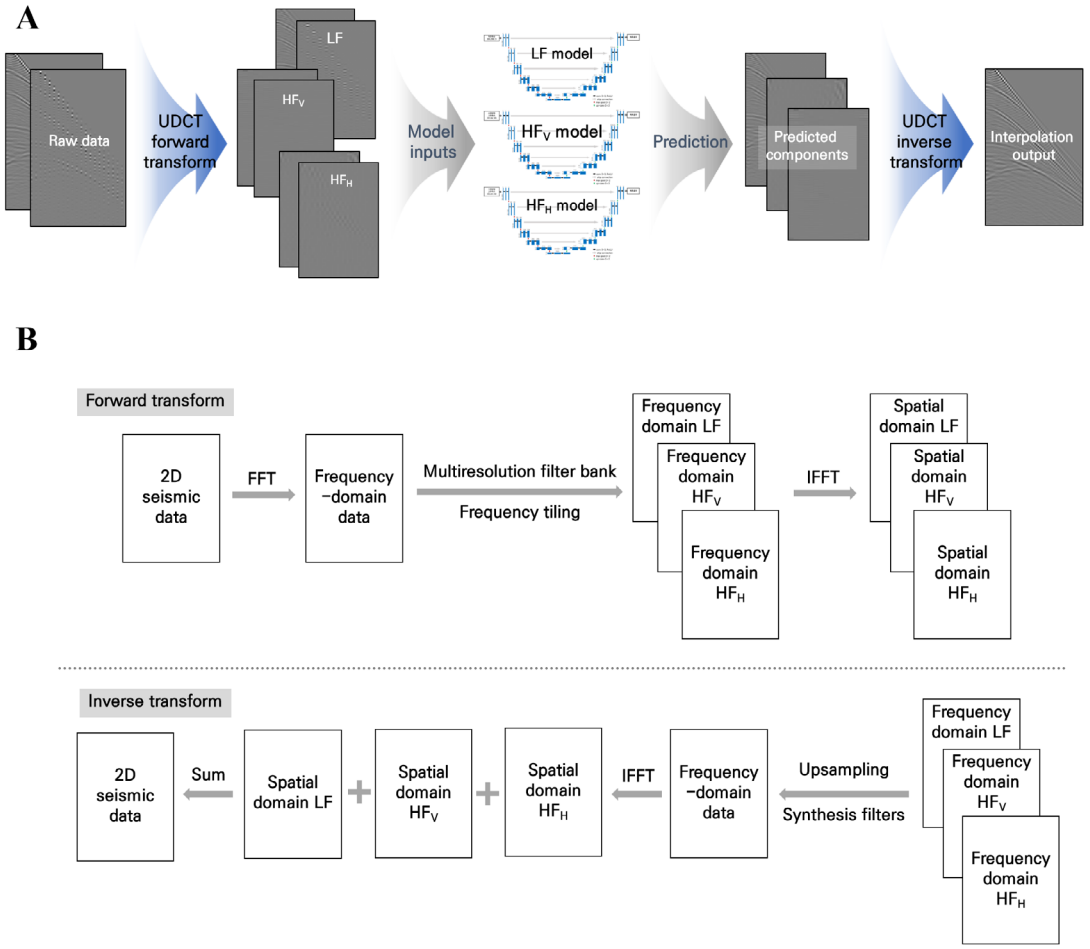

Figure 1. Overall workflow of CT-UNet, where (A) illustrates the process of component decomposition, component-wise interpolation, and inverse transform synthesis, and (B) shows the schematic of the UDCT forward and inverse transforms
Abbreviations: 2D: Two-dimensional; CT: Curvelet transform; FFT: Fast Fourier Transform; HF: High-frequency component; IFFT: Inverse Fast Fourier Transform; LF: Low-frequency component; UDCT: Uniform discrete curvelet transform.

Second, in the frequency tiling stage, the frequency plane of each scale-decomposed band component is subdivided into multiple directional tiles, so that components corresponding to directional events (dip) are mapped to distinct directional tiles.

In this study, the level configuration was set to [8,8], where the first parameter (8) specifies the number of directional decompositions per scale (8 directions) and the second parameter (8) specifies the resolution/scale depth parameter governing the multi-resolution filter bank. Reflecting the downsampling results, the tiled components are extracted at sizes smaller than the original input size (64, 256). For example, the LF is represented as (64, 256, 1), while the HFs take forms such as (32, 64, 8) and (16, 128, 8) with 8 directional channels (Figure 2B).

The selection of the level configuration [8,8] is based on the following rationale. First, with eight directions, the spatial sizes of the decomposed HFs are extracted as powers of two (e.g., 32 × 64, 16 × 128), maintaining an integer-multiple relationship with the 2 × 2 MaxPooling operations in the U-Net. Increasing the number of directions to 16 would excessively reduce the spatial size of the components, making meaningful feature extraction infeasible at the bottleneck stage of the four-level encoder. Second, according to Candès and Donoho,[27] eight directions in a single-level decomposition are consistent with the theoretical structure, whereas 4 directions are insufficient to capture the diversity of dips. Third, under the 64 × 256 patch-size condition, an eight-direction decomposition represents a practical balance that simultaneously provides sufficient spatial information and directional separation. The results of the structural compatibility analysis for alternative configurations ([4,4], [16,16]) are discussed in

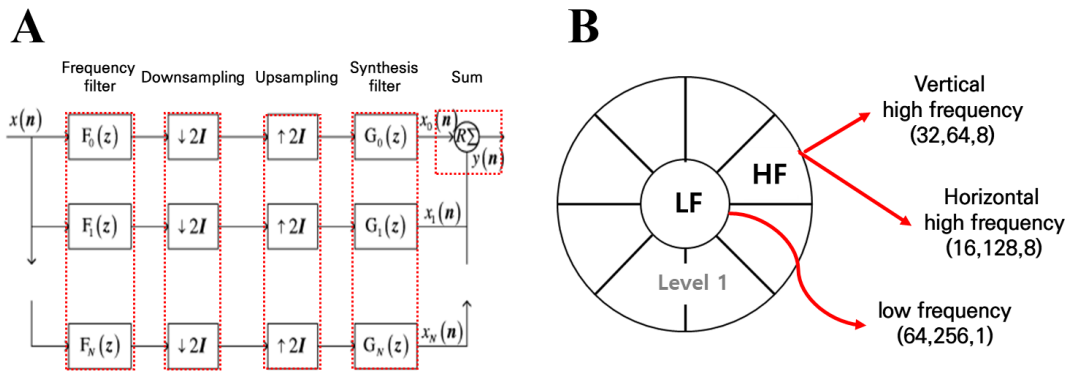

Figure 2. Examples of the UDCT multi-resolution filter bank and frequency tiling, where (A) shows the filter bank structure in which analysis filters $F_0(z)$ through $F_N(z)$ and downsampling constitute the forward transform while upsampling followed by synthesis filters $G_0(z)$ through $G_N(z)$ and band summation are used in the inverse transform, and (B) illustrates the frequency tiling and component configuration for the level setting [8,8]
Abbreviations: HF: High-frequency component; LF: Low-frequency component.

Section 4.

2.3. Component-wise interpolation and inverse transform

According to the theoretical structure of the UDCT, multi-directional HFs are naturally classified into two groups based on the characteristics of the decimation matrices in the frequency plane. The decimation matrices applied to the high-frequency directional subbands are defined in two forms, $D_{J,0} = diag\left\{2, \frac{2N_j}{3}\right\} \cdot 2^{J-j}$ and $D_{j,1} = diag\left\{\frac{2N_j}{3}, 2\right\} \cdot 2^{J-j}$, indicating that the mostly horizontal group and the mostly vertical group are arranged on different lattice structures.[35] In this study, we directly utilize this 2-lattice structure, defining the LF, the vertically dominant HF as HF_V, and the horizontally dominant HF as HF_H.

Denoting the UDCT components of each group as C_{LF}, C_{HF_V}, and C_{HF_H}, and defining the corresponding reconstruction networks as $f_{LF}(\cdot)$, $f_{HF_V}(\cdot)$, and $f_{HF_H}(\cdot)$, respectively, three independent U-Net networks predict each group component in parallel, and the final interpolation result is generated through inverse transform synthesis (**Equation 2**).

$$\hat{\boldsymbol{C}}_{LF} = \boldsymbol{f}_{LF}\left(\boldsymbol{C}_{LF}\right),\ \hat{\boldsymbol{C}}_{HF_H} = \boldsymbol{f}_{HF_H}\left(\boldsymbol{C}_{HF_H}\right) \quad \hat{\boldsymbol{C}}_{HF_V} = \boldsymbol{f}_{HF_V}\left(\boldsymbol{C}_{HF_V}\right) \tag{2}$$

where, C_{LF}, C_{HF_V}, and C_{HF_H} are the group-wise UDCT components (coefficient maps) obtained from the frequency tiling, and $\hat{C}_{LF}$, $\hat{C}_{HF_V}$, and $\hat{C}_{HF_H}$ denote the interpolation result components predicted by each network.

The component-wise reconstructed results are synthesized into the original domain through the inverse UDCT operator $C^{-1}(\cdot)$ to generate the final reconstructed section. This synthesis process can be summarized as **Equation 3**:

$$\hat{\boldsymbol{X}} = \boldsymbol{C}^{-1}\left(\hat{\boldsymbol{C}}_{LF}, \boldsymbol{C}_{HF_V}, \boldsymbol{C}_{HF_H}\right) \tag{3}$$

where, $C^{-1}(\cdot)$ is the inverse UDCT operator, which aggregates the predicted components from the three networks according to the original scale–direction decomposition structure to produce the final interpolation result $\hat{X}$. The inverse transform stage combines the independently reconstructed components in accordance with the original scale–direction decomposition structure, ensuring that the information in the frequency–direction region covered by each group is preserved without loss.

2.4. Network architecture

The interpolation model is constructed as a two-dimensional U-Net-based convolutional neural network (Figure 3). The encoder consists of a four-stage downsampling path, where each stage performs 3 × 3 convolution followed by 2 × 2 max pooling, with the number of channels increasing as 32 → 64 → 128 → 256. The bottleneck has 512 channels, and the decoder adopts a symmetric structure to the encoder with skip connections. The activation function is the rectified linear unit, and the output layer uses 1 × 1 convolution with linear activation. The loss function employed is the mean squared error (MSE).

The same U-Net architecture is applied to all three components (LF, HF_V, HF_H), with only the spatial size

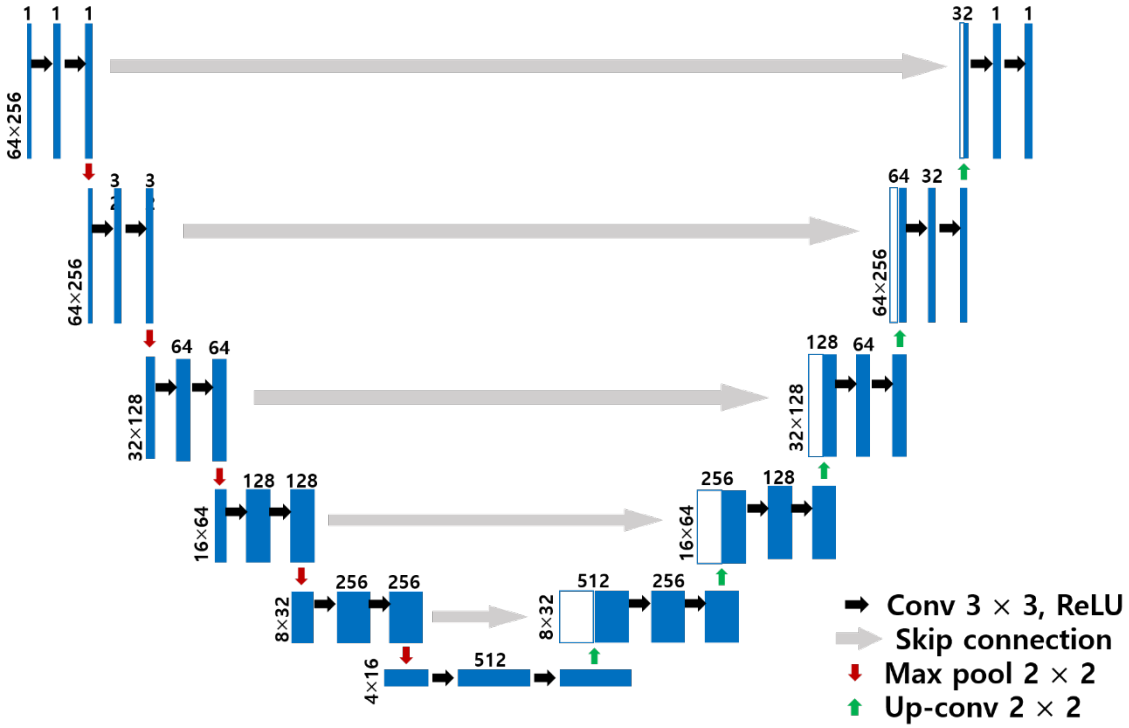

Figure 3. Architecture of the two-dimensional U-Net used in this study
Abbreviation: ReLU: Rectified linear unit.

of the input tensor varying according to the UDCT decomposition results. Training was configured with the Adam optimizer[36] (initial learning rate of 1×10^{-3}), a batch size of 128, and a maximum of 500 epochs, with early stopping applied when the validation loss did not improve for 10 consecutive epochs. Weight initialization used He initialization. The experimental environment consisted of an Intel Xeon Silver 4210R CPU (2.40 GHz, 2 × 10 cores), 125 GB RAM, and an NVIDIA TITAN RTX graphics processing unit (GPU) (24 GB VRAM).

The comparative experiments were designed to verify the contribution of curvelet-based component separation to interpolation performance. (i) F–x interpolation is a conventional frequency-domain interpolation method.[1] (ii) Constrained Diffusion-Driven Deep Image Prior (CDDIP) is a diffusion model-based self-supervised generative interpolation method.[16] (iii) U-Net serves as the baseline model that directly interpolates in the original domain without any transform. (iv) WT-UNet is a hybrid structure consisting of one original-domain U-Net and one wavelet-domain U-Net, where the wavelet-domain model takes the four subbands (low–low, low–high, high–low, high–high) of the two-dimensional discrete wavelet transform concatenated along the channel dimension as input. U-Net-Wide is a parameter-matched baseline that uses a single U-Net with increased channel widths to match the total parameter count of CT-UNet, without any transform-based decomposition. This baseline is included to verify whether the performance improvement of CT-UNet is attributable to curvelet-based decomposition or simply to increased model capacity. The comparative methods are selected to address distinct questions: F–x interpolation and CDDIP represent conventional and generative paradigms, respectively, situating the proposed method within the broader landscape of seismic interpolation. The standard U-Net serves as the primary ablation baseline, isolating the effect of curvelet-based decomposition from the underlying network architecture. WT-UNet evaluates the effect of transform selection (wavelet vs. curvelet) under a similar component-separation philosophy. U-Net-Wide controls for model capacity to confirm that the observed gains are attributable to the curvelet representation rather than to increased parameter count.

3. Experiments

3.1. Data generation and model training process

For synthetic data, the Narrow-azimuth data from the Society of Exploration Geophysicists (SEG)/European Association of Geoscientists and Engineers (EAGE) Salt Model (receiver spacing 20 m, streamer spacing 40 m)[37]

was used. For field data, Mobil Amplitude Versus Offset (AVO) Viking Graben Line 12 (1001 shot records, 120 channels, recording time 6 s, sampling interval 4 ms, shot/receiver spacing 25 m)[38] was used.

Regular missing patterns were applied to the original data to generate input data with missing rates of 67%, 75%, and 80%, with the complete data prior to missing trace removal serving as ground truth. Specifically, 67% missing corresponds to retaining one trace and removing the following two traces (every three-trace cycle), 75% missing corresponds to retaining one trace and removing the following three traces (every four-trace cycle), and 80% missing corresponds to retaining one trace and removing the following four traces (every five-trace cycle). A patch-based training approach was adopted, with synthetic data configured as 64 × 256 patches (250 patches in the test set) and field data as 64 × 1,024 patches (505 patches in the test set). The difference in patch size reflects the spatial extent and event scale of each dataset, while the UDCT decomposition ratio and component structure remain identical under the level configuration [8,8]. Dataset splitting was performed by first randomly assigning all shot locations to training (70%), validation (20%), and test (10%) sets, and then extracting patches from the shots assigned to each set. This prevented data leakage where patches extracted from the same shot could be included in both the training and test sets simultaneously, and ensured the reliability of generalization performance evaluation by distributing shots from different spatial locations across each set.

A separate CT-UNet system (three component-wise U-Nets) was trained independently for each combination of dataset and missing rate. Missing traces were 0-filled prior to UDCT decomposition, and no binary sampling mask was provided as an auxiliary input to the networks. For the [8,8] level configuration, the real and imaginary parts of the complex-valued high-frequency coefficients were concatenated along the channel dimension, resulting in 16 input channels (eight directions × 2) for both the HF_V and HF_H networks, while the LF network received a single-channel real-valued input.

Irregular missing scenarios were generated by randomly removing 50% and 70% of all traces from the synthetic data, while maintaining all other conditions identical to those in the regular missing experiments. The UDCT forward transform was applied to decompose each dataset into three groups: LF, HF_V, and HF_H (Figure 4). The HFs are expressed in complex form, and in this study, the real and imaginary parts were separated and concatenated along the channel dimension to construct the U-Net input tensor. This approach maintains continuous real-valued inputs suitable for CNN training while avoiding the 2π periodic discontinuity (phase wrapping) problem that arises in the alternative magnitude/phase separation approach. The validity of the real/imaginary separation method has been verified in image processing and MRI reconstruction.[39,40] However, a limitation is that the phase coherence between the two channels is only implicitly learned, and the introduction of complex-valued convolution or a phase consistency loss is left for future work.

The three decomposed components were trained and predicted independently using U-Net models, and during prediction, the same UDCT decomposition followed by component-wise prediction and inverse transform synthesis was applied.

3.2. Results of synthetic data

Figure 5 shows the reconstruction results for missing rates of 67%, 75%, and 80%; Figure 6 presents the enlarged regions of interest (ROI); and Figure 7 compares the f–k spectra.

The f–x interpolation exhibits ringing and ripple residuals near the missing traces under varying dip conditions. CDDIP shows weak fidelity to the observed data, producing results that approximate plausible structure generation rather than precisely reproducing the phase and amplitude of the ground truth. U-Net performs stable interpolation overall; however, as the missing rate increases, event continuity in the ROI weakens, and a smoothing tendency is observed. U-Net-Wide, despite having a comparable total parameter count to CT-UNet, exhibited reconstruction quality similar to or slightly lower than U-Net across all missing rates, indicating that simply increasing model capacity without transform-based decomposition does not yield the improvement observed in CT-UNet. WT-UNet tends to over-amplify weak components in non-dominant directions. CT-UNet most naturally reproduces the continuity and curvature variations of curvilinear events in the ROI. In particular, in regions containing conflicting-dip events (i.e., reflections with dip opposite to the dominant event direction), U-Net and WT-UNet exhibit noticeable reconstruction degradation, while CT-UNet preserves these events with high fidelity — a pattern that is quantitatively supported by the ROI-based analysis below. In the f–k spectrum, CT-UNet maintains an energy distribution closest to the ground truth while effectively suppressing aliasing components.

Quantitative evaluation (Tables 1 and 2) shows that CT-UNet achieved the highest peak signal-to-noise ratio (PSNR) and structural similarity index measure (SSIM) across all missing rates. Paired *t*-test results indicate

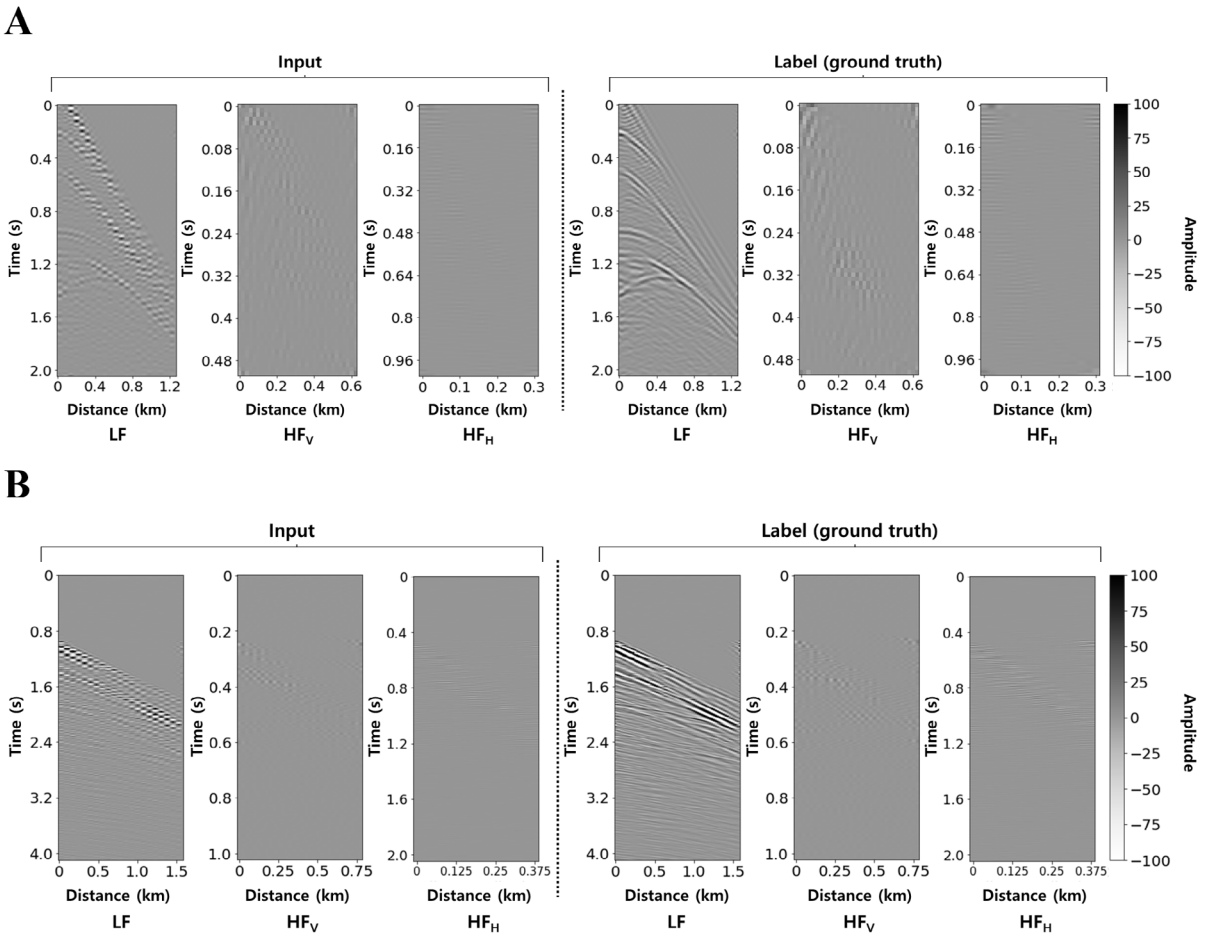

Figure 4. Example of UDCT decomposition for synthetic data (A) and field data (B). For each row, the left three panels show the decomposed components (LF, HF_V, HF_H) of the input with missing traces, and the right three panels show those of the ground truth. The dashed line separates the input and ground truth groups.
Abbreviations: HF: High-frequency component; LF: Low-frequency component.

that the PSNR difference between CT-UNet and U-Net was not statistically significant at 67% (p = 0.139) and 75% (p = 0.878), but was significant at 80% (p = 0.039). In terms of SSIM, consistent improvement was observed across all conditions. CT-UNet showed highly significant improvement over f–x interpolation, CDDIP, and WT-UNet across all conditions (all $p < 0.001$).

To further examine the reconstruction quality in the region containing curvature-varying events, the normalized correlation coefficient (CC) and SSIM were additionally computed over the ROI (blue boxes in Figure 5). Tables 3 and 4 present the ROI-based CC and SSIM, respectively. CT-UNet achieved the highest values across all missing rates, with a larger margin over U-Net than in the global metrics. This indicates that the advantage of curvelet-based decomposition is particularly evident in regions where complex dip variations are concentrated.

3.3. Results of field data

Figure 8 shows the reconstruction results of field data, and Figure 9 presents the corresponding f–k spectra. Field data contain noise, non-stationarity, and complex reflection patterns, requiring simultaneous event continuity and spectral consistency. The overall performance trend is similar to that of the synthetic data, with CT-UNet reproducing the continuity of major reflection events most naturally and maintaining the energy distribution closest to the ground truth in the f-k spectra.

Quantitative evaluation (Tables 1 and 2) shows that CT-UNet achieved the highest PSNR across all missing rates. At 67%, the difference from U-Net was only 0.01 dB, indicating equivalent performance (p = 0.918), while the gap widened to 0.60 dB at 75% ($p = 5.63 \times 10^{-8}$) and 1.61 dB at 80% ($p = 1.48 \times 10^{-66}$). U-Net-Wide achieved PSNR values of 35.29 dB (67%), 34.08 dB (75%), and 31.22

Table 1. Peak signal-to-noise results

Data	Missing ratio (%)	F–x interpolation	CDDIP	U-Net	U-Net-Wide	WT-UNet	CT-UNet
Synthetic data	67	23.64 (± 0.84)	22.63 (± 1.21)	31.96 (± 1.43)	31.52 (± 1.37)	28.82 (± 1.35)	32.14 (± 1.28)$^{n.s.}$
	75	22.91 (± 0.91)	22.23 (± 1.18)	30.18 (± 1.51)	30.01 (± 1.45)	29.42 (± 1.47)	30.20 (± 1.39)$^{n.s.}$.
	80	22.06 (± 1.02)	22.04 (± 1.09)	29.42 (± 1.58)	29.08 (± 1.49)	28.73 (± 1.52)	29.70 (± 1.44)*
	Irregular missing traces 50%	24.76 (± 0.73)	27.24 (± 1.12)	32.61 (± 1.45)	32.33 (± 1.29)	31.92 (± 1.47)	32.76 (± 1.11)$^{n.s.}$
	Irregular missing traces 70%	23.48 (± 0.89)	24.65 (± 1.15)	30.32 (± 1.50)	30.46 (± 1.44)	30.56 (± 1.41)	30.98 (± 1.33)*
Field data	67	27.17 (± 1.12)	26.31 (± 1.38)	36.29 (± 1.61)	35.29 (± 1.54)	34.84 (± 1.55)	36.30 (± 1.48)$^{n.s.}$
	75	26.67 (± 1.08)	23.93 (± 1.72)	33.86 (± 1.83)	34.08 (± 1.69)	34.00 (± 1.71)	34.46 (± 1.65)***
	80	25.05 (± 0.97)	23.85 (± 1.31)	29.88 (± 1.42)	31.22 (± 1.36)	31.18 (± 1.38)	31.49 (± 1.33)***

Notes: For paired *t*-test results (CT-UNet vs. U-Net), *$p < 0.05$; ***$p < 0.001$; Values represent the mean (± standard deviation) computed over all test patches (250 patches for synthetic data, 505 patches for field data); All metrics were computed on the original amplitude scale after denormalization; CDDIP is a self-supervised method that does not use training data and is included to provide insight into the performance characteristics across different reconstruction paradigms rather than for direct comparison with supervised methods.
Abbreviations: CDDIP: Constrained Diffusion-Driven Deep Image Prior; CT: Curvelet transform; n.s.: Not significant; WT: Wavelet transform.

Table 2. Structural similarity index measure results

Data	Missing ratio (%)	F–x interpolation	CDDIP	U-Net	U-Net-Wide	WT-UNet	CT-UNet
Synthetic data	67	0.71 (± 0.03)	0.58 (± 0.15)	0.89 (± 0.03)	0.89 (± 0.03)	0.82 (± 0.04)	0.92 (± 0.02)
	75	0.62 (± 0.03)	0.54 (± 0.05)	0.86 (± 0.03)	0.83 (± 0.04)	0.81 (± 0.04)	0.87 (± 0.03)
	80	0.56 (± 0.04)	0.51 (± 0.05)	0.84 (± 0.04)	0.83 (± 0.04)	0.82 (± 0.04)	0.85 (± 0.03)
	Irregular missing traces 50%	0.74 (± 0.06)	0.76 (± 0.11)	0.90 (± 0.06)	0.90 (± 0.05)	0.90 (± 0.06)	0.91 (± 0.05)
	Irregular missing traces 70%	0.61 (± 0.06)	0.62 (± 0.10)	0.83 (± 0.05)	0.85 (± 0.05)	0.86 (± 0.05)	0.87 (± 0.04)
Field data	67	0.87 (± 0.02)	0.82 (± 0.05)	0.98 (± 0.01)	0.97 (± 0.01)	0.98 (± 0.01)	0.98 (± 0.01)
	75	0.82 (± 0.02)	0.78 (± 0.02)	0.97 (± 0.01)	0.97 (± 0.01)	0.97 (± 0.01)	0.98 (± 0.01)
	80	0.79 (± 0.02)	0.75 (± 0.02)	0.96 (± 0.01)	0.96 (± 0.01)	0.96 (± 0.01)	0.97 (± 0.01)

Note: Values represent the mean (± standard deviation) over 250 patches (synthetic data) and 505 patches (field data).
Abbreviations: CDDIP: Constrained Diffusion-Driven Deep Image Prior; CT: Curvelet transform; WT: Wavelet transform.

Table 3. Region of interest-based normalized correlation coefficient for synthetic data

Missing ratio (%)	F–x interpolation	CDDIP	U-Net	U-Net-Wide	WT-UNet	CT-UNet
67	0.42 (± 0.20)	0.25 (± 0.14)	0.88 (± 0.06)	0.89 (± 0.06)	0.82 (± 0.09)	0.90 (± 0.05)
75	0.28 (± 0.16)	0.22 (± 0.13)	0.80 (± 0.10)	0.81 (± 0.10)	0.75 (± 0.11)	0.82 (± 0.09)
80	0.21 (± 0.13)	0.15 (± 0.11)	0.77 (± 0.11)	0.78 (± 0.10)	0.73 (± 0.12)	0.79 (± 0.10)

Note: Values were computed over the region of interest (blue boxes in Figure 5) and represent the mean (± standard deviation) over 250 test patches.
Abbreviations: CDDIP: Constrained Diffusion-Driven Deep Image Prior; CT: Curvelet transform; WT: Wavelet transform.

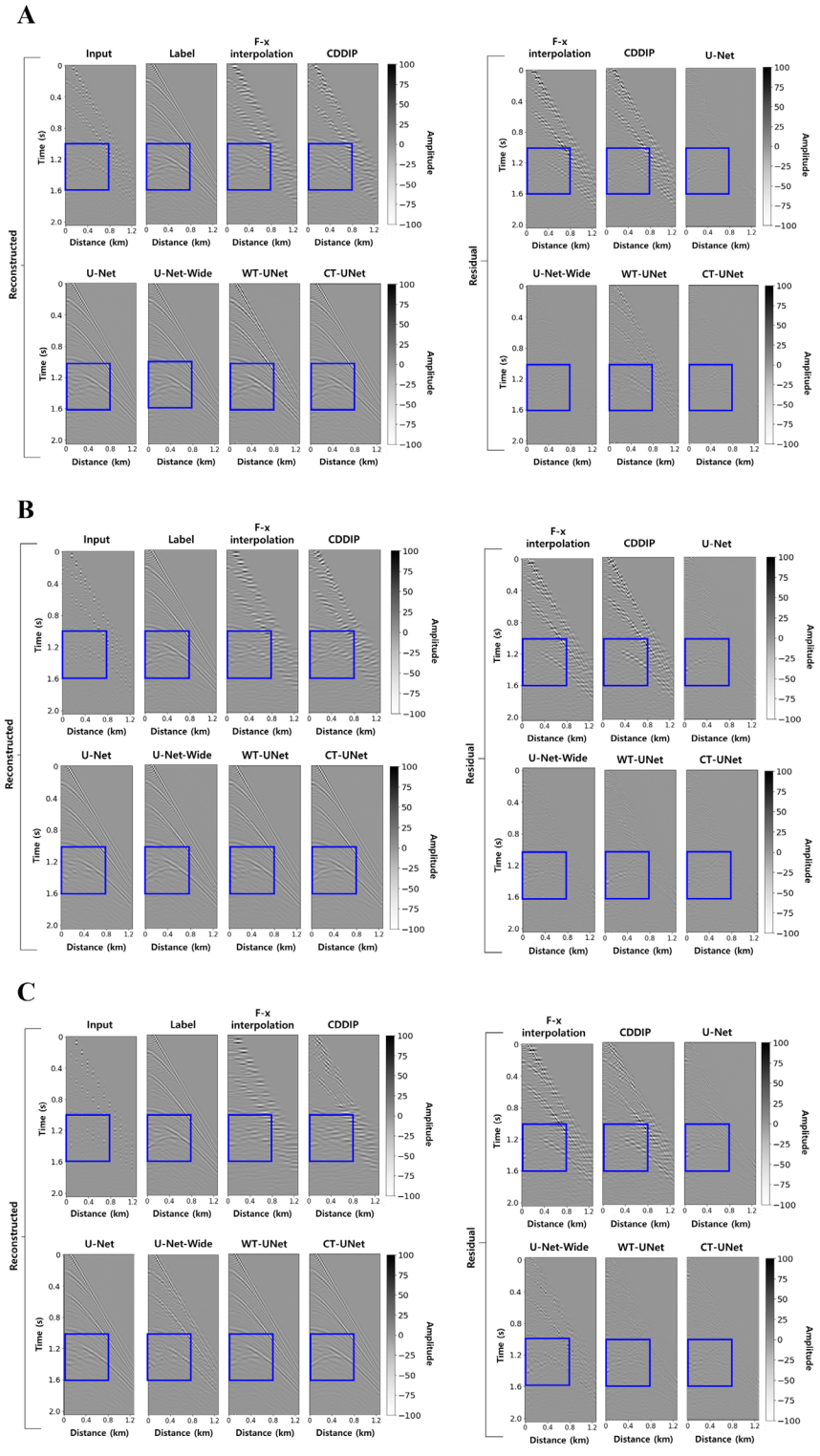

Figure 5. Reconstruction results and residuals of synthetic data under regular missing rates of (A) 67%, (B) 75%, and (C) 80%. The top row of each panel shows the reconstructed results, and the bottom row shows the residuals. From left to right, the reconstructed results are the input, ground truth, f–x interpolation, Constrained Diffusion-Driven Deep Image Prior (CDDIP), U-Net, U-Net-Wide, wavelet transform (WT)-UNet, and curvelet transform (CT)-UNet. The residual panels, from left to right, correspond to f–x interpolation, CDDIP, U-Net, U-Net-Wide, WT-UNet, and CT-UNet.

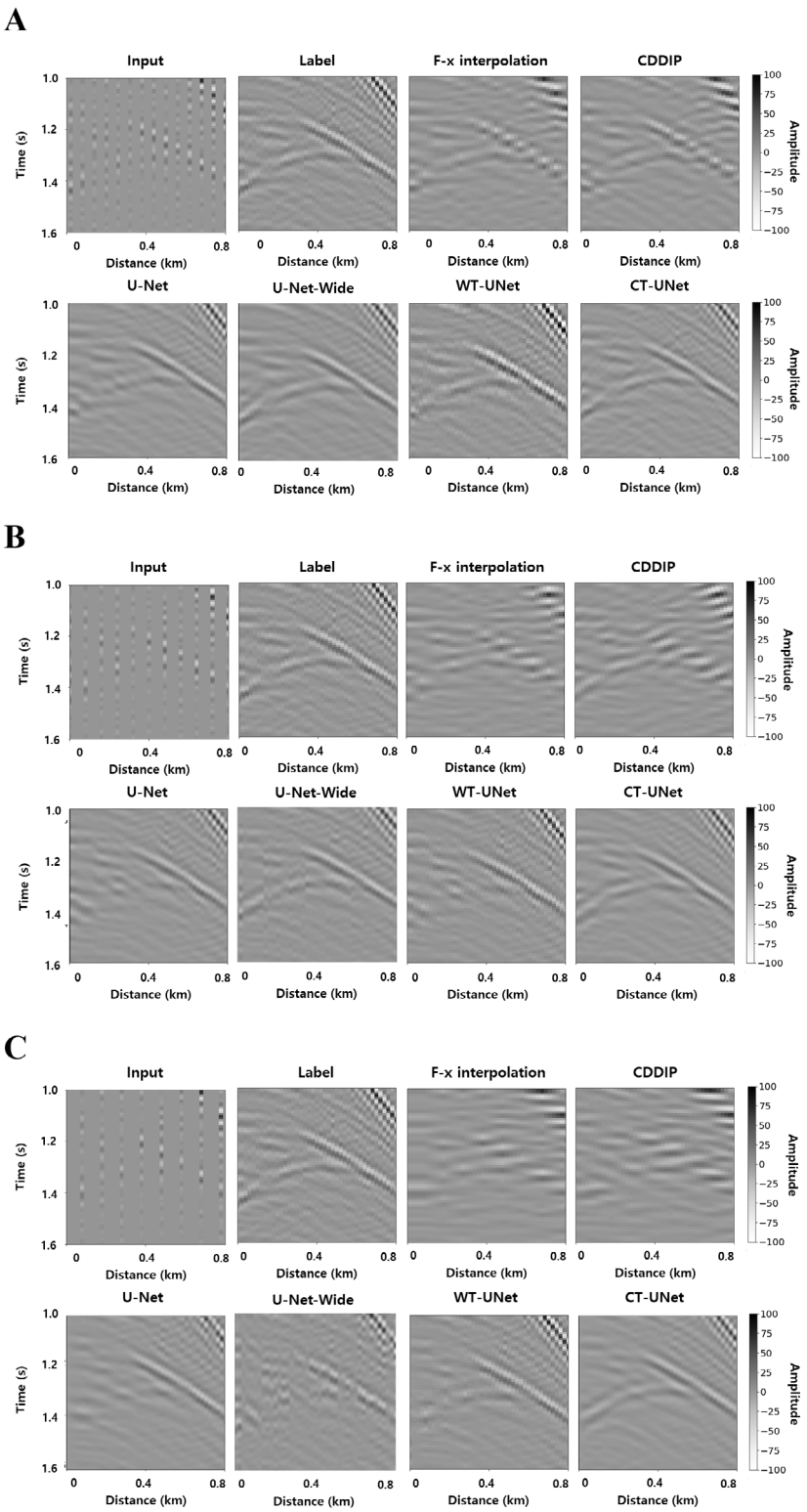

Figure 6. Enlarged views of the region of interest (blue boxes in Figure 5) for synthetic data under regular missing rates of (A) 67%, (B) 75%, and (C) 80%. From left to right, the top row shows the input, ground truth, f–x interpolation, and Constrained Diffusion-Driven Deep Image Prior results, while the bottom row shows the U-Net, U-Net-Wide, wavelet transform-UNet, and curvelet transform-UNet results.

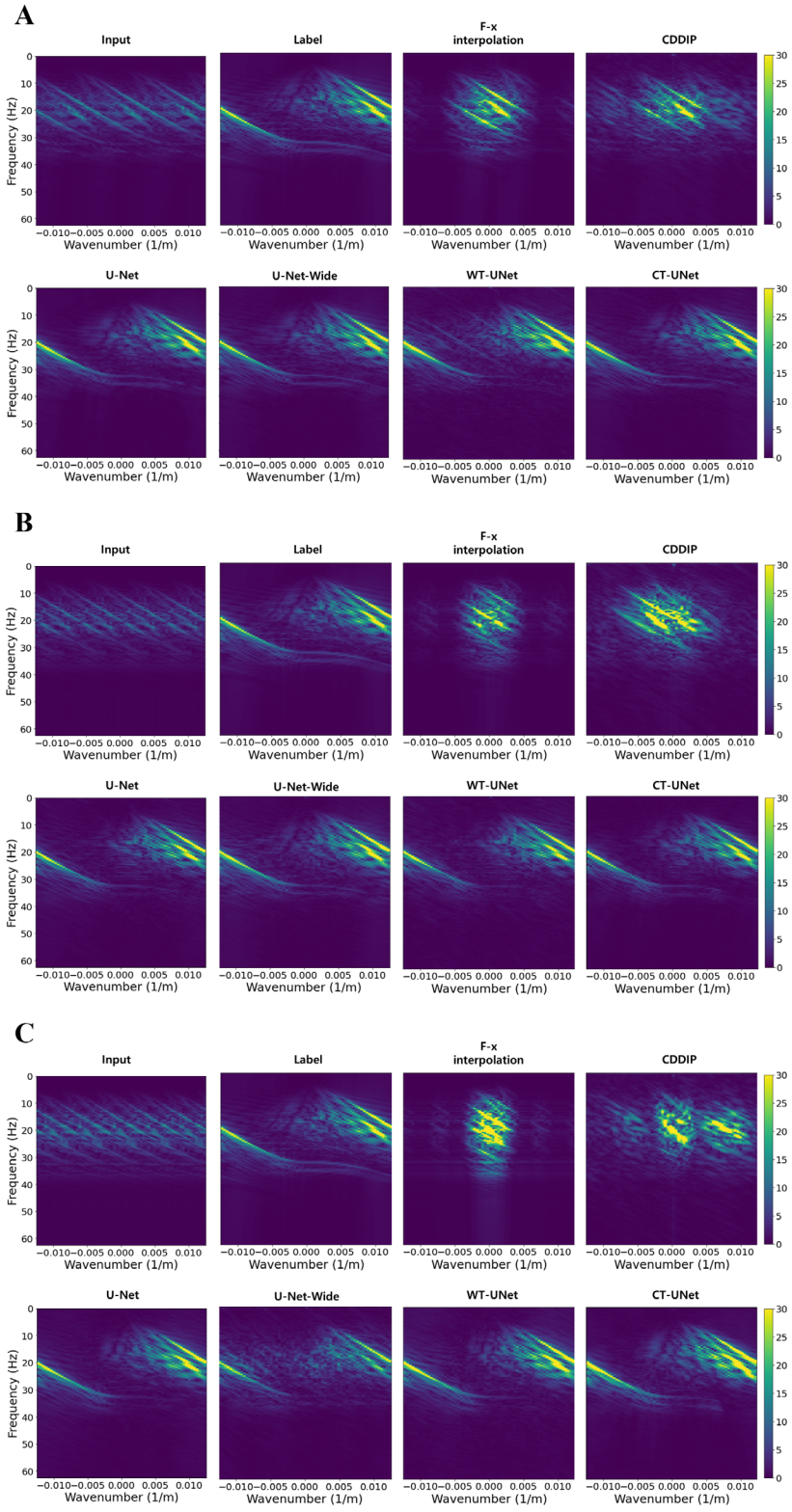

Figure 7. The f–k spectra corresponding to the reconstructed results in Figure 5 under regular missing rates of (A) 67%, (B) 75%, and (C) 80%. From left to right, the top row shows the input, ground truth, f–x interpolation, and Constrained Diffusion-Driven Deep Image Prior results, while the bottom row shows the U-Net, U-Net-Wide, wavelet transform-UNet, and curvelet transform-UNet results.

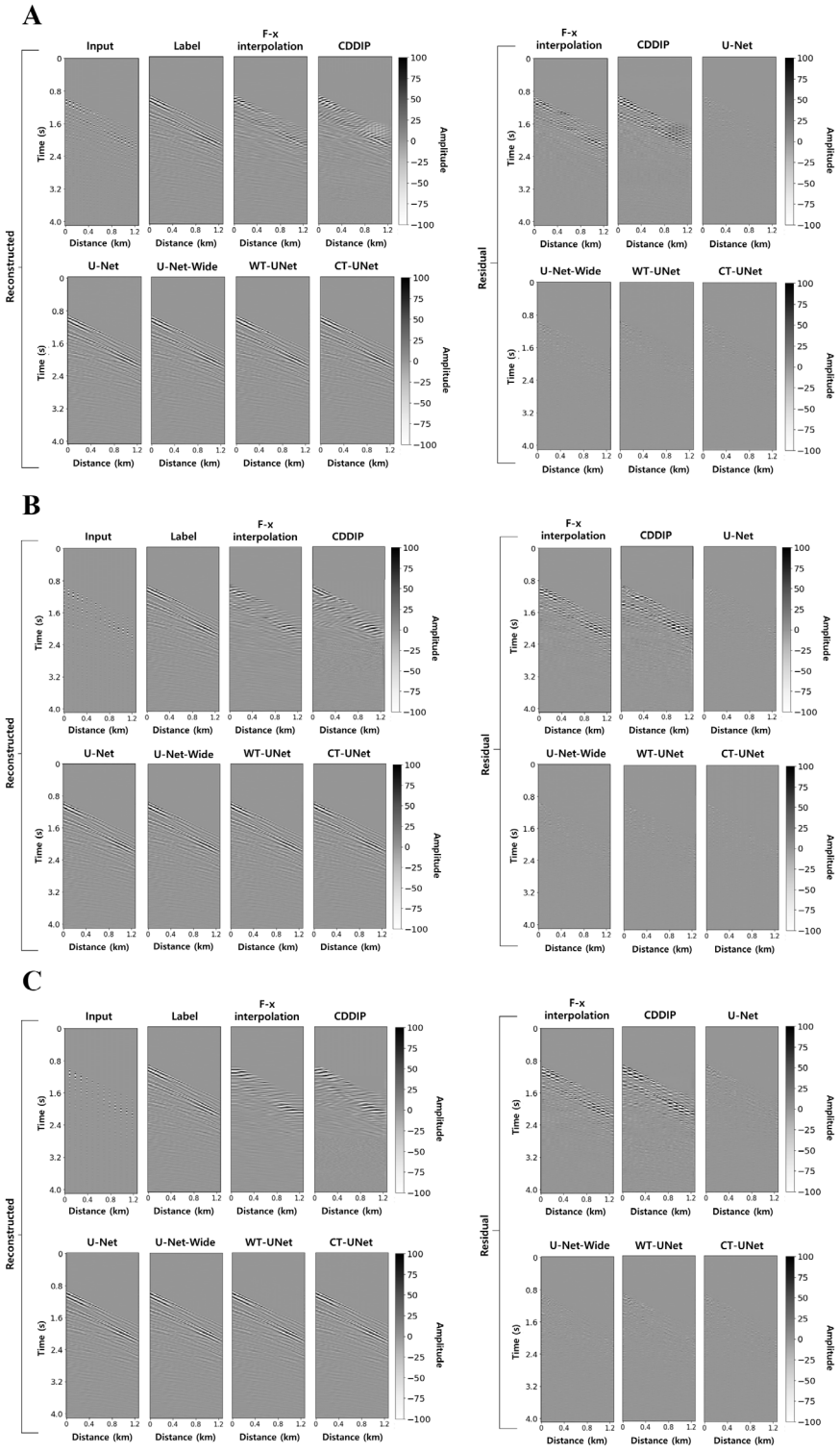

Figure 8. Reconstruction results and residuals of field data under regular missing rates of (A) 67%, (B) 75%, and (C) 80%. For each missing-rate case, the reconstructed results are shown in the first two rows, and the corresponding residuals are shown in the last two rows. From left to right, the reconstructed results are the input, ground truth, f–x interpolation, Constrained Diffusion-Driven Deep Image Prior (CDDIP), U-Net, U-Net-Wide, wavelet transform (WT)-UNet, and curvelet transform (CT)-UNet. The residual panels, from left to right, correspond to f–x interpolation, CDDIP, U-Net, U-Net-Wide, WT-UNet, and CT-UNet.

dB (80%). At 75% and 80%, U-Net-Wide outperformed U-Net but remained below CT-UNet, confirming that the curvelet-based decomposition provides an additional benefit beyond what increased model capacity alone can achieve. CT-UNet showed highly significant improvement over WT-UNet, f–x interpolation, and CDDIP across all conditions (all $p < 0.001$).

To examine the frequency-dependent reconstruction characteristics, band-limited PSNR and SSIM were computed for three frequency bands (Tables 5 and 6). In both synthetic and field data, CT-UNet achieved the highest PSNR and SSIM across all three bands. The advantage over U-Net was most pronounced in the mid-frequency band, where CT-UNet achieved 31.0 dB on synthetic data and 33.5 dB on field data, compared with 30.6 dB and 32.4 dB, respectively, for U-Net. U-Net-Wide showed intermediate performance between U-Net and CT-UNet in most bands, confirming that increased model capacity alone does not fully account for CT-UNet's improvement.

To provide a quantitative comparison of the frequency-dependent reconstruction accuracy, the spectral residual energy profiles under the 80% regular missing condition are presented in Figure 10. For both synthetic and field data, CT-UNet exhibits the lowest residual energy across the entire frequency range, indicating the most balanced reconstruction among all compared methods. Notably, U-Net-Wide, despite having a comparable total parameter count to CT-UNet, shows higher residual energy than CT-UNet, particularly in the mid-frequency range (normalized frequency 0.1–0.3), confirming that the improvement is attributable to curvelet-based decomposition rather than increased model capacity.

3.4. Results of irregular missing data

To examine the behavior of CT-UNet beyond regular undersampling, two irregular (random) missing scenarios at 50% and 70% missing rates were tested on synthetic data (Figures 11 and 12). Unlike regular missing, no periodic aliasing pattern forms in the f-k domain, and the damaged components spread incoherently across the spectrum.

In the spatial domain, f–x interpolation and CDDIP exhibit relatively large residuals along event structures across both missing rates, whereas U-Net, U-Net-Wide, WT-UNet, and CT-UNet stably reconstruct the major reflection events. The visual differences among the learning-based methods are smaller compared to the regular missing conditions. In the f-k spectra, U-Net, U-Net-Wide, and CT-UNet show nearly identical levels of energy distribution recovery at both missing rates.

Quantitative evaluation (Tables 1 and 2) shows that at 50% irregular missing, CT-UNet achieved the highest PSNR of 32.76 ± 1.11 dB and SSIM of 0.91 ± 0.05, with U-Net at 32.61 ±1.45 dB and U-Net-Wide at 32.33 ± 1.29 dB. At the more challenging 70% irregular missing rate, CT-UNet maintained the highest PSNR of 30.98 ± 1.33 dB ($p < 0.05$) and SSIM of 0.87 ± 0.04, outperforming U-Net (30.32 ± 1.50 dB; 0.83 ± 0.05), U-Net-Wide (30.46 ± 1.44 dB; 0.85 ± 0.05), and WT-UNet (30.56 ± 1.41 dB; 0.86 ± 0.05). These results indicate that CT-UNet remains effective under a more challenging random, irregular, and missing condition.

Across both tested random irregular missing rates, CT-UNet maintained the highest PSNR and SSIM among the compared methods. These results suggest that curvelet-based component separation can remain effective beyond periodic regular undersampling, although further evaluation is required for more realistic acquisition-gap scenarios, such as blocky, mixed regular–irregular, consecutive, and spatially varying missing patterns.

To control for potential spatial autocorrelation between patches, paired *t*-tests were additionally conducted on shot-aggregated PSNR and SSIM values ($n = 50$ for synthetic and $n = 101$ for field data). Results for CT-UNet versus U-Net are summarized in Table 7. CT-UNet shows consistently non-negative differences across all tested conditions, with statistically significant PSNR advantages at synthetic 80% (+0.28 dB, $p < 0.05$), synthetic 70% irregular missing (+0.66 dB, $p < 0.05$), field 75% (+0.60 dB, $p < 0.001$), and field 80% (+ 1.61 dB, $p < 0.001$). For SSIM, CT-UNet maintains consistent advantages across all conditions. This pattern indicates that CT-UNet's improvement over U-Net is most pronounced under high regular missing rates and challenging irregular missing scenarios, consistent with the patch-level results in Tables 1 and 2.

4. Discussion

This section discusses the experimental results in terms of (i) the contribution of curvelet-based component separation, (ii) performance characteristics according to missing type and level configuration, (iii) design differences among comparison methods, (iv) computational cost, and (v) limitations and future work.

4.1. Contribution of curvelet-based component separation

The core of CT-UNet lies in separating components in the curvelet domain and performing learning tailored to the statistical characteristics of each component. The curvelet transform provides a near-optimal sparse representation for curvilinear discontinuities, and according to Candès and Donoho[27] and Candès *et al.*,[28] the approximation error decay rate for C^2 discontinuities is $O(k^{-2}(\log k)^3)$, which

Table 4. ROI-based structural similarity index measure for synthetic data

Missing ratio (%)	F–x interpolation	CDDIP	U-Net	U-Net-Wide	WT-UNet	CT-UNet
67	0.45 (± 0.11)	0.20 (± 0.13)	0.83 (± 0.10)	0.84 (± 0.09)	0.77 (± 0.15)	0.86 (± 0.09)
75	0.31 (± 0.09)	0.20 (± 0.10)	0.70 (± 0.14)	0.69 (± 0.14)	0.62 (± 0.18)	0.73 (± 0.13)
80	0.23 (± 0.07)	0.15 (± 0.08)	0.65 (± 0.15)	0.63 (± 0.16)	0.59 (± 0.17)	0.68 (± 0.14)

Notes: Values were computed over the ROI (blue boxes in Figure 5); mean (± standard deviation) over 250 test patches.
Abbreviations: CDDIP: Constrained Diffusion-Driven Deep Image Prior; CT: Curvelet transform; ROI: Region of interest; WT: Wavelet transform.

Table 5. Band-limited PSNR (dB) and SSIM for synthetic data under 80% regular missing

Metric	F–x interpolation	CDDIP	U-Net	U-Net-Wide	WT-UNet	CT-UNet
Low PSNR (dB)/SSIM	27.6/0.78	27.1/0.73	34.6/0.93	34.8/0.92	33.3/0.90	35.0/0.94
Mid PSNR (dB)/SSIM	24.8/0.65	24.1/0.60	30.6/0.87	30.8/0.86	29.7/0.84	31.0/0.88
High PSNR (dB)/SSIM	22.9/0.54	22.2/0.49	28.8/0.80	29.0/0.79	27.9/0.77	29.2/0.81

Note: Metrics were computed separately for low (0–12.5 Hz), mid (12.5–37.5 Hz), and high (37.5–62.5 Hz) frequency bands using Butterworth bandpass filtering (dt = 0.008 s, Nyquist frequency = 62.5 Hz).
Abbreviations: CDDIP: Constrained Diffusion-Driven Deep Image Prior; CT: Curvelet transform; PSNR: Peak signal-to-noise ratio; SSIM: Structural similarity index measure; WT: Wavelet transform.

Table 6. Band-limited PSNR (dB) and SSIM for field data under 80% regular missing

Metric	F–x interpolation	CDDIP	U-Net	U-Net-Wide	WT-UNet	CT-UNet
Low PSNR (dB)/ SSIM	29.5/0.86	28.8/0.82	34.9/0.98	35.9/0.98	35.7/0.98	36.1/0.98
Mid PSNR(dB)/ SSIM	27.6/0.82	26.9/0.78	32.4/0.96	33.2/0.97	33.0/0.97	33.5/0.97
High PSNR (dB)/ SSIM	24.2/0.78	23.4/0.74	29.7/0.95	30.6/0.96	30.4/0.96	30.8/0.96

Note: Band definitions are identical to Table 5.
Abbreviations: CDDIP: Constrained Diffusion-Driven Deep Image Prior; CT: Curvelet transform; PSNR: Peak signal-to-noise ratio; SSIM: Structural similarity index measure; WT: Wavelet transform.

Table 7. Shot-level comparison between CT-UNet and U-Net

Data	Condition	*n*_shots	ΔPSNR (dB)	ΔSSIM	Significance
Synthetic	Regular 67%	50	+0.18	+0.03	n.s.
Synthetic	Regular 75%	50	+0.02	+0.01	n.s.
Synthetic	Regular 80%	50	+0.28	+0.01	*
Synthetic	Irregular 50%	50	+0.15	+0.01	n.s.
Synthetic	Irregular 70%	50	+0.66	+0.04	*
Field	Regular 67%	101	+0.01	+0.00	n.s.
Field	Regular 75%	101	+0.60	+0.01	***
Field	Regular 80%	101	+1.61	+0.01	***

Notes: PSNR and SSIM were aggregated at the shot level ($n = 50$ for synthetic, $n = 101$ for field) to reduce spatial dependence among neighboring patches; Δ = mean(CT-UNet) − mean(U-Net); positive values indicate CT-UNet advantage; *$p < 0.05$; ***$p < 0.001$.
Abbreviations: CT: Curvelet transform; n.s.: Not significant; PSNR: Peak signal-to-noise ratio; SSIM: Structural similarity index measure.

challenges for conventional interpolation methods because of their opposing dip orientations relative to the dominant reflections. The ROI-based analysis (Tables 3 and 4) quantitatively confirms this, with CT-UNet exhibiting a more pronounced margin over U-Net in regions containing such events compared to the global metrics.

The band-limited analysis (Tables 5 and 6) quantitatively confirms that CT-UNet reduces reconstruction error more uniformly across frequency bands compared to all other methods, with consistent superiority in the mid-frequency band where complex dip components are concentrated.

The spectral residual energy analysis (Figure 10) provides further evidence for this conclusion. In the synthetic 80% condition, CT-UNet maintains the lowest residual energy across all frequencies, whereas U-Net and U-Net-Wide concentrate residuals in the mid-to-high frequency range. This pattern is consistent with the theoretical prediction that curvelet-based decomposition reduces the complexity of the reconstruction problem for each component-wise network, enabling more balanced recovery across the full bandwidth. The same trend is reproduced in the field data, where CT-UNet achieves the lowest residual energy despite noise and non-stationarity, reinforcing the generalizability of the observed benefit.

4.2. Performance characteristics according to missing type

In the regular case, aliasing components exhibit a periodic structure in the f–k domain, allowing the directional decomposition of curvelets to effectively separate signal and aliasing components. Under irregular missing, the damaged components spread incoherently across the f–k domain rather than forming periodic aliasing patterns. Despite this loss of structured aliasing, CT-UNet maintained the highest PSNR and SSIM among the compared methods at both 50% and 70% random irregular missing rates. These results suggest that curvelet-based separation remains beneficial even when the missing pattern is not periodic. However, because only random irregular missing was examined, further evaluation is required for more realistic acquisition-gap scenarios, including blocky, mixed regular–irregular, consecutive, and spatially varying missing patterns.

4.3. Influence of uniform discrete curvelet transform level configuration

With the [4,4] configuration, the HFs produced only two types of spatial sizes, making 3-group classification impossible. With the [16,16] configuration, the spatial size of the HF_H component was extracted as 7×128, which was incompatible with the 2×2 MaxPooling operations of the U-Net. These findings confirm the theoretical rationale presented in Section 2.2 and demonstrate that [8,8] is the only practical configuration that can fully constitute the CT-UNet framework under the combination of patch size (64×256) and a four-stage U-Net. The effects of asymmetric configurations (e.g., [8,4], [4,8]) and increased patch sizes are set as future tasks.

4.4. Design differences among comparison methods

The structural difference between WT-UNet and CT-UNet stems from the inherent decomposition characteristics of each transform. For wavelets, it is natural to concatenate four subbands along the channel dimension and feed them into a single network, whereas the UDCT produces components with different lattice structures for each direction, making group-wise independent networks consistent with the transform structure. Forcing an identical framework would distort the inherent advantages of each transform; therefore, this comparison is interpreted as evaluating the performance when each transform is applied in its optimal structure.

Given that CT-UNet employs three independent U-Nets and thus has approximately three times the total parameters of the baseline U-Net, the question may arise whether the performance improvement is attributable to curvelet decomposition or simply to increased model capacity. To directly address this concern, U-Net-Wide was included as a capacity-matched control: a single U-Net with channel widths scaled to match CT-UNet's total parameter count (~23M) without applying any transform. U-Net-Wide achieved results comparable to, and in some conditions slightly better than, the standard U-Net, but it remained below CT-UNet in the key high-missing-rate cases. This indicates that increasing model capacity alone is insufficient to reproduce the performance of CT-UNet. The spectral residual energy profiles further support this interpretation, showing that U-Net-Wide does not match CT-UNet despite having a comparable parameter count.

Curvelet-based sparsity-promoting reconstruction methods (e.g., curvelet-POCS, L1-regularized inversion) utilize the same transform domain but follow an iterative-optimization paradigm rather than data-driven learning. The comparative experiments in this study are deliberately scoped to evaluate the effect of transform selection within the learning-based interpolation paradigm, where all compared methods (U-Net, U-Net-Wide, WT-UNet, CT-UNet) share a supervised learning framework. This design provides a controlled comparison for assessing the contribution of curvelet-domain decomposition within the learning-based interpolation framework. Comparison with optimization-based curvelet methods addresses a

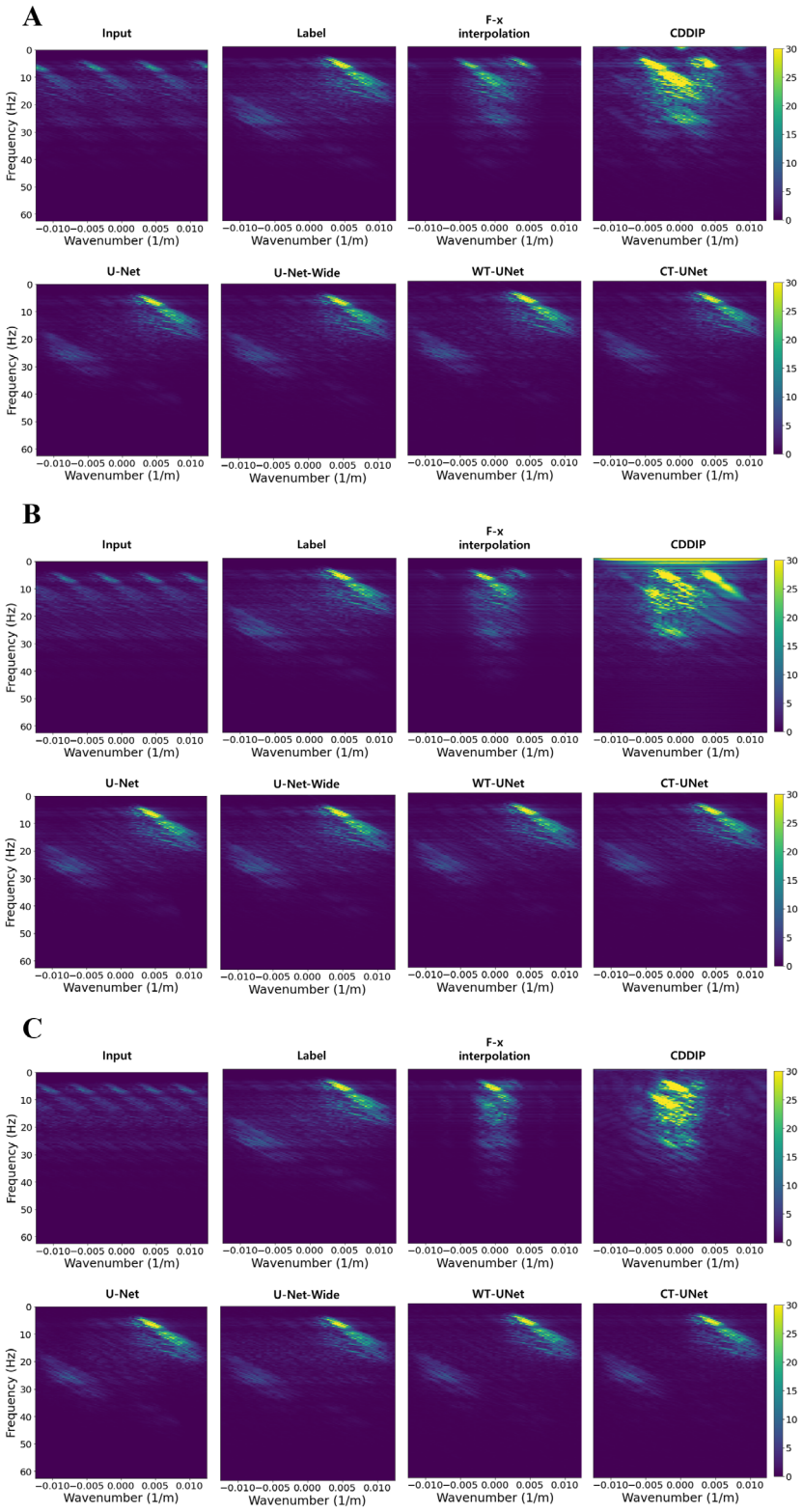

Figure 9. The f–k spectra corresponding to the reconstructed results in Figure 8 under regular missing rates of (A) 67%, (B) 75%, and (C) 80%. From left to right, the top row shows the input, ground truth, f–x interpolation, and Constrained Diffusion-Driven Deep Image Prior results, while the bottom row shows the U-Net, U-Net-Wide, wavelet transform-UNet, and curvelet transform-UNet results.

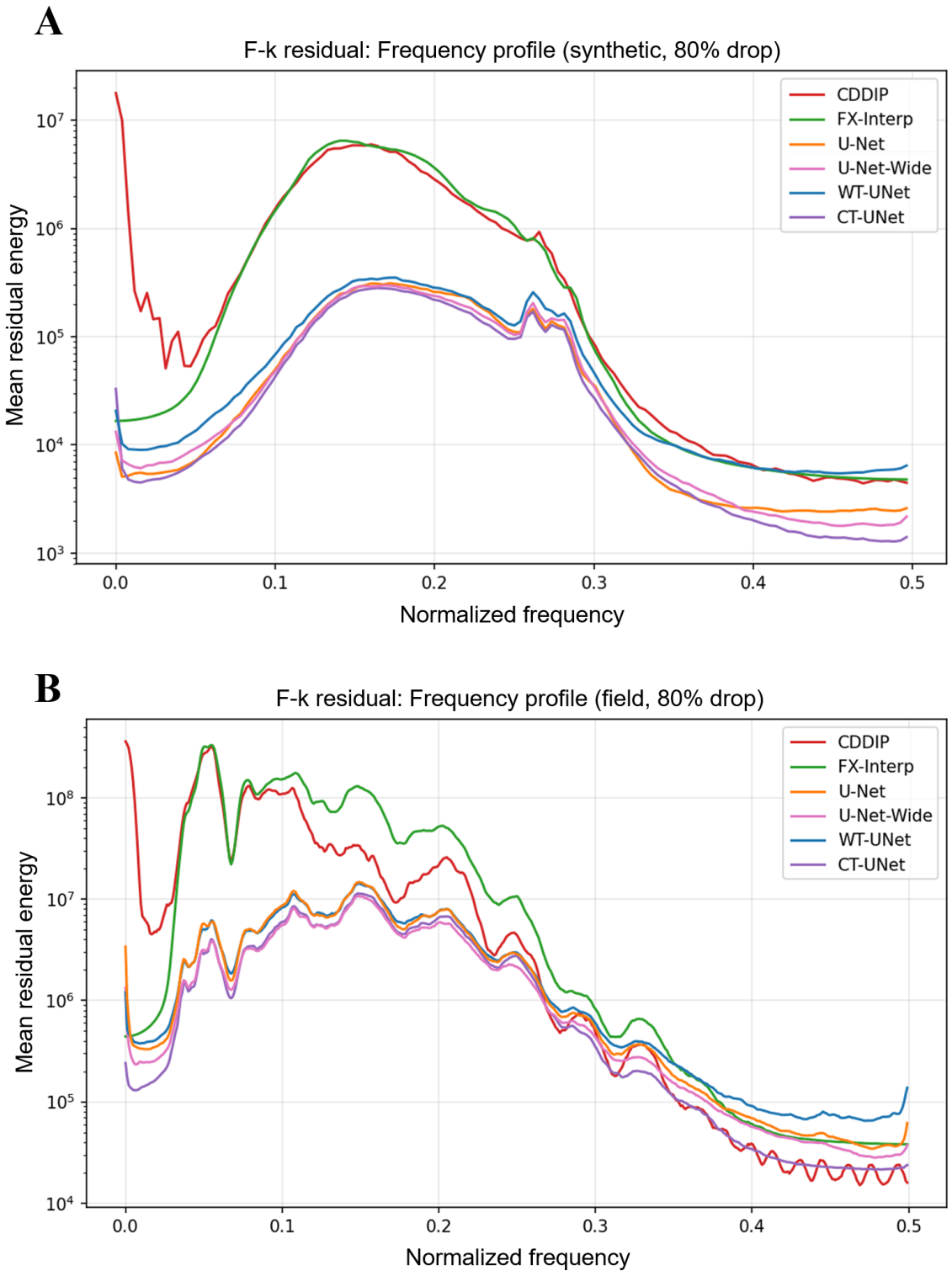

Figure 10. Spectral residual energy profiles under 80% regular missing for (A) synthetic data and (B) field data. Each curve represents the mean residual energy in the f–k domain, computed by averaging the squared magnitude of the residual spectrum along the wavenumber axis at each frequency. Lower values indicate a more accurate reconstruction.
Abbreviations: CDDIP: Constrained Diffusion-Driven Deep Image Prior; CT: Curvelet transform; WT: Wavelet transform.

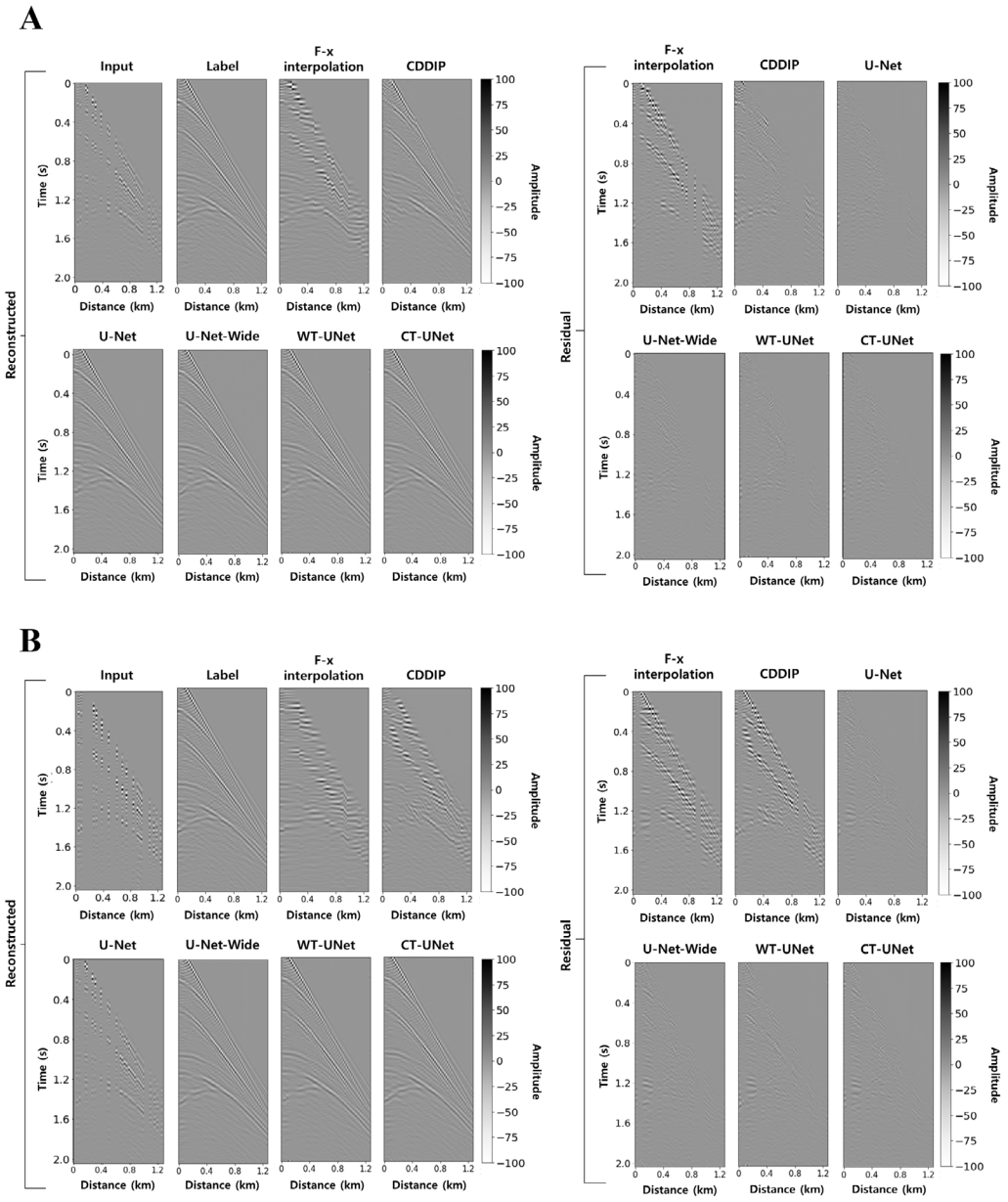

Figure 11. Reconstruction results and residuals of synthetic data under irregular (random) missing: (A) 50% missing rate and (B) 70% missing rate. In each panel, the top row shows the reconstructed results and the bottom row shows the residuals. From left to right, the reconstructed results are the input, ground truth, f–x interpolation, Constrained Diffusion-Driven Deep Image Prior (CDDIP), U-Net, U-Net-Wide, wavelet transform (WT)-UNet, and curvelet transform (CT)-UNet. The residual panels, from left to right, correspond to f–x interpolation, CDDIP, U-Net, U-Net-Wide, WT-UNet, and CT-UNet.

exhibits fundamentally faster convergence compared to $O(k^{-1})$ for wavelets. This reduces the complexity of the residuals that each component-wise U-Net must learn, and mitigates the spectral bias of a single network through component-wise learning.[41]

The experimental results are consistent with this theoretical prediction. Under high missing-rate conditions (80%), CT-UNet achieved PSNR improvements of 0.28 dB on synthetic data and 1.61 dB on field data compared to U-Net, with the difference statistically significant. In contrast, no significant difference was observed under low missing-rate conditions. This theoretical property also translates into a practical advantage for reconstructing conflicting-dip events, which are known to pose significant

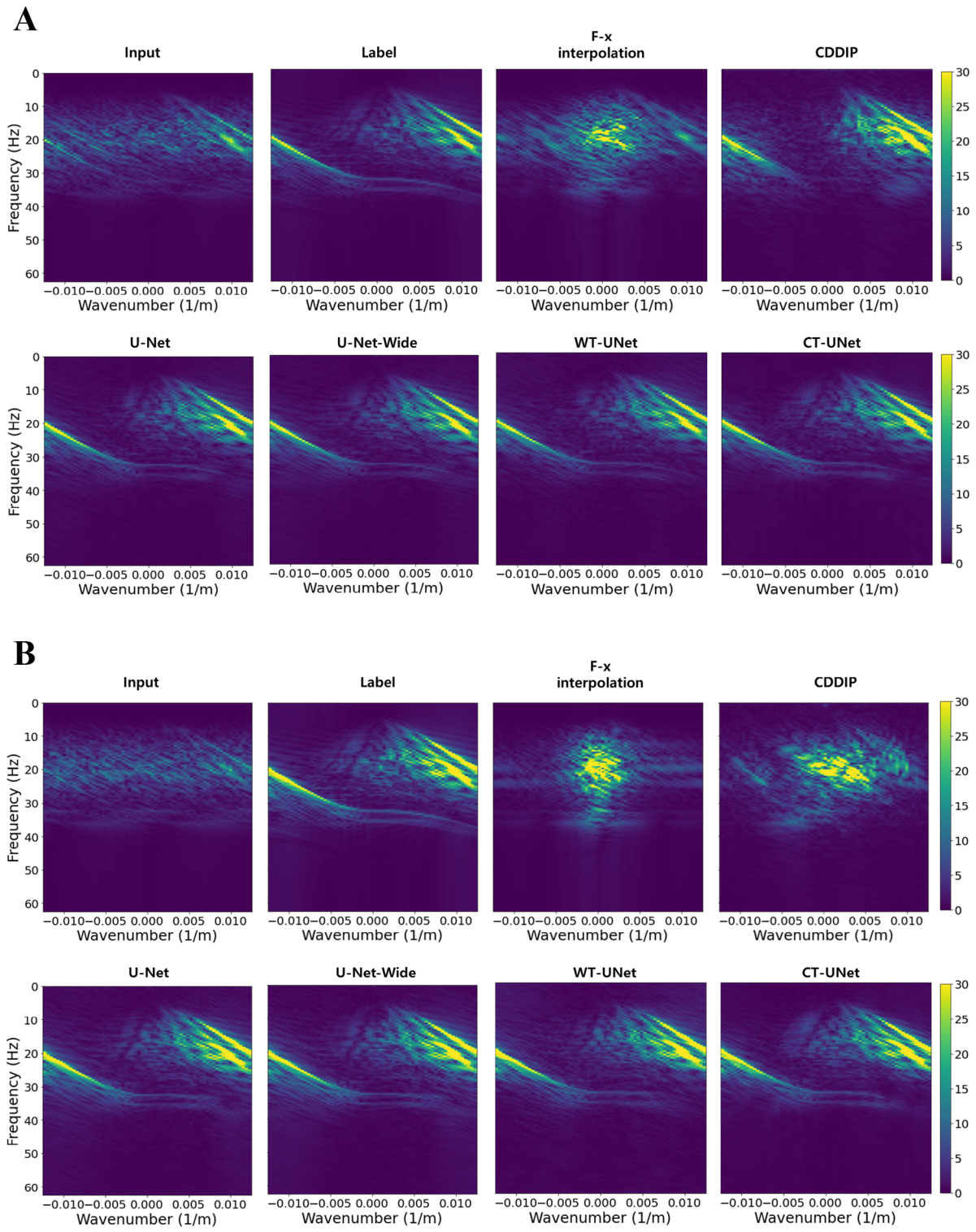

Figure 12. The f–k spectra corresponding to the reconstructed results in Figure 11 under irregular (random) missing: (A) 50% missing rate and (B) 70% missing rate. In each panel, from left to right, the top row shows the input, ground truth, f–x interpolation, and Constrained Diffusion-Driven Deep Image Prior results, while the bottom row shows the U-Net, U-Net-Wide, wavelet transform-UNet, and curvelet transform-UNet results.

fundamentally different research question—learning-based versus iterative-optimization-based reconstruction—and requires dedicated investigation of optimization hyperparameters (iteration count, thresholding schedule, regularization weights). Such a comparison is therefore outside the present scope and is left for independent investigation.

In comparison with CDDIP, it should be noted that CDDIP is fundamentally different, performing iterative optimization without training data, and the purpose of this comparison is to examine performance characteristics across different reconstruction paradigms.

4.5. Computational cost and recommended use cases

The CT-UNet incurs approximately a threefold increase in training time (~30 GPU·hours) and inference time (~30 s) compared to a single U-Net (Table 8); however, this can be reduced in a parallel GPU environment, and the peak memory remains identical at ~6 GB (training)/< 0.25 GB (inference). The practical value of this additional cost is supported by the consistent quantitative gains: shot-level paired t-tests confirm statistically significant PSNR improvements over U-Net at synthetic 80% (+0.28 dB), synthetic 70% irregular missing (+0.66 dB), field 75% (+0.60 dB), and field 80% (+1.61 dB). CT-UN*et al*so maintains SSIM values comparable to or higher than those of the baseline methods across the tested conditions, suggesting that its structural reconstruction quality is at least preserved and often improved beyond the high-missing regime. In conflicting-dip regions where conventional methods fail (ROI analysis, Tables 3 and 4), CT-UNet's advantage is particularly pronounced. Furthermore, the component-wise architecture enables selective deployment: in scenarios where only specific frequency bands require enhanced reconstruction, individual component networks can be applied independently - an operational flexibility unavailable in single-network architectures. CT-UNet is therefore most recommended for applications where high missing rates, structural continuity, or conflicting-dip event recovery are critical. For lower-missing-rate cases where the performance gap relative to a standard U-Net is small, the simpler U-Net may remain a more cost-effective choice.

4.6. Validation methodology for field data

The field data validation in this study employed Mobil AVO Viking Graben Line 12,[38] a fully sampled, publicly available benchmark dataset widely used in seismic interpolation research. Controlled missing patterns were applied to the original data, which served as ground truth, enabling rigorous quantitative evaluation through PSNR and SSIM. This semi-synthetic validation protocol is a standard approach in the field, providing quantifiable benchmarks for objective comparison across methods, reproducibility through publicly available data, and systematic control over missing rate and pattern. Application to datasets with naturally occurring acquisition gaps constitutes a natural application study downstream of the methodological validation presented here.

4.7. Limitations and future work

This study has the following limitations: First, the real/imaginary separation of complex coefficients means that phase coherence is only implicitly learned, necessitating the introduction of complex-valued convolution or phase consistency loss. Second, only random irregular missing was examined in this study. More realistic acquisition-gap scenarios, including blocky missing traces, mixed regular–irregular missing, consecutive missing traces, and spatially varying missing patterns, require systematic evaluation with dedicated mask-generation protocols and

Table 8. Computational cost comparison

Method	Training time (GPU·hours)	Inference time (min)	GPU memory (train/infer)
F–x interpolation	–	~0.5	<1 GB
CDDIP	~16.7	~2.5	~1.5 GB/<0.5 GB
U-Net	~10	~0.17	~6 GB/<0.25 GB
U-Net-Wide	~12	~0.20	~7 GB/<0.3 GB
WT-UNet	~10	~0.17	~6 GB/<0.25 GB
CT-UNet	~30	~0.5	~6 GB/<0.25 GB

Abbreviations: CDDIP: Constrained Diffusion-Driven Deep Image Prior; CT: Curvelet transform; GPU: Graphics processing unit; WT: Wavelet transform.

mask-aware learning strategies. These cases are therefore left as future work. Third, only MSE loss was applied, but component-specific customized losses (e.g., MSE for LF and frequency-domain loss for HF) represent an extension direction naturally permitted by the modular framework of CT-UNet. Fourth, the standard U-Net can be replaced with attention-based models, transformers, or diffusion models. Fifth, the synthetic data were generated under relatively clean conditions, and robustness evaluation under controlled noise environments (signal-to-noise ratio 10/20 dB) remains a future task.

5. Conclusion

In this study, we proposed CT-UNet, a seismic data interpolation framework based on the curvelet transform. The proposed method decomposes seismic data into multi-scale and multi-directional components using the UDCT, reconstructs each component with independent U-Net models, and synthesizes them via inverse transformation, aiming to simultaneously enhance event continuity and preserve frequency components even under high missing-rate conditions.

The performance of CT-UNet was evaluated on synthetic data (SEG/EAGE Salt Model) and field data (Mobil AVO Viking Graben Line 12) at regular missing rates of 67%, 75%, and 80%, as well as on synthetic data at 50% and 70% random irregular missing rates. Combining spatial-domain reconstruction results, f–k spectral analysis, and PSNR/SSIM quantitative evaluation, CT-UNet showed performance comparable to U-Net under lower missing-rate conditions, while its advantages became more evident under challenging conditions, including synthetic 80%, synthetic 70% irregular missing, field 75%, and field 80%. The shot-level analysis further supports the conclusion that these gains are most robust under high missing-rate and challenging irregular-missing conditions. In the tested irregular missing scenarios, CT-UNet maintained the highest PSNR and SSIM among the compared methods, suggesting that curvelet-based component decomposition can remain effective beyond periodic regular undersampling. However, more realistic missing patterns, such as blocky, mixed regular–irregular, consecutive, and spatially varying gaps, require further investigation.

In summary, the results indicate that integrating curvelet-based multi-scale and multi-directional representation into deep learning interpolation is an effective strategy for improving event continuity and spectral consistency, particularly under high-rate regular undersampling and in regions containing curvature-varying, conflicting-dip events. The proposed CT-UNet is therefore expected to be most useful in acquisition scenarios where high missing rates, structural continuity, and recovery from conflicting dip events are critical.

Acknowledgments

None.

Funding

This study was supported by the Basic Science Research Program through the National Research Foundation of Korea (NRF), funded by the Ministry of Education (No. RS-2025-25435564), and by the Korea Institute of Marine Science and Technology Promotion grant funded by the Ministry of Oceans and Fisheries (No. 20220254, Development of technology for seabed classification based on machine learning).

Conflict of interest

The authors declare they have no competing interests.

Author contributions

Conceptualization: Daeung Yoon
Formal analysis: Jiyun Yu
Investigation: Jiyun Yu
Methodology: Daeung Yoon, Young Kim
Writing–original draft: Jiyun Yu
Writing–review & editing: Jiyun Yu, Daeung Yoon

Availability of data

The data underlying this article are available in the SEG Wiki (https://wiki.seg.org/wiki/SEG_C3_NA) and the Mobil AVO Viking Graben Line 12 (https://wiki.seg.org/wiki/Mobil_AVO_viking_graben_line_12).

Further disclosure

The methodology (Section 2) and the synthetic-data results (Sections 3.1 and 3.2) of this study were presented at the 2025 Spring Conference of the Korean Society of Earth and Exploration Geophysicists (KSEG), held at the Korea Institute of Geoscience and Mineral Resources (KIGAM), Daejeon, Republic of Korea, on April 3, 2025.

References

1. Spitz S. Seismic trace interpolation in the F-X domain. *Geophysics*. 1991;56(6):785-794.

   doi: 10.1190/1.1443096

2. Abma R, Kabir N. 3D interpolation of irregular data with a POCS algorithm. *Geophysics*. 2006;71(6):E91-E97.

   doi: 10.1190/1.2356088

3. Ronneberger O, Fischer P, Brox T. U-Net: Convolutional networks for biomedical image segmentation. In: *Proceedings of MICCAI 2015*. LNCS 9351. 2015:234-241.

   doi: 10.1007/978-3-319-24574-4_28

4. He K, Zhang X, Ren S, Sun J. Deep residual learning for image recognition. In: *Proceedings of the IEEE Conference on Computer Vision and Pattern Recognition (CVPR)*. June 27–30, 2016; Las Vegas, NV, USA. 2016:770-778.

   doi: 10.1109/CVPR.2016.90

5. Wang B, Zhang N, Lu W, Wang J. Deep-learning-based seismic data interpolation: A preliminary result. *Geophysics*. 2019;84(1):V11-V20.

   doi: 10.1190/geo2017-0495.1

6. Yu J, Wu B. Attention and hybrid loss guided deep learning for consecutively missing seismic data reconstruction. *IEEE Trans Geosci Remote Sens*. 2022;60:1-8.

   doi: 10.1109/TGRS.2021.3068279

7. Li X, Wu B, Zhu X, Yang H. Consecutively missing seismic data interpolation based on coordinate attention Unet. *IEEE Geosci Remote Sens Lett*. 2022;19:3005005.

   doi: 10.1109/LGRS.2021.3128511

8. He T, Wu B, Zhu X. Seismic data consecutively missing trace interpolation based on multistage neural network training process. *IEEE Geosci Remote Sens Lett*. 2022;19:7504105.

   doi: 10.1109/LGRS.2021.3089585

9. Tian Y, Fu L, Fang W, Li T. FR-UNet: A feature restoration-based UNet for seismic data consecutively missing trace interpolation. *IEEE Trans Geosci Remote Sens*. 2025;63:1-10.

   doi: 10.1109/TGRS.2025.3531934

10. Yu J, Joo Y, Yoon D. Transposed arrangement strategy-based deep learning for seismic data crossline interpolation. *J Seism Explor*. 2025;34(5):66-80.

    doi: 10.36922/JSE025330056

11. Mukherjee B, Kar S, Banerjee R, Sain K. Seismic data recovery with the aid of 3D U-Net deep learning approach: A case study from Amguri prospect, Upper Assam Shelf, India. *J Appl Geophys*. 2026;250:106214.

    doi: 10.1016/j.jappgeo.2026.106214

12. Yu J, Yoon D. Crossline reconstruction of 3D seismic data using 3D cWGAN: A comparative study on Sleipner seismic survey data. *Appl Sci*. 2023;13(10):5999.

    doi: 10.3390/app13105999

13. Oliveira DAB, Ferreira RS, Silva R, Brazil EV. Interpolating seismic data with conditional generative adversarial networks. *IEEE Geosci Remote Sens Lett*. 2018;15(12):1952-1956.

    doi: 10.1109/LGRS.2018.2866199

14. Guo Y, Fu L, Li H. Seismic data interpolation based on multi-scale Transformer. *IEEE Geosci Remote Sens Lett*. 2023;20:1-5.

    doi: 10.1109/LGRS.2023.3298101

15. Ho J, Jain A, Abbeel P. Denoising diffusion probabilistic models. In: *Advances in Neural Information Processing Systems (NeurIPS)*. 2020;33:6840-6851. Accessed January 20, 2026. https://proceedings.neurips.cc/paper/2020/hash/4c5bcfec8584af0d967f1ab10179ca4b-Abstract.html

16. Goyes-Peñafiel P, Kamilov US, Arguello H. CDDIP: Constrained diffusion-driven deep image prior for seismic data reconstruction. *IEEE Geosci Remote Sens Lett*. 2025;22:7504105.

    doi: 10.1109/LGRS.2025.3545860

17. Wei X, Zhang C, Wang H, Tan C, Xiang D, Jiang B. Seismic data interpolation via denoising diffusion implicit models with coherence-corrected resampling. *IEEE Trans Geosci Remote Sens*. 2024;62:1-14.

    doi: 10.1109/TGRS.2024.3485573

18. Durall R, Ghanim A, Fernandez MR, Ettrich N, Keuper J. Deep diffusion models for seismic processing. *Comput Geosci*. 2023;177:105377.

    doi: 10.1016/j.cageo.2023.105377

19. Liu Q, Ma J. Generative interpolation via a diffusion probabilistic model. *Geophysics*. 2024;89(1):65-85.

    doi: 10.1190/geo2023-0182.1

20. Fang W, Fu L, Zhang M, Li Z. Seismic data interpolation based on U-net with texture loss. *Geophysics*. 2021;86(1):V41-V54.

    doi: 10.1190/geo2019-0615.1

21. Chang D, Yang W, Yong X, *et al*. Seismic Data Interpolation Using Dual-Domain Conditional Generative Adversarial Networks. *IEEE Geosci Remote Sens Lett*. 2021;18(10):1856-1860.

    doi: 10.1109/LGRS.2020.3008478

22. Chang DK, Yang WY, Yong XS, Li HS. Seismic data interpolation with conditional generative adversarial network in time and frequency domain. In: *SEG Technical Program Expanded Abstracts*. Houston, TX: Society of Exploration Geophysicists; 2019:2589-2593.

    doi: 10.1190/segam2019-3210118.1

23. Lou Y, Wu L, Liu L, *et al*. Irregularly sampled seismic data interpolation via wavelet-based convolutional block attention deep learning. *Artif Intell Geosci*. 2022;3:192-202.

    doi: 10.1016/j.aiig.2022.12.001

24. Dodda VC, Kuruguntla L, Mandpura AK, Elumalai K. Simultaneous seismic data denoising and reconstruction with attention-based wavelet-convolutional neural network. *IEEE Trans Geosci Remote Sens*. 2023;61:1-14.

doi: 10.1109/TGRS.2023.3267037

25. Liu N, Wu L, Wang J, Wu H, Gao J, Wang D. Seismic data reconstruction via wavelet-based residual deep learning. *IEEE Trans Geosci Remote Sens*. 2022;60:4508213.

doi: 10.1109/TGRS.2022.3152984

26. Kong F, Picetti F, Lipari V, Bestagini P, Tang X, Tubaro S. Deep prior-based unsupervised reconstruction of irregularly sampled seismic data. *IEEE Geosci Remote Sens Lett*. 2022;19:7501305.

doi: 10.1109/LGRS.2020.3044455

27. Candès EJ, Donoho DL. New tight frames of curvelets and optimal representations of objects with C2 singularities. *Commun Pure Appl Math*. 2003;57(2):219-266.

doi: 10.1002/cpa.10116

28. Candès EJ, Demanet L, Donoho DL, Ying L. Fast discrete curvelet transforms. *Multiscale Model Simul*. 2006;5(3):861-899.

doi: 10.1137/05064182X

29. Herrmann FJ, Hennenfent G. Non-parametric seismic data recovery with curvelet frames. *Geophys J Int*. 2008;173(1):233-248.

doi: 10.1111/j.1365-246X.2007.03698.x

30. Sun B, Ma J, Chauris H, Yang H. Solving wave equation in the curvelet domain: A multi-scale and multi-directional approach. *J Seism Explor*. 2009;18(4):385-399.

doi: 10.36922/JSE402

31. Sitzmann V, Martel JNP, Bergman AW, Lindell DB, Wetzstein G. Implicit neural representations with periodic activation functions. In: *Advances in Neural Information Processing Systems (NeurIPS)*. 2020;33:7462-7473. Accessed February 2, 2026. https://proceedings.neurips.cc/paper/2020/hash/53c04118df112c13a8c34b38343b9c10-Abstract.html

32. Gao W, Liu D, Chen W, Sacchi MD, Wang X. NeRSI: Neural implicit representations for 5D seismic data interpolation. *Geophysics*. 2025;90(1):V29-V42.

doi: 10.1190/geo2023-0767.1

33. Lee G, Cheong S, Choi Y. Implicit neural representations for unsupervised seismic data interpolation from single gather. *Geophys Prospect*. 2025;73(9):e70110.

doi: 10.1111/1365-2478.70110

34. Do MN, Vetterli M. The contourlet transform: An efficient directional multiresolution image representation. *IEEE Trans Image Process*. 2005;14(12):2091-2106.

doi: 10.1109/TIP.2005.859376

35. Nguyen TT, Chauris H. Uniform discrete curvelet transform. *IEEE Trans Signal Process*. 2010;58(7):3618-3634.

doi: 10.1109/TSP.2010.2047666

36. Kingma DP, Ba J. Adam: A method for stochastic optimization. In: *Proceedings of the 3rd International Conference on Learning Representations (ICLR)*. 2015. Accessed February 20, 2026. https://arxiv.org/abs/1412.6980

37. Aminzadeh F, Brac J, Kunz T. *SEG/EAGE 3-D Salt and Overthrust Models*. SEG/EAGE 3-D Modeling Series, No. 1. Tulsa, OK: Society of Exploration Geophysicists; 1997.

38. Keys RG, Foster DJ. A data set for evaluating and comparing seismic inversion methods. In: Keys RG, Foster DJ, eds. *Comparison of Seismic Inversion Methods on a Single Real Data Set*. Tulsa, OK: Society of Exploration Geophysicists; 1998:1-12.

doi: 10.1190/1.9781560802082.ch1

39. Wang S, Su Z, Ying L, *et al*. Accelerating magnetic resonance imaging via deep learning. In: *2016 IEEE 13th International Symposium on Biomedical Imaging (ISBI)*. IEEE; 2016:514-517.

doi: 10.1109/ISBI.2016.7493320

40. Cole EK, Ong F, Vasanawala SS, Pauly JM. Fast unsupervised MRI reconstruction without fully-sampled ground truth data using generative adversarial networks. In: *Proceedings of the IEEE/CVF International Conference on Computer Vision Workshops*. 2021:3988-3997.

doi: 10.1109/ICCVW54120.2021.00444

41. Rahaman N, Baratin A, Arpit D, *et al*. On the spectral bias of neural networks. In: *Proceedings of the 36th International Conference on Machine Learning (ICML)*. 2019;97:5301-5310. Accessed February 20, 2026. https://proceedings.mlr.press/v97/rahaman19a.html

ACCSCIENCE PUBLISHING

Journal of Seismic Exploration

ARTICLE

Deep learning for three-dimensional seismic fault prediction using convolutional neural networks

Yasir Bashir[1]*, Dilek Yüksel[1], Begüm Akin[1], Derin Gezer[1], Muhsan Ehsan[2], Muhammad Khan[3], and Syed Haroon Ali[4]

[1]Department of Geophysical Engineering, Faculty of Mines, İstanbul Technical University, İstanbul, Turkey

[2]Department of Earth and Environmental Sciences, Bahria School of Engineering and Applied Sciences, Bahria University, Islamabad, Pakistan

[3]Saudi Aramco, Dhahran, Saudi Arabia

[4]Department of Earth Sciences, Faculty of Science, University of Sargodha, Sargodha, Punjab, Pakistan

Abstract

Understanding seismic faults is essential for generating prospects, modeling reservoirs, and assessing carbon dioxide storage. Identifying faults in complex tectonic regimes presents significant challenges, especially in areas that have undergone multiple phases of tectonic activity. Even with advances in structural seismic attributes and machine learning, interpreters often rely on manual methods to examine complex fault systems. This work introduces a method for predicting three-dimensional seismic faults using convolutional neural networks (CNNs), effectively overcoming the constraints of conventional interpretation techniques. The research uses CNNs to demonstrate the effectiveness of seismic attributes in training models that identify faults with high accuracy and consistency. This approach, unlike manual interpretation, reduces time, costs, and subjective errors by leveraging automated learning techniques, thereby improving reproducibility and efficiency while reducing interpreter bias. The research highlights the growing importance of solid computational tools in geophysics, especially as seismic datasets become more complex and wider. The approach significantly enhances confidence in artificial intelligence-assisted geological analysis by validating its performance with real-world data. The validation accuracy rises from 0.936 to 0.9436 across configurations, while the validation loss increases from 0.5635 to 0.9941 across diverse patches of the trained model.

Keywords: Deep learning; Convolutional neural networks; Fault likelihood; Fault cube; Fault prediction

***Corresponding author:**
Yasir Bashir
(ybashir@itu.edu.tr)

Citation: Bashir Y, Yüksel D, Akin B, *et al*. Deep learning for three-dimensional seismic fault prediction using convolutional neural networks. *J Seismic Explor.* 2026;35(3):026180079. doi: 10.36922/JSE026180079

Received: April 30, 2026

Revised: May 21, 2026

Accepted: May 28, 2026

Published online: June 18, 2026

Copyright: © 2026 Author(s). This is an Open-Access article distributed under the terms of the Creative Commons Attribution License, permitting distribution, and reproduction in any medium, provided the original work is properly cited.

Publisher's Note: AccScience Publishing remains neutral with regard to jurisdictional claims in published maps and institutional affiliations.

1. Introduction

In geophysics, the entire process of seismic structural interpretation depends significantly on the expertise and specialized knowledge of the interpreters involved. This dependence increases the chances of human error and variability, particularly in

complex geological settings.[1] Recently, artificial intelligence and machine learning (ML) have become significant tools in geophysical exploration, capable of replicating human expertise and enhancing their performance through training on a broader range of datasets.[2-6] Geophysical explorations require seismic fault detection. The problem is that this method is complicated and time-consuming. Conventional interpretation methods rely on human interpreters' knowledge and judgment, which increases variability and error risk, especially when handling large datasets or complex geological features. Manual methods are becoming insufficient as seismic data volumes and complexity increase.[6] The issue at present limits scalability and the detection of shortcomings, emphasizing the necessity for more effective, objective, and automated solutions, particularly those based on ML.

Existing geophysical methods lack tuning and automation to handle the variety and complexity. Without these answers, human error and fault identification across geological contexts remain issues. The scenarios demonstrate the importance of detailed fault mapping for hydrocarbon exploration and reservoir characterization to reduce risk and boost production. Recently, Wu *et al.*[7] proposed an automatic defect interpretation method based on a convolutional neural network (CNN). A 7-layer CNN was used to estimate fault orientations, notably dips and strikes, from small patches of entire seismic pictures. The estimated orientations yielded anisotropic Gaussian functions that extend in the projected fault directions.[7] By arranging locally oriented Gaussian functions, a fault probability image is generated that enhances the clarity and continuity of fault features. Despite being trained on synthetic seismic data, the CNN shows the capability to accurately estimate fault orientations from actual seismic images. This approach offers greater accuracy and clarity than conventional fault-attribute techniques. Guo *et al.*[8] used CNN to interpret faults and horizons in a coalfield case study. Structurally modeled datasets achieved high accuracy, eliminating the need for manual labeling.[8] Both Wu *et al.*[7] and Guo *et al.*[8] highlighted the potential of CNNs for seismic structural interpretation; however, there are several methodological gaps that this study explicitly addresses. Initially, Wu *et al.*[7] focused on estimating fault orientation through patch classification. However, their method did not yield spatially coherent fault-probability volumes that could be directly interpreted geologically, nor did it address the simultaneous prediction of faults and horizons. Guo *et al.*[8] achieved joint fault–horizon prediction; however, their approach to label generation via structural modeling, although innovative, was tested only on relatively simple geological configurations. Furthermore, it did not explicitly address the significant class imbalance in fault detection tasks, where fault pixels typically constitute only 5–10% of the total labeled volume. Additionally, neither study conducted a systematic validation of label quality nor reported metrics for inter-annotator agreement regarding the training data. The present study advances the current understanding in several important areas: (i) A patch-based training strategy that includes targeted oversampling of fault-bearing patches to address class imbalance; (ii) the implementation of a weighted focal loss function to further tackle the frequency imbalance between fault and non-fault classes during training; (iii) a thorough binary mask quality assurance protocol that involves independent verification and spatial consistency checks; and (iv) validation on both synthetic and real coalfield seismic data, utilizing quantitative performance metrics such as precision, recall, and the F1-score, which offers a more detailed evaluation of model generalization than previously established.

Research indicates that seismic facies analysis methodologies have evolved, highlighting a transition from manual interpretation to ML-based techniques. The study describes the difficulties associated with identifying seismic features, particularly for new interpreters, and introduces a method that integrates UVQ and beam forming seismic.[9] This approach employs computational weights to pinpoint the key seismic features, thereby enhancing objectivity and reproducibility. The article recommends using spectral decomposition in conjunction with ML for interpretation and initial validation. Spectral decomposition helps interpreters identify lithological and stratigraphic changes by providing frequency-based information from seismic volumes instead of well log data. A detailed Gulf of Guinea case study shows how attribute combinations affect facies classifications. It shows how the selection of input data affects unsupervised techniques. Zhao *et al.*[10] perform a comparative analysis of six commonly used classification techniques for seismic facies recognition, tackling the escalating challenges posed by increasingly large three-dimensional (3D) seismic datasets and the variety of available seismic attributes.[10] Since manually reading seismic lines and time slices is difficult, this research evaluates supervised and unsupervised ML systems. This study integrates a semblance-based fault-likelihood assessment with the widely used ant-tracking method to reduce the inefficiencies and subjectivity of manual fault interpretation. This integration creates high-resolution discontinuity volumes that enable interpreters to automatically extract defects with less input.[11,12] The study's use of directed semblance, based on Dave Hale's fault-oriented semblance algorithm, improves alignment with fault geometry over coherency-based methods. The approach was tested on a fractured reservoir in a Malaysian

basin, demonstrating its reliability in noisy, gas-related signal-attenuated settings. The method improves fault mapping accuracy and efficiency and shows potential for detecting fractures, stratigraphic discontinuities, and gas chimneys.

Recent studies have shown the increasing efficacy of CNNs and sophisticated deep learning frameworks in complex medical imaging applications.[13,14] Methods including privacy-preserving federated learning paired with extended reality for analyzing pediatric cerebral palsy, lightweight deep learning alongside virtual reality visualization for offline tumor segmentation, spiking CNNs employing spike-timing-dependent plasticity for glioma segmentation, and advanced U-Net and ConvNeXt architectures incorporating attention mechanisms and data augmentation for breast tumor segmentation have demonstrated notable advancements in feature extraction, segmentation accuracy, computational efficiency, and the intelligent interpretation of high-dimensional datasets.[15,16] These advancements underscore the extensive potential of CNN-based models for automated pattern recognition and semantic interpretation, which can also be tailored for seismic data analysis, subsurface characterization, and geophysical feature detection.

A hybrid method is developed that employs variable-mode decomposition and support vector machines for the detection of small-scale faults in coal mining, where vertical displacements range from 2 to 5 m. Their approach effectively minimized seismic noise, enhancing fault detection under challenging conditions.[17,18] We also discussed the growing interest in semi-supervised and unsupervised methods, which reduce labeling while maintaining model efficacy. Recent advancements in seismic interpretation leverage sophisticated hybrid architectures, such as combining CEEMDAN multiscale fuzzy entropy with NSGA-III-optimized CNNs for event recognition, or integrating graph attention networks with gradient-boosted decision trees for enhanced impedance inversion prediction.[19,20] A deep convolutional neural network model for automatic fault detection was introduced by An *et al.*,[21] framed as an image segmentation problem.[21] The model achieved performance comparable to that of humans across multiple datasets while significantly decreasing processing time.

1.1. The study area

Structurally complex, the F3 Block in the northern Dutch offshore is impacted by Devonian to Paleogene tectonic periods. Ter Borgh *et al.*[22] and Terranubis' 2020 high-resolution 3D seismic dataset show that the F3 area is important for regional fault reactivation, salt tectonics, and basin development. The study area is between the Elbow Spit Platform and the Step Graben. Terranubis seismic data confirms pre-Zechstein deformation, fault reactivation, and salt as a mechanical decoupling horizon. The traits align with regional structural evolution and help explain trap formation, fault sealing, and compartmentalization. The F3 Block captures Ter Borgh *et al.*'s[22] regional tectonic evolution, while the Terranubis 2020 seismic dataset provides substantial image support for local and regional fault system correlation.

A unique extensional regime formed N360° (N–S)-trending faults during the Triassic and Early Cretaceous periods, which helped construct the Step and Dutch Central Grabens. These faults have large throws in the F3 Block and play a major role in the distribution of Zechstein salt and in structural deformation. Finally, N070° (WSW–ENE)-trending dextral strike-slip faults, active from the Jurassic to the Paleogene, locally overprint earlier structures and present as subtle flower structures within coherence and attribute displays of the F3 volume, especially in salt-free areas[22] (Figure 1).

1.2. Convolutional neural networks

Research indicates a significant transition towards supervised ML methods for seismic interpretation, with CNNs recognized as the most prevalent and efficient technique for fault detection. CNNs exhibit greater precision and resilience in pattern recognition, particularly compared with conventional manual or attribute-driven interpretation techniques. The ability to autonomously extract spatial characteristics from seismic data makes them especially effective at detecting geological discontinuities, including faults. Research consistently shows that CNNs outperform traditional algorithms in terms of precision and generalizability, especially in complex or noisy subsurface settings. Hybrid models that combine CNNs with signal processing techniques or temporal frameworks, such as long short-term memory networks, show greater potential to improve detection sensitivity and maintain fault continuity.

The main goal of this research is to develop a robust, automated system for detecting seismic faults using supervised ML methods. The study focuses on training CNN models that can accurately identify and highlight fault features within seismic volumes. CNNs serve as the primary algorithm because of their established success in intricate pattern recognition challenges and their flexibility in handling geophysical data formats. The integration of these models into seismic interpretation workflows aims to improve interpreters' productivity and accuracy. This is achieved by generating suggestive fault frameworks and

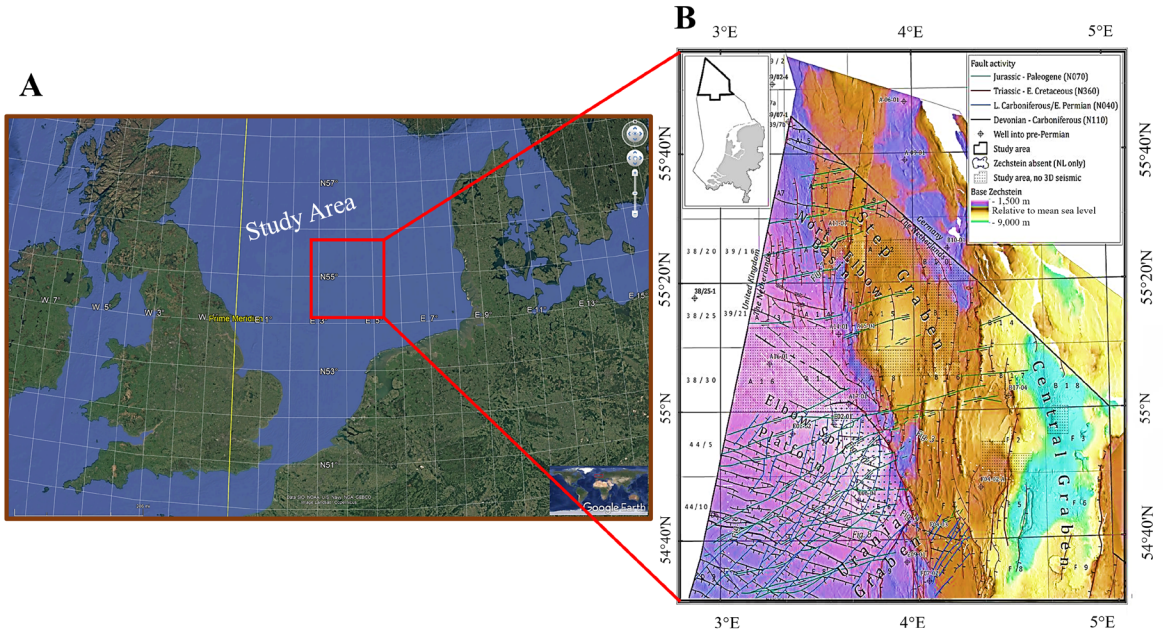

Figure 1. Location of the dataset used for research. (A) Google Earth map of the study area, and (B) Focusing on the structural framework of the northern Dutch offshore. Faults are displayed at the Base Permian level or, for older structures, at the highest affected stratigraphic horizon. The map also shows the depth to the base of the Zechstein Group, or to the next overlying unit where Zechstein is absent, adapted from Ref.[22]
Abbreviation: 3D: Three-dimensional.

associated confidence levels, which, in turn, reduce manual effort and enhance consistency in subsurface structural analysis.

2. Materials and methods

The method for identifying seismic faults uses ML techniques, with a particular focus on CNNs. The work begins with an overview of the core principles of CNNs, explaining their importance and advantages in seismic data analysis, particularly for segmentation tasks. CNNs are chosen for their ability to independently extract features and recognize complex spatial patterns in seismic data, making them well-suited for detecting fault zones.

A comprehensive overview of the theoretical foundations of CNNs is followed by an in-depth explanation of the specific workflow in this research. The next phase of the workflow involves preprocessing real field seismic data. The process of selecting seismic attributes for fault detection is carefully carried out, ensuring that only the most relevant features are retained for the model. Following this, the model architecture is defined, with the U-Net selected for its demonstrated efficacy in segmentation tasks. The process involves training the CNN model using labeled seismic data patches, followed by evaluation and performance testing.

The workflow is thoughtfully explained, incorporating patch-based training, model evaluation using accuracy and loss metrics, and visualization techniques for assessing fault detection. This methodology is designed to develop an automated solution for detecting seismic faults that is both effective and efficient. The method relies on ML to improve both the precision and efficiency of seismic interpretation.

2.1. Machine learning approaches for fault detection

Machine learning algorithms can be classified into two main categories: supervised learning, which functions with labeled datasets, and unsupervised learning, which operates on unlabeled datasets. As indicated in Table 1,[9] supervised learning techniques are especially advantageous when the dataset includes predefined output values or labels. This method enables the model to identify patterns by analyzing the connection between the input data and the associated output labels. Conversely, unsupervised learning is used when the output labels are unavailable, requiring the algorithm to identify hidden patterns or clusters in the data without predefined classifications.

For fault detection in seismic data, we chose supervised ML because it can be applied to datasets with labeled values. Supervised learning provides significant benefits by enabling the model to learn directly from labeled data, resulting in enhanced accuracy and reliability. By leveraging the established geophysical values, supervised

learning enhances the model's ability to accurately identify and predict fault zones, making it a more appropriate choice for this application.

Table 1. Primary categories of machine learning methodologies, along with their corresponding algorithms

Supervised machine learning	Unsupervised machine learning
- Convolutional neural networks - Support vector machines - Random forest - Convolutional recurrent neural networks - Probabilistic neural networks	- Self-organizing maps - K-means clustering -Principal component analysis -Independent component analysis -Generative topographic maps -Unsupervised vector quantizer -Convolutional autoencoder

Supervised ML techniques have demonstrated effectiveness in seismic interpretation tasks by reducing the need for manual intervention and improving the accuracy of structural identification. CNNs have proven significant potential due to their ability to autonomously extract features and identify spatial patterns within seismic data.[23] CNNs are particularly effective for binary segmentation tasks, such as distinguishing between faulted and non-faulted regions, making them an ideal option for this work, as shown in Figure 2.

A typical CNN architecture comprises three essential components: convolutional layers, pooling layers, and fully connected layers. The convolutional layers play a crucial role in identifying low- and high-level features in the input seismic slices, including edges, discontinuities, and textures, by using learnable filters. Pooling layers subsequently reduce the dimensionality of the extracted features, thereby helping the model generalize and mitigate overfitting (Figure 2A). The fully connected layers at the conclusion of the network aggregate these features into a definitive classification output, signifying the presence or absence of faults.[24]

2.2. Convolutional neural networks

Convolutional neural networks represent an innovative deep learning approach for detecting seismic faults, offering notable benefits over conventional techniques. The main factor contributing to their success is the computational power of contemporary graphics processing units. These

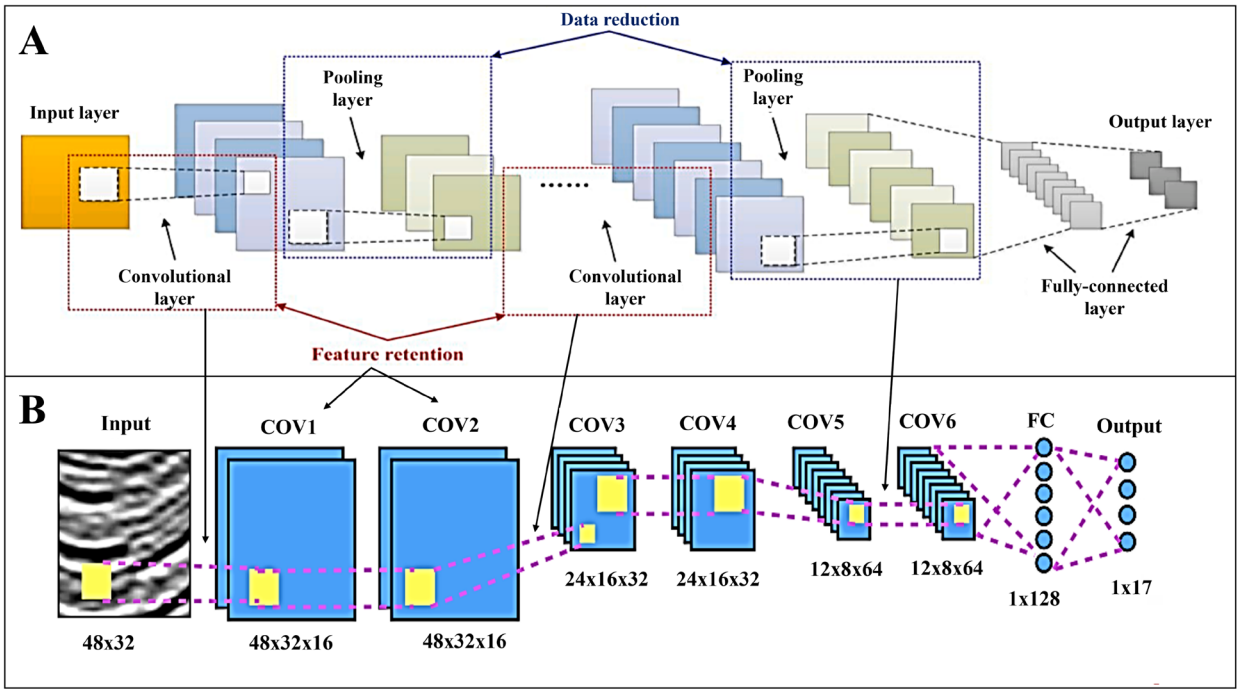

Figure 2. The working of a convolutional neural network (CNN) and internal process. (A) Generalized scheme of CNN including convolutional, pooling, and fully connected layer for output, and (B) specific flow of the machine learning model explaining the CNN architecture used to estimate fault orientation from an input seismic patch.[7]
Abbreviations: COV: Convolutional layer; FC: Fully connected.

enable CNNs to concentrate on local feature connections while streamlining the overall architecture of neural networks. This feature allows CNNs to handle large seismic datasets with exceptional efficiency, eliminating the requirement for extensive libraries of waveform templates that were once crucial in conventional methods. Avoiding this dependency allows CNNs to reduce computational complexity and achieve robust generalization, enabling the detection of seismic features in waveforms that were not part of the training set.[25] Additionally, CNNs excel at extracting significant features directly from raw seismic data (uninterpreted), enabling them to model intricate, non-linear relationships among variables. This feature proves particularly advantageous for analyzing the complex, often subtle patterns encountered in seismic fault-detection tasks, establishing CNNs as a formidable asset in the domain, as shown in Figure 2A.

Additionally, CNNs extend beyond the scope of seismic fault detection and demonstrate significant adaptability across a range of seismic applications. Their primary strength lies in the capacity to generalize beyond the specific training data, enabling them to manage the inherent variability present in geological structures and seismic signals. This capability holds particular significance in areas with limited labeled data, as CNNs can leverage patterns acquired from one dataset to enhance others, thereby markedly increasing the accuracy of predictions (Figure 3). The capacity to generalize across datasets, manage complex and noisy data, and optimize the computational process establishes them as a transformative technology in the field, serving as a fundamental element for progressing both research and practical applications in seismic interpretation.

2.3. Workflow of research

The workflow for this research is a systematic, structured

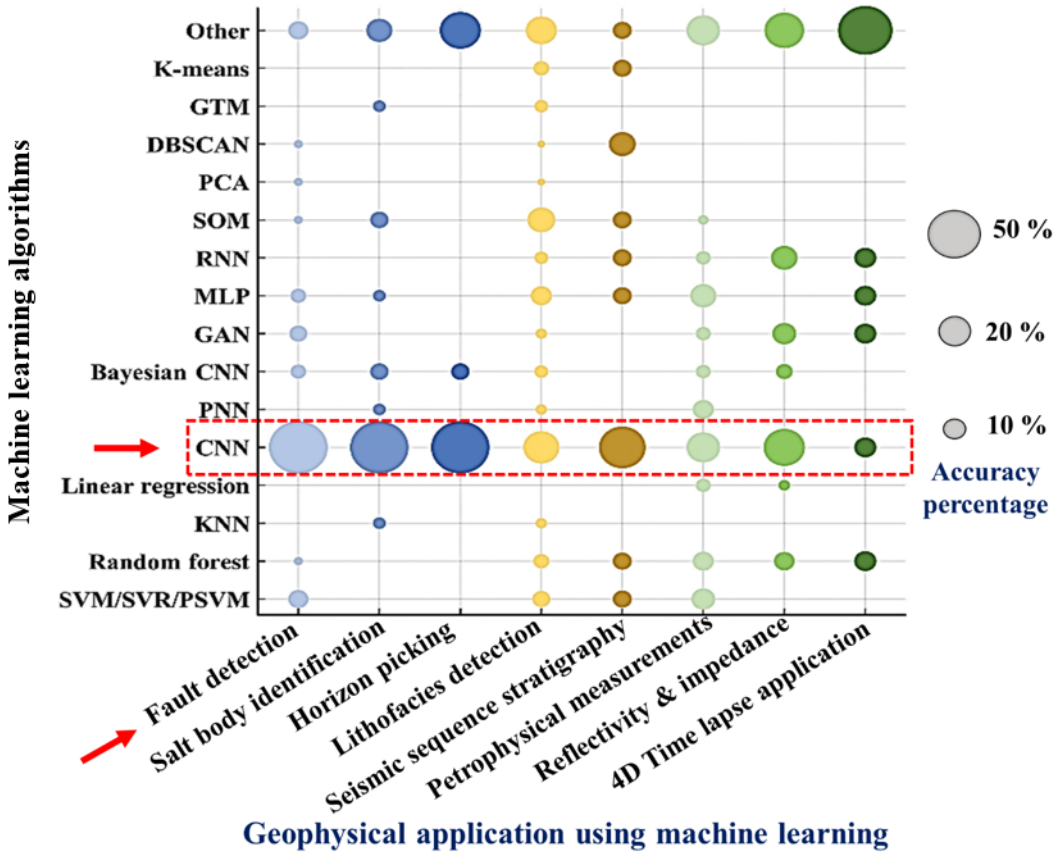

Figure 3. The machine learning algorithms have been used for the most common interpretation applications. The three gray circles illustrate the relationship between their dimensions and the fractions they represent in the applications.[1]
Abbreviations: 4D: Four-dimensional; CNN: Convolutional neural network; DBSCAN: Density-based spatial clustering of applications with noise; GAN: Generative adversarial network; GTM: Generative topographic mapping; KNN: k-nearest neighbor; MLP: Multilayer perceptron; PCA: Principal component analysis; PNN: Probabilistic neural network; PSVM: Proximal support vector machine; RNN: Recurrent neural network; SOM: Self-organizing map; SVM: Support vector machine; SVR: Support vector regression.

approach that ensures each component of the ML model's development and application is comprehensively examined. The main goal is to use CNNs to detect seismic faults. Each phase is structured to ensure optimal model performance while addressing the complexities of interpreting seismic data, as illustrated in Figure 4.

The process begins with data collection and preparation. The study used real-world open-access seismic datasets. The Dutch F3 offshore block (Terranubis F3-Demo-2020) has a high-resolution 3D seismic volume and a detailed fault system description. The dataset is model-ready. Seismic properties are chosen to find faults, preserving geological features such as reflection terminations for study. The next step is model selection and configuration. The CNN using the U-Net architecture is chosen for its segmentation performance. U-Net's balanced encoder-decoder architecture and skip links retain spatial precision needed for geophysical data interpretation, making it effective for seismic fault detection. To improve model performance and accuracy, the number of epochs and patch sizes were tested. This technique identified the best training configuration, improving fault detection accuracy and reliability.

The results highlight the strengths and drawbacks of the seismic fault identification model. Future proposals include improving model accuracy, integrating more seismic datasets, and modifying model hyperparameters. The following suggestions will guide seismic fault detection and improve the model's ability to handle more complex geological formations. The approach to developing the seismic fault detection ML framework relies on supervised learning and CNNs. These networks can automatically extract characteristics and identify spatial patterns, making them ideal for segmentation and seismic fault detection. The methodology begins with seismic data collection and preprocessing, followed by fault detection and seismic attribute identification. After data preparation, the CNN model is patch-trained. This method solves memory restrictions and improves model generalization. Different epochs and patch sizes were tested to increase training performance and accuracy.

3. Results

The application of the ML model to seismic data is followed by a detailed study of its performance and implications for fault detection. The main goal is to evaluate the CNN model's performance in identifying fault zones in seismic sections using North Sea seismic data. The model is trained and tested on a publicly available 3D seismic dataset using a patch-based approach to optimize memory usage and increase the diversity of training samples. The extensive training process, model configuration, and assessment measures indicate that CNNs can accurately detect errors in complex, noisy datasets. This section examines how TensorFlow, Keras, and Matplotlib are used to build, train, and visualize the model. Probability maps of the model's fault predictions allow comparisons between projected fault zones and seismic structures.

3.1. Machine learning training and testing

The architecture is a U-Net-based CNN. Due to its balanced encoder–decoder architecture and skip connections that preserve spatial resolution, the U-Net is well-suited for segmentation tasks such as seismic volume analysis. Consequently, this architecture influenced the data management strategy during experimentation. The raw seismic data were evaluated and grouped into a 3D array with inline, crossline, and temporal (or depth) dimensions before training. After extracting and organizing each trace, the amplitude values were normalized to (0, 1). This preprocessing step ensured numerical stability and consistency during model training. Six manually labeled binary masks aided supervised learning. Seismic inline slices 100, 200, 300, 400, 500, and 600 correspond to masks. The original tutorial includes tested and labeled inlines 100–500. This project used inline 600 to improve model learning and evaluation (Figures 5 and 6).

Each mask was a PNG image with binary pixel values indicating defects. However, these label masks had uneven beginning size and did not match the seismic slice resolution. Using masks directly in training and evaluation is difficult due to dimensional irregularity, which prevents identified defects from aligning with their counterparts in the raw data. This issue was fixed by resizing all masks to 462 pixels high and 951 pixels wide. By preventing interpolation artifacts, nearest-neighbor interpolation preserved mask binary integrity during resizing. After scaling, masks were converted to binary to ensure pixel values represented fault or non-fault circumstances. Standardizing mask dimensions ensured spatial alignment between seismic inlines and labels. If this phase is skipped, the array shapes will differ, preventing the model from accurately learning correlations between seismic features and fault structure. Applying this modification consistently to all six labeled inlines created a consistent and compatible training and validation dataset.

The high dimensionality and complexity of seismic data make direct training of a CNN on complete seismic slices computationally intensive and inefficient. A patch-based approach was employed to enhance the model's training efficiency. This approach entails extracting smaller, square subimages, referred to as patches, from the seismic inline

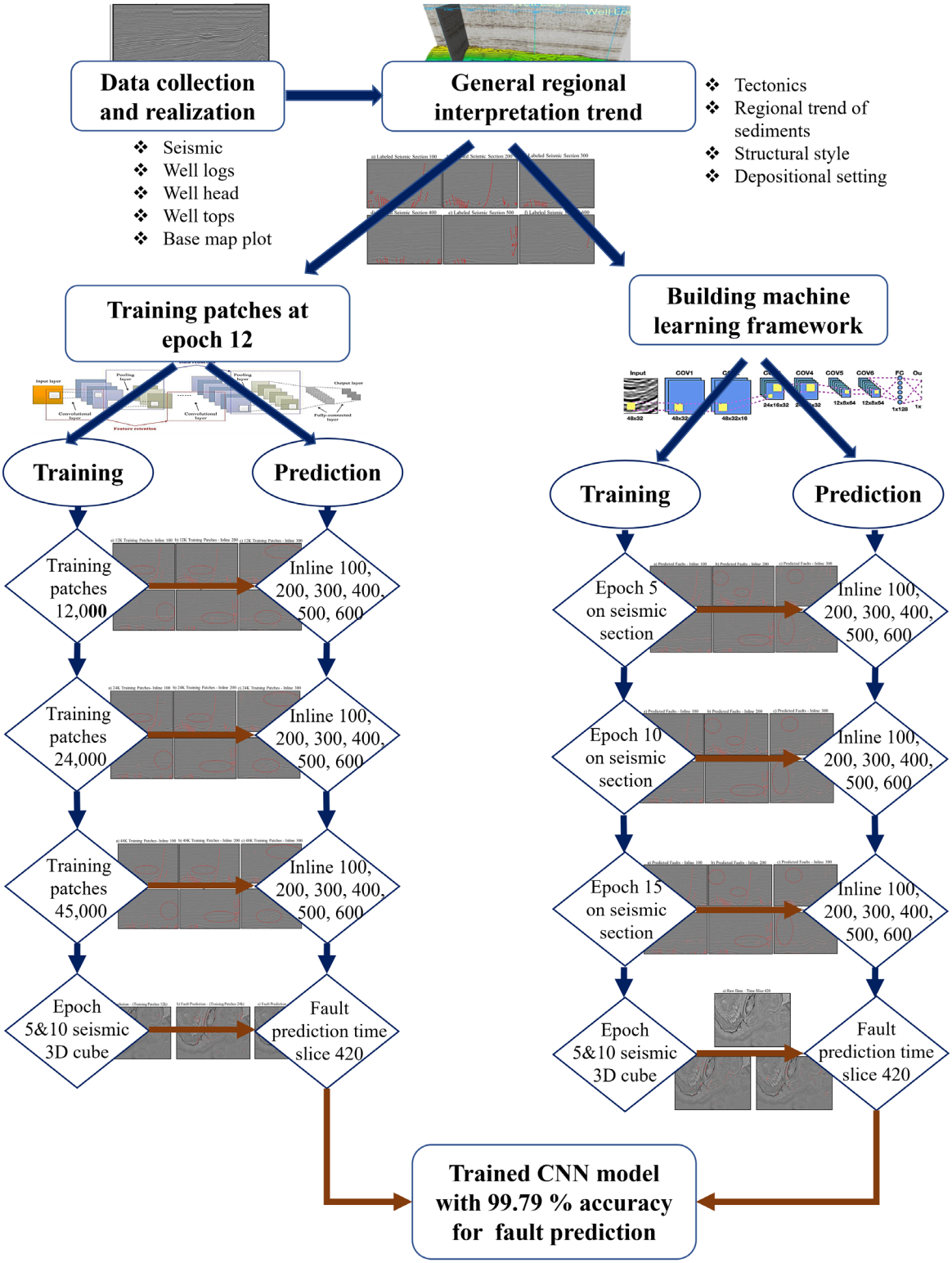

Figure 4. Workflow of the research: A convolutional neural network (CNN)-based fault detection method using a multi-epoch and training patches approach
Abbreviation: 3D: Three-dimensional.

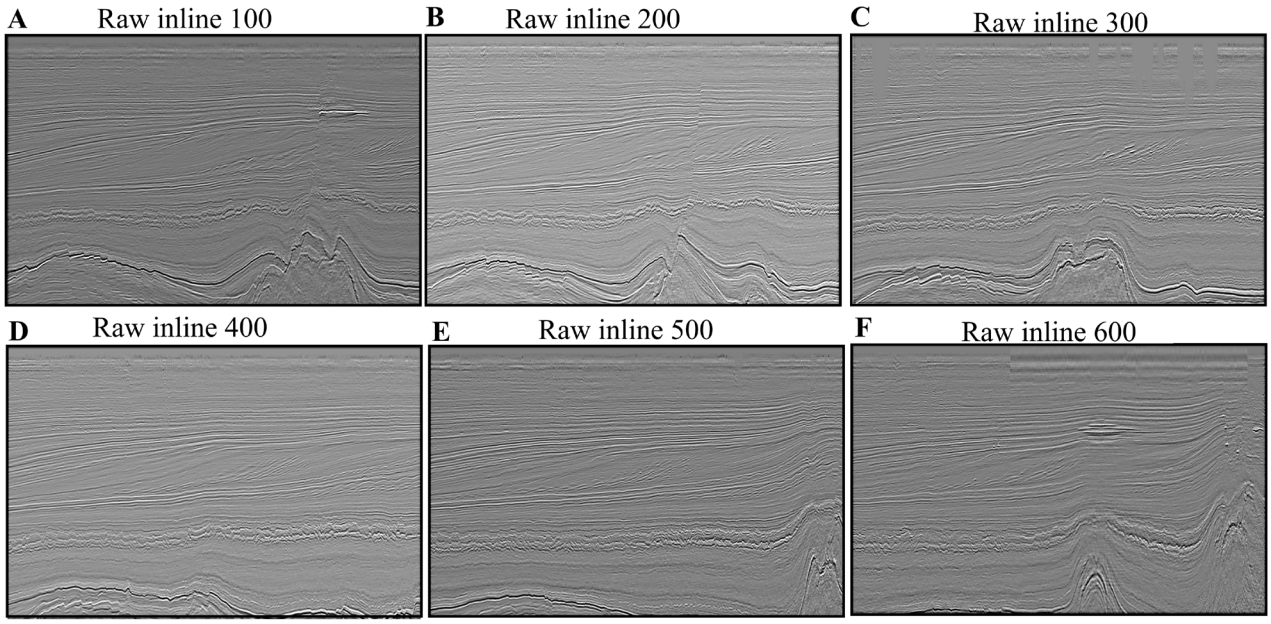

Figure 5. Seismic inline slices from 100 to 600 at 100-interval steps. Panels (A) through (F) correspond to inline 100, 200, 300, 400, 500, and 600, respectively.

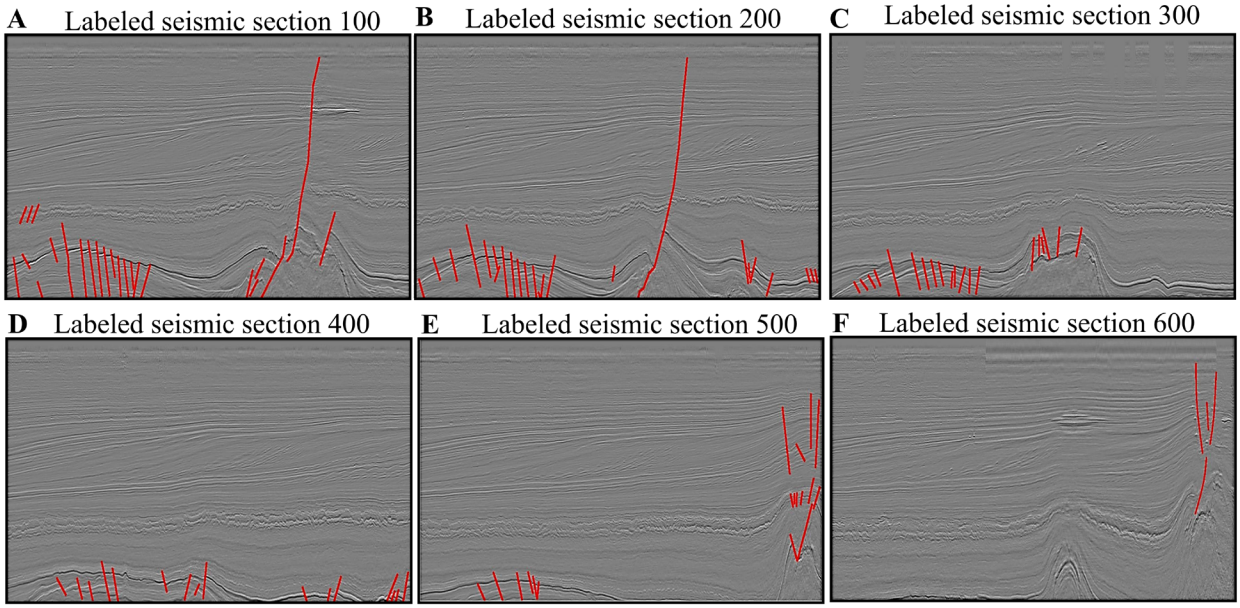

Figure 6. Seismic inline slices with labeled fault masks from 100 to 600 at 100-interval steps. Panels (A) through (F) correspond to inline 100, 200, 300, 400, 500, and 600, respectively.

slices, along with their associated binary label masks. A specialized function for patch extraction was created to accomplish this task. It randomly selects square regions of size 64 × 64 pixels from both the seismic data and the label mask. Each patch from the seismic image is spatially aligned with its corresponding label patch to maintain pixel-level correspondence, a crucial requirement for supervised learning (Figure 7).

A threshold condition was used to ensure that extracted patches contained significant features. Only patches containing a sufficient number of fault-indicating pixels

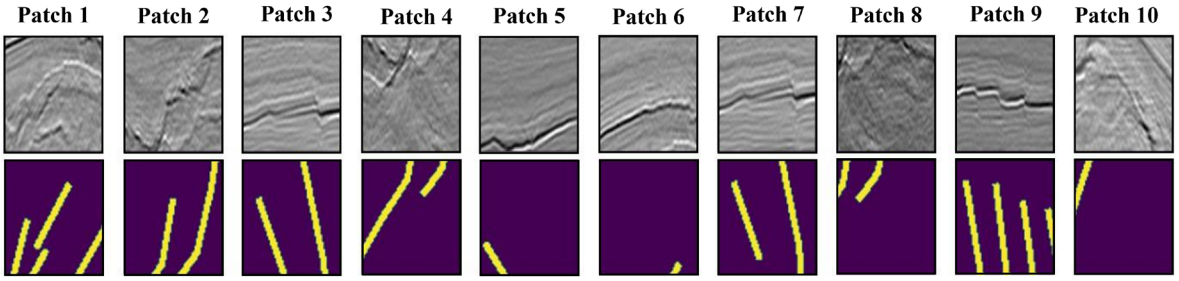

Figure 7. Patch samples along with their associated faults (yellow lines indicate faults)

were retained. Filtering removes irrelevant or empty regions of seismic volume from the training data. Patch extraction continues until a sufficient number of high-quality samples are collected. Array orientation discrepancies are corrected using the function. If the seismic slice and label mask differ in shape due to axis ordering, the function automatically transposes the data to align their dimensions.

For each training session, accuracy and loss metrics for the training and validation datasets were recorded. Table 2 and Figure 8 show the performance evolution plotted and examined. Figure 8A–D shows the model's learning behavior over time by plotting accuracy and loss values for each training period. A confusion matrix was created to evaluate classification performance using predictions from the validation dataset. The confusion matrix lists the true positives, false positives, true negatives, and false negatives for all patches. Normalizing and visualizing the data as a heatmap showed the model's ability to distinguish fault and non-fault classes. Even with the typical class imbalance in seismic fault datasets, background classification was accurate, and fault pixels were detected well (Figure 9). This method reliably assessed the model's generalization to full-scale data and demonstrated its capacity to recognize major and complex geological features (Figures 10 and 11).

Model performance was evaluated in the third dimension by selecting a depth level within the seismic volume. A horizontal time slice at depth index 420 showed a consistent time sample across all inlines and crosslines (Figure 12A). The two-dimensional slice showed subsurface structures at the selected depth as amplitude values. The patch-based prediction algorithm for vertical inlines was modified to use a sliding window in this horizontal plane. During the training phase, a 64 × 64-pixel window was used to traverse the slice and provide predictions at the center of each patch. The model systematically scanned the time slice to create a fault probability map (Figure 12B and 12C).

3.2. Machine learning output

The patchification procedure expanded the training dataset and augmented the data, allowing the model to encounter more fault patterns and improve its fault-detection generalization (Figure 7). Epoch counts were tested and compared during training for the U-Net-structured CNN model. By analyzing accuracy and loss measurements across multiple epochs, it is possible to determine when additional training continues to improve performance and to reduce the risk of overfitting. Despite limited processing resources and a short dataset, the model learned from the data. A validated design, adequate filter depths, and regulated training helped the model to recognize and pinpoint geological fault structures with sufficient precision.

Table 2 summarizes U-Net model training and validation performance metrics for epochs 3–15. Training accuracy, validation accuracy, and validation loss are used. The objective was to determine an appropriate number of training epochs to improve generalization while avoiding overfitting. Training accuracy rises from 96.81% in epoch 3 to 99.47% in epoch 15. Similarly, training loss drops from 0.0821 to 0.0124. This shows that the model learned and fit the training data better with each epoch. Validation accuracy is steady and high throughout all epochs, with minimal changes between 93.12% and 94.2%, peaking at 94.2% in epoch 14. The validation loss trend is different. Starts at 0.335 in epoch 3, rises to 0.9141 in epoch 11, and varies between 0.75 and 0.76 thereafter.

Overfitting begins when both training accuracy (A) and validation loss (D) increase. The model starts to remember training data patterns at epoch 8 or 9, rather than generic characteristics. The validation accuracy remains good, but the rising validation loss suggests that the model may be overconfident in its predictions, especially when applied to unseen data, reducing reliability. Epochs 8 to 10 show a good balance, with epoch 10 achieving 99.19% training accuracy, 93.62% validation accuracy, and a validation loss of 0.6878, demonstrating control before overfitting.

Table 2. A comparison of accuracy and loss is presented as a function of epoch number, with validation accuracy and loss also calculated

Epoch no	Accuracy	Loss	Validation accuracy	Validation loss
3	0.9681	0.0821	0.9359	0.3350
4	0.9746	0.0630	0.9327	0.3953
5	0.9861	0.0336	0.9342	0.5120
6	0.9888	0.0269	0.9353	0.5371
7	0.9859	0.0334	0.9326	0.5443
8	0.9917	0.0196	0.9387	0.6434
9	0.9922	0.0184	0.9390	0.6069
10	0.9919	0.0192	0.9362	0.6878
11	0.9928	0.0171	0.9312	0.9141
12	0.9932	0.0161	0.9361	0.5953
13	0.9949	0.0120	0.9397	0.7290S
14	0.9943	0.0136	0.9420	0.7584
15	0.9947	0.0124	0.9347	0.7607

In the early training phases (Figure 8A, epochs 3–5), the model improves training accuracy while maintaining validation accuracy, with a slight divergence after epoch 4. Overfitting begins when validation loss rises while training loss decreases. Although the model has modest generalization, it fails to understand the complexity of fault structures. In epochs 10–12 (Figure 8A), training accuracy saturates above 99%, and loss approaches zero. However, validation accuracy plateaus while validation loss increases, showing a performance disparity. The model improves on the training set, but its generalization performance declines. Due to its high accuracy and good validation performance, epoch 12 (Figure 8A) was chosen for final implementation. In the final phases of training (Figure 8A, epochs 13–15), training accuracy remains high, whereas validation accuracy plateaus or declines. Meanwhile, validation loss is rising, indicating that the model is overconfident in its predictions and that these improvements are not matched by generalization gains. The latter epochs exhibit overfitting, indicating that additional training yields diminishing returns and degrades the model's performance on new seismic data.

The confusion matrix is a tool for assessing a model's classification performance by comparing predicted labels to actual labels. This provides a summary of the correct and incorrect predictions for each class, offering insights into the model's ability to differentiate between fault and non-fault pixels. The matrix allows for the derivation of key metrics, including true positives, false positives, true negatives, and false negatives, which are essential for evaluating accuracy, precision, and recall, as demonstrated in Figure 9.

The confusion matrices in Figure 9 show that the model achieves 98–99% accuracy in detecting no-fault pixels across all epochs, due to their abundance in the sample. Despite advances, fault identification remains limited, especially in the earlier epochs (3–5), where true-positive rates drop to 19% (Figure 9A–C). In epochs 10–12, defect detection reaches 25%, suggesting model sensitivity improvement after training (Figure 9D–F). In epochs 13–15, fault prediction accuracy stabilizes or decreases, suggesting overfitting. This suggests that while the model improves the dominant class, it does not generalize to fault locations (Figure 9G–I).

To visually evaluate the model, predicted fault probability maps were overlaid on seismic inlines. The results for epochs 5 (Figure 10) and 10 (Figure 11) were reviewed to evaluate fault identification progress during training.

The findings show that epoch 10 forecasts are more advanced and more consistent across all inline portions than epoch 5 forecasts. Both sets of overlays show fault detection in red highlights on the seismic amplitude background, but there are numerous key differences. Epoch 5 shows many expected fault patterns, some broken and others partially aligned with geological discontinuities. The model identifies major fault regions, though it still misses parts, especially on faint or low-contrast seismic lines. At epoch 10, predictions are more consistent and aligned with seismic structures. In complex sections such as lines 300 and 500 (Figure 5C and 5E), faults are more accurately identified. Epoch 10's red overlays align more closely with fault planes and exhibit less noise, improving the model's ability to recognize both significant and subtle fault characteristics. This visual upgrade confirms the quantitative data that epoch 10 showed improved training accuracy and validation performance. It appears the model has increased its capacity to generalize from labeled data, leading to more geologically relevant predictions.

Fault prediction was performed on a time-slice segment at depth index 420, removed from training and without labeled data, to evaluate model generalization (Figure 12A). To assess the model's performance on unseen data, the results from epochs 5 and 10 were compared (Figure 12B and 12C).

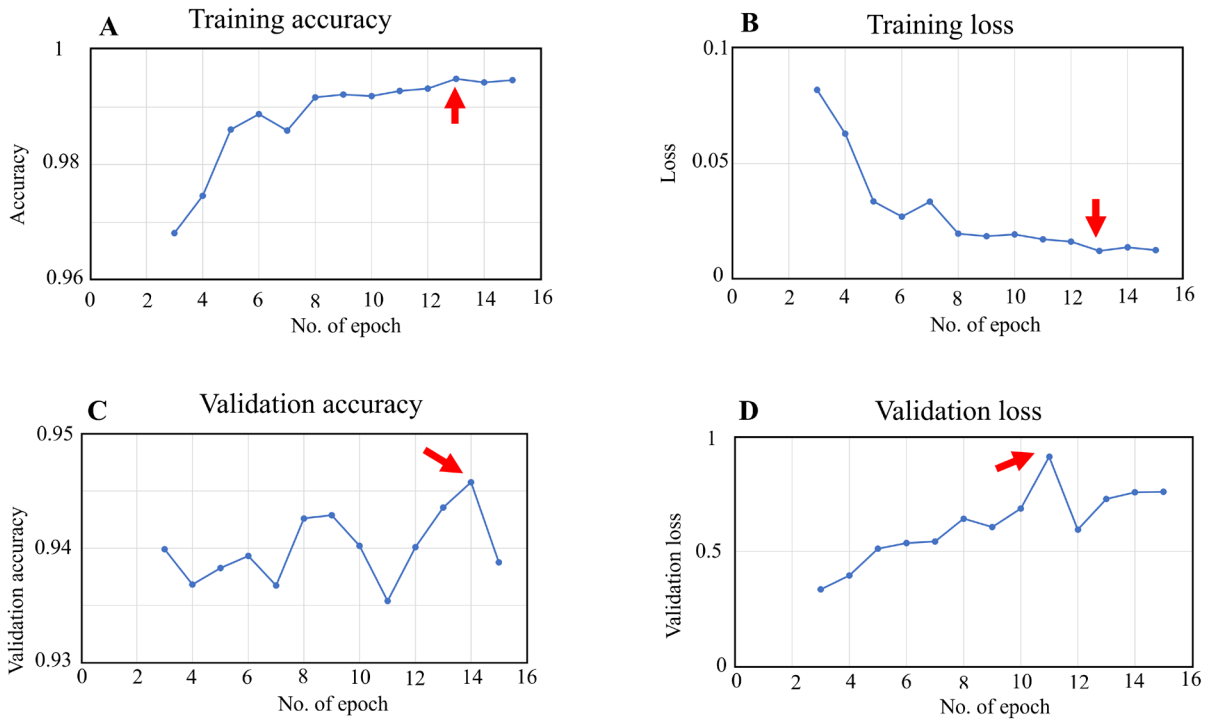

Figure 8. Performance metrics for training and validation are illustrated across epochs. (A) Accuracy during training, (B) loss during training, (C) accuracy during validation, and (D) loss during validation.

The prediction overlays show that model performance varied from epochs 5 to 10, especially in a segment of the data that was not used during training and lacked labeled input. At epoch 5, fault forecasts are scattered and less continuous, with multiple discontinuities and isolated false positives (Figure 12B). Many fault structures are underrepresented or partially recognized, suggesting the model has not fully generalized from the training data. The predictions at epoch 10 are clearer, more consistent, and aligned with the seismic imaging fault patterns (Figure 12C). The model covers more fault network locations, especially curved or branched ones, while limiting noise and isolated detections. This improvement shows enhanced generalization and fault sensitivity after lengthy training. In epoch 10, the model recognized intricate fault structures even in areas without explicit supervision, indicating a considerable improvement in prediction quality.

After selecting an appropriate epoch number (epoch = 12), research was conducted to test model performance by varying the number of training patches while maintaining a constant number of epochs. Epoch 12 was chosen for its accuracy and low validation loss. Patch extraction settings aid this process. Each patch was 64 × 64 pixels, with a threshold of 0, suggesting that no minimum defect-pixel count was required. The lesson set the training patch count to 8,000. However, this count was raised to 12,000 to test the effect of data volume on model learning in this study. By adding 24,000 and 48,000 training patches, the data volume impact was better analyzed. The validation set was always 2,000 patches from one labeled inline. This ensured that validation results were unaffected by changes to the data source, enabling trustworthy comparisons of training configurations.

Table 3. A comparison of accuracy and loss for 12K, 24K, and 48K training patches at epoch 12 is shown in the following list

No. of training	Accuracy	Loss	Validation accuracy	Validation loss
12,000	0.9929	0.0168	0.936	0.5636
24,000	0.9966	0.0082	0.9403	0.8801
45,000	0.9979	0.0053	0.9436	0.9941

The data show that adding training patches gradually improves performance (Table 3). Training accuracy rises

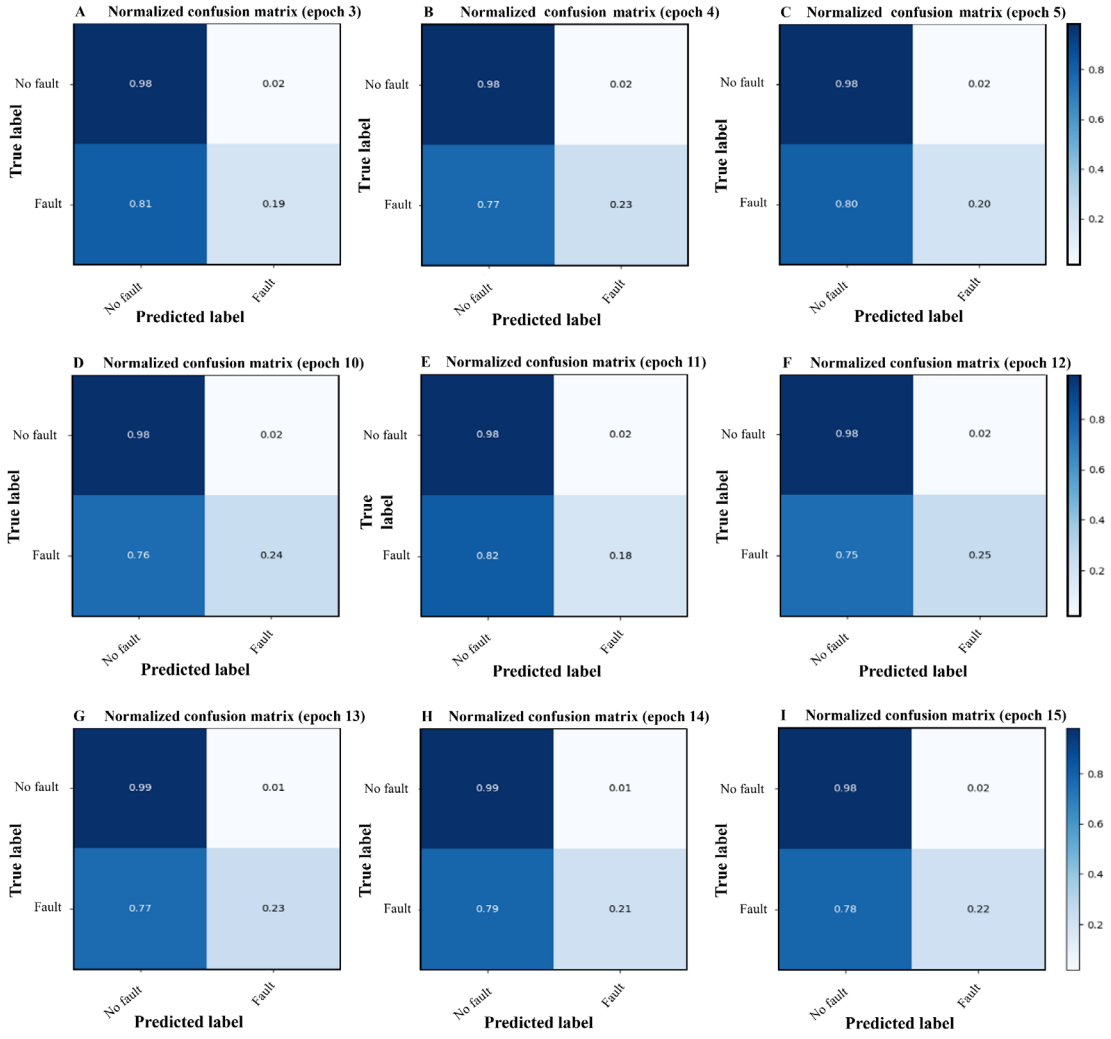

Figure 9. Normalized confusion matrices for (A) epoch 3, (B) epoch 4, (C) epoch 5, (D) epoch 10, (E) epoch 11, (F) epoch 12, (G) epoch 13, (H) epoch 14, and (I) epoch 15

from 0.9929 to 0.9979 with 48,000 patches. Meanwhile, training loss drops from 0.0168 to 0.0053. Trends show that a larger training set helps the model grasp data better. Validation metrics show no comparable improvement. Validation accuracy increases from 0.936 to 0.9436 across the three configurations, whereas validation loss increases from 0.5635 with 12,000 patches to 0.9941 with 48,000 patches. Validation accuracy peaks at 24,000 patches (0.9403), whereas validation loss rises to 0.8801. The model's inconsistency implies that its confidence in its predictions is rising, but this does not ensure increased accuracy, suggesting overfitting as training data grows. Additional training patches may enhance performance on the training dataset, but they do not reliably improve generalization to unseen data. The model, trained with 12,000 patches, balances accuracy with validation loss. This indicates enough learning capacity without overfitting (Figure 13). The accuracy and loss graphs for 12,000, 24,000, and 48,000 patch models show consistent trends.

In all three circumstances, training accuracy rapidly increases and stabilizes at over 99%. Training loss decreases steadily, reaching zero in the final epochs. The observed trends show that the model learns from training data regardless of dataset size. Validation accuracy is steady and much lower than training accuracy, demonstrating little improvement as patches grow. The validation loss increases throughout training, peaking for the model trained with 48,000 patches (Figure 13A).

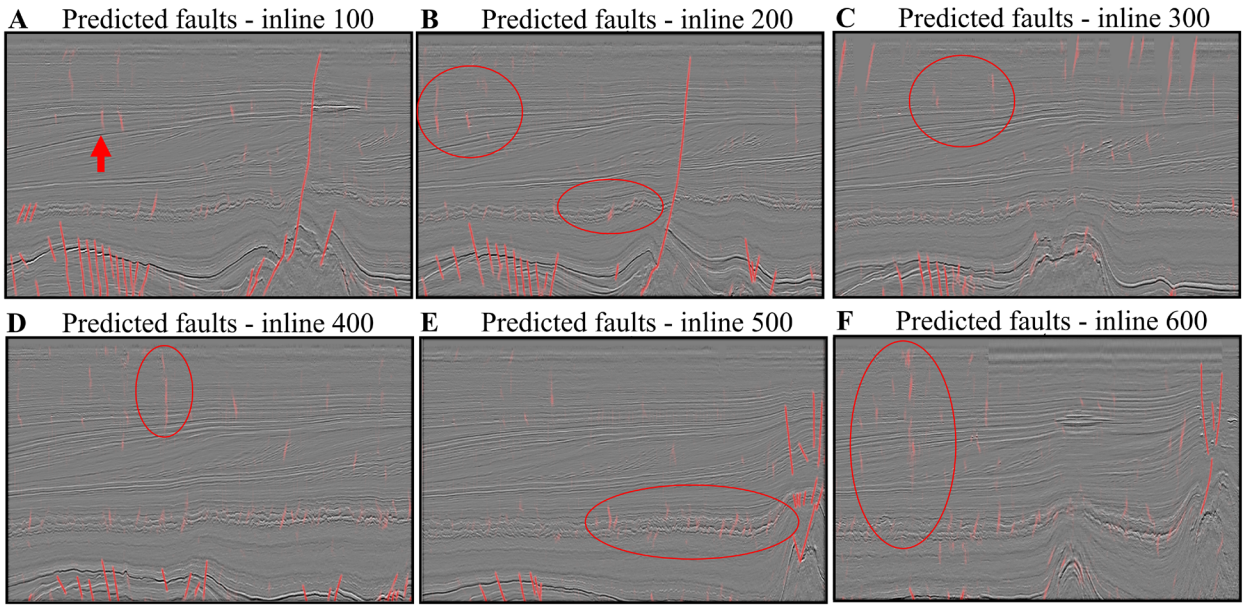

Figure 10. Predicted fault overlays for epoch 5 on inline slices (A) 100, (B) 200, (C) 300, (D) 400, (E) 500, and (F) 600

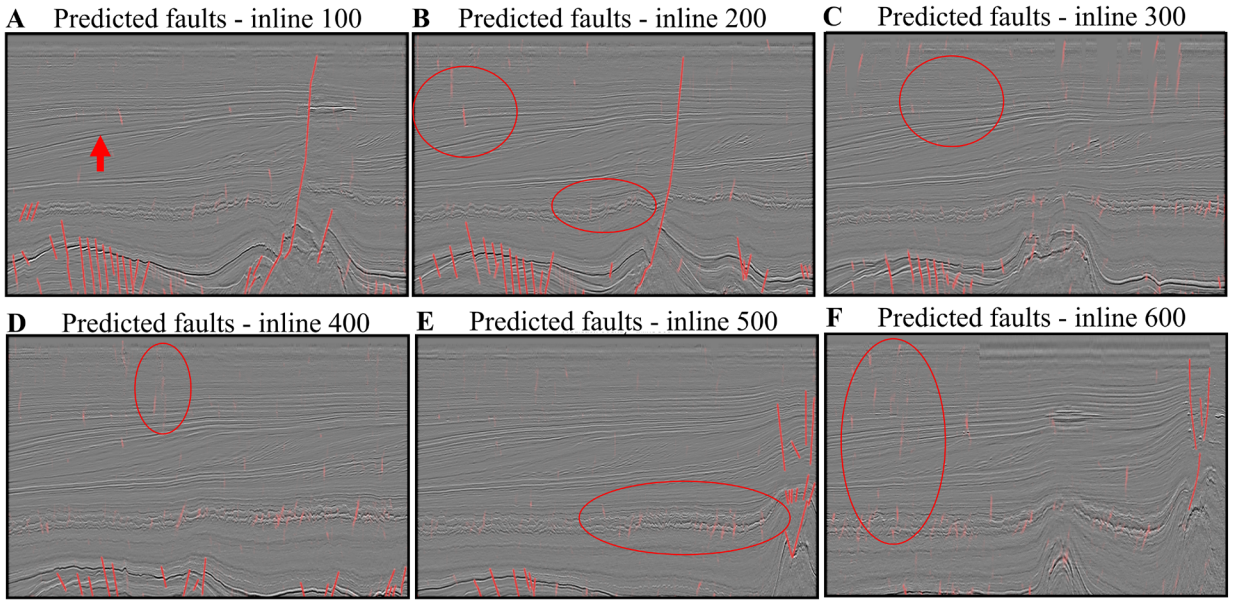

Figure 11. Predicted fault overlays for epoch 10 on inline slices (A) 100, (B) 200, (C) 300, (D) 400, (E) 500, and (F) 600

The confusion matrices show that the model accurately detects the no-fault class across all three patch volumes (Figure 14). High performance is expected because of the dataset's no-fault pixels. True positive rates for fault classification are consistent, with the model recognizing 25% of problem pixels with 12,000 patches and 24% with 24,000 and 48,000 patches. Despite adding training data, false negatives—fault pixels misclassified as no-fault—remain at 75–76%. The results show that adding patches does not improve the model's fault structure sensitivity. Despite the robustness of no-fault detection, the fault detection rate has stabilized, supporting the idea that higher patch volumes do not help model generalization.

To enhance comprehension, the outcomes of the training with a progressively larger number of training patches are analyzed (Figures 15–17).

Distinct structural discontinuities suggest that core fault detection is unaffected by patch volume. Figure 15 shows that the 12,000 patch model captures key fault zones

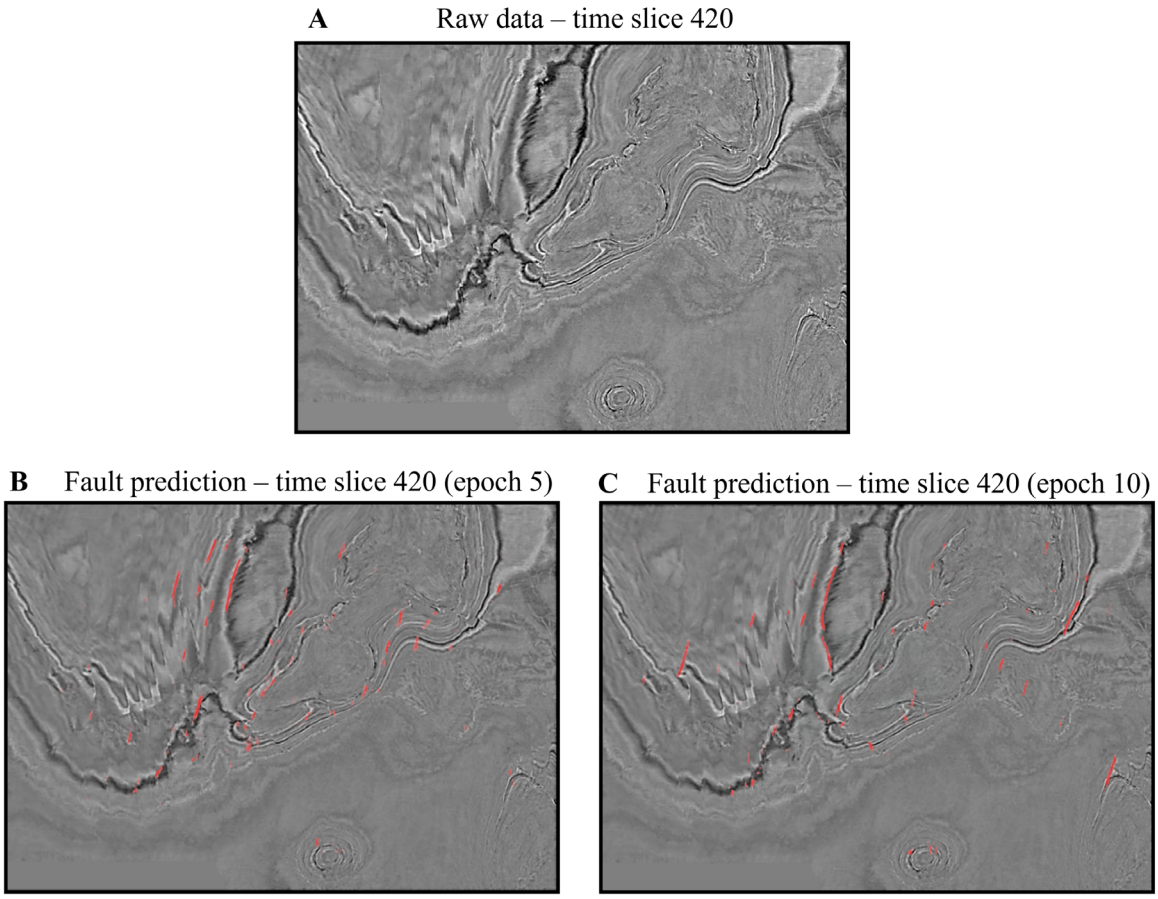

Figure 12. Results of fault prediction at time slice 420: (A) Input data (uninterpreted), (B) epoch 5, and (C) epoch 10

with sparse forecasts. The model focuses on critical traits, reducing false positives and scattered noise. The 24,000 patch model has slightly more expected flaws (Figure 16). Additional minor characteristics have been found, but continuity and alignment are no better than with the 12,000-patch scenario. The 48,000 patch model predicts a wider spread, especially in low-contrast locations (Figure 17). However, this increases visual clutter by creating more disconnected fault segments that do not correspond with seismic structures. According to earlier quantitative data, training accuracy improved, but validation loss rose, suggesting overfitting.

Figure 18A shows that the 12,000-patch model predicts fault lines that are confined and focused along major reflector terminations and structural boundaries. Highlighting only the most significant and geologically relevant discontinuities, the model shows restraint. This generates a low-noise, high-precision output that matches the seismic backdrop. The 24,000 patch model (Figure 18B) predicts more fault segments in more nuanced locations. Some forecasts are accurate, but others look inconsistent with seismic texture, indicating overprediction. The model becomes more sensitive but loses selectivity. The density of anticipated fault segments increases in the 48,000-patch model (Figure 18C). Many marked regions no longer match geological discontinuities. Essential faults are still found, but the findings are noisier, resulting in more isolated predictions and misinterpretations of non-fault reflectors. This suggests that the model is over-adapting to tiny training data properties that do not apply to new situations. Validation loss increased with performance, suggesting overfitting.

4. Discussion

This research validates the effectiveness of CNNs, particularly the U-Net architecture, in identifying 3D seismic faults. Labelled seismic inlines assisted the model's identification of fault structures in space, proving its ability to recognize geologic discontinuities. The tests involved a comprehensive assessment of model training

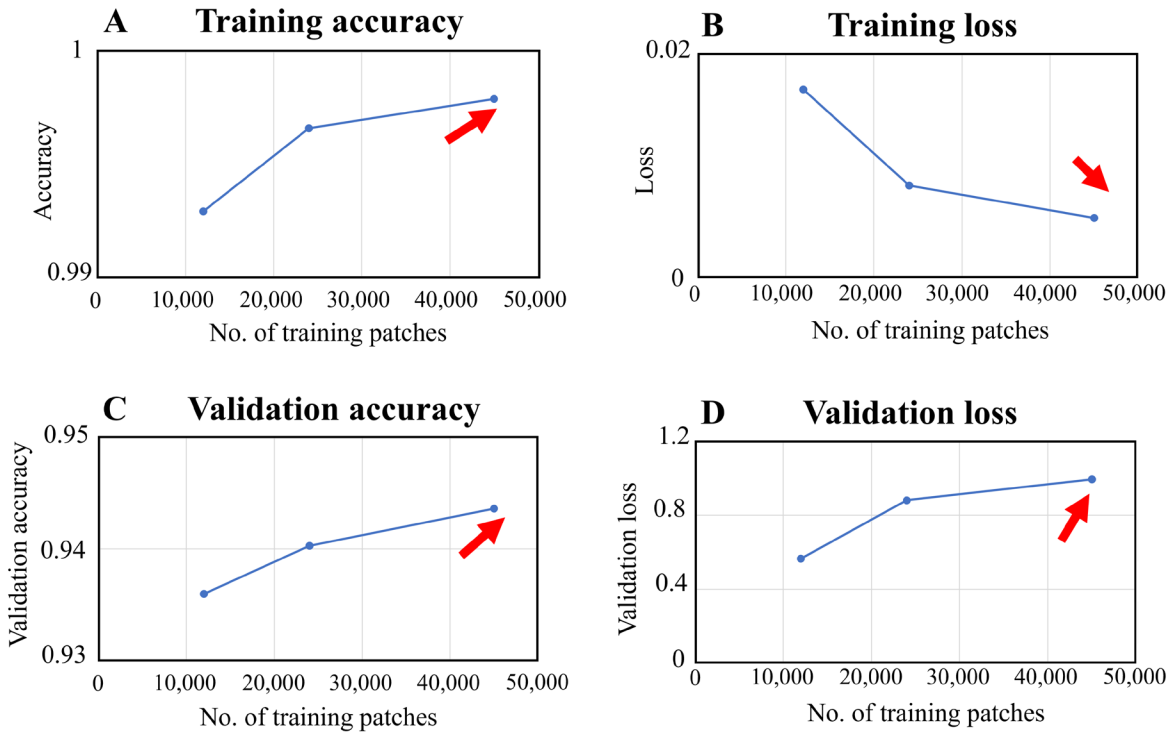

Figure 13. Graphs depicting training and validation accuracy and loss for 12K, 24K, and 48K training patches at epoch 12: (A) Training accuracy, (B) training Loss, (C) validation precision, and (D) validation error

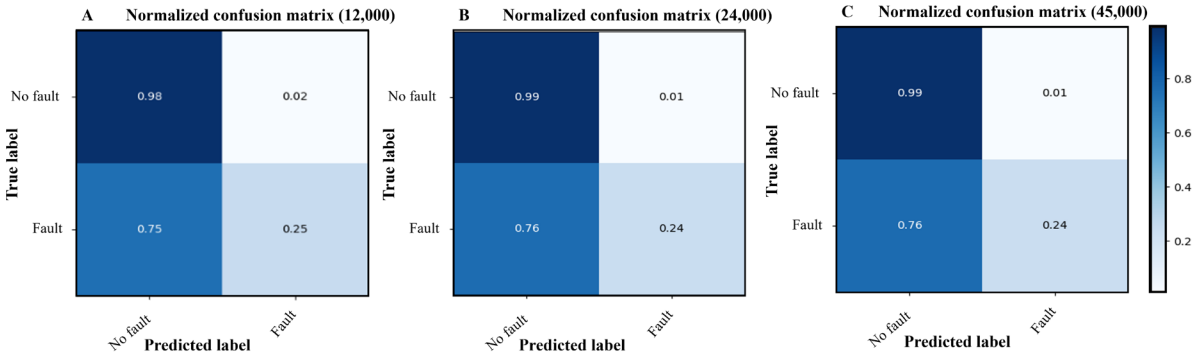

Figure 14. Normalized confusion matrices for (A) 12K, (B) 24K, and (C) 48K training patches at epoch 12

and performance. The implementation of multiple training epochs resulted in a significant impact. The curves for training and validation accuracy showed initial improvements in model learning but reached an average and began to diverge around the tenth epoch. The training accuracy continued to grow up to this threshold; however, the validation accuracy reached a peak while the validation loss exhibited an increasing trend. This pattern indicates overfitting, where the model becomes excessively developed for the training data and is unable to generalize. Therefore, epoch 12 represented the optimal balance between training performance and generalization.

We also considered training patch volume and observed that increased patches from 12,000 to 48,000 improved training data fit but not validation metrics. More patches increased validation loss, and fault prediction overlays had more noise and false positives at higher volumes. In imbalanced datasets with non-fault pixels, adding data may enhance noise patterns or non-essential features above a threshold. The algorithm trained with 12,000 patches consistently made clearer, geologically interpretable predictions. This shows that moderately well-

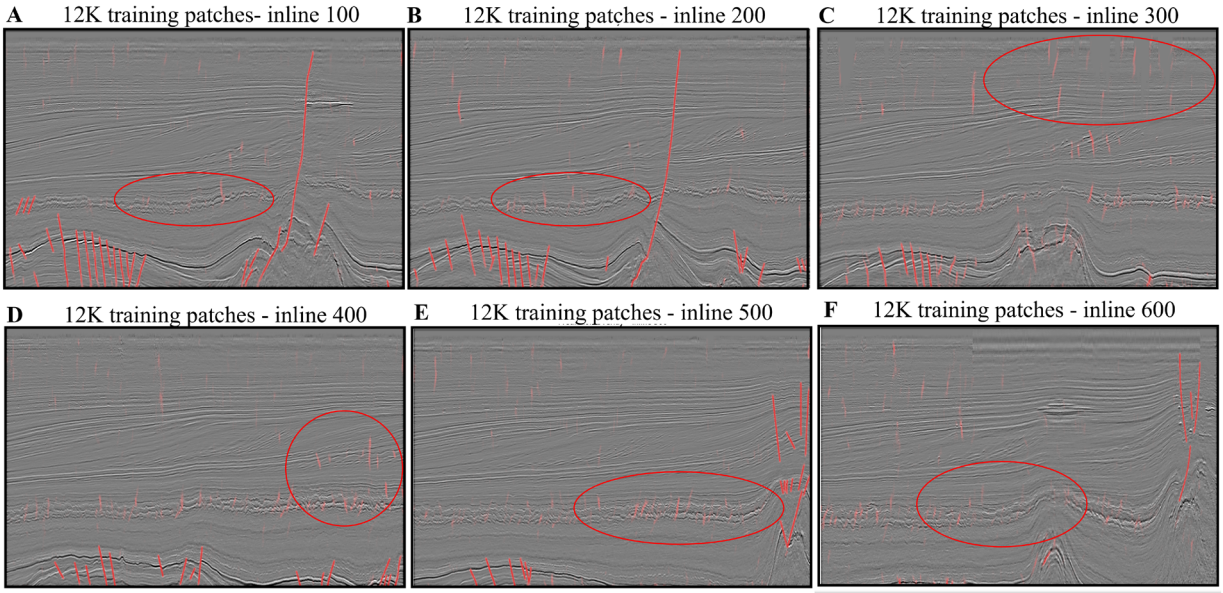

Figure 15. Fault prediction was conducted for 12,000 training patches at epoch 12 on the inline seismic section for line numbers (A) 100, (B) 200, (C) 300, (D) 400, (E) 500, and (F) 600

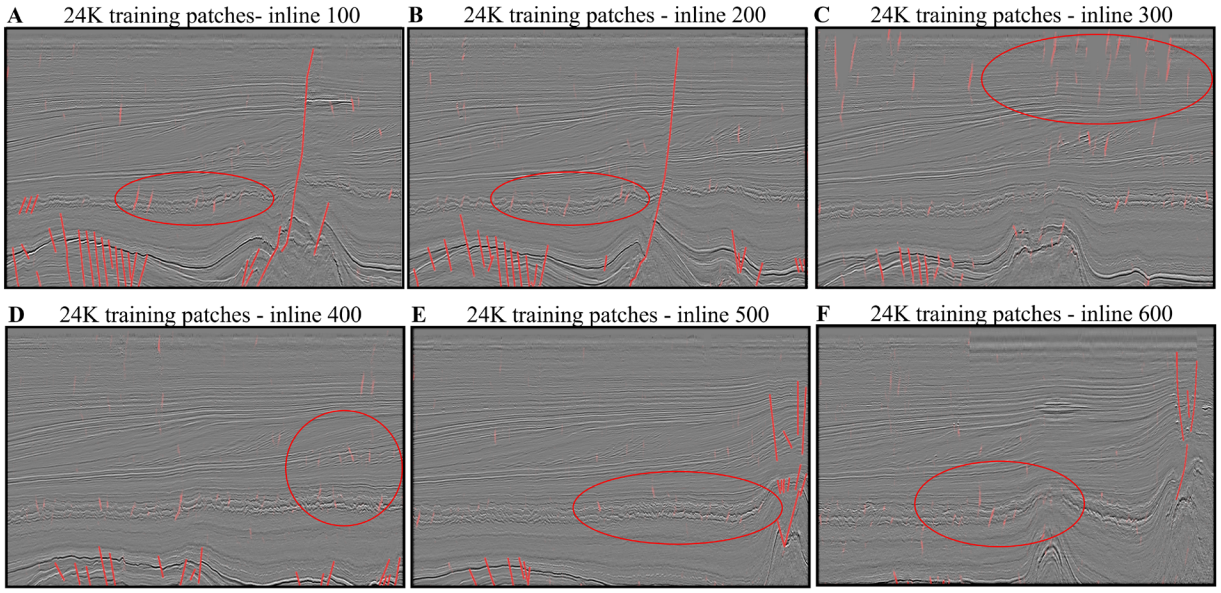

Figure 16. Fault prediction results for 24,000 training patches at epoch 12 on the Inline seismic section line numbers (A) 100, (B) 200, (C) 300, (D) 400, (E) 500, and (F) 600

prepared data is more beneficial than excessive volume. Confusion matrices supported the findings. All models had high classification performance for the dominating non-fault class, but fault pixel identification did not improve with more training data. Fault true positive rates leveled at 24–25%, indicating that minority characteristics in imbalanced datasets are challenging to categorize. The findings suggest that future research should consider class-weighting or loss function adjustments.

The model's performance was evaluated by predicting a time-slice part that was not used during training of the model. The model trained with 12,000 patches produced the most structurally consistent and interpretable outputs.

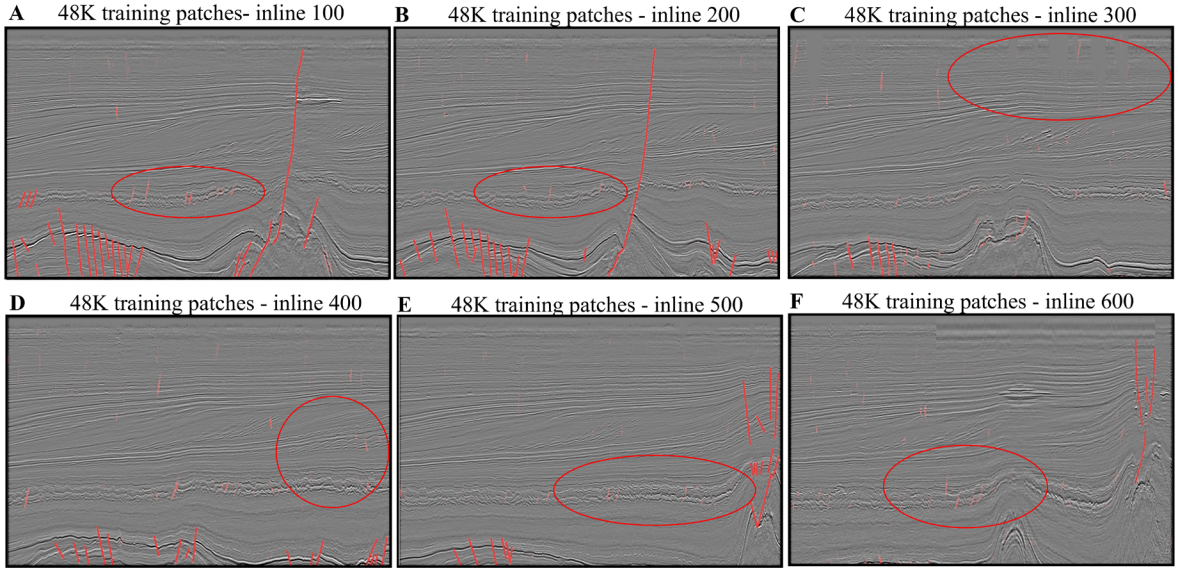

Figure 17. Fault prediction results for 48,000 training patches at epoch 12 on inline seismic section line numbers (A) 100, (B) 200, (C) 300, (D) 400, (E) 500, and (F) 600

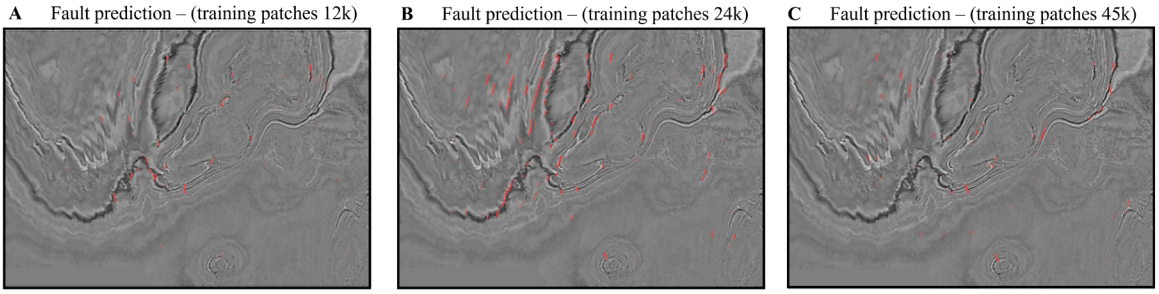

Figure 18. Prediction overlays at time slice 420 for (A) 12K, (B) 24K, and (C) 48K training patches at epoch 12

Models with 24,000 and 48,000 patches produced larger, noisier fault networks, indicating less geological alignment. This supports the earlier finding that increased patch volume sensitivity may weaken precision without regularization or validation-guided training. The findings show that deep learning's seismic interpretation performance is not solely dependent on model complexity or dataset quantity, but also on the dependable, interpretable, and generalizable results; parameter selection, data preparation, and validation must be done carefully. The findings indicate that deep learning has the capability to identify faults; however, there is a necessity for methodological enhancements.

5. Conclusion

U-Net, a CNN developed and implemented for seismic fault detection. A carefully constructed training procedure using 3D seismic data assesses the model's effectiveness in identifying fault structures within 3D seismic data. The research's final results are listed below:

- A patch-based CNN approach for detecting seismic faults using 64 × 64 picture segments was demonstrated, enabling efficient training with limited resources. 12,000 patches of training data yield optimal generalization, resulting in more accurate fault predictions than bigger datasets.
- Excessive training data volume leads to overfitting and decreased prediction quality, emphasizing the importance of data balance over quantity. Training accuracy improved, but class imbalance remained, with true positive fault detection stabilizing at 24–25%.
- The conventional binary cross-entropy loss proves insufficient for highly unbalanced seismic datasets, requiring a larger loss function or data sampling methods. The model effectively picked faults on unlabeled seismic time-slices, proving the developed model's ability.

The research demonstrates that deep learning techniques serve as an effective tool for automated seismic interpretation. The results validate the use of a U-Net architecture for fault detection and define a systematic approach for integrating CNN-based models into geophysical analysis. Conclusions emphasize essential components for upcoming applications, including the impact of data volume, class imbalance, and overfitting, which must be considered to ensure accuracy and reliability in structural interpretation.

Acknowledgments

The authors would like to thank Geophysical Engineering at Istanbul Technical University for providing the facilities used in this research. This research is associated with the ITU DAP project (Code: TDA-2023-44996).

Funding

None.

Conflict of interest

The authors declare that they have no competing interests, financial or non-financial, that could have appeared to influence the work reported in this paper. The authors also declare that there are no personal relationships, affiliations, funding-related conflicts, or institutional interests that could be perceived as influencing the publication of this study.

Author contributions

Conceptualization: Yasir Bashir, Dilek Yüksel, Begüm Akin, Derin Gezer
Formal analysis: Yasir Bashir, Dilek Yüksel, Begüm Akin, Derin Gezer, Muhammad Khan
Investigation: Yasir Bashir, Dilek Yüksel, Begüm Akin, Derin Gezer
Methodology: Yasir Bashir, Dilek Yüksel, Begüm Akin, Derin Gezer
Supervision: Yasir Bashir, Muhsan Ehsan, Muhammad Khan, Syed Haroon Ali
Validation: Yasir Bashir, Dilek Yüksel, Begüm Akin, Derin Gezer
Writing–original draft: Yasir Bashir, Dilek Yüksel, Begüm Akin, Derin Gezer
Writing–review & editing: Yasir Bashir, Muhsan Ehsan, Muhammad Khan, Syed Haroon Ali

Availability of data

Data are available from the corresponding author upon reasonable request, and the codes are available online at the GitHub repository.

Code availability section

Name of the code/library: CNN-fault-prediction
Contact: (Email) dryasir.bashir@live.com, ybashir@itu.edu.tr; (Phone) +905366224503
Hardware requirements: Intel(R) Xeon(R) CPU E5-2678 v3 @ 2.50 GHz and an NVIDIA GeForce GTX 1080 Ti GPU.
Program language: Python
Software required: Anaconda, Jupyter Notebook
Program size: 5 Gigabytes
The source codes are available for download at: https://github.com/dryasir/CNN-Fault-Prediction

References

1. Khosro Anjom F, Vaccarino F, Socco LV. Machine learning for seismic exploration: Where are we and how far are we from the holy grail? *Geophysics*. 2024;89(1):WA157-WA178.

   doi: 10.1190/geo2023-0129.1

2. Xiong W, Ji X, Ma Y, *et al*. Seismic fault detection with convolutional neural network. *Geophysics*. 2018;83(5):O97-O103.

   doi: 10.1190/geo2017-0666.1

3. Babikir I, Elsaadany M. Machine learning-based seismic characterization of deepwater turbidites in the Dangerous Grounds area, Northwest Sabah, offshore Malaysia. *Acta Geophys*. 2024;73(1):379-391.

   doi: 10.1007/s11600-024-01396-2

4. Bashir Y, Khan M, Mahgoub M, *et al*. Machine Learning Application on Seismic Diffraction Detection and Preservation for High Resolution Imaging. In: *International Petroleum Technology Conference*. IPTC; 2024:IPTC-23668.

   doi: 10.2523/IPTC-23668-EA

5. Ismail A, Radwan AA, Leila M, Abdelmaksoud A, Ali M. Unsupervised machine learning and multi-seismic attributes for fault and fracture network interpretation in the Kerry Field, Taranaki Basin, New Zealand. *Geomech Geophys Geo-Energy Geo-Resour*. 2023;9(1).

   doi: 10.1007/s40948-023-00646-9

6. Khan M, Bery AA, Bashir Y, Sharoni SMH, Ali SS. Automated Fault Network Extraction in Complex Tectonic Regimes: A Hybrid Machine Learning and Structural Attributes Approach. *Appl Comput Geosci*. 2025;27:100264.

   doi: 10.1016/j.acags.2025.100264

7. Wu X, Shi Y, Fomel S, Liang L. Convolutional neural networks for fault interpretation in seismic images. In: *SEG Technical Program Expanded Abstracts 2018*. Tulsa, OK: Society of Exploration Geophysicists; 2018:1946-1950.

   doi: 10.1190/segam2018-2995341.1

8. Guo Y, Peng S, Du W, Li D. Fault and horizon automatic

interpretation by CNN: A case study of coalfield. *J Geophys Eng*. 2020;17(6):1016-1025.

doi: 10.1093/jge/gxaa060

9. Owusu BA, Boateng CD, Asare VDS, Danuor SK, Adenutsi CD, Quaye JA. Seismic facies analysis using machine learning techniques: a review and case study. *Earth Sci Inform*. 2024;17(5):3899-3924.

doi: 10.1007/s12145-024-01395-3

10. Zhao T, Jayaram V, Roy A, Marfurt KJ. A comparison of classification techniques for seismic facies recognition. *Interpretation*. 2015;3(4):SAE29-SAE58.

doi: 10.1190/INT-2015-0044.1

11. Imran QS, Siddiqui NA, Latiff AHA, *et al*. Automated fault detection and extraction under gas chimneys using hybrid discontinuity attributes. *Appl Sci*. 2021;11(16):7218.

doi: 10.3390/app11167218

12. Khan M, Bery AA, Bashir Y, Sharoni SMH, Gnapragasan J, Imran QS. Optimizing petrophysical property prediction in fluvial-deltaic reservoirs: a multi-seismic attribute transformation and probabilistic neural network approach. *J Pet Explor Prod Technol*. 2025;15(2):29.

doi: 10.1007/s13202-024-01912-6

13. Kamsari M, Sadeghi S, de Oliveira GG, *et al*. The role of data augmentation and attention mechanisms in UNet and ConvNeXt architectures for optimizing breast tumor segmentation. *Sci Rep*. 2025;15:45268.

doi: 10.1038/s41598-025-29841-2

14. Anari S, Ranjbarzadeh R, Cunneen M, Bendechache M. Privacy-Preserving Federated Learning for Human Intention Modeling in Pediatric Cerebral Palsy Using Extended Reality. In: *2025 IEEE 49th Annual Computers, Software, and Applications Conference (COMPSAC)*. IEEE; 2025:1-6.

doi: 10.1109/COMPSAC65507.2025.00209

15. Ranjbarzadeh R, Anari S, Cunneen M, Bendechache M. Lightweight Deep Learning with Virtual Reality Visualization for Offline Tumor Segmentation in Rural Environments. In: *2025 IEEE 49th Annual Computers, Software, and Applications Conference (COMPSAC)*. IEEE; 2025:1577-1582.

doi: 10.1109/COMPSAC65507.2025.00211

16. Bagherian Kasgari A, Sadeghi S, Zarbakhsh P, Jafarzadeh Ghoushchi S, Ranjbarzadeh R. A spiking convolutional neural network for glioma brain tumor segmentation using a spike-timing-dependent plasticity method. *Neurocomputing*. 2026;660:131903.

doi: 10.1016/j.neucom.2025.131903

17. Zeng A, Yan L, Huang Y, Ren E, Liu T, Zhang H. Intelligent detection of small faults using a support vector machine. *Energies*. 2021;14(19):6242.

doi: 10.3390/en14196242

18. Bashir Y, Babasafari AA, Alashloo SYM, Muztaza NM, Ali SH, Imran QS. Seismic wave propagation characteristics using conventional and advance modelling algorithm for d-data imaging. *J Seism Explor*. 2021;30:21-44.

19. Zhao T, Chen G, Pang C, *et al*. Hybrid convolutional neural network–graph attention network–gradient boosting decision tree model for seismic impedance inversion prediction. *J Seism Explor*. 2025;34(5):81-98.

doi: 10.36922/JSE025310051

20. Pang C, Zhao T, Chen G, *et al*. Earthquake and blast recognition based on CEEMDAN multiscale fuzzy entropy and NSGAIII optimized 1D-CNN neural networks. *J Seism Explor*. 2025;34(1):22-42.

doi: 10.36922/JSE025260029

21. An Y, Guo J, Ye Q, Childs C, Walsh J, Dong R. Deep convolutional neural network for automatic fault recognition from 3D seismic datasets. *Comput Geosci*. 2021;153:104776.

doi: 10.1016/j.cageo.2021.104776

22. Ter Borgh MM, Jaarsma B, Rosendaal EA. Structural development of the northern Dutch offshore: Paleozoic to present. In: *Geological Society, London, Special Publications*. Vol 471. London, UK: Geological Society; 2019:115-131.

doi: 10.1144/SP471.4

23. Lima G, Zeiser FA, Da Silveira A, Rigo S, de Oliveira Ramos G. An encoder–decoder deep neural network for binary segmentation of seismic facies. *Comput Geosci*. 2024;183:105507.

doi: 10.1016/j.cageo.2023.105507

24. Waldeland AU, Jensen AC, Gelius LJ, Solberg AHS. Convolutional neural networks for automated seismic interpretation. *Leading Edge*. 2018;37(7):529-537.

doi: 10.1190/tle37070529.1

25. Wei XL, Zhang CX, Kim SW, *et al*. Seismic fault detection using convolutional neural networks with focal loss. *Comput Geosci*. 2022;158:104968.

doi: 10.1016/j.cageo.2021.104968

26. Jozinović D, Lomax A, Štajduhar I, Michelini A. Rapid prediction of earthquake ground shaking intensity using raw waveform data and a convolutional neural network. *Geophys J Int*. 2020;222(2):1379-1389.

doi: 10.1093/gji/ggaa233

ACCSCIENCE PUBLISHING

OUR JOURNALS

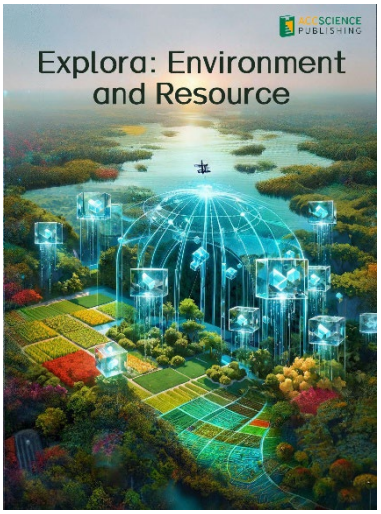

Explora: Environment and Resource (EER) is an international and multidisciplinary journal covering all aspects of the environmental impacts of socio-economic development. It is concerned with the complex interactions among society, development, and the environment, aiming to explore ways and means of achieving sustainability in all human activities related to development.

EER covers subject areas, including but not limited to the following:

- Water reclamation, wastewater treatment and waste management for eco-environment sustainability
- Innovative nanotechnology, catalysis, photocatalysis and nano materials for decontamination practices and renewable energy resources.
- Climate change-related sustainable resource and environment quality analysis
- Microorganisms and plants-oriented low-carbon processes and strategies for clean energy, water and resource management

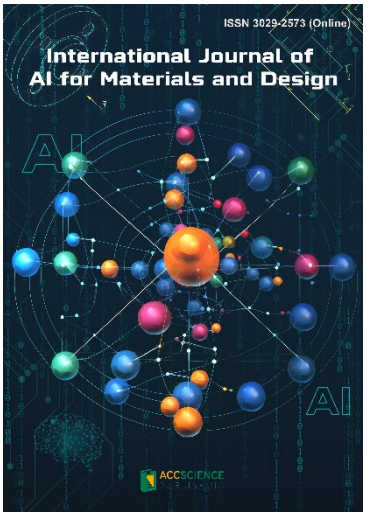

International Journal of AI for Materials and Design is an international, peer-reviewed open-access journal that aims to bridge the cutting-edge research between AI and materials, AI and design. In recent years, the tremendous progress in AI is leading a radical shift of AI research from a mainly academic endeavor to a much broader field with increasing industrial and governmental investments. The maturation of AI technology brings about a step change in the scientific research of various domains, especially in the world of materials and design. Machine learning (ML) algorithms enable researchers to analyze extensive datasets on material properties and accurately predict their behavior in different conditions. This subsequently impact the industry to leverage on big data and advanced analytics to build scientific strategies, scale operational performance of processes and drive innovation. In addition, AI and ML are uniquely positioned to enable advanced manufacturing technologies across the value chain of different industries. Integration of multiple and complementary AI techniques, such as ML, search, reasoning, planning, and knowledge representation, will further accelerate advances in scientific discoveries, engineering excellence and the future of cyber-physical systems manufacturing.

International Journal of AI for Materials and Design covers the following topics: AI or machine learning for material discovery, AI for process optimization, AI and data-driven approaches for product or systems design, application of AI in advanced manufacturing processes such as additive manufacturing, IoT, sensors, robotics, cloud-based manufacturing, intelligent manufacturing for various applications, autonomous experiments, material intelligence, energy intelligence, and AI-linked decarbonization technologies.

Start a new journal

Write to us via email if you are interested to start a new journal with AccScience Publishing. Please attach your CV, professional profile page and a brief pitch proposal in your email. We shall inform you of our decision whether we are interested to collaborate in starting a new journal.

Contact: info@accscience.com

https://accscience.com/journal/JSE

ACCSCIENCE PUBLISHING

Access Science Without Barriers

Contact

www.accscience.com
2 Venture Drive, #07-06 Vision Exchange, Singapore 608526
E-mail: editorial@accscience.com
Phone: +65 6348 3650